remote sensing

Special Issue Reprint

Planetary Geologic Mapping and Remote Sensing (Second Edition)

Edited by
Kaichang Di, Long Xiao and Jan-Peter Muller

mdpi.com/journal/remotesensing

MDPI

Planetary Geologic Mapping and Remote Sensing (Second Edition)

Planetary Geologic Mapping and Remote Sensing (Second Edition)

Guest Editors

Kaichang Di
Long Xiao
Jan-Peter Muller

MDPI

Basel • Beijing • Wuhan • Barcelona • Belgrade • Novi Sad • Cluj • Manchester

Guest Editors

Kaichang Di
State Key Laboratory of
Remote Sensing and
Digital Earth
Chinese Academy of Sciences
Beijing
China

Long Xiao
School of Earth Sciences
China University
of Geosciences
Wuhan
China

Jan-Peter Muller
Department of Space &
Climate Physics
University College
London (UCL)
Holmbury St Mary
UK

Editorial Office
MDPI AG
Grosspeteranlage 5
4052 Basel, Switzerland

This is a reprint of the Special Issue, published open access by the journal *Remote Sensing* (ISSN 2072-4292), freely accessible at: https://www.mdpi.com/journal/remotesensing/special_issues/V96W1X7FD4.

For citation purposes, cite each article independently as indicated on the article page online and as indicated below:

Lastname, A.A.; Lastname, B.B. Article Title. *Journal Name* **Year**, *Volume Number*, Page Range.

ISBN 978-3-7258-7853-6 (Hbk)
ISBN 978-3-7258-7854-3 (PDF)
https://doi.org/10.3390/books978-3-7258-7854-3

© 2026 by the authors. Articles in this reprint are Open Access and distributed under the Creative Commons Attribution (CC BY) license. The reprint as a whole is distributed by MDPI under the terms and conditions of the Creative Commons Attribution-NonCommercial-NoDerivs (CC BY-NC-ND) license (https://creativecommons.org/licenses/by-nc-nd/4.0/).

Contents

About the Editors . . . . . **vii**

Yexin Wang, Jing Nan, Chenxu Zhao, Bin Xie, Sheng Gou, Zongyu Yue, et al.
A Catalogue of Impact Craters and Surface Age Analysis in the Chang'e-6 Landing Area
Reprinted from: *Remote Sens.* **2024**, *16*, 2014, https://doi.org/10.3390/rs16112014 . . . . . **1**

Naihuan Zheng, Chunyu Ding, Yan Su and Roberto Orosei
Water Ice Resources on the Shallow Subsurface of Mars: Indications to Rover-Mounted Radar Observation
Reprinted from: *Remote Sens.* **2024**, *16*, 824, https://doi.org/10.3390/rs16050824 . . . . . **15**

Fei He, Zhaojin Rong, Zhaopeng Wu, Jiawei Gao, Kai Fan, Xu Zhou, et al.
Martian Dust Storms: Reviews and Perspective for the Tianwen-3 Mars Sample Return Mission
Reprinted from: *Remote Sens.* **2024**, *16*, 2613, https://doi.org/10.3390/rs16142613 . . . . . **46**

Yaqi Zhao and Hongxia Ye
Crater Detection and Population Statistics in Tianwen-1 Landing Area Based on Segment Anything Model (SAM)
Reprinted from: *Remote Sens.* **2024**, *16*, 1743, https://doi.org/10.3390/rs16101743 . . . . . **72**

Shuangshuang Wu, Jianping Chen, Chenli Xue, Yiwen Pan and Cheng Zhang
Global Inversion of Lunar Surface Oxides by Adding Chang'e-5 Samples
Reprinted from: *Remote Sens.* **2024**, *16*, 1812, https://doi.org/10.3390/rs16101812 . . . . . **92**

Xinyu Ma, Meixi Chen, Teng Hu, Zhizhong Kang and Meng Xiao
Study on the Degradation Pattern of Impact Crater Populations in Yutu-2's Rovering Area
Reprinted from: *Remote Sens.* **2024**, *16*, 2356, https://doi.org/10.3390/rs16132356 . . . . . **109**

Xinbao Liu, Ming Jin, Xiangnan Liu, Zhiming Yang, Zengqian Hou and Xiaozhong Ding
Quantitative Inversion of Martian Hydrous Minerals Based on LSTM-1DCNN Model
Reprinted from: *Remote Sens.* **2024**, *17*, 94, https://doi.org/10.3390/rs17010094 . . . . . **128**

Hengxi Liu, Yongzhi Wang, Shibo Wen, Sheng Zhang, Kai Zhu and Jianzhong Liu
Comprehensive Evaluation of the Lunar South Pole Landing Sites Using Self-Organizing Maps for Scientific and Engineering Purposes
Reprinted from: *Remote Sens.* **2025**, *17*, 1579, https://doi.org/10.3390/rs17091579 . . . . . **149**

Yan Zhou, Yu-Yan Sara Zhao, Xiaoting Xu and Yiran Wang
Characteristics and Climatic Indications of Ice-Related Landforms at Low Latitudes (0°–±30°) on Mars
Reprinted from: *Remote Sens.* **2025**, *17*, 1939, https://doi.org/10.3390/rs17111939 . . . . . **185**

Tianhao Chen, Yexin Wang, Jing Nan, Chenxu Zhao, Biao Wang, Bin Xie, et al.
A Generative Adversarial Network for Pixel-Scale Lunar DEM Generation from Single High-Resolution Image and Low-Resolution DEM Based on Terrain Self-Similarity Constraint
Reprinted from: *Remote Sens.* **2025**, *17*, 3097, https://doi.org/10.3390/rs17173097 . . . . . **217**

About the Editors

Kaichang Di

Kaichang Di is a Professor at Aerospace Information Research Institute, Chinese Academy of Sciences, Beijing, China, where he is also the founding director of the Planetary Mapping and Remote Sensing Lab (PMRS Lab) at the institute. He was the chair of Inter-Commission Working Group III/II "Planetary Remote Sensing and Mapping" of International Society for Photogrammetry and Remote Sensing from 2016 to 2022. His research interests include planetary photogrammetry and remote sensing, visual localization and navigation, and planetary science. He is a core member of the scientific research teams for Chang'e-3 and Chang'e-4 lunar missions and Tianwen-1 Mars mission, and a member landing site selection working group for China's crewed lunar exploration. He led the PMRS Lab and developed technologies and software of high-precision topographic mapping and visual localization, which have been operationally applied to the Chang'e-3, 4, 5, 6, and Tianwen-1 missions, and greatly contributed to landing site mapping and evaluation, lander localization, rover localization and navigation in these missions. He has also made a series of research achievements in lunar control network and global mapping, lunar and Mars target recognition, topographic and geomorphologic analysis, mineral inversion, and geological evolution. He has authored 2 academic books, 196 academic journal papers, and 128 conference papers. His achievements have been recognized through more than ten international and national awards.

Long Xiao

Long Xiao is a distinguished professor at the China University of Geosciences (Wuhan), a leading scholar in planetary geology, and the chief editor of the Planetary Geology textbook for the national "101 Plan". His research focuses on planetary volcanism, lunar and Martian geological evolution, impact processes, and terrestrial analogs for planetary exploration, with core contributions to deep space exploration missions including China's Chang'E and Tianwen projects.

He has led and participated in groundbreaking studies on young lunar mare volcanism, Martian sedimentary and volcanic features, and lunar soil geochemistry, publishing over 200 high-impact papers in top journals such as *Science*, *Nature Astronomy*, *Nature Geoscience*, and *Geology*. His work on Chang'E-3/4/5/6 lunar mission data and Zhurong rover's Martian observations has advanced the understanding of lunar thermal evolution and Martian paleoenvironment.

He has authored/edited 6 academic books and textbooks including Mars on Earth: A study of the Qaidam Basin and Planetary Geology, and his popular science work Unveiling Mars won the Outstanding Popular Science Work Award of Hubei Province. As a PI, he leads key national research projects, and his team has identified critical planetary analog sites (e.g., Qaidam Basin) and provided scientific support for lunar and Martian landing site selection. His research bridges planetary geoscience research and deep space exploration engineering, making pivotal contributions to China's planetary science development and national deep space exploration strategy.

Jan-Peter Muller

Jan-Peter Muller is an emeritus professor of image understanding and remote sensing at University College London's Mullard Space Science Laboratory in the Department of Space and Climate Physics. His research focuses on the development of 3D retrieval methods including digital stereo photogrammetry using computer vision in the 1980's, stereo and interferometric SAR in the 1990's, application of stereo to operational retrieval of cloud-top height and motion from the NASA

MISR (Multi-angle Imaging SpectroRadiometer) and DTMs of the ESA Mars Express HRSC (High Resolution Stereo Camera) in the 2000's, MAISR (multi-angle Image Super Resolution) applied to long time sequences of NASA HiRSE and SIHE (Single Image Height Estimates) and SISR (Single Image Super Resolution) combined together to provide sub-pixel Super-3D of Martian and Lunar surfaces. He was an Associate science team member of the NASA Mars Science Laboratory, Curiosity, the ESA Rosland Franklin ExoMars2032 rover PanCam team and has worked for JPL to build SIHE models of the von Karman crater (where Chang'e-4 rover operated) as well as 7/13 of the ARTEMIS landing sites. He is author of over 200 peer review papers and editor of 2 books and contributor to 6 other books. He was former chair of the UK government Aurora Advisory Committee that helped rescue the ExoMars mission after NASA pulled out and is a PIFI fellow at the Chinese Academy of Sciences Centre for Big Data and Sustainable Development (CBAS) centre in Beijing, currently working on the development of a telescopic imaging system based on the Moon for observation of the terrestrial atmosphere.

remote sensing

MDPI

Technical Note

A Catalogue of Impact Craters and Surface Age Analysis in the Chang'e-6 Landing Area

Yexin Wang [1], Jing Nan [1,2], Chenxu Zhao [1,2], Bin Xie [1,2], Sheng Gou [3], Zongyu Yue [3,4], Kaichang Di [1,4,*], Hong Zhang [5], Xiangjin Deng [5] and Shujuan Sun [1,6]

[1] State Key Laboratory of Remote Sensing Science, Aerospace Information Research Institute, Chinese Academy of Sciences, Beijing 100101, China; wangyx@aircas.ac.cn (Y.W.); nanjing23@mails.ucas.ac.cn (J.N.); zhaochenxu22@mails.ucas.ac.cn (C.Z.); xiebin21@mails.ucas.ac.cn (B.X.); sunshujuan@cdu.edu.cn (S.S.)
[2] University of Chinese Academy of Sciences, Beijing 100101, China
[3] Key Laboratory of Earth and Planetary Physics, Institute of Geology and Geophysics, Chinese Academy of Sciences, Beijing 100029, China; gousheng@mail.iggcas.ac.cn (S.G.); yuezy@mail.iggcas.ac.cn (Z.Y.)
[4] Center for Excellence in Comparative Planetology, Chinese Academy of Sciences, Hefei 230026, China
[5] Beijing Institute of Spacecraft System Engineering, China Academy of Space Technology, Beijing 100094, China; dengxiangjin@sina.com (X.D.)
[6] School of Architecture and Civil Engineering, Chengdu University, Chengdu 610106, China
* Correspondence: dikc@aircas.ac.cn

Abstract: Chang'e-6 (CE-6) is the first sample-return mission from the lunar farside and will be launched in May of 2024. The landing area is in the south of the Apollo basin, inside the South Pole Aitken basin. Statistics and analyses of impact craters in the landing area are essential to support safe landing and geologic studies. In particular, the crater size–frequency distribution information of the landing area is critical to understanding the provenance of the CE-6 lunar samples to be returned and can be used to verify and refine the lunar chronology model by combining with the radioisotope ages of the relevant samples. In this research, a digital orthophoto map (DOM) mosaic with a resolution of 3 m/pixel of the CE-6 landing area was generated from the 743 Narrow Angle Camera of the Lunar Reconnaissance Orbiter Camera. Based on the DOM, craters were extracted by an automated method and checked manually. A total of 770,731 craters were extracted in the whole area of 246 km × 135 km, 374,684 of which were within the mare area. Systematic analyses of the crater distribution, completeness, spatial density, and depth-to-diameter ratio were conducted. Geologic model age estimation was carried out in the mare area that was divided into three geologic units according to the TiO_2 abundance. The result showed that the east part of the mare had the oldest model age of $\mu 3.27^{+0.036}_{-0.045}$ Ga, and the middle part of the mare had the youngest model age of $\mu 2.49^{+0.072}_{-0.073}$ Ga. The crater catalogue and the surface model age analysis results were used to support topographic and geologic analyses of the pre-selected landing area of the CE-6 mission before the launch and will contribute to further scientific research after the lunar samples are returned to Earth.

Keywords: Chang'e-6; landing area; crater catalogue; surface age; lunar farside

1. Introduction

Lunar samples have been returned to Earth by six Apollo missions (Apollo 11, 12, 14, 15, 16, and 17), three Luna missions (Luna 16, 20, and 24), and the Chang'e-5 mission. The analysis results of these samples are invaluable to our fundamental understanding of lunar origin and evolution [1–4]. Based on the lunar sample radiometric ages, the Moon also provides the foundation of crater size–frequency distribution chronologies for the solar system [5–8]. However, all of the samples were returned from the lunar nearside, and the samples from the farside, especially from the lunar South Pole Aitken (SPA) basin, are crucial to address other fundamental questions such as the nature of the Moon's asymmetry, the composition and structure of the lunar mantle, etc. The Chang'e-6 (CE-6) mission is

scheduled to launch in May of 2024. The pre-selected landing area of CE-6 is in the south of the Apollo basin, a ~490 km diameter crater, within the SPA basin [9,10]. It is the first sample-return mission to the lunar farside and is expected to return the farside basalts.

Impact craters are one of the most prominent surface features of the lunar surface, and they are important in studying the subsurface structure of the Moon [11], tracing the sample source area [12], analyzing the impact flux of the meteorites [8], etc. For comprehensive studies of the impact craters, many global or regional crater catalogues have been established [13–16]. The completeness diameter of the current global crater databases is too large for the CE-6 landing area (e.g., 1 km in [13]) in carrying out scientific analysis on the lunar samples. Zeng et al. mapped 26,785 craters using the 7 m/pixel resolution Chang'e-2 (CE-2) digital orthophoto map (DOM) in the pre-selected CE-6 landing area [10]. However, their work mainly focused on studying the geologic background of the CE-6 landing area, with no particular analysis on the mapped craters such as the completeness diameter that would greatly hinder its further application. Therefore, a detailed study of the impact craters in the CE-6 landing area using higher-resolution images is still necessary.

In this research, we utilized a seamless DOM mosaic based on the Lunar Reconnaissance Orbiter Camera (LROC) Narrow Angle Camera (NAC) images and SLDEM2015 (a lunar digital elevation model generated by co-registration and combining SELENE TC digital elevation model with LRO laser altimetric data) [17], to obtain a crater catalogue in the pre-selected CE-6 landing area. The resolution of the mosaic was 3.0 m/pixel, and the original images were in suitable illumination conditions. As a result, a more reliable and accurate crater catalogue could be obtained. In addition, with the SLDEM2015, the depth of craters was also automatically measured. The obtained crater catalogue and the analysis results can contribute to the studying of the returned lunar samples and other important issues such as the lunar Late Heavy Bombardment. Combined with the radioisotope ages of the samples, the crater size–frequency distribution information can be used to verify and refine the lunar chronology model, which is of fundamental importance for lunar and planetary sciences.

2. Data and Methods

2.1. LROC NAC Images and SLDEM2015

A high-resolution DOM mosaic of the landing area was generated using 743 LROC NAC images as a base map to extract and measure craters in the CE-6 landing area (Figure 1). The LROC NAC images covered most of the lunar surface with a horizontal resolution of 0.5–2 m and were the highest-resolution orbiter images currently available in the pre-selected landing area [18]. A method for large-area DOM generation was proposed and used to produce the high-resolution orthophoto mosaic of the CE-5 landing area [19] and was also used in this research. According to this method, 743 NAC images were selected first, and the Planetary Data System (PDS) experiment data record (EDR) files of them were downloaded from the PDS Geosciences Node Lunar Orbital Data Explorer website. Next, the SPICE kernels were attached, and radiometric corrections were performed for each image using the Integrated System for Imagers and Spectrometers (ISIS) software (v7.2.0). The planar block adjustment was then utilized to improve the relative positional consistencies of the LROC NAC images of the sub-areas to subpixel level and simultaneously align the NAC images to the control source (SLDEM2015). Subsequently, TPS (Thin Plate Spline)-based image registration was used to reduce geometric inconsistencies between the adjacent sub-area DOM mosaics, ensuring that the final DOM was seamlessly mosaicked over the entire area. Finally, a geometrically seamless DOM mosaic was produced, covering 149°–160° west longitude and 39.7°–44.1° south latitude with a resolution of 3 m/pixel. The detailed mapping method can be found in [19].

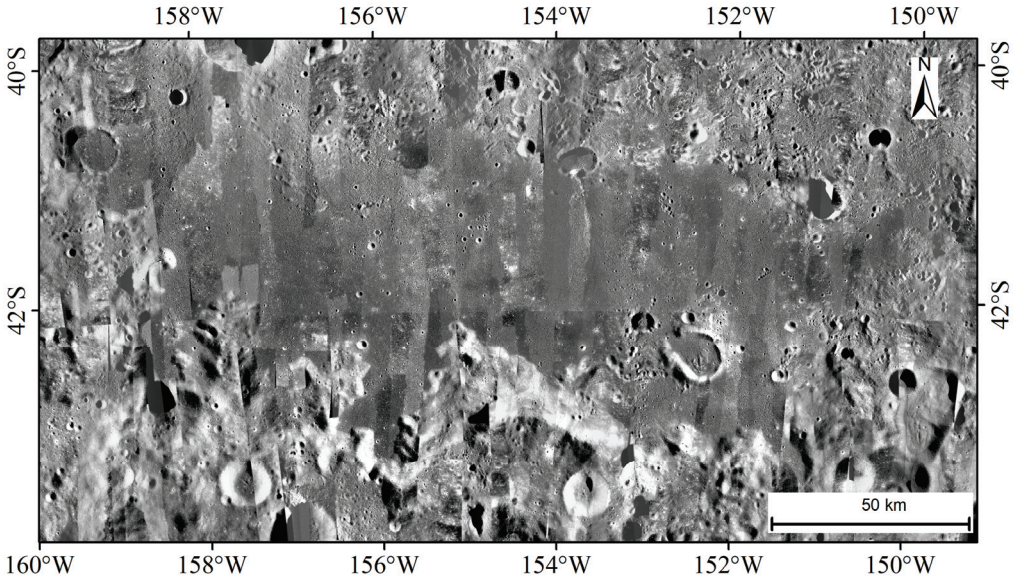


Figure 1. The base map of the CE-6 landing area generated from LROC NAC images with a pixel size of 3 m. The Lambert conformal conic projection was adopted.

SLDEM2015 covered latitudes within ±60° with a horizontal resolution of approximately 60 m in the equator area and a vertical accuracy of 3–4 m. It can be downloaded at the PDS LOLA data node (http://imbrium.mit.edu/EXTRAS/SLDEM2015/, accessed on 10 May 2023). In this research, SLDEM2015 provided the necessary elevation information when generating the DOM mosaic and measuring crater depths in the CE-6 landing area.

2.2. Crater Extraction and Mapping in CE-6 Landing Area

In this research, the impact craters within the CE-6 landing area were extracted using a deep-learning-based automated method followed by manual inspection. Our method was based on the YOLOv8 model (https://github.com/ultralytics/ultralytics, accessed on 15 June 2023), which combines object classification and localization in the same network, directly regressing the position and class information of the object in an end-to-end manner [20]. Our improved YOLOv8-LCNET (YOLOv8-lunar crater net) integrated more pyramid levels to extract craters with a wide range of diameter spans. Comparing with the former versions of YOLO, our improved YOLOv8-LCNET demonstrated higher recall rate in the lunar crater extraction task. As the focus of this paper was the analysis of the extracted craters of the landing area, the technical details of YOLOv8-LCNET will not be elaborated. A comparison of the performance of our improved method with the original method can be found in Appendix A. The training of the network and validation of the results are briefly described below.

Within the CE-6 landing area, a local mosaic DOM map with a resolution better than one meter was produced, based on which the crater sample dataset was established using the same approach of automatic extraction followed by manual inspection. The local DOM mosaic was cropped to sub images of 512 × 512 pixels to form the dataset, which contained 66,030 impact crater samples with a range in diameter from 3.7 m to 609 m. In addition, in order to improve the generalization of YOLOv8-LCNET, random data augmentation techniques such as flipping, rotation, adding noise, and image enhancement were applied to generate a dataset comprising 209,627 sample images. The dataset was split into training and validation datasets in the ratio of 8:2 for model training and performance evaluation.

To assess the rim accuracy of the impact craters automatically extracted by YOLOv8-LCNET, the diameters of the extracted craters and the manually confirmed true values were compared (Figure 2). As shown in Figure 2, an optimal straight line fitted from the scattering points plotted by the diameters automatically measured from the extracted craters and the true diameters had a slope of 1.034 and an intercept of 0.411 in meters. Additionally,

the mean relative error (MRE) of the diameters was calculated to be 0.1042 (i.e., 10.42% diameter difference). These findings indicated that the automatically extracted impact crater diameters were consistent with the true diameters. This consistency verified the agreement between automatic extraction and manual extraction methods, thus demonstrating that the YOLOv8-LCNET algorithm could replace most of the manual efforts in impact crater extraction. It is worth mentioning that for manual crater mapping, different workers would generate different results, with up to 10% diameter differences [21]. In this research, the approach of automatic crater extraction and manual checking proved to be practical and time-saving.

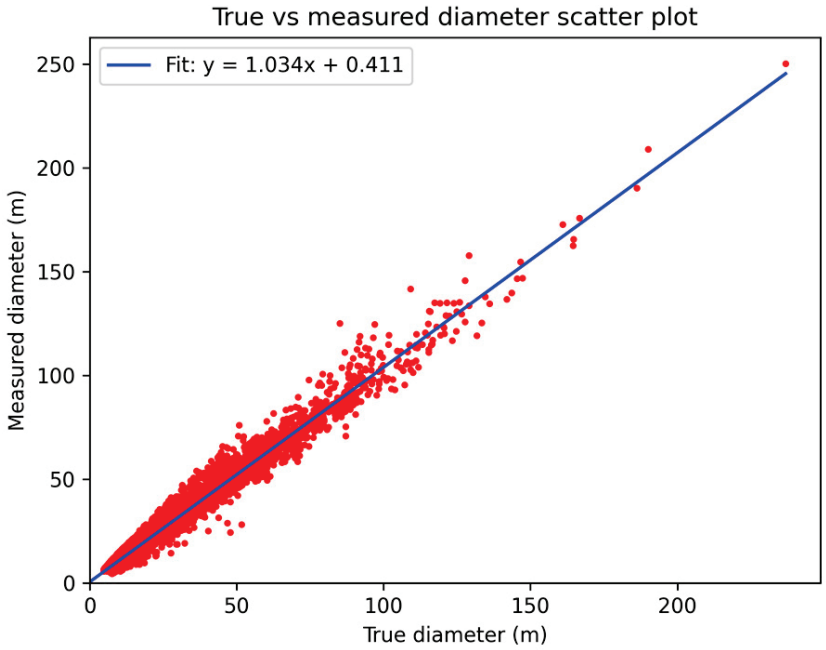


Figure 2. Comparison between the diameters automatically measured from extracted craters and diameters of the manually confirmed craters.

Note that the rims of the craters were first extracted and then transformed into local projection coordinate systems, ensuring that the crater measurements were not affected by map projection. After the automatic extraction by YOLOv8-LCNET, manual inspection work was conducted to erase some false detections and add missing detections from the DOM mosaic with an ArcGIS extension named "CraterTools" [22]. All crater extraction results were manually examined using this tool, especially for impact craters larger than 200 m for dating purposes. Due to significant differences in the solar azimuth and elevation angles of some images forming the DOM mosaic, the manual examination was mainly needed in regions with extreme solar elevation angles or where large craters were in two images with contrary azimuth angles.

To calculate the crater rim-to-floor depth, an automatic tool developed by [23] was utilized. For each crater, profiles crossing the crater center were generated every 22.5° to form a total number of 8. Then a local maximum of the topographic curvature in each profile was found within 10% of the diameter on both sides of the crater circle. The resultant 16 rim points were used to represent the crater rims in order to obtain an averaged rim-to-floor depth of the crater. Note that in some cases such as craters intersecting with other craters, the interfered rim points were eliminated automatically. If fewer than 6 rim points were left, manually added rim points were needed. More details about the automatic crater rim-to-floor tool can be found in [23]. As the resolution of SLDEM2015 constrained small crater rim-to-floor depth calculation, craters larger than 8 pixels were selected for this automatic depth measurement [15,24].

In order to carry out surface dating, secondary craters needed to be removed from the dataset. Based on the appearance of clusters and chains around a primary crater with ejecta patterns, secondary craters were recognized and removed manually.

2.3. Surface Dating with Craters

Absolute ages can provide vital information in establishing the geologic history of the Moon, and currently, the widely used surface dating method is based on the crater size–frequency distribution (CSFD). The method was elaborated by [5] and was the subject of many papers (e.g., [25,26]). The rationale of the method was to fit the observed CSFD of a counting area to a known crater production function (PF) (e.g., [27,28]), which was further used to derive the absolute age along with a chronology function (CF) calibrated to radiometric dating of the returned lunar samples [5]. The detailed steps of the method can be summarized as follows: (1) obtaining the CSFD of a counting area belonging to the same geologic unit, (2) comparing it with a known crater production function (PF) [27,28], and (3) deriving the absolute age according to a CF that has been calibrated to radiometric dating of the returned lunar samples [5]. In practical work, these calculations are often completed with the aid of CraterStats software (v2.0) [28].

The titanium dioxide (TiO_2) content of lunar mare basalt represents an important indicator in magma evolution and is widely used to classify lunar basalt types [29]. According to the TiO_2 abundance derived from LROC WAC imageries by [30] and the basalt classification schema [29], three areas (i.e., A1, A2, and A3) within the basalt unit [31] for the CE-6 potential landing and sampling region inside the Apollo basin were outlined for crater dating in this study (shown in Figure 3), with the TiO_2 abundances of them being $4.6 \pm 1.0\%$, $6.2 \pm 1.3\%$, and $3.8 \pm 0.8\%$, respectively.

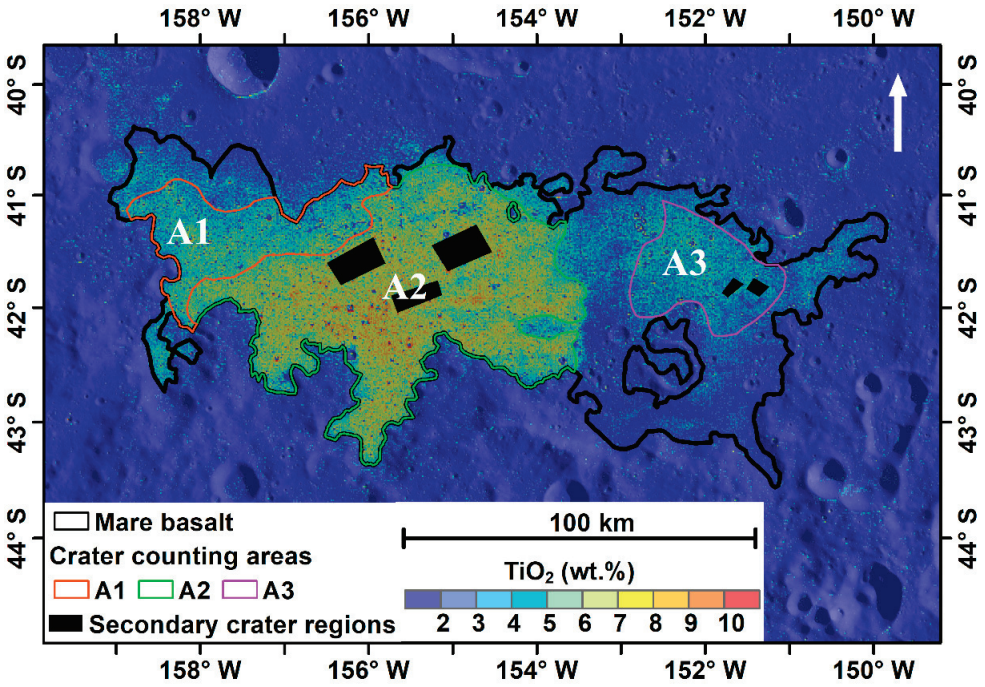


Figure 3. Crater dating areas (i.e., A1, A2, and A3) of the basalt inside the Apollo basin. The basemap is the TiO_2 abundance [30] overlying the LROC Wide Angle Camera global mosaic [32]. The black polygon is the mare extent defined by [31]. The red, green, and magenta polygons are the crater counting areas of A1, A2, and A3. The black patches inside A2 and A3 are regions excluded for counting due to contamination of secondary craters.

3. Results

3.1. Catalogue of Craters in CE-6 Landing Area

In this 246 km × 135 km landing area, a total number of 770,731 craters were extracted using the approach introduced in Section 2.2. According to the properties of the area surface, the whole area could be divided into mare and highland. The number of impact craters in the mare region is 374,684. The completeness diameter size for these craters was calculated within the mare area and is shown in Figure 4.

The completeness value of a crater dataset means that all the craters with diameters larger than this value are included [33]. Previous studies developed three different approaches of estimating the crater diameter completeness [33–35]. Salamunićcar et al. considered the completeness diameter as the inflection point of the slope in the cumulative CSFD curve of impact craters [34]. Robbins and Hynek adopted the value of the completeness diameter from the diameter of the bin one size larger than the bin with the highest number of impact craters in the incremental CSFD [35]. According to Robbins [33], the value was estimated by the Nth diameter bin larger than where the derivative of the slope was zero in an incremental CSFD.

Figure 4a,b illustrate the incremental and cumulative CSFD, respectively, of the craters in the mare area. In Figure 4a, the diameter of the crater cluster with the maximum number is approximately 25 m, yielding a completeness diameter of approximately 30 m according to the definition of Robbins and Hynek [35]. In Figure 4b, the inflection point of the slope is approximately 20 m. In Figure 4c, the value given by Robbins' method is approximately 170 m [33]. Robbins' value was larger compared with the other two, which may have been due to crater saturation equilibrium in the mare region. As the resolution of the mosaic map was 3 m/pixel, the completeness analysis result illustrated by Figure 4a,b indicates that the craters with diameters no less than 10 pixels were extracted. This dense crater catalogue can provide rich information for multiple applications such as landing safety evaluation, crater formation mechanisms, and impact gardening effects, etc. [36].

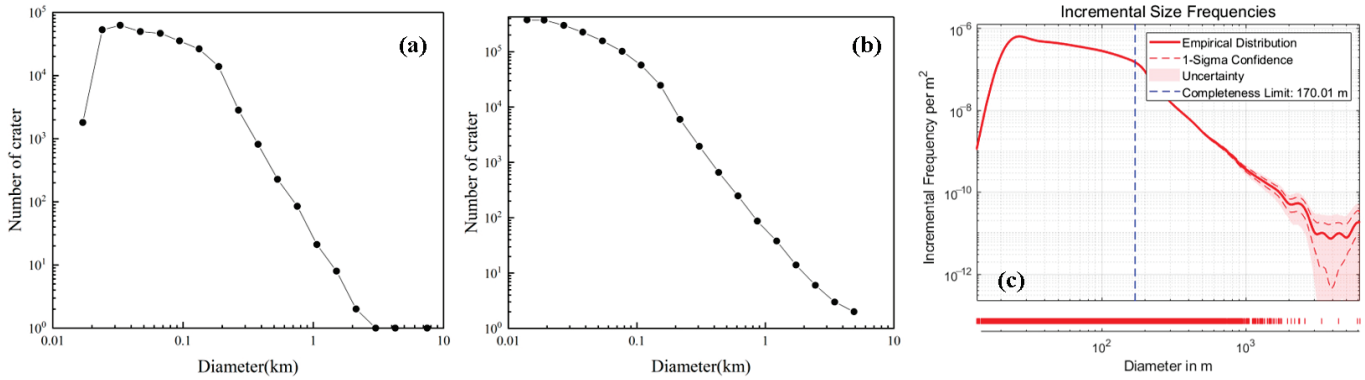


Figure 4. The (**a**) incremental and (**b**) cumulative size–frequency distributions of craters in the crater catalogue with the diameter internal of $\sqrt{2}$D in a log-log plot. Note that the diameter axis is the crater median in each bin. (**c**) The incremental size–frequency distribution established by robust kernel density estimation [33].

In this crater catalogue of the whole area, 38,471 possible secondary crater clusters were identified and eliminated by the easily applicable criteria of irregular shape, clustered distribution, and auxiliary information of shallow depth. In the original crater catalogue, there were 511,484 craters with diameters larger than 30 m, 15,575 craters with diameters larger than 200 m, and 456 craters with diameters larger than 1 km. The mapping results showing craters with diameters ≥200 m are illustrated in Figure 5. After secondary crater elimination, there were 484,410 craters with diameters larger than 30 m, 14,142 craters with diameters larger than 200 m, and 415 craters with diameters larger than 1 km.

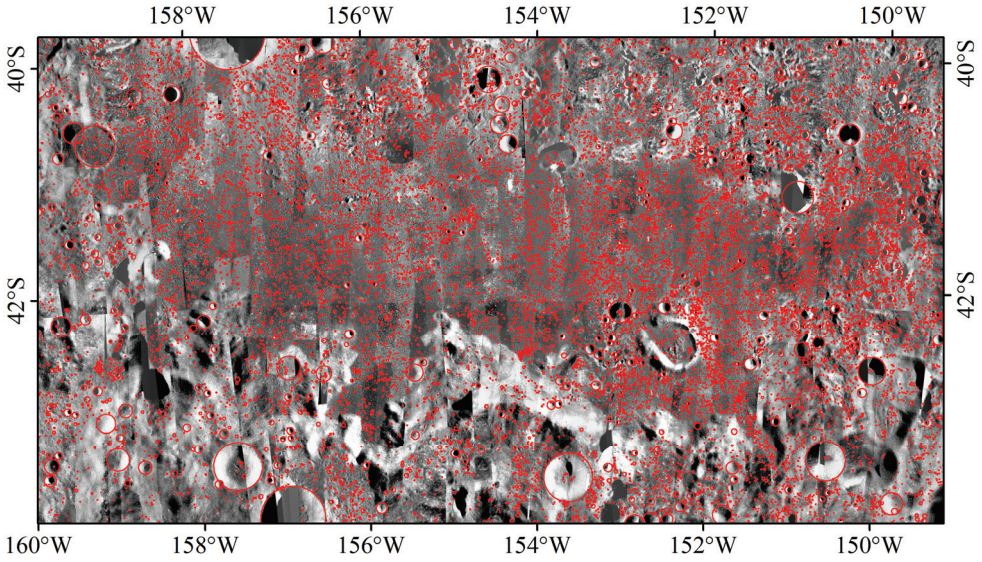


Figure 5. The mapped craters annotated in red with diameters larger than 200 m in the CE-6 landing area overlaying on the LROC NAC DOM mosaic.

Spatial density analysis was conducted on the catalogue after exclusion of secondary craters and on two subsets of greater than 30 m and greater than 1 km, respectively. As shown in Figure 6a,b, the spatial density of impact craters ranging from 30 m to 1 km was greater in the mare region at the center of the landing area than in the highlands. For craters with diameters greater than 1 km, they were more commonly found in the highlands than in the mare. This was because some of the small impact craters in the highlands were expunged due to topographic relief, while the large impact craters were preserved.

The estimation of crater depth was based on SLDEM2015, which is described in Section 2.2. Considering the grid size of SLDEM2015, only craters with diameters larger than 480 m were considered for depth estimation. Craters with depths larger than 12 m were utilized for subsequent analysis, considering the vertical accuracy of SLDEM2015 to be 3–4 m. A total of 1547 craters were ultimately measured for depth, with depths ranging from 12.1 to 2583.8 m. The majority of craters (94.2%) had depths less than 200 m. Six craters were deeper than 1 km, and nearly all of these craters were located in the geological units of the highlands. Figure 7 shows the crater depth distribution with a depth interval of 50 m.

In this work, the depth-to-diameter ratio was used to assess the morphology of craters. The depth-to-diameter ratios of a total number of 1,547 craters were calculated in the mare and highlands (as shown in Figure 3). The statistical results of the depth-to-diameter ratios are shown in Figure 8. As shown in Figure 8a, the depth-to-diameter ratio in the mare region was higher than that of the highland, which was because of the younger age of the mare, as well as the crater size difference illustrated in Figure 6. In the highlands, there were 1132 craters with diameters ranging from 480 to 19,882 m and depths from 12.1 to 2583.8 m, resulting in an average depth-to-diameter ratio of 0.058. In the mare area, there were 415 craters with diameters ranging from 481 to 6179 m and depths from 12.3 to 313.2 m, resulting in an average depth-to-diameter ratio of 0.071. Although the average depth-to-diameter ratios differed, the ranges of them were almost the same in both regions as shown in Figure 8b. Qualitative morphological analyses were also carried out, some examples can be found in Appendix B.

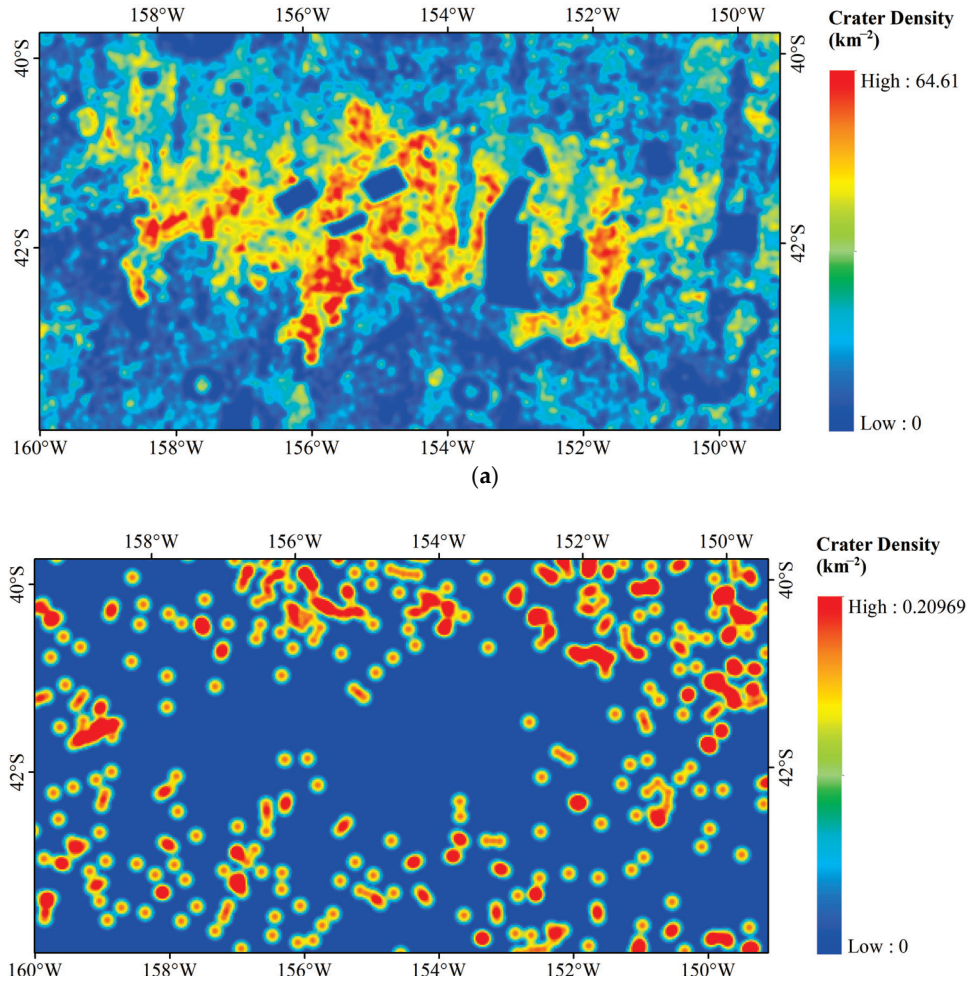


Figure 6. Spatial densities of craters in the CE-6 landing area: (**a**) spatial density of the crater diameters within 30 m to 1 km excluding possible secondary craters and (**b**) spatial density of craters with D $\geq$ 1 km excluding possible secondary craters. The Lambert conformal conic projection is adopted. Note that the colors represent different density values in different plots.

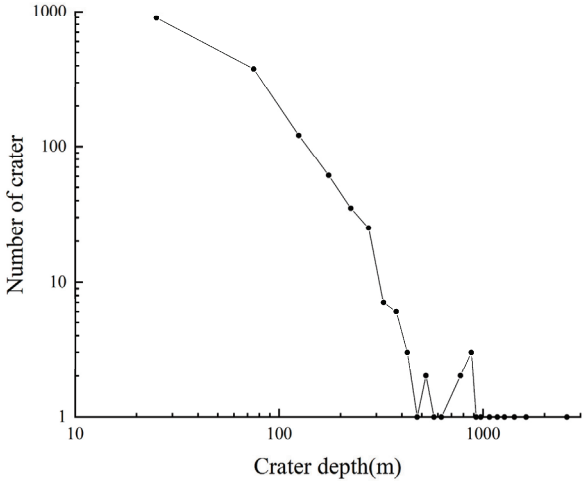


Figure 7. Crater depth (D > 480 m) distribution of CE-6 landing area in a log-log plot. There are 1547 craters catalogued with a depth interval of 50 m.

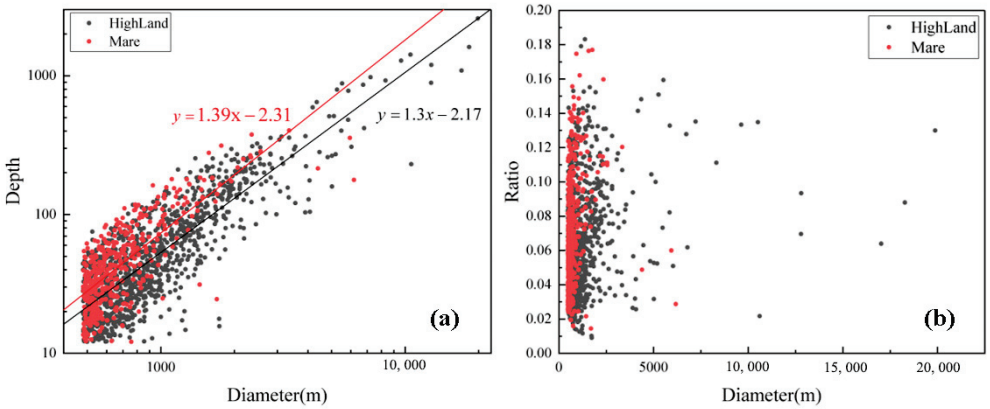


Figure 8. The relationships between the crater diameter and (**a**) the crater depth (in a log-log plot) and (**b**) the d-D ratio. The results for mare craters are shown in red, while the results for highland are shown in black.

3.2. Surface Model Ages of CE-6 Landing Area

By inputting impact crater extraction results into the CraterStats software, the absolute model ages (AMAs) of the A1, A2, and A3 basalt units were $\mu 2.62^{+0.093}_{-0.095}$ Ga, $\mu 2.49^{+0.072}_{-0.073}$ Ga, and $\mu 3.27^{+0.036}_{-0.045}$ Ga, respectively (Figure 9a–c). The AMAs of A1 and A2 were within each other's uncertainty range, suggesting there might be either two basalt flooding events or only one flooding event, but the surface of A1 was masked/contaminated by materials with low TiO_2 content (e.g., ejecta) that resulted in a decrease in TiO_2 abundance. If the latter was the case, dating on the A1 + A2 unit would indicate the flooding happened around $\mu 2.58^{+0.063}_{-0.064}$ Ga (Figure 9d).

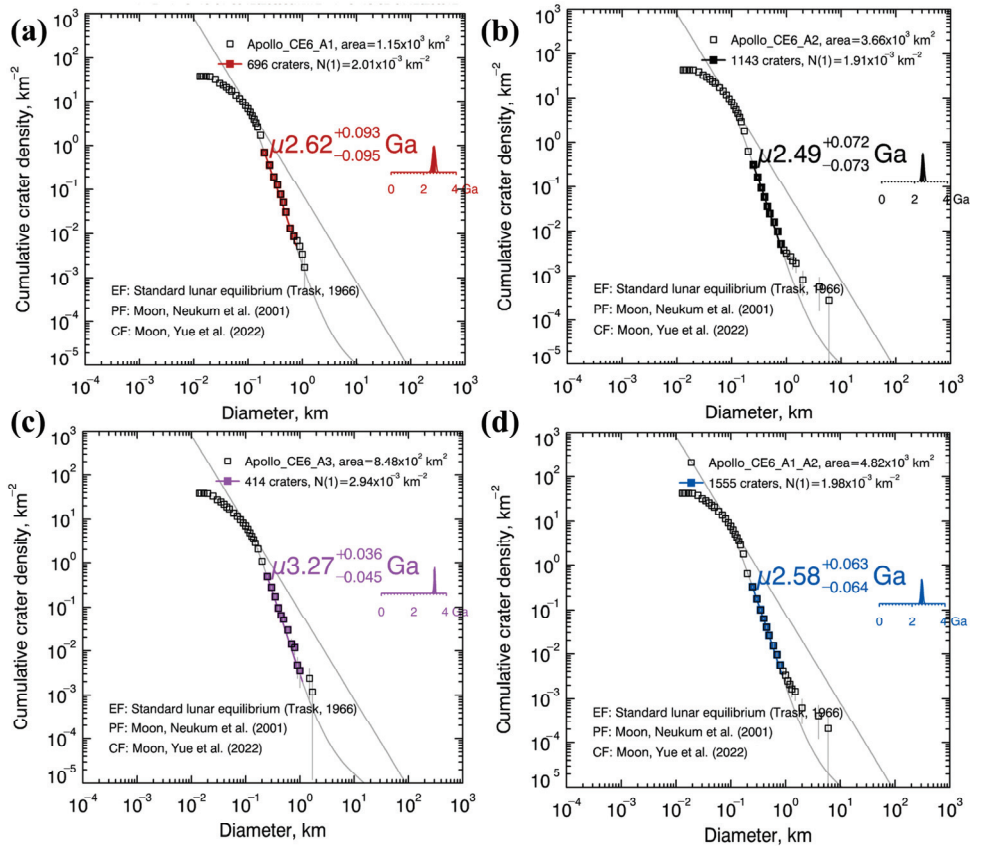


Figure 9. AMAs of the crater dating areas: (**a**) A1; (b) A2; (**c**) A3; (**d**) A1 + A2. The standard lunar crater equilibrium line is from [37], the PF is from [38], and the CF is from [8].

4. Discussion

4.1. Comparison with the Craters in CE-5 Landing Area

The completeness analysis of the mare region using three different methods provided varying values, which is introduced in Section 3.2. The value provided by Robbins' method was much larger than the other two methods. This was because the method adopted the production function, which took the crater saturation equilibrium into account [33]. From Figure 9a–c, the three basalt units, covering most of the mare region, also showed that the craters were essentially saturated at diameters greater than 100 m.

As described in Section 3.2, the depth–diameter ratios of the mare and highland areas in the CE-6 landing area were 0.071 and 0.058, respectively, which coincided with the conclusion from [39] that small craters (less than ~4 km in diameter) on the lunar maria were found to be deeper than those on the highlands. The highland area in the CE-6 landing area contained 415 craters larger than 1 km, which was almost twice the amount of the CE-5 landing area; therefore, the overall depth–diameter ratio distributions showed smaller values than that of the CE-5 landing area.

4.2. Dating Results Compared with Previous Study

Ref. [10] also carried out crater dating on the basalt units of the CE-6 landing area, with approximately similar dating areas of A2 and A3. They used the classic chronology system, i.e., [5]. If the chronology system from [5] was used for dating in this study, the AMAs of the A1, A2, A3, and A1 + A2 basalt units were $\mu 2.51^{+0.092}_{-0.094}$ Ga, $\mu 2.38^{+0.07}_{-0.07}$ Ga, $\mu 3.25^{+0.043}_{-0.056}$ Ga, and $\mu 2.46^{+0.062}_{-0.062}$ Ga, respectively (Figure 10a–c). Compared with their dating results (i.e., $2.40^{+0.11}_{-0.11}$ Ga for the F_A unit and $3.43^{+0.044}_{-0.061}$ for the L_A unit), the AMA of the A2 unit was about the same in both studies, while the AMA of the A3 unit estimated in this study was younger than that of [10]. The difference might be because the dating regions and data sources for crater counting were not completely consistent. Overall, as we mapped craters based on higher-resolution DOM and used more craters in dating the surface units after eliminating secondary craters, our surface dating results should be more reliable.

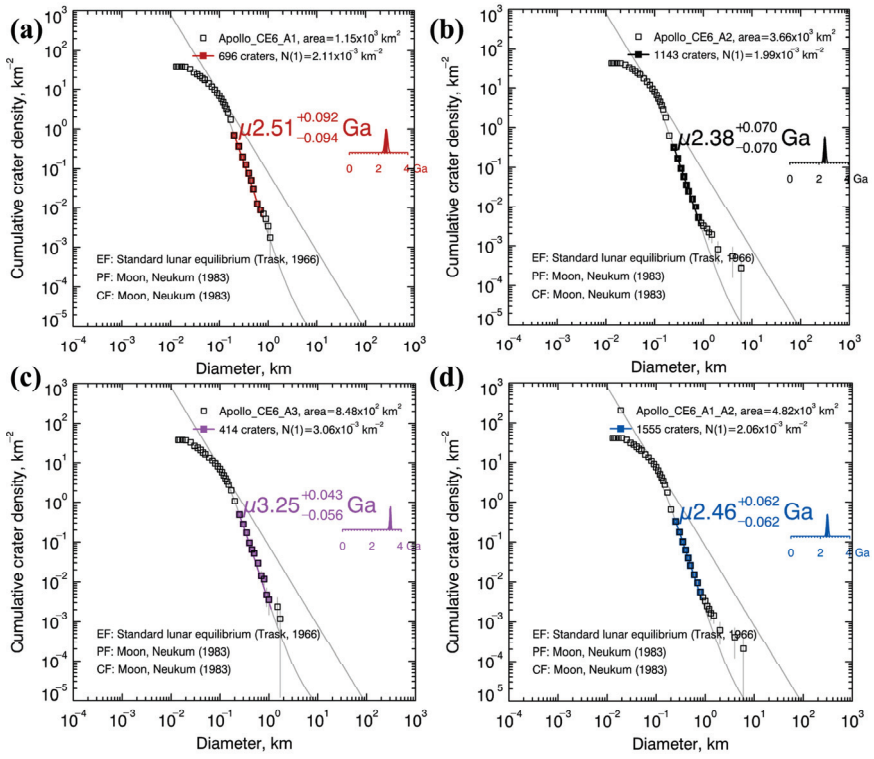


Figure 10. AMAs of the crater dating areas: (**a**) A1; (**b**) A2; (**c**) A3; (**d**) A1 + A2. The standard lunar crater equilibrium line is from [37], the PF is from [5], and the CF is from [5].

5. Conclusions

We established a catalogue of 770,731 craters with the completeness diameter of 30 m in the CE-6 landing area based on an LROC NAC DOM mosaic with resolution of 3 m/pixel. The craters were extracted by our improved YOLOv8-LCNET deep-learning algorithm and examined manually. The morphology and distribution of all the craters and the depth analysis of craters larger than 480 m were included in this catalogue. The crater size-frequencies of different surface units delineated by TiO_2 abundance were analyzed to obtain the absolute model ages. The results showed that the oldest unit lay in the right of the mare and had a model age of $\mu 3.27^{+0.036}_{-0.045}$ Ga, and the youngest unit was the middle part of the mare, which had a model age of $\mu 2.49^{+0.072}_{-0.073}$ Ga. The established crater catalogue was used to support topographic and geologic analyses of the pre-selected landing area of the CE-6 mission for landing safety evaluation and scientific research before the launch. The catalogue and the derived surface ages have multiple potential applications after the lunar samples are returned. This catalogue and the CSFD analysis results will be helpful for the interpretation of the samples and understanding their provenances, the lunar chronology model refinement when combined with the radioisotope ages of the relevant samples, and better understanding of the geologic properties of the landing site, the Apollo basin, and the SPA basin.

Author Contributions: Conceptualization, Y.W., K.D. and Z.Y.; methodology, J.N., B.X., Z.Y., S.G. and S.S.; formal analysis, C.Z. and S.G.; investigation, C.Z., S.G., H.Z. and X.D.; resources, B.X.; data curation, J.N., C.Z. and B.X.; writing—original draft preparation, all the authors; writing—review and editing, Y.W., S.G., Z.Y., K.D. and S.S.; visualization, C.Z. and S.G.; supervision, K.D.; project administration, Y.W.; funding acquisition, K.D. All authors have read and agreed to the published version of the manuscript.

Funding: This research was funded by the National Key Research and Development Program of China (Grant No. 2022YFF0503100), the Strategic Priority Research Program of the Chinese Academy of Sciences (grant No. XDB41000000), and the Open Fund of State Key Laboratory of Remote Sensing Science (Grant No. OFSLRSS202206).

Data Availability Statement: The craters used for surface model ages dating presented in the study are openly available in Zenodo at https://doi.org/10.5281/zenodo.11385444 (accessed on 31 May 2024). The remaining data supporting the conclusions of this article will be made available by the authors on request.

Acknowledgments: The authors gratefully acknowledge all those who worked on the Planetary Data System archive (https://ode.rsl.wustl.edu/moon/index.aspx, accessed on 10 May 2023) to make the LROC NAC imagery and SLDEM2015 publicly available.

Conflicts of Interest: The authors declare that they have no known competing financial interests or personal relationships that could have appeared to influence the work reported in this paper.

Appendix A

To evaluate the performance of the proposed YOLOv8-LCNET network, we compared the crater extraction results using this improved and the original YOLOv8 networks. The training dataset and training parameters used for two networks were the same. The crater extraction results tested on the validation dataset are shown in Table A1. Table A1 indicates that compared with the original YOLOv8 algorithm, the proposed YOLOv8-LCNET network had significant improvements on Precision, Recall, mAP50, and mAP50-95 of 0.228, 0.312, 0.439, and 0.350, respectively, which meant YOLOv8-LCNET reduced manual work better than using YOLOv8.

Table A1. Performance comparisons of YOLOv8 and YOLOv8-LCNET.

Model	Precision	Recall	mAP50	mAP50-95
YOLOv8	0.630	0.516	0.547	0.325
YOLOv8-LCNET	0.858	0.828	0.906	0.675

Appendix B

In this work, simple qualitative morphological analyses of the extracted craters have also been conducted. Figure A1 provides some examples showing different depth-to-diameter ratios of craters at various degradation stages. From Figure A1a–c, it is obvious to distinguish the different stages of the crater degradation according to the morphological characteristics. And the quantitative calculation of the depth-to-diameter ratios coincides with the intuition of visual interpretation. The crater catalogue we established provides a base dataset to carry out more comprehensive work on integrating qualitative and quantitative analyses for better understanding of crater degradation mechanism.

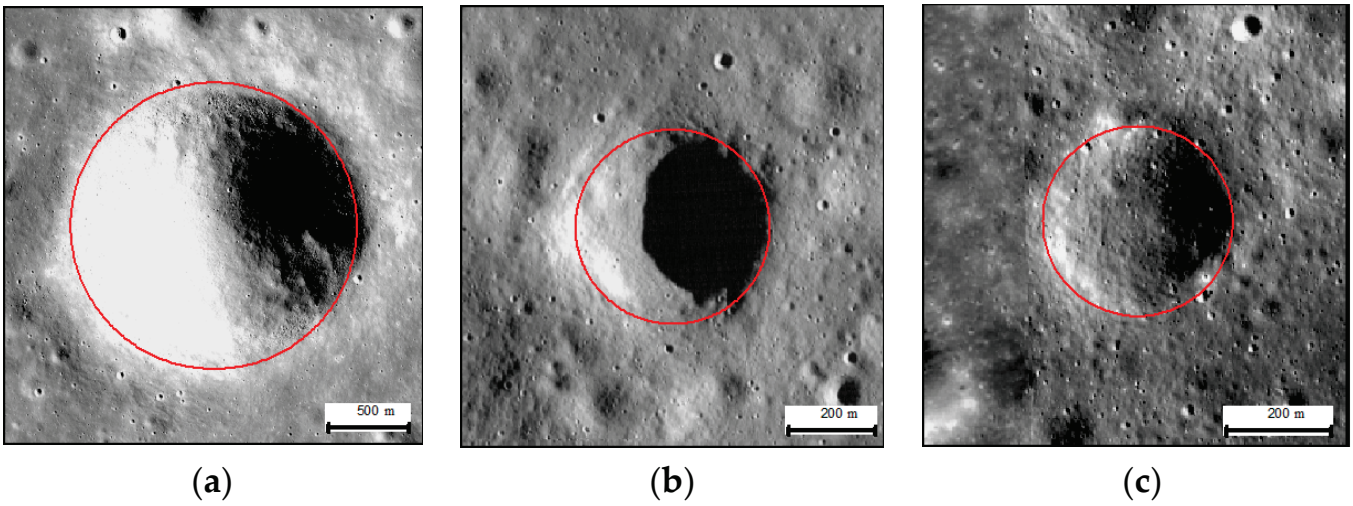


Figure A1. Different depth-to-diameter ratios of craters at various degradation stages: (**a**) a fresh crater (location: 156.07°W, 41.59°S) with diameter of 1769.7 m and depth-to-diameter ratio of 0.177, (**b**) a degraded crater (location: 152.80°W, 40.58°S) with diameter of 453.2 m and depth-to-diameter ratio of 0.07, and (**c**) a heavily degraded crater (location: 158.02°W, 41.59°S) with diameter of 364 m and depth-to-diameter ratio of 0.023.

References

1. Smith, J.V.; Anderson, A.T.; Newton, R.C.; Olsen, E.J.; Crewe, A.V.; Isaacson, M.S. Petrologic history of the moon inferred from petrography, mineralogy and petrogenesis of Apollo 11 rocks. In Proceedings of the Apollo 11 Lunar Science Conference, Houston, TX, USA, 5–8 January 1970; p. 897.
2. Wood, J.A.; Dickey, J.J.S.; Marvin, U.B.; Powell, B.N. Lunar anorthosites and a geophysical model of the moon. In Proceedings of the Apollo 11 Lunar Science Conference, Houston, TX, USA, 5–8 January 1970; p. 965.
3. Stevenson, D.J. Origin of the Moon-The Collision Hypothesis. *Annu. Rev. Earth Planet Sci.* **1987**, *15*, 271–315. [CrossRef]
4. Hu, S.; He, H.; Ji, J.; Lin, Y.; Hui, H.; Anand, M.; Tartèse, R.; Yan, Y.; Hao, J.; Li, R.; et al. A dry lunar mantle reservoir for young mare basalts of Chang'e-5. *Nature* **2021**, *600*, 49–53. [CrossRef] [PubMed]
5. Neukum, G. *Meteoriten Bombardement und Datierung Planetarer Oberflächen (Meteorite Bombardment and Dating of Planetary Surfaces)*; Ludwig-Maximilians University: Munich, Germany, 1983.
6. Ivanov, B.A. Mars/Moon Cratering Rate Ratio Estimates. *Space Sci. Rev.* **2001**, *96*, 87–104. [CrossRef]
7. Yue, Z.; Di, K.; Michael, G.; Gou, S.; Lin, Y.; Liu, J. Martian surface dating model refinement based on Chang'E-5 updated lunar chronology function. *Earth Planet Sci. Lett.* **2022**, *595*, 117765. [CrossRef]
8. Yue, Z.; Di, K.; Wan, W.; Liu, Z.; Gou, S.; Liu, B.; Peng, M.; Wang, Y.; Jia, M.; Liu, J.; et al. Updated lunar cratering chronology model with the radiometric age of Chang'e-5 samples. *Nat. Astron.* **2022**, *6*, 541–545. [CrossRef]
9. Li, C.; Wang, C.; Wei, Y.; Lin, Y. China's present and future lunar exploration program. *Science* **2019**, *365*, 238–239. [CrossRef] [PubMed]
10. Zeng, X.; Liu, D.; Chen, Y.; Zhou, Q.; Ren, X.; Zhang, Z.; Yan, W.; Chen, W.; Wang, Q.; Deng, X.; et al. Landing site of the Chang'e-6 lunar farside sample return mission from the Apollo basin. *Nat. Astron.* **2023**, *7*, 1188–1197. [CrossRef]
11. Yue, Z.; Di, K.; Liu, Z.; Michael, G.; Jia, M.; Xin, X.; Liu, B.; Peng, M.; Liu, J. Lunar regolith thickness deduced from concentric craters in the CE-5 landing area. *Icarus* **2019**, *329*, 46–54. [CrossRef]

12. Jia, B.; Fa, W.; Zhang, M.; Di, K.; Xie, M.; Tai, Y.; Li, Y. On the provenance of the Chang'E-5 lunar samples. *Earth Planet Sci. Lett.* **2022**, *596*, 117791. [CrossRef]
13. Robbins, S.J. A New Global Database of Lunar Impact Craters >1–2 km: 1. Crater Locations and Sizes, Comparisons With Published Databases, and Global Analysis. *J. Geophys. Res. Planets* **2019**, *124*, 871–892. [CrossRef]
14. Wang, Y.; Wu, B.; Xue, H.; Li, X.; Ma, J. An Improved Global Catalog of Lunar Impact Craters ($\geq$1 km) With 3D Morphometric Information and Updates on Global Crater Analysis. *J. Geophys. Res. Planets* **2021**, *126*, e2020JE006728. [CrossRef]
15. Jia, M.; Yue, Z.; Di, K.; Liu, B.; Liu, J.; Michael, G. A catalogue of impact craters larger than 200 m and surface age analysis in the Chang'e-5 landing area. *Earth Planet Sci. Lett.* **2020**, *541*, 116272. [CrossRef]
16. Bo, Z.; Di, K.; Liu, Z.; Yue, Z.; Liu, J.; Shi, K. A catalogue of meter-scale impact craters in the Chang'e-5 landing area measured from centimeter-resolution descent imagery. *Icarus* **2022**, *378*, 114943. [CrossRef]
17. Barker, M.K.; Mazarico, E.; Neumann, G.A.; Zuber, M.T.; Haruyama, J.; Smith, D.E. A new lunar digital elevation model from the Lunar Orbiter Laser Altimeter and SELENE Terrain Camera. *Icarus* **2016**, *273*, 346–355. [CrossRef]
18. Robinson, M.S.; Brylow, S.M.; Tschimmel, M.; Humm, D.; Lawrence, S.J.; Thomas, P.C.; Denevi, B.W.; Bowman-Cisneros, E.; Zerr, J.; Ravine, M.A.; et al. Lunar Reconnaissance Orbiter Camera (LROC) Instrument Overview. *Space Sci. Rev.* **2010**, *150*, 81–124. [CrossRef]
19. Di, K.; Jia, M.; Xin, X.; Wang, J.; Liu, B.; Li, J.; Xie, J.; Liu, Z.; Peng, M.; Yue, Z.; et al. High-Resolution Large-Area Digital Orthophoto Map Generation Using LROC NAC Images. *Photogramm. Eng. Remote Sensing* **2019**, *85*, 481–491. [CrossRef]
20. Juan, T.; Diana-Margarita, C.; Julio-Alejandro, R. A Comprehensive Review of YOLO Architectures in Computer Vision: From YOLOv1 to YOLOv8 and YOLO-NAS. *Mach. Learn. Knowl. Extr.* **2023**, *5*, 1680–1716. [CrossRef]
21. Robbins, S.J.; Antonenko, I.; Kirchoff, M.R.; Chapman, C.R.; Fassett, C.I.; Herrick, R.R.; Singer, K.; Zanetti, M.; Lehan, C.; Huang, D.; et al. The variability of crater identification among expert and community crater analysts. *Icarus* **2014**, *234*, 109–131. [CrossRef]
22. Kneissl, T.; van Gasselt, S.; Neukum, G. Map-projection-independent crater size-frequency determination in GIS environments—New software tool for ArcGIS. *Planet Space Sci.* **2011**, *59*, 1243–1254. [CrossRef]
23. Liu, Z.; Yue, Z.; Michael, G.; Gou, S.; Di, K.; Sun, S.; Liu, J. A global database and statistical analyses of (4) Vesta craters. *Icarus* **2018**, *311*, 242–257. [CrossRef]
24. Gou, S.; Yue, Z.; Di, K.; Liu, Z. A global catalogue of Ceres impact craters $\geq$ 1 km and preliminary analysis. *Icarus* **2018**, *302*, 296–307. [CrossRef]
25. Stöffler, D.; Ryder, G. Stratigraphy and Isotope Ages of Lunar Geologic Units: Chronological Standard for the Inner Solar System. *Space Sci. Rev.* **2001**, *96*, 9–54. [CrossRef]
26. Stöffler, D.; Ryder, G.; Ivanov, B.A.; Artemieva, N.A.; Cintala, M.J.; Grieve, R.A.F. Cratering History and Lunar Chronology. *Rev. Mineral Geochem.* **2006**, *60*, 519–596. [CrossRef]
27. Hiesinger, H.; Jaumann, R.; Neukum, G.; Head III, J.W. Ages of mare basalts on the lunar nearside. *J. Geophys. Res. Planets* **2000**, *105*, 29239–29275. [CrossRef]
28. Michael, G.; Neukum, G. Planetary surface dating from crater size–frequency distribution measurements: Partial resurfacing events and statistical age uncertainty. *Earth Planet Sci. Lett.* **2010**, *294*, 223–229. [CrossRef]
29. Giguere, T.A.; Taylor, G.J.; Hawke, B.R.; Lucey, P.G. The titanium contents of lunar mare basalts. *Meteorit. Planet. Sci.* **2000**, *35*, 193–200. [CrossRef]
30. Sato, H.; Robinson, M.S.; Lawrence, S.J.; Denevi, B.W.; Hapke, B.; Jolliff, B.L.; Hiesinger, H. Lunar mare TiO_2 abundances estimated from UV/Vis reflectance. *Icarus* **2017**, *296*, 216–238. [CrossRef]
31. Nelson, D.; Koeber, S.; Daud, K.; Robinson, M.; Watters, T.; Banks, M.; Williams, N. Mapping Lunar Maria Extents and Lobate Scarps Using LROC Image Products. In Proceedings of the 45th Lunar and Planetary Science Conference, The Woodlands, TX, USA, 17–21 March 2014; p. 2861.
32. Wagner, R.V.; Speyerer, E.J.; Robinson, M.S.; The LROC Team. New Mosaicked Data Products from the LROC Team. In Proceedings of the 46th Lunar and Planetary Science Conference, The Woodlands, TX, USA, 16–20 March 2015; p. 1473.
33. Robbins, S.J.; Riggs, J.D.; Weaver, B.P.; Bierhaus, E.B.; Chapman, C.R.; Kirchoff, M.R.; Singer, K.N.; Gaddis, L.R. Revised recommended methods for analyzing crater size-frequency distributions. *Meteorit. Planet. Sci.* **2018**, *53*, 891–931. [CrossRef]
34. Salamunićcar, G.; Lončarić, S.; Mazarico, E. LU60645GT and MA132843GT catalogues of Lunar and Martian impact craters developed using a Crater Shape-based interpolation crater detection algorithm for topography data. *Planet Space Sci.* **2012**, *60*, 236–247. [CrossRef]
35. Robbins, S.J.; Hynek, B.M. A new global database of Mars impact craters $\geq$1 km: 2. Global crater properties and regional variations of the simple-to-complex transition diameter. *J. Geophys. Res. Planets* **2012**, *117*, E06001. [CrossRef]
36. Shi, K.; Yue, Z.; Di, K.; Liu, J.; Dong, Z. The gardening process of lunar regolith by small impact craters: A case study in Chang'E-4 landing area. *Icarus* **2022**, *377*, 114908. [CrossRef]
37. Trask, N.J. Size and spatial distribution of craters estimated from the ranger photographs. In *Ranger VIII and IX, Part II—Experimenters' Analyses and Interpretations*; 32-800; Jet Propulsion Laboratory, California Institute of Technology: Pasadena, CA, USA, 1966; pp. 252–263.

38. Neukum, G.; Ivanov, B.A.; Hartmann, W.K. Cratering records in the inner solar system in relation to the lunar reference system. *Space Sci. Rev.* **2001**, *96*, 55–86. [CrossRef]
39. Wu, B.; Wang, Y.; Werner, S.C.; Prieur, N.C.; Xiao, Z. A global analysis of crater depth/diameter ratios on the Moon. *Geophys. Res. Lett.* **2022**, *49*, e2022GL100886. [CrossRef]

Disclaimer/Publisher's Note: The statements, opinions and data contained in all publications are solely those of the individual author(s) and contributor(s) and not of MDPI and/or the editor(s). MDPI and/or the editor(s) disclaim responsibility for any injury to people or property resulting from any ideas, methods, instructions or products referred to in the content.

remote sensing

MDPI

Review

Water Ice Resources on the Shallow Subsurface of Mars: Indications to Rover-Mounted Radar Observation

Naihuan Zheng [1], Chunyu Ding [1,2,*], Yan Su [3,4] and Roberto Orosei [5]

[1] Institute for Advanced Study, Shenzhen University, Shenzhen 518060, China; 2020281080@email.szu.edu.cn
[2] Tiandu-Shenzhen University Deep Space Exploration Joint Laboratory, Shenzhen 518060, China
[3] Key Laboratory of Lunar and Deep Space Exploration, National Astronomical Observatories, Chinese Academy of Sciences, Beijing 100049, China; suyan@nao.cas.cn
[4] School of Astronomy and Space Science, University of Chinese Academy of Sciences, Beijing 100049, China
[5] Istituto di Radioastronomia, Istituto Nazionale di Astrofisica, Via Piero Gobetti 101, 40129 Bologna, Italy; roberto.orosei@inaf.it
* Correspondence: dingchunyu@szu.edu.cn

Abstract: The planet Mars is the most probable among the terrestrial planets in our solar system to support human settlement or colonization in the future. The detection of water ice or liquid water on the shallow subsurface of Mars is a crucial scientific objective for both the Chinese Tianwen-1 and United States Mars 2020 missions, which were launched in 2020. Both missions were equipped with Rover-mounted ground-penetrating radar (GPR) instruments, specifically the RoPeR on the Zhurong rover and the RIMFAX radar on the Perseverance rover. The in situ radar provides unprecedented opportunities to study the distribution of shallow subsurface water ice on Mars with its unique penetrating capability. The presence of water ice on the shallow surface layers of Mars is one of the most significant indicators of habitability on the extraterrestrial planet. A considerable amount of evidence pointing to the existence of water ice on Mars has been gathered by previous researchers through remote sensing photography, radar, measurements by gamma ray spectroscopy and neutron spectrometers, soil analysis, etc. This paper aims to review the various approaches utilized in detecting shallow subsurface water ice on Mars to date and to sort out the past and current evidence for its presence. This paper also provides a comprehensive overview of the possible clues of shallow subsurface water ice in the landing area of the Perseverance rover, serving as a reference for the RIMFAX radar to detect water ice on Mars in the future. Finally, this paper proposes the future emphasis and direction of rover-mounted radar for water ice exploration on the Martian shallow subsurface.

Keywords: Mars; water ice; shallow subsurface; Martian-based ground-penetrating radars; RoPeR radar; RIMFAX radar

1. Introduction

The search for extraterrestrial water resources has been a key scientific objective in the human exploration of the solar system, with Mars being the second closest terrestrial planet and the most likely candidate to have water resources. Scientists have been exploring Mars with space probes since 1960 (Masursky [1], Zheng [2], Li et al. [3]), and after more than sixty years of exploration, the red planet is slowly revealing its secrets to mankind.

In 2002, the Mars Odyssey spacecraft discovered possible frozen water on the surface layer of Mars (Boynton et al. [4]). Back in the 1960s, it was thought that the two polar caps consisted mainly of frozen carbon dioxide and a small amount of water ice (McDougal et al. [5]). In the late 1970s, it was shown that there was water ice underneath the carbon dioxide ice covering of the north polar cap according to the observation of the Viking orbiters. However, experts continued to believe that the southern polar cap was made of

carbon dioxide ice (Kieffer [6]). In 2003, Byrne and Ingersoll [7] argued, based on high-resolution images from Mars Global Surveyor and thermal images from Mars Odyssey, that the Martian polar ice caps are made almost entirely of water ice, with only a thin layer of carbon dioxide ice on its surface. This was confirmed through direct spectroscopic observations by Bibring et al. [8]. In 2008, the Phoenix mission confirmed water existed on Mars by identifying water vapor when heating Martian soil samples (Rennó et al. [9]). Remote sensing data suggest that Mars once had large oceans and lakes (Clifford and Parker [10], McEwen et al. [11], Michalski et al. [12]). Moreover, recurring slope lineae suggest there may be seasonal flowing liquid water on Mars (McEwen et al. [13]). The presence of water ice on the surface of Mars can also be inferred by measuring the concentration of hydrogen on the shallow subsurface of Mars through neutron detectors and calculating the abundance of hydrogen. However, these observations are not penetrating and only reflect the physical properties of very thin areas of the Martian surface. The Martian-based ground-penetrating radar is a unique way to explore the presence of water ice on the shallow surface layer of Mars within a few meters to tens of meters (Hamran et al. [14], Zhou et al. [15], Chen et al. [16], Zhang et al. [17]).

Martian orbiter-based radars are mainly focused on the observation of water ice over the entirety of Mars, which includes the Mars Advanced Radar for Subsurface and Ionosphere Sounding (MARSIS) on the Mars Express spacecraft, Shallow Radar (SHARAD) on the Mars Reconnaissance Orbiter (MRO) and The Mars orbiter subsurface investigation radar (MOSIR) on China's Tianwen-1 mission (Picardi et al. [18,19]). But orbiter-based radars are not sensitive to the detection of water ice at depths of several meters due to their limited vertical resolution (Li et al. [3], Seu et al. [20,21], Hong et al. [22,23], Qiu and Ding [24]). In 2020, China and the United States launched the Tianwen-1 and Mars 2020 missions, respectively. China's Tianwen-1 mission landed on the Utopian Planitia (109°55′30″E, 25°3′58″N) (Li et al. [3]), and the Perseverance rover landed on the Jezero crater (77°27′3″E, 18°26′4″N) (Hamran et al. [25]). These missions carry advanced detection instruments, such as in situ spectrometers and highly accurate ground-penetrating radars. The Rover-mounted Subsurface Penetrating Radar (RoPeR) is onboard the Zhurong Rover (Zhou et al. [15], Chen et al. [16], Li et al. [26]), while the Radar Imager for Mars' Subsurface Experiment (RIMFAX) is onboard the Perseverance rover (Hamran et al. [14], Casademont et al. [27]). Both of the Martian-based ground-penetrating radars can detect water ice within a few meters or tens of meters of the shallow surface of Mars (Hamran et al. [14], Zhou et al. [15]). In addition, the European Space Agency (ESA) plans to launch the Exomars Mars exploration mission in 2028, which also will carry WISDOM (the Water Ice Subsurface Deposit Observation on Mars), a ground penetrating radar, onboard the rover (Herve et al. [28]). These Martian-based ground-penetrating radars will be used primarily to reveal the geologic framework of the subsurface layers of Mars and the evolutionary history of its surface processes, and to detect water ice, or even liquid water, on the shallow subsurface of Mars.

This paper reviews the evidence for water ice on Mars obtained from previous studies using various observations, which are discussed in Section 2, including remote sensing photography (see Section 2.1), radar observation (see Section 2.2), measurements by gamma-ray spectroscopy and neutron spectrometers (see Section 2.3), soil analysis (see Section 2.4), and other observation methods (see Section 2.5); Section 3 reviews the evidence of water ice on the shallow surface layers of Mars in the old days, including canyon network features (see Section 3.1), paleolake features (see Section 3.2), marine remains (see Section 3.3), rampart craters and polygonal terrain (see Section 3.4), and other surface geological features (see Section 3.5); Section 4 provides an overview of the current evidence of water ice in the shallow subsurface of Mars, including results from in situ spectroscopic observation (see Section 4.1) and radar detection (see Section 4.2); Section 5 summarizes the findings derived from the ground-penetrating radar in the landing area of the Perseverance rover; Section 6 discusses the limitations and breakthroughs in ground-penetrating radar to detect water ice on the Martian shallow subsurface. Finally, the advantages and development

trends of in situ ground-penetrating radar for detecting water ice in the shallow surface layer of Mars are presented (see Section 7). Assessing the feasibility of human colonization on Mars greatly depends on comprehending the spatial distribution of water ice and liquid water within the shallow subsurface layer of Mars, alongside the evolutionary patterns of water ice resources.

2. Detection Techniques of Shallow Surface Water Ice

Since 1961, more than forty Mars exploration missions have been conducted by humans. The detection of water ice in the shallow surface layers of Mars has long been a primary objective of these missions, as it is a crucial factor in the search for signs of life on the planet Mars. A comprehensive review of the successful missions reveals that the historical detection of water ice in the shallow surface layers of Mars can be categorized into several methods, including remote-sensing photography, radar, gamma-ray spectroscopy, neutron spectrometers, soil analysis, and other ancillary analyses.

2.1. Remote Sensing Photography

Remote sensing photography utilizes high-resolution imaging cameras onboard orbiters or rovers to capture images of the surface of Mars. This method enables direct observation of the presence or absence of landforms formed by liquid water on the planet's surface. Several typical Mars imaging cameras include the Mars Orbiting Camera (MOC) carried by the Mars Global Surveyor (MGS), which can capture images with high resolution, e.g., the captured images have a resolution of 1.5–12 m/pixel (Malin et al. [29]). MRO is equipped with several cameras, e.g., the Mars Color Imager (MARCI), the High-Resolution Imaging Science Equipment (HiRISE), and the Context Camera (CTX). The SuperCam onboard the Perseverance rover is equipped with the remote micro-imager (RMI); the RMI can distinguish the grains as small as 160 μm at a distance of 2 m from the instrument with a resolution $\leq$ 80 μrad (Wiens et al. [30]). The Colour and Stereo Surface Imaging System (CaSSIS) onboard ESA's Exomars Trace Gas Orbiter (TGO) can acquire surface images at a resolution of ∼4.6 m/pixel, including stereo imaging and color information (Thomas et al. [31]).

Extensive remote sensing photography has enabled the acquisition of imagery of the Martian surface, such as Figure 1a, which depicts the Acidalia mesas captured by HiRISE. The interpretation of this image suggests similarities to the Tuya landscape on Earth, indicating the possible existence of volcano–ice interaction terrain on Mars (Martínez-Alonso et al. [32]). This observation provides evidence that the mysterious landforms on Mars have been influenced by water and ice (Martínez-Alonso et al. [32]). The Galaxias Fossae region photographed by CTX (Figure 1b) is interpreted as exhibiting possible ice-fall-like and ice-flow morphologies (Pedersen et al. [33]). Furthermore, by comparison of recurring slope lineae (RSL) images captured by HiRISE with surface temperature and water vapor images at the same time at Martian solar longitude (Ls) 142.7° and Ls 348.7° (Figure 2), the temperature increases from 158 K to 261 K, while the water vapor increases from 0.0013 kg/m^2 to 0.0097 kg/m^2. It reinforces the possibility that the triggering mechanism of RSL requires sufficient water and temperature (Howari et al. [34]). Additionally, the orbiter of the Chinese Tianwen-1 mission is equipped with medium- and high-resolution cameras (0.5 m@265 km) for imaging of key areas where water may be present (Li et al. [3]).

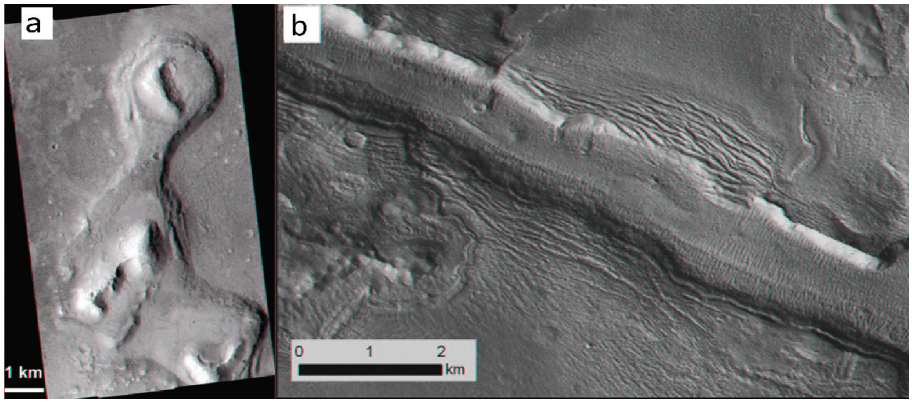


Figure 1. (**a**) The Acidalia mesas are considered to be flat-topped mountains (adapted from Martínez-Alonso et al. [32]); (**b**) an example from Galaxias Fossae (adapted from Pedersen and Head [35]).

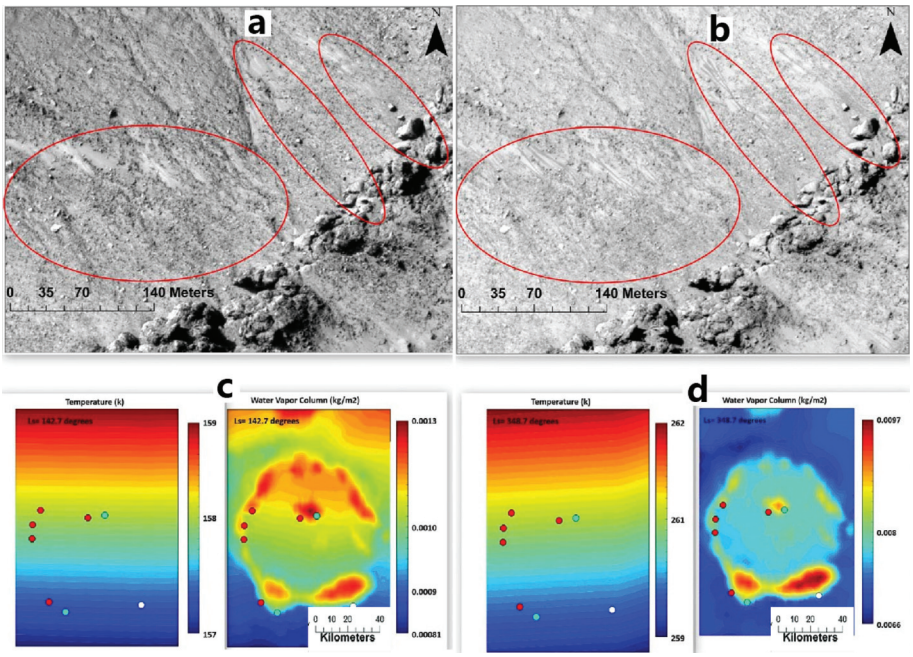


Figure 2. (**a**,**b**) display HiRISE data for Asimov crater (47°S, 5°E) at Ls 142.7° and Ls 348.7°, respectively, showcasing variations in recurring slope lineae (red circles) in the images. (**c**,**d**) depict relevant atmospheric parameters that were captured at the same time as the HiRISE data acquisition on the Martian surface (adapted from Howari et al. [34]).

2.2. Radar Observation

The detection of shallow surface water ice on Mars is primarily accomplished through the use of radar equipment on orbiters or Mars rovers (Zhou et al. [15], Picardi et al. [18,19], Seu et al. [20,21], Zhou et al. [36]). The working principle of the Martian-based ground-penetrating radar can be summarized as follows (Zhou et al. [15], Qiu and Ding [24]): The radar antenna emits radar pulses towards the subsurface of Mars. When the radar electromagnetic waves encounter differences in impedance from subsurface materials, reflections and scattering of the electromagnetic waves occur at the interfaces between different materials. These echo signals are then captured by the radar antenna. The data received by the radar are then analyzed to calculate the subsurface stratification and thickness of the soil on Mars (Chen et al. [16]), as well as the dielectric properties of the subsurface material, such as the value of dielectric loss and relative permittivity. By determining the polarization of the radar signal, it is potentially feasible to ascertain the presence of water ice in the superficial layers of the detection area (Zhou et al. [36], Dong et al. [37], Liu et al. [38]). By processing these echo

signals, the subsurface structure of Mars' surface and the composition of the subsurface materials can also be revealed (Grima et al. [39], Nouvel et al. [40]).

Orbiter-based radars such as MARSIS, SHARAD, and MOSIR are used to detect the global scale of Mars, with the advantage of a wide detection range. In situ ground-penetrating radars, such as RoPeR and the RIMFAX, are used for localized detection in the landing areas and have the advantage of higher precision to examine the localized subsurface structure with an unprecedented resolution compared to those of orbiter-based ground-penetrating radar.

Installed on the ESA's Mars Express space probe, the Mars Advanced Radar for Subsurface and Ionosphere Sounding (MARSIS) operates at central frequencies of 1.8, 3, 4, and 5 MHz (Picardi et al. [18,19]). With a theoretical penetration depth of 0.5–5 km, the radar is primarily used to detect the distribution of water ice beneath the Martian subsurface, local geological stratigraphy, and subsurface aquifers (Jordan et al. [41]).

Similarly, the Mars Reconnaissance Orbiter (MRO) carries shallow radar (SHARAD) with a central frequency of 20 MHz and a theoretical penetration depth of 0.1–1 km (Seu et al. [21]). SHARAD is capable of detecting stratified structures up to one kilometer below the Martian surface and is primarily used for detecting water ice, geological subsurface structure, and subsurface aquifers below the subsurface of Mars (Seu et al. [20], Xiong et al. [42]).

For instance, Bramson et al. [43] compared the time delay between surface and subsurface radar reflector from SHARAD (Figure 3c) with the terrace depth (Figure 3b) of terrace-type crater within the Arcadia Planitia determined by digital terrain models (DTMs) from HiRISE (Figure 3a), to work out the dielectric constant and constrain the materials' composition, and finally suggested that much of the upper region of the area is likely to be water ice. Anomalously bright subsurface reflections were identified in MARSIS radar observations collected from May 2012 to December 2015 over Planum Australe (Figure 4), which were construed as due to the presence of liquid water at the bottom of the SPLDs (Orosei et al. [44]).

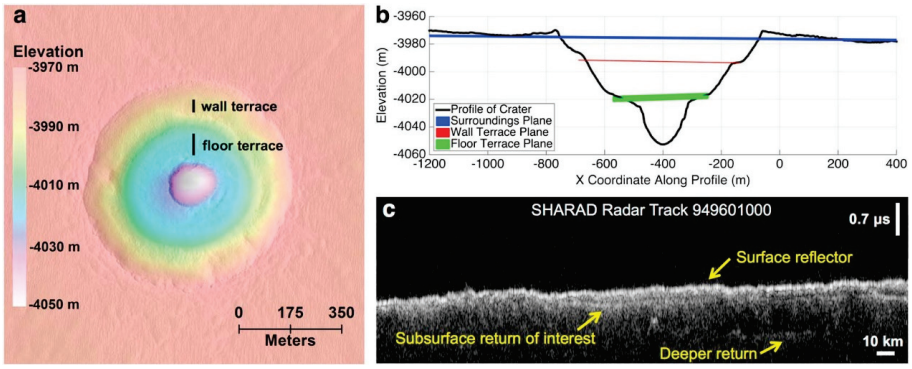


Figure 3. (**a**) DTM of the double terrace crater. (**b**) Crater profile with planes close to the surroundings and the elevation of each terrace. (**c**) SHARAD radar observations through Badger Crater. (Adapted from Bramson et al. [43]).

China's Tianwen-1 spacecraft with MOSIR subsurface detection radar is currently exploring Mars, but the relevant detection data and research results have not yet been officially released (Li et al. [3], Fan et al. [45]). Its high-frequency mode operates at a center frequency ranging from 30 to 50 MHz, while its low-frequency mode operates at a center frequency of 10–15 MHz and 15–20 MHz (Fan et al. [45]). It has a subsurface structure penetration depth of about 100 m and an ice penetration depth of about 1000 m (Fan et al. [45]). Its thickness resolution capability is at the meter level, and it is primarily utilized for detecting water ice and subsurface structure on Mars (Li et al. [3], Hong et al. [22], Fan et al. [45]).

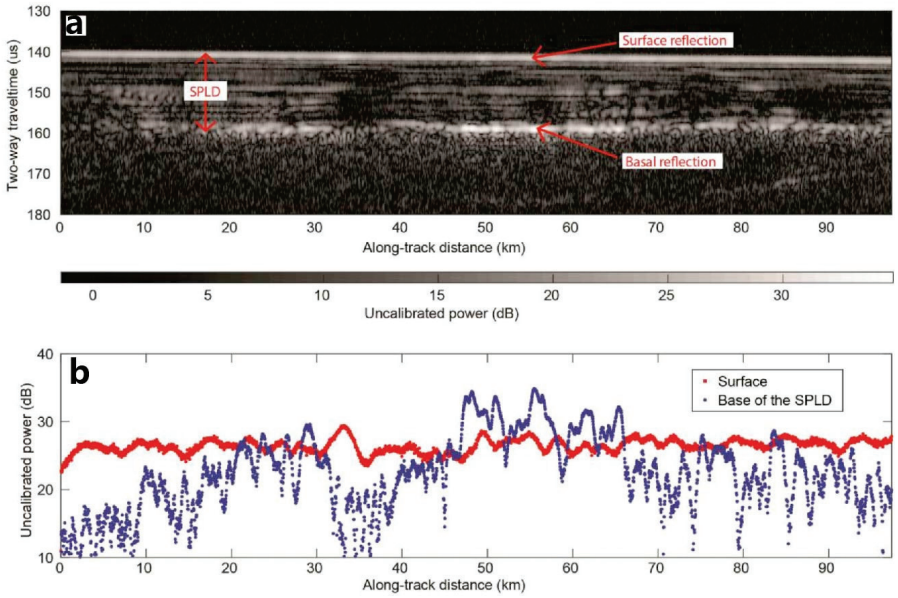


Figure 4. Radar data collected by MARSIS radar for the Planum Australe region on the southern pole of Mars. (**a**) Radargram for MARSIS orbit 10737. the bottom reflector corresponds to the South Polar Layered Deposits (SPLDs)/basal material interface. (**b**) Plot of surface and basal echo power for the radargram in (a) (adapted from Orosei et al. [44]).

Martian-based ground-penetrating radars are also beginning to be deployed on the surface of Mars to reveal the secrets beneath its surface (Hamran et al. [25], Li et al. [26]). For instance, the Zhurong rover carries an in situ detection radar, RoPeR, which is a Martian-based ground-penetrating radar (Zhou et al. [15]). It operates at 15–95 MHz for the low-frequency channel and 450–2150 MHz for the high-frequency channel (Table 1), with thickness resolution at the meter and centimeter levels, respectively. It can be used to detect the regions with depths of tens of meters below the Martian surface (Zhou et al. [15], Chen et al. [16], Li et al. [26]). The Perseverance rover also carries a Martian-based ground-penetrating radar, RIMFAX, primarily used to detect shallow surface geological structures and water ice on Mars [46]. Additionally, the ESA plans to carry a Martian-based ground-penetrating radar named WISDOM on board the ExoMars Rover soon (Herve et al. [28]).

Table 1. The carried ground-penetrating radars and their basic parameters both in Mars and lunar exploration missions.

Mission	GPR Name	Center Frequency	Frequency Band	Depth Resolution	Penetration Depth	References
China's Zhurong Rover	RoPeR	55 MHz	15–95 MHz	A few meters	10–100 m	Zhou et al. [15]
		1300 MHz	450–2150 MHz	A few centimeters	3–10 m	Zhou et al. [15]
Perseverance Rover	RIMFAX	675 MHz	150–1200 MHz	10–40 cm	>10 m	Hamran et al. [14]
ExoMars	WISDOM	1750 MHz	500–3000 MHz	≈3 cm	3–10 m	Ciarletti et al. [47]
Chang'e-3/-4	LPR	60 MHz	40–80 MHz	meter-scale	>100 m	Fang et al. [48]
	LPR	500 MHz	250–750 MHz	≤30 cm	>30 m	Fang et al. [48]
Chang'e-5	LRPR	2000 MHz	1000–3000 MHz	≈5 cm	>3 m	Xiao et al. [49]

2.3. Measurements by Gamma Ray Spectroscopy and Neutron Spectrometers

The Gamma Ray Spectrometer (GRS) onboard NASA's Mars Odyssey allows for the mapping of the chemical makeup on Mars to depths of 10 cm to 1 m below the surface through the measurement of gamma rays from space and their interactions with various surface materials (Evans et al. [50], Saunders et al. [51]). The GRS consists of the

Gamma Sensor (GS), the Neutron Spectrometer (NS), and the High-Energy Neutron Detector (HEND). The neutron detector equipment like NS and HEND measures neutrons with different energy levels liberated from the near-surface of Mars by cosmic rays. It analyzes the energy reaction between neutrons and hydrogen nuclei and measures the gamma rays to obtain the content of hydrogen atoms (water and potential organic matter) in the soil at different depths, thus inferring water ice does exist on the near-surface (Saunders et al. [51]). This enables the identification of the number and type of chemical elements present, as well as the distribution of hydrogen, which can provide evidence of water ice (Evans et al. [50], Saunders et al. [51]). The GRS is capable of planet-wide mapping of hydrogen abundance on Mars at a spatial resolution of approximately 600 km, enabling inferences to be made that water ice may exist near the Martian surface (Saunders et al. [51]).

Boynton et al. [4] utilized the GRS observation to create a superthermal neutron flux map from the neutron energy spectrometer (Figure 5). Through this analysis, two hydrogen-rich regions near the Martian northern pole and southern pole were identified, suggesting that the source of this hydrogen in the subsurface may be ice. The globally distributed superthermal neutron flux map can be used to assist in the interpretation of whether Martian-based ground-penetrating radar detects regions of water ice.

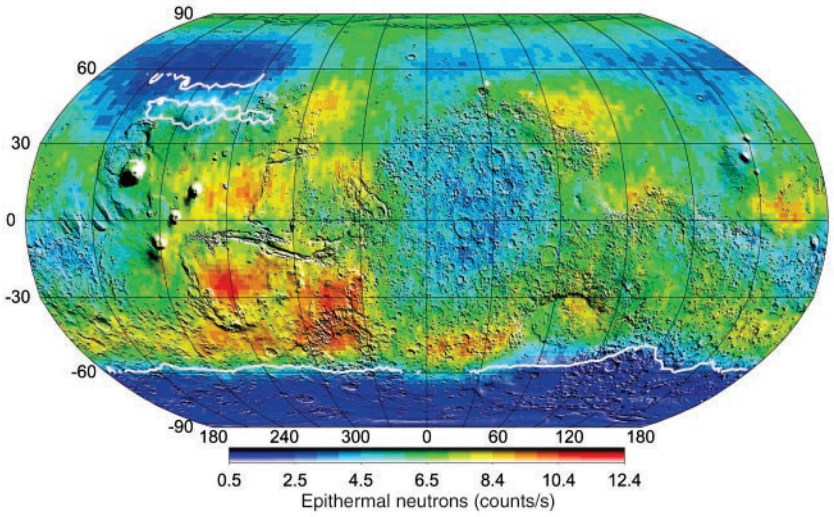


Figure 5. Super thermal neutron flux map created using data from the neutron energy spectrometer (adapted from Boynton et al. [4]).

The distribution of superthermal neutrons for 55 days at energies ranging from 0.4 eV to 100 keV plotted by HEND (Figure 6) suggested that the deviation of the mean and maximum neutron count rates in the northern and southern hemispheres corresponds to 5% water by weight in the homogeneous subsurface layer, with the higher content likely related to chemically bound water in the subsurface layer. The low superthermal neutron flux in the south is due to the higher water ice content within the lower subsurface layer than the upper subsurface. Under this hypothesis, Mars has large areas at low-elevation regions of the northern hemisphere and high-elevation regions of the southern hemisphere that contain the uppermost subsurface hydrogen, which may be bound in water ice. This hypothesis requires support from the global surface and subsurface water transport mechanisms on Mars (Mitrofanov et al. [52]).

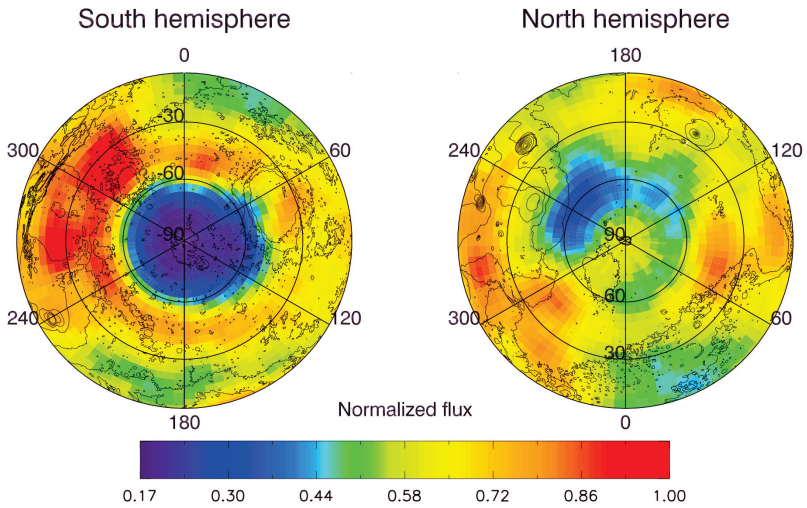


Figure 6. Initial plot of HEND measurements of Mars' superthermal neutron orbit during the first 55 days of mapping at energies ranging from 0.4 eV to 100 keV (adapted from Mitrofanov et al. [52]).

The Fine-Resolution Epithermal Neutron Detector (FREND) onboard TGO is an orbital neutron telescope, capable of detecting hydrogen on the subsurface of Mars up to 1 m depth (Mitrofanov et al. [53]). Mitrofanov et al. [54] analyzed FREND data for the Valles Marineris (VM) region and interpreted the average water-equivalent hydrogen value of Candor Chaos in the central region of VM should be 40.3 wt%. The result points to the presence of water ice permafrost or large amounts of highly hydrated minerals in the subsurface at equatorial latitudes.

The Curiosity rover is equipped with the Dynamic Albedo Detector of Neutrons (DAN), which enables the rover to characterize the soil composition at depths of 0.5–1 m and search for ice and water-bearing minerals beneath the Martian surface (Nikiforov et al. [55], Mitrofanov et al. [56]). This instrument operates by emitting a neutron beam at the surface and then measuring the speed at which the beam reflects. Water and water-bearing minerals are the only hydrogen-containing compounds detected on Mars in significant concentration (Busch and Aharonson [57]). Hydrogen atoms in the subsurface tend to slow down neutrons, and the magnitude of this slowing can indicate the presence of water or ice. Nikiforov et al. [55] proposed a method for estimating the hydrogen content equivalent to water using neutron-sensing data from the DAN instrument on the Curiosity rover and suggested the possible existence of water-containing material in the shallow subsurface of the Vera Rubin Ridge (Nikiforov et al. [55]). In situ radar electromagnetic sounding is also sensitive to the water content of the subsurface, which affects the penetration depth of radar electromagnetic waves. Therefore, this technique can provide important information for other regions of Mars where in situ radar sounding is performed to study the Martian subsurface.

2.4. Soil Analysis

The lander and rover missions were able to analyze the water-ice content of the exploration areas by collecting soil samples or by conducting a direct analysis of soil composition. For example, the Phoenix lander landed in the permafrost zone of the Martian surface and subsequently explored the subsurface ice by collecting soil samples (Smith et al. [58]). Excavations at the landing site revealed the presence of white material beneath the ground (Figure 7), which provides evidence for the presence of liquid brine on Mars (Rennó et al. [9]). The Zhurong rover, equipped with the Mars Surface Composition Explorer, is expected to discover indications of water ice in the Utopian Plainita by directly analyzing the composition of materials in the soil (Li et al. [3]).

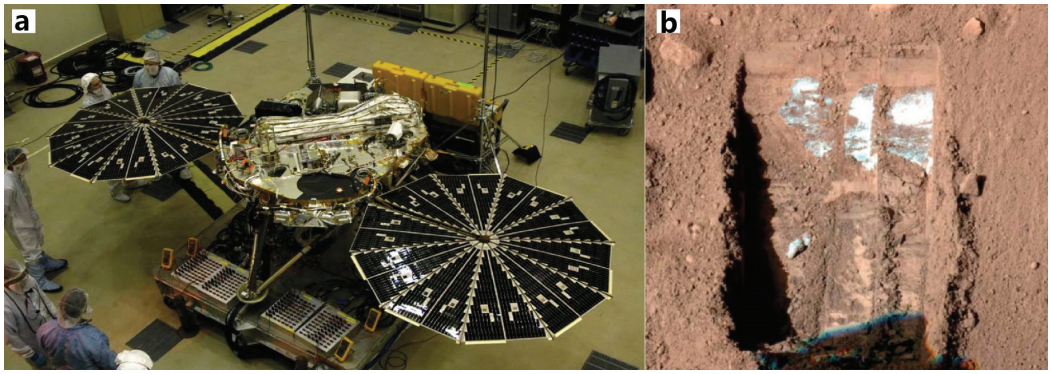


Figure 7. (**a**) Image of the Phoenix lander during the testing phase (adapted from Smith et al. [58]), and (**b**) an image showing the Phoenix robotic arm positioned to excavate the Martian surface. The white area in the image indicates the location of the water ice (adapted from Rennó et al. [9]).

2.5. Other Observation Methods

The widespread presence of clay, rounded gravels, salt patches at lower elevations, and hydrates containing iron compounds, as well as the occurrence of small channels on Mars, all provide evidence of past water flow on the planet (Bibring et al. [59]). The specific minerals found in Martian rocks provide insight into the previous environmental conditions that existed on the planet, including those suitable for life. For instance, the presence of sulfates and water-bearing carbonates in certain Martian meteorites, known as basaltic snow crystals, suggests that they were in an environment containing liquid water before being ejected (Nazari-Sharabian et al. [60]).

The recurring slope lineae (RSL) that form on present-day Mars are characterized by low albedo and are believed to be the result of transient liquid water flow (Stillman et al. [61]). Different parts of Mars produce RSL through various mechanisms, and all slopes containing RSL display evidence of hydrated salts, as shown in Figure 8. Moreover, warm slopes in the Martian seasons can produce liquid water in contemporary Mars (Ojha et al. [62]). Subsequently, through spectral data obtained from OMEGA (Observatoire pour la Mineralogie, l'Eau, la Glace et l'Activite), two forms of water presence on Mars have been identified. They are extensive water ice deposits in the polar regions of Mars and water-containing minerals on the Martian surface, respectively (Bibring et al. [59]). Analysis of near-infrared data from CRISM (Compact Reconnaissance Imaging Spectrometer for Mars) and OMEGA has revealed a widespread distribution of water-bearing minerals on Mars. Specifically, hydrous silicates are primarily distributed in the south highlands, while water-bearing minerals in the northern lowlands exhibit greater compositional diversity and are found in various geological epochs (Bibring et al. [59]). This indicates that the forms of water present on Mars are highly diverse and span multiple geological eras.

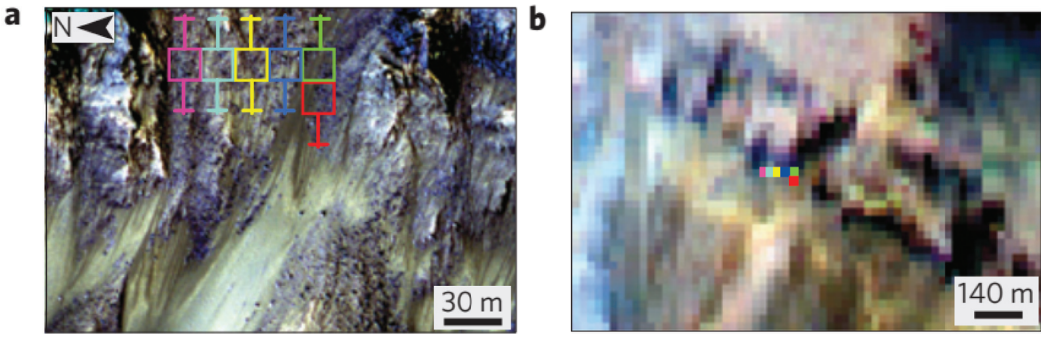


Figure 8. Recurring slope lineae in Palikir Crater (adapted from Ojha et al. [62]). (**a**) Infrared images of RSL on the slope of Palikir Crater. Colored boxes indicate the uncertainty of CRISM pixel locations; (**b**) synchronized CRISM observations.

In mineralogical surveys, it has been found that water-bearing minerals on Mars are mainly composed of Fe/Mg smectites, chlorite, and hydrated silica (Carter et al. [63]). Most of these water-bearing minerals formed before the middle of the Noachian, with a smaller portion continuing to form into the Hesperian and early Amazonian. Subsequent analysis, through crater age dating, has revealed that water-bearing minerals predominantly formed during the Noachian and the early period of Hesperian. The formation of these minerals decreased during the late Hesperian and Amazonian. Analysis of water-bearing minerals within impact melt materials inside craters has confirmed the presence of groundwater or previously existing hydrated minerals, subsurface ice, and impactor ice throughout Mars' history (Sun and Milliken [64], Wernicke and Jakosky [65]).

Based on estimations of the global water content on Mars, the water stored in and required for the formation of water-bearing minerals is estimated to range from 130–260 m of Global Equivalent Layer (GEL), with a theoretical range of 70–860 m GEL (Wernicke and Jakosky [65]). The estimated global water equivalent on Mars falls between 173–317 GEL, with a potential range of 110–1114 m GEL (Wernicke and Jakosky [65]). This underscores the significance of water-bearing minerals as a crucial reservoir of water on Mars, providing valuable insights for future endeavors in detecting water ice reserves and extracting water resources on the planet Mars.

3. Evidence for the Past Presence of Water Ice in the Shallow Surface

The past existence of water in the shallow surface layers of Mars is strongly supported by the existence of various geological formations, including canyons, outflow channels, oceans, washes, riverbeds, and lake basins. (McEwen et al. [11]). The analysis of these features sheds light on the planet's geological evolution, providing insights into past crustal activity and the climatic environment of Mars. Currently, remote sensing photography, terrain exploration, and mineral analysis are the primary methods for identifying and analyzing geological features on Mars. The Martian surface is primarily composed of basalt, a type of fine-grained magmatic rock comprising plagioclase, pyroxene, and the basal silicate mineral olivine, which can combine with water to form crystalline structures during chemical weathering (Ehlmann and Edwards [66], Yen et al. [67], Chevrier and Mathé [68]). The formation of secondary minerals requires water, and although they generally do not contain water themselves, they can serve as evidence to determine the past presence of water in the shallow surface layers (Craddock and Howard [69]).

3.1. Canyon Network Features

Branching channel systems, also called canyon networks, on Mars have been considered some of the strongest evidence for past water flow on the surface of Mars (Carr and Chuang [70]). These valleys bear similarities to river valleys found on Earth. To understand the origins of the river channels on Mars, scientists compared the density of craters on Earth and Mars with the density of the Martian river network. They concluded that valley formation on Mars likely involved slow erosion by flowing water over a short duration. The rock structure of Mars differs significantly from that of Earth (Carr and Chuang [70]). Viking observations suggest that during the Noachian period, upland grading was a long-term, slow process with possible brief periods of strong erosional fluvial activity from the late Noachian to early Hesperian, which resulted in an immature valley network. Martian global river valley drainage age densities were mapped using Mars Odyssey spectral data with Viking Mars images (Figure 9), and a high correlation was found between high drainage densities and river sediments (Hynek et al. [71]). The widespread distribution of hypothetical ancient lakes, fan delta sediments, and chlorides detected by THEMIS data indicates that most of Martian valleys and associated sediments were attributed to prolonged surface precipitation runoff.

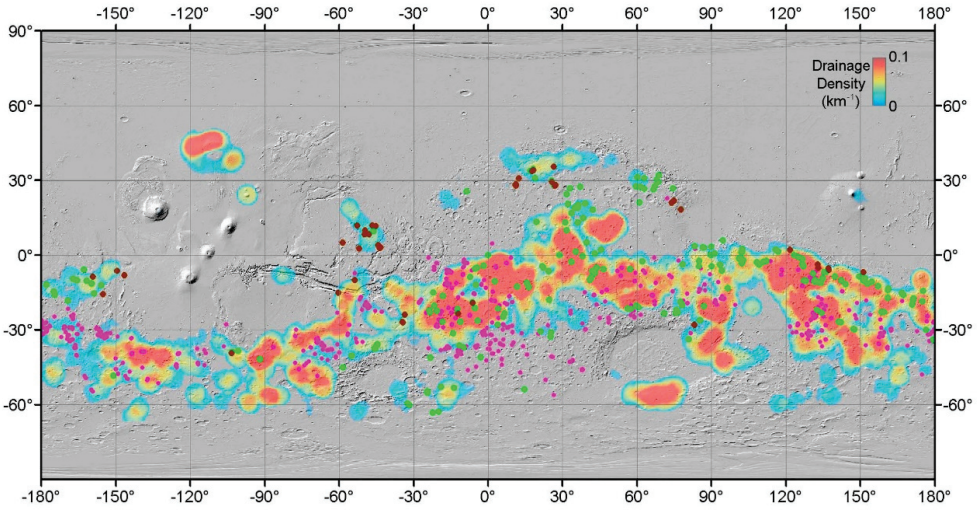


Figure 9. Map of the density distribution of full Martian river valleys, along with the distribution of river valleys on Mars that are believed to have ancient lake deposits (indicated by green circles, (adapted from Fassett and Head III [72]), fan deltas (shown as dark red circles, (adapted from Di Achille and Hynek [73,74]), and chlorine deposition (represented by pink circles).

Additionally, a climate model for ancient Mars, a 3D simulation of climate for the late Noachian and early Hesperian periods, and a river transport model were developed (Kamada et al. [75]). These models revealed that a CO_2 atmosphere, with a small amount of hydrogen at surface pressures exceeding two bar, could generate an environment conducive to the presence of stable liquid water on the surface. This would explain the observed distribution of certain valley networks, which can be attributed to river runoff. It suggests that the Martian valley networks may also be due to seasonal or transient snowmelt (Kamada et al. [75]).

3.2. Paleolake Features

Both on Earth and Mars, lakes are areas of high atmospheric activity and energy flow at the intersection of the hydrosphere, lithosphere, and cryosphere, making ancient Martian lakes a key target for Mars exploration. In recent years, the Spirit, Curiosity, and Perseverance rovers have landed in Gusev Crater, Gale Crater, and Jezero Crater, respectively, all of which have been identified as, or are believed to be, sites of paleolake (Farley et al. [46], Golombek et al. [76], Grotzinger et al. [77]). Over 400 paleolake basins have been identified on Mars using remote sensing techniques and can be divided into three categories: valley network-fed closed-basin lakes (Figure 10a), isolated inlet valley closed-basin lakes (Figure 10b), and valley network-fed open-basin lakes (Figure 10c). These findings suggest that the early Martian paleolake basins required a significant inflow of water to become filled and submerged (Goudge et al. [78]). To date, there is sufficient evidence confirming the presence of approximately 500 ancient lakes on Mars, as observed through visible imaging, infrared imaging, multispectral hyperspectral analysis, and stereo imaging (Figure 11) (Michalski et al. [12]).

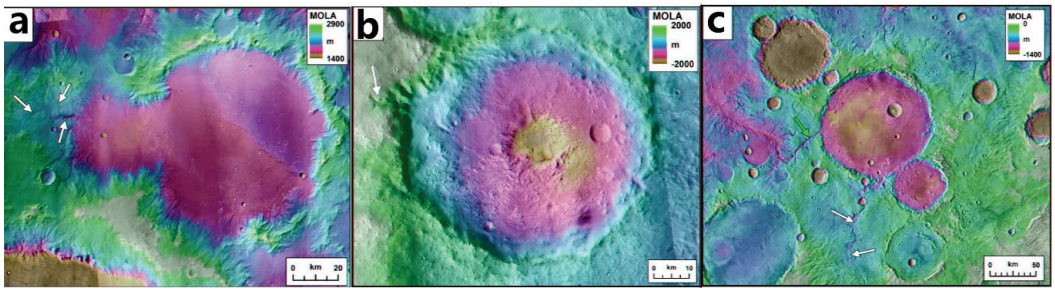


Figure 10. Examples of paleolakes on Mars (adapted from Goudge et al. [78]). White arrows indicate inlet valleys and green arrows indicate outlet valleys. (**a**) Valley network-fed closed-basin lake at −11.3°N, 131.4°E. (**b**) Isolated inlet valley closed-basin lake at 21.4°N, 58.1°E. (**c**) Valley network-fed open-basin lake at −10.6°N, 2.8°E.

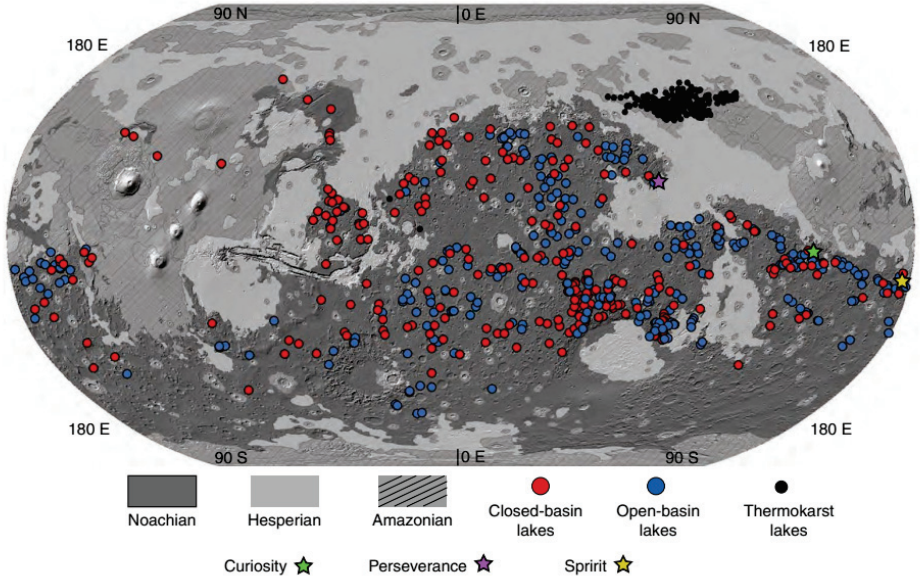


Figure 11. Global distribution of lake basins on Mars (adapted from Michalski et al. [12]).

The detection of paleolakes in the diverse landscapes of Mars has been of great significance in the present time. To examine the hypothesis of the presence of paleolakes, sediment analysis was conducted on the crater interiors of five craters (Figure 12) larger than 10 km in diameter situated in the westernmost lobes of the Medusae Fossae Formation (Aeolis and Zephyria Planum), approximately 800 km east of Gale Crater (Burr et al. [79]). A sedimentary unit with wind-formed paleoenvironment and fluvial paleoenvironment as the main supporting features were eventually identified, with another possible lacustrine sedimentary paleoenvironment (Peel and Burr [80]), providing a basis for later verification of the paleolakes. Moreover, the Jezero crater is also believed to be a paleolake at the Perseverance landing site (Farley et al. [46]). The RIMFAX radar carried on its Mars rover is expected to detect direct evidence of water ice in the area of the paleolake.

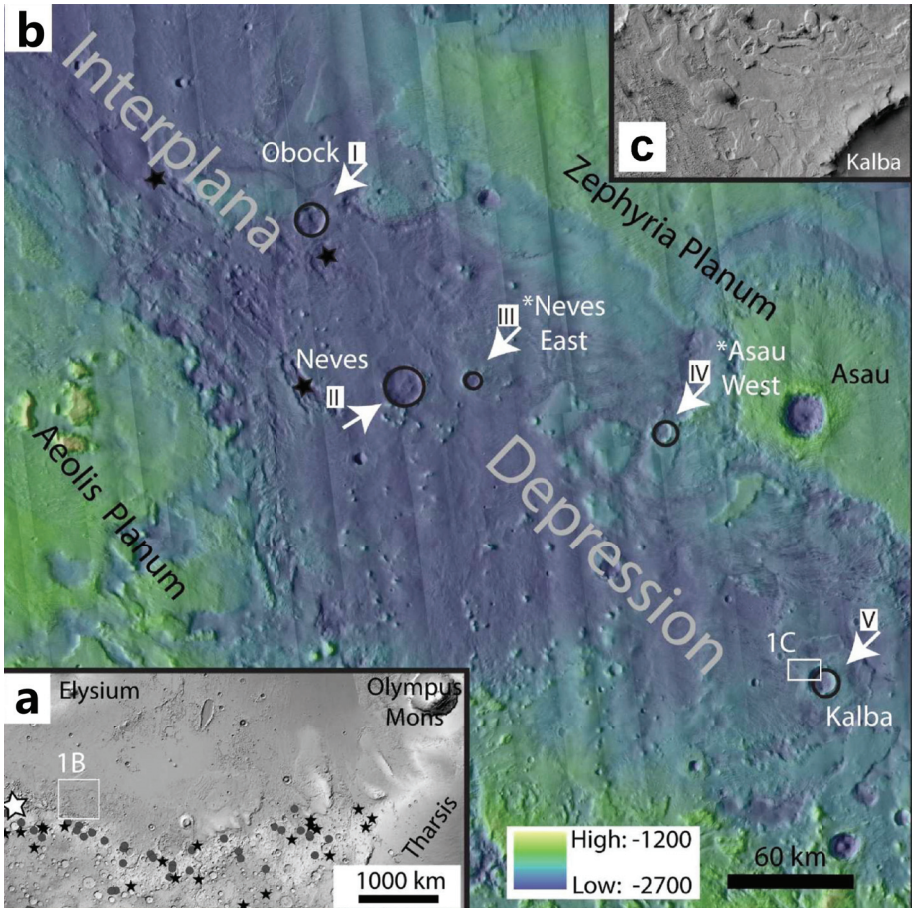


Figure 12. Part of the Medusae Fossae Formation region spanning the western Tharsis and eastern Gale crater, with black circles indicating impact crater lakes, adopted from Peel and Burr [80]. (**a**) MFF region of Mars, spanning the dichotomy boundary west of Tharsis and east of Gale crater (white star) and showing the locations of catalogued crater lakes that overflowed, forming an outlet channel (circles) and those that did not (black stars) on MOLA grayscale. Figure 1B in original paper represent Figure 12b in this paper. (**b**) Aeolis Dorsa region of Mars shown in CTX images with MOLA colorshade overlay. The craters mapped in this project are outlined with black circles and labeled by roman numerals and formal and ∗informal names. Figure 1C in original paper represent Figure 12c in this paper. (**c**) portion morphology of Kalba crater.

3.3. Marine Remains

Besides paleolakes, the presence of primitive oceans covering over 30% of the Martian surface can be inferred by exploring the hydraulic and thermal characteristics in the source areas of the Late Hesperian outflow channels and comparing them with the topographic and geomorphological evidence. It is suggested that these oceans once occupied the present northern plains of Mars (Clifford and Parker [10]). Measurements of the dielectric constant of the Vastitas Borealis Formation (VBF) within the shoreline of the paleo-ocean by MARSIS radar, which reveal that the VBF has a low dielectric constant (Figure 13), indicating that it is sediment or sediment mixed with significant amounts of ice deposited from water, supporting the claim of the existence of the northern paleo-ocean (Mouginot et al. [81]).

The Zhurong rover's Surface Composition Explorer has examined the VBF soil composition of the Utopia Plain. Through the utilization of laser-induced breakdown spectrometry (LIBS) and shortwave infrared spectroscopy (SWIR) to compare the spectra of opal, allophane, imogolite, and pyroxene from the RELAB database with the spectra of six selected VBF target layers (see Figure 14), it has been determined that the soils at the Zhurong rover landing site are a mixture of igneous minerals containing allophane and imogolite/opal, which have undergone minimal chemical alteration. These sediments are believed to have

formed due to extensive erosion of volcanic clastic soils in a cold environment with short-lived water (Liu et al. [82]). Xiao et al. [83] reported the first in situ observations of VBF and interpreted the layered features as sedimentary structures typical of marine environments detected by the Zhurong rover.

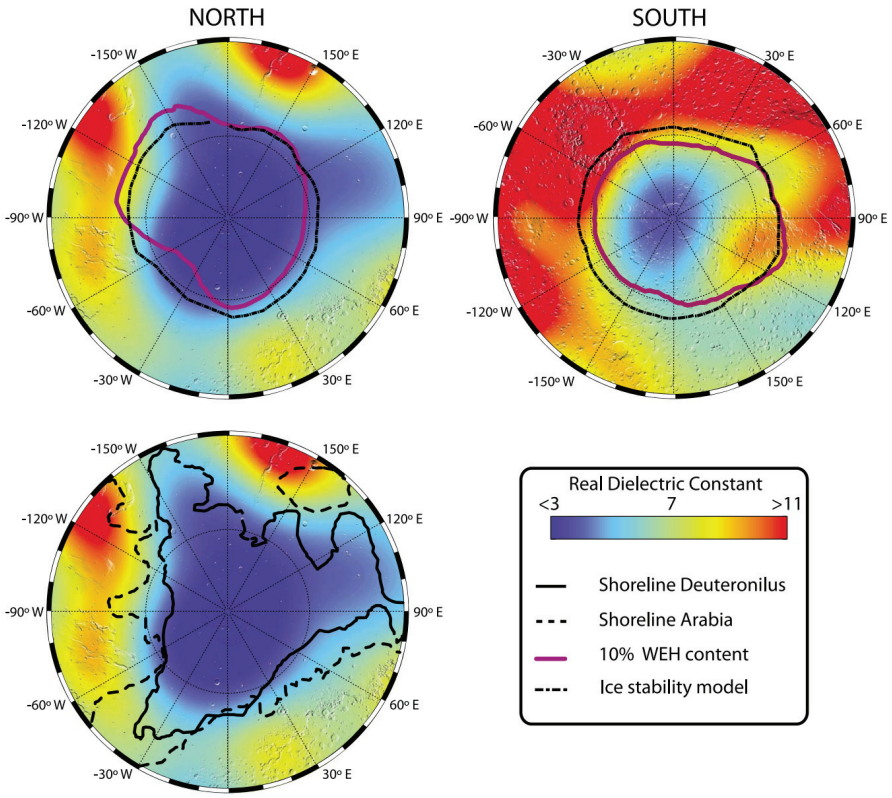


Figure 13. Distribution values of dielectric constants on the surface of Mars from MARSIS radar inversions (adapted from Mouginot et al. [81]).

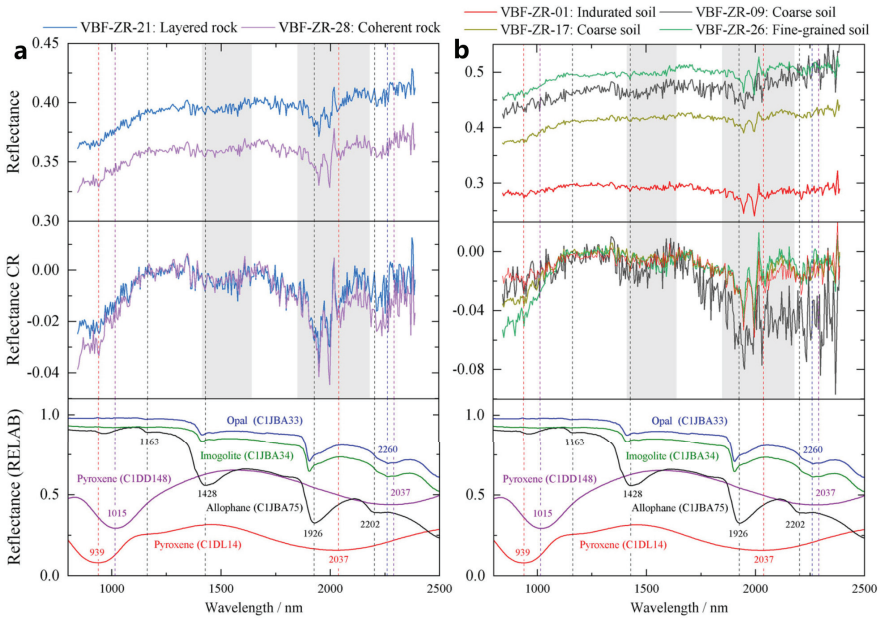


Figure 14. SWIR absolute spectra and mineral identification maps (adapted from Liu et al. [82]). (**a**) selected VBF rocks; (**b**) selected VBF soils (reflectance CR is the spectrum after removal of the continuum, the dashed lines indicate the absorption centers of these phases and the grey areas indicate the absorption features of the Martian atmosphere).

3.4. Rampart Craters and Polygonal Terrain

There is a unique type of impact crater known as the rampart crater on Mars. These craters exhibit multiple layers of continuous ejecta deposits (Carr et al. [84], Osinski [85], Mantegazza et al. [86]). The surface of the ejecta deposits features closely spaced radial stripes, discontinuous concentric ridges, and steep troughs. What makes them particularly distinctive is that each layer of ejecta is bordered by a low ridge or cliff extending from the crater's rim to a distance equal to twice the crater's diameter. This layered arrangement resembles successive barriers encircling the crater, hence the name rampart crater (Carr et al. [84], McCauley [87], Wulf et al. [88]). The formation of these rampart craters is explained by the presence of permafrost or subsurface water in the impacted region, which imparts fluidity to the ejected material (Carr et al. [84,89]). By simulating impacts on mixtures of ice and rock, it has been observed that the resulting craters display elevated ejection angles, fluidized ejecta blankets, and increased crater uplifts. This serves as further evidence supporting the role of water ice in the creation of rampart craters (Stewart et al. [90]). In the northern plains region of Mars, there are extensive polygonal terrains, which are cut by complex grooves and fissures ([89,91]), these polygonal terrains are primarily found in low-lying areas where evident deposits exist on Mars. Several hypotheses have been proposed for the formation mechanism of these polygonal terrains, e.g., the disappearance of water body loads leading to ground uplift and deformation, infiltration of surface water into frozen soil fissures resulting in the formation of ice wedges combined with the drying process, and the shrinkage of dry sediments and the cooling of volcanic rocks (Helfenstein and Mouginis-Mark [92], Hiesinger and Head III [93], McGill and Hills [94], Pechmann [95], Seibert and Kargel [96], Wenrich and Christensen [97]). On a smaller scale, the likelihood of mud-dry crack formations, contraction from cooling lava, or thermal contraction cracks is higher, and this cracking mechanism is closely related to fine-grained materials rich in water ice, indicating the presence of seasonal liquid water traces on the Martian surface (Seibert and Kargel [96], Mellon [98]). It is worth noting that impact craters on the polygonal terrains exhibit the morphology of rampart ejecta (Hiesinger and Head III [93]).

According to the radar data of Zhurong, it was found that there existed a wide distribution of buried polygonal terrain under Utopia Planitia. These polygons are interpreted as being produced by freeze-thaw cycles, where thermal contraction cracks first, and then water or soil material fills the cracks (Zhang et al. [17]). Wang et al. [99] investigated the transverse aeolian ridges (TARs) in the Zhurong landing region and identified polygonal features with hydrated minerals. They proposed the possible formation mechanisms of the polygons were contractional cracks formed during groundwater evaporation or fracture of indurated sand crust and the latter is the most possible mechanism. Either way, it may be related to recent water activity and atmosphere–surface water exchange on Mars.

Therefore, based on speculation regarding the formation mechanism of the rampart craters and the polygonal terrains, they can be considered significant evidence of the past presence of liquid water, interstitial water, or water ice on the Martian surface. These landforms, widely found in Utopia Planitia and Argyre Planitia, are also preferred landing areas for various countries' Mars exploration missions to investigate water ice (Seibert and Kargel [96], Liu et al. [100]). It is expected that the ground-penetrating radar carried by the Zhurong rover will detect such impact craters along its traverse route and conduct more in situ investigations of the distribution and properties of water ice beneath the Martian surface.

3.5. Other Surface Geological Features

Several distinctive characteristics can be also indicative of past water presence on Mars. The widespread occurrence of rootless volcanic cones and cratered terrain in the Tartarus colles region suggests the existence of a significant fossil hydrothermal system. The evolution process of this lava–ice interaction is as follows: At the beginning, the Tartarus colles lava flow is situated above a basement containing ice. The concentrated flow of lava towards the central path resulted in a thickness of approximately 60 m in the central location, while the edges of the

lateral flow remained around 30 m thick. (Hamilton et al. [101]). The heat of the lava melted the ice in the basement, causing the lava to sink and form a deformable base. Heat transfer from the lava to the basement allowed water to gradually escape and form a space beneath the lava. Eventually, the lava collapsed into the basement, along with fragments of the rootless cone, creating the observed features (Hamilton et al. [101]). This hydrothermal system was formed through interactions between lava and surface ice during the late to mid-Amazonian period, indicating the presence of water ice on Mars during this period (Hamilton et al. [101]). The use of ground-penetrating radar, especially the Mars in situ detection equipment, enables the detection of water ice beneath the surface of this geological feature.

In 2022, hydrated sulfate/silica material was identified in the Amazonian strata at the landing site through short-wave infrared spectroscopic data collected by the Zhurong rover in southern Utopia Planitia. These materials were interpreted as crusts that formed in situ and suggested that strata containing large amounts of liquid water formed as a result of groundwater uplift or melting. Evidence at the Zhurong rover landing site also suggests that the Amazonian hydrosphere on Mars is more active than previously thought (Liu et al. [102]).

The radar data from the RoPeR has unveiled subsurface layering in the Utopia basin of Mars, pointing to sedimentation resulting from intermittent hydraulic flooding. This is interpreted as representing the infilling of Utopia Planitia during the Late Hesperian to Amazonian periods (Li et al. [26]).

A recent work using LIBS onboard the Zhurong rover is analyzing the surface targets of the landing zone. The lithified duricrusts were detected to have a high water content. The cemented duricrusts may be formed through water vapor-frost cycling at the atmosphere–soil interface, and soils and sands contain hydrated magnesium salts and adsorbed water. Those evidences indicate potential Amazonian brine (Zhao et al. [103]).

Zhurong rover also observed some surface features inferred to have formed 1.4 to 0.4 million years ago in the southern Utopia Planitia, which includes cracks, aggregates, bright polygonal ridges, and crusts. These geological features are most likely caused by saline water from thawed frost/snow (Qin et al. [104]).

In the transitional area between Elysium and Utopia Planitia, significant deposits of material with a relatively high albedo have been observed. This material is located in extensive deposits around terraces, in cratons, and valley systems. It is believed that these deposits consist of modified ice-rich material, lineated valley fills, lobate debris aprons and degraded deposits of concentric crater fill. The presence of degraded ice-rich sediments at all elevations and latitudes in the study area suggests that ice-mantle material was originally deposited over a wide area and remained stable for a long period. Long-term sediment interaction processes are hypothesized to have ultimately played a part in forming the transition zone between Elysium and Utopia Planitia (Pedersen et al. [33], Pedersen and Head [35]).

The glacial and periglacial landforms on Mars are also a form of water storage. Rock glaciers (lobate-shaped landforms of unconsolidated sediment and rock debris) may have evolved from glaciers. Williams et al. [105] compiled morphometric data from the lobate feature on Mount Sharp (the northern slopes of Aeolis Mons), using orbitally derived imagery of HiRISE and CTX. These lobate features are evaluated as terrestrial rock glacier analogs. The periglacial features on Mount Sharp suggest the existence of water for the production of ice in the past equatorial region (Williams et al. [105]).

4. Evidence for the Current Presence of Water Ice in the Shallow Surface

The current presence of water ice has significant implications for studying the Martian climate's evolution and habitability for human exploration. Mellon predicted the distribution of water ice on Mars based on thermal inertia, albedo, and insolation calculations, which led to the conclusion that subsurface ice is stable in the high inclination range but not stable in the low inclination range (between $\pm 60°$) (Mellon and Jakosky [106]). As Mars exploration missions have progressed, NASA's Mars Odyssey, Curiosity, Perseverance, and China's Tianwen-1 have deployed advanced equipment such as spectrometers and radar. Recent Mars exploration missions will provide more evidence to find water ice in the shallow subsurface of Mars.

4.1. In Situ Spectrometer Detection

Since hydrogen atoms block high-energy cosmic rays, the absence of high-energy neutrons produced by cosmic rays on Mars indicates a widespread subsurface distribution of hydrogen elements, presumably present in water ice (Mitrofanov et al. [52]). Subsequently, the Thermal Emission Imaging System (THEMIS) onboard Mars Odyssey made a noteworthy finding of water ice, which was distributed near the periphery of the southern perennial polar cap of Mars. Daily and seasonal temperature trends on Mars based on observations from THEMIS suggest the presence of water ice on the Martian surface. Combined with Viking observations and a small number of other relevant observations from THEMIS, water ice on the Martian surface may be widely distributed around and beneath a perennial carbon dioxide ice cap (Titus et al. [107]). This result coincides with HEND's detection of large amounts of hydrogen in the southern polar subsurface (Mitrofanov et al. [52]).

Possible signs of liquid water on the Martian surface include recurring slope lineae observed on sloping terrain. These recurring slope lines (RSLs) (Figure 15) appear and gradually lengthen on low albedo surfaces during the warm season, which is observed as a narrow, dark mark on steep slopes (Stillman et al. [61]). RSL fades out during the cold season and occurs repeatedly in multiple Martian years (the statistical period ranges from Mars year 28 to 32). Data analysis from MRO has revealed the extensive occurrence of RSLs in the equatorial regions of Mars, particularly in the deep valleys of VM. RSLs are most active during seasons when the slopes are often facing the Sun. The abundance of RSLs in VM indicates a higher concentration of liquid water close to the surface in the equatorial region, surpassing the predictions of equilibrium models. This assumption is based on the association of RSL abundance in VM with the presence of flowing water (McEwen et al. [13]). This finding suggests that the high value of mean water equivalent hydrogen detected by FREND (Mitrofanov et al. [54]) is probably caused by the abundance of RSLs. Containing huge volumes of fossil ice from ancient glaciers, VM also has fossil glacial land systems, probably contributed by accumulated ice of chasma floors and valley walls at low elevations. And wet-based glaciers can flow and slide over the bed of the glacial system (Gourronc et al. [108]).

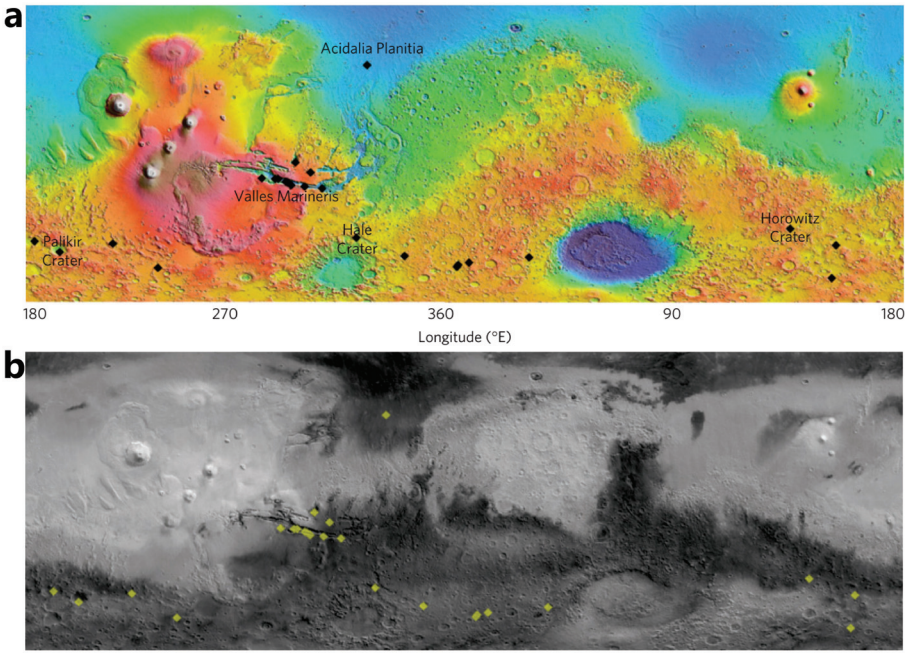


Figure 15. Locations of confirmed recurring slope lineae (RSLs) (adapted from McEwen et al. [13]). (**a**) Locations of confirmed RSLs as black diamonds; (**b**) the same set of RSLs on the Thermal Emission Spectrometer global radiative heat albedo map as yellow diamonds.

In 2020, discoveries of water ice on steep walls within two craters in the northern mid-latitudes of Mars were reported based on high-resolution images and spectral data from the Mars Reconnaissance Orbiter (Figure 16) (Vijayan et al. [109]). The exposed water ice deposits were shallow, with absorption bands at 1.5 μm and 2 μm, and the exposed ice remained stable after a 1-week interval in one location. It complements earlier research indicating the wide distribution of shallow water ice on Mars and aligns with the detection of subsurface water ice by the Neutron Star Spectrometer. The final interpretation is that the presence of shallow surface water ice in the origin deposits of polar-facing and equatorial-facing Martian rock walls in mid-latitude craters in the Northern Hemisphere implies the potential abundance of water ice resources in the shallow surface layers of Mars (Vijayan et al. [109]). Butcher [110] further summarized water ice at mid-latitudes on Mars: water ice is present as regolith and deposits of excess ice with bigger volume; most of the known excess ice deposits were probably formed under climatic conditions within the last few million to 1 billion years.

Currently, in situ spectrometers on Mars are more oriented towards detecting the abundance of water vapor in the Martian atmosphere and analyzing the distribution of water in the Martian atmosphere and climate change. For example, the "Nadir and Occultation for Mars Discovery" spectrometer suite (NOMAD) is designed to investigate the composition of Mar's atmosphere (Vandaele et al. [111]); CRISM is designed to measure spatial and seasonal variations in the atmosphere (Murchie et al. [112]). Spectrographic analysis remains the most convincing evidence for water ice and water-bearing minerals exposed outside or near the surface of Mars.

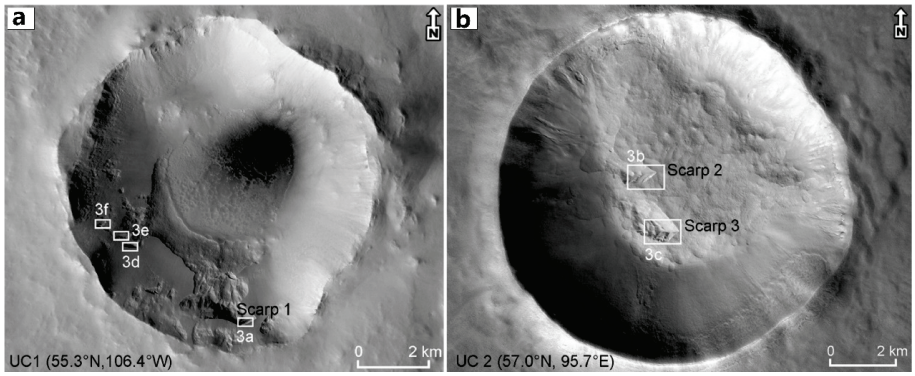


Figure 16. Two unnamed craters in the northern lowlands of Mars, referred to as UC1 and UC2 (adapted from Vijayan et al. [109]). (**a**) Crater UC1 with steep slopes on the polar face wall. Picture 3a/b/c/d/e/f are relative to original paper (Vijayan et al. [109]). (**b**) UC2 crater with steep slopes on the floor.

4.2. Radar Observation

The primary types of radar currently available for observing Mars are Mars-orbiting penetrating radar and the in-situ ground penetrating radar (Zhou et al. [15], Seu et al. [21], Hamran et al. [25]). Those two kinds of radars can detect the thickness and stratification of the Martian soil beneath the surface, as well as the distribution of water ice. MARSIS, SHARAD, and MOSIR are orbiter penetrating radars currently in operation on Mars, and the rovers Perseverance and Zhurong carry the in situ ground-penetrating radars.

MARSIS recently detected bright reflections at the base of SPLDs. Orosei et al. [44] suggested these indicate liquid water due to lowered freezing points from high brine concentrations. Lauro et al. [113] then identified multiple reflections, proposing the presence of multiple liquid water bodies. However, some researchers dispute this, citing temperature and heat flux limitations, suggesting the different dielectric properties of minerals or clay as potential causes (Ojha et al. [114], Bierson et al. [115], Smith et al. [116]). Layered interference within the SPLDs and high-density igneous material with metallic inclusions are also thought to cause (Lalich et al. [117], Grima et al. [118]). Laboratory

experiments have been conducted to measure the dielectric properties of relevant materials under similar conditions, and materials like clay cannot produce such bright reflections (Mattei et al. [119], Cosciotti et al. [120]).

To determine resources available for human exploration of Mars, NASA is promoting the Mapping Project (SWIM), which aims to map the water ice resources on Mars (Bain et al. [121]). The ice resources of the Deuteronilus Mensae region were mapped through SHARAD's radar analysis of glacial and mantle sediments. The results show an average dielectric constant of 3.4 $\pm$ 0.5 for ice and 4.0 $\pm$ 1.0 for mantle sediments in the region. A newly developed radar surface analysis technique was used to compare the mantle and glacier units. It was found that the radar surface analysis on the mantle unit (see Figure 17) resulted in higher return power than on the glacier (Morgan et al. [122]).

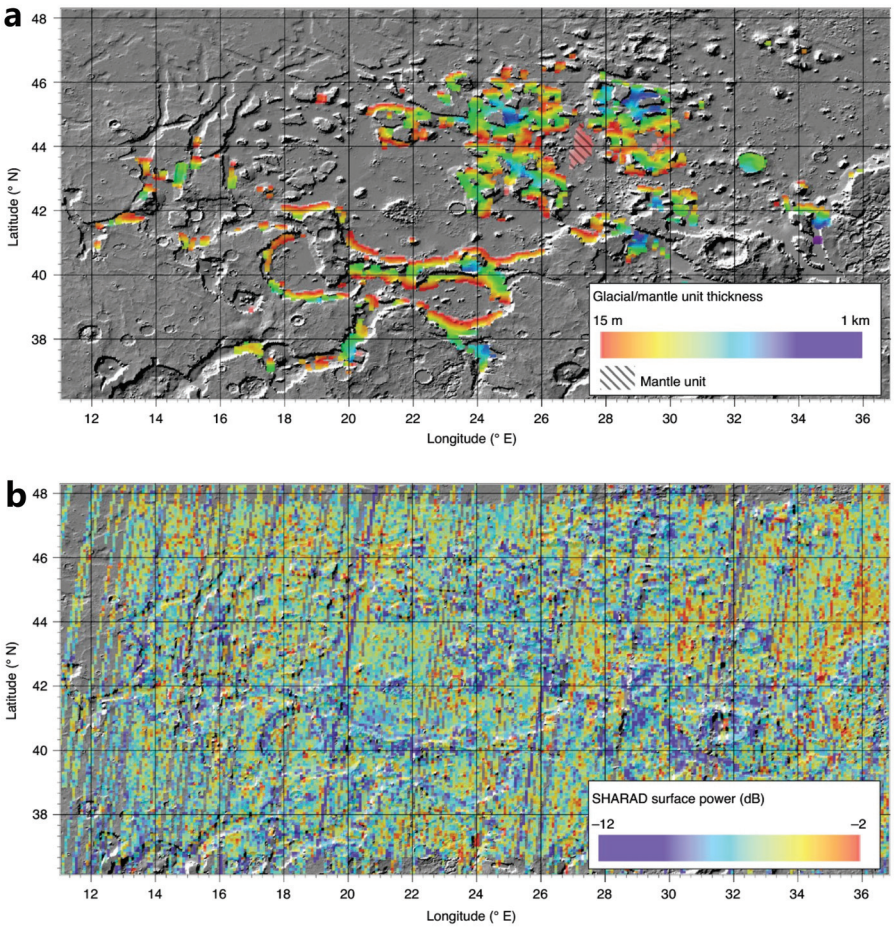


Figure 17. Radar analysis of glacial and mantle deposits within the Deuteronilus Mensae region (adapted from Morgan et al. [122]). (**a**) Depth of glacial sediment and mantle unit to the basement. (**b**) Regional correspondence radar surface analysis. Notably, the low power returns, which are consistent with the presence of ice above 5 m, are associated with the glacier surface.

Regarding the exploration of water ice on Mars, investigations in the polar regions of Mars have revealed extensive ice caps, similar to those at Earth's poles, with thicknesses reaching up to several kilometers (Farrell et al. [123], Grima et al. [124], Levrard et al. [125], Zhou et al. [126], Garvin et al. [127], Putzig et al. [128]). In the southern polar region, due to the thick ice layer, deep reflection signals could not be detected by SHARAD. However, in the region spanning from 310° E to 0° E, MARSIS detected a reflection layer with a thickness of approximately 3.7 km. This layer is interpreted as the boundary between ice-rich south-polar layered deposit materials and the bedrock (Plaut et al. [129]). In the northern polar region, both MARSIS and SHARAD radars detected reflection signals indicating the

boundary between the ice layer and the substrate (Picardi et al. [19], Phillips et al. [130], Putzig et al. [131]). In the mid-latitude regions of Mars, as temperatures rise, surface water ice sublimates, revealing various forms of water ice in different areas, such as glacier deposits in the eastern part of the Hellas basin, abundant water ice in the Deuteronilus Mensae region, and extensive subsurface ice water in the Utopia Planitia (Bramson et al. [43], Stuurman et al. [132], Plaut et al. [133]). Dundas et al. [134] through comparative analysis of high-resolution images combined with radar data analysis, discovered substantial water ice at eight different cliff locations in mid-latitude regions of Mars, extending from depths of 1 to 2 m to over 100 m thick. However, the question of whether water ice exists in lower latitude or equatorial regions of Mars has long intrigued scientists. The Medusae Fossae Formation is a unique, young deposit spanning thousands of kilometers along the equator of Mars, the structural origin of which remains unclear. Both MARSIS and SHARAD radars have probed this region, with Watters et al. [135] calculating an electromagnetic attenuation coefficient of $\sim$0.0048 ± 0.0024 dB/m and a dielectric constant of $\sim$2.9 ± 0.4 using MARSIS data orbit 02896, suggesting that the dielectric properties of this region are similar to pure water ice, although the possibility of dry, low-density materials such as volcanic ash cannot be ruled out. Carter et al. [136] calculated electromagnetic attenuation and dielectric property parameters using SHARAD radar data in this region, essentially obtaining research results similar to those of Watters et al. [135]. Recent studies have reported a significant presence of underground water ice in the Medusae Fossae Formation on Mars Campbell et al. [137], Watters et al. [138], although further research is still needed.

5. Shallow Subsurface of the Perseverance Landing Site

Perseverance is the centerpiece of NASA's 2020 Mars mission (Figure 18), carrying a set of scientific instruments to interpret the geology of the landing site, detect potential biological features, collect and record Martian rock and soil samples, and map the near-surface Martian environment (Farley et al. [46]).

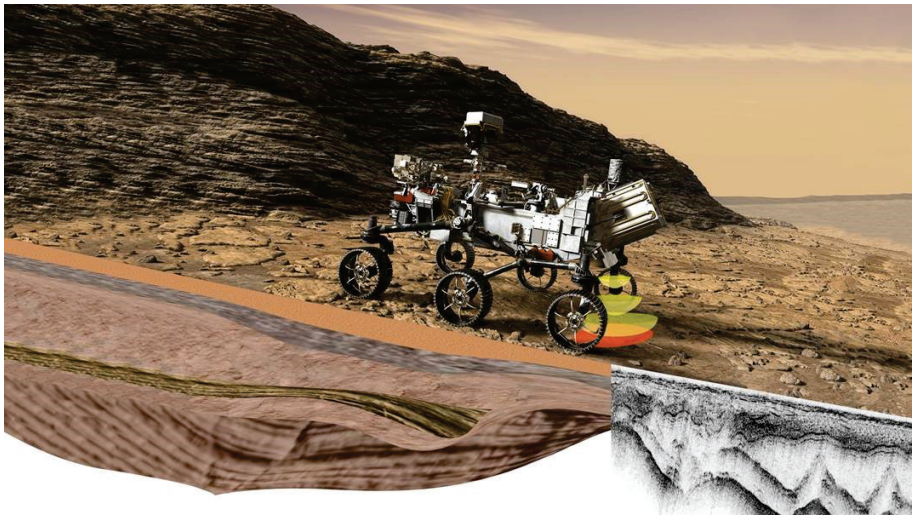


Figure 18. Martian-based ground-penetrating radar, RIMFAX onboard Perseverance rover. Credit from NASA/JPL-Caltech/FFI.

Of these instruments, RIMFAX is a ground-penetrating radar that operates within the frequency range of 150 MHz to 1200 MHz, utilizing frequency-modulated continuous wave technology. It possesses the capability to observe at different depths over a dynamic range of approximately 100 dB (Hamran et al. [14]). Shallow imaging with full bandwidth (effective center frequency of 675 MHz) is used to image the subsurface to a depth of a few meters, while deeper imaging with lower bandwidth (center frequency of 375 MHz) is used for deeper ranges. RIMFAX is designed to study the stratigraphic structure and dielectric properties of the subsurface layers in the landing zone, and the depositional sequences

observed by the radar will provide information for the study of the subsurface stratigraphy of the landing area (Hamran et al. [14,25], Farley et al. [46]).

On 18 February 2021, the Perseverance rover successfully landed in the Jezero crater, which is located in the Nili Fossae region of Mars (Hamran et al. [25]). The Jezero crater, formed in the mid to late Noachian period, has a diameter of about 45 km (Goudge et al. [139]). Orbiter observation identified two river valley networks forming an alluvial fan to the west and one to the north in the Nili Fossae region (Figure 19). They suggested that the climatic conditions in the Noachian Nili Fossae region could have supported the flow and accumulation of liquid water on the surface (Fassett and Head III [140]). This is one of the reasons why Perseverance chose the Jezero crater as its landing site. After the Perseverance rover landed, images of the western sedimentary fan (Figure 20) were obtained using remote microimaging with the Mastcam-Z camera and SuperCam instrument. These images revealed the presence of hills (Kodiak) on the sedimentary fan that was invisible from orbit. The hills were interpreted as erosional remains of an originally more extensive fan deposit, with overall stratigraphic features suggesting an incoming western deltaic system and a long-term retreat of the lake level (Mangold et al. [141]). The presence of inclined strata in the hills can thus be interpreted as evidence that the sedimentary fans here are lacustrine deltas (Mangold et al. [141]).

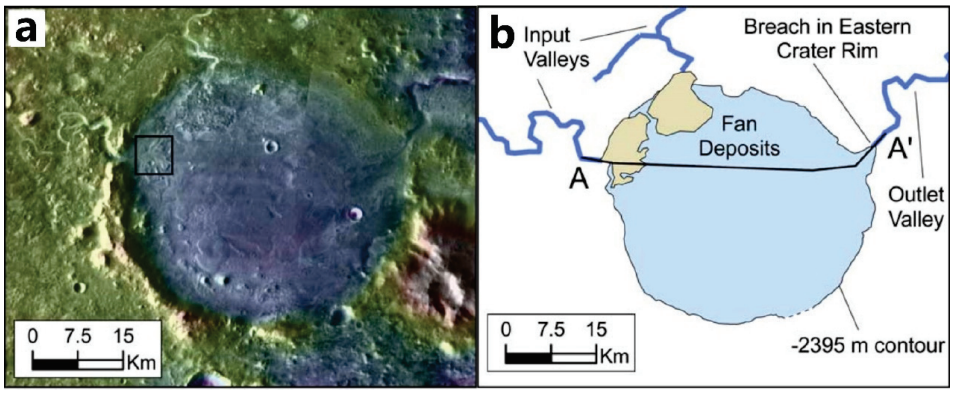


Figure 19. (**a**) Image of the Jezero crater and its alluvial fan, and (**b**) the two inlet valley networks and one outlet valley network of the crater, as identified in a previous study (adapted from Fassett and Head III [140]).

There is an interesting observation regarding the uppermost fan stratigraphy at the Jezero crater, which is composed of boulder conglomerates indicating intermittent high-energy floods. This suggests a shift from continuous hydrological activity in a persistent lacustrine environment to a high-energy, short-duration fluvial flow. Furthermore, Mastcam-Z images and multispectral data of the rocks at the floor of the Jezero crater revealed their morphology, lithology, and mineralogy to be consistent with lightly aqueous altered igneous rocks that have undergone varying degrees of local impact damage. Wind metamorphism has then formed superficial fine-grained soil material containing evidence of pyroxene, olivine, and crystalline hematite (Bell III et al. [142]).

After the Perseverance rover's initial exploration of the Martian subsurface, electromagnetic properties, and bedrock stratigraphy were obtained at a depth of 15 m below the surface of Jezero Crater (Hamran et al. [25]). The radargram was segmented by defining 286 marker points during the nearly 3-kilometer journey of the rover. The travel path (Figure 21a), the radargram (Figure 21b), and the cross-sectional interpretation (Figure 21c) correspond to the journey from sol 201 to 202 (Hamran et al. [25]). Strongly reflective layers that dip from the surface to a depth of about 15 m are associated with erosion-resistant rock outcrops parallel to the Artuby Ridge, and these reflective layers, along with the dip layer represented by the surface ridge, are the Séitah Formation's outermost layer. A zone of lower reflectivity exists between the strongly reflective layers, which is interpreted as a zone of sediment from the dust weathering layer (Hamran et al. [25]).

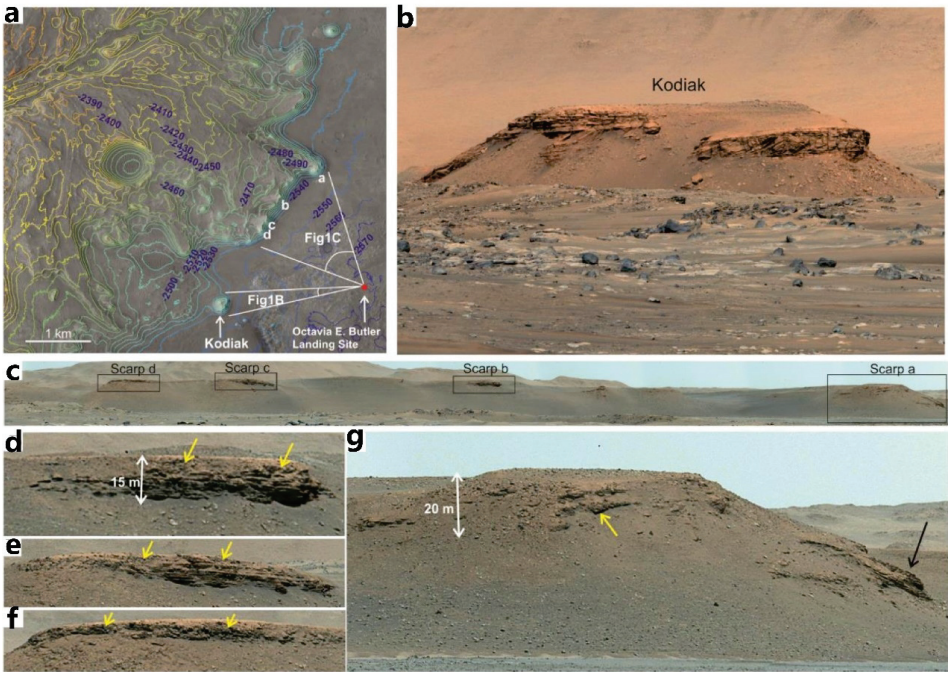


Figure 20. The topography of Jezero Crater as observed by the Perseverance rover (adapted from Mangold et al. [141]). (**a**) The High-Resolution Imaging Science Experiment (HiRISE) data, which display the western fan and the landing site located in the interior of Jezero Crater, are referred to as Octavia E. Butler (indicated by the red dot). Figure 1B and 1C are relative to original paper (Mangold et al. [141]). (**b**) Mastcam-Z photograph of the hills of Kodiak. (**c**) Mastcam-Z image of the landing area delta. Panels (**d**–**g**) show different steep slopes in the landing area. Yellow arrows indicate the location of boulder-rich material. The black arrow indicates an exposure with dipping strata.

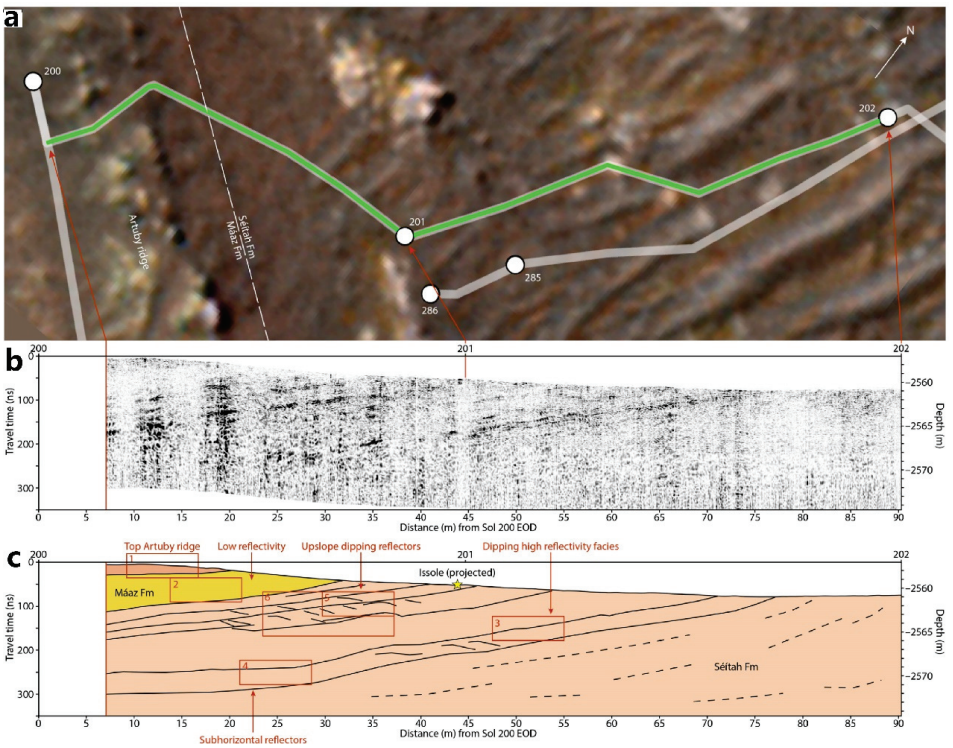


Figure 21. RIMFAX radar image of Perseverance and its geological interpretation (adapted from Hamran et al. [25]). (**a**) Route map of the Mars rover (green line) between sol 201 and 202. (**b**) RIMFAX radar observation image. (**c**) Geological interpretation.

The geological layering detected in the radargram is interpreted as igneous structures associated with the in situ laminated magma bodies (Hamran et al. [25]). At the highest resolution, there are multiple lenticular reflective surfaces with S-shaped profiles between the inclined high-reflectivity layers (Figure 21c), which are interpreted as magmatic flows and shear structures or as cyclic step structures. Radar images show the prevalence of strongly reflective sequences (intrusive strata), which are interpreted as sedimentary layers formed by igneous activity and multiple aqueous depositions, further validating the claim of a paleolake at Jezero Crater. However, the Perseverance radar currently does not find evidence of water ice at the landing zone. Nevertheless, it is anticipated that the rover, traveling longer distances, is expected to find evidence of water ice on the shallow surface layers of Mars (Hamran et al. [25]).

6. Prospect of In Situ Ground-Penetrating Radar on Mars: Detection of Water Ice

The main parameters of the ground-penetrating radar (GPR) radargram for distinguishing subsurface materials are relative permittivity and dielectric loss. The permittivity is complex, where the real part represents the relative permittivity and can be estimated by calculating the propagation velocity of the radar electromagnetic waves in the subsurface materials. The imaginary part represents the loss of electromagnetic waves in the medium, and the dielectric loss tangent is the ratio of the imaginary part to the real part of the complex permittivity. By calculating the values of the relative permittivity and the dielectric loss tangent from the radar echoes, it is possible to infer the subsurface structure and composition on Mars and potentially obtain evidence of the presence of water ice. However, when detecting water ice with radar, it is not possible to determine the uniqueness of the detected substance solely based on the relative permittivity and the dielectric loss of the medium. For instance, water ice typically exhibits a relative permittivity of $\sim$3, with a dielectric loss of less than 10^{-3} (Grima et al. [124], Orosei et al. [143], Nerozzi and Holt [144]), while low-density porous materials (e.g., Martian soil or volcanic ash) have similar those of values to water ice (Watters et al. [135], Carter et al. [136]). Therefore, it is insufficient to determine whether the detected material is water ice or low-density material based solely on these two parameters. It is necessary to approach the identification of water ice from multiple perspectives. This paper suggests several approaches to determine whether subsurface water ice is observed by the ground-penetrating radar:

1. Calculating the relative permittivity and the dielectric loss of the subsurface material based on the radar observations. If the calculated relative permittivity is greater than 4 and the value of the dielectric loss tangent is higher than 10^{-2}, it can be concluded that the detected region almost certainly does not contain water ice but possibly consists of volcanic basalt or other dense deposits.
2. Observing the echo features of the GPR radargram. Typically, water ice has an isotropic composition, which should result in fewer interior echoes and clean echoes with distinct interfaces between the water ice and the underlying layer in the radargram. However, Martian soil is primarily formed by impact cratering and space weathering, and its internal uniformity depends on the duration of weathering. It inevitably contains fragmented rocks internally, which can cause multiple reflections within the radar echoes.
3. Using multi-frequency radar observations. Laboratory studies have shown that the electromagnetic attenuation characteristics differ for different frequencies in basalt sand, pure water ice, and mixtures of water ice with different ratios (Mattei et al. [145]). The attenuation coefficient of electromagnetic waves in basalt sand is directly proportional to frequency, while the attenuation coefficient of water ice is independent of frequency.

In 2013, the Chinese Chang'e-3 mission carried the Moon-based GPR observing the geological stratigraphy of the Mare Imbrium on the nearside of the Moon (Fang et al. [48]). The subsequent Chang'e-4 and Chang'e-5 missions also carried the GPR instruments (Xiao et al. [49], Ding et al. [146,147], Su et al. [148]). Detailed parameters can be found

in Table 1. Currently, two deployed GPRs are operating on Mars: the RoPeR radar on the Zhurong rover (Zhou et al. [15]) and the RIMFAX radar on the Perseverance rover (Hamran et al. [14]). Table 1 contains the detailed parameters of those two radars. The RoPeR radar consists of a high-frequency channel and a low-frequency channel (Zhou et al. [15], Chen et al. [16], Li et al. [26]). The low-frequency channel's center frequency is 55 MHz, with a depth resolution of meters, theoretically capable of penetrating several tens of meters beneath the Martian surface (Zhou et al. [15], Li et al. [26]). The high-frequency channel operates at a center frequency of 1.30 GHz, with a depth resolution in the centimeter, capable of penetrating several meters below the Martian surface (Zhou et al. [15], Chen et al. [16]). RIMFAX has only one channel with a center frequency of 675 MHz and a depth resolution of 10–40 cm, capable of penetrating depths greater than 10 m beneath the Martian surface (Hamran et al. [14]). Additionally, the future ExoMars mission will also carry the WISDOM radar to detect the Martian surface. The center frequency of this radar is 1.75 GHz, with a depth resolution of $\sim$3 cm, capable of penetrating several meters beneath the Martian surface (Ciarletti et al. [47]). It is foreseeable that GPRs will play an important role in current and future surface exploration missions on Mars. This provides opportunities for the detection of subsurface water ice but also poses challenges in distinguishing low-density materials and water ice. Currently, none of the deployed Martian-based GPRs have more than two channels (Table 1). Therefore, to effectively detect shallow subsurface water ice on Mars, our paper suggests that future Martian surface exploration missions can consider GPR systems with more than two frequency channels. Analyzing the radar electromagnetic wave attenuation at different frequencies will be a key breakthrough in proving the presence of water ice detected by the in situ GPR.

7. Conclusions and Perspectives

Detecting water ice on Mars has been a crucial aspect of the Mars exploration project as it directly influences the planet's habitability and the potential for extraterrestrial life. The current approach to detecting Mars water ice is becoming more diverse, incorporating remote sensing photography, radar, measurements by gamma ray spectroscopy and neutron spectrometers, soil analysis, and the recent SWIM mapping project, which is a collaborative effort involving multiple devices. This expansion of detection methods is expected to provide more compelling evidence of Martian water ice soon.

The existence that there could have been liquid water on Mars in the past is becoming an increasingly robust argument, supported by the study of features such as the network of canyons, ancient lakes, oceanic remains, and the presence of hydrated minerals at various locations. Regarding the present presence of water ice on Mars, the widespread detection of hydrogen by spectroscopy suggests the possible abundance of water on the planet. Additionally, recurring slope lines (RSL) that have been observed in recent years are evidence of the current flow of liquid water on the Martian surface. Furthermore, bodies of liquid water have been observed below the ice caps in Mars' polar regions, making it one of the current research hotspots for Mars radar observations (Lauro et al. [113], Orosei et al. [149], Diez [150]).

Currently, Mars exploration primarily targets areas with remnants of paleolakes or oceans. These regions are ideal for investigating the geological evolution of Mars and the distribution of water ice. For instance, the Chryse Planitia, Utopia Plain, and Isidis Plain have numerous clues to the presence of subsurface water ice. The implementation of the SWIM mapping project has also revealed that future Mars radar exploration will likely rely on subsurface radar-based and multi-equipment collaboration.

The Jezero crater, where the Perseverance rover has recently landed, contains alluvial fans indicating paleolakes and strata formed by aqueous deposition. Although the short time available to Perseverance has prevented it from finding evidence of current water ice presence, the area remains ideal for exploring the geological evolution of Mars and the distribution of water ice hidden below the surface. Although Martian-based ground-penetrating radar is set to be deployed on the surface of Mars in 2020, ground-

penetrating radar technology was previously deployed on the nearside of the Moon in 2013 (Xiao et al. [151], Ding et al. [152]). Researchers can adapt from the experience gained through the Moon-based ground-penetrating radar for data processing (Ding et al. [152], Su et al. [153]), the inversion of the subsurface medium's dielectric property parameters (Feng et al. [154], Ding et al. [155], Li et al. [156]), and the construction of numerical models for the subsurface layers of Mars (Ding et al. [157,158]). We believe that with long-term and continuous observation of the Perseverance rover's ground-penetrating radar, as well as advanced data-processing methods and modeling simulations, it is possible to detect the existence of subsurface water ice or liquid water on Mars.

Author Contributions: Conceptualization, C.D.; methodology, N.Z., C.D. and R.O.; software, N.Z., C.D. and R.O.; validation, N.Z., C.D. and R.O.; formal analysis, N.Z., C.D. and Y.S.; investigation, N.Z., C.D. and R.O. resources, C.D., Y.S. and R.O.; data curation, N.Z. and C.D.; writing—original draft preparation, N.Z. and C.D.; writing—review and editing, C.D., Y.S. and R.O.; visualization, C.D.; project administration, C.D., Y.S. and R.O.; supervision, C.D. and R.O. funding acquisition, C.D. All authors have read and agreed to the published version of the manuscript.

Funding: This work is supported by the National Natural Science Foundation of China with Grant No. 42241139, 62227901 and 42004099, the Opening Fund of the Key Laboratory of Lunar and Deep Space Exploration, Chinese Academy of Sciences (No. LDSE202005), the National Innovation and Entrepreneurship Training Program for College Students (No. 202310590016), and Shenzhen Municipal Government Investment Project (No. 2106-440300-04-03-901272).

Acknowledgments: This work has been supported by the team "Searching for Subglacial Water on Mars with Orbiting Ground Penetrating Radars" of the International Space Science Institute (ISSI).

Conflicts of Interest: The authors declare no conflicts of interest.

References

1. Masursky, H. On Mars: Exploration of the Red Planet. *Eos Trans. Am. Geophys. Union* **1985**, *66*, 642–643. [CrossRef]
2. Zheng, Y.C. Mars exploration in 2020. *Innovation* **2020**, *1*, 100036. [CrossRef] [PubMed]
3. Li, C.; Zhang, R.; Yu, D.; Dong, G.; Liu, J.; Geng, Y.; Sun, Z.; Yan, W.; Ren, X.; Su, Y.; et al. China's Mars exploration mission and science investigation. *Space Sci. Rev.* **2021**, *217*, 57. [CrossRef]
4. Boynton, W.; Feldman, W.; Squyres, S.; Prettyman, T.; Bruckner, J.; Evans, L.; Reedy, R.; Starr, R.; Arnold, J.; Drake, D.; et al. Distribution of hydrogen in the near surface of Mars: Evidence for subsurface ice deposits. *Science* **2002**, *297*, 81–85. [CrossRef]
5. McDougal, M.S.; Lasswell, H.D.; Vlasic, I.A.; Smith, J.C. Enjoyment and Aquisition of Resources in Outer Space. *Penn Law Leg. Scholarsh. Repos.* **1962**, *111*, 521.
6. Kieffer, H.H. Mars south polar spring and summer temperatures: A residual CO_2 frost. *J. Geophys. Res.* **1979**, *84*, 8263–8288. [CrossRef]
7. Byrne, S.; Ingersoll, A.P. A sublimation model for Martian south polar ice features. *Science* **2003**, *299*, 1051–1053. [CrossRef]
8. Bibring, J.P.; Langevin, Y.; Poulet, F.; Gendrin, A.; Gondet, B.; Berthé, M.; Soufflot, A.; Drossart, P.; Combes, M.; Bellucci, G.; et al. Perennial water ice identified in the south polar cap of Mars. *Nature* **2004**, *428*, 627–630. [CrossRef]
9. Rennó, N.O.; Bos, B.J.; Catling, D.; Clark, B.C.; Drube, L.; Fisher, D.; Goetz, W.; Hviid, S.F.; Keller, H.U.; Kok, J.F.; et al. Possible physical and thermodynamical evidence for liquid water at the Phoenix landing site. *J. Geophys. Res. Planets* **2009**, *114*, E00E03. [CrossRef]
10. Clifford, S.M.; Parker, T.J. The evolution of the Martian hydrosphere: Implications for the fate of a primordial ocean and the current state of the northern plains. *Icarus* **2001**, *154*, 40–79. [CrossRef]
11. McEwen, A.S.; Hansen, C.; Delamere, W.A.; Eliason, E.; Herkenhoff, K.E.; Keszthelyi, L.; Gulick, V.; Kirk, R.L.; Mellon, M.; Grant, J.A.; et al. A closer look at water-related geologic activity on Mars. *Science* **2007**, *317*, 1706–1709. [CrossRef]
12. Michalski, J.R.; Goudge, T.A.; Crowe, S.A.; Cuadros, J.; Mustard, J.F.; Johnson, S.S. Geological diversity and microbiological potential of lakes on Mars. *Nat. Astron.* **2022**, *6*, 1133–1141. [CrossRef]
13. McEwen, A.S.; Dundas, C.M.; Mattson, S.S.; Toigo, A.D.; Ojha, L.; Wray, J.J.; Chojnacki, M.; Byrne, S.; Murchie, S.L.; Thomas, N. Recurring slope lineae in equatorial regions of Mars. *Nat. Geosci.* **2014**, *7*, 53–58. [CrossRef]
14. Hamran, S.E.; Paige, D.A.; Amundsen, H.E.; Berger, T.; Brovoll, S.; Carter, L.; Damsgård, L.; Dypvik, H.; Eide, J.; Eide, S.; et al. Radar imager for Mars' subsurface experiment—RIMFAX. *Space Sci. Rev.* **2020**, *216*, 1–39. [CrossRef]
15. Zhou, B.; Shen, S.; Lu, W.; Liu, Q.; Tang, C.; Li, S.; Fang, G. The Mars rover subsurface penetrating radar onboard China's Mars 2020 mission. *Earth Planet. Phys.* **2020**, *4*, 345–354. [CrossRef]
16. Chen, R.; Zhang, L.; Xu, Y.; Liu, R.; Bugiolacchi, R.; Zhang, X.; Chen, L.; Zeng, Z.; Liu, C. Martian soil as revealed by ground-penetrating radar at the Tianwen-1 landing site. *Geology* **2023**, *51*, 315–319. [CrossRef]

17. Zhang, L.; Li, C.; Zhang, J.; Zhou, B.; Zhao, Y.Y.S.; Liu, Y.; Di, K.; Mitchell, R.N.; Li, J.; Zhang, Z.; et al. Buried palaeo-polygonal terrain detected underneath Utopia Planitia on Mars by the Zhurong radar. *Nat. Astron.* **2024**, *8*, 69–76. [CrossRef]
18. Picardi, G.; Biccari, D.; Seu, R.; Plaut, J.; Johnson, W.; Jordan, R.; Safaeinili, A.; Gurnett, D.; Huff, R.; Orosei, R.; et al. MARSIS: Mars advanced radar for subsurface and ionosphere sounding. In *Mars Express: The Scientific Payload*; NASA/ADS: Cambridge, MA, USA, 2004; Volume 1240, pp. 51–69.
19. Picardi, G.; Plaut, J.J.; Biccari, D.; Bombaci, O.; Calabrese, D.; Cartacci, M.; Cicchetti, A.; Clifford, S.M.; Edenhofer, P.; Farrell, W.M.; et al. Radar soundings of the subsurface of Mars. *Science* **2005**, *310*, 1925–1928. [CrossRef]
20. Seu, R.; Biccari, D.; Orosei, R.; Lorenzoni, L.; Phillips, R.; Marinangeli, L.; Picardi, G.; Masdea, A.; Zampolini, E. SHARAD: The MRO 2005 shallow radar. *Planet. Space Sci.* **2004**, *52*, 157–166. [CrossRef]
21. Seu, R.; Phillips, R.J.; Biccari, D.; Orosei, R.; Masdea, A.; Picardi, G.; Safaeinili, A.; Campbell, B.A.; Plaut, J.J.; Marinangeli, L.; et al. SHARAD sounding radar on the Mars Reconnaissance Orbiter. *J. Geophys. Res. Planets* **2007**, *112*, E05S05. [CrossRef]
22. Hong, T.; Su, Y.; Fan, M.; Dai, S.; Lv, P.; Ding, C.; Zhang, Z.; Wang, R.; Liu, C.; Du, W.; et al. Flight Experiment Validation of Altitude Measurement Performance of MOSIR on Tianwen-1 Orbiter. *Remote Sens.* **2021**, *13*, 5049. [CrossRef]
23. Hong, T.; Su, Y.; Dai, S.; Zhang, Z.; Du, W.; Liu, C.; Liu, S.; Wang, R.; Ding, C.; Li, C. An Improved Method of Surface Clutter Simulation Based on Orbiting Radar in Tianwen-1 Mars Exploration. *Radio Sci.* **2022**, *57*, e2022RS007491. [CrossRef]
24. Qiu, X.; Ding, C. Radar Observation of the Lava Tubes on the Moon and Mars. *Remote Sens.* **2023**, *15*, 2850. [CrossRef]
25. Hamran, S.E.; Paige, D.A.; Allwood, A.; Amundsen, H.E.; Berger, T.; Brovoll, S.; Carter, L.; Casademont, T.M.; Damsgård, L.; Dypvik, H.; et al. Ground penetrating radar observations of subsurface structures in the floor of Jezero crater, Mars. *Sci. Adv.* **2022**, *8*, eabp8564. [CrossRef] [PubMed]
26. Li, C.; Zheng, Y.; Wang, X.; Zhang, J.; Wang, Y.; Chen, L.; Zhang, L.; Zhao, P.; Liu, Y.; Lv, W.; et al. Layered subsurface in Utopia Basin of Mars revealed by Zhurong rover radar. *Nature* **2022**, *610*, 308–312. [CrossRef] [PubMed]
27. Casademont, T.; Eide, S.; Shoemaker, E.; Liu, Y.; Nunes, D.; Russell, P.; Dypvik, H.; Amundsen, H.; Berger, T.; Hamran, S.E. RIMFAX Ground Penetrating Radar Reveals Dielectric Permittivity and Rock Density of Shallow Martian Subsurface. *J. Geophys. Res. Planets* **2023**, *128*, e2022JE007598. [CrossRef]
28. Herve, Y.; Ciarletti, V.; Le Gall, A.; Corbel, C.; Hassen-Khodja, R.; Benedix, W.; Plettemeier, D.; Humeau, O.; Vieau, A.J.; Lustrement, B.; et al. The WISDOM radar on board the ExoMars 2022 Rover: Characterization and calibration of the flight model. *Planet. Space Sci.* **2020**, *189*, 104939. [CrossRef]
29. Malin, M.; Danielson, G.; Ravine, M.; Soulanille, T. Design and development of the Mars Observer Camera. *Int. J. Imaging Syst. Technol.* **1991**, *3*, 76–91. [CrossRef]
30. Wiens, R.C.; Maurice, S.; Robinson, S.H.; Nelson, A.E.; Cais, P.; Bernardi, P.; Newell, R.T.; Clegg, S.; Sharma, S.K.; Storms, S.; et al. The SuperCam Instrument Suite on the NASA Mars 2020 Rover: Body Unit and Combined System Tests. *Space Sci. Rev.* **2020**, *217*, 4. [CrossRef] [PubMed]
31. Thomas, N.; Cremonese, G.; Ziethe, R.; Gerber, M.; Brändli, M.; Bruno, G.; Erismann, M.; Gambicorti, L.; Gerber, T.; Ghose, K.; et al. The Colour and Stereo Surface Imaging System (CaSSIS) for the ExoMars Trace Gas Orbiter. *Space Sci. Rev.* **2017**, *212*, 1897–1944. [CrossRef]
32. Martínez-Alonso, S.; Mellon, M.T.; Banks, M.E.; Keszthelyi, L.P.; McEwen, A.S.; Team, T.H. Evidence of volcanic and glacial activity in Chryse and Acidalia Planitiae, Mars. *Icarus* **2011**, *212*, 597–621. [CrossRef]
33. Pedersen, G.; Head, J., III; Wilson, L. Formation, erosion and exposure of Early Amazonian dikes, dike swarms and possible subglacial eruptions in the Elysium Rise/Utopia Basin Region, Mars. *Earth Planet. Sci. Lett.* **2010**, *294*, 424–439. [CrossRef]
34. Howari, F.M.; Sharma, M.; Xavier, C.M.; Nazzal, Y.; Alaydaroos, F. Atmospheric, Geomorphological, and Compositional Analysis of Martian Asimov and Hale Craters: Implications for Recurring Slope Lineae. *Front. Astron. Space Sci.* **2022**, *8*, 244. [CrossRef]
35. Pedersen, G.B.M.; Head, J.W. Evidence of widespread degraded Amazonian-aged ice-rich deposits in the transition between Elysium Rise and Utopia Planitia, Mars: Guidelines for the recognition of degraded ice-rich materials. *Planet. Space Sci.* **2010**, *58*, 1953–1970. [CrossRef]
36. Zhou, H.; Feng, X.; Zhou, B.; Dong, Z.; Fang, G.; Zeng, Z.; Liu, C.; Li, Y.; Lu, W. Polarized Orientation Calibration and Processing Strategies for Tianwen-1 Full-Polarimetric Mars Rover Penetrating Radar Data. *IEEE Trans. Geosci. Remote Sens.* **2022**, *60*, 5119914. [CrossRef]
37. Dong, Z.; Feng, X.; Zhou, H.; Liu, C.; Lu, Q.; Liang, W. Assessing the effects of induced field rotation on water ice detection of Tianwen-1 full-polarimetric Mars rover penetrating radar. *IEEE Trans. Geosci. Remote Sens.* **2021**, *60*, 1–13. [CrossRef]
38. Liu, H.; Li, J.; Meng, X.; Zhou, B.; Fang, G.; Spencer, B.F. Discrimination Between Dry and Water Ices by Full Polarimetric Radar: Implications for China's First Martian Exploration. *IEEE Trans. Geosci. Remote Sens.* **2022**, *61*, 5100111. [CrossRef]
39. Grima, C.; Kofman, W.; Herique, A.; Orosei, R.; Seu, R. Quantitative analysis of Mars surface radar reflectivity at 20 MHz. *Icarus* **2012**, *220*, 84–99. [CrossRef]
40. Nouvel, J.F.; Herique, A.; Kofman, W.; Safaeinili, A. Radar signal simulation: Surface modeling with the facet method. *Radio Sci.* **2004**, *39*, RS1013. [CrossRef]
41. Jordan, R.; Picardi, G.; Plaut, J.; Wheeler, K.; Kirchner, D.; Safaeinili, A.; Johnson, W.; Seu, R.; Calabrese, D.; Zampolini, E.; et al. The Mars express MARSIS sounder instrument. *Planet. Space Sci.* **2009**, *57*, 1975–1986. [CrossRef]
42. Xiong, S.; Muller, J.P.; Tao, Y.; Ding, C.; Zhang, B.; Li, Q. Combination of MRO SHARAD and deep-learning-based DTM to search for subsurface features in Oxia Planum, Mars. *Astron. Astrophys.* **2023**, *676*, A16. [CrossRef]

43. Bramson, A.M.; Byrne, S.; Putzig, N.E.; Sutton, S.; Plaut, J.J.; Brothers, T.C.; Holt, J.W. Widespread excess ice in arcadia planitia, Mars. *Geophys. Res. Lett.* **2015**, *42*, 6566–6574. [CrossRef]
44. Orosei, R.; Lauro, S.E.; Pettinelli, E.; Cicchetti, A.; Coradini, M.; Cosciotti, B.; Di Paolo, F.; Flamini, E.; Mattei, E.; Pajola, M.; et al. Radar evidence of subglacial liquid water on Mars. *Science* **2018**, *361*, 490–493. [CrossRef]
45. Fan, M.; Lyu, P.; Su, Y.; Du, K.; Zhang, Q.; Zhang, Z.; Dai, S.; Hong, T. The Mars orbiter subsurface investigation radar (MOSIR) on China's Tianwen-1 mission. *Space Sci. Rev.* **2021**, *217*, 8. [CrossRef]
46. Farley, K.A.; Williford, K.H.; Stack, K.M.; Bhartia, R.; Chen, A.; de la Torre, M.; Hand, K.; Goreva, Y.; Herd, C.D.; Hueso, R.; et al. Mars 2020 mission overview. *Space Sci. Rev.* **2020**, *216*, 1–41. [CrossRef]
47. Ciarletti, V.; Clifford, S.; Plettemeier, D.; Le Gall, A.; Hervé, Y.; Dorizon, S.; Quantin-Nataf, C.; Benedix, W.S.; Schwenzer, S.; Pettinelli, E. The WISDOM radar: Unveiling the subsurface beneath the ExoMars Rover and identifying the best locations for drilling. *Astrobiology* **2017**, *17*, 565–584. [CrossRef]
48. Fang, G.Y.; Zhou, B.; Ji, Y.C.; Zhang, Q.Y.; Shen, S.X.; Li, Y.X.; Guan, H.F.; Tang, C.J.; Gao, Y.Z.; Lu, W. Lunar Penetrating Radar onboard the Chang'e-3 mission. *Res. Astron. Astrophys.* **2014**, *14*, 1607. [CrossRef]
49. Xiao, Y.; Su, Y.; Dai, S.; Feng, J.; Xing, S.; Ding, C.; Li, C. Ground experiments of Chang'e-5 lunar regolith penetrating radar. *Adv. Space Res.* **2019**, *63*, 3404–3419. [CrossRef]
50. Evans, L.G.; Reedy, R.C.; Starr, R.D.; Kerry, K.E.; Boynton, W.V. Analysis of gamma ray spectra measured by Mars Odyssey. *J. Geophys. Res. Planets* **2006**, *111*, E03S04. [CrossRef]
51. Saunders, R.; Arvidson, R.; Badhwar, G.; Boynton, W.; Christensen, P.; Cucinotta, F.; Feldman, W.; Gibbs, R.; Kloss, C.; Landano, M.; et al. 2001 Mars Odyssey mission summary. *Space Sci. Rev.* **2004**, *110*, 1–36. [CrossRef]
52. Mitrofanov, I.; Anfimov, D.; Kozyrev, A.; Litvak, M.; Sanin, A.; Tret'Yakov, V.; Krylov, A.; Shvetsov, V.; Boynton, W.V.; Shinohara, C.; et al. Maps of subsurface hydrogen from the high energy neutron detector, Mars Odyssey. *Science* **2002**, *297*, 78–81. [CrossRef]
53. Mitrofanov, I.; Malakhov, A.; Bakhtin, B.; Golovin, D.; Kozyrev, A.; Litvak, M.; Mokrousov, M.; Sanin, A.; Tretyakov, V.; Vostrukhin, A.; et al. Fine Resolution Epithermal Neutron Detector (FREND) Onboard the ExoMars Trace Gas Orbiter. *Space Sci. Rev.* **2018**, *214*, 86. [CrossRef]
54. Mitrofanov, I.; Malakhov, A.; Djachkova, M.; Golovin, D.; Litvak, M.; Mokrousov, M.; Sanin, A.; Svedhem, H.; Zelenyi, L. The evidence for unusually high hydrogen abundances in the central part of Valles Marineris on Mars. *Icarus* **2022**, *374*, 114805. [CrossRef]
55. Nikiforov, S.; Mitrofanov, I.; Litvak, M.; Lisov, D.; Djachkova, M.; Jun, I.; Tate, C.; Sanin, A. Assessment of water content in martian subsurface along the traverse of the Curiosity rover based on passive measurements of the DAN instrument. *Icarus* **2020**, *346*, 113818. [CrossRef]
56. Mitrofanov, I.G.; Litvak, M.L.; Varenikov, A.B.; Barmakov, Y.N.; Behar, A.; Bobrovnitsky, Y.I.; Bogolubov, E.P.; Boynton, W.V.; Harshman, K.; Kan, E.; et al. Dynamic Albedo of Neutrons (DAN) Experiment Onboard NASA's Mars Science Laboratory. *Space Sci. Rev.* **2012**, *170*, 559–582. [CrossRef]
57. Busch, M.W.; Aharonson, O. Measuring subsurface water distribution using the Dynamic Albedo of Neutrons instrument on Mars Science Laboratory. *Nucl. Instrum. Methods Phys. Res. Sect. A Accel. Spectrometers Detect. Assoc. Equip.* **2008**, *592*, 393–399. [CrossRef]
58. Smith, P.; Tamppari, L.; Arvidson, R.; Bass, D.; Blaney, D.; Boynton, W.; Carswell, A.; Catling, D.; Clark, B.; Duck, T.; et al. Introduction to special section on the phoenix mission: Landing site characterization experiments, mission overviews, and expected science. *J. Geophys. Res. Planets* **2008**, *113*, E00A18. [CrossRef]
59. Bibring, J.P.; Langevin, Y.; Gendrin, A.; Gondet, B.; Poulet, F.; Berthé, M.; Soufflot, A.; Arvidson, R.; Mangold, N.; Mustard, J.; et al. Mars surface diversity as revealed by the OMEGA/Mars Express observations. *Science* **2005**, *307*, 1576–1581. [CrossRef] [PubMed]
60. Nazari-Sharabian, M.; Aghababaei, M.; Karakouzian, M.; Karami, M. Water on Mars—A literature review. *Galaxies* **2020**, *8*, 40. [CrossRef]
61. Stillman, D.E.; Michaels, T.I.; Grimm, R.E. Characteristics of the numerous and widespread recurring slope lineae (RSL) in Valles Marineris, Mars. *Icarus* **2017**, *285*, 195–210. [CrossRef]
62. Ojha, L.; Wilhelm, M.B.; Murchie, S.L.; McEwen, A.S.; Wray, J.J.; Hanley, J.; Massé, M.; Chojnacki, M. Spectral evidence for hydrated salts in recurring slope lineae on Mars. *Nat. Geosci.* **2015**, *8*, 829–832. [CrossRef]
63. Carter, J.; Poulet, F.; Bibring, J.P.; Mangold, N.; Murchie, S. Hydrous minerals on Mars as seen by the CRISM and OMEGA imaging spectrometers: Updated global view. *J. Geophys. Res. Planets* **2013**, *118*, 831–858. [CrossRef]
64. Sun, V.Z.; Milliken, R.E. Ancient and recent clay formation on Mars as revealed from a global survey of hydrous minerals in crater central peaks. *J. Geophys. Res. Planets* **2015**, *120*, 2293–2332. [CrossRef]
65. Wernicke, L.J.; Jakosky, B.M. Martian hydrated minerals: A significant water sink. *J. Geophys. Res. Planets* **2021**, *126*, e2019JE006351. [CrossRef]
66. Ehlmann, B.L.; Edwards, C.S. Mineralogy of the Martian surface. *Annu. Rev. Earth Planet. Sci.* **2014**, *42*, 291–315. [CrossRef]
67. Yen, A.S.; Gellert, R.; Schröder, C.; Morris, R.V.; Bell, J.F., III; Knudson, A.T.; Clark, B.C.; Ming, D.W.; Crisp, J.A.; Arvidson, R.E.; et al. An integrated view of the chemistry and mineralogy of Martian soils. *Nature* **2005**, *436*, 49–54. [CrossRef] [PubMed]

68. Chevrier, V.; Mathé, P.E. Mineralogy and evolution of the surface of Mars: A review. *Planet. Space Sci.* **2007**, *55*, 289–314. [CrossRef]
69. Craddock, R.A.; Howard, A.D. The case for rainfall on a warm, wet early Mars. *J. Geophys. Res. Planets* **2002**, *107*, 21-1–21-36. [CrossRef]
70. Carr, M.H.; Chuang, F.C. Martian drainage densities. *J. Geophys. Res. Planets* **1997**, *102*, 9145–9152. [CrossRef]
71. Hynek, B.M.; Beach, M.; Hoke, M.R. Updated global map of Martian valley networks and implications for climate and hydrologic processes. *J. Geophys. Res. Planets* **2010**, *115*, E09008. [CrossRef]
72. Fassett, C.I.; Head, J.W., III. The timing of Martian valley network activity: Constraints from buffered crater counting. *Icarus* **2008**, *195*, 61–89. [CrossRef]
73. Di Achille, G.; Hynek, B.M. Ancient ocean on Mars supported by global distribution of deltas and valleys. *Nat. Geosci.* **2010**, *3*, 459–463. [CrossRef]
74. Di Achille, G.; Hynek, B.M. Deltas and valley networks on Mars: Implications for a global hydrosphere. In *Lakes on Mars*; Elsevier Science: Amsterdam, The Netherlands, 2010; pp. 223–248.
75. Kamada, A.; Kuroda, T.; Kasaba, Y.; Terada, N.; Nakagawa, H. Global climate and river transport simulations of early Mars around the Noachian and Hesperian boundary. *Icarus* **2021**, *368*, 114618. [CrossRef]
76. Golombek, M.; Grant, J.A.; Parker, T.; Kass, D.; Crisp, J.; Squyres, S.W.; Haldemann, A.; Adler, M.; Lee, W.; Bridges, N.; et al. Selection of the Mars Exploration Rover landing sites. *J. Geophys. Res. Planets* **2003**, *108*, 8072. [CrossRef]
77. Grotzinger, J.P.; Crisp, J.A.; Vasavada, A.R.; Team, M.S. Curiosity's mission of exploration at Gale Crater, Mars. *Elements* **2015**, *11*, 19–26. [CrossRef]
78. Goudge, T.A.; Fassett, C.I.; Head, J.W.; Mustard, J.F.; Aureli, K.L. Insights into surface runoff on early Mars from paleolake basin morphology and stratigraphy. *Geology* **2016**, *44*, 419–422. [CrossRef]
79. Burr, D.; Jacobsen, R.; Lefort, A.; Borden, R.; Peel, S. Summary of Findings from a USGS Scientific Investigations Map (SIM) at 1:500 k of the Aeolis Dorsa Region, Mars. In Proceedings of the 52nd Lunar and Planetary Science Conference, virtual event, 15–19 March 2021; Number 2548, p. 1315.
80. Peel, S.; Burr, D. Lack of evidence for paleolakes in the Aeolis Dorsa region, Mars; A mapping investigation. *Planet. Space Sci.* **2022**, *216*, 105445. [CrossRef]
81. Mouginot, J.; Pommerol, A.; Beck, P.; Kofman, W.; Clifford, S.M. Dielectric map of the Martian northern hemisphere and the nature of plain filling materials. *Geophys. Res. Lett.* **2012**, *39*, L02202. [CrossRef]
82. Liu, C.; Ling, Z.; Wu, Z.; Zhang, J.; Chen, J.; Fu, X.; Qiao, L.; Liu, P.; Li, B.; Zhang, L.; et al. Aqueous alteration of the Vastitas Borealis Formation at the Tianwen-1 landing site. *Commun. Earth Environ.* **2022**, *3*, 280. [CrossRef]
83. Xiao, L.; Huang, J.; Kusky, T.; Head, J.; Zhao, J.; Wang, J.; Wang, L.; Yu, W.; Shi, Y.; Wu, B.; et al. Evidence for marine sedimentary rocks in Utopia Planitia: Zhurong rover observations. *Natl. Sci. Rev.* **2023**, *10*, nwad137. [CrossRef]
84. Carr, M.; Crumpler, L.; Cutts, J.; Greeley, R.; Guest, J.; Masursky, H. Martian impact craters and emplacement of ejecta by surface flow. *J. Geophys. Res.* **1977**, *82*, 4055–4065. [CrossRef]
85. Osinski, G.R. Effect of volatiles and target lithology on the generation and emplacement of impact crater fill and ejecta deposits on Mars. *Meteorit. Planet. Sci.* **2006**, *41*, 1571–1586. [CrossRef]
86. Mantegazza, M.; Spagnuolo, M.G.; Rossi, A.P. Multidisciplinary analysis of pit craters at Hale Crater, Mars. *Icarus* **2023**, *397*, 115495. [CrossRef]
87. McCauley, J.F. Mariner 9 evidence for wind erosion in the equatorial and mid-latitude regions of Mars. *J. Geophys. Res.* **1973**, *78*, 4123–4137. [CrossRef]
88. Wulf, G.; Hergarten, S.; Kenkmann, T. Combined remote sensing analyses and landform evolution modeling reveal the terrestrial Bosumtwi impact structure as a Mars-like rampart crater. *Earth Planet. Sci. Lett.* **2019**, *506*, 209–220. [CrossRef]
89. Carr, M.H.; Masursky, H.; Baum, W.A.; Blasius, K.R.; Briggs, G.A.; Cutts, J.A.; Duxbury, T.; Greeley, R.; Guest, J.E.; Smith, B.A. Preliminary results from the Viking orbiter imaging experiment. *Science* **1976**, *193*, 766–776. [CrossRef]
90. Stewart, S.; O'Keefe, J.; Ahrens, T. The relationship between rampart crater morphologies and the amount of subsurface ice. In Proceedings of the 32nd Lunar and Planetary Science Conference, Houston, TX, USA, 12–16 March 2001; p. 2092.
91. Scott, D.H.; Tanaka, K.L. *Geologic Map of the Western Equatorial Region of Mars*; Citeseer: Forest Grove, OR, USA, 1986; Volume 1.
92. Helfenstein, P.; Mouginis-Mark, P. Morphology and distribution of fractured terrain on Mars. In Proceedings of the Lunar and Planetary Science Conference, Houston, TX, USA, 17–21 March 1980; Volume 11, pp. 429–431.
93. Hiesinger, H.; Head, J.W., III. Characteristics and origin of polygonal terrain in southern Utopia Planitia, Mars: Results from Mars Orbiter Laser Altimeter and Mars Orbiter Camera data. *J. Geophys. Res. Planets* **2000**, *105*, 11999–12022. [CrossRef]
94. McGill, G.E.; Hills, L.S. Origin of giant Martian polygons. *J. Geophys. Res. Planets* **1992**, *97*, 2633–2647. [CrossRef]
95. Pechmann, J.C. The origin of polygonal troughs on the northern plains of Mars. *Icarus* **1980**, *42*, 185–210. [CrossRef]
96. Seibert, N.M.; Kargel, J.S. Small-scale Martian polygonal terrain: Implications for liquid surface water. *Geophys. Res. Lett.* **2001**, *28*, 899–902. [CrossRef]
97. Wenrich, M.; Christensen, P. A formational model for the Martian polygonal terrains. In Proceedings of the Lunar and Planetary Science Conference, Houston, TX, USA, 18–22 March 1996; Volume 27.
98. Mellon, M.T. Small-scale polygonal features on Mars: Seasonal thermal contraction cracks in permafrost. *J. Geophys. Res. Planets* **1997**, *102*, 25617–25628. [CrossRef]

99. Wang, J.; Zhao, J.; Xiao, L.; Peng, S.; Zhang, L.; Zhang, Z.; Gao, A.; Qiao, H.; Wang, L.; Zhang, S.; et al. Recent Aqueous Activity on Mars Evidenced by Transverse Aeolian Ridges in the Zhurong Exploration Region of Utopia Planitia. *Geophys. Res. Lett.* **2023**, *50*, e2022GL101650. [CrossRef]
100. Liu, J.; Li, C.; Zhang, R.; Rao, W.; Cui, X.; Geng, Y.; Jia, Y.; Huang, H.; Ren, X.; Yan, W.; et al. Geomorphic contexts and science focus of the Zhurong landing site on Mars. *Nat. Astron.* **2021**, *6*, 65–71. [CrossRef]
101. Hamilton, C.W.; Fagents, S.A.; Thordarson, T. Lava–ground ice interactions in Elysium Planitia, Mars: Geomorphological and geospatial analysis of the Tartarus Colles cone groups. *J. Geophys. Res. Planets* **2011**, *116*, E03004. [CrossRef]
102. Liu, Y.; Wu, X.; Zhao, Y.Y.S.; Pan, L.; Wang, C.; Liu, J.; Zhao, Z.; Zhou, X.; Zhang, C.; Wu, Y.; et al. Zhurong reveals recent aqueous activities in Utopia Planitia, Mars. *Sci. Adv.* **2022**, *8*, eabn8555. [CrossRef]
103. Zhao, Y.S.; Yu, J.; Wei, G.; Pan, L.; Liu, X.; Lin, Y.; Liu, Y.; Sun, C.; Wang, X.; Wang, J.; et al. In situ analysis of surface composition and meteorology at the Zhurong landing site on Mars. *Natl. Sci. Rev.* **2023**, *10*, nwad056. [CrossRef]
104. Qin, X.; Ren, X.; Wang, X.; Liu, J.; Wu, H.; Zeng, X.; Sun, Y.; Chen, Z.; Zhang, S.; Zhang, Y.; et al. Modern water at low latitudes on Mars: Potential evidence from dune surfaces. *Sci. Adv.* **2023**, *9*, eadd8868. [CrossRef] [PubMed]
105. Williams, J.M.; Scuderi, L.A.; Newsom, H.E. Numerical Analysis of Putative Rock Glaciers on Mount Sharp, Gale Crater, Mars. *Remote Sens.* **2022**, *14*, 1887. [CrossRef]
106. Mellon, M.T.; Jakosky, B.M. Geographic variations in the thermal and diffusive stability of ground ice on Mars. *J. Geophys. Res. Planets* **1993**, *98*, 3345–3364. [CrossRef]
107. Titus, T.N.; Kieffer, H.H.; Christensen, P.R. Exposed water ice discovered near the south pole of Mars. *Science* **2003**, *299*, 1048–1051. [CrossRef] [PubMed]
108. Gourronc, M.; Bourgeois, O.; Mmaoge, D.; Pochat, S.; Bultel, B.; Massmao, M.; Le Deit, L.; Le Moumaolic, S.; Mercier, D. One million cubic kilometers of fossil ice in Valles Marineris: Relicts of a 3.5 Gy old glacial landsystem along the Martian equator. *Geomorphology* **2014**, *204*, 235–255. [CrossRef]
109. Vijayan, S.; Mangold, N.; Bhardwaj, A. Water-Ice Exposing Scarps within the Northern Midlatitude Craters on Mars. *Geophys. Res. Lett.* **2020**, *47*, e2020GL089057.
110. Butcher, F.E.G. *Water Ice at Mid-Latitudes on Mars*; Oxford University Press: Oxford, UK, 2022. [CrossRef]
111. Vandaele, A.C.; Lopez-Moreno, J.J.; Patel, M.R.; Bellucci, G.; Daerden, F.; Ristic, B.; Robert, S.; Thomas, I.R.; Wilquet, V.; Allen, M.; et al. NOMAD, an Integrated Suite of Three Spectrometers for the ExoMars Trace Gas Mission: Technical Description, Science Objectives and Expected Performance. *Space Sci. Rev.* **2018**, *214*, 80. [CrossRef]
112. Murchie, S.; Arvidson, R.; Bedini, P.; Beisser, K.; Bibring, J.P.; Bishop, J.; Boldt, J.; Cavender, P.; Choo, T.; Clancy, R.T.; et al. Compact Reconnaissance Imaging Spectrometer for Mars (CRISM) on Mars Reconnaissance Orbiter (MRO). *J. Geophys. Res. Planets* **2007**, *112*, E05S03. [CrossRef]
113. Lauro, S.E.; Pettinelli, E.; Caprarelli, G.; Guallini, L.; Rossi, A.P.; Mattei, E.; Cosciotti, B.; Cicchetti, A.; Soldovieri, F.; Cartacci, M.; et al. Multiple subglacial water bodies below the south pole of Mars unveiled by new MARSIS data. *Nat. Astron.* **2021**, *5*, 63–70. [CrossRef]
114. Ojha, L.; Karimi, S.; Buffo, J.; Nerozzi, S.; Holt, J.W.; Smrekar, S.; Chevrier, V. Martian Mantle Heat Flow Estimate From the Lack of Lithospheric Flexure in the South Pole of Mars: Implications for Planetary Evolution and Basal Melting. *Geophys. Res. Lett.* **2021**, *48*, e2020GL091409. [CrossRef]
115. Bierson, C.J.; Tulaczyk, S.; Courville, S.W.; Putzig, N.E. Strong MARSIS Radar Reflections from the Base of Martian South Polar Cap May Be Due to Conductive Ice or Minerals. *Geophys. Res. Lett.* **2021**, *48*, e2021GL093880. [CrossRef]
116. Smith, I.B.; Lalich, D.E.; Rezza, C.; Horgan, B.H.N.; Whitten, J.L.; Nerozzi, S.; Holt, J.W. A Solid Interpretation of Bright Radar Reflectors under the Mars South Polar Ice. *Geophys. Res. Lett.* **2021**, *48*, e2021GL093618. [CrossRef]
117. Lalich, D.E.; Hayes, A.G.; Poggiali, V. Explaining Bright Radar Reflections Below The South Pole of Mars without Liquid Water. *Nat. Astron.* **2022**, *6*, 1142–1146. [CrossRef]
118. Grima, C.; Mouginot, J.; Kofman, W.; Hmaorique, A.; Beck, P. The Basal Detectability of an Ice-Covered Mars by MARSIS. *Geophys. Res. Lett.* **2022**, *49*, e2021GL096518. [CrossRef]
119. Mattei, E.; Pettinelli, E.; Lauro, S.E.; Stillman, D.E.; Cosciotti, B.; Marinangeli, L.; Tangari, A.C.; Soldovieri, F.; Orosei, R.; Caprarelli, G. Assessing the role of clay and salts on the origin of MARSIS basal bright reflections. *Earth Planet. Sci. Lett.* **2022**, *579*, 117370. [CrossRef]
120. Cosciotti, B.; Mattei, E.; Brin, A.; Lauro, S.E.; Stillman, D.E.; Cunje, A.; Hickson, D.; Caprarelli, G.; Pettinelli, E. Can Clay Mimic the High Reflectivity of Briny Water Below the Martian SPLD? *J. Geophys. Res. Planets* **2023**, *128*, e2022JE007513. [CrossRef]
121. Bain, Z.; Morgan, G.; Putzig, N.; Campbell, B.; Bramson, A.; Petersen, E.; Mastrogiuseppe, M.; Perry, M.; Baker, D.H.; Smith, I.; et al. MARS Subsurface Water Ice Mapping (SWIM): Radar Surface Reflectivity. In Proceedings of the 50th Lunar and Planetary Science Conference, The Woodlands, TX, USA, 18–22 March 2019.
122. Morgan, G.A.; Putzig, N.E.; Perry, M.R.; Sizemore, H.G.; Bramson, A.M.; Petersen, E.I.; Bain, Z.M.; Baker, D.M.; Mastrogiuseppe, M.; Hoover, R.H.; et al. Availability of subsurface water-ice resources in the northern mid-latitudes of Mars. *Nat. Astron.* **2021**, *5*, 230–236. [CrossRef]
123. Farrell, W.; Plaut, J.; Gurnett, D.; Picardi, G. Detecting sub-glacial aquifers in the north polar layered deposits with Mars Express/MARSIS. *Geophys. Res. Lett.* **2005**, *32*. [CrossRef]

124. Grima, C.; Kofman, W.; Mouginot, J.; Phillips, R.J.; Hérique, A.; Biccari, D.; Seu, R.; Cutigni, M. North polar deposits of Mars: Extreme purity of the water ice. *Geophys. Res. Lett.* **2009**, *36*, L03203. [CrossRef]
125. Levrard, B.; Forget, F.; Montmessin, F.; Laskar, J. Recent ice-rich deposits formed at high latitudes on Mars by sublimation of unstable equatorial ice during low obliquity. *Nature* **2004**, *431*, 1072–1075. [CrossRef] [PubMed]
126. Zhou, J.; Ding, C.; Xiong, S.; Su, Y.; Li, J.; Chen, M.; Dai, S. Radar Observations of Liquid Water in the South Polar Region of Mars: Indications from Astrobiology Perspectives. *Universe* **2024**, *10*, 43. [CrossRef]
127. Garvin, J.B.; Soare, R.J.; Hepburn, A.J.; Koutnik, M.; Godin, E. Ice Exploration on Mars: Where to and when? In *Ices in the Solar-System*; Elsevier: Amsterdam, The Netherlands, 2024; pp. 193–219.
128. Putzig, N.E.; Morgan, G.A.; Sizemore, H.G.; Hollibaugh Baker, D.M.; Petersen, E.I.; Pathare, A.V.; Dundas, C.M.; Bramson, A.M.; Courville, S.W.; Perry, M.R.; et al. Ice resource mapping on Mars. In *Handbook of Space Resources*; Springer: New York, NY, USA, 2023; pp. 583–616.
129. Plaut, J.J.; Picardi, G.; Safaeinili, A.; Ivanov, A.B.; Milkovich, S.M.; Cicchetti, A.; Kofman, W.; Mouginot, J.; Farrell, W.M.; Phillips, R.J.; et al. Subsurface radar sounding of the south polar layered deposits of Mars. *Science* **2007**, *316*, 92–95. [CrossRef] [PubMed]
130. Phillips, R.J.; Zuber, M.T.; Smrekar, S.E.; Mellon, M.T.; Head, J.W.; Tanaka, K.L.; Putzig, N.E.; Milkovich, S.M.; Campbell, B.A.; Plaut, J.J.; et al. Mars north polar deposits: Stratigraphy, age, and geodynamical response. *Science* **2008**, *320*, 1182–1185. [CrossRef] [PubMed]
131. Putzig, N.E.; Seu, R.; Morgan, G.A.; Smith, I.B.; Campbell, B.A.; Perry, M.R.; Mastrogiuseppe, M.; the MRO SHARAD team. Science results from sixteen years of MRO SHARAD operations. *Icarus* **2023**, *2023*, 115715. [CrossRef]
132. Stuurman, C.; Osinski, G.; Holt, J.; Levy, J.; Brothers, T.; Kerrigan, M.; Campbell, B. SHARAD detection and characterization of subsurface water ice deposits in Utopia Planitia, Mars. *Geophys. Res. Lett.* **2016**, *43*, 9484–9491. [CrossRef]
133. Plaut, J.J.; Safaeinili, A.; Holt, J.W.; Phillips, R.J.; Head, J.W., III; Seu, R.; Putzig, N.E.; Frigeri, A. Radar evidence for ice in lobate debris aprons in the mid-northern latitudes of Mars. *Geophys. Res. Lett.* **2009**, *36*, L02203. [CrossRef]
134. Dundas, C.M.; Bramson, A.M.; Ojha, L.; Wray, J.J.; Mellon, M.T.; Byrne, S.; McEwen, A.S.; Putzig, N.E.; Viola, D.; Sutton, S.; et al. Exposed subsurface ice sheets in the Martian mid-latitudes. *Science* **2018**, *359*, 199–201. [CrossRef]
135. Watters, T.R.; Campbell, B.; Carter, L.; Leuschen, C.J.; Plaut, J.J.; Picardi, G.; Orosei, R.; Safaeinili, A.; Clifford, S.M.; Farrell, W.M.; et al. Radar sounding of the Medusae Fossae Formation Mars: Equatorial ice or dry, low-density deposits? *Science* **2007**, *318*, 1125–1128. [CrossRef]
136. Carter, L.M.; Campbell, B.A.; Watters, T.R.; Phillips, R.J.; Putzig, N.E.; Safaeinili, A.; Plaut, J.J.; Okubo, C.H.; Egan, A.F.; Seu, R.; et al. Shallow radar (SHARAD) sounding observations of the Medusae Fossae Formation, Mars. *Icarus* **2009**, *199*, 295–302. [CrossRef]
137. Campbell, B.A.; Watters, T.R.; Morgan, G.A. Dielectric properties of the medusae fossae formation and implications for ice content. *J. Geophys. Res. Planets* **2021**, *126*, e2020JE006601. [CrossRef]
138. Watters, T.R.; Campbell, B.A.; Leuschen, C.J.; Morgan, G.A.; Cicchetti, A.; Orosei, R.; Plaut, J.J. Evidence of Ice-Rich Layered Deposits in the Medusae Fossae Formation of Mars. *Geophys. Res. Lett.* **2024**, *51*, e2023GL105490. [CrossRef]
139. Goudge, T.A.; Mustard, J.F.; Head, J.W.; Fassett, C.I.; Wiseman, S.M. Assessing the mineralogy of the watershed and fan deposits of the Jezero crater paleolake system, Mars. *J. Geophys. Res. Planets* **2015**, *120*, 775–808. [CrossRef]
140. Fassett, C.I.; Head, J.W., III. Fluvial sedimentary deposits on Mars: Ancient deltas in a crater lake in the Nili Fossae region. *Geophys. Res. Lett.* **2005**, *32*. [CrossRef]
141. Mangold, N.; Gupta, S.; Gasnault, O.; Dromart, G.; Tarnas, J.; Sholes, S.; Horgan, B.; Quantin-Nataf, C.; Brown, A.; Le Mouélic, S.; et al. Perseverance rover reveals an ancient delta-lake system and flood deposits at Jezero crater, Mars. *Science* **2021**, *374*, 711–717. [CrossRef]
142. Bell, J.F., III; Maki, J.N.; Alwmark, S.; Ehlmann, B.L.; Fagents, S.A.; Grotzinger, J.P.; Gupta, S.; Hayes, A.; Herkenhoff, K.E.; Horgan, B.H.; et al. Geological, multispectral, and meteorological imaging results from the Mars 2020 Perseverance rover in Jezero crater. *Sci. Adv.* **2022**, *8*, eabo4856. [CrossRef]
143. Orosei, R.; Rossi, A.P.; Cantini, F.; Caprarelli, G.; Carter, L.M.; Papiano, I.; Cartacci, M.; Cicchetti, A.; Noschese, R. Radar sounding of Lucus Planum, Mars, by MARSIS. *J. Geophys. Res. Planets* **2017**, *122*, 1405–1418. [CrossRef]
144. Nerozzi, S.; Holt, J. Buried ice and sand caps at the north pole of Mars: Revealing a record of climate change in the cavi unit with SHARAD. *Geophys. Res. Lett.* **2019**, *46*, 7278–7286. [CrossRef]
145. Mattei, E.; Lauro, S.; Vannaroni, G.; Cosciotti, B.; Bella, F.; Pettinelli, E. Dielectric measurements and radar attenuation estimation of ice/basalt sand mixtures as martian Polar Caps analogues. *Icarus* **2014**, *229*, 428–433. [CrossRef]
146. Ding, C.; Xiao, Z.; Wu, B.; Li, Y.; Prieur, N.C.; Cai, Y.; Su, Y.; Cui, J. Fragments delivered by secondary craters at the Chang'E-4 landing site. *Geophys. Res. Lett.* **2020**, *47*, e2020GL087361. [CrossRef]
147. Ding, C.; Su, Y.; Lei, Z.; Zhang, Z.; Song, M.; Liu, Y.; Wang, R.; Li, Q.; Li, C.; Huang, S. Electromagnetic Signal Attenuation Characteristics in the Lunar Regolith Observed by the Lunar Regolith Penetrating Radar (LRPR) Onboard the Chang'E-5 Lander. *Remote Sens.* **2022**, *14*, 5189. [CrossRef]
148. Su, Y.; Wang, R.; Deng, X.; Zhang, Z.; Zhou, J.; Xiao, Z.; Ding, C.; Li, Y.; Dai, S.; Ren, X.; et al. Hyperfine structure of regolith unveiled by Chang'E-5 lunar regolith penetrating radar. *IEEE Trans. Geosci. Remote Sens.* **2022**, *60*, 1–14. [CrossRef]

149. Orosei, R.; Ding, C.; Fa, W.; Giannopoulos, A.; Hérique, A.; Kofman, W.; Lauro, S.E.; Li, C.; Pettinelli, E.; Su, Y.; et al. The global search for liquid water on Mars from orbit: Current and future perspectives. *Life* **2020**, *10*, 120. [CrossRef] [PubMed]
150. Diez, A. Liquid water on Mars. *Science* **2018**, *361*, 448–449. [CrossRef]
151. Xiao, L.; Zhu, P.; Fang, G.; Xiao, Z.; Zou, Y.; Zhao, J.; Zhao, N.; Yuan, Y.; Qiao, L.; Zhang, X.; et al. A young multilayered terrane of the northern Mare Imbrium revealed by Chang'E-3 mission. *Science* **2015**, *347*, 1226–1229. [CrossRef]
152. Ding, C.; Li, C.; Xiao, Z.; Su, Y.; Xing, S.; Wang, Y.; Feng, J.; Dai, S.; Xiao, Y.; Yao, M. Layering structures in the porous material beneath the Chang'e-3 landing site. *Earth Space Sci.* **2020**, *7*, e2019EA000862. [CrossRef]
153. Su, Y.; Xing, S.; Feng, J.; Dai, S.; Ding, C.; Xiao, Y.; Zhang, H.; Zhao, S.; Xue, X.; Zhang, X.; et al. Data Processing and Primary results of Lunar Penetrating Radar on Board the Chinese Yutu Rover. In Proceedings of the EGU General Assembly Conference Abstracts, Vienna, Austria, 12–17 April 2015; p. 4282.
154. Feng, J.; Su, Y.; Ding, C.; Xing, S.; Dai, S.; Zou, Y. Dielectric properties estimation of the lunar regolith at CE-3 landing site using lunar penetrating radar data. *Icarus* **2017**, *284*, 424–430. [CrossRef]
155. Ding, C.; Xiao, Z.; Su, Y.; Zhao, J.; Cui, J. Compositional variations along the route of Chang'e-3 Yutu rover revealed by the lunar penetrating radar. *Prog. Earth Planet. Sci.* **2020**, *7*, 1–11. [CrossRef]
156. Li, C.; Su, Y.; Pettinelli, E.; Xing, S.; Ding, C.; Liu, J.; Ren, X.; Lauro, S.E.; Soldovieri, F.; Zeng, X.; et al. The Moon's farside shallow subsurface structure unveiled by Chang'E-4 Lunar Penetrating Radar. *Sci. Adv.* **2020**, *6*, eaay6898. [CrossRef]
157. Ding, C.; Su, Y.; Xing, S.; Dai, S.; Xiao, Y.; Feng, J.; Liu, D.; Li, C. Numerical simulations of the lunar penetrating radar and investigations of the geological structures of the lunar regolith layer at the Chang'E 3 landing site. *Int. J. Antennas Propag.* **2017**, *2017*, 3013249. [CrossRef]
158. Ding, C.; Xiong, S.; Li, J.; Su, Y.; Huang, S. Yutu-2 radar observation of the lunar regolith heterogeneity at the Chang'E-4 landing site. *Astron. Astrophys.* **2022**, *664*, A43. [CrossRef]

Disclaimer/Publisher's Note: The statements, opinions and data contained in all publications are solely those of the individual author(s) and contributor(s) and not of MDPI and/or the editor(s). MDPI and/or the editor(s) disclaim responsibility for any injury to people or property resulting from any ideas, methods, instructions or products referred to in the content.

remote sensing

MDPI

Review

Martian Dust Storms: Reviews and Perspective for the Tianwen-3 Mars Sample Return Mission

Fei He [1,2,*], Zhaojin Rong [1,2], Zhaopeng Wu [1], Jiawei Gao [1,2], Kai Fan [1], Xu Zhou [1], Limei Yan [1,2], Yuqi Wang [1] and Yong Wei [1,2]

[1] Key Laboratory of Earth and Planetary Physics, Institute of Geology and Geophysics, Chinese Academy of Sciences, Beijing 100029, China; rongzhaojin@mail.iggcas.ac.cn (Z.R.); wuzp@mail.iggcas.ac.cn (Z.W.); gaojw@mail.iggcas.ac.cn (J.G.); kaif@mail.iggcas.ac.cn (K.F.); zx0601@mail.iggcas.ac.cn (X.Z.); lmyan@mail.iggcas.ac.cn (L.Y.); wangyq@mail.iggcas.ac.cn (Y.W.); weiy@mail.iggcas.ac.cn (Y.W.)

[2] College of Earth and Planetary Sciences, University of Chinese Academy of Sciences, Beijing 100049, China

* Correspondence: hefei@mail.iggcas.ac.cn

Abstract: Dust storms play a crucial role in the climate system and the space environment of Mars, significantly impacting human exploration activities on the planet. The Martian dust storms exhibit significant regional, seasonal and interannual variations due to various controlling factors such as large-scale atmospheric circulation, varying solar radiation forcing, and Martial orbital and rotational motions and their coupling to the atmospheric dynamics. This paper aims to review current understandings of Martian dust storms. This paper begins by elucidating the basic properties of dust storms, their driving mechanisms, and their impacts on atmospheric dynamics, atmospheric electric property, space environment, topography, and Mars explorations. The paper then introduces the observation methods on different platforms, including orbiters and landers/rovers, along with datasets constructed based on these historical observations of Martian dust storms. Finally, we propose dust storm monitoring and predicting for the upcoming Chinese Tianwen-3 Mars sample return mission. It concludes by depicting the future research topics aimed at systematically understanding Martian dust storms.

Keywords: Mars; dust storm; remote sensing; monitor and prediction; tianwen-3 mission

1. Introduction

Mars is the fourth terrestrial planet and the second smallest planet in the solar system after Mercury. It is known as the "Red Planet" due to its surface being covered with hematite. The radius of Mars is 3390 km, significantly smaller than Earth. The aphelion and perihelion of the Mars orbit are 1.666 AU (1 AU $\approx 1.5 \times 10^8$ km) and 1.381 AU, respectively, with an eccentricity of 0.933941 and a sidereal orbital period of 686.98 Earth days. Mars lacks a global dipolar magnetic field [1] and has lost most of its atmosphere to space over billions of years [2]. Presently, Mars is frigid and arid because most of its water has escaped through various processes influenced by several factors [3–9], such as solar wind variations, solar extreme ultraviolet (EUV) radiations, and dust storms.

The lack of a protective global dipolar magnetic field leads to persistent escape of the Martian atmosphere, resulting in an extremely thin and cold atmosphere with surface atmospheric pressure only reaching 0.6% that of Earth's. Dominated by carbon dioxide (95.3%) [10], the Martian atmosphere undergoes significant seasonal variations due to the large difference between the aphelion and perihelion of Mars orbit, which generates clear seasonal variations in climate and environment. The seasonal cycle on Mars results in changes in surface atmospheric pressure by up to 20% due to sublimation and condensation of carbon dioxide in polar regions [11]. Additionally, the high eccentricity of Mars' orbit causes dramatic variation in solar radiation, fluctuating by as much as 30% during a

Martian year (MY) [12]. Various textbooks, e.g. [10,13,14] and reviews, e.g. [15,16], offer detailed insights into satellite observations and understanding of the Martian atmosphere.

Mars' surface features include river channels, canyons, ravines, and alluvial plains. Research suggests that Mars may have been habitable around 3 billion years ago, with a global dipole magnetic field, abundant liquid water, and a dense atmosphere [17]. This history makes Mars a focal point for human planetary exploration driven by the search for extraterrestrial life. Over fifty missions, including orbiters, landers, and rovers, have significantly advanced our understanding of Mars' environment [18,19]. Surface missions face challenges due to Martian environmental factors. Among Mars' seasonal variations, dust storms are particularly prominent and significantly influence Martian climate, surface conditions, space environment, and atmospheric escape [20]. Dust storms have become the biggest threat to missions landing on the surface of Mars.

Extensive reviews on Martian dust storms, e.g. [21–25], provide valuable insights. This paper focuses on summarizing current knowledge of Martian dust storms in order to guide China's Tianwen-3 Mars sample return mission. It aims to offer comprehensive information for scientific researchers and mission planners, focusing on dust storm properties, driving mechanisms, impacts, detection principles and methods. Section 2 introduces basic dust storm properties, reviews driving mechanisms, and summarizes impacts on Mars' surface and space environment. Section 3 covers the history of observing dust storms on Mars and outlines observation principles and methods (including orbiters and landers/rovers). Section 4 includes statistical predictions of dust activity for Tianwen-3 and discusses our proposed dust storm monitoring scheme, which was officially accepted for the mission. Concluding remarks are provided in Section 5.

2. Martian Dust Storms

Dust storms on Mars are the most dramatic activity in its climate system, involving both the surface and atmosphere, and exhibit significant seasonal variations. Each Martian year, particularly as Mars approaches its southern summer solstice, local, regional, and sometimes global dust storms (Figure 1) become highly active. In this section, we will review the fundamental properties of dust storms and their impacts on the Martian environment.

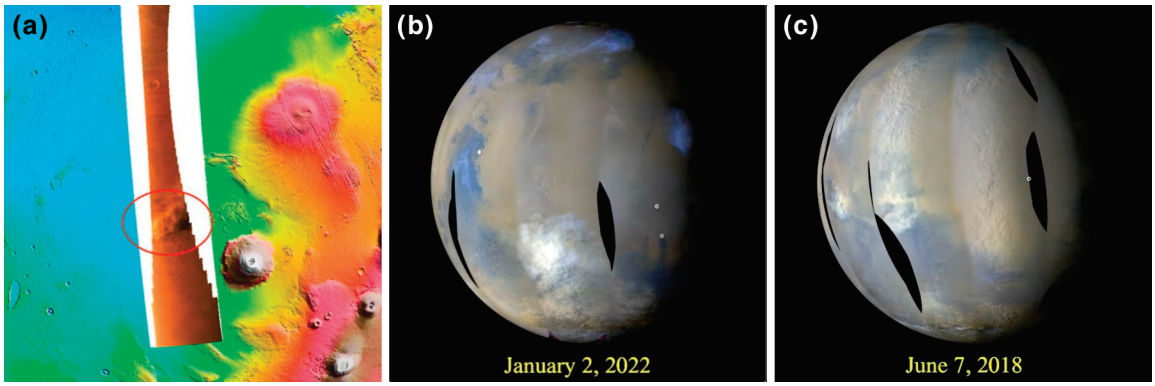


Figure 1. Illustrations of local, regional, and global dust storms. (**a**) A local dust storm in the Amazonis Planitia near Olympus Mountain was captured by the Moderate Resolution Imaging Camera (MoRIC) onboard the Tianwen-1 mission on 6 January 2022. The red circle denotes the local dust storm. (**b**) A regional dust storm in the southern hemisphere was captured by the Mars Color Imager (MARCI) onboard Mars Reconnaissance Orbiter (MRO) [26]. (**c**) A global dust storm in 2018 was captured by the MARCI onboard MRO [27].

2.1. Basic Properties of Dust Storms

Martian dust storms can be categorized based on different criteria. According to their scales, they are classified as local dust storms, regional dust storms, and global dust storms [22,28], as depicted in Figure 1. A regional dust storm is defined by dust events

covering an area $\geq 1.6 \times 10^6$ km^2 and lasting longer than 2 days. Dust lofted during these events can travel significant distances, sometimes encircling Mars within a latitude zone and settling far from its source region. Smaller or shorter-duration events are classified as local dust storms, typically lasting less than 3 days. Global dust storms, known as planet-encircling dust storms, sweep the entire Martian globe. These storms rapidly expand and merge with multiple local and regional dust storms, often lasting tens of days.

Local dust storms can occur on Mars in any season at any location, although certain regional patterns have been identified [29–32]. Regional dust storms are particularly common during southern spring and summer seasons, occurring within a solar longitude range (L_S) between 180° and 360° (L_S = 0°, 90°, 180°, and 270° are defined as northern hemisphere spring equinox, summer solstice, autumn equinox, and winter solstice, respectively.), except during the solstitial pause period. These storms often concentrated in specific regions, such as Acidalia, Utopia, Arcadia, and Hellas [29]. Global dust storms, on the other hand, are unpredictable and non-periodic events in terms of both timing and location. Only seven confirmed global dust storms were observed in the years 1956, 1971, 1973, 1977, 2001, 2007, and 2018 [33].

In terms of seasonal and timescale characteristics, Martian regional-scale dust storms can be classified into three types: A, B and C [34], as illustrated in MY 36 shown in Figure 2a. The data presented in Figure 2 are derived from the global maps of the 9.3 μm absorption column dust optical depth (CDOD) database compiled by Montabone et al. [35,36] (refer to Section 3.3 for more details). It is important to note that types A, B, or C do not refer to specific dust storms but rather phases during the entire storm season, each potentially resulting from multiple regional and/or global dust storms. These storms are most active during the southern spring and summer seasons (L_S range 180°~360°), while the southern autumn and winter seasons (L_S range 0°~180°) generally experience lower dust activity levels.

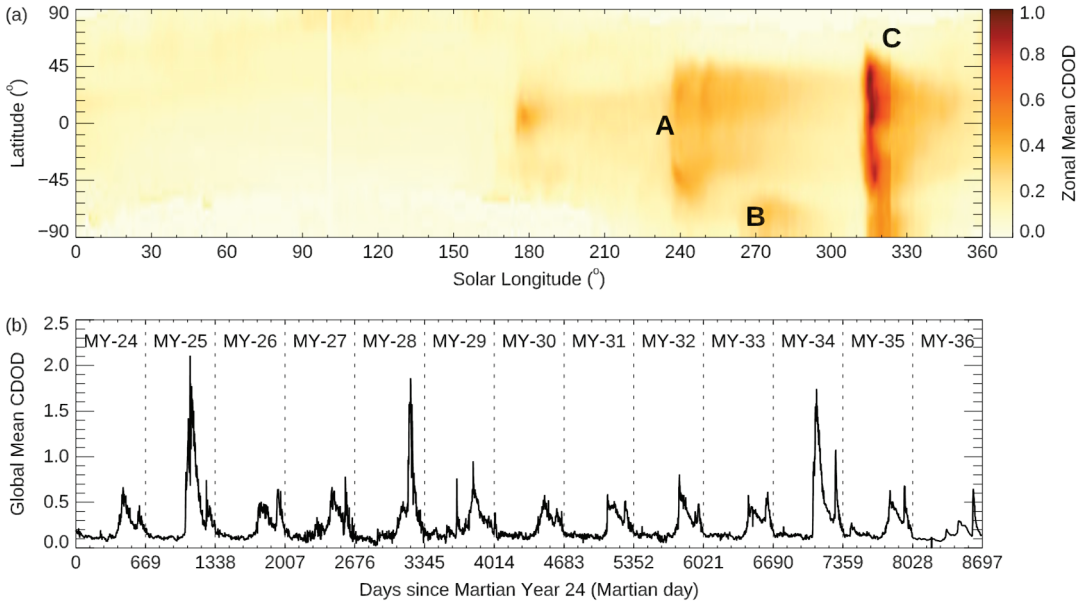


Figure 2. Variation of absorption column dust optical depth (CDOD) on Mars from MY 24 to 36. (**a**) An example of a zonal mean is 9.3 μm CDOD in MY 36. The three types of dust storms are denoted by A, B, and C. (**b**) Temporal variations of the global mean CDOD from MY 24 to 26.

Type A dust storms typically intensify in the middle and low latitudes between L_S = 180° and L_S = 270°, covering more than two-thirds of Mars' latitude and lasting approximately four months. Type A dust storms are characterized by their longer duration and broader coverage, with occasional evolution into global dust storms in certain Martian years (e.g., 2001, 2007, 2018). Near the end of a Type A dust storm, close to the summer solstice in the southern hemisphere, Type B dust storms erupt primarily in the south-polar region of Mars, lasting about two months. These storms are predominately local and

regional, confined mainly to latitudes near the South Pole (south of 60° S). Following the conclusion of Type A and B dust storms, Type C dust storms typically occur around L_S = 330° in the middle and low latitudes, lasting one to two months. Type C dust storms may also develop into global dust storms that cease before the southern autumn equinox, marking a return to a calmer period and beginning a new cycle in the next Martian year.

Overall, Martian dust activity follows a seasonal pattern as described above. For example, Fourier analysis of long-term global mean CDOD during MY 24–36 (Figure 2b) reveals a precise periodicity of 668.615 days. However, there are significant irregular interannual variations in the intensity, frequency, onset, and duration of dust storms, as well as their impact range. This variability presents substantial challenges in predicting Martian dust storms. Furthermore, accurately quantifying the contribution of dust storms to atmospheric suspended dust levels indicated by CDOD remains challenging due to factors other than dust storms (e.g., dust devils, convections, gusts) contributing to atmospheric dust levels.

The effective radius of lofted dust particles on Mars is typically around 1.5 μm, but it varies depending on the intensity of dust storms. Weak local dust storms near the Martian northern summer solstice have particles averaging about ~1 μm in size, whereas, during regional and global dust storms in the southern spring and summer, particle size can increase to approximately ~2 μm, as observed by the Curiosity rover [37,38]. Generally, the effective radius of dust particles correlates with atmospheric dust content, with larger particles prevalent during the southern hemisphere's spring and summer compared to autumn and winter [39–41].

In the vertical direction (10–70 km height range), the distribution of dust particle sizes in the Martian atmosphere exhibits a bimodal pattern: the primary peak ranges from 0.7 to 1.2 μm, and a secondary peak ranges from 0.04 to 0.07 μm [42], as observed by the Spectroscopy for the Investigation of the Characteristics of the Atmosphere of Mars (SPICAM) instrument on Mars Express [43]. The altitude-dependent distribution of particle sizes significantly influences how incoming solar radiation is absorbed, scattered, and re-radiated, thereby impacting the radiative balance. These effects play a crucial role in large-scale atmospheric circulation and climate variability on Mars [44,45]. During the dust season, particularly following the onset of Type A dust storms, smaller dust particles tend to dominate the lower atmosphere and persist longer [25]. A higher proportion of smaller particles can intensify heating rates, temperatures, westerly winds, and meridional winds associated with the Hadley circulation [46]. Changes in meridional circulation due to adiabatic heating further contribute to temperature fluctuations on Mars [45].

2.2. Driving Mechanisms of Dust Storms

The interannual variability of dust storms during the southern hemisphere summer season significantly influences the seasonal climate on Mars. Therefore, it is crucial to understand the driving mechanisms behind these dust storms in order to comprehend Martian climate dynamics. In this section, we review the current understanding of the mechanisms responsible for dust lifting and the factors contributing to seasonal and interannual variability in dust storms.

The fundamental prerequisite for a dust storm is dust lifting. When Mariner 9 arrived at Mars in 1971, it observed the decaying phase of a global encircling dust storm from Martian orbit [47]. Subsequent studies have focused on elucidating the driving mechanisms of these storms. Leovy et al. [48] reviewed early work and proposed an energy balance model. During the southern hemisphere spring, local dust storms are initially generated by phenomena such as dust devils and cyclonic dust storms [49], intense surface winds in baroclinic regions [50], or strong mass outflow wind [51], which accumulate dust in southern, middle, and subtropical latitudes. Intense insolation, low static stability, and high atmospheric absorptivity and emissivity facilitate strong meridional circulations that can trigger global storm events [48]. Observations at the Viking Lander #1 suggested that

local dust storms can also be triggered by baroclinic wave activity with a threshold wind speed of 25–30 m s^{-1} [52].

Dust particles are lifted through exchanges of momentum and heat between the Martian surface and atmosphere. Gierasch and Goody [49] initially proposed the existence of an axisymmetric swirling flow field around a central dusty core, where solar radiation heating strengthens horizontal temperature gradients, accelerating the cyclonic swirling flow inward into the core. Ryan and Lucich [53] further found that dust devils occur more frequently during the southern hemisphere spring and summer. The coexistence of multiple dust devils has been suggested as a possible mechanism for generating local dust storms [24,54]. Currently, two primary mechanisms are recognized for lifting dust particles: surface wind stress lifting and convective vortex lifting (such as dust devils), supported by various numerical simulations [55–59] using Martian global circulation models (GCMs) [60]. Dust particles are lifted during the saltation of more easily mobilized sand-size particles above a certain threshold [55,56]. It has been proposed that background dust haze on Mars is sustained by dust devil lifting [57,58]. Simulation studies combining convective schemes with high-threshold and high-rate stress lifting have successfully simulated spontaneous and interannually variable global dust storms [57]. Further simulations indicated that both wind stress and dust devil are essential and contribute equally to the total dust lifted [58].

Current consensus indicates that seasonal dust storms on Mars are primarily driven by variations in solar radiation forcing on the Martian surface and atmosphere system. In this system, the planetary boundary layer is recognized as playing a critical role in the Martian dust cycle [61]. As solar radiation increases near the southern spring equinox, it heats the lower Martian atmosphere, leading to accelerated atmospheric circulation. This enhanced near-surface wind stress lifts dust particles into the atmosphere [55,56], which in turn further heats the atmosphere and creates zonal temperature gradients. These gradients strengthen equatorial easterly winds, establishing positive feedback mechanisms that lift more dust particles into the atmosphere and ultimately result in large regional or global dust storms.

The mechanisms discussed above primarily pertain to the coupling of Mars' atmosphere and surface modulated by solar radiation. However, other potential mechanisms link dust storms to changes in Martian orbital and rotational motions, influencing atmospheric dynamics [12,62–65]. Shirley [12] found that all regional dust storms escalated into global dust storms during periods when Mars's orbital angular momentum relative to the solar system barycenter was increasing or at its maximum. Recent simulations [64,65] further illustrated that global dust storms occur around times of peak orbital-spin coupling torques and during periods of rapid torque changes. Orbital-spin coupling induces intensified, and relaxed circulations overlaid on the normal annual cycles of atmospheric circulation driven by external solar forcing. The asynchrony of these two cycles introduces interannual variability in dust storms [12,62–64].

To summarize, the precise mechanisms governing interannual variations in Martian dust storms, particularly global dust storms, remain unclear. Modeling efforts over recent decades have incorporated Mars global circulation models, such as the Mars GCM, e.g. [55,56] and the Ames Mars Global Climate Model (AMGCM), e.g. [58,66], achieving significant success by embedding dust lifting schemes. Detailed reviews on the status of the Martian whole atmosphere model and dust activities can be found in Wu et al. [67] and Zhou et al. [68]. Incorporating accelerations from orbit-spin coupling [65] into these models could further enhance their ability to replicate interannual variability in Martian dust storms.

2.3. Impacts of Dust Storms

Dust storms on Mars have profound effects on various aspects of the planet's environment and pose potential hazards for exploration and manned missions. Here, we review their impacts on atmospheric dynamics, atmospheric electrical properties, the space environment, topography, and Mars exploration.

During a dust storm, dust lifted into the atmosphere significantly absorbs solar radiation, causing temperatures in the Martian atmosphere to rise by at least 20 °C above the altitude of 25 km [69,70] while the surface temperatures decrease. The nighttime surface temperature is raised during the main phase of dust storms, making the diurnal temperature difference significantly lower during dust storms [71]. The radiation effect of dust changes the thermal structure and dynamic conditions of the atmosphere, which further affect the atmospheric tides and intensify meridional wind and Hadley circulation of Mars [72,73], strengthening the interhemispheric transport of dust. Furthermore, dust storms affect the sublimation and condensation of the CO_2 ice sheet in the polar region [74], thereby altering the atmospheric pressure.

Simulations, experiments, and calculations have demonstrated that Martian dust storms can generate friction discharge due to dust driven by strong winds, leading to low-frequency electromagnetic disturbances [75–78]. Additionally, during periods of high dust activities, the increased dust aerosols are favorable to attaching ions, resulting in a decrease in atmosphere conductivity [79,80].

The dust activities in the lower atmosphere will significantly influence the upper atmosphere, ionosphere and magnetosphere through vertical transportation and coupling. During dust storms, the rise in lower atmospheric temperature induces an increase in CO_2 density in the upper atmosphere [81,82]. As a result, the ionospheric peak height will be raised by tens of kilometers but without significant variation in peak electron density [83–85]. The variations of atmospheric ion densities are species-dependent, with CO_2^+ ions significantly increased, O^+ ions decreased, while no obvious change in O_2^+ ions [84]. More water vapor is transported to higher altitudes during dust storms. These water molecules undergo dissociation and ionization, which can lead to an increased hydrogen escape rate of 5–10 times [3,5,86]. At the same time, the escape rate is CO_2^+ ions can be increased by 3 times [83]. Apart from the strong orbital forcing on the vertical profile of water vapor saturation [87], dust storms will significantly increase vertical water vapor transportation, further depleting the ozone [88].

On the surface of Mars, dust storms have a direct impact on the topography. Dust storms can affect the deposition of dust [89] and volatile (ice/snow) [90] in the polar ice caps, which in turn can significantly influence the analysis of Mars' climate evolution history. Furthermore, dust storms are capable of driving the redistribution of dust across the Mars surface, and the strong winds (reaching speed of up to 100 km h^{-1}) play an important role in reshaping and evolving the topography and landform [91]. Additionally, dust storms also contribute to exposing organic matter in the surface soil that has not been degraded by cosmic rays, thereby aiding in assessing potential signs of life on Mars surface [92].

Apart from the environmental effects mentioned above, dust storms have a direct impact on the operations of landers and rovers on the surface of Mars [19]. The accuracy of landing will be reduced due to the large uncertainties in the atmospheric density, strong winds, and poor observing conditions during dust storms [93]. Martian dust particles range in size from 0.1 to 2000 μm and can take on plate-like, angle-like, or round shapes with a particle density of 2.6 to 3.0 g cm^{-3} [94]. They are rich in elements such as Si, Al, Fe, Mg, Ca, Ti, S, Cl, and Br [95]. These tiny dust particles can cover or penetrate the surface of instruments, causing mechanical failure and affecting the operation of related hardware and electronics. For example, dust activities have been shown to reduce the efficiency of solar panels and even cause damage [96–98]. When the atmosphere becomes dusty, the communication between Mars landers/rovers and Earth will be attenuated or even interrupted [99]. The Opportunity rover worked for fourteen years on Mars until it lost contact during the global dust storm in 2018. In December 2022, the National Aeronautics and Space Administration (NASA) announced that the Insight mission launched in May 2018 was ending due to power loss after a strong dust storm. Any landers or rovers using solar panels as their power source will be significantly impacted by dust storms and may even suffer fatal damages. Additionally, it has been found that Martian soil is rich in Cr

(hexavalent chromium ions are highly toxic), S, and Cl elements [95,100]; therefore, Martian dust could be toxic and acidic, posing a significant threat to the health of astronauts. The great temperature, pressure, and wind variations during dust storms will significantly affect the entry, descending, and landing process and the returning process.

In summary, comprehensive monitoring and forecasting are essential for the study of Mars' multi-layer coupling system and for safe Mars exploration missions due to the significant impacts of dust storms on Martian environments and exploration activities.

3. Detection Methods for Dust Storms

In the 1950s, the global encircling dust storm on Mars was first observed through ground optical telescopes [101]. Since then, detection and investigation of dust storms have always been a primary focus of Mars exploration missions. This section reviews the detection methods for dust storms, with an emphasis on those performed by Martian orbiters and landers/rovers.

3.1. Historical Views on Dust Storms

Before human detectors arrived at Mars, qualitative observation and analysis of dust storms on Mars were mainly carried out using ground-based telescopes. The interannual variation characteristics of Martian dust storms have been identified; specifically, changes in color and albedo near the perihelion of Mars indicate frequent occurrence of large dust storms [22,23].

One of the crucial physical parameters for quantifying the content and spatial distribution of dust particles in the Martian atmosphere is the vertical profile of the dust optical depth (DOD). This parameter is associated with the attenuation of light in the propagation direction due to absorption and scattering (i.e., extinction) by dust particles in the atmosphere when the radiation of a specific wavelength passes through. The column-integrated DOD from the surface to the top of the atmosphere gives the CDOD, where a larger value indicates more serious attenuation and stronger dust activity. The vertical profile of optical depth can be retrieved from the radiation measured by a limb observation instrument, which offers important information about the vertical transport of dust. It should be noted that while relative changes in optical depth can be easily obtained from remote sensing observations, obtaining absolute values is much more challenging as it requires an accurate understanding of key properties related to dust, such as particle size distribution and optical parameters. In order to obtain CDOD for Mars, most US and European probes since Mariner 9 have been equipped with optical instruments capable of detecting dust storm activity, including spectrometers, radiometers, imagers/cameras, LiDAR, etc. Table 1 summarizes the dust-related measurements in Mars exploration history. Currently, methods for monitoring Martian dust storms can roughly be divided into three categories: orbiter multicolor cameras, orbiter infrared (IR) and/or ultraviolet (UV) spectrometers, and lander/rover cameras.

Table 1. Successful dust-related measurements in the Mars exploration history.

Mission	Type	Instruments	Years	References
Mariner 6	Flyby	IR Spectrometer (IRS)	1969	[102,103]
Mariner 7	Flyby	IR Spectrometer (IRS)	1969	[103]
Mariner 9	Orbiter	IR Spectrometer (IRS) UV Spectrometer (UVS) Television (TV)	1971~1972	[47,104,105]
Viking 1	Orbiter Lander	IR Thermal Mapper (IRTM) Visual Imaging Subsystem (VIS) Cameras	1976~1980 1976~1982	[106,107]
Viking 2	Orbiter Lander	IR Thermal Mapper (IRTM) Visual Imaging Subsystem (VIS) Cameras	1976~1978 1976~1980	[106,107]

Table 1. *Cont.*

Mission	Type	Instruments	Years	References
Mars Global Surveyor (MGS)	Orbiter	Thermal Emission Spectrometer (TES) Mars Orbit Camera (MOC)	1997~2006	[108–110]
Mars Pathfinder	Lander Rover	Imager for Mars Pathfinder (IMP) Atmospheric Structure Instrument Navigation Camera (ASINC) Alpha Proton X-Ray Spectrometer (APXS)	1997 1997	[95,111,112]
Mars Odyssey	Orbiter	Thermal Emission Imaging System (THEMIS)	2004~present	[113]
Mars Express	Orbiter	Spectroscopy for the Investigation of the Characteristics of the Atmosphere of Mars (SPICAM) Observatoire pour la Mineralogie, l'Eau, les Glaces et l'Activité (OMEGA) High Resolution Stereo Camera (HRSC)	2003~present	[43,114–116]
Mars Exploration Rovers: Spirit Opportunity	Rover Rover	Panoramic Cameras (Pancam) Miniature Thermal Emission Spectrometer (Mini-TES) Alpha Particle X-ray Spectrometer (APXS)	2004~2009 2004~2022	[117–119]
Mars Reconnaissance Orbiter (MRO)	Orbiter	Mars Color Imager (MARCI) Compact Reconnaissance Imaging Spectrometer for Mars (CRISM) Mars Climate Sounder (MCS)	2006~present	[120–122]
Phoenix	Lander	Surface Stereo Imager (SSI)	2008~2009	[123]
Mars Science Laboratory (MSL) Curiosity	Rover	Rover Environmental Monitoring Station (REMS) Mast Camera (Mastcam)	2012~present	[41,124]
ExoMars 2016 Trace Gas Orbiter (TGO)	Orbiter	Nadir and Occultation for Mars Discovery (NOMAD) Color and Stereo Surface Imaging System (CaSSIS) Atmospheric Chemistry Suit (ACS)	2016~present	[125–127]
Insight	Lander	Color Cameras Auxiliary Payload Sensor Suite	2018~2022	[128,129]
Perseverance	Rover	Mastcam-Z SuperCam Mars Environmental Dynamics Analyzer (MEDA)	2021~	[130–132]
Hope	Orbiter	Emirates Exploration Imager (EXI)	2021~	[133]
Tianwen-1	Orbiter	High-Resolution Imaging Camera (HiRiC) Medium Resolution Imaging Camera (MoRiC) Multispectral Camera (MSCam)	2021~	[134–136]

3.2. Orbiter Multicolor Imaging

Optical imaging is a valuable tool for monitoring the occurrence and development trends of dust storms on Mars. It provides the most intuitive way to track dust storm activities. Two important cameras, the MGS MOC [108,109] and the MRO MARCI [120], have been operated on Mars orbiters. These instruments have provided daily global maps of Mars from 1999 to the present, offering an extensive database for investigating Martian dust storms [28,29,137]. More recently, the EXI instrument on the Emirates Mars Mission (EMM) Hope mission [133] has been acquiring both regional and global images in a completely different orbit with different spatiotemporal coverage compared to MGS and MRO [138].

The most successful imager in Mars orbit is the MARCI onboard MRO. The MRO operates in a polar near-circular orbit of Mars, with an apogee of approximately 320 km

and a perigee of around 255 km. At this altitude, large-field optical images with a spatial resolution of 1~10 km can be obtained. With the help of Mars' rotation, a global image of Mars can be captured every day. The wave bands covered by MARCI range from ultraviolet to visible and near-IR bands, which are selected by seven filters with central wavelengths of approximately 260 nm, 320 nm, 425 nm, 550 nm, 600 nm, 650 nm, and 725 nm, respectively [120]. MARCI operates in push-frame mode, with the camera's optical axis always pointing at the nadir point. The cross-track field of view (FOV) is 180° while the along-track FOV is 26° for the visible and near-IR channels and 20° for the ultraviolet channel, respectively [120]. The angular resolution is 0.13° in both along-track and cross-track directions [120].

The design of MARCI is very sophisticated, utilizing a dual optical path single-focal plane design. The optical system of the visible and near-IR channels and the ultraviolet channels are independent to ensure the transmittance of different channels and optical image quality. In front of the Charge Coupling Device (CCD), two prisms were utilized to redirect the beams at different wavelengths to the appropriate parts of the CCD based on the principle that light with different wavelengths has different refractive indices in the same medium. Furthermore, according to the focusing position of different bands on the CCD, narrowband interference multilayer filters are directly deposited on the CCD's photosensitive surface. This further realizes a narrowband filter and suppresses light crosstalk of different wavelengths while enabling simultaneous imaging of different wavelengths, which is essential for joint scientific research involving multi-band images. These ingenious designs significantly reduce the size and weight of MARCI. The volume is controlled within 10 $cm^{3,}$ and the weight is controlled under 1 kg [120]. These specifications align with the requirements of having a small volume and light weight in deep space exploration.

The images of each band can be individually utilized for the study of the Martian atmosphere and surface. This includes analysis of clouds, circulation, dust storms, atmospheric ozone, polar surface processes, local albedo properties, surface color properties, mineralogical constraints, and surface physical constraints. For example, the images at wavelengths around 425 nm, 600 nm and 725 nm have been synthesized to create global color images of Mars (Figure 1b,c) in order to identify the ranges and evolution paths of dust storms [29], which are of great significance for revealing the generation and evolution laws of dust storms on Mars, especially the regional characteristics and spatiotemporal evolution laws of large dust storms. Based on the Mars Daily Global Maps (MDGM) from MGS MOC and MRO MARCI [139], a comprehensive Mars Dust Activity Database (MDAD) covering eight MYs (24~32) has been compiled. This database includes records of 14,974 dust storms with an area greater than 10^5 km^2 [140]. Analysis using this database by Battalio and Wang [140] revealed that many dust storm sequences originated from the northern mid-latitudes before flushing into the southern hemisphere across the equator following more coherent tracks (Figure 3). In contrast, sequence paths were found to be less organized in the southern hemisphere.

Recently, the Tianwen-1 orbiter from China was equipped with a MoRiC [135], which is a standard RGB color camera. The main objective was to capture images of the surface of Mars, produce global remote sensing images of Mars, explore the topography and changes of Mars, and study the geological structure, topography, and landforms. MoRIC had a FOV of 53.3° × 41.2° and provided a spatial resolution at a nadir point of about 98 m at an orbital altitude of 400 km [135]. Dust storms were directly observed in the images captured by MoRIC (as shown in Figure 1a). The Tianwen-1 orbiter was also equipped with a HiRiC capable of acquiring images with a spatial resolution of ~1 m [134]. The HiRiC was primarily used to obtain detailed images of key areas on the Martian surface, especially to determine the Tianwen-1 landing site [141].

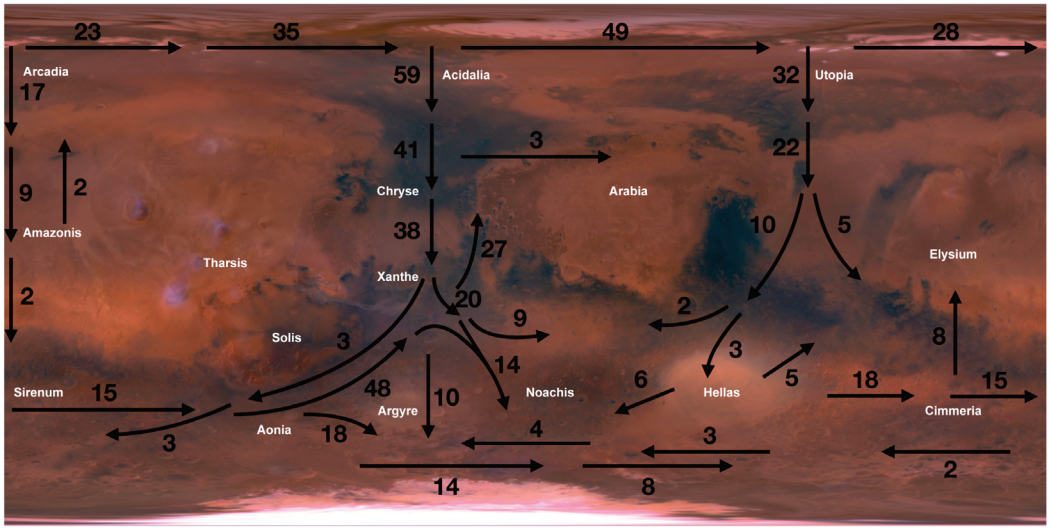


Figure 3. Paths of dust storm sequences observed by MGS MOC and MRO MARCI during MY 24 and 32. The numbers near the arrows indicate the number of sequences traveling along that path. (Adapted from Battalio and Wang [140]).

3.3. Orbiter Infrared Spectroscopy

The visible light images captured by the orbiter cameras can monitor the global distribution and spatiotemporal changes of the dust storms (e.g., area, lifetime, and moving speed), but there are challenges in quantitatively estimating the strengths of dust storms without an accurate Martian surface albedo model. Herein referred to as the strength of a dust storm, it is mainly related to the amount of dust in the atmosphere, namely dust opacity profile and CDOD. With this parameter, particularly through global measurements, the area, lifetime, and moving speed of dust storms can be estimated. A time series analysis using this parameter is also crucial for atmospheric numerical simulations. Currently, IR spectrometers and radiometers are primarily used to estimate dust optical depth from Mars orbit due to their greater sensitivity at larger optical depths.

The observation of IR spectra by Mars orbiters has a long history, dating back to Mariner 6 & 7 [102,103]. With the maturation of IR spectroscopy and radiative transfer models, starting with the MGS, NASA's Mars orbiters have been equipped with IR/thermal IR spectrometers to continuously monitor the Martian atmosphere and dust storms. These instruments include the TES on MGS [110], the THEMIS on Odyssey [113], and the MCS on MRO [122]. Together, these three spectrometers have provided continuous and complete quantitative monitoring data of global dust activities on Mars since MY 24 (1998–present). Apart from THEMIS, which just adopted the nadir viewing mode, both TES and MCS adopted scanning mode to realize nadir and limb observations [142]. The SPICAM on Mars Express [43] was an ultraviolet-IR (UV-IR) dual spectrometer, which was the first instrument to perform stellar occultations at Mars in order to retrieve aerosol vertical distributions [114]. Recently, data from the OMEGA instrument [115] on Mars Express were also used to retrieve DOD [143].

The basic method for retrieving DOD in infrared involves searching for optimized profiles of temperature, dust, and water ice that best match observed radiation profiles based on the radiative transfer models of the Martian atmosphere. Nadir viewing data can be used to retrieve the CDOD, while the limb viewing data can be used to retrieve vertical profiles of DOD. Both retrieving processes must consider the contributions of temperature and other aerosols such as water, ice, and CO_2. To retrieve CDOD from the nadir view, the general radiative transfer equation is [144–146]

$$I_{obs}(\nu) = \epsilon(\nu)B\left[\nu, T_{surf}\right]e^{-\frac{\tau_0(\nu)}{\mu}} + \int_0^{\tau_0(\nu)} B[\nu, T(\tau)]e^{-\frac{\tau(\nu)}{\mu}}d\tau, \quad (1)$$

where $I_{obs}(\nu)$ represents the observed monochromatic radiance of Mars at wave number ν, $\epsilon(\nu)$ is the surface emissivity at wave number ν, $B[\nu, T(\tau)]$ stands for the Planck function, $\tau_0(\nu)$ denotes the normal column-integrated aerosol optical depth, μ is the cosine of emission angle, T_{surf} is the surface temperature, $T(\tau)$ refers to the atmospheric temperature. The integration is performed from the spacecraft to the surface. The total aerosol optical depth is mainly contributed by dust particles, water ice, and CO_2. Assuming a plane-parallel atmosphere and uniform mixing of dust, water, ice, and CO_2, Equation (1) can be solved to obtain CDOD.

To retrieve the vertical profiles of temperature, dust, and water ice, Kleinböhl et al. utilized a modified Chahine method and a fast radiative transfer scheme based on the Curtis-Godson approximation [147]. The basic radiative transfer equation is

$$R = \int_{\nu} F(\nu) \int_{z} B(\nu, T(z)) K(\nu, z) dz d\nu \quad (2)$$

where R is the radiance seen at a specific viewing direction in a certain channel, $F(\nu)$ is the frequency response function of the channel, and $K(\nu, z)$ is the vertical response function at frequency ν, respectively. This retrieving algorithm was successfully applied to the MCS onboard the MRO.

Apparently, the CDOD obtained from observed radiance at different wavebands will have different values. For example, the 9.3 μm CDOD represents dust-induced absorption at 9.3 μm, while the 21.6 μm CDOD represents dust-induced absorption at 21.6 μm [147]. The 21.6 μm CDOD can be converted to 9.3 μm CDOD by multiplying a factor of 2.7 [35]. The CDOD retrieved from TES, THEMIS, MCS, and other IR spectrometers listed in Table 1 formed the most important and the longest time series of daily global maps of CDOD, which significantly improved our understanding of the climatology of Martian dust storms [36]. These daily global column-integrated dust scenarios greatly benefited the numerical simulations of the Martian climate system, e.g. [36,148]. Strong diurnal variations in the vertical distribution of dust during the global dust storm in 2018 were observed by MRO MCS and were attributed to meridional circulation exhibiting diurnal tidal variations [149]. Fast changes in water abundance observed by TGO NOMAD during the same storm suggested that the impact of dust storms on the Martian atmosphere is very fast [150]. Based on retrieved dust, temperature, ice, and water profiles during the Type C dust storm in January 2019, it was found that regional dust storms can enhance Martian water loss to space by a factor of five to ten [3]. It should be pointed out that, in this work [3], water vapor was measured by TGO ACS and NOMAD higher up, while MCS estimated water vapor in the middle atmosphere by assuming that vapor was at its condensation threshold given by their measured temperature.

3.4. Landers/Rovers Monitoring

On the surface of Mars, the visible solar radiations received can be utilized to measure dust storm activity. According to the Beer-Lambert Law, the solar radiation flux (F) reaching the Mars surface can be expressed as $F = F_{\mathrm{TOA}} \times \mathrm{e}^{-\tau\eta}$, where τ represents the visible CDOD (VDOD), F_{TOA} is the solar radiation flux at the top of the atmosphere, and η denotes the airmass [117]. This method has been successfully applied on MER Opportunity and Spirit rovers, as well as other landers/rovers. The panoramic cameras on both rovers routinely image the Sun near local noon each day on Mars at 440 nm and 880 nm [117,118]. Other small multispectral cameras on the landers/rovers, such as SSI [123], Mastcam [124], and Mastcam-Z [130], are all valuable for dust storm monitoring, not only for DOD but also for surface property and mineral characteristics.

The VDOD retrieved from two wavelengths are nearly identical, as demonstrated by the VDOD series during the lifetime of the Opportunity rover in Figure 4. The Opportunity rover survived the global dust storm in 2007 but, unfortunately, was completely lost during the global dust storm in 2018. Images taken by Opportunity rover during the eruption of this 2018 global dust storm clearly show drastic attenuation of visible solar radiations

on Mars' surface due to the strong absorption of dust particles (Figure 5). When VDOD reached 11, the visible light can be attenuated by nearly 100%, with IR band attenuation also at 98%, resulting in a darkened Martian surface.

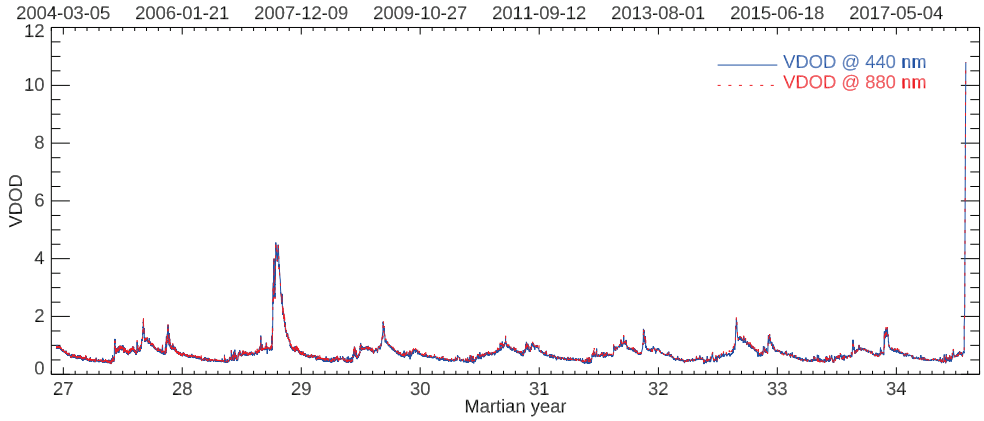


Figure 4. The VDOD was recorded by the Opportunity rover. VDOD observed in 440 nm (blue solid) and 880 nm (red dashed) are shown.

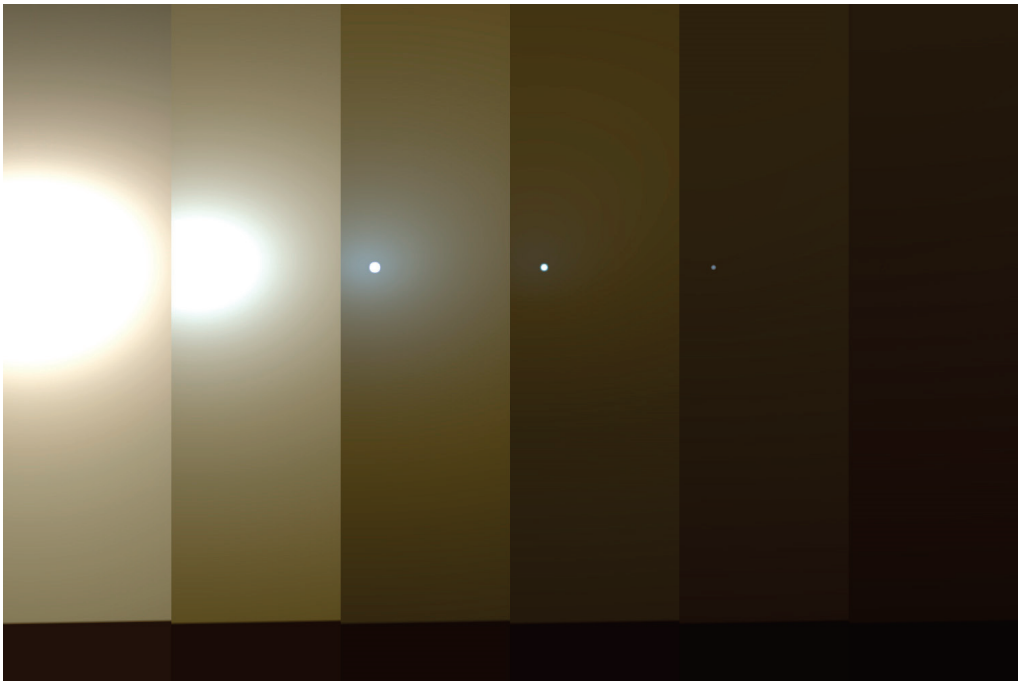


Figure 5. Photographs of the Sun in visible light captured by the panoramic camera onboard Opportunity rover during the eruption phase of the global dust storm in June 2018. The VDOD for each frame is 1, 3, 5, 7, 9, and 11, from left to right. (Image taken from https://www.jpl.nasa.gov/images/pia22521-shades-of-martian-darkness, accessed on 15 May 2024. Credit: NASA/JPL-Caltech/TAMU).

Based on the operation status and record of landers and rovers on Mars over the past two decades, it has been observed that different levels of dust storms have varying effects on the landers/rovers. The engineering team at NASA has developed a guidebook for dust storm operations [99], which classifies dust storms into six levels based on VDOD values, as outlined in Table 2.

Table 2. Classification of dust storm levels according to VDOD values [99].

Levels	VDOD Values	Actions
Level 1	<0.7	No restrictions.
Level 2	0.7 < VDOD < 1.0	No restrictions but watch the VDOD closely.
Level 3	1.0 < VDOD < 2.0	Scientific activities can only be carried out within reasonable limits during the day, with no overnight activities, and the operation team searches for possible parking points for rovers and protective measures for landers.
Level 4	2.0 < VDOD < 3.0	Start driving to a parking point to safely ride out the dust storm, allowing ONLY essential activities (VDOD observation and battery control board history).
Level 5	3.0 < VDOD < 3.5	Final drive to parking point, minimal activities ONLY (VDOD observation and battery control board history), begin ultra-high frequency (UHF) overflights per a couple of days, and wait for VDOD to drop.
Level 6	VDOD > 3.5	Minimal activities ONLY (VDOD observation and battery control board history), UHF overflights per couple of days, and wait for VDOD to drop.

It is important to note that the trend of large dust storms is different to predict, making continuous monitoring and treatment according to the actual situation particularly crucial. For example, during the 2017 global dust storm, it took four days for the VDOD value to increase from 1 to 2, while it only took one day during the 2018 global dust storm. The rapid growth of the dust storm made following a guidebook impossible.

For landers/rovers using solar arrays as their power source, dust storms—especially global dust storms—can dramatically accelerate the rate of dust deposition, leading to a rapid degradation of power supply. The average decrease rate in the power supply due to dust accumulation is 0.2% per Martian day [96]. During large dust storms, however, the dust can be seasonally removed benefit from the large winds. The loss of solar energy mainly results from decreased solar insolation. During the 2018 global dust storm, when the VDOD values increased from 0.6 to 10.8 in eight days (3–10 June 2018), energy output from solar arrays dropped by an alarming 96.7% [99]. From 10 June, the Opportunity rover was officially dead, successfully exploring Mars for 15 years. These missions have provided valuable lessons: seasonal dust storms have significant impacts on landers/rovers, and real-time monitoring of the dust storm activities—from both orbiters and landers/rovers—is crucial for ensuring security and successful scientific explorations on Mar's surface.

4. Dust Storm Monitoring and Predicting for Tianwen-3

China has announced the implementation of a Mars sample return mission around 2030 [151]. Throughout the entire mission, the entry, descending and landing process, sampling process, and the launch process on the Martian surface are highly likely to be affected by Martian dust storms. In this section, we will discuss the potential characteristics of dust storm activity during the Tianwen-3 mission and propose a dust monitoring scheme for Tianwen-3.

4.1. Statistical Predictions

Based on long-term observation data of dust storms, primarily the CDOD retrieved from TES, THEMIS, and MCS, Montabone et al. [35,36] conducted systematic data processing, cross-calibration, and quality control on these data and established a comprehensive CDOD database covering MY 24 to present. The database is global, with a spatial resolution of 6° (longitude) by 5° (latitude) and a temporal resolution of one Martian day. The CDOD data in the database are all 9.3 μm CDOD. The 9.3 μm CDOD is converted to VDOD by multiplying a factor of 2.7 [35,152] to facilitate the assessment of the degree of dust storm impact according to the classification criteria in Table 2.

The sampling will take place in flat areas in the low-latitude regions in the northern hemisphere. Based on recommended landing site candidates, four zones in the northern

hemisphere have been selected for statistical prediction of the dust storm levels using the following procedure:

- The four zones are located in Utopia Planitia, Isidis Basin, Amazonis Planitia, and Chryse Planitia, respectively. Each zone covers a range of 18° in longitude and 15° in latitude, creating a 3 × 3 grid in the VDOD database;
- The VDOD data in the grid during MY 24–35 (12 MYs) are extracted from the database to form a subset for each region, resulting in 108 samples for each zone (=3 × 3 × 12);
- For each Martian day, the numbers of the six dust activity levels in the 108 samples are counted, and their probabilities are calculated;
- Since Martian dust storms are seasonal, we extend the date to MY 40 and 41 according to the orbit of Mars;
- Finally, the predicted results are presented in Figure 6.

Taking the zone in Utopian Planitia as an example (Figure 6a), it is observed that:

- Before the southern spring equinox (L_S < 180°), the dust activity remains weak, generally below the safety line (VDOD < 1.0), occasionally exceeding 1.0 but with very short duration;
- After the southern spring equinox (L_S > 180°), there is a significant increase in the probability of VDOD exceeding 1.0. The trend is particularly noticeable between L_S of 200°~240° (i.e., 7 October to 11 December, 2029 in MY 40 and 25 August to 29 October, 2031 in MY 41), with the probability of VDOD exceeding 2.0 being greater than 30%. Dust activity generally peaks near L_S of 210°~220°, and then begins to weaken and recover. During this period, it is important for operators to closely monitor the changing trend of dust activity;
- After the southern summer solstice (L_S > 270°), dust activity experiences a significant weakening but remains at an active level. As shown in Figure 6a, just before L_S = 270°, the probabilities for Level 2 and Level 3 are both about 50%. Subsequently, dust activity will recover to quiet conditions and begin another seasonal trend.

In general, prior to July–September 2029 in MY 40 or May–July 2031 in MY 41, the overall level of Martian dust storms is very low, making it relatively safe to conduct sampling and returning activities during these periods. However, after July–September 2029 in MY 40 or May–July 2031 in MY 41, a significant increase in regional or global dust activity may significantly impact sampling and returning activities. A comparison between different zones in Figure 6 indicates that higher latitudes generally experience lower levels of dust activity compared to areas near the equator. It is therefore recommended that higher latitudes be selected as far as scientific requirements and engineering technology allow while completing the relevant science and engineering tasks by July 2029 or May 2031.

It is important to note that Figure 6 represents a preliminary statistical analysis, providing an initial reference for engineering task planning. It is recommended that other dust storm databases (such as the MDAD) be considered in conjunction with this analysis to ensure comprehensive and robust results. For instance, although Figure 6d indicates relatively low probabilities of Levels 2 and 3, it should be noted that Chryse Planitia lies in the middle of the paths of the outstanding dust storm sequences flushing into the southern hemisphere (Figure 3). Therefore, safety evaluations in this region should be conducted using multiple databases if the landing site is determined in the future. In order to minimize the impact of dust storms on the Mars sample return mission, it is essential to establish a Mars dust storm monitoring and early warning system prior to mission implementation [20]. Besides, once the landing site and window for Tianwen-3 are determined, dynamic forecasting methods, such as those proposed by Montabone and Forget [154], can be done in the future.

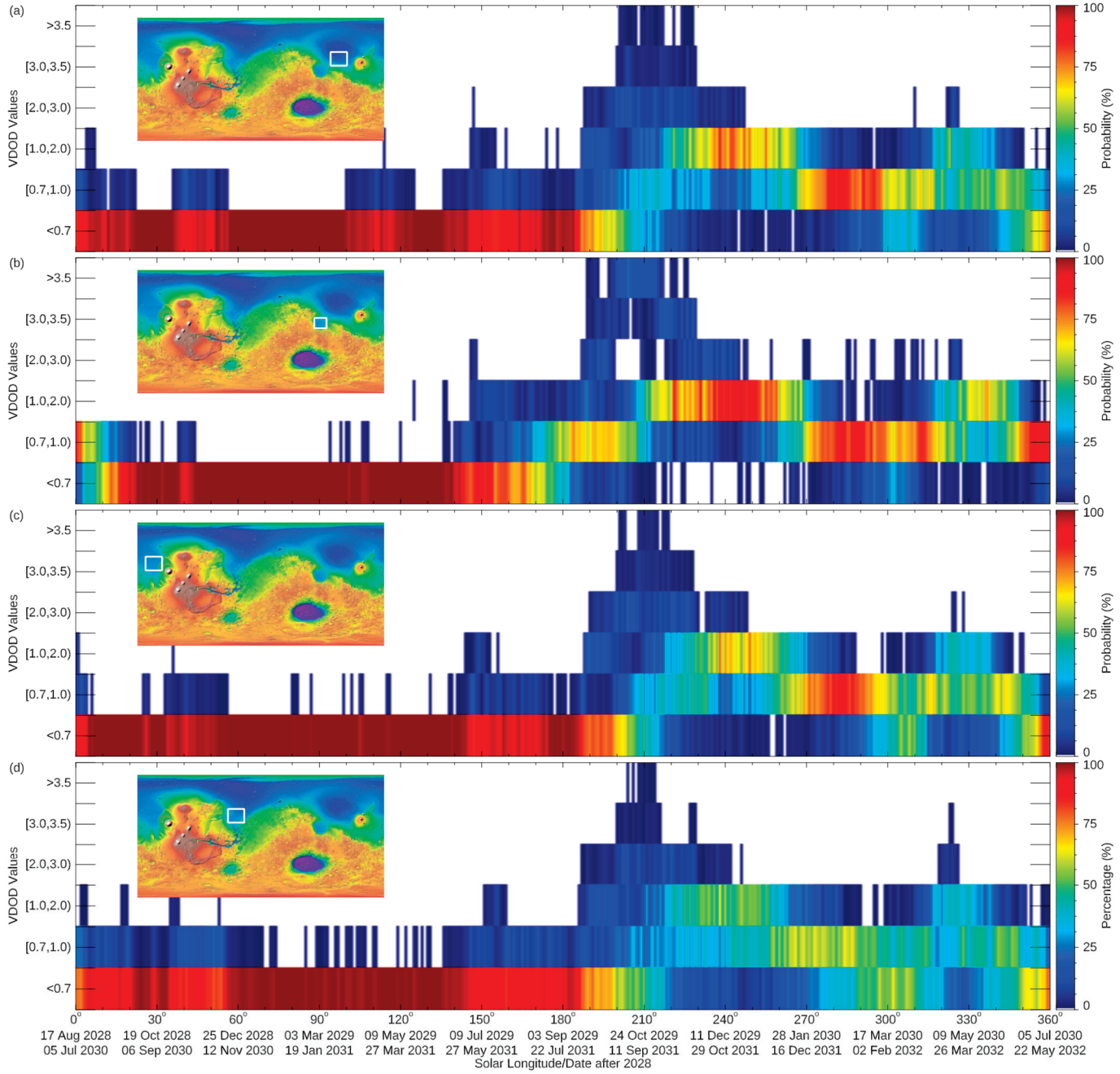


Figure 6. Statistical predictions of the dust storm activity level at five zones in the low-latitude regions of Mars. (**a**) Utopia Planitia, (**b**) Isidis Basin, (**c**) Amazonis Planitia, and (**d**) Chryse Planitia. Modified from He et al. [153]. The white rectangles represent the area of 3 × 3 grid used in the statistics.

Using the aforementioned method, we further statistically predicted dust storm activity levels across the entire northern hemisphere (Figure 7). The Martian year was divided into six periods, each spanning a L_S interval of 60° as shown at the top of each panel in Figure 7. Probabilities for each dust activity level during each period were then calculated within zones having a longitudinal range of 6° and a latitudinal range of 5°. The six rows in Figure 7 correspond to Level 1 to Level 6 from top to bottom.

Before the southern spring equinox (L_S < 180°), the dust activity is generally weak throughout the entire northern hemisphere, remaining below the safety line (VDOD < 1.0) as shown in Figure 7(a1–a3,b1–b3). Regions for VDOD > 1.0 are primarily concentrated in the Tharsis Montes, Chryse Planitia, and Utopia Planitia for L_S < 60° (Figure 7(c1)), in the polar region for 60° < L_S < 180° (Figure 7(c2,c3)), and in low latitude regions for

120° < L_S < 180° (Figure 7(c3)). However, these occurrences have a probability of less than 10%.

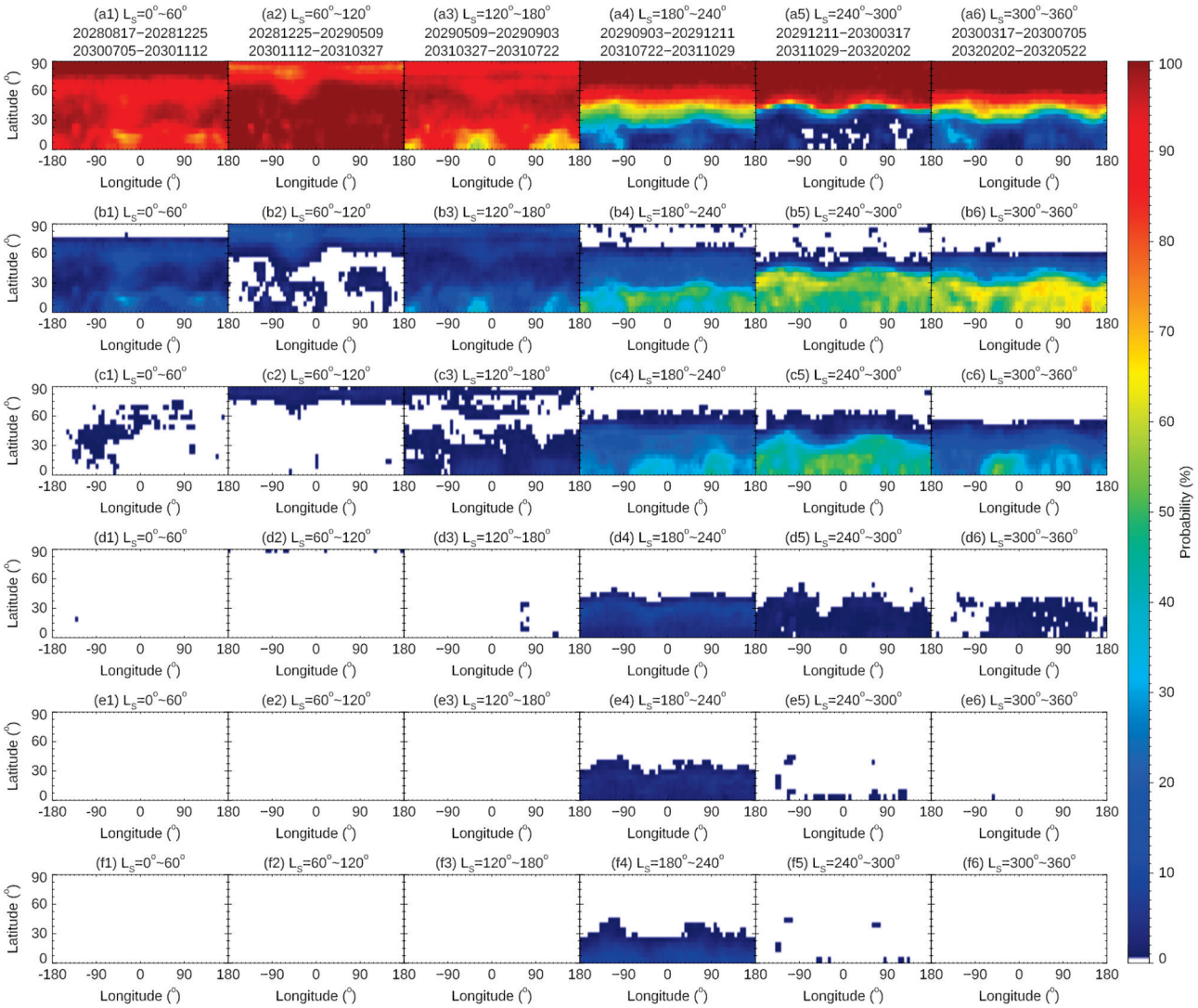


Figure 7. Statistical predictions of the VDOD levels (Table 2) in the entire northern hemisphere. (**a1**–**a6**) Probability for Level 1. (**b1**–**b6**) Probability for Level 2. (**c1**–**c6**) Probability for Level 3. (**d1**–**d6**) Probability for Level 4. (**e1**–**e6**) Probability for Level 5. (**f1**–**f6**) Probability for Level 6. The color bar is shown on the right. The L_S ranges are shown at the top of each panel. The date ranges in MY 40 and 41 are shown at the top of the first row. White areas indicate a zero probability.

Following the southern spring equinox (L_S > 180°), the VDOD remains low in the high latitude regions but increases in the low latitudes, especially below the latitude of 30°. In the latitudinal belt of 0°~25°, the probabilities for Level 3 are 16%~46% (180° < L_S < 240° in Figure 7(c4)), 29%~56% (240° < L_S < 300° in Figure 7(c5)), 14%~55% (300° < L_S < 360° in Figure 7(c6)), respectively, with the situation the most serious around the southern summer solstice (Figure 7(c5)). In Figure 7(c4), the peak is located in the Isidis Basin and the south of Utopia Planitia. In Figure 7(c6), the peak is located in the south of Chryse Planitia, which is in the middle of the paths of the outstanding dust storm sequences flushing into the southern hemisphere [140]. The probabilities for activities higher than Level 3 are generally below 10%. Extreme activities (higher than Level 4) are predominantly observed between 180° < L_S < 240°, primarily attributed to the two global dust storms in MY 25 (2001) and MY 34 (2018). The global dust storm in MY 28 (2007, 270° < L_S < 300°) was stronger in the southern hemisphere and thus not conspicuous in Figure 7(e5,f5).

4.2. Dust Storm Monitoring for Tianwen-3

During the sampling and returning phases of the mission, an orbiter will be utilized to provide high-resolution mapping of the landing site and measurements of environmental parameters, including dust storm activity. We have proposed to carry a Mars Multicolor Camera (MMC) to monitor dust storms because of the simplicity of instrumentation (e.g., lower power and mass and data rates). The main scientific objectives of MMC are as follows:

- Martian dust storm monitoring and early warning: Conducting large-field multicolor imaging of mid-low latitude dust storm activities on Mars to obtain information such as location, coverage and moving speed of dust storms on Mars.
- Spatial and temporal distribution of atmospheric ozone on Mars: Conducting large-field ultraviolet imaging of the column content of middle- and low-latitude ozone on Mars to obtain its spatial and temporal distributions. This will also improve the accuracy of dust storm identification in combination with water-ice cloud identification in visible light channels.

The Tianwen-3 orbiter is expected to operate in a circular orbit with an altitude of approximately 350 km, an orbital inclination of around 30°, and an orbital period close to 1.8 h. This orbit is an idea for global imaging of Martian dust storms at the middle and low latitudes. At this altitude, a camera with a FOV of 130° will achieve the largest surface coverage of ~3000 km cross-track. Considering the rotation of Mars, a global image of Mars will be generated each Martian day, covering an area below 52° latitude in both hemispheres, as indicated by the white circles in Figure 8. Due to the combined effects of orbital motion and Mars rotation, the revisit times for MMC over the same area are shown in Figure 9.

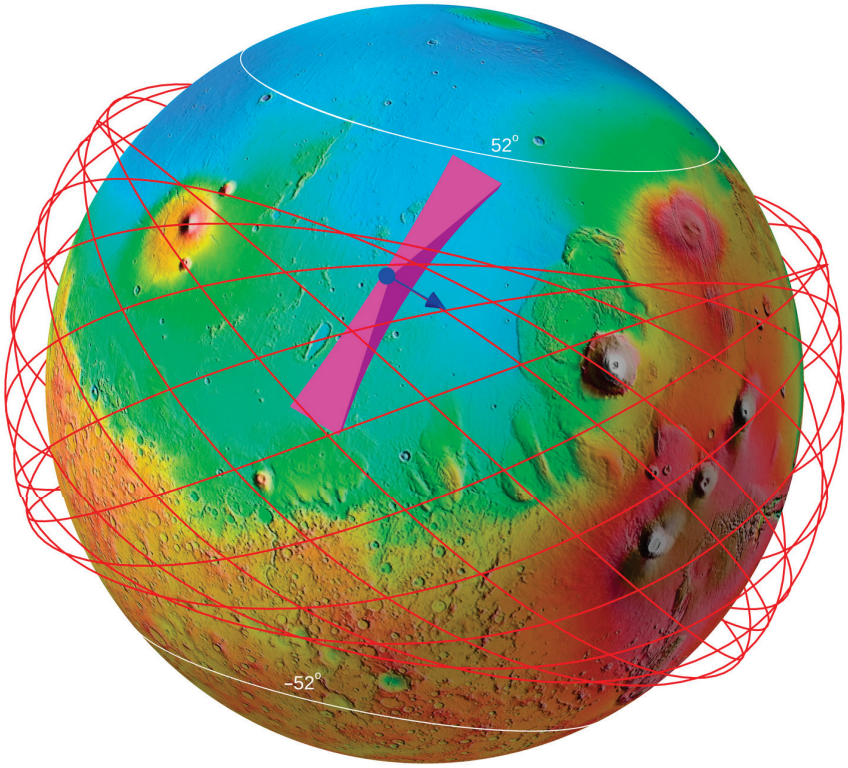


Figure 8. A demo of the orbit of the Tianwen-3 orbiter. The orbit is plotted by red lines. The orbiter is denoted by the blue dot, and its velocity is shown by the blue arrow. The pink surfaces demonstrate the FOV of the MCC. The background Mars digital elevation map is available at the U.S. Geological Survey Astrogeology Science Center (https://astrogeology.usgs.gov/search/map/Mars/, accessed on 17 May 2024).

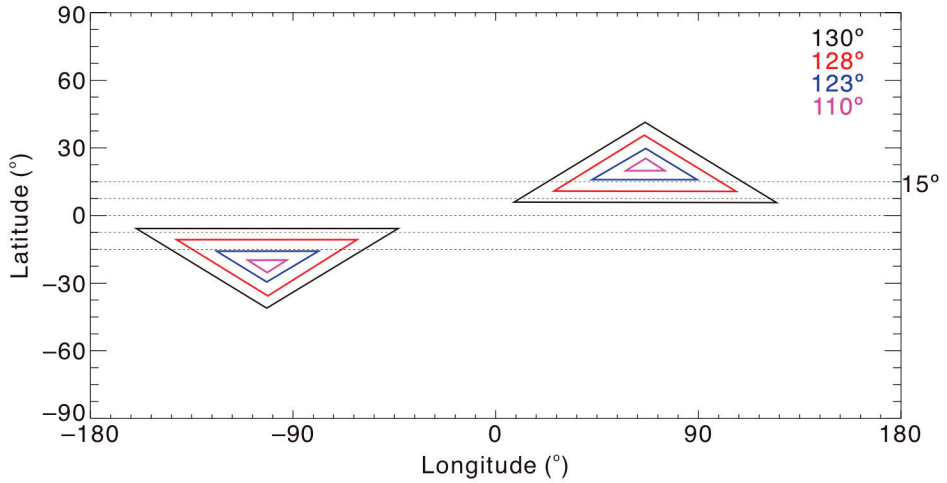


Figure 9. The surface areas can be revisited by MMC six times during Martian daytime with different cross-track FOV as shown by different colors.

The rotation period of Mars is ~24.62 h, and the orbital period of the Tianwen-3 orbiter is ~1.8 h. It is important to consider the coverage of the MMC FOV to the same area during the daytime period of each Martian day. As shown in Figure 9, an area of about 2000 km × 3000 km below 30° latitude can be continuously observed during six orbits throughout the daytime of each Martian day. In other words, for such an area of 2000 km × 3000 km, the MMC can achieve continuous monitoring with a time resolution of better than 2 h. Other regions with latitude lower than 30° in both hemispheres will be revisited at least three times during one Martian day. This is of great significance for early warning and prediction of dust storms during the landing, sampling and return phases of the mission.

The revisited area for different cross-track FOV of MMC is further shown in Figure 9. When the cross-track FOV decreases from 130° (black) to 110° (pink), there is a significant reduction in the area that can be revisited by MMC six times. When the cross-track FOV is smaller than 110°, no area can be revisited six times over. Therefore, it is determined that the cross-track FOV of MMC should achieve 130°. The along-track FOV is not so critical since the MMC will operate in a push frame mode, and it will be kept as small as feasible to reduce the data rate. Currently, the along-track FOV is determined to be 20°. We propose that once the landing and sampling site is determined, the tilt of the orbit should be as small as possible, and the orbital phase of the orbiter should be optimized to revisit the landing site six times or more.

For the demonstration orbit depicted in Figure 8, the westward longitudinal drift speed of the orbit in Mars body-fixed coordinate is ~24.8° per orbit. As a result, there will be a time difference of ~1.5 h between the orbital regression period and the Mars rotation period, and the opportunity for six observations per day will have a time interval of ~15 Martian days. If the orbital altitude is slightly decreased to ~300 km (although this may lead to a slight decrease in cross-track FOV coverage), and the orbital period is shortened to ~1.76 h, this time difference between the orbital regression period and the Mars rotation period will be reduced to only 0.02 h, making it almost equal to the Mars rotation period. Consequently, six observations per day can be guaranteed for every Martian day. Reducing the orbital inclination will also be beneficial, even though it may necessitate landing the lander in a narrower belt in lower latitudes. It is recommended that the satellite suitably reduces the altitude and orbital inclination during the mission operations. Once the sampling and returning phases are completed, the orbital inclination could be increased to provide better coverage in high latitudes.

To achieve the scientific objectives of MMC, the selection of wavelengths is essential. Since the MRO MARCI has been a great success, the operation wavelengths of MMC will be similar to those of MARCI. We have decided to design seven channels centered at ~260 nm,

~320 nm, ~425 nm, ~550 nm, ~600 nm, ~770 nm, and ~860 nm, respectively. The expected spatial resolution of the MMC images will be 1 km near nadir points. The images from each channel can be used individually to study various aspects of the Martian atmosphere and surface, such as clouds, circulation, dust swirls and dust storms, atmospheric ozone, surface processes, local albedo properties, surface color properties, mineralogical constraints, and surface physical constraints. These images can also be used to synthesize different channel colors for the identification of Martian dust storms. For example, the false color RGB composite generated from channels at ~425 nm, ~600 nm and ~600 nm could help identify the locations, ranges and evolutions of dust storms, while the false color RGB composite generated from channels at ~260 nm, ~320 nm, and ~425 nm would be suitable for identifying ice clouds thus improving reliability in dust storm identification.

5. Conclusions

Dust storms play a crucial role in the climate system and the space environment of Mars, significantly impacting human Mars exploration activities. The Martian dust storms involve the geological and geochemical processes, surface chemistry and physics, atmospheric chemistry and physics, Mars orbital motion, and solar energy input. Therefore, advancements in understanding the driving mechanisms of Martian dust storms and their environmental effects will promote our understanding of the habitable environment on Mars.

This paper begins by introducing the basic properties, driving mechanisms, and impacts of Martian dust storms. It also provides a brief overview of the history of observing dust storms on Mars while summarizing observation principles and methods for dust storms. Our knowledge of Martian dust storms has advanced considerably through long-term (since the first successful Mars mission) comprehensive observations using spectrometers and cameras as well as simulation efforts.

For the upcoming Tianwen-3 sample return mission, we have statistically predicted the dust activity for potential landing sites. Finally, we proposed an MMC for the Tianwen-3 orbiter to monitor Martian dust storms. The specifications and performance of MMC were simulated to determine that an orbiter altitude of ~300 km with an inclination of ~30° can observe a landing site in the low latitude region during six orbits if its orbital regression period matches the Mars's rotation period. This is critical for the sample return mission as it provides high time resolution monitoring images (~1.76 h) capturing global dust activity on Mars.

At present, the international Mars exploration is in full swing and is expected to enter the era of multi-satellite and multi-lander explorations [155]. In order to conduct an in-depth and systematic study of Martian dust storms, it is essential to establish a stereo observation network in the future that could quantitatively monitor the three-dimensional spatial distribution and dynamic evolution of global dust activities on Mars. To truly understand mechanisms that control the outbreak, development, and decline of dust storms, as well as the interannual variation of global dust storms, missions spanning as many local times and latitudes as possible across the lower, middle, and upper atmosphere are necessary. For orbiters, multicolor cameras and ultraviolet and IR spectrometers will be valuable tools. Small multispectral cameras in visible and near IR bands will be essential for the safe and smooth operation of landers and rovers on Mars.

On the other hand, although models produce dust storms, they do not produce them at the right times and places where such storms are observed without artificial adjustments. The advancement in this field relies on the development of a more comprehensive general circulation model for the whole atmosphere, an improved dust parameterization scheme, and a deeper understanding of dust activities [68]. Observations are the basis for these insights. A stereo observation network would provide a fine climatology, and the attendant monitoring could provide advance notification of dust storms that could impact lander (and aerial) operations. However, a thorough understanding of storm drivers may also necessitate in-situ observations of dust lifting by landers on the surface or laboratory

studies focusing on atmospheric dust coagulation and scavenging at far more localized scales.

The proposed MMC will achieve better spatiotemporal resolution for observing dust activity. For specific areas (depending on the orbit of the orbiter), the time resolution of the dust storm image will reach better than 2 h. We can track the onset time of dust storms much more precisely than with day-resolution images. Apart from MMC, a multi-spectral camera will be carried by the lander of the Tianwen-3 mission, which will not only monitor local dust optical depth but also assess the surface property and mineral characteristics near the landing site. The combination of these two instruments will effectively ensure the safe and smooth implementation of the Mars sample return mission. Together with other available observations from instruments, such as MARCI, MCS, ACS, and NOMAD, it is expected that a more comprehensive understanding of the origins and mechanisms behind dust storms will be achieved in future research endeavors.

Author Contributions: Conceptualization, F.H. and Z.R.; methodology, F.H.; software, F.H.; validation, F.H.; formal analysis, F.H.; investigation, F.H., Z.R. and Y.W. (Yong Wei); resources, F.H.; data curation, F.H.; writing—original draft preparation, F.H.; writing—review and editing, F.H., Z.R., Z.W., J.G., K.F., X.Z., L.Y., Y.W. (Yuqi Wang) and Y.W. (Yong Wei); visualization, F.H.; supervision, F.H.; project administration, F.H. and Z.R.; funding acquisition, F.H. and Z.R. All authors have read and agreed to the published version of the manuscript.

Funding: This research was funded by the National Natural Science Foundation of China (42222408, 41931073) and the National Key R&D Program of China (2021YFA0718600). F.H. was supported by the Youth Innovation Promotion Association of the Chinese Academy of Sciences (Y2021027). Z.R. was supported by the Key Research Program of the Chinese Academy of Sciences (ZDBS-SSW-TLC00103) and the Key Research Program of the Institute of Geology and Geophysics, CAS (IGGCAS-202102).

Data Availability Statement: The Opportunity rover's visible dust optical depth data are publicly available at https://pds-geosciences.wustl.edu/mer/mer1_mer2-m-pancam-5-atmos-opacity-v1/merao_1xxx/data/ (accessed on 17 May 2024). The Mars digital elevation map is publicly available at the U.S. Geological Survey Astrogeology Science Center at https://astrogeology.usgs.gov/search/map/Mars/ (accessed on 17 May 2024). The Mars 9.3 μm absorption column dust optical depth database is publicly available at the Mars Climate Database at https://www-mars.lmd.jussieu.fr/mars/dust_climatology/index.html (accessed on 8 March 2023). The Mars Daily Global Maps are publicly available at https://www.msss.com/view.php?page=subject/weather_reports (accessed on 9 March 2024).

Acknowledgments: The authors thank the L. Montabone for providing the Mars dust optical depth database.

Conflicts of Interest: The authors declare no conflicts of interest.

References

1. Connerney, J.E.P.; Acuña, M.H.; Wasilewski, P.J.; Ness, N.F.; Rème, H.; Mazelle, C.; Vignes, D.; Lin, R.P.; Mitchell, D.L.; Cloutier, P.A. Magnetic lineations in the ancient crust of Mars. *Science* **1999**, *284*, 794–798. [CrossRef] [PubMed]
2. Jakosky, B.M. Atmospheric loss to space and the history of water on Mars. *Ann. Rev. Earth Planet. Sci.* **2021**, *49*, 71–93. [CrossRef]
3. Chaffin, M.S.; Kass, D.M.; Aoki, S.; Fedorova, A.A.; Deighan, J.; Connour, K.; Heavens, N.G.; Kleinböhl, A.; Jain, S.K.; Chaufray, J.-Y.; et al. Martian water loss to space enhanced by regional dust storms. *Nat. Astronom.* **2021**, *5*, 1036–1042. [CrossRef]
4. Dubinin, E.; Fraenz, M.; Pätzold, M.; McFadden, J.; Halekas, J.S.; DiBraccio, G.A.; Connerney, J.E.P.; Eparvier, F.; Brain, D.; Jakosky, B.M.; et al. The effect of solar wind variations on the escape of oxygen ions from Mars through different channels: MAVEN observations. *J. Geophys. Res. Space Phys.* **2017**, *122*, 11285–11301. [CrossRef]
5. Heavens, N.G.; Kleinböhl, A.; Chaffin, M.S.; Halekas, J.S.; Kass, D.M.; Hayne, P.O.; McCleese, D.J.; Piqueux, S.; Shirley, J.H.; Schofield, J.T. Hydrogen escape from Mars enhanced by deep convection in dust storms. *Nat. Astronom.* **2018**, *2*, 126–132. [CrossRef]
6. Lillis, R.J.; Brain, D.A.; Bougher, S.W.; Leblanc, F.; Luhmann, J.G.; Jakosky, B.M.; Modolo, R.; Fox, J.; Deighan, J.; Fang, X.; et al. Characterizing atmospheric escape from Mars today and through time, with MAVEN. *Space Sci. Rev.* **2015**, *195*, 357–422. [CrossRef]

7. Lundin, R.; Barabash, S.; Andersson, H.; Holmström, M.; Grigoriev, A.; Yamauchi, M.; Sauvaud, J.-A.; Fedorov, A.; Dudnik, E.; Thocaven, J.J.; et al. Solar wind-induced atmospheric erosion at Mars: First results from ASPERA-3 on Mars Express. *Science* **2004**, *305*, 1933–1936. [CrossRef]
8. Ramstad, R.; Barabash, S.; Futaana, Y.; Nilsson, H.; Wang, X.-D.; Holmström, M. The Martian atmospheric ion escape rate dependence on solar wind and solar EUV conditions: 1. Seven years of Mars Express observations. *J. Geophys. Res. Planets* **2015**, *120*, 1298–1309. [CrossRef]
9. Wei, Y.; Fraenz, M.; Dubinin, E.; Woch, J.; Lühr, H.; Wan, W.; Zong, Q.-G.; Zhang, T.L.; Pu, Z.Y.; Fu, S.Y.; et al. Enhanced atmospheric oxygen outflow on Earth and Mars driven by a corotating interaction region. *J. Geophys. Res.* **2012**, *117*, A03208. [CrossRef]
10. Barlow, N. *Mars: An Introduction to Its Interior, Surface and Atmosphere*; Cambridge University Press: New York, NY, USA, 2008; pp. 163–186.
11. Leovy, C. Weather and climate on Mars. *Nature* **2001**, *412*, 245–249. [CrossRef]
12. Shirley, J.H. Solar system dynamics and global-scale dust storms on Mars. *Icarus* **2015**, *251*, 128–144. [CrossRef]
13. Keiffer, H.H.; Jakosky, B.M.; Snyder, C.W.; Matthews, M.S. *Mars*; Univ. Ariz. Press: Tucson, AZ, USA, 1992.
14. Haberle, R.M.; Clancy, R.T.; Forget, F.; Smith, M.D.; Zurek, R.W. *The Atmosphere and Climate of Mars*; Cambridge University Press: New York, NY, USA, 2007.
15. Encrenaz, T. The atmosphere of Mars as constrained by remote sensing. *Space Sci. Rev.* **2001**, *96*, 411–424. [CrossRef]
16. Smith, M.D. Spacecraft observations of Martian atmosphere. *Ann. Rev. Earth Planet. Sci.* **2008**, *36*, 191–219. [CrossRef]
17. Schmidt, F.; Way, M.J.; Costard, F.; Bouley, S.; Séjourné, A.; Aleinov, I. Circumpolar ocean stability on Mars 3 Gy ago. *Proc. Natl. Acad. Sci. USA* **2022**, *119*, e2112930118. [CrossRef] [PubMed]
18. Wei, Y.; He, F.; Fan, K.; Rong, Z.; Wang, Y. Preliminary predictions of the dust storm activity at the landing site of China's Zhurong Mars rover in 2022. *Chin. Sci. Bull.* **2022**, *67*, 1938–1944. (In Chinese) [CrossRef]
19. Wang, Y.; Wei, Y.; Fan, K.; He, F.; Rong, Z.; Zhou, X.; Tan, N. The impact of dust storms on Mars surface rovers: Review and prospect. *Chin. Sci. Bull.* **2023**, *68*, 368–379. (In Chinese) [CrossRef]
20. Rong, Z.; Wei, Y.; He, F.; Gao, J.; Fan, K.; Wang, Y.; Cao, L.; Yan, L.; Ren, Z.; Zhou, X.; et al. The orbit schemes to monitor Martian dust storms: Benefits to China's future mars missions. *Chin. Sci. Bull.* **2023**, *68*, 716–728. (In Chinese) [CrossRef]
21. James, P.B. Martian local dust storms. In *Recent Advances in Planetary Meteorology*; Hunt, G., Ed.; Cambridge University Press: New York, NY, USA, 1985; pp. 85–100.
22. Martin, L.J.; Zurek, R.W. An analysis of the history of dust activity on Mars. *J. Geophys. Res.* **1993**, *98*, 3221–3246. [CrossRef]
23. Zurek, R.W.; Martin, L.J. Interannual variability of planet-encircling dust storms on Mars. *J. Geophys. Res.* **1993**, *98*, 3247–3259. [CrossRef]
24. Fernández, W. Martian dust storms: A review. *Earth Moon Planet.* **1997**, *77*, 19–46. [CrossRef]
25. Kahre, M.A.; Murphy, J.R.; Newman, C.E.; Wilson, R.J.; Cantor, B.A.; Lemmon, M.T.; Wolff, M.J. The Mars Dust Cycle. In *The Atmosphere and Climate of Mars*; Haberle, R.M., Clancy, R.T., Forget, F., Smith, M.D., Zurek, R.W., Eds.; Cambridge University Press: New York, NY, USA, 2007; pp. 295–337.
26. Malin, M.C.; Cantor, B.A. MRO MARCI Weather Report for the week of 27 December 2021–2 January 2022. Malin Space Science Systems Captioned Image Release, 2022, MSSS-603. Available online: https://www.msss.com/msss_images/2022/01/05/ (accessed on 9 March 2024).
27. Malin, M.C.; Cantor, B.A.; Britton, A.W. MRO MARCI Weather Report for the week of 4 June 2018–10 June 2018, Malin Space Science Systems Captioned Image Release, 2018, MSSS-534. Available online: https://www.msss.com/msss_images/2018/06/13/ (accessed on 9 March 2024).
28. Cantor, B.A.; James, P.B.; Caplinger, M.; Wolff, M.J. Martian dust storms: 1999 Mars Orbiter Camera observations. *J. Geophys. Res.* **2001**, *106*, 23653–23688. [CrossRef]
29. Wang, H.; Richardson, M.I. The origin, evolution, and trajectory of large dust storms on Mars during Mars Year 24–30 (1999–2011). *Icarus* **2015**, *251*, 112–127. [CrossRef]
30. Kulowski, L.; Wang, H.; Toigo, A.D. The seasonal and spatial distribution of textured dust storms observed by Mars Global Surveyor Mars Orbiter Camera. *Adv. Space Res.* **2017**, *59*, 715–721. [CrossRef]
31. Guzewich, S.D.; Fedorova, A.A.; Kahre, M.A.; Toigo, A.D. Studies of the 2018/Mars Year 34 planet-encircling dust storm. *J. Geophys. Res. Planets* **2020**, *125*, e2020JE006700. [CrossRef]
32. Wang, H.; Saidel, M.; Richardson, M.I.; Toigo, A.D.; Battalio, J.M. Martian dust storm distribution and annual cycle from Mars daily global map observations. *Icarus* **2023**, *394*, 115416. [CrossRef]
33. Sánchez-Lavega, A.; del Río-Gaztelurrutia, T.; Hernández-Bernal, J.; Delcroix, M. The onset and growth of the 2018 Martian Global Dust Storm. *Geophys. Res. Lett.* **2019**, *46*, 6101–6108. [CrossRef]
34. Kass, D.M.; Kleinböhl, A.; McCleese, D.J.; Schofield, J.T.; Smith, M.D. Interannual similarity in the Martian atmosphere during the dust storm season. *Geophys. Res. Lett.* **2016**, *43*, 6111–6118. [CrossRef]
35. Montabone, L.; Forget, F.; Millour, E.; Wilson, R.J.; Lewis, S.R.; Cantor, B.; Kass, D.; Kleinböhl, A.; Lemmon, M.T.; Smith, M.D.; et al. Eight-year climatology of dust optical depth on Mars. *Icarus* **2015**, *251*, 65–95. [CrossRef]

36. Montabone, L.; Spiga, A.; Kass, D.M.; Kleinböhl, A.; Forget, F.; Millour, E. Martian year 34 column dust climatology from Mars Climate Sounder observations: Reconstructed maps and model simulations. *J. Geophys. Res. Planets* **2020**, *125*, e2019JE006111. [CrossRef]
37. Lemmon, M.T.; Guzewich, S.D.; McConnochie, T.; de Vicente-Retortillo, A.; Martínez, G.; Smith, M.D.; Bell, J.F., III; Wellington, D.; Jacob, S. Large dust aerosol sizes seen during the 2018 Martian global dust event by the Curiosity rover. *Geophys. Res. Lett.* **2019**, *46*, 9448–9456. [CrossRef]
38. Chen-Chen, H.; Pérez-Hoyos, S.; Sánchez-Lavega, A. Dust particle size, shape and optical depth during the 2018/MY34 Martian global dust storm retrieved by MSL Curiosity rover Navigation Cameras. *Icarus* **2021**, *354*, 114021. [CrossRef]
39. Clancy, R.T.; Wolff, M.J.; Christensen, P.R. Mars aerosol studies with the MGS TES emission phase function observations: Optical depths, particle sizes, and ice cloud types versus latitude and solar longitude. *J. Geophys. Res.* **2003**, *108*, 5098. [CrossRef]
40. Wolff, M.J.; Clancy, R.T. Constraints on the size of Martian aerosols from thermal emission spectrometer observations. *J. Geophys. Res.* **2003**, *108*, 5097. [CrossRef]
41. Vicente-Retortillo, Á.; Martínez, G.; Rennó, N.; Lemmon, M.T.; de la Torre Juarez, M. Determination of dust aerosol particle size at Gale crater using REMS UVS and Mastcam measurements. *Geophys. Res. Lett.* **2017**, *44*, 3502–3508. [CrossRef]
42. Fedorova, A.A.; Montmessin, F.; Rodin, A.V.; Korablev, O.I.; Maattanen, A.; Maltagliati, L.; Bertaux, J.-L. Evidence for a bimodal size distribution for the suspended aerosol particles on Mars. *Icarus* **2014**, *231*, 239–260. [CrossRef]
43. Bertaux, J.-L.; Korablev, O.; Perrier, S.; Quémerais, E.; Montmessin, F.; Leblanc, F.; Lebonnois, S.; Rannou, P.; Lefèvre, F.; Forget, F.; et al. SPICAM on Mars Express: Observing modes and overview of UV spectrometer data and scientific results. *J. Geophys. Res.* **2006**, *111*, E10S90. [CrossRef]
44. Guzewich, S.D.; Tiogo, A.D.; Richardson, M.I.; Newman, C.E.; Talaat, E.R.; Waugh, D.W.; McConnochie, T.H. The impact of a realistic vertical dust distribution on the simulation of the Martian General Circulation. *J. Geophys. Res. Planet.* **2013**, *118*, 980–993. [CrossRef]
45. Medvedev, A.S.; Yiğit, E.; Kuroda, T.; Hartogh, P. General circulation modeling of the Martian upper atmosphere during global dust storms. *J. Geophys. Res. Planet.* **2013**, *118*, 2234–2246. [CrossRef]
46. Wang, Y.; Chow, K.-C.; Xiao, J.; Wang, C.-F. Effect of dust particle size on the climate of Mars. *Planet. Space Sci.* **2021**, *208*, 105346. [CrossRef]
47. Hanel, R.; Conrath, B.; Hovis, W.; Kunde, V.; Lowman, P.; Maguire, W.; Pearl, J.; Pirraglia, J.; Prabhakara, C.; Schlachman, B.; et al. Investigation of the Martian environment by infrared spectroscopy on Mariner 9. *Icarus* **1972**, *17*, 423–442. [CrossRef]
48. Leovy, C.B.; Zurek, R.W.; Pollack, J.B. Mechanisms for Mars dust storms. *J. Atmos. Sci.* **1973**, *30*, 749–762. [CrossRef]
49. Gierasch, P.J.; Goody, R.M. A model of a Martian great dust storm. *J. Atmos. Sci.* **1973**, *30*, 169–179. [CrossRef]
50. Leovy, C.B.; Briggs, G.A.; Young, A.T.; Smith, B.A.; Pollack, J.B.; Shipley, E.N.; Wildey, R.L. The Martian atmosphere: Mariner 9 television experiment progress report. *Icarus* **1972**, *17*, 373–393. [CrossRef]
51. Cross, C.A. The heat balance of the Martian polar caps. *Icarus* **1971**, *15*, 110–114. [CrossRef]
52. Ryan, J.A.; Sharman, R.D.; Lucich, R.D. Local Mars dust storm generation mechanism. *Geophys. Res. Lett.* **1981**, *8*, 899–901. [CrossRef]
53. Ryan, J.A.; Lucich, R.D. Possible dust devils, vortices on Mars. *J. Geophys. Res.* **1983**, *88*, 11005–11011. [CrossRef]
54. Hess, S.L. Martian winds and dust clouds. *Planet. Space Sci.* **1973**, *21*, 1549–1557. [CrossRef]
55. Newman, C.E.; Lewis, S.R.; Read, S.R.; Forget, F. Modeling the Martian dust cycle, 1, Representations of dust transport processes. *J. Geophys. Res.* **2002**, *107*, 5123. [CrossRef]
56. Newman, C.E.; Lewis, S.R.; Read, S.R.; Forget, F. Modeling the Martian dust cycle, 2, Multiannual radiatively active dust transport simulations. *J. Geophys. Res.* **2002**, *107*, 5124. [CrossRef]
57. Basu, S.; Wilson, J.; Richardson, M.; Ingersoll, A. Simulation of spontaneous and variable global dust storms with the GFDL Mars GCM. *J. Geophys. Res.* **2006**, *111*, E09004. [CrossRef]
58. Kahre, M.A.; Murphy, J.R.; Haberle, R.M. Modeling the Martian dust cycle and surface dust reservoirs with the NASA Ames general circulation model. *J. Geophys. Res.* **2006**, *11*, E06008. [CrossRef]
59. Xiao, J.; Chow, K.C.; Chan, K. Dynamical processes of dust lifting in the northern mid-latitude region of Mars during the dust storm season. *Icarus* **2019**, *317*, 94–103. [CrossRef]
60. Forget, F.; Hourdin, F.; Fournier, R.; Hourdin, C.; Talagrand, O.; Collins, M.; Lewis, S.R.; Read, P.L.; Huot, J.P. Improved general circulation model for the Martian atmosphere from the surface to above 80 km. *J. Geophys. Res.* **1999**, *104*, 24155–24175. [CrossRef]
61. Petrosyan, A.; Galperin, B.; Larsen, S.E.; Lewis, S.R.; Määttänen, A.; Read, P.L.; Renno, N.; Rogberg, L.P.H.T.; Savijärvi, H.; Siili, T.; et al. The Martian atmospheric boundary layer. *Rev. Geophys.* **2011**, *49*, RG3005. [CrossRef]
62. Shirley, J.H.; Mischna, M.A. Orbit-spin coupling and the interannual variability of global-scale dust storm occurrence on Mars. *Planet. Space Sci.* **2017**, *139*, 37–50. [CrossRef]
63. Mischna, M.A.; Shirley, J.H. Numerical modeling of orbit-spin coupling accelerations in a Mars general circulation model: Implications for global dust storm activity. *Planet. Space Sci.* **2017**, *141*, 45–72. [CrossRef]
64. Newman, C.E.; Lee, C.; Mischna, M.A.; Richardson, M.I.; Shirley, J.H. An initial assessment of the impact of postulated orbit-spin coupling on Mars dust storm variability in fully interactive dust simulations. *Icarus* **2019**, *317*, 649–668. [CrossRef]
65. Shirley, J.H.; McKim, R.J.; Battalio, J.M.; Kass, D.M. Orbit-Spin Coupling and the Triggering of the Martian Planet-Encircling Dust Storm of 2018. *J. Geophys. Res. Planets* **2020**, *125*, e2019JE006077. [CrossRef]

66. Bertrand, T.; Wilson, R.J.; Kahre, M.A.; Urata, R.; Kling, A. Simulation of the 2018 global dust storm on Mars using the NASA Ames Mars GCM: A multitracer approach. *J. Geophys. Res. Planets* **2020**, *125*, e2019JE006122. [CrossRef]
67. Wu, Z.; Li, T.; Heavens, N.G.; Newman, C.E.; Richardson, M.I.; Yang, C.; Li, J.; Cui, J. Earth-like thermal and dynamical coupling processes in the Martian climate system. *Earth Sci. Rev.* **2022**, *229*, 104023. [CrossRef]
68. Zhou, X.; Wei, Y.; Wu, Z.; Ren, Z.; Tan, N.; Fan, S.; He, F.; Rong, Z.; Yan, L.; Wang, Y.; et al. Martian whole atmosphere model and dust activities: Review and prospect. *Chin. Sci. Bull.* **2024**, *69*, 1058–1067. (In Chinese) [CrossRef]
69. Fenton, L.K.; Geissler, P.E.; Haberle, R.M. Global warming and climate forcing by recent albedo changes on Mars. *Nature* **2007**, *446*, 646–649. [CrossRef]
70. Kass, D.M.; Schofield, J.T.; Kleinböhl, A.; McCleese, D.J.; Heavens, N.G.; Shirley, J.H.; Steele, L.J. Mars Climate Sounder observation of Mars' 2018 global dust storm. *Geophys. Res. Lett.* **2020**, *47*, e2019GL083931. [CrossRef]
71. Guzewich, S.D.; Lemmon, M.; Smith, C.L.; Martínez, G.; de Vicente-Retortillo, Á.; Newman, C.E.; Baker, M.; Campbell, C.; Cooper, B.; Gómez-Elvira, J.; et al. Mars Science Laboratory observations of the 2018/Mars year 34 global dust storm. *Geophys. Res. Lett.* **2019**, *46*, 71–79. [CrossRef]
72. Haberle, R.M.; Pollack, J.B.; Barnes, J.R.; Zurek, R.W.; Leovy, C.B.; Murphy, J.R.; Lee, H.; Schaeffer, J. Mars atmospheric dynamics as simulated by the NASA Ames General Circulation Model: 1. The zonal-mean circulation. *J. Geophys. Res.* **1993**, *98*, 3093–3123. [CrossRef]
73. Wu, Z.; Li, T.; Zhang, X.; Li, J.; Cui, J. Dust tides and rapid meridional motions in the Martian atmosphere during major dust storms. *Nat. Commun.* **2020**, *11*, 614. [CrossRef] [PubMed]
74. Zhao, Y.; Zhong, L.; Yuan, R.; Zhao, C.; Li, R.; Wang, Y.; Lian, Y.; Richardson, M. Simulation of Martian dust effects on polar CO_2 ice caps and atmospheric circulation using the MarsWRF model. *J. Geophys. Res. Planet.* **2021**, *126*, e2021JE006937. [CrossRef]
75. Melnik, O.; Parrot, M. Electrostatic discharge in Martian dust storms. *J. Geophys. Res.* **1998**, *103*, 29107–29117. [CrossRef]
76. Farrell, W.M.; Kaiser, M.L.; Desch, M.D.; Houser, J.G.; Cummer, S.A.; Wilt, D.M.; Landis, G.A. Detecting electrical activity from Martian dust storms. *J. Geophys. Res.* **1999**, *104*, 3795–3801. [CrossRef]
77. Krauss, C.E.; Horanyi, M.; Robertson, S. Experimental evidence for electrostatic discharging of dust near the surface of Mars. *New J. Phys.* **2003**, *5*, 70. [CrossRef]
78. Merrison, J.; Jensen, J.; Kinch, K.; Mugford, R.; Nørnberg, P. The electrical properties of Mars analogue dust. *Planet Space Sci.* **2004**, *52*, 279–290. [CrossRef]
79. Michael, M.; Tripathi, S.N. Effect of charging of aerosols in the lower atmosphere of Mars during the dust storm of 2001. *Planet Space Sci.* **2008**, *56*, 1696–1702. [CrossRef]
80. Haider, S.A.; Sheel, V.; Smith, M.D.; Maguire, W.C.; Molina-Cuberos, G.J. Effect of dust storms on the D region of the Martian ionosphere: Atmospheric electricity. *J. Geophys. Res. Space Phys.* **2010**, *115*, A12336. [CrossRef]
81. McDunn, T.L.; Bougher, S.W.; Murphy, J.; Smith, M.D.; Forget, F.; Bertaux, J.-L.; Montmessin, F. Simulating the density and thermal structure of the middle atmosphere (80–130 km) of Mars using the MGCM–MTGCM: A comparison with MEX/SPICAM observations. *Icarus* **2010**, *206*, 5–17. [CrossRef]
82. Chaufray, J.Y.; Chaffin, M.S.; Deighan, J.; Jain, S.; Schneider, N.; Mayyasi, M.; Jakosky, B. Effect of the 2018 Martian global dust storm on the CO2 density in the lower nightside thermosphere observed from MAVEN/IUVS Lyman-alpha absorption. *Geophys. Res. Lett.* **2020**, *47*, e2019GL082889. [CrossRef]
83. Fang, X.; Ma, Y.; Lee, Y.; Bougher, S.; Liu, G.; Benna, M.; Mahaffy, P.; Montabone, L.; Pawlowski, D.; Dong, C.; et al. Mars dust storm effects in the ionosphere and magnetosphere and implications for atmospheric carbon loss. *J. Geophys. Res. Space Phys.* **2020**, *125*, e2019JA026838. [CrossRef]
84. Niu, D.D.; Cui, J.; Wu, S.Q.; Gu, H.; Cao, Y.-T.; Wu, Z.-P.; Wu, X.-S.; Zhong, J.-H.; Wu, M.-Y.; Wei, Y.; et al. Species-dependent response of the Martian ionosphere to the 2018 global dust event. *J. Geophys. Res. Planets* **2021**, *126*, e2020JE006679. [CrossRef]
85. Mukundan, V.; Thampi, S.V.; Bhardwaj, A.; Fang, X. Impact of the 2018 Mars global dust storm on the ionospheric peak: A study using a photochemical model. *J. Geophys. Res. Planets* **2021**, *126*, e2021JE006823. [CrossRef]
86. Stone, S.W.; Yelle, R.V.; Benna, M.; Lo, D.Y.; Elrod, M.K.; Mahaffy, P.R. Hydrogen escape from Mars is driven by seasonal and dust storm transport of water. *Science* **2020**, *370*, 824–831. [CrossRef]
87. Clancy, R.T.; Nair, H. Annual (perihelion-aphelion) cycles in the photochemical behavior of the global Mars atmosphere. *J. Geophys. Res. Planets* **1996**, *101*, 12785–12790. [CrossRef]
88. Clancy, R.T.; Wolff, M.J.; Lefèvre, F.; Cantor, B.A.; Malin, M.C.; Smith, M.D. Daily global mapping of Mars ozone column abundances with MARCI UV band imaging. *Icarus* **2016**, *266*, 112–133. [CrossRef]
89. Hvidberg, C.S.; Fishbaugh, K.E.; Winstrup, M.; Svensson, A.; Byrne, S.; Herkenhoff, K.E. Reading the climate record of the Martian polar layered deposits. *Icarus* **2012**, *221*, 405–419. [CrossRef]
90. Colaprete, A.; Barnes, J.; Haberle, R.; Hollingsworth, J.L.; Kieffer, H.H.; Titus, T.N. Albedo of the south pole on Mars determined by topographic forcing of atmosphere dynamics. *Nature* **2005**, *435*, 184–188. [CrossRef] [PubMed]
91. Golombek, M.P.; Warner, N.H.; Ganti, V.; Lamb, M.P.; Parker, T.J.; Fergason, R.L.; Sullivan, R. Small crater modification on Meridiani Planum and implications for erosion rates and climate change on Mars. *J. Geophys. Res. Planets* **2014**, *119*, 2522–2547. [CrossRef]

92. Farley, K.A.; Malespin, C.; Mahaffy, P.; Grotzinger, J.P.; Vasconcelos, P.M.; Milliken, R.E.; Malin, M.; Edgett, K.S.; Pavlov, A.A.; Hurowitz, J.A.; et al. In Situ Radiometric and Exposure Age Dating of the Martian Surface. *Science* **2013**, *343*, 1247166. [CrossRef] [PubMed]
93. Vasavada, A.R.; Chen, A.; Barnes, J.R.; Burkhart, P.D.; Cantor, B.A.; Dwyer-Cianciolo, A.M.; Fergason, R.L.; Hinson, D.P.; Justh, H.L.; Kass, D.M.; et al. Assessment of environments for mars science laboratory entry, descent, and surface operations. *Space Sci. Rev.* **2012**, *170*, 793–835. [CrossRef]
94. Team, R. Characterization of the Martian Surface Deposits by the Mars Pathfinder Rover, Sojourner. *Science* **1997**, *278*, 1765–1767. [CrossRef]
95. Rieder, R.T.; Economou, T.E.; Wänke, H.; Turkevich, A.; Crisp, J.; Brückner, J.; Dreibus, G.; McSween, H.Y., Jr. The Chemical Composition of Martian Soil and Rocks Returned by the Mobile Alpha Proton X-ray Spectrometer: Preliminary Results from the X-ray Mode. *Science* **1998**, *278*, 1771–1774. [CrossRef]
96. Lorenz, R.D.; Martínez, G.M.; Spiga, A.; Vicente-Retortillo, A.; Newman, C.E.; Murdoch, N.; Forget, F.; Millour, E.; Pierron, T. Lander and rover histories of dust accumulation on and removal from solar arrays on Mars. *Planet. Space Sci.* **2021**, *207*, 105337. [CrossRef]
97. Landis, G.A.; Jenkins, P.P. Measurement of the settling rate of atmospheric dust on Mars by the MAE instrument on Mars Pathfinder. *J. Geophys. Res.* **2000**, *105*, 1855–1857. [CrossRef]
98. Crisp, D.; Pathare, A.; Ewell, R.C. The performance of gallium arsenide/germanium solar cells at the Martian surface. *Acta Astronaut.* **2004**, *54*, 83–101. [CrossRef]
99. Staab, M.S.; Herman, J.A.; Reich, K.; Reich, K.; Sridhar, V.; Nelson, R.W. MER Opportunity dust-storm recovery operations and implications for future Mars surface missions. In Proceedings of the 2020 IEEE Aerospace Conference, Big Sky, MT, USA, 7–14 March 2020.
100. Yen, A.; Gellert, R.; Schröder, C.; Morris, R.V.; Bell, J.F., III; Knudson, A.T.; Clark, B.C.; Ming, D.M.; Crisp, J.A.; Arvidson, R.E.; et al. An integrated view of the chemistry and mineralogy of Martian soils. *Nature* **2005**, *436*, 49–54. [CrossRef] [PubMed]
101. Slipher, E.C. *Mars—The Photographic Story*; Northland Press: Flagstaff, AZ, USA, 1962.
102. Horn, D.; McAfee, J.M.; Winer, A.M.; Herr, K.C.; Pimentel, G.C. The composition of the Martian atmosphere: Minor constituents. *Icarus* **1972**, *16*, 543–556. [CrossRef]
103. Cimino, G.; Clavin, W.M. Calibration and analysis of Mariner 7 infrared spectra. *Bull. Am. Astron. Soc.* **1996**, *28*, 1068.
104. Hord, C.W.; Barth, C.A.; Stewart, A.I.; Lane, A.L. Mariner 9 ultraviolet spectrometer experiment: Photometry and topography of Mars. *Icarus* **1972**, *17*, 433–456. [CrossRef]
105. Anderson, E.; Loevy, C. Mariner 9 television limb observations of dust and ice hazes on Mars. *J. Atmos. Sci.* **1978**, *35*, 723. [CrossRef]
106. Martin, T.Z.; Richardson, M.I. New dust opacity mapping from Viking infrared thermal mapper data. *J. Geophys. Res.* **1993**, *98*, 10941–10949. [CrossRef]
107. Biggs, G.A.; Baum, W.A.; Barnes, J. Viking Orbiter imaging observations of dust in the martian atmosphere. *J. Geophys. Res.* **1979**, *84*, 2795. [CrossRef]
108. Malin, M.C.; Danielson, G.E.; Ravine, M.A.; Soulanille, T.A. Design and development of the Mars Observer Camera. *Int. J. Imaging Syst. Technol.* **1991**, *3*, 76–91. [CrossRef]
109. Malin, M.C.; Danielson, G.E.; Ingersoll, A.P.; Masursky, H.; Veverka, J.; Ravine, M.A.; Soulanille, T.A. Mars Observer Camera. *J. Geophys. Res.* **1992**, *97*, 7699–7718. [CrossRef]
110. Christensen, P.R.; Bandfield, J.L.; Hamilton, V.E.; Ruff, S.W.; Kieffer, H.H.; Titus, T.N.; Malin, M.C.; Morris, R.V.; Lane, M.D.; Clark, R.L.; et al. Mars Global Surveyor Thermal Emission Spectrometer experiment: Investigation description and surface science results. *J. Geophys. Res.* **2001**, *106*, 23823–23871. [CrossRef]
111. Tomasko, M.G.; Doose, L.R.; Lemmon, M.; Smith, P.H.; Wegryn, E. Properties of dust in Martian atmosphere from the Imager on Mars Pathfinder. *J. Geophys. Res.* **1999**, *104*, 8987–9007. [CrossRef]
112. Smith, P.H.; Lemmon, M. Opacity of the Martian atmosphere measured by the Imager for Mars Pathfinder. *J. Geophys. Res.* **1999**, *104*, 8975–8985. [CrossRef]
113. Christensen, P.R.; Jakosky, B.M.; Kieffer, H.H.; Malin, M.C.; McSween, H.Y., Jr.; Nealson, K.; Mehall, G.L.; Silverman, S.H.; Ferry, S.; Caplinger, M.; et al. The Thermal Emission Imaging System (THEMIS) for the Mars 2001 Odyssey mission. *Space Sci. Rev.* **2004**, *110*, 85–130. [CrossRef]
114. Määttänen, A.; Listowski, C.; Montmessin, F.; Maltagliati, L.; Reberac, A.; Joly, L.; Bertaux, L.J. A complete climatology of the aerosol vertical distribution on Mars from MEx/SPICAM UV solar occultations. *Icarus* **2013**, *223*, 892–941. [CrossRef]
115. Bibring, J.-P.; Soufflot, A.; Berthé, M.; Langevin, Y.; Gondet, B.; Drossart, P.; Bouyé, M.; Combes, M.; Puget, P.; Semery, A.; et al. OMEGA: Observatoire pour la Mineralogie, l'Eau, les Glaces et l'Activité. *Eur. Space Agency Spec. Pub.* **2004**, *1240*, 37.
116. Gwinner, K.; Jaumann, R.; Hauber, E.; Hoffmann, H.; Heipke, C.; Oberst, J.; Neukum, G.; Ansan, V.; Bostelmann, J.; Dumke, A.; et al. The High Resolution Stereo Camera (HRSC) of Mars Express and its approach to science analysis and mapping for Mars and its satellites. *Planet. Space Sci.* **2016**, *126*, 93–138. [CrossRef]
117. Lemmon, M.T.; Wolff, M.J.; Bell, J.F., III; Smith, M.D.; Cantor, B.A.; Smith, P.H. Dust aerosol, clouds, and the atmospheric optical depth record over 5 Mars years of the Mars Exploration Rover mission. *Icarus* **2015**, *251*, 96–111. [CrossRef]

118. Bell, J.F., III; Squyres, S.W.; Herkenhoff, K.E.; Maki, J.N.; Arneson, H.M.; Brown, D.; Collins, S.A.; Dingizian, A.; Elliot, S.T.; Hagerott, E.C.; et al. Mars Exploration Rover Athena Panoramic Camera (Pancam) investigation. *J. Geophys. Res. Planets* **2003**, *108*, 8063. [CrossRef]
119. Chistensen, P.R.; Mehall, G.L.; Silverman, S.H.; Anwar, S.; Cannon, G.; Gorelick, N.; Kheen, R.; Tourville, T.; Bates, D.; Ferry, S.; et al. Miniature Thermal Emission Spectrometer for the Mars Exploration Rovers. *J. Geophys. Res. Planets* **2003**, *108*, 8064.
120. Bell, J.F., III; Wolff, M.J.; Malin, M.C.; Calvin, W.M.; Cantor, B.A.; Caplinger, M.A.; Clancy, R.T.; Edgett, K.S.; Edwards, L.J.; Fahle, J.; et al. Mars Reconnaissance Orbiter Mars Color Imager (MARCI): Instrument description, calibration, and performance. *J. Geophys. Res. Planets* **2009**, *114*, E08S92. [CrossRef]
121. Murchie, S.; Arvidson, R.; Bedini, P.; Beisser, K.; Bibring, J.-P.; Bishop, J.; Boldt, J.; Cavender, P.; Choo, T.; Clancy, R.T.; et al. Compact Reconnaissance Imaging Spectrometer for Mars (CRISM) on Mars Reconnaissance Orbiter (MRO). *J. Geophys. Res. Planets* **2007**, *112*, E05S03. [CrossRef]
122. McCleese, D.J.; Schofield, J.T.; Taylor, F.W.; Calcutt, S.B.; Foote, M.C.; Kass, D.M.; Leovy, C.B.; Paige, D.A.; Read, P.L.; Zurek, R.W. Mars Climate Sounder: An investigation of thermal and water vapor structure, dust and condensate distributions in the atmosphere, and energy balance of the polar regions. *J. Geophys. Res. Planets* **2007**, *112*, E05S06. [CrossRef]
123. Smith, P.H.; Tamppari, L.; Arvidson, R.E.; Bass, D.; Blaney, D.; Boynton, W.; Carswell, A.; Catling, D.; Clark, B.; Duck, T.; et al. Introduction to special section on the Phoenix Mission: Landing Site Characterization Experiments, Mission Overviews, and Expected Science. *J. Geophys. Res. Planets* **2008**, *113*, E00A18. [CrossRef]
124. Grotzinger, J.P.; Crisp, J.; Vasavada, A.R.; Anderson, R.C.; Baker, C.J.; Barry, R.; Blake, D.F.; Conrad, P.; Edgett, K.S.; Ferdowski, B.; et al. Mars Science Laboratory mission and science investigation. *Space Sci. Rev.* **2012**, *170*, 5–56. [CrossRef]
125. Vandaele, A.C.; Neefs, E.; Drummond, R.; Thomas, I.R.; Daerden, F.; Lopez-Moreno, J.-J.; Rodriguez, J.; Patel, M.R.; Bellucci, G.; Allen, M.; et al. Science objectives and performances of NOMAD, a spectrometer suite for the ExoMars TGO mission. *Planet. Space Sci.* **2015**, *119*, 233–249. [CrossRef]
126. Thomas, N.; Cremonese, G.; Ziethe, R.; Gerber, M.; Brändli, M.; Bruno, G.; Erismann, M.; Gambicorti, L.; Gerber, T.; Ghose, K.; et al. The Colour and Stereo Surface Imaging System (CaSSIS) for the ExoMars Trace Gas Orbiter. *Space Sci. Rev.* **2017**, *212*, 1897–1944. [CrossRef]
127. Korablev, O.; Montmessin, F.; Trokhimovskiy, A.; Fedorova, A.A.; Shakun, A.V.; Grigoriev, A.V.; Moshkin, B.E.; Ignatiev, N.I.; Forget, F.; Lefèvre, F.; et al. The Atmospheric Chemistry Suite (ACS) of Three Spectrometers for the ExoMars 2016 Trace Gas Orbiter. *Space Sci. Rev.* **2018**, *214*, 7. [CrossRef]
128. Maki, J.N.; Golombek, M.; Deen, R.; Abarca, H.; Sorice, C.; Goodsall, T.; Schwochert, M.; Lemmon, M.; Trebi-Ollennu, A.; Banerdt, W.B. The Color Cameras on the InSight Lander. *Space Sci. Rev.* **2018**, *214*, 105. [CrossRef]
129. Banfield, D.; Rodriguez-Manfredi, J.A.; Russell, C.T.; Rowe, K.M.; Leneman, D.; Lai, H.R.; Cruce, P.R.; Means, J.D.; Johnson, C.L.; Mittelholz, A.; et al. Insight Auxiliary Payload Sensor Suite (APSS). *Space Sci. Rev.* **2019**, *215*, 4. [CrossRef]
130. Bell, J.F., III; Maki, J.N.; Mehall, G.L.; Ravine, M.A.; Caplinger, M.A.; Bailey, Z.J.; Brylow, S.; Schaffner, J.A.; Kinch, K.M.; Madsen, M.B.; et al. The Mars 2020 Perseverance Rover Mast Camera Zoom (Mastcam-Z) Multispectral, Stereoscopic Imaging Investigation. *Space Sci. Rev.* **2021**, *217*, 24. [CrossRef]
131. Maurice, S.; Wiens, R.C.; Bernardi, P.; Caïs, P.; Robinson, S.; Nelson, T.; Gasnault, O.; Reess, J.-M.; Deleuze, M.; Rull, F.; et al. The SuperCam Instrument Suite on the Mars 2020 Rover: Science Objectives and Mast-Unit Description. *Space Sci. Rev.* **2021**, *217*, 47. [CrossRef]
132. Rodriguez-Manfredi, J.A.; de la Torre Juárez, M.; Alonso, A.; Apéstigue, V.; Arruego, I.; Atienza, T.; Banfield, D.; Boland, J.; Carrera, M.A.; Castañer, L.; et al. The Mars Environmental Dynamics Analyzer, MEDA. A Suite of Environmental Sensors for the Mars 2020 Mission. *Space Sci. Rev.* **2021**, *217*, 48. [CrossRef] [PubMed]
133. Jones, A.R.; Wolff, M.; Alshamsi, M.; Osterloo, M.; Bay, P.; Brennan, N.; Bryant, K.; Castleman, Z.; Curtin, A.; DeVito, E.; et al. The Emirates Exploration Imager (EXI) Instrument on the Emirates Mars Mission (EMM) Hope Mission. *Space Sci. Rev.* **2021**, *217*, 81. [CrossRef]
134. Meng, Q.; Wang, D.; Wang, X.; Li, W.; Yang, X.; Yan, D.; Li, Y.; Cao, Z.; Ji, Q.; Sun, T.; et al. High Resolution Imaging Camera (HiRiC) on China's first Mars exploration Tianwen-1 mission. *Space Sci. Rev.* **2021**, *217*, 42. [CrossRef]
135. Yu, G.B.; Liu, E.H.; Liu, G.L.; Zhou, L.; Zeng, J.Z.; Chen, Y.P.; Zhou, X.D.; Zhao, R.J.; Zhu, S.Y. Moderate Resolution Imaging Camera (MoRIC) of China's First Mars Mission Tianwen-1. *Earth Planet. Phys.* **2020**, *4*, 364–370. [CrossRef]
136. Yang, J.-F.; Liu, D.-W.; Xue, B.; Lyu, J.; Liu, J.-J.; Li, F.; Ren, X.; Ge, W.; Liu, B.; Ma, X.-L.; et al. Design and ground verification for Multispectral Camera on the Mars Tianwen-1 Rover. *Space Sci. Rev.* **2022**, *218*, 19. [CrossRef]
137. Li, B.; Yue, Z.; Qu, S.; Yao, P.; Fu, X.; Ling, Z.; Chen, S. Spatio-Temporal Analysis of Dust Storm Activity in Chryse Planitia Using MGS-MOC Observations from Mars Years 24–28. *Universe* **2021**, *7*, 433. [CrossRef]
138. Guha, B.K.; Gebhardt, C.; Young, R.M.B.; Wolff, M.J.; Montabone, L. Seasonal and diurnal variations of dust storms in Martian year 36 based on the EMM-EXI database. *J. Geophys. Res. Planets* **2024**, *129*, e2023JE008156. [CrossRef]
139. Wang, H.; Ingersoll, A.P. Martian clouds observed by Mars Global Surveyor Mars Orbiter Camera. *J. Geophys. Res.* **2002**, *107*, 5078. [CrossRef]
140. Battalio, M.; Wang, H. The Mars Dust Activity Database (MDAD): A comprehensive statistical study of dust storm sequences. *Icarus* **2021**, *354*, 114059. [CrossRef]

141. Wu, B.; Dong, J.; Wang, Y.; Rao, W.; Sun, Z.Z.; Li, Z.; Tan, Z.; Chen, Z.; Wang, C.; Liu, W.C.; et al. Landing Site Selection and Characterization of Tianwen-1 (Zhurong Rover) on Mars. *J. Geophys. Res. Planets* **2022**, *127*, e2021JE007137. [CrossRef]
142. Shirley, J.H.; McConnochie, T.H.; Kass, D.M.; Kleinböhl, A.; Schofield, J.T.; Heavens, N.G.; McCleese, D.J.; Benson, J.; Hinson, D.P.; Bandfield, J.L. Temperature and aerosol opacities of the Mars atmosphere at aphelion: Validation and inter-comparison of limb sounding profiles from MRO/MCS and MGS/TES. *Icarus* **2015**, *251*, 26–49. [CrossRef]
143. Laseigneur, Y.; Vincendon, M. OMEGA/Mars Express: A new Martian atmospheric dust hunter. *Icarus* **2023**, *392*, 115366. [CrossRef]
144. Smith, M.D.; Pearl, J.C.; Conrath, B.J.; Christensen, P.R. Mars Global Surveyor Thermal Emission Spectrometer (TES) observations of dust opacity during aerobraking and science phasing. *J. Geophys. Res.* **2000**, *105*, 9539–9552. [CrossRef]
145. Smith, M.D.; Bandfield, J.L.; Christensen, P.R.; Richardson, M.I. Thermal Emission Imaging System (THEMIS) infrared observations of atmospheric dust and water ice cloud optical depth. *J. Geophys. Res.* **2003**, *108*, 5115. [CrossRef]
146. Smith, M.D. Interannual variability in TES atmospheric observations of Mars during 1999-2003. *Icarus* **2004**, *167*, 148–165. [CrossRef]
147. Kleinböhl, A.; Schofield, J.T.; Kass, D.M.; Abdou, W.A.; Backus, C.R.; Sen, B.; Shirley, J.H.; Lawson, W.G.; Richardson, M.I.; Taylor, F.W.; et al. Mars Climate Sounder limb profile retrieval of atmospheric temperature, pressure and dust and water ice opacity. *J. Geophys. Res.* **2009**, *114*, E10006. [CrossRef]
148. Millour, E.; Forget, F.; Spiga, A.; Navarro, T.; Madeleine, J.B.; Montabone, L.; Pottier, A.; Lefevre, F.; Montmessin, F.; Chaufray, J.-Y.; et al. The Mars Climate Database (MCD version 5.2). In Proceedings of the European Planetary Science Congress 2015, Nantes, France, 27 September 2015.
149. Kleinböhl, A.; Spiga, A.; Kass, D.M.; Shirley, J.H.; Millour, E.; Montabone, L.; Forget, F. Diurnal variations of dust during the 2018 global dust storm observed by the Mars Climate Sounder. *J. Geophys. Res. Planets* **2020**, *125*, e2019JE006115. [CrossRef]
150. Vandaele, A.C.; Korablev, O.; Daerden, F.; Aoki, S.; Thomas, I.R.; Altieri, F.; López-Valverde, M.; Villanueva, G.; Liuzzi, G.; Smith, M.D.; et al. Martian dust storm impact on atmospheric H_2O and D/H observed by ExoMars Trace Gas Orbiter. *Nature* **2019**, *568*, 521–525. [CrossRef]
151. Information Office of the State Council of the People's Republic of China. *China's Spaceflight in 2021*; People's Publishing House: Beijing, China, 2022. (In Chinese)
152. Kleinböhl, A.; Schofield, J.T.; Abdou, W.A.; Irwin, P.G.J.; de Kok, R.J. A single-scattering approximation for infrared radiative transfer in limb geometry in the Martian atmosphere. *J. Quant. Spectrosc. Radiat. Transfer.* **2011**, *112*, 1568–1580. [CrossRef]
153. He, F.; Wei, Y.; Rong, Z.; Reng, Z.; Yan, L.; Tan, N.; Wang, Y.; Fan, K.; Zhou, X.; Gao, J. Monitoring methods for Martian dust storms. *Chin. Sci. Bull.* **2023**, *68*, 2046–2057. (In Chinese) [CrossRef]
154. Montabone, L.; Forget, F. On forecasting dust storms on Mars. In Proceedings of the 48th International Conference on Environmental Systems, Albuquerque, NM, USA, 8–12 July 2018.
155. Fan, K.; Wei, Y. Prospection of multi-spacecraft planetary exploration missions in upcoming future. *Chin. Sci. Bull.* **2021**, *66*, 4350–4353. (In Chinese) [CrossRef]

Disclaimer/Publisher's Note: The statements, opinions and data contained in all publications are solely those of the individual author(s) and contributor(s) and not of MDPI and/or the editor(s). MDPI and/or the editor(s) disclaim responsibility for any injury to people or property resulting from any ideas, methods, instructions or products referred to in the content.

remote sensing

MDPI

Article

Crater Detection and Population Statistics in Tianwen-1 Landing Area Based on Segment Anything Model (SAM)

Yaqi Zhao and Hongxia Ye *

Key Laboratory for Information Sciences of Electromagnetic Waves (MoE), Fudan University, Shanghai 200433, China; 21210720309@m.fudan.edu.cn
* Correspondence: yehongxia@fudan.edu.cn

Abstract: Crater detection is useful for research into dating a planetary surface's age and geological mapping. The high-resolution imaging camera (HiRIC) carried by the Tianwen-1 rover provides digital image model (DIM) datasets with a resolution of 0.7 m/pixel, which are suitable for detecting meter-scale craters. The existing deep-learning-based automatic crater detection algorithms require a large number of crater annotation datasets for training. However, there is currently a lack of datasets of optical images of small-sized craters. In this study, we propose a model based on the Segment Anything Model (SAM) to detect craters in Tianwen-1's landing area and perform statistical analysis. The SAM network was used to obtain a segmentation mask of the craters from the DIM images. Then non-circular filtering was used to filter out irregular craters. Finally, deduplication and removal of false positives were performed to obtain accurate circular craters, and their center's position and diameter were obtained through circular fitting analysis. We extracted 841,727 craters in total, with diameters ranging from 1.57 m to 7910.47 m. These data are useful for further Martian crater catalogs and crater datasets. Additionally, the crater size–frequency distribution (CSFD) was also analyzed, indicating that the surface ages of the Tianwen-1 landing area are ~3.25 billion years, with subsequent surface resurfacing events occurring ~1.67 billion years ago.

Keywords: Mars; crater detection; Tianwen-1; segmentation; segment anything model

1. Introduction

China's first Mars exploration mission, Tianwen-1, was launched on 23 July 2020, with the aim of completing orbital, landing, and roving tasks. The high-resolution imaging camera (HiRIC) [1] carried by the Tianwen-1 orbiter provided detailed images of the landing area. The landing area is dotted with numerous craters, which can offer crucial information about the evolution of the landing region. Craters, as one of the most prominent features on the planetary surface, play a key role in planetary science. The distribution of craters provides valuable clues for revealing the aging process of geological structures [2,3] and is also one of the important factors in selecting landing sites for planetary probes [4]. Calculating the size–frequency distribution of craters is a primary method for estimating the surface age of celestial bodies [5,6], making it a key technique in planetary geological research. Therefore, the automatic segmentation and statistical analysis of the features of Martian surface craters are crucial in Martian exploration missions. Traditional methods [2,7] rely on planetary scientists manually labeling craters on remote sensing images, which is time-consuming and labor-intensive, and cannot detect craters in real time. Therefore, an efficient, accurate, and unsupervised method for automatic crater detection is highly necessary.

Currently, several methods for automatic crater detection have been developed, which can be roughly categorized into methods based on extraction of the morphological features and methods based on deep learning. Methods based on extraction of the morphological features utilize intuitive and simple features, such as the craters' shape or spectral characteristics, such as the Canny edge contour algorithm [8], the Hough transform [9],

and template matching [10]. Yang et al. [8] used a multi-scale Canny operator to detect the edges of craters. However, variations in the illumination conditions between different images may affect the performance of edge detection, resulting in suboptimal crater detection, Leroy et al. [11] utilized template matching and probability volume analysis to identify Martian craters larger than 5 pixels (an image resolution of 250 m/pixel). However, the experimental scenarios were relatively simple, with mostly regular circular craters. Galloway et al. [12] investigated the impact of preprocessing via Canny edge detection on the performance of the Hough transform, finding that edge detection significantly affected the performance of the Hough transform, and they considered the Hough transform to be a more practical method than edge detection. However, their approach requires computing gradients for each edge pixel, which is time-consuming, and they did not test the performance when detecting multiple-sized craters in larger images. These methods based on the extraction of morphological features can effectively detect simple craters in small datasets. However, due to the complexity of the terrain conditions and the common occurrence of densely distributed craters in real-world scenarios, these methods exhibit relatively lower detection rates and efficiency when dealing with large-scale datasets.

To improve the efficiency of automatic crater detection, deep learning has been widely applied in crater detection tasks. Convolutional Neural Network (CNN)-based deep learning algorithms have achieved tremendous success in segmentation and detection tasks in remote sensing images [13,14]. Li et al. [15] introduced a novel encoder-decoder-based network, MarsSeg, specifically tailored for segmentation of the Martian landscape, and demonstrated its advanced performance. Silburt et al. [16] successfully used the U-Net [17,18] model and template matching algorithm to extract craters on lunar DEM images. Since the U-Net network layers they used were relatively shallow, the segmentation ability for the craters' outlines was poor. Lee et al. [19] utilized the U-Net model trained on lunar DEM images by Silburt et al. to identify and extract craters in Martian DEM images, confirming the effectiveness of the U-Net model in crater detection. In order to enhance the efficiency of crater detection and the accuracy of identifying large Martian craters, Chen et al. [20] proposed a novel CNN called MC-UNet. They incorporated average pooling and embedded channel attention into the skip-connection process between the encoder and decoder layers to identify craters in optical images of Mars. To improve the performance and accuracy of automatic crater identification, Zhao et al. [21] explored a novel embedded U-Net structure based on U-Net, named Square U-Net (SqUNet). They used the embedded U-Net architecture to replace traditional convolutional modules, successfully achieving high-precision identification and extraction of lunar DEM craters, and demonstrating high-precision test results on Martian DEM as well. However, these algorithms for automatic crater detection are supervised models, requiring many labeled crater datasets for training. The currently available global catalogs of lunar craters [2,7,22] include craters with diameters greater than 1 km, while the global catalog of Martian craters includes craters with diameters greater than 1 km [23]. The Chang'e-5's landing area has a catalog of craters with diameters larger than 200 m [24]. However, most landing areas lack a catalog of meter-sized craters. Therefore, in the absence of a crater catalog, a model that does not require additional training would be highly valuable.

In the remote sensing field, several foundational large models tailored for segmentation tasks have emerged, such as RSPrompter [25] and SAM [26]. These foundational large models are typically trained on extremely large annotated datasets, endowing them with strong generalization capabilities for segmentation tasks. Therefore, they can be easily extended to other segmentation tasks. SAM [26], in particular, is suitable for unsupervised segmentation tasks. SAM was initially designed to address a fundamental challenge in image segmentation: how to effectively identify and segment objects in images without training data that are specific to a particular task. SAM aims to create a universal model that is capable of adapting to different types and sizes of images, automatically identifying and segmenting target objects in these images, even if these objects have never been encountered by the model before. SAM networks have achieved significant success in various domains.

In the field of medical imaging, SAM has been used for the automatic identification and segmentation of structures in various medical images [27], which is particularly important in situations with a scarcity of annotated medical images. In processing remote sensing images, Giannakis et al. [28] validated the effectiveness of SAM in identifying planetary craters by providing examples from different celestial bodies and types of data. However, extracting crater targets from high-resolution planetary images remains challenging due to SAM's ability to extract any type of target from images.

The Tianwen-1 mission landed in the southern part of Utopia Planitia, located in the northern lowlands of Mars (25.1°N, 109.9°E). Tianwen-1 is a comprehensive mission aiming to study the morphology, mineralogy, spatial environment, and distribution of water ice on Mars [29]. Many researchers have conducted detailed geological surveys of the Tianwen-1 landing area, gaining a deep understanding of the geological background and evolutionary history of Utopia Planitia [30–33]. However, studies on impact craters in the Tianwen-1 landing area have only extracted partial areas or a small number of large craters for an analysis of their distribution, lacking a detailed catalog of craters in the landing area. Currently, the Tianwen-1 landing area has a catalog of craters with diameters larger than 80 m [34]. Cao et al. [35] annotated over 7000 craters larger than 1 m in three subregions of the Tianwen-1 landing area, providing labels for small-sized craters. Providing a complete catalog of meter-sized impact craters for the landing area is crucial. Understanding the distribution, quantity, size, and other important parameters of craters not only helps deepen our understanding of the geological environment near the Mars landing site but also provides important references for future scientific research and exploration missions. This study aimed to extract multi-scale craters in the landing area and make a more detailed and in-depth analysis of the age and geological evolution of the landing area.

In this work, we used SAM to identify and extract craters from the digital image model (DIM) of the Tianwen-1 landing area. The SAM was used to identify craters in the DIM and obtain their segmentation mask, and a series of postprocessing steps was performed to extract the positions and sizes of craters. Through analyzing the CSFD of the craters, we estimated their specific surface age to be approximately ~3.25 Ga, with subsequent surface resurfacing events occurring around ~1.67 Ga. The main contributions of this article are as follows:

(a) We proposed a complete solution for automatic crater identification based on SAM, which was applied to extract craters from the DIM of the Tianwen-1 landing area.
(b) Experiments were conducted in three subregions of the Tianwen-1 landing area, where SAM achieved a recall rate of 100%. Many new craters were detected, confirming its effectiveness in the task of crater extraction.
(c) On the basis of the DIM of the Tianwen-1 landing area, we provided a relatively comprehensive crater dataset, including information on the position and diameter of the craters.
(d) We analyzed the CSFD of the craters and estimated the surface age of the landing area, conducting an analysis of the geological evolution of the landing region.

The structure of this article is as follows: Section 2 introduces the complete process of using SAM to extract craters from the DIM of the Tianwen-1 landing area. Section 3 describes the experimental results of SAM on the lunar crater dataset. Section 4 presents the results of crater extraction, including an analysis of the number of craters extracted, an analysis of the craters' size and distribution frequency, and an explanation of the catalog of craters. Section 5 discusses the limitations of the study and outlines future work. Finally, Section 6 draws some conclusions.

2. Materials and Methods

We utilized the DIM data of the Tianwen-1 landing area captured by the high-resolution imaging camera (HiRIC) [1] installed on the Tianwen-1 orbiter. The resolution is 0.7 m per pixel, allowing for the detection of small-sized craters at the meter scale. The

complete process of extracting craters from the Tianwen-1 landing area's DIM consisted of three steps. Firstly, preprocessing of the data was conducted by performing multi-scale cropping and down-sampling of the Tianwen-1 landing area DIM to generate a multi-scale dataset. Next, the SAM was applied to segment the newly generated multi-scale dataset [26]. Subsequently, each segmented mask was analyzed, non-circular masks were filtered out, and circular fitting was applied to the filtered mask edges. Next, deduplication and removal of false positives were performed on the information on the craters extracted from the multi-scale dataset. Finally, the pixel coordinates of the impact craters' centers were converted to latitude and longitude coordinates.

2.1. Data Preprocessing

Figure 1a shows the DIM of the entire landing area, which was obtained by stitching together 15 DIMs with a pixel size of 28,583 × 42,869 on the basis of their latitude and longitude. The pixel size of DIM images for the entire landing area is 85,749 × 214,345 (https://moon.bao.ac.cn/web/zhmanager/mars1, accessed on 3 August 2021). Figure 1b shows the details of one image, where some craters of different sizes can be seen. Due to the different scales of the craters in the images, we adopted a multi-scale cropping strategy, which helped the network model adapt better to the objects' size. We performed overlapping cropping using five different scales with cropping sizes of 1024 × 1024, 2048 × 2048, 4096 × 4096, 8192 × 8192, and 16,384 × 16,384, corresponding to overlap sizes of 128, 256, 512, 1024, and 2048, respectively. The corresponding pixel diameter range of the main craters detected were 2∼100, 4∼200, 8∼400, 16∼800, and 32~1600, respectively. This approach allowed for the extraction of as many craters of all sizes as possible.

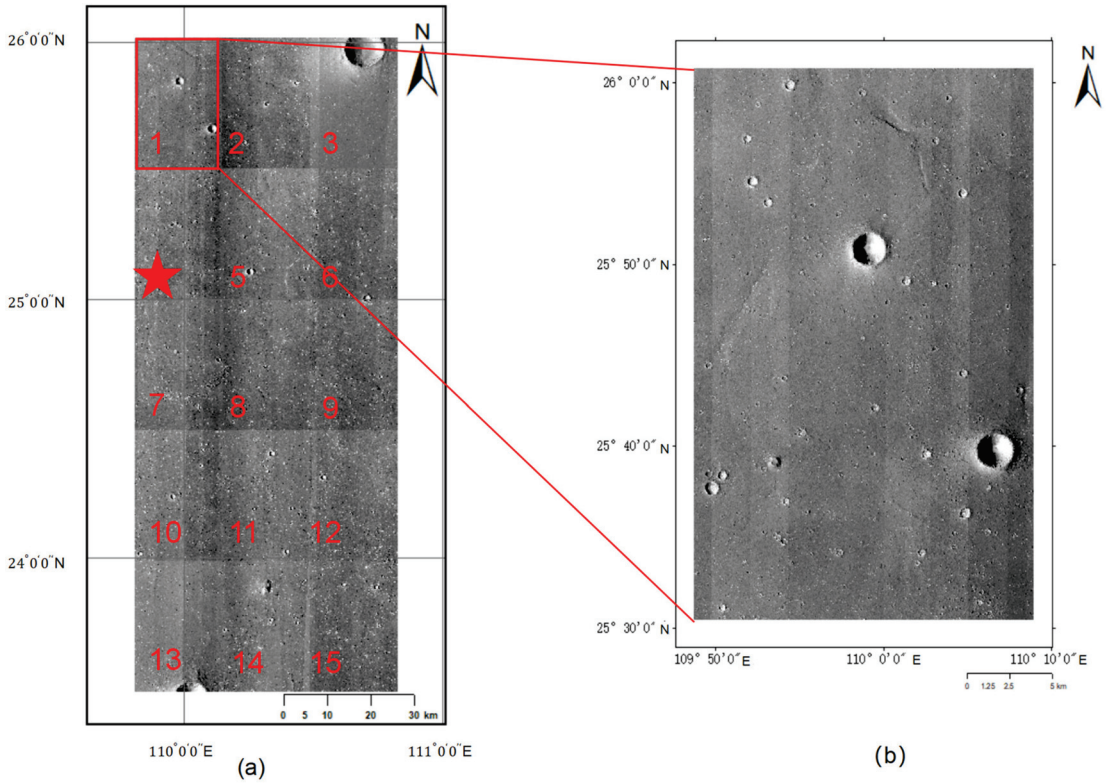


Figure 1. Digital image map (DIM) of Tianwen-1's landing area. (**a**) The 15 DIMs of the landing area. The red star in the image represents the landing location of the Zhurong rover. (**b**) DIM of the first region in the landing area (HX1_GRAS_HIRIC_DIM_0.7_0001_254537N1095850E_A).

2.2. SAM

The SAM [26] is an advanced deep learning image segmentation model that has been trained on a total of over 1.1 billion masks from more than 11 million images [26],

demonstrating exceptional image segmentation capabilities. The model consists of three main components: a prompt encoder, an image encoder, and a lightweight mask decoder. The image is processed through the image encoder. The prompts, such as points, boxes, masks, or text, are transformed into a form that is understandable by the model through the prompt encoder. The mask decoder receives representations of the prompts and images to produce plausible masks.

Figure 2 shows the data flow of the SAM's network in generating crater masks from the DIM's outputs. The default parameters of the SAM network were used. First, the image was preprocessed by resizing its longest side to 1024 while maintaining the aspect ratio and then normalizing it. The image encoder used was the Vision Transformer (ViT) [36], which treated the image as a sequence of patches and captures complex relationships between these patches using a self-attention mechanism. After preprocessing, the image was segmented into patches through patch embedding, and each patch was converted into a deep feature vector. Here, patch embedding used a 2D convolution with a kernel size of 16 $\times$ 16, a stride of 16, and an output dimension of 1280, resulting in 64 $\times$ 64 $\times$ 1280 feature maps. Next, position encoding was added to help the model understand the spatial arrangement of the objects in the image. Then these vectors were processed using the transformer architecture [37] to enhance the features' representation and obtain high-dimensional image embeddings. Finally, a convolutional neural network (CNN) was used for reducing the dimensionality and adjustment of the channel for the segmentation task. The prompt encoder can encode points, boxes, masks, and text, but in this case, automatic segmentation was adopted. In this form, 32 $\times$ 32 independent prompt points were evenly distributed across the image region, and the prompt points contained information on the location. These points were divided into 16 batches, each with 64 points. Through the mask decoder, the masks and the corresponding confidence IOU prediction values were generated. The masks were filtered using the box non-maximum suppression (Box NMS) [26] technique to retain the most relevant bounding boxes and eliminate redundant ones, resulting in 112 masks. The results included the following information:

(a) Segmentation masks and the area of each mask;
(b) Boundary boxes for each mask;
(c) A quality score (ranging from 0 to 1) for the boundary box of each mask, measuring the reliability of the mask;
(d) A stability score (ranging from 0 to 1) for each mask, assessing the stability of the mask at different input coordinates.

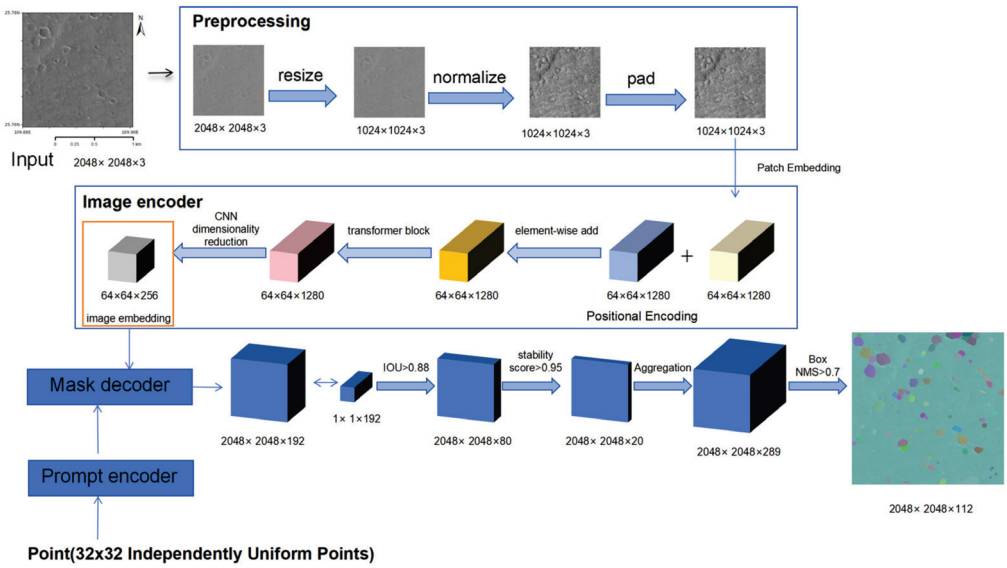


Figure 2. Network structure of the SAM for the automatic identification of craters (Different colors in the output image represent different segmentation targets).

In summary, SAM is suitable for crater detection tasks, as it can identify craters and estimate the size of craters by providing direct information about the mask's edges and region. Figure 3 illustrates an example of using SAM to identify craters in the DIM of the Tianwen-1 landing area, in which different colors represent different segmented objects. Despite not being specifically trained for high-resolution images of Mars, SAM appeared to capture all major features in the image, demonstrating its effectiveness in crater detection. Additionally, SAM could identify craters and provide information about the masks' edges and regions for estimations of the craters' size, offering significant advantages in creating crater datasets.

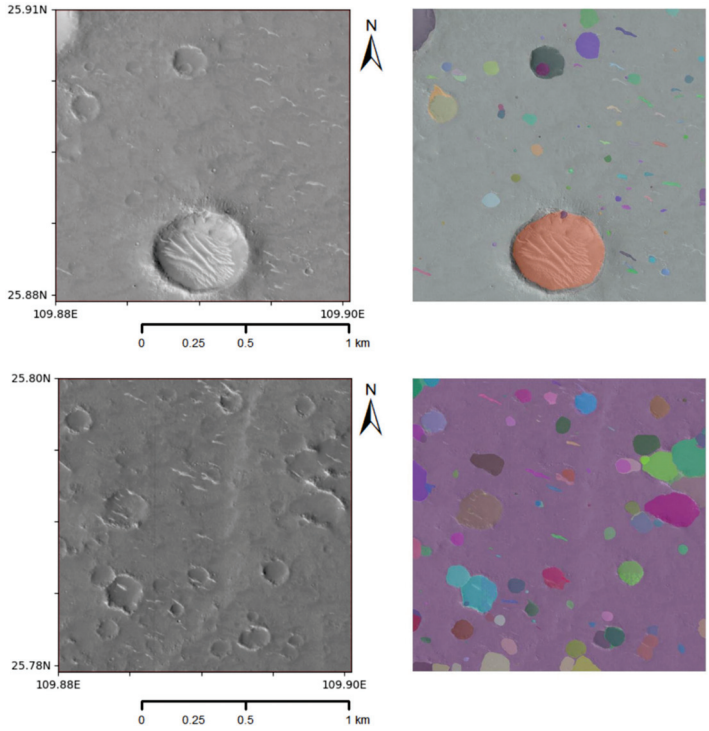


Figure 3. Segmented images from SAM (Different colors in the output image represent different segmentation targets). (**a**) DIM of the landing area. (**b**) Segmented images outputted by SAM.

2.3. Crater Extraction

The main process for extracting craters from the DIM images of the Tianwen-1 landing area was as follows:

(a) Using SAM model to obtain segmentation masks for DIM images of different sizes;
(b) Filtering out non-circular edges from the segmented edges;
(c) Performing circular fitting with the edges of the segmentation masks;
(d) Removing duplicates and false circles;
(e) Converting pixel coordinates to geographic coordinates.

2.3.1. Circular Metrics

The above SAM extracts segmentation masks with different morphological features from input images. We used the "findContours" function in OpenCV [38] to obtain the coordinates of edge pixels in the mask. Most craters have a circular shape, so we needed to filter out the non-circular masks. We defined n as a measure to evaluate the circularity of each mask, and the formula was defined as follows [39].

$$n = \frac{C}{P} = \frac{2\sqrt{\pi A}}{P} \quad (1)$$

Here, A is the area of the mask (number of pixels), and P is the sum of distances between any two adjacent pixels on the boundary.

This study aimed to create a dataset of craters, including the centers' coordinates and radius, and only regular circular craters were considered. Therefore, a circularity threshold parameter was used to filter irregular circular craters. Figure 4 shows the circularity statistics of all the extracted objects in the dataset. We found that 57% of the objects had a circularity above 0.75. Subsequently, a circularity threshold of 0.75 was set to filter irregular circular craters. Objects with a circularity greater than 0.75 were retained for subsequent circular fitting. A detailed analysis for this threshold is in Section 3.2.

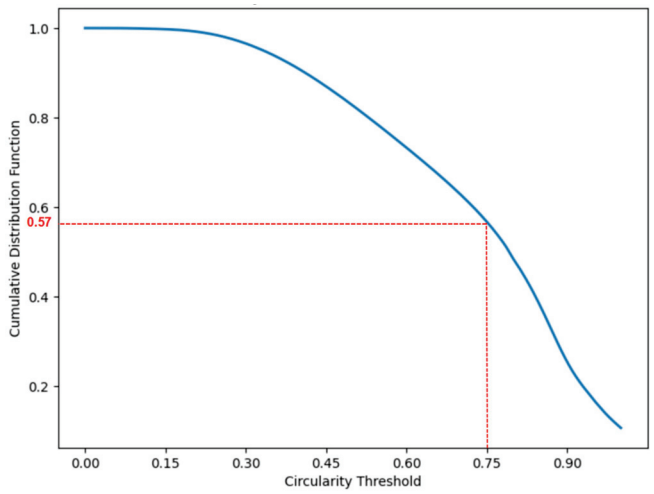


Figure 4. Cumulative distribution curve of the circularity of objects segmented using SAM.

Figure 5 shows the images before (Figure 5a) and after (Figure 5b) removing non-circular masks. It can be observed that almost all the non-circular masks (green) were removed, while the remaining circular masks (red) proceeded to the subsequent circular fitting step.

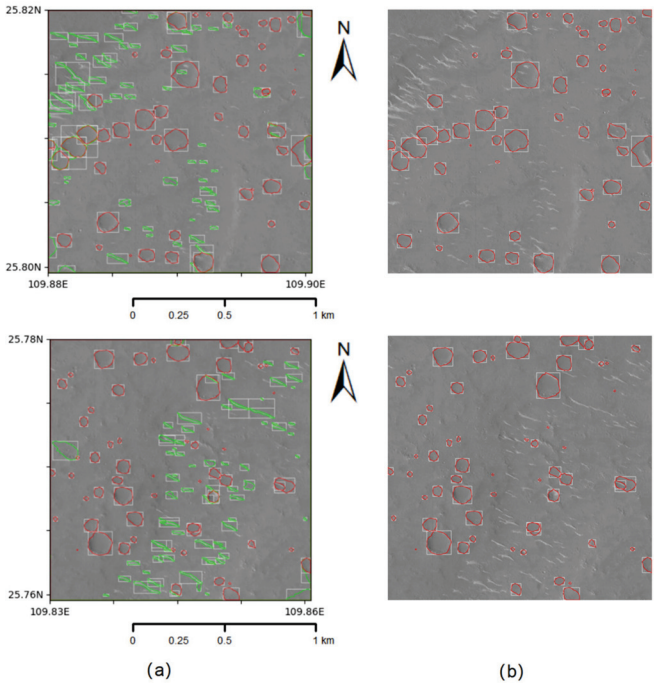


Figure 5. Non-circular filtering of the segmentation objects generated by SAM (Green represents non circular segmentation targets, while red represents circles). (**a**) Segmentation results outputted by SAM. (**b**) Results after filtering non-circular objects.

2.3.2. Circular Fitting

We used the least squares method to perform circular fitting on the edges of the remaining masks. Initially, an estimation of the circle's center and radius is made for each mask. The initial estimation of the center was the mean of the point set, and the initial estimation of the radius was the average distance from the points to that mean. The least squares method was then utilized to minimize the distance errors between the fitted circle and the actual edge points, providing the optimal fit for the circle's center and radius. The formula for the distance error is as follows:

$$S(x_0, y_0, r) = \sum_{i=1}^{n} \left[(x_i - x_0)^2 + (y_i - y_0)^2 - r^2 \right]^2 \quad (2)$$

Here, x_i and y_i represent the coordinates of each edge point, (x_0, y_0) represents the central coordinates of the fitted circle, and r represents the radius of the fitted circle. Finally, the parameter information of the fitted circle was updated in the data for further analysis and statistics.

Figure 6 illustrates the images before (a) and after (b) circular fitting. It can be observed that the fitted circles accurately represent the size and position of the craters in the results of extraction across different sizes.

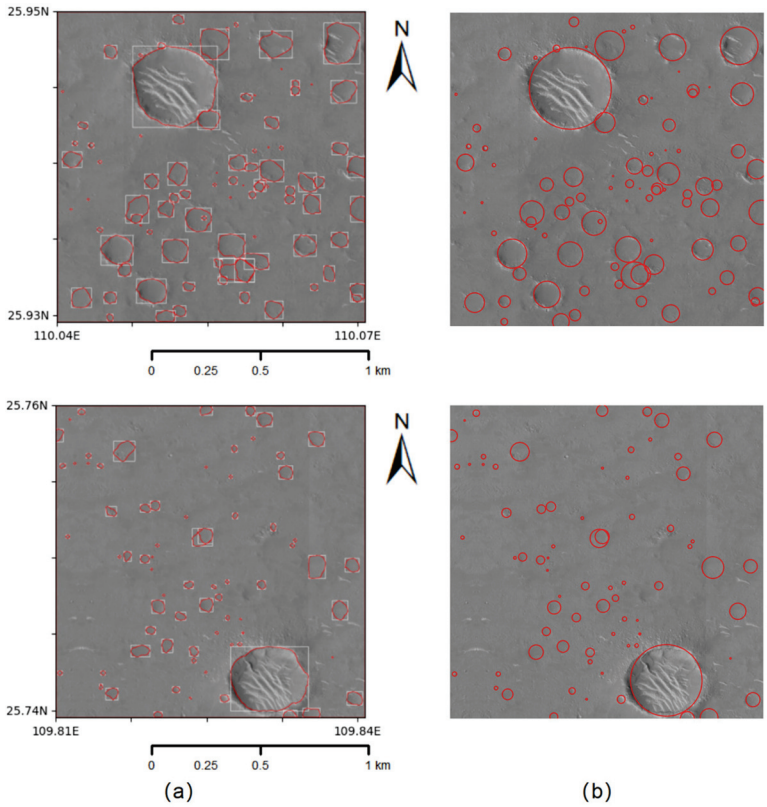


Figure 6. Circular fitting of the mask edges extracted by SAM: (**a**) before circular fitting; (**b**) after circular fitting.

2.3.3. Remove of Duplicates and False Craters

We merged the segmentation results of datasets cropped at different scales back into the original large image. Figure 7 shows the distribution of the size and quantity of craters at different cropping sizes. The results indicated that with an increase in the cropping size, the range of the diameters of successfully extracted craters also expanded. This further validated the necessity of multi-scale cropping for extracting craters of various sizes. Figure 8 displays the craters extracted from datasets cropped at five different sizes.

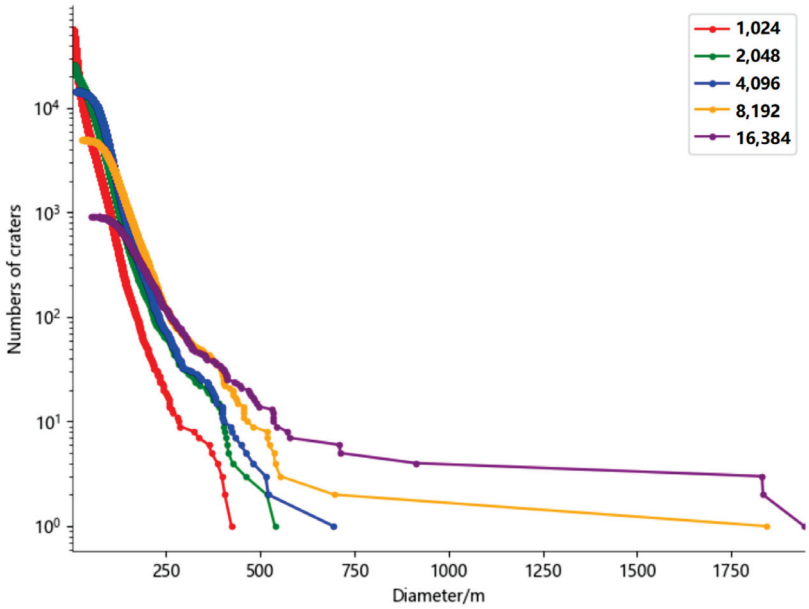
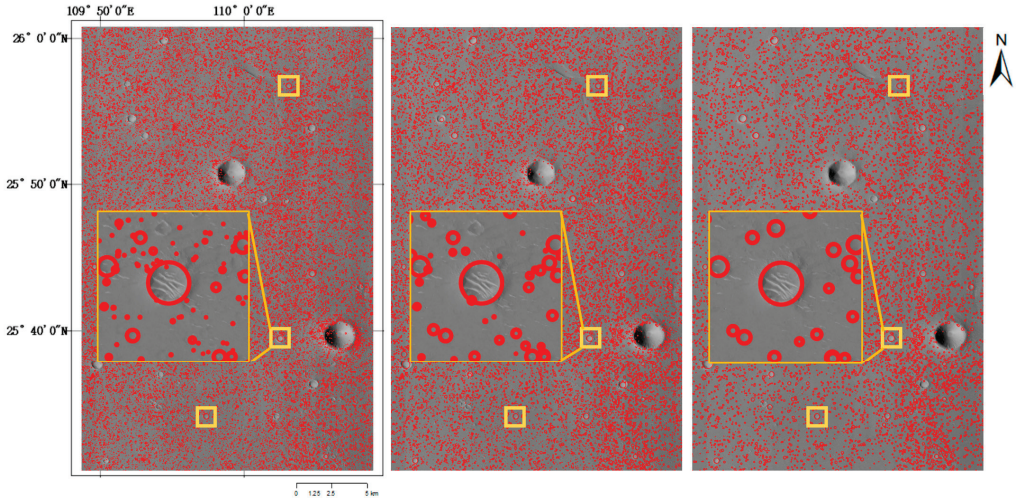
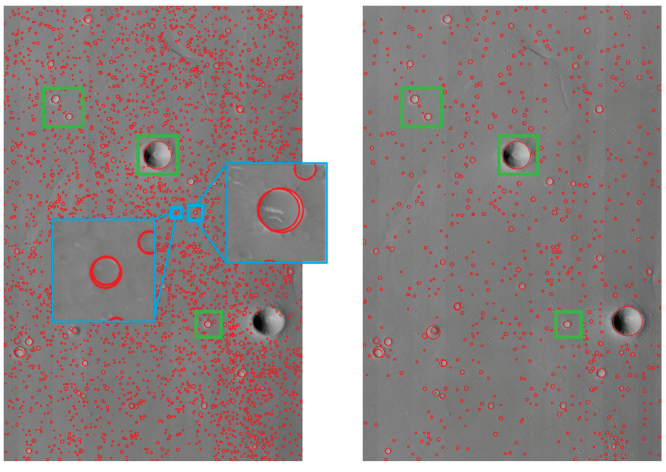


Figure 7. The distribution of crater sizes and quantities resulting from different cropping sizes.



(a) 1,024×1,024 (b) 2,048×2,048 (c) 4,096×4,096



(d) 8,192×8,192 (e) 16,384×16,384

Figure 8. Results of extracting craters from datasets with different cropping sizes.

However, there are duplicates in the results of extracting crater at different sizes. For example, craters highlighted in the yellow boxes in Figure 8a–c, and the green boxes in Figure 8d,e show duplicates. Additionally, due to overlapping during the cropping process, craters extracted from datasets with the same cropping size may also have a partial overlap, as exemplified by the crater highlighted in the blue boxes in Figure 8d. To ensure the uniqueness of the final crater data extracted, we performed a deduplication process. A crater's information was recorded as (x_i, y_i, r_i), and another crater's information was labeled as $(\widehat{x}_j, \widehat{y}_j, \widehat{r}_j)$. If two craters satisfied Equations (3) and (4), they were labeled as duplicate craters and removed. Here, to improve the computational efficiency, we only calculated the distance between a crater and other craters located in an 8192 × 8192 grid centered at the crater's center.

$$\left(\left(x_i - \widehat{x}_j\right)^2 + \left(y_i - \widehat{y}_j\right)^2\right) / min\left(r_i, \widehat{r}_j\right)^2 < D_{x,y} \tag{3}$$

$$abs\left(r_i - \widehat{r}_j\right) / min\left(r_i, \widehat{r}_j\right) < D_r \tag{4}$$

Here, $D_{x,y}$ = 1.8 and D_r = 1.0 are hyperparameters [16].

Upon examining the images after deduplication, we observed that there was some texture at the bottom of the crater. This type of texture is formed by transverse aeolian ridges (TARs) resulting from weathering [40]. The shaded areas formed by the TARs exhibit circular features in the optical images and were consequently incorrectly identified as craters. as shown by the green crater in Figure 9a. To address this issue, we introduced an intersection over union (IOU) threshold, defined as in Equation (5)

$$\text{IOU} = \frac{A \cap B}{A \cup B} \tag{5}$$

where A and B represent the areas of the two circles. Figure 9a shows the result with the IOU set to 0.8, and Figure 9b shows the result with the IOU set to 0.7. It can be seen that when the IOU was 0.7, false craters were removed. Therefore, we set the IOU threshold to 0.7. If the IOU was greater than 0.7, the smaller one of the two circles was deemed to be a pseudo-crater. Figure 9b displays the image after the removal of these false craters.

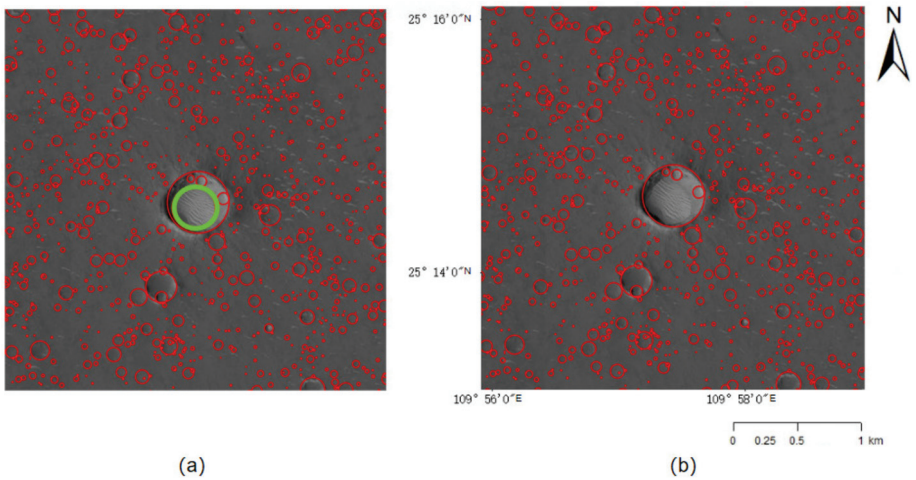


Figure 9. (**a**) Before removing false craters(IOU = 0.8). (**b**) After removing false craters (IOU = 0.7).

2.3.4. Transformation of Coordinates

We merged the segmentation results of datasets cropped at different scales back into the original large image. Finally, we needed to convert the pixel coordinates of the craters to latitude and longitude coordinates using Equations (6) and (7).

$$la = \frac{x}{L}(La_r - La_l) + La_l \tag{6}$$

$$lo = Lo_l - \frac{y}{H}(Lo_l - Lo_r) \tag{7}$$

Here, (la, lo) and (x, y) represent the latitude and longitude coordinates and pixel coordinates of a point, respectively. L and H are the given pixel length and height of the cropping area, and (La_l, Lo_l) and (La_r, Lo_r) are the latitude and longitude coordinates of the upper left and lower right corners of the cropping area, respectively.

3. Experimental Results and Analysis

This section presents the experimental results of SAM in extracting Martian craters, including the evaluation metrics and an analysis of the results. The experiments verified the effectiveness of SAM in the task of crater extraction.

3.1. Evaluate Metrics

To evaluate the effectiveness of SAM in the task of crater extraction, we used the precision P and recall R to measure the accuracy of the model in terms of Equations (8) and (9)

$$P = T_p / \left(T_p + F_p\right) \tag{8}$$

$$R = T_p / \left(T_p + F_n\right) \tag{9}$$

where T_p are true positives, representing the correctly identified craters; F_p are false positives, representing the craters in the results of prediction that do not match the real craters; and F_n are false negatives, representing missed craters. Here, we were more concerned about the number of detectable craters, so we cared more about the recall rate.

3.2. Experimental

To verify the effectiveness of SAM in extracting craters, we conducted validation experiments using the crater catalog annotated by Cao et al. [35] in three subregions of the landing area as labels. As shown in Figure 10, the three areas had areas of 10 × 20, 20 × 10, and 20 × 10 km^2, with the centers located at (110°2′E, 25°41′N), (110°18′E, 24°56′N), and (110°8′E, 24°24′N), respectively.

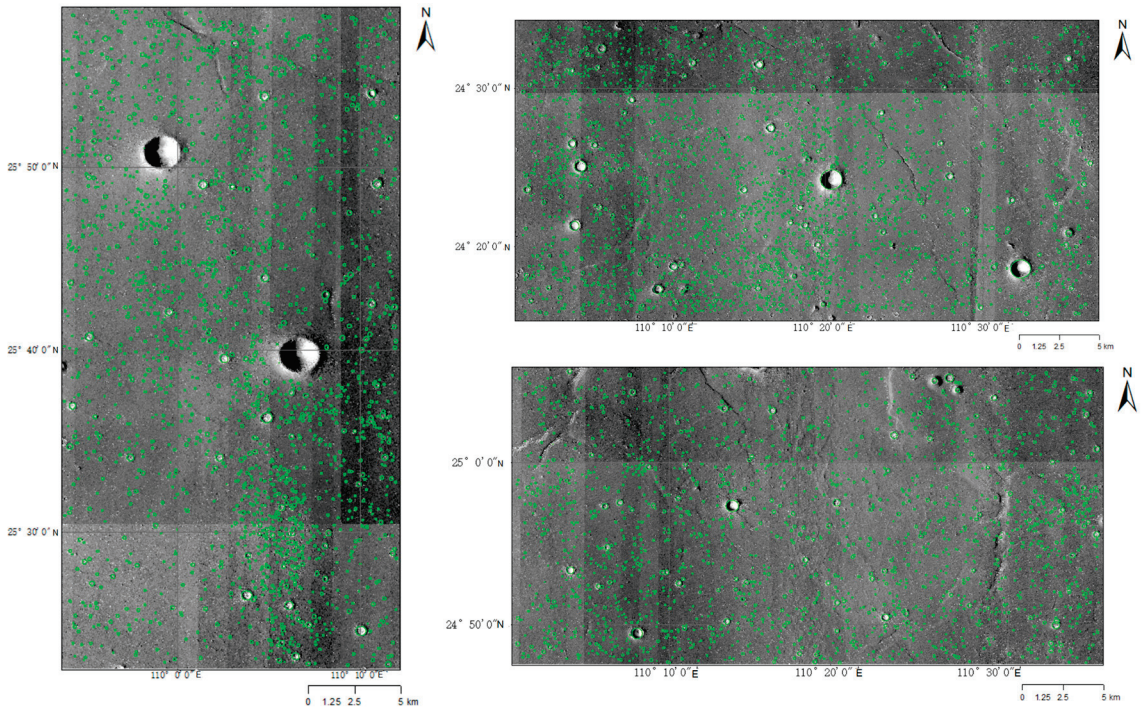


Figure 10. Crater labels for the three subregions of the landing area.

First, we evaluated the results of applying different circularity threshold filters to the craters extracted from one of the subregions. The experimental results are shown in Table 1. According to the results in Table 1, when the circularity threshold was set to less than or equal to 0.75, the recall was 1, indicating that all craters in the ground truth were detected. However, the precision significantly decreased when the circularity threshold was less than 0.75, suggesting that many non-crater objects were extracted. On the other hand, when the circularity threshold was greater than 0.75, the recall decreased significantly, indicating that many craters were missed. Since our goal was to detect as many craters as possible, we set the circularity threshold to 0.75. To verify the robustness of the method, we calculated the precision metrics of three subregions separately, and the results are shown in Table 2. The results indicated that the recall rate was 1 in each subregion, indicating that the method extracted all the craters from the labels, demonstrating the method's strong robustness in effectively extracting craters.

Table 1. The results of different circularity thresholds on the dataset.

Metrics \ Circularity Threshold	0.5	0.55	0.6	0.65	0.7	0.75	0.8	0.85	0.9	0.95
R	1	1	1	1	1	1	92.7%	79.7%	56.8%	43.8%
P	2.8%	3.0%	3.2%	3.4%	3.7%	4.7%	4.8%	6.1%	9.1%	13.8%

Table 2. The metric results for the three subregions.

Metricsc \ Central Positions of the Subregions	110°2′E, 25°41′N	110°18′E, 24°56′N	110°8′E, 24°24′N
R	1	1	1
P	3.5%	4.7%	3.8%

We then compared several models, namely MC-UNet [20], ERU-Net [41], UNet++ [42], and DeepMoon [16]. These network models are relatively new and competitive architectures in the field of crater detection. The experimental results are shown in Table 3, from which it can be seen that SAM, as a model that can extract craters without training, achieved a 100% recall rate compared with several supervised models. However, the precision was lower. We conducted an analysis of the reasons and found that SAM extracted 58,724 craters, but there were only 2103 craters with the crater label. This means that we extracted many new craters, leading to a higher F_p when calculating precision; hence the calculated precision was lower.

Table 3. Comparison of different competing models on the datasets.

Metrics \ Model	SAM	MC-UNet	ERU-Net	U-Net++	DeepMoon
R	1	89.2%	88.1%	86.3%	76.3%
P	3.5%	80.1%	82.3%	81.5%	91.6%

Next, we conducted a statistical analysis of the results of extraction for the three subregions, and the statistical results are shown in Table 4. The results indicated that the size range of the craters we extracted was much wider, and the number of extracted craters was significantly greater than the number of craters in the labels.

Figure 11 shows the extraction results of two small regions. The blue circles represent the craters matching the labels, while the green circles represent newly extracted craters. Compared with the craters in the ground truth, the craters extracted by SAM exhibited a wider size distribution, and SAM could extract overlapping craters. The extracted craters in the red boxes indicate that SAM identified some craters with higher degrees of edge

degradation. These results validated the high performance of SAM in the task of detecting impact craters.

Table 4. The results of extraction for the three subregions.

Central Positions of the Subregions	**110°2′E, 25°41′N**		**110°18′E, 24°56′N**		**110°8′E, 24°24′N**	
	GT	SAM	GT	SAM	GT	SAM
Size range (m)	12.1–567.9	1.9–1943.2	1.9–1300.9	1.9–1367.4	12.2–733.9	1.6–744.0
Quantity	2103	58,724	3135	65,477	2084	53,610

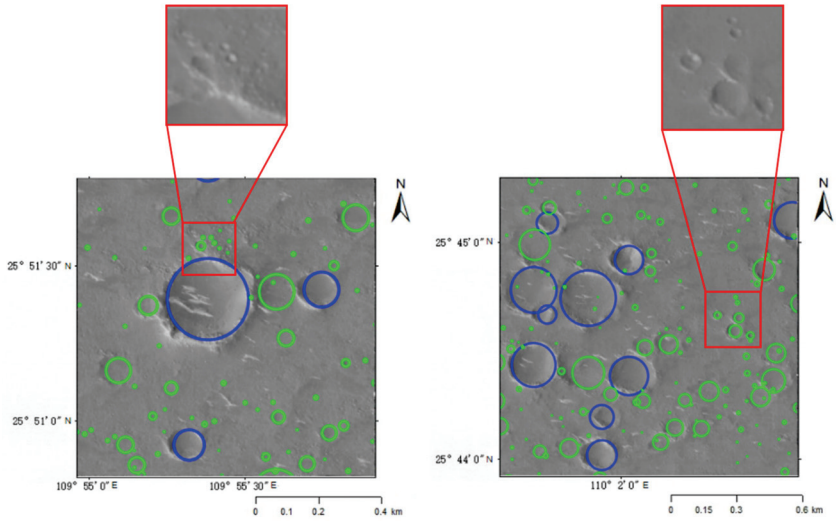


Figure 11. The results of extracting craters in two small regions.

4. Statistics and Distribution of The Landing Area's Crater

This section introduces the results of crater extraction, including an analysis of the number of extracted craters, an analysis of the craters' size and distribution frequency, and an explanation of the crater catalog.

4.1. Counting the Craters

We performed crater identification and extraction on 15 DIM images, and the extracted results are shown in Table 5. According to the statistics, we extracted a total of 841,727 craters in the entire landing area, with diameters ranging from 1.57 m to 7910.47 m. Figure 12 shows the results of crater identification for two subregions from different DIM images. Figure 12a demonstrates that small craters within a large crater could also be detected, while Figure 12b shows that multiple craters of different scales were detected as well.

Additionally, we performed statistical analysis on the extracted craters, categorizing them on the basis of their diameter into different ranges and plotting the crater count for each range, as shown in Figure 13a. We can see that the number of craters with diameters less than 30 m exceeded 10^5, accounting for approximately 73% of the total. Craters with diameters in the range of 30–60 m constituted around 14%, while those in the range of 60–100 m accounted for approximately 8%. The proportion of craters larger than 100 m was relatively small, with a total of 40,932 craters. These findings indicated that within the landing area, small-sized craters are widely distributed. With an increase in diameter, the number of craters exhibited an exponential decline. This result is consistent with observations on the surfaces of other planets [32], as the distribution of impacting objects also follows this pattern. Additionally, over time, the number of larger craters may decrease due to erosion and geological activities [43].

Table 5. Statistics of the number of craters in 15 digital image models (DIMs) of the landing area.

ID	Range of Craters' Diameters (m)	Quantity (Count)	ID	Range of Craters' Diameters (m)	Quantity (Count)
HX1_GRAS_HIRIC_DIM_0.7_0001_254537N1095850E_A	1.93–1943.17	53,428	HX1_GRAS_HIRIC_DIM_0.7_0009_244453N1103919E_A	1.98–1060.23	54,670
HX1_GRAS_HIRIC_DIM_0.7_0002_254537N1101905E_A	1.57–831.91	44,950	HX1_GRAS_HIRIC_DIM_0.7_0010_241431N1095850E_A	2.14–1143.70	54,937
HX1_GRAS_HIRIC_DIM_0.7_0003_254537N1103919E_A	1.66–1528.68	51,029	HX1_GRAS_HIRIC_DIM_0.7_0011_241431N1101905E_A	1.98–1609.63	48,865
HX1_GRAS_HIRIC_DIM_0.7_0004_251515N1095850E_A	1.83–948.05	61,423	HX1_GRAS_HIRIC_DIM_0.7_0012_241431N1095850E_A	1.68–744.02	49,424
HX1_GRAS_HIRIC_DIM_0.7_0005_251515N1101905E_A	1.95–1794.37	47,557	HX1_GRAS_HIRIC_DIM_0.7_0013_234409N1095850E_A	1.64–1142.47	70,031
HX1_GRAS_HIRIC_DIM_0.7_0006_251515N1103919E_A	1.97–1240.55	69,949	HX1_GRAS_HIRIC_DIM_0.7_0014_234409N1101905E_A	1.98–1367.44	56,653
HX1_GRAS_HIRIC_DIM_0.7_0007_244453N1095850E_A	1.89–7910.47	54,900	HX1_GRAS_HIRIC_DIM_0.7_0015_234409N1103919E_A	1.57–879.72	62,522
HX1_GRAS_HIRIC_DIM_0.7_0008_244453N1101905E_A	1.95–1196.73	61,389			

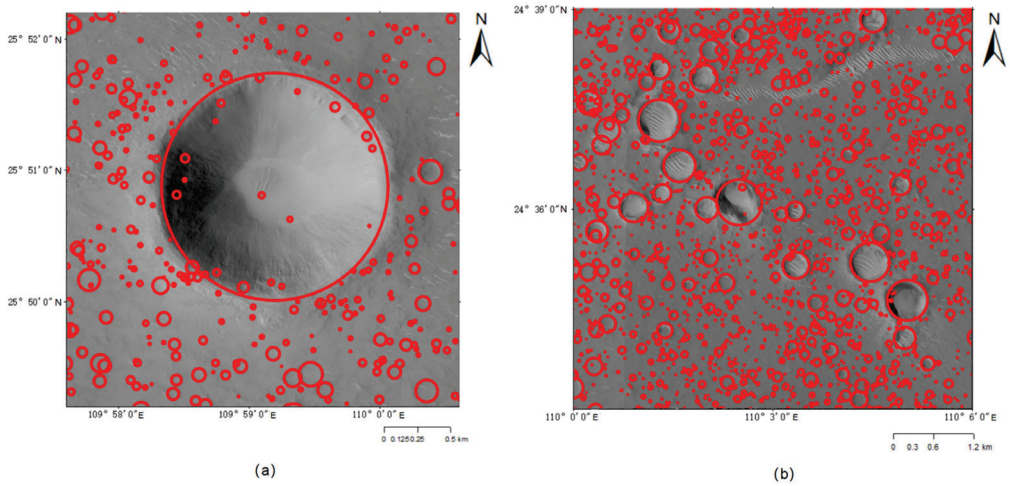


Figure 12. Crater extraction results from different regions of the two landing areas. (**a**) HX1_GRAS_HIRIC_DIM_0.7_0001_254537N1095850E_A. (**b**) HX1_GRAS_HIRIC_DIM_0.7_0007_244453N1095850E_A.

We calculated the values of crater density, which is defined as the percentage of the coverage area of the craters (with a diameter $\geq$ 10 m) within a square window of 2 km $\times$ 2 km. Figure 13b shows the crater density map of Tianwen-1's landing region. The crater density map revealed that craters are concentrated in local regions, such as the southern and northwestern parts of the main landing region. The central-northern region exhibited lower crater densities. The area marked with a red box in the figure represents the small region where the Tianwen-1 landing site is located, and the purple star indicates the landing site, where the crater density is relatively low. The average crater density was approximately 19.3%. The maximum crater density of 100% occurred in several large craters within the main landing region.

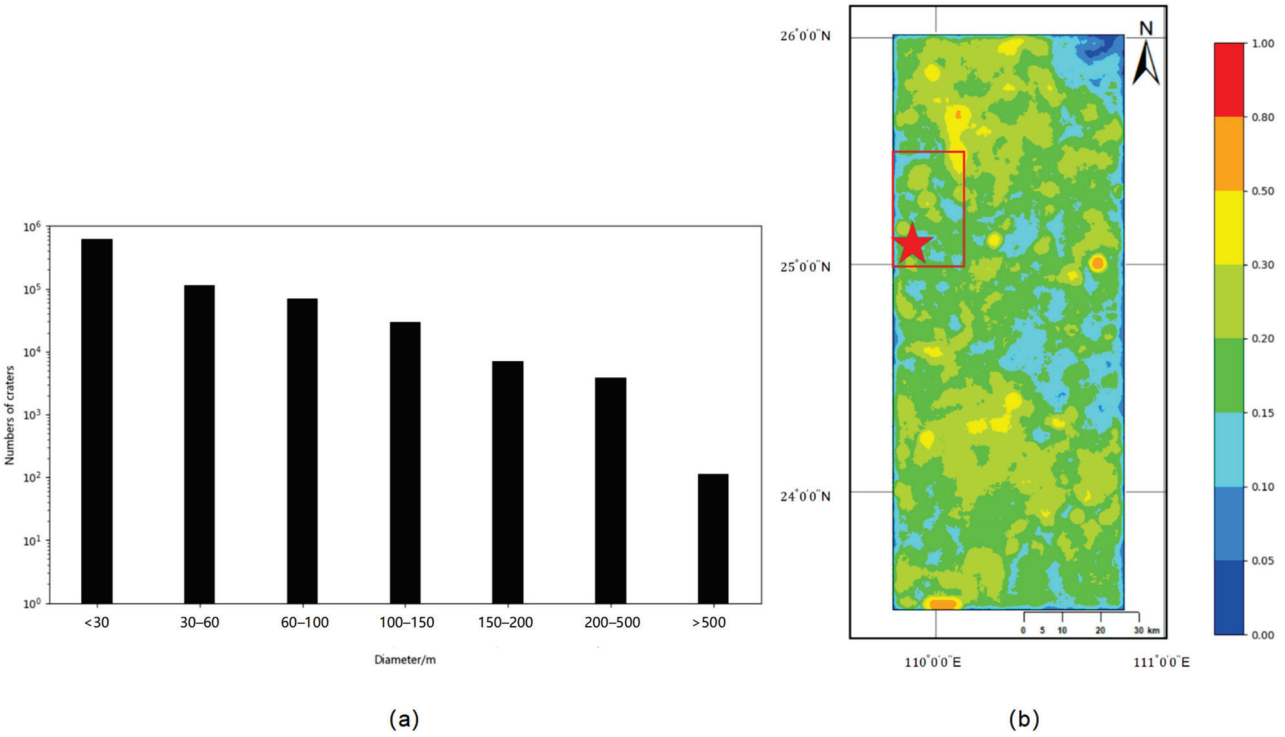


Figure 13. (**a**) Statistics of craters with different diameter ranges. (**b**) Map of crater density in the main landing region.

4.2. Crater Size–Frequency Distribution (CSFD)

To obtain information about the surface age of the landing area, we conducted an analysis of the CSFD using the smaller-sized craters (diameter $\geq$ 50 m) detected in the landing area DIM [5]. We used the production function of Ivanov et al. [44] and the chronology function of Neukum et al. [45] for estimating the age in the landing area, resulting in a size–frequency diagram of the craters (Figure 14). The shaded regions on the map represent different Martian epochs [5,44–46], from left to right, including the Late, Middle, and Early Amazonian; Late and Early Hesperian; and Late, Middle, and Early Noachian periods.

The extracted craters with diameters greater than 1 km (black) were used to estimate the age of the landing area of Tianwen-1 as $3.25^{+0.16}_{-0.56}$. Age estimation was also conducted using the crater labels of the landing area in the RH_2012 dataset [23] (green), yielding an age of $3.21^{+0.18}_{-0.61}$. The determinations of the age of the craters we extracted are consistent with the results obtained using the RH_2012 dataset. According to the geological time division provided by Tanaka et al. [47], the landing area of Tianwen-1 belongs to the Late Hesperian Lowland Unit ($3.34^{+0.02}_{-0.02}$ Ga), which is consistent with the results obtained in our study.

However, estimation of the age of the craters with diameters ranging from 50 to 800 m extracted by SAM (red) revealed an age of $1.67^{+0.0045}_{-0.0045}$, indicating a younger age. The relatively young age of the small craters may indicate the possibility of local resurfacing events around the landing area. However, further investigation of the geological and geomorphological features of the region on a larger scale is needed to determine the nature of these resurfacing events. This study aligns with the results of some previous research [34,47–49].

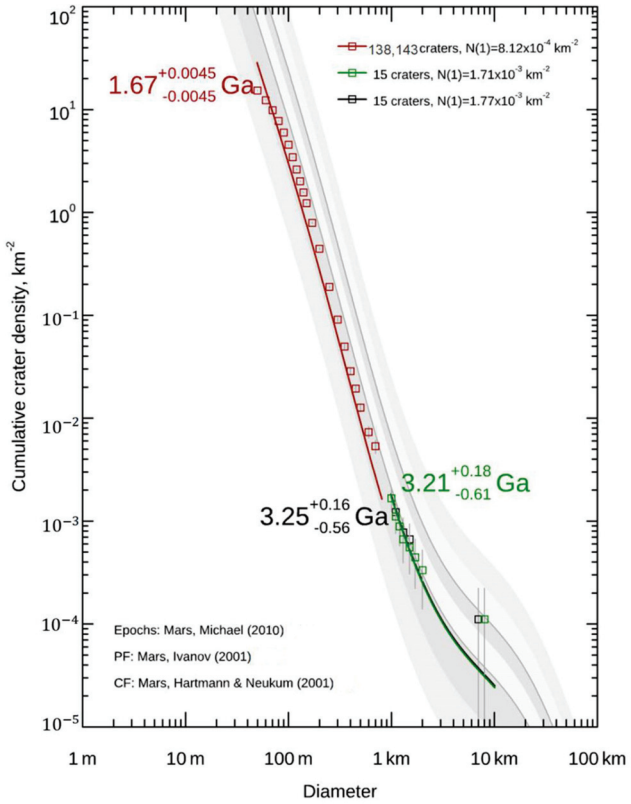


Figure 14. Craters' size–frequency distribution and estimation of the age of the landing area. Craters with diameters greater than 1 km, black; diameters ranging from 50 to 800 m, red; estimation of the age using the RH_2012 dataset, green [5,44,46].

4.3. Documentation of the Crater Catalog

We compiled the extracted craters from the landing area of the Tianwen-1 mission into a comprehensive catalog of craters within the landing zone. A detailed description of the data contained in this crater catalog is provided in Table 6. This table provides an example of a crater, originating from the fifth region of the landing zone's DIM, with a diameter of approximately 19.62 m. Its coordinates are approximately (25.45°N, 110.44°E). The pixel coordinates relative to the entire landing zone DIM are approximately (52,881.7, 48,093.1), and relative to the DIM of the fifth region of the landing area, the pixel coordinates are approximately (24,298.7, 5224.1).

Table 6. Documentation of the crater catalog.

Index	Meaning	Example
ID	Representing the region in the DIM	HX1_GRAS_HIRIC_DIM_0.7_0005_ 251515N1101905E_A
Latitude (degrees)	Longitude of the crater's center	25.445545541679884
Longitude (degrees)	Latitude of the crater's center	110.4361572920686
Global_x_center	X-coordinate of the center of thecrater relative to the entire landing zone's DIM (in pixels)	52,881.735497283
Global_y_center	Y-coordinate of the center of the crater relative to the entire landing zone's DIM (in pixels)	48,093.05926101379
Local_x_center	X-coordinate of the center of the crater relative to the local landing area's DIM (in pixels)	24,298.735497283
Local_y_center	Y-coordinate of the center of the crater relative to the local landing area' s DIM (in pixels)	5224.059261013788
Diameter (km)	Diameter of the crater	0.0196223768624538

5. Discussion

The current approach for extracting craters based on SAM can essentially capture all craters in the DIM, but there are still some issues that need discussion and improvement. Firstly, during the process of crater extraction, we only identified masks with a circular shape as craters. However, craters may undergo a series of geological processes, such as erosion, deposition, and reshaping, resulting in irregular shapes, as seen in the crater in Figure 15a. These craters are detected by SAM, but they may be overlooked during the process of filtering out non-circular ones, indicating that relying solely on the geometric property of circularity is not enough. The diversity in craters' morphology demands the development of more sophisticated recognition algorithms that can identify and process craters with various irregular shapes, including those shaped irregularly due to their impact angles, geological processes, or erosion.

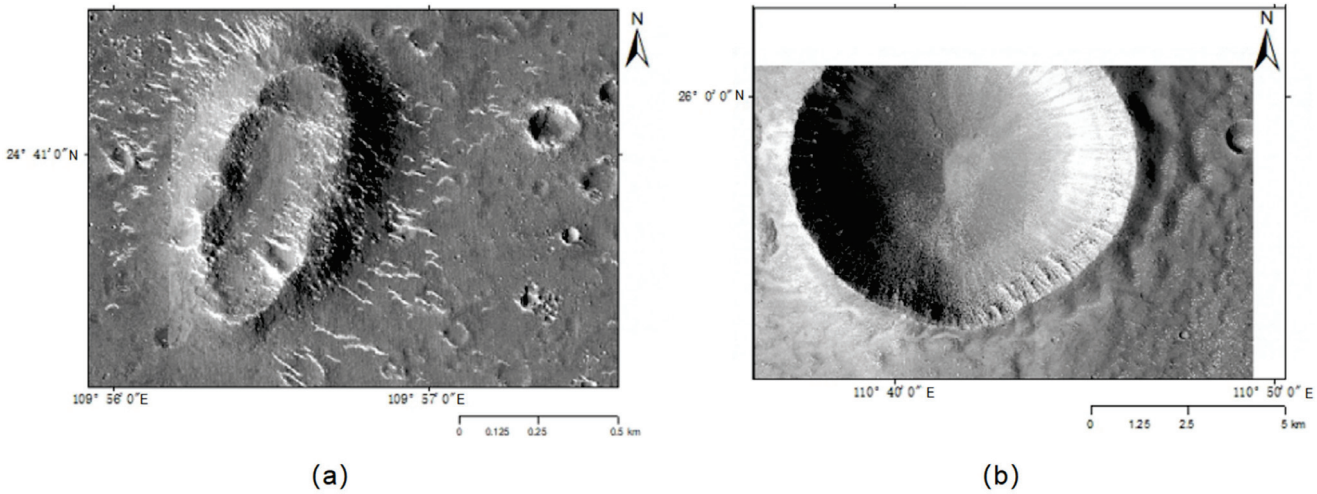


Figure 15. Morphological analysis of undetected craters: (**a**) irregularly shaped craters; (**b**) overlooked large-sized craters.

In addition, there was a case where the large crater in Figure 15b was not successfully extracted. The diameter of this crater is approximately 9.4 km, corresponding to a pixel diameter of 13,428. The cropping process did not fully encompass this crater, and its substantial area in the cropped image resulted in reduced contrast between the target and the background, making the extraction challenging. However, these types of craters exhibited clear features in the digital elevation model (DEM), and the resolution of the DEM was relatively lower than that of the DIM. This provides a significant advantage for detecting large-sized craters. In the subsequent steps, we will use a crater automatic extraction model based on the DEM to extract these potentially overlooked large-sized craters from the landing area's DEM.

6. Conclusions

This article presents a comprehensive solution for automatic crater recognition based on the Segment Anything Model (SAM), aiming to extract craters in the DIM of the landing area of the Tianwen-1 mission. We utilized SAM to obtain segmentation masks for the craters and used a series of postprocessing steps, including non-circular filtering, circular fitting, deduplication, and removal of false positives, to extract the positions and sizes of craters. Experimental validation demonstrated the effectiveness of SAM in planetary crater identification tasks. In the DIM of the Tianwen-1 landing area, we extracted a total of 841,727 craters with diameters ranging from 1.57 m to 7910.47 m, providing a comprehensive crater dataset that contributes valuable data for future missions of detecting Martian crater detection. The distribution of the number of craters reflected the geological structure and characteristics of historical impact events in the Tianwen-1 landing area.

Additionally, through the craters' size–frequency distribution, we estimated the specific surface age of the landing area to be ~3.25 billion years, with subsequent surface resurfacing events occurring ~1.67 billion years ago.

In future work, we plan to further optimize and improve the crater extraction solution using SAM. This involves optimizing postprocessing algorithms for crater extraction by considering the diversity of craters. In addition, we also plan to explore the use of multi-source data fusion techniques for crater extraction, aiming to obtain more comprehensive and accurate information on craters. Multi-source data fusion techniques can integrate data from different sensors and observation platforms, providing more comprehensive information on craters' feature. This not only enhances the accuracy and reliability of our existing models but also offers richer data support for scientific research. Furthermore, we plan to expand and improve the existing crater dataset, which will be crucial for future Martian exploration and research. Finally, we hope to apply these techniques to the study of craters on other celestial bodies such as the Moon, asteroids, etc., to further extend the reach of our research and provide more data and insights for the geological study of these celestial bodies. Through these efforts, we aim to offer more comprehensive and in-depth support for the geological exploration and research of Mars and other celestial bodies.

Author Contributions: Conceptualization, H.Y.; methodology, Y.Z.; writing, Y.Z.; supervision, H.Y. All authors have read and agreed to the published version of the manuscript.

Funding: This work was funded by the National Natural Science Foundation of China, grant 62271152.

Data Availability Statement: The extracted crater dataset is available at https://drive.google.com/file/d/1pKRlC0Zh2fe1taZcFpwB-QysfxXy2doi/view?usp=drive_link (accessed on 1 May 2024).

Conflicts of Interest: The authors declare no conflicts of interest.

References

1. Meng, Q.; Wang, D.; Wang, X.; Li, W.; Yang, X.; Yan, D.; Li, Y.; Cao, Z.; Ji, Q.; Sun, T.; et al. High Resolution Imaging Camera (HiRIC) on China's First Mars Exploration Tianwen-1 Mission. *Space Sci. Rev.* **2021**, *217*, 42. [CrossRef]
2. Head, J.W., 3rd; Fassett, C.I.; Kadish, S.J.; Smith, D.E.; Zuber, M.T.; Neumann, G.A.; Mazarico, E. Global distribution of large lunar craters: Implications for resurfacing and impactor populations. *Science* **2010**, *329*, 1504–1507. [CrossRef] [PubMed]
3. Hu, T.; Yang, Z.; Kang, Z.; Lin, H.; Zhong, J.; Zhang, D.; Cao, Y.; Geng, H. Population of Degrading Small Impact Craters in the Chang'E-4 Landing Area Using Descent and Ground Images. *Remote Sens.* **2022**, *14*, 3608. [CrossRef]
4. Wu, B.; Huang, J.; Li, Y.; Wang, Y.; Peng, J. Rock Abundance and Crater Density in the Candidate Chang'E-5 Landing Region on the Moon. *J. Geophys. Res. Planets* **2018**, *123*, 3256–3272. [CrossRef]
5. Hartmann, W.K.; Neukum, G. Cratering chronology and the evolution of Mars. In *Chronology and Evolution of Mars: Proceedings of an ISSI Workshop, Bern, Switzerland, 10–14 April 2000*; Springer Netherlands: Dordrecht, The Netherlands, 2001; pp. 165–194.
6. Neukum, G. Meteoritenbombardement und Datierung Planetarer Oberflachen. Habilitation Dissertation, Faculty Membership, Ludwig-Maximilians-University, Munchen, Germany, 1983.
7. Povilaitis, R.Z.; Robinson, M.S.; van der Bogert, C.H.; Hiesinger, H.; Meyer, H.M.; Ostrach, L.R. Crater density differences: Exploring regional resurfacing, secondary crater populations, and crater saturation equilibrium on the moon. *Planet. Space Sci.* **2018**, *162*, 41–51. [CrossRef]
8. Cheng, Y.; Johnson, A.E.; Matthies, L.H.; Olson, C.F. Optical landmark detection for spacecraft navigation. In Proceedings of the 13th Annual AAS/AIAA Space Flight Mechanics Meeting, Ponce, Puerto Rico, 9–13 February 2003; pp. 1–19.
9. Illingworth, J.; Kittler, J. A survey of the Hough transform. *Comput. Vis. Graph. Image Process.* **1988**, *44*, 87–116. [CrossRef]
10. Briechle, K.; Hanebeck, U.D. Template matching using fast normalized cross correlation. *Proc. SPIE Int. Soc. Opt. Eng.* **2001**, *4387*, 1–8.
11. Leroy, B.; Medioni, G.; Johnson, E.; Matthies, L. Crater detection for autonomous landing on asteroids. *Image Vis. Comput.* **2001**, *19*, 787–792. [CrossRef]
12. Galloway, M.J.; Benedix, G.K.; Bland, P.A.; Paxman, J.; Towner, M.C.; Tan, T. Automated crater detection and counting using the Hough transform. In Proceedings of the 2014 IEEE International Conference on Image Processing (ICIP), Paris, France, 27–30 October 2014; pp. 1579–1583.
13. Dong, S.; Wang, L.; Du, B.; Meng, X. ChangeCLIP: Remote sensing change detection with multimodal vision-language representation learning. *ISPRS J. Photogramm. Remote Sens.* **2024**, *208*, 53–69. [CrossRef]
14. Li, Y.; Du, L.; Wei, D. Multiscale CNN Based on Component Analysis for SAR ATR. *IEEE Trans. Geosci. Remote Sens.* **2022**, *60*, 5211212. [CrossRef]

15. Li, J.; Chen, K.; Tian, G.; Li, L.; Shi, Z. MarsSeg: Mars Surface Semantic Segmentation with Multi-level Extractor and Connector. *arXiv* **2024**, arXiv:2404.04155.
16. Silburt, A.; Ali-Dib, M.; Zhu, C.; Jackson, A.; Valencia, D.; Kissin, Y.; Tamayo, D.; Menou, K. Lunar crater identification via deep learning. *Icarus* **2019**, *317*, 27–38. [CrossRef]
17. Speyerer, E.; Robinson, M.; Denevi, B.; Team, L.S. Lunar Reconnaissance Orbiter Camera Global Morphological Map of the Moon. In Proceedings of the 42nd Annual Lunar and Planetary Science Conference, The Woodlands, TX, USA, 7–11 March 2011; p. 2387.
18. Ronneberger, O.; Fischer, P.; Brox, T. U-net: Convolutional networks for biomedical image segmentation. In *Medical Image Computing and Computer-Assisted Intervention–MICCAI 2015, Proceedings of the 18th International Conference, Munich, Germany, 5–9 October 2015*; Proceedings, Part III; Springer International Publishing: Berlin/Heidelberg, Germany, 2015; pp. 234–241.
19. Lee, C. Automated crater detection on Mars using deep learning. *Planet. Space Sci.* **2019**, *170*, 16–28. [CrossRef]
20. Chen, D.; Hu, F.; Mathiopoulos, P.T.; Zhang, Z.; Peethambaran, J. MC-UNet: Martian Crater Segmentation at Semantic and Instance Levels Using U-Net-Based Convolutional Neural Network. *Remote Sens.* **2023**, *15*, 266. [CrossRef]
21. Zhao, Y.; Ye, H. SqUNet: An High-Performance Network for Crater Detection With DEM Data. *IEEE J. Sel. Top. Appl. Earth Obs. Remote Sens.* **2023**, *16*, 8577–8585. [CrossRef]
22. Yang, C.; Zhao, H.; Bruzzone, L.; Benediktsson, J.A.; Liang, Y.; Liu, B.; Zeng, X.; Guan, R.; Li, C.; Ouyang, Z. Lunar impact crater identification and age estimation with Chang'E data by deep and transfer learning. *Nat. Commun.* **2020**, *11*, 6358. [CrossRef]
23. Robbins, S.J.; Hynek, B.M. A new global database of Mars impact craters $\geq$1 km: 1. Database creation, properties, and parameters. *J. Geophys. Res. Planets* **2012**, *117*. [CrossRef]
24. Jia, M.; Yue, Z.; Di, K.; Liu, B.; Liu, J.; Michael, G. A catalogue of impact craters larger than 200 m and surface age analysis in the Chang'e-5 landing area. *Earth Planet. Sci. Lett.* **2020**, *541*, 116272. [CrossRef]
25. Chen, K.; Liu, C.; Chen, H.; Zhang, H.; Li, W.; Zou, Z.; Shi, Z. RSPrompter: Learning to prompt for remote sensing instance segmentation based on visual foundation model. *IEEE Trans. Geosci. Remote Sens.* **2024**, *62*, 4701117. [CrossRef]
26. Kirillov, A.; Mintun, E.; Ravi, N.; Mao, H.; Rolland, C.; Gustafson, L.; Xiao, T.; Whitehead, S.; Berg, A.C.; Lo, W.-Y. Segment anything. *arXiv* **2023**, arXiv:2304.02643.
27. Mazurowski, M.A.; Dong, H.; Gu, H.; Yang, J.; Konz, N.; Zhang, Y. Segment anything model for medical image analysis: An experimental study. *Med. Image Anal.* **2023**, *89*, 102918. [CrossRef]
28. Giannakis, I.; Bhardwaj, A.; Sam, L.; Leontidis, G. A flexible deep learning crater detection scheme using Segment Anything Model (SAM). *Icarus* **2024**, *408*, 115797. [CrossRef]
29. Wan, W.X.; Wang, C.; Li, C.L.; Wei, Y. China's first mission to Mars. *Nat. Astron.* **2020**, *4*, 721. [CrossRef]
30. Niu, S.; Zhang, F.; Di, K.; Gou, S.; Yue, Z. Layered Ejecta Craters in the Candidate Landing Areas of China's First Mars Mission (Tianwen-1): Implications for Subsurface Volatile Concentrations. *J. Geophys. Res. Planets* **2022**, *127*, e2021JE007089. [CrossRef]
31. Zhao, J.; Xiao, Z.; Huang, J.; Head, J.W.; Wang, J.; Shi, Y.; Wu, B.; Wang, L. Geological Characteristics and Targets of High Scientific Interest in the Zhurong Landing Region on Mars. *Geophys. Res. Lett.* **2021**, *48*, e2021GL094903. [CrossRef]
32. Wu, B.; Dong, J.; Wang, Y.; Li, Z.; Chen, Z.; Liu, W.C.; Zhu, J.; Chen, L.; Li, Y.; Rao, W. Characterization of the Candidate Landing Region for Tianwen-1—China's First Mission to Mars. *Earth Space Sci.* **2021**, *8*, e2021EA001670. [CrossRef]
33. Wu, X.; Liu, Y.; Zhang, C.; Wu, Y.; Zhang, F.; Du, J.; Liu, Z.; Xing, Y.; Xu, R.; He, Z.; et al. Geological characteristics of China's Tianwen-1 landing site at Utopia Planitia, Mars. *Icarus* **2021**, *370*, 114657. [CrossRef]
34. Wu, B.; Dong, J.; Wang, Y.; Rao, W.; Sun, Z.; Li, Z.; Tan, Z.; Chen, Z.; Wang, C.; Liu, W.C.; et al. Landing Site Selection and Characterization of Tianwen-1 (Zhurong Rover) on Mars. *J. Geophys. Res. Planets* **2022**, *127*, e2021JE007137. [CrossRef]
35. Cao, Z.; Kang, Z.; Hu, T.; Yang, Z.; Zhu, L.; Ye, C. Cross-attention induced multilayer domain adaptation network for extraction of sub-kilometer craters from HiRIC images. *Icarus* **2024**, *407*, 115776. [CrossRef]
36. Dosovitskiy, A.; Beyer, L.; Kolesnikov, A.; Weissenborn, D.; Zhai, X.; Unterthiner, T.; Dehghani, M.; Minderer, M.; Heigold, G.; Gelly, S. An image is worth 16x16 words: Transformers for image recognition at scale. *arXiv* **2020**, arXiv:2010.11929.
37. Vaswani, A.; Shazeer, N.; Parmar, N.; Uszkoreit, J.; Jones, L.; Gomez, A.N.; Kaiser, Ł.; Polosukhin, I. Attention is all you need. *Adv. Neural Inf. Process. Syst.* **2017**, *30*, 600–610.
38. Mordvintsev, A.; Abid, K. Opencv-Python Tutorials Documentation. 2014. Available online: https://buildmedia.readthedocs.org/media/pdf/opencv-python/latest/opencv-python.pdf (accessed on 10 January 2024).
39. Bottema, M.J. Circularity of objects in images. In Proceedings of the 2000 IEEE International Conference on Acoustics, Speech, and Signal Processing (Cat. No. 00CH37100), Istanbul, Turkey, 5–9 June 2000; pp. 2247–2250.
40. Gou, S.; Yue, Z.; Di, K.; Zhao, C.; Bugiolacchi, R.; Xiao, J.; Cai, Z.; Jin, S. Transverse aeolian ridges in the landing area of the Tianwen-1 Zhurong rover on Utopia Planitia, Mars. *Earth Planet. Sci. Lett.* **2022**, *595*, 117764. [CrossRef]
41. Wang, S.; Fan, Z.; Li, Z.; Zhang, H.; Wei, C. An effective lunar crater recognition algorithm based on convolutional neural network. *Remote Sens.* **2020**, *12*, 2694. [CrossRef]
42. Jia, Y.; Liu, L.; Zhang, C. Moon impact crater detection using nested attention mechanism based UNet++. *IEEE Access* **2021**, *9*, 44107–44116. [CrossRef]
43. Grant, J.A.; Schultz, P.H. Degradation of selected terrestrial and Martian impact craters. *J. Geophys. Res. Planets* **1993**, *98*, 11025–11042. [CrossRef]
44. Ivanov, B.A. Mars/Moon cratering rate ratio estimates. *Space Sci. Rev.* **2001**, *96*, 87–104. [CrossRef]

45. Neukum, G.; Ivanov, B.A.; Hartmann, W.K. Cratering records in the inner solar system in relation to the lunar reference system. In *Chronology and Evolution of Mars, Proceedings of an ISSI Workshop, Bern, Switzerland, 10–14 April 2000*; Springer: Dordrecht, The Netherlands, 2001; pp. 55–86.
46. Michael, G.; Neukum, G. Planetary surface dating from crater size–frequency distribution measurements: Partial resurfacing events and statistical age uncertainty. *Earth Planet. Sci. Lett.* **2010**, *294*, 223–229. [CrossRef]
47. Tanaka, K.L.; Skinner, J.A., Jr.; Dohm, J.M.; Irwin, R.P., III; Kolb, E.J.; Fortezzo, C.M.; Platz, T.; Michael, G.G.; Hare, T.M. *Geologic Map of Mars*; U.S. Geological Survey: Reston, VA, USA, 2014; p. 3292. [CrossRef]
48. Ivanov, M.A.; Hiesinger, H.; Erkeling, G.; Reiss, D. Mud volcanism and morphology of impact craters in Utopia Planitia on Mars: Evidence for the ancient ocean. *Icarus* **2014**, *228*, 121–140. [CrossRef]
49. Huang, H.; Wang, X.; Chen, Y.; Zhang, Q.; Zhao, F.; Ren, X.; Zeng, X.; Yan, W.; Chen, W.; Liu, B. Observations and interpretations of geomorphologic features in the Tianwen-1 landing area on Mars by using orbital imagery data. *Earth Planet. Phys.* **2022**, *7*, 331–346. [CrossRef]

Disclaimer/Publisher's Note: The statements, opinions and data contained in all publications are solely those of the individual author(s) and contributor(s) and not of MDPI and/or the editor(s). MDPI and/or the editor(s) disclaim responsibility for any injury to people or property resulting from any ideas, methods, instructions or products referred to in the content.

remote sensing

MDPI

Article

Global Inversion of Lunar Surface Oxides by Adding Chang'e-5 Samples

Shuangshuang Wu [1,2], Jianping Chen [1,2,*], Chenli Xue [1,2], Yiwen Pan [1,2] and Cheng Zhang [1,2]

[1] School of Earth Sciences and Resources, China University of Geosciences, Beijing 100083, China; wss@email.cugb.edu.cn (S.W.); xcl@email.cugb.edu.cn (C.X.); panyw@email.cugb.edu.cn (Y.P.); chengzhang@email.cugb.edu.cn (C.Z.)

[2] Beijing Key Laboratory of Development and Research for Land Resources Information, Beijing 100083, China

* Correspondence: 3s@cugb.edu.cn

Abstract: The chemical distribution on the lunar surface results from the combined effects of both endogenic and exogenic geological processes. Exploring global maps of chemical composition helps to gain insights into the compositional variation among three major geological units, unraveling the geological evolution of the Moon. The existing oxide abundance maps were obtained from spectral images of remote sensing and geochemical data from samples returned by Apollo and Luna, missing the chemical characteristics of the Moon's late critical period. In this study, by adding geochemical data from Chang'e (CE)-5 lunar samples, we construct inversion models between the Christiansen feature (CF) and oxide abundance of lunar samples using the particle swarm optimization–extreme gradient boosting (PSO-XGBoost) algorithm. Then, new global oxide maps (Al_2O_3, CaO, FeO, and MgO) and Mg# with the resolution of 32 pixels/degree (ppd) were produced, which reduced the space weathering effect to some extent. The PSO-XGBoost models were compared with partial least square regression (PLSR) models and four previous results, indicating that PSO-XGBoost models possess the capability to effectively describe nonlinear relationships between CF and oxide abundance. Furthermore, the average contents of our results and the Diviner results for 21 major maria demonstrate high correlations, with R^2 of 0.95, 0.82, 0.95, and 0.86, respectively. In addition, a new Mg# map was generated, which reveals different magmatic evolutionary processes in the three geologic units.

Keywords: lunar surface; LRO Diviner; Christiansen feature; lunar oxide; Chang'e-5

1. Introduction

Al, Ca, Fe, and Mg, as major components of lunar regolith, reflect a variety of complex geological processes, including volcanism and impact events, providing insight into the petrological characteristics and geological evolution of the Moon. Although chemical abundance within lunar samples can be assessed through laboratory measurements, the limited geochemical information from lunar samples represents only a small range of their composition [1–3]. It is not yet possible to gain an overall understanding of the compositional distribution across the Moon through limited sample data.

Nowadays, remote sensing techniques, including high-energy and optical techniques, such as Lunar Prospector (LP) gamma ray spectroscopy (GRS) data [4–7], LP neutron spectroscopy data [8–12], Clementine ultraviolet/visible (UV/VIS) data [1,13–15], Lunar Reconnaissance Orbiter wide angle camera (WAC) ultraviolet/visible (UV/VIS) data [16], KAGUYA multiband imager (MI) data [2,17–20] and Chang'e-1 (CE-1) interference imaging spectrometer (IIM) data [3,21–24], are widely used in oxide abundance inversion on the lunar surface. Compared with high-energy techniques, optical techniques offer the advantage of higher resolution, which has led to their predominant use for lunar surface oxide abundance inversion in existing studies [13,22]. However, they also present some

problems that need to be considered. (1) Sensitivity of visible near-infrared (VNIR) data: Only Fe and Ti, as transition metals, possess the ability for ligand field transitions that have absorption diagnostic features in the visible to near-infrared range [25–27]. Previous models for FeO and TiO_2 have relied on reflectance and a two-band ratio targeting the 1 micron iron band [15]. (2) Limitations of previous models: The use of band ratio methods, which rely on only two bands to describe the non-linear relationship between reflectance and oxide abundance, has limited capability in accurately estimating oxide content [23]. The accuracy of oxide content estimation is highly dependent on the inversion model [3,23]. (3) Photometric effects on reflectance values: Differences in solar elevation angle at different times of the lunar day result in varying terrain shadow effects, which have an impact on the reflectance of the lunar surface and consequently increase the uncertainty in oxide content inversion [28]. Additionally, the topographic effects also contribute to lower coverage in optical images [23], particularly in polar regions [3,23].

To overcome these problems, many studies have turned their attention to thermal infrared (TIR) remote sensing [28–34]. The thermal infrared spectra of silicate minerals exhibit a prominent emissivity maximum near 8 μm, known as the Christiansen feature (CF). The CF can be used as an indicator for identifying the composition of silicate minerals, such as plagioclase, pyroxene, and olivine [35], compensating for the limitations of visible and NIR remote sensing [36]. Additionally, the wavelength position of the CF is closely related to the degree of polymerization of silicate minerals and the content of cations in the minerals [29,37,38]. Therefore, the CF map derived by Lucey et al. [32], with the correction of space weathering effects and a resolution of 32 pixels/degree (ppd), provides a different perspective for quantitative inversion of oxide abundance on the lunar surface.

In addition to remote sensing data, geochemical information from returned lunar samples and in situ measurements are also the basis of compositional inversion, providing a reliable ground truth for compositional modeling of the lunar surface. The lunar regolith samples used in previous studies were obtained from six Apollo and three Luna missions, which represent chemical features only from 3.1–4.3 Ga [39,40], missing the later stage of lunar evolution. In November 2020, the Chang'e-5 (CE-5) mission returned lunar regolith samples from the Mons Rümker in the northern Oceanus Procellarum (43.06°N, 51.92°W), with a radiometric age of 2.0 Ga [41–43]. The CE-5 sample represents the youngest volcanic eruption, and its inclusion holds significant importance in updating the lunar surface oxide maps.

The distribution of oxides on the lunar surface exhibits significant heterogeneity, which is particularly evident in samples from the highlands and maria, with corresponding differences in the number of samples from these regions [7]. This heterogeneity, combined with the inconsistency in sample quantities, imposes potential limitations in predicting using single-model algorithms. However, ensemble machine learning algorithms can help alleviate these limitations by integrating multiple models to improve the accuracy and robustness of predictions [44]. Among these, the extreme gradient boosting (XGBoost) algorithm, as an efficient integrated learning technique, has demonstrated excellent performance in several fields [45–47]. Meanwhile, the partial least squares regression (PLSR) algorithm, as a well-established linear regression analysis method, is particularly suitable for datasets in which the number of predictor variables is larger than the number of observed samples, and it has been widely used in soil spectral analysis [48–50]. Therefore, we choose the results of the PLSR model as the control group for the XGBoost model, aiming to explore the feasibility of machine learning algorithms to estimate the abundance of oxides and improve the accuracy of the inversion results.

Given the above limitations and challenges, this study aims to (1) employ the particle swarm optimization–extreme gradient boosting (PSO-XGBoost) algorithm to construct inversion models for exploring updated maps of oxide (Al_2O_3, CaO, FeO, and MgO) abundance, (2) evaluate the predictive accuracy of our model in comparison to the PLSR model and other previous work, (3) investigate the new Mg# map that delineates the lunar surface into three geological units (maria, highlands, and SPA basin) with distinct Mg#

features, and discuss the differences in the magmatic processes undergone in these units. According to the results, the oxide distribution maps in this work provide valuable data support for understanding the geological evolution of the Moon.

2. Data

2.1. Christiansen Feature

CF refers to the phenomenon in the spectra of silicate samples involving a strong minimum reflectance and maximum emission near 8 μm [35]. The CF feature is mainly related to the Si-O stretching vibrations in the crystals. Although fine grain sizes characteristic of lunar soil can somewhat suppress the spectral contrast of vibrational features [51], the CF and its wavelength sensitivity to composition still persist, making the CF important in lunar remote sensing [32]. Plagioclase, pyroxene, olivine, and ilmenite are the major minerals on the Moon, all of which, except for ilmenite, are silicate minerals and exhibit distinctly different CF values. Among them, the CF values of plagioclase, pyroxene, and olivine are 7.84 μm, 8.25 μm, and 8.67 μm, respectively [31].

2.2. Diviner CF Map

Diviner is a nine-channel radiometer carried on the Lunar Reconnaissance Orbiter (LRO) satellite, with a wavelength range from ultraviolet to far-infrared, approximately 0.35–400 μm [52,53]. Diviner's three narrow channels near 8 μm were utilized to estimate the spectral position of maximum emission, known as CF [33]. The CF maps were based on three-point spectral data from Diviner and there are uncertainties relating to those CF positions based on the position of the Diviner spectral filters. Recently, Lucey et al. [32] corrected the effects of space weathering and generated a new CF map with a resolution of 32 ppd (948 m/pixel at the equator), providing strong support for chemical (Al_2O_3, CaO, FeO, and MgO) inversion (Figure 1).

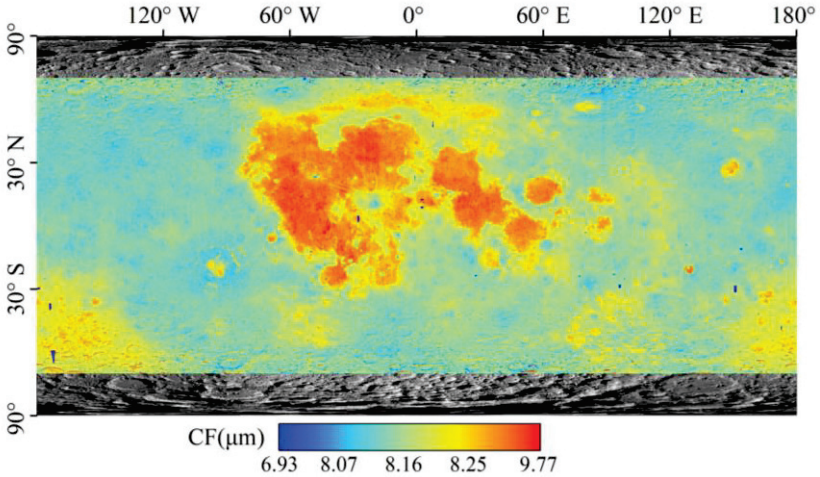


Figure 1. The corrected CF map derived by Lucey et al. [32].

2.3. Lunar Sampling Sites

Lunar sample data are the basis of compositional inversion and also the standard of model accuracy evaluation. In this study, forty-nine lunar samples from the Apollo, Luna, and Chang'e projects [3,19,20,28] were utilized to represent the ground truth of oxide content (Table 1). Additionally, the CF value of CE-5 was extracted based on the criteria stated by Ma et al. [28] and the other CF values were derived from Ma et al. [28].

Table 1. Four oxide (Al_2O_3, CaO, FeO, and MgO) contents and CF positions of 49 lunar sampling sites. Abundances are shown in wt.%, and CF values are shown in μm.

Site	Al_2O_3	CaO	FeO	MgO	CF
A11	13.45	12.01	15.80	7.81	8.286
A12	13.86	10.58	15.40	9.66	8.255
A14-LM	17.69	10.32	10.53	9.52	8.214
A14-Cone	17.50	11.00	10.30	9.60	8.209
A15-LM	14.45	10.25	14.95	10.65	8.257
A15-S1	13.15	10.58	15.79	10.81	8.253
A15-S2	17.52	11.75	11.52	10.54	8.290
A15-S4	13.22	10.46	15.96	11.19	8.272
A15-S6	16.47	11.29	12.14	10.51	8.247
A15-S7	15.92	10.12	12.37	11.17	8.247
A15-S8	14.46	10.38	14.98	10.35	8.257
A15-S9	12.54	10.31	16.61	10.98	8.250
A15-S9a	10.31	9.39	20.19	11.36	8.250
A16-LM	27.60	15.42	5.44	5.70	8.165
A16-S1	26.60	15.60	5.40	6.10	8.177
A16-S2	27.00	15.60	5.50	6.00	8.177
A16-S4	27.60	15.70	4.60	5.40	8.176
A16-S5	26.20	15.10	5.90	6.20	8.170
A16-S6	27.10	16.40	6.00	6.90	8.170
A16-S8	26.50	15.40	5.40	6.20	8.203
A16-S9	26.30	15.50	5.70	6.30	8.203
A16-S11	28.60	16.70	4.20	4.50	8.180
A16-S13	27.70	15.80	4.66	5.32	8.145
A17-LM	12.10	11.10	16.60	9.80	8.257
A17-S1	10.90	10.80	17.80	9.60	8.279
A17-S2	20.70	12.80	8.70	9.90	8.201
A17-S3	20.40	12.90	8.70	10.20	8.220
A17-S5	10.90	10.80	17.70	9.60	8.260
A17-S6	18.30	12.20	10.70	10.80	8.224
A17-S7	17.30	11.90	11.60	10.10	8.228
A17-S8	16.60	11.80	12.30	10.20	8.223
A17-S9	13.90	11.30	15.40	10.00	8.286
A17-LRV1	12.60	11.20	16.30	9.40	8.281
A17-LRV2	16.10	11.90	13.40	10.30	8.223
A17-LRV3	14.40	11.30	14.80	10.40	8.223
A17-LRV4/S2a	21.40	12.80	8.50	9.60	8.216
A17-LRV5	19.90	12.80	9.80	8.90	8.220
A17-LRV6	19.40	12.50	10.30	9.90	8.241
A17-LRV7	12.80	10.70	16.10	10.30	8.259
A17-LRV8	13.50	11.30	15.70	9.90	8.266
A17-LRV9	14.30	11.30	14.60	9.80	8.276
A17-LRV10	17.50	12.10	11.20	10.50	8.224
A17-LRV11	16.30	11.90	12.70	10.00	8.267
A17-LRV12	11.20	10.80	17.40	9.40	8.251
Luna16	15.24	12.50	16.70	8.80	8.295
Luna20	22.90	14.50	7.50	9.20	8.203
Luna24	11.10	11.10	20.50	10.20	8.296
CE-3	11.90	10.60	21.60	9.60	8.301
CE-5	10.80	10.90	22.20	6.48	8.280

3. Methods

3.1. Oxide Inversion Model

We used PSO-XGBoost and PLSR algorithms to construct mathematical models for describing the relationship between the four oxide contents and CF values. The XGBoost algorithm is one of the supervised machine learning models proposed by Chen and Guestrin [44] and is essentially a gradient boosting decision tree (GBDT) model. The fundamental idea of

the XGBoost algorithm is to integrate multiple weak estimators into a strong estimator [54], demonstrating excellent performance in parallel computing efficiency, handling missing values, controlling overfitting, and predicting generalization ability [55,56].

There are two important parameters in the XGBoost model: n_estimators and learning_rate. The n_estimators parameter represents the number of trees built during training. The larger the n_estimators value, the better is the learning capacity of the model and the easier is the overfitting. The other parameter is learning_rate, also known as shrinkage, which controls the iteration rate and can be used to prevent overfitting. After each iteration, the XGBoost algorithm determines the weights of new features to control the weights of the subtrees and mitigate overfitting [47].

The PSO algorithm, proposed by J. Kennedy and R. Eberhart [57], is a stochastic search algorithm based on collective collaboration, which was developed through simulating the foraging behavior of birds [57,58]. In the PSO algorithm, each potential solution is called a particle [54] and consists of the velocity vector and geometric position vector [59]. The core of the PSO algorithm is to update the velocity and position of the particles, enabling the continuous search for the optimal solution within the search space [60]. The PSO algorithm helps to find the optimal combination of parameters which can improve the performance of the XGBoost model.

In addition, the PLSR algorithm is a linear regression model proposed by de Jong [61]. The core idea of PLSR is to find a new space that can simultaneously explain the variation in both the predictor and response variables [62]. In the PLSR model, coefficients and intercepts are two important parameters. PLSR simplifies the model by extracting latent variables and captures the relationships between variables through coefficients and intercepts, thereby enhancing the model's predictive power.

3.2. Model Parameters and Evaluation Index

In this study, the oxide abundances and CF values of 49 lunar samples were input into the PSO-XGBoost and PLSR algorithms to construct oxide inversion models. To ensure the training effectiveness of the designed oxide inversion models, it was necessary to optimize relevant parameters of the models. In each oxide model constructed by the PSO-XGBoost algorithm, the optimal values of two hyperparameters were obtained through iteratively updating the location vectors and velocity vectors of the PSO (Table 2). The optimal parameters of the oxide model based on the PLSR algorithm are shown in Table 3. Based on these optimal parameters, the functional relationships between CF values and oxide abundances were constructed. In addition, random sampling was adopted to select 80% of the 49 lunar samples (39 samples) as the training set and 20% of the 49 samples (10 samples) as the testing set.

Table 2. Optimal values of parameters for four major oxides based on the PSO-XGBoost algorithm.

Parameters	Al_2O_3	CaO	FeO	MgO
n_estimators	582	518	530	584
learning_rate	0.1	0.1	0.1	0.1

Table 3. Optimal values of parameters for four major oxides based on the PLSR algorithm.

Parameters	Al_2O_3	CaO	FeO	MgO
intercept	1067.8859	355.0624	−831.7237	−247.5031
coefficient	−127.5548	−41.6391	102.4634	31.1801

To assess the performance of the oxide inversion models, the determination coefficient (R^2) and the root mean square error (RMSE) were utilized as evaluation indicators and calculated as follows:

$$R^2 = 1 - \frac{\sum_{i=1}^{m}(\check{c}_i - c_i)^2}{\sum_{i=1}^{m}(c_i - \overline{c_i})^2} \quad (1)$$

$$RMSE = \sqrt{\frac{\sum_{i=1}^{m}(\check{c}_i - c_i)^2}{n}} \quad (2)$$

where $\check{c}_i$, c_i and $\overline{c_i}$ denote the true, predicted, and mean values of the ith sample, respectively, and n denotes the number of samples.

Finally, the corrected CF values of the Moon (70°N/S) were used as input for predicting, and the Al_2O_3, CaO, FeO and MgO abundances of the Moon (70°N/S) were output, respectively.

4. Results

4.1. Correlation Coefficients between Oxides and CF Values

Correlation analysis of CF values and oxide abundances at 49 sampling sites showed high Pearson correlation coefficients (Figure 2). In general, Al_2O_3 and CaO exhibited negative correlation with CF values, whereas FeO and MgO demonstrated positive correlation. Among them, the linear correlation between CF values and FeO abundance was 0.7737, and the nonlinear correlation between CF values and abundance of oxides (Al_2O_3, CaO, and MgO) were maintained at 0.8110, 0.7360, and 0.6641, respectively. However, the relationship between CF values and oxide content was not always univariate linear regression. For some oxides (e.g., Al_2O_3, CaO, and MgO), it was difficult to describe their complex relationship with CF values using traditional univariate regression.

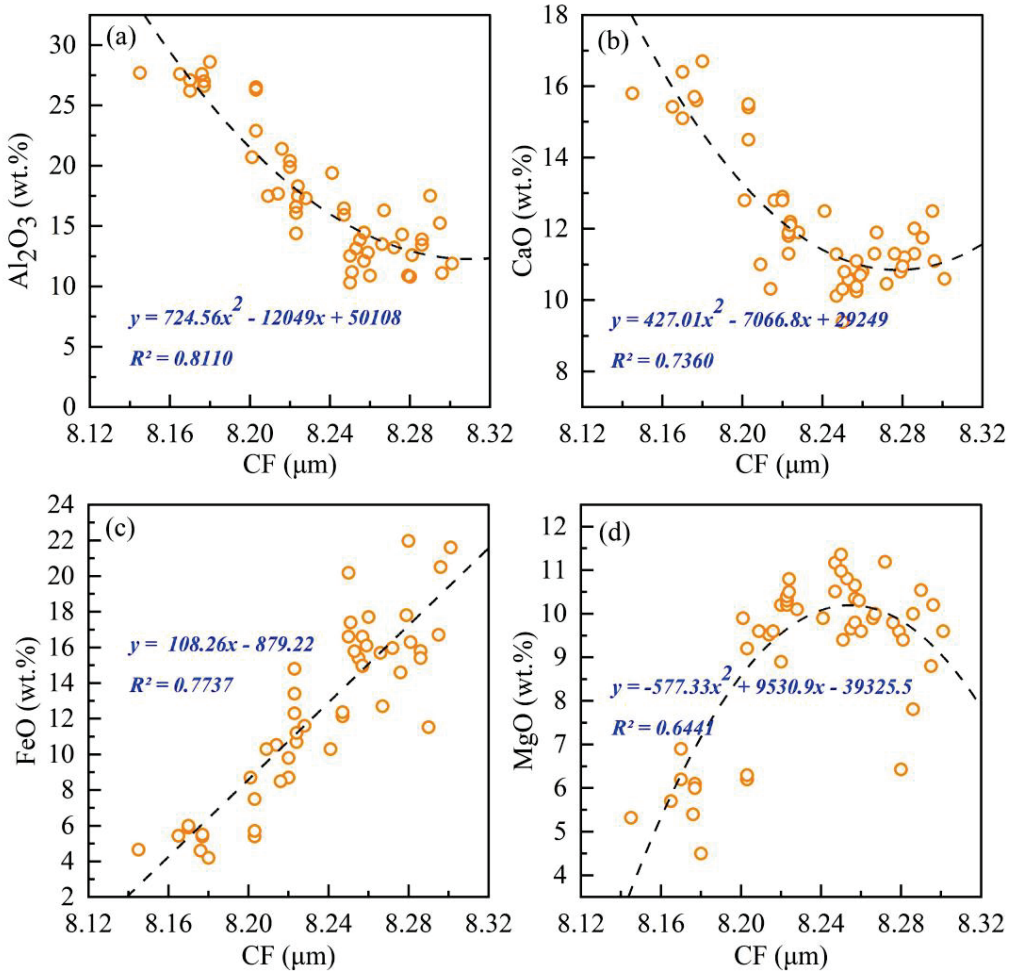


Figure 2. Linear or nonlinear relationships between (**a**) Al_2O_3, (**b**) CaO, (**c**) FeO, and (**d**) MgO and the CF values for 49 lunar sampling points.

4.2. Model Accuracy Evaluation

The prediction accuracies of the PSO-XGBoost models are shown in Figure 3. The R^2 values of the oxide (Al_2O_3, CaO, FeO, and MgO) abundance prediction models were 0.8806, 0.754, 0.8755, and 0.79, respectively, all greater than 0.75. The RMSE for these predictive models was also notably low, at 2.2698, 1.0392, 2.1327, and 0.9922. In contrast, the PLSR models (Figure 4), while possessing some predictive capability, demonstrate slightly inferior R^2 values of 0.769, 0.5116, 0.6827, and 0.2569, and relatively higher RMSE values of 3.1577, 1.4643, 2.2641, and 1.8664, respectively. Therefore, compared with the PLSR model, the PSO-XGBoost model demonstrated superior performance in capturing nonlinear relationships, enabling it to provide more precise predictions of oxide abundance.

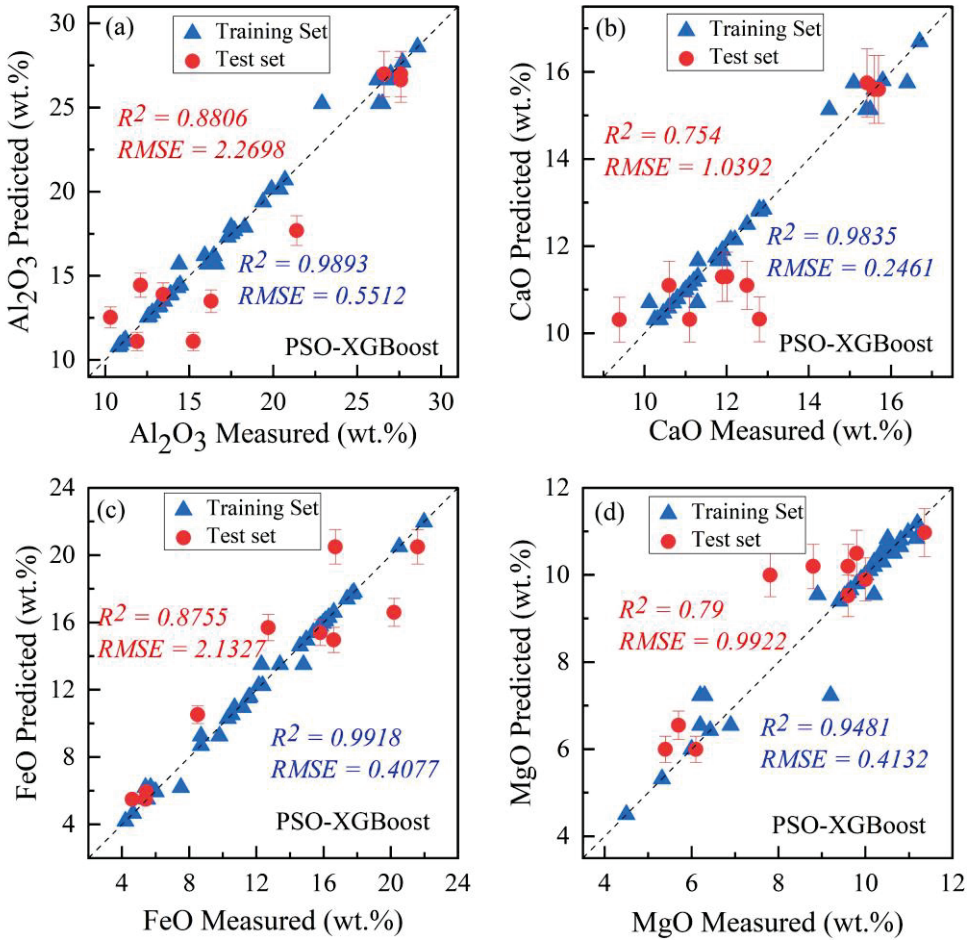


Figure 3. Scatter plots of the measured and predicted values for (**a**) Al_2O_3, (**b**) CaO, (**c**) FeO, and (**d**) MgO from PSO-XGBoost models. Error bars represent 95% confidence intervals around the oxides' predicted values.

4.3. Global Maps of Oxides

The global distribution maps of the four oxides' abundances with a resolution of 32 ppd were derived from the CF map based on the PSO-XGBoost model, as shown in Figure 5. From a global perspective, the average abundances of Al_2O_3, CaO, FeO, and MgO were 23.63 wt.%, 14.42 wt.%, 7.78 wt.%, and 7.14 wt.% respectively, and the standard deviations of Al_2O_3, CaO, FeO, and MgO were 5.64, 2.10, 4.47 and 2.15 (Table 4). Among them, the highest average of Al_2O_3 across the global Moon indicates that Al_2O_3 is present in a relatively significant proportion in the lunar oxides. Additionally, standard deviation is a statistical measure that quantifies the amount of variation or dispersion in a set of values, and the highest standard deviation of Al_2O_3 implies significant differences in Al_2O_3 abundance between different regions on the lunar surface.

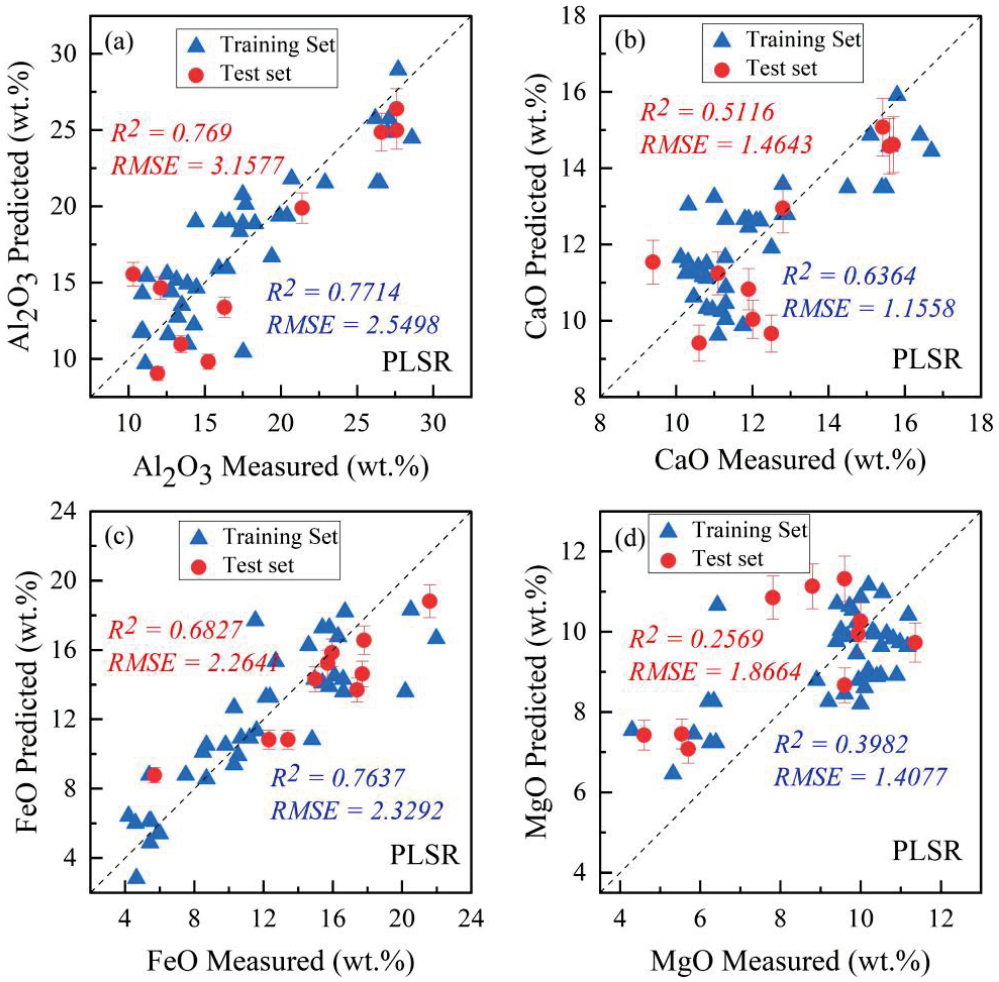


Figure 4. Scatter plots of the measured and predicted values for (**a**) Al_2O_3, (**b**) CaO, (**c**) FeO, and (**d**) MgO from PLSR models.

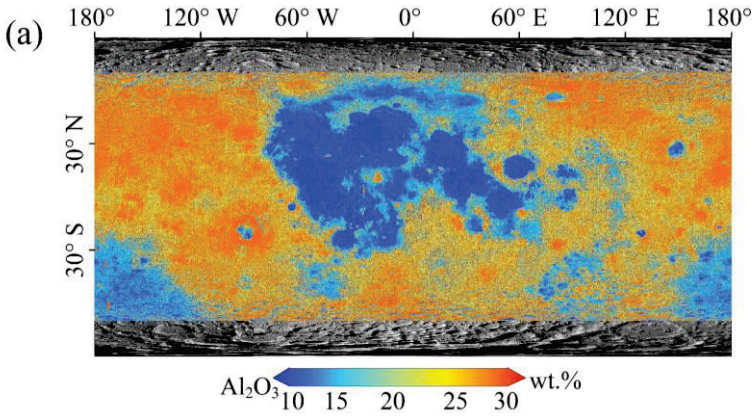


Figure 5. *Cont*.

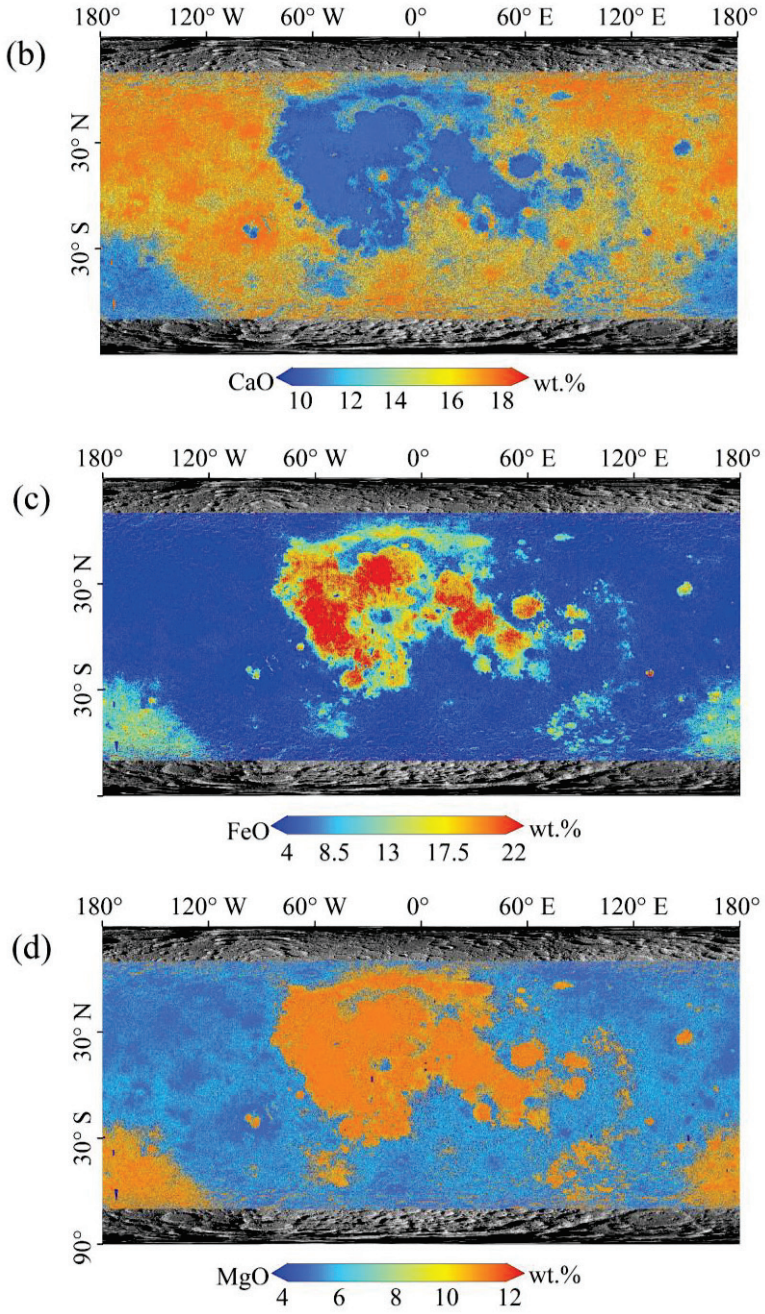


Figure 5. Global distribution maps of (**a**) Al_2O_3, (**b**) CaO, (**c**) FeO and (**d**) MgO abundances.

Table 4. Average (AVG) and standard deviation (STD) values for the abundance of four oxides and Mg# in maria, highlands, and SPA basin (wt.%).

	Global		**Maria**		**Highlands**		**SPA**	
	AVG	**STD**	**AVG**	**STD**	**AVG**	**STD**	**AVG**	**STD**
Al_2O_3	23.63	5.64	14.71	3.98	25.66	3.86	19.80	5.18
CaO	14.42	2.10	11.45	1.18	15.12	1.66	12.74	2.20
FeO	7.78	4.47	15.09	4.31	6.16	2.64	10.01	3.98
MgO	7.14	2.15	9.88	1.10	6.46	1.80	8.81	2.04
Mg#	0.50	5.65	0.41	6.77	0.52	2.90	0.48	5.40

4.4. Three Geological Units and Interesting Regions of Chemical Abundances

As shown in Table 4, the four oxides' average abundance in the Moon (70°N/S) and the SPA basin follows the order Al_2O_3 > CaO > FeO > MgO. In maria, the order of four oxides average abundance is FeO > Al_2O_3 > CaO > MgO, while the order of the four oxides' average abundance in the highlands is Al_2O_3 > CaO > MgO > FeO. The average abundances of Al_2O_3 (25.66 wt.%) and CaO (15.12 wt.%) in the highlands are higher than (Al_2O_3: 14.71 wt.% and CaO: 11.45 wt.%) in maria, while the average abundances of FeO (6.16 wt.%) and MgO (6.46 wt.%) in the highlands are lower than in the maria (FeO: 15.09 wt.% and MgO: 9.88 wt.%). MgO exhibited the lowest average abundance among these four oxides in maria and the SPA basin, and the average FeO content was the lowest in the highlands. In the SPA basin, the average contents of each oxide were intermediate between the maria and highlands.

The average and STD of the four oxides' abundances in the major lunar maria are shown in Table 5. Except for the lowest value of Ca, which is in Mare Spumans, the maximum and minimum values of the other oxides are in Mare Australe and Mare Tranquillitatis. Among the 21 major maria, the STD values of Al_2O_3 and FeO abundances are larger than those of CaO and MgO content, indicating large changes in the distribution of Al_2O_3 and FeO abundances, especially in Mare Orientale.

The compositional distributions of three interesting regions are shown in Figure 6. The oxide compositions are inconsistent within and around the Kepler impact crater. The high Al_2O_3 and CaO contents inside the Kepler crater are similar to those in the highlands, which may be due to the exposure of plagioclase material after the impact broke through the mare basalt. The higher FeO content in the interior of the Moscoviense Basin was formed by the filling of the basin with iron-and titanium-rich basaltic magma after its formation. In addition, the composition of the Helmet dome is relatively similar to the highland material, with higher Al_2O_3 and CaO and lower FeO and MgO.

Table 5. The AVG and STD of oxide abundances in major lunar maria (wt.%).

Mare	Al_2O_3		CaO		FeO		MgO	
	AVG	**STD**	**AVG**	**STD**	**AVG**	**STD**	**AVG**	**STD**
Mare Anguis	19.39	4.91	12.59	1.97	10.34	3.77	9.02	1.85
Mare Australe	**19.85**	4.72	**12.70**	2.04	**9.87**	3.47	**8.94**	1.91
Mare Cognitum	13.62	2.77	11.16	0.71	16.00	3.26	10.03	0.82
Mare Crisium	13.84	3.19	11.27	0.84	15.94	3.67	9.98	0.91
Mare Fecunditatis	14.24	3.13	11.28	0.78	15.38	3.65	10.02	0.78
Mare Frigoris	15.97	3.12	11.45	0.94	13.18	2.99	10.08	0.67
Mare Humorum	13.47	2.97	11.17	0.89	16.36	3.70	10.03	0.91
Mare Imbrium	13.19	2.71	11.18	0.66	16.85	3.55	10.06	0.75
Mare Marginis	14.34	3.03	11.21	0.83	14.98	3.19	10.01	0.83
Mare Moscoviense	14.84	3.08	11.29	0.84	14.41	3.21	10.04	0.75
Mare Nectaris	16.96	3.95	11.76	1.41	12.28	3.42	9.76	1.21
Mare Nubium	15.49	3.66	11.45	1.13	13.77	3.51	9.91	1.00
Mare Orientale	19.44	**5.01**	12.64	2.02	10.34	**3.79**	8.99	1.92
Mare Serenitatis	13.02	2.29	11.15	0.46	16.97	3.20	10.05	0.73
Mare Smythii	13.99	2.73	11.16	0.69	15.39	3.06	10.04	0.78
Mare Spumans	14.05	2.69	**11.12**	0.70	15.19	2.85	10.04	0.78
Mare Tranquillitatis	**12.57**	2.26	11.16	0.37	**17.93**	3.28	**10.11**	0.58
Mare Undarum	14.42	3.01	11.23	0.78	14.95	3.29	10.04	0.76
Mare Vaporum	13.18	2.79	10.93	1.46	15.90	3.48	9.89	1.45
Mare Insularum	15.51	4.10	11.43	1.58	13.59	3.84	9.77	1.39
Oceanus Procellarum	13.19	2.77	11.21	0.60	16.97	3.65	10.07	0.69

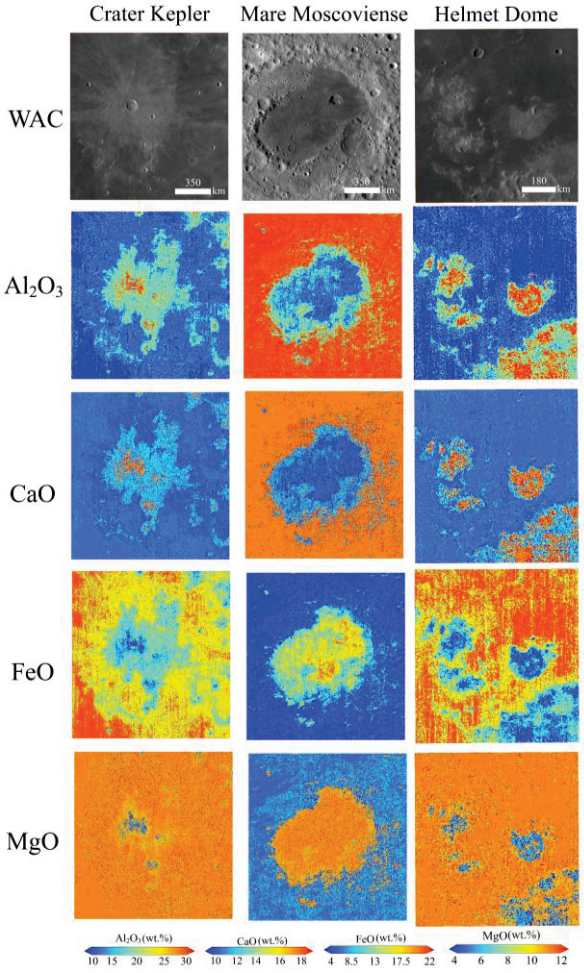


Figure 6. The LRO WAC and compositional distributions of three interesting regions including the Kepler crater (8.1°N, 38.0°W), Mare Moscoviense (148°E, 27°N), and the Helmet dome (16.6°S, 31.4°W).

5. Discussion

5.1. Comparison with Previous Studies

The four oxides' distributions were estimated using LP GRS [7], CE-1 IIM (~200 m/pixel) [3,23], and LRO Diviner (32 ppd) data [28]. Based on the global maps of the four oxides, their average content in the Moon (70°N/S) and its different terrains can be obtained (Figure 7). Figure 8 illustrates the spatial distribution of maria, highlands, and SPA basin. Based on the boundaries of different terrains, bar charts (Figure 7) were produced for comparative analysis by extracting the oxide abundances for the different geological units (global, maria, highlands, and SPA basin).

The average abundances of the four oxides in this study fell between the ranges of the other inversion results (Figure 7). For the Moon (70°N/S), the smallest differences of average abundances in Al_2O_3, CaO, FeO, and MgO were 0.16, 0.10, 0.03, and 0.29, respectively. Apart from CaO derived from LP GRS in maria and the SPA basin and FeO obtained from Diviner in maria, the average abundance of inversion results in this study was similar to the other results, especially those from CE-1 [23] and Diviner [28], which showed the closest resemblance. Relatively significant differences in levels of CaO in maria and the SPA basin were observed between this study and LP GRS, which may be due to the different resolution. The LP GRS and the Diviner data exhibit different spatial resolution, implying a variance in their capacity to discern the smallest pixels. Data characterized by a lower resolution may not adequately capture the fine-scale characteristics observable within higher resolution datasets, which could lead to the neglect of subtle variations in

the CaO distribution. Despite the differences in their absolute abundances, the trends in their relative abundances are consistent.

We compared the average and standard deviation of oxide abundance in 21 major maria with previous work conducted by Ma et al. [28], and the scatter plots with error bars for the four oxide abundances are shown in Figure 9. For the four oxides (Al_2O_3, CaO, FeO, and MgO), the average contents determined through this study and the LRO Diviner maps [28] in each maria demonstrated a relatively proximity to the 1:1 line, with R^2 values of 0.95, 0.82, 0.95 and 0.86, respectively.

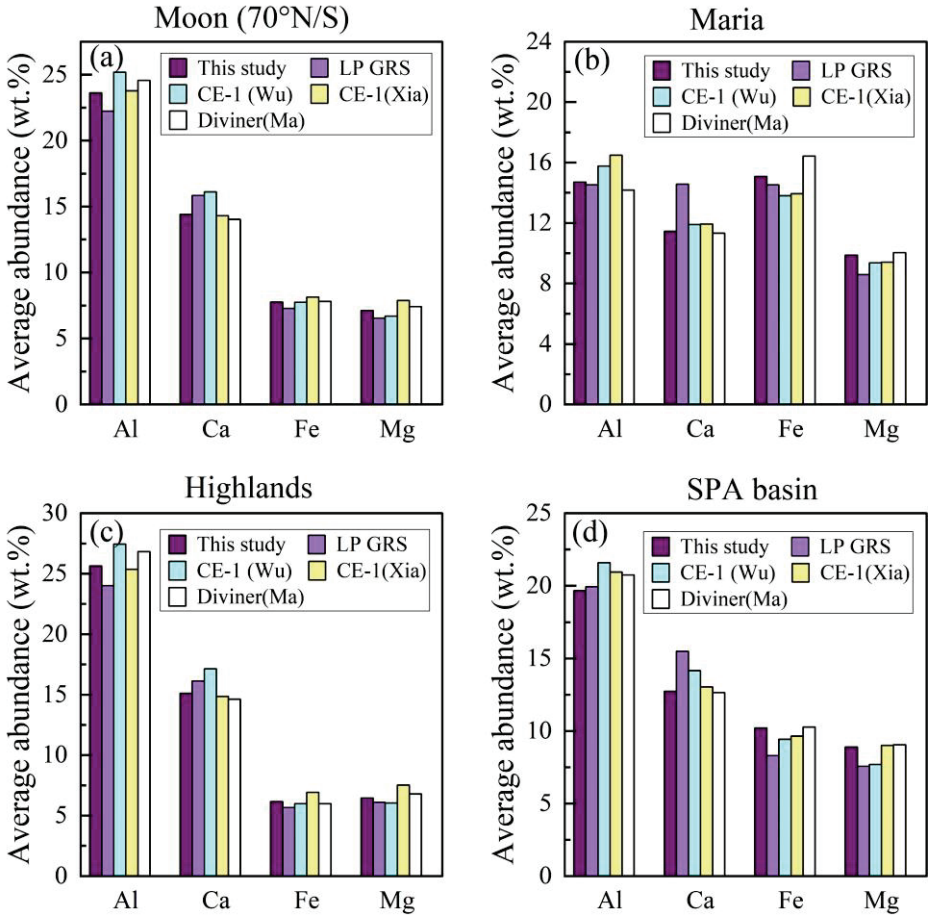


Figure 7. Average abundances of four oxides in the (**a**) Moon (70°N/S), (**b**) maria, (**c**) highlands, and (**d**) SPA basin, according to five sets of results.

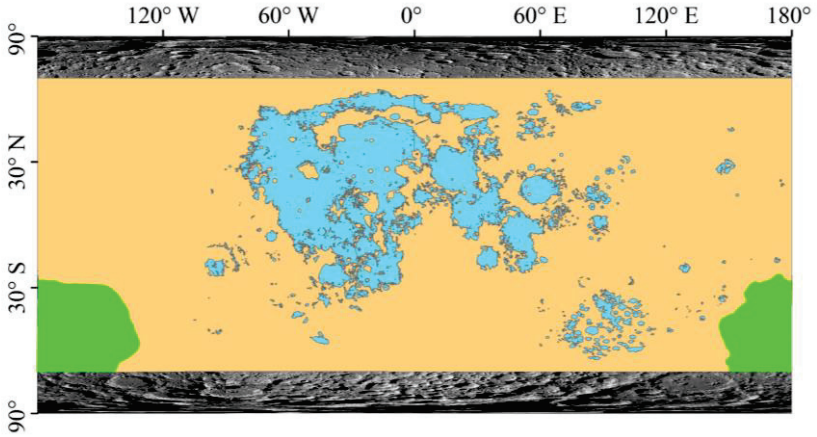


Figure 8. Sketch map showing the locations of the three geological units (maria are marked in blue, highlands are marked in orange, and the SPA basin is identified in green).

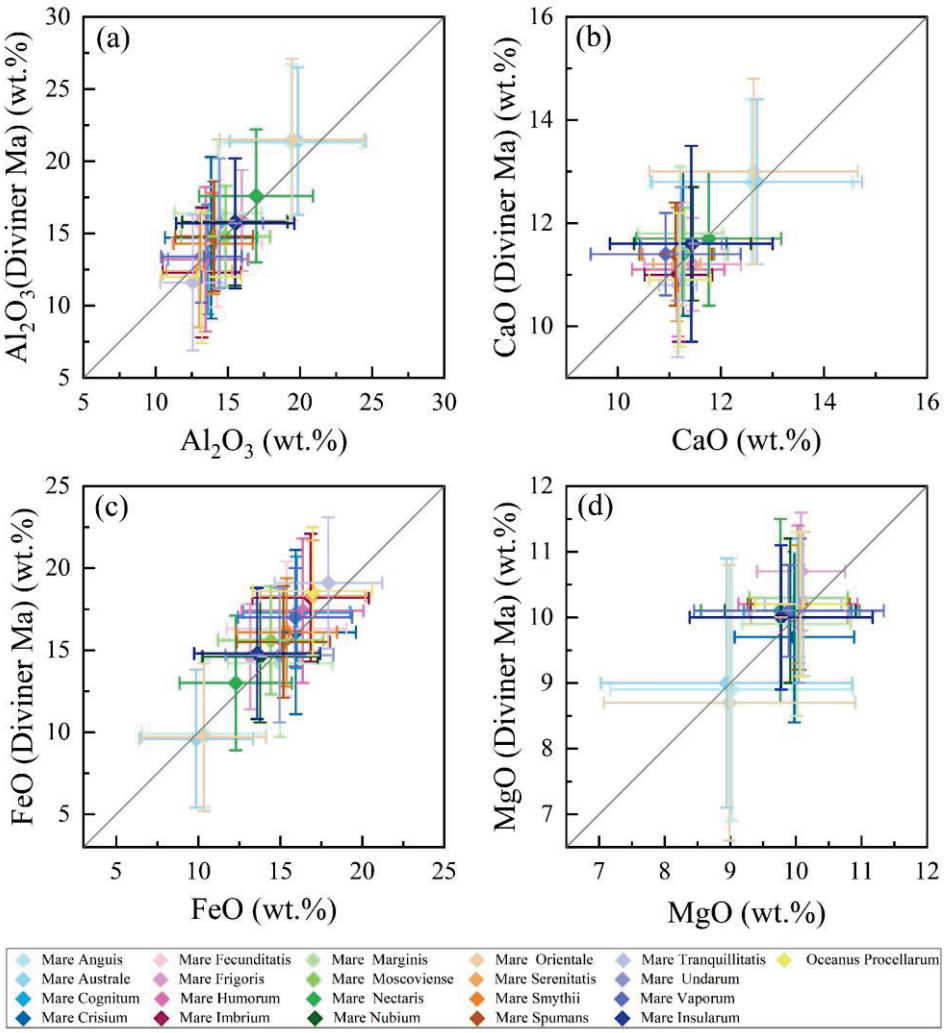


Figure 9. Scatter plot with error bars for (**a**) Al_2O_3 (**b**) CaO (**c**) FeO and (**d**) MgO abundances from Ma et al. [28] and this study, for 21 major maria. Error bar indicates the standard deviation.

5.2. Implications of the Mg# Map

For the four major oxides estimated in this study, the Mg# (Mg# = mole percent MgO/(MgO + FeO)) was obtained with a resolution of 32 ppd. The global distribution of Mg# is shown in Figure 10, and exhibits an obvious trichotomy. The average Mg# values across the Moon (70°N/S) and in the three geological units (maria, highlands, and SPA basin) were 0.50, 0.41, 0.52, and 0.48, which are close to the multiband imager (MI) Mg# values [19] of 0.53, 0.40, 0.58, and 0.46, respectively. The average Mg# value in the highlands was higher than in the maria, which is consistent with the fact that FeO was higher than MgO in the maria regions, while MgO was higher than FeO in the highland regions [3]. In addition, the regions with low Mg# values in the new Mg# map correspond to the distribution of mare basalts on the Moon [63], which indicates that mare basalts exhibit low Mg#.

Mg# is an important indicator in lunar petrology for studying the compositional variation during magma crystallization [28,59], and a higher Mg# value represents an earlier magma ocean event with more primitive materials [2]. The different Mg# values observed in these three geological units are similar to those described by Otake et al. [2], indicating that they have undergone different magma evolution processes resulting in the lava flow filling with diverse composition and minerals [2,64]. Therefore, the maria have undergone a higher degree of evolution, primarily crystallized from the iron- and magnesium-rich magma, while the formation of the highlands marks the early stages

of the lunar magma crystallization process, formed by the crystallization of relatively primitive magma.

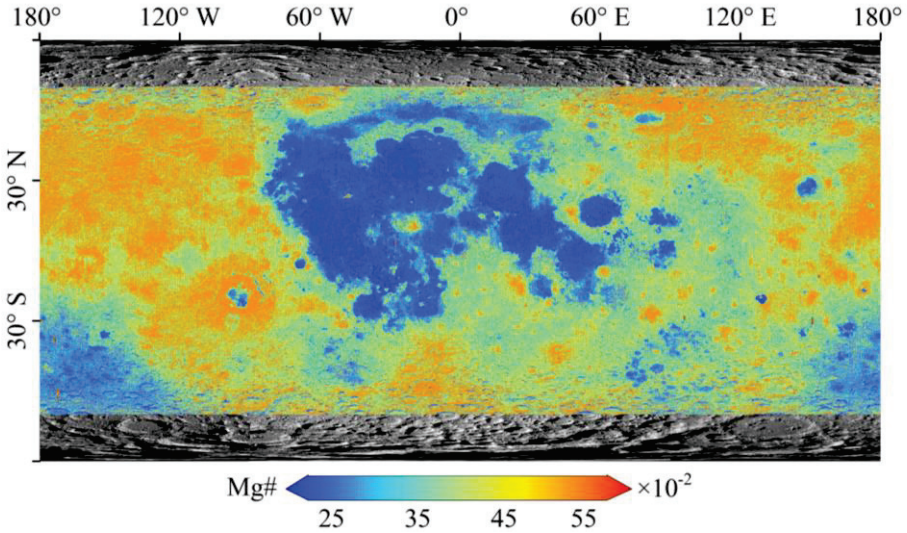


Figure 10. Mg# map across the Moon (70°N/S).

5.3. Limitations and Prospects

The limited quantity of lunar samples poses an obstacle to compositional modelling. A total of 49 samples were utilized, including the Apollo and Luna missions, CE-3 in situ measurements, and the CE-5 mission, all of which were distributed in the low-latitude regions on the lunar near side, except for the CE-5 samples. Moreover, the small sample size and limited geographic coverage led to limitations in both quantity and spatial distribution, resulting in uncertainties in the prediction results. It is hoped that more samples can be obtained in the future, especially from the lunar far side and high-latitude regions, which is expected to improve the accuracy of the inversion results.

The study of minerals through spectral features, particularly the CF, has a long history in planetary science. Indeed, the CF has demonstrated capability in identifying silicate minerals and estimating lunar surface composition [29,30,52]. However, both space weathering and viewing geometry influence the CF values. Recently, Greenhagen et al. [31] performed terrain-dependent photometric correction to map the latest -normalized-to-equatorial-noon (NEN) CF map. Meanwhile, Lucey et al. [32] corrected the effects of space weathering to generate a new surface optical maturity parameter (OMAT) CF map. With the advancement of remote sensing technology, exploring new methods to mitigate the effects of space weathering and viewing geometry can help to reduce the uncertainty of inversion results.

In addition, machine learning and deep learning algorithms can be further applied to lunar oxide inversion. In this paper, the PSO-XGBoost algorithm was used to predict the abundance of oxides with satisfactory results, although there is still space for further improvement.

6. Conclusions

Based on previous lunar samples, this study incorporated samples from the CE-5 mission to produce the new maps of oxide abundance and Mg# on the lunar surface. Except for FeO, the oxide (Al_2O_3, CaO, and MgO) abundances exhibited complex nonlinear relationships with CF values, making the PSO-XGBoost model a better choice for inversion. The higher R^2 values and lower RMSE in this study indicate the satisfactory performance and generalization ability of the models. The distinctive distribution of oxides and Mg# across the three geological units indicate differences in the source of the magma, resulting in mare basalts with different composition. Incorporating data from the Chang'e-5 mission

has supplemented and refined our understanding of the Moon's late-stage magmatic activities, enabling updating of the lunar oxide distribution maps.

Author Contributions: Conceptualization, S.W. and J.C.; methodology, S.W.; software, S.W.; validation, S.W., J.C. and C.X.; formal analysis, S.W.; resources, C.Z. and Y.P.; data curation, S.W., J.C. and C.X.; writing—original draft preparation, S.W.; writing—review and editing, S.W., J.C. and C.X.; visualization, S.W., C.Z. and Y.P.; supervision, S.W. and J.C.; funding acquisition, J.C. All authors have read and agreed to the published version of the manuscript.

Funding: This research was funded by the Geological Survey Project of China Geological Survey, grant number DD20221645.

Data Availability Statement: The corrected CF map was provided by Lucey et al. and is available at https://doi.org/10.5281/zenodo.4558194 (accessed on 23 February 2021).

Conflicts of Interest: The authors declare no conflicts of interest.

References

1. Lucey, P.G.; Taylor, G.J.; Malaret, E. Abundance and Distribution of Iron on the Moon. *Science* **1995**, *268*, 1150–1153. [CrossRef] [PubMed]
2. Otake, H.; Ohtake, M.; Hirata, N. Lunar Iron and Titanium Abundance Algorithms Based on SELENE (KAGUYA) Multiband Imager Data. In Proceedings of the 43rd Annual Lunar and Planetary Science Conference, Woodlands, TX, USA, 19–23 March 2012.
3. Wu, Y. Major Elements and Mg# of the Moon: Results from Chang'E-1 Interference Imaging Spectrometer (IIM) Data. *Geochim. Cosmochim. Acta* **2012**, *93*, 214–234. [CrossRef]
4. Lawrence, D.J.; Feldman, W.C.; Barraclough, B.L.; Binder, A.B.; Elphic, R.C.; Maurice, S.; Miller, M.C.; Prettyman, T.H. Thorium Abundances on the Lunar Surface. *J. Geophys. Res. Planets* **2000**, *105*, 20307–20331. [CrossRef]
5. Lawrence, D.J.; Feldman, W.C.; Barraclough, B.L.; Binder, A.B.; Elphic, R.C.; Maurice, S.; Miller, M.C.; Prettyman, T.H. High Resolution Measurements of Absolute Thorium Abundances on the Lunar Surface. *Geophys. Res. Lett.* **1999**, *26*, 2681–2684. [CrossRef]
6. Lawrence, D.J.; Feldman, W.C.; Barraclough, B.L.; Binder, A.B.; Elphic, R.C.; Maurice, S.; Thomsen, D.R. Global Elemental Maps of the Moon: The Lunar Prospector Gamma-Ray Spectrometer. *Science* **1998**, *281*, 1484–1489. [CrossRef] [PubMed]
7. Prettyman, T.H.; Hagerty, J.J.; Elphic, R.C.; Feldman, W.C.; Lawrence, D.J.; McKinney, G.W.; Vaniman, D.T. Elemental Composition of the Lunar Surface: Analysis of Gamma Ray Spectroscopy Data from Lunar Prospector. *J. Geophys. Res. Planets* **2006**, *111*, E12007. [CrossRef]
8. Elphic, R.C.; Lawrence, D.J.; Feldman, W.C.; Barraclough, B.L.; Gasnault, O.M.; Maurice, S.; Lucey, P.G.; Blewett, D.T.; Binder, A.B. Lunar Prospector Neutron Spectrometer Constraints on TiO_2. *J. Geophys. Res. Planets* **2002**, *107*, 8-1–8-9. [CrossRef]
9. Elphic, R.C.; Lawrence, D.J.; Feldman, W.C.; Barraclough, B.L.; Maurice, S.; Binder, A.B.; Lucey, P.G. Lunar Rare Earth Element Distribution and Ramifications for FeO and TiO_2: Lunar Prospector Neutron Spectrometer Observations. *J. Geophys. Res. Planets* **2000**, *105*, 20333–20345. [CrossRef]
10. Elphic, R.C.; Lawrence, D.J.; Feldman, W.C.; Barraclough, B.L.; Maurice, S.; Binder, A.B.; Lucey, P.G. Lunar Fe and Ti Abundances: Comparison of Lunar Prospector and Clementine Data. *Science* **1998**, *281*, 1493–1496. [CrossRef]
11. Feldman, W.C.; Lawrence, D.J.; Elphic, R.C.; Vaniman, D.T.; Thomsen, D.R.; Barraclough, B.L.; Maurice, S.; Binder, A.B. Chemical Information Content of Lunar Thermal and Epithermal Neutrons. *J. Geophys. Res. Planets* **2000**, *105*, 20347–20363. [CrossRef]
12. Feldman, W.C.; Barraclough, B.L.; Maurice, S.; Elphic, R.C.; Lawrence, D.J.; Thomsen, D.R.; Binder, A.B. Major Compositional Units of the Moon: Lunar Prospector Thermal and Fast Neutrons. *Science* **1998**, *281*, 1489–1493. [CrossRef] [PubMed]
13. Gillis, J.J.; Jolliff, B.L.; Korotev, R.L. Lunar Surface Geochemistry: Global Concentrations of Th, K, and FeO as Derived from Lunar Prospector and Clementine Data. *Geochim. Cosmochim. Acta* **2004**, *68*, 3791–3805. [CrossRef]
14. Gillis, J.J.; Jolliff, B.L.; Elphic, R.C. A Revised Algorithm for Calculating TiO_2 from Clementine UVVIS Data: A Synthesis of Rock, Soil, and Remotely Sensed TiO_2 Concentrations. *J. Geophys. Res. Planets* **2003**, *108*, 5009. [CrossRef]
15. Lucey, P.G.; Blewett, D.T.; Jolliff, B.L. Lunar Iron and Titanium Abundance Algorithms Based on Final Processing of Clementine Ultraviolet-Visible Images. *J. Geophys. Res.* **2000**, *105*, 20297–20305. [CrossRef]
16. Sato, H.; Robinson, M.S.; Lawrence, S.J.; Denevi, B.W.; Hapke, B.; Jolliff, B.L.; Hiesinger, H. Lunar Mare TiO_2 Abundances Estimated from UV/Vis Reflectance. *Icarus* **2017**, *296*, 216–238. [CrossRef]
17. Lemelin, M.; Lucey, P.G.; Song, E.; Taylor, G.J. Lunar Central Peak Mineralogy and Iron Content Using the Kaguya Multiband Imager: Reassessment of the Compositional Structure of the Lunar Crust: LUNAR CENTRAL PEAK MINERALOGY AND IRON. *J. Geophys. Res. Planets* **2015**, *120*, 869–887. [CrossRef]
18. Qiu, D.; Li, F.; Yan, J.; Gao, W.; Chong, Z. Machine Learning for Inversing FeO and TiO_2 Content on the Moon: Method and Comparison. *Icarus* **2022**, *373*, 114778. [CrossRef]

19. Yang, C.; Zhang, X.; Bruzzone, L.; Liu, B.; Liu, D.; Ren, X.; Benediktsson, J.A.; Liang, Y.; Yang, B.; Yin, M.; et al. Comprehensive Mapping of Lunar Surface Chemistry by Adding Chang'e-5 Samples with Deep Learning. *Nat. Commun.* **2023**, *14*, 7554. [CrossRef] [PubMed]
20. Zhang, L.; Zhang, X.; Yang, M.; Xiao, X.; Qiu, D.; Yan, J.; Xiao, L.; Huang, J. New Maps of Major Oxides and Mg # of the Lunar Surface from Additional Geochemical Data of Chang'E-5 Samples and KAGUYA Multiband Imager Data. *Icarus* **2023**, *397*, 115505. [CrossRef]
21. Sun, L.; Ling, Z.; Zhang, J.; Li, B.; Chen, J.; Wu, Z.; Liu, J. Lunar Iron and Optical Maturity Mapping: Results from Partial Least Squares Modeling of Chang'E-1 IIM Data. *Icarus* **2016**, *280*, 183–198. [CrossRef]
22. Wu, S.; Chen, J.; Li, L.; Zhang, C.; Huang, R.; Zhang, Q. Quantitative Inversion of Lunar Surface Chemistry Based on Hyperspectral Feature Bands and Extremely Randomized Trees Algorithm. *Remote Sens.* **2022**, *14*, 5248. [CrossRef]
23. Xia, W.; Wang, X.; Zhao, S.; Jin, H.; Chen, X.; Yang, M.; Wu, X.; Hu, C.; Zhang, Y.; Shi, Y.; et al. New Maps of Lunar Surface Chemistry. *Icarus* **2019**, *321*, 200–215. [CrossRef]
24. Yan, B.; Xiong, S.Q.; Wu, Y.; Wang, Z.; Dong, L.; Gan, F.; Yang, S.; Wang, R. Mapping Lunar Global Chemical Composition from Chang'E-1 IIM Data. *Planet. Space Sci.* **2012**, *67*, 119–129. [CrossRef]
25. Burns, R.G. *Mineralogical Applications of Crystal Field Theory*, 2nd ed.; Cambridge University Press: Cambridge, UK, 1993; ISBN 978-0-521-43077-7.
26. Jaumann, R. Spectral-Chemical Analysis of Lunar Surface Materials. *J. Geophys. Res. Planets* **1991**, *96*, 22793–22807. [CrossRef]
27. Pieters, C. Statistical Analysis of the Links among Lunar Mare Soil Mineralogy, Chemistry, and Reflectance Spectra. *Icarus* **2002**, *155*, 285–298. [CrossRef]
28. Ma, M.; Li, B.; Chen, S.; Lu, T.; Lu, P.; Lu, Y.; Jin, Q. Global Estimates of Lunar Surface Chemistry Derived from LRO Diviner Data. *Icarus* **2022**, *371*, 114697. [CrossRef]
29. Allen, C.C.; Greenhagen, B.T.; Donaldson Hanna, K.L.; Paige, D.A. Analysis of Lunar Pyroclastic Deposit FeO Abundances by LRO Diviner. *J. Geophys. Res. Planets* **2012**, *117*, E00H28. [CrossRef]
30. Donaldson Hanna, K.L.; Greenhagen, B.T.; Patterson, W.R.; Pieters, C.M.; Mustard, J.F.; Bowles, N.E.; Paige, D.A.; Glotch, T.D.; Thompson, C. Effects of Varying Environmental Conditions on Emissivity Spectra of Bulk Lunar Soils: Application to Diviner Thermal Infrared Observations of the Moon. *Icarus* **2017**, *283*, 326–342. [CrossRef]
31. Greenhagen, B.T.; Lucey, P.G.; Wyatt, M.B.; Glotch, T.D.; Allen, C.C.; Arnold, J.A.; Bandfield, J.L.; Bowles, N.E.; Hanna, K.L.D.; Hayne, P.O.; et al. Global Silicate Mineralogy of the Moon from the Diviner Lunar Radiometer. *Science* **2010**, *329*, 1507–1509. [CrossRef]
32. Lucey, P.G.; Greenhagen, B.; Donaldson Hanna, K.; Bowles, N.; Flom, A.; Paige, D.A. Christiansen Feature Map From the Lunar Reconnaissance Orbiter Diviner Lunar Radiometer Experiment: Improved Corrections and Derived Mineralogy. *J. Geophys. Res. Planets* **2021**, *126*, e2020JE006777. [CrossRef]
33. Lucey, P.G.; Greenhagen, B.T.; Song, E.; Arnold, J.A.; Lemelin, M.; Hanna, K.D.; Bowles, N.E.; Glotch, T.D.; Paige, D.A. Space Weathering Effects in Diviner Lunar Radiometer Multispectral Infrared Measurements of the Lunar Christiansen Feature: Characteristics and Mitigation. *Icarus* **2017**, *283*, 343–351. [CrossRef]
34. Bian, C.; Zhang, K.; Wu, Y.; Wu, S.; Lu, Y.; Shi, H.; Li, H.; Zhao, D.; Duan, Y.; Zhao, L.; et al. Mapping the Spatial Distributions of Oxide Abundances and Mg# on the Lunar Surface Using Multi-Source Data and a New Ensemble Learning Algorithm. *Planet. Space Sci.* **2024**, *245*, 105894. [CrossRef]
35. Conel, J.E. Infrared Emissivities of Silicates: Experimental Results and a Cloudy Atmosphere Model of Spectral Emission from Condensed Particulate Mediums. *J. Geophys. Res.* **1969**, *74*, 1614–1634. [CrossRef]
36. Kusuma, K.N.; Sebastian, N.; Murty, S.V.S. Geochemical and Mineralogical Analysis of Gruithuisen Region on Moon Using M3 and DIVINER Images. *Planet. Space Sci.* **2012**, *67*, 46–56. [CrossRef]
37. Logan, L.M.; Hunt, G.R.; Salisbury, J.W.; Balsamo, S.R. Compositional Implications of Christiansen Frequency Maximums for Infrared Remote Sensing Applications. *J. Geophys. Res.* **1973**, *78*, 4983–5003. [CrossRef]
38. Salisbury, J.W.; Hunt, G.R.; Logan, L.M. Infrared Spectra of Apollo 16 Fines. *Lunar Planet. Sci. Conf. Proc.* **1973**, *4*, 3191.
39. Nyquist, L.E.; Bogard, D.D.; Chi-Yu, S. Radiometric Chronology of the Moon and Mars. In *The Century of Space Science*; Bleeker, J.A.M., Geiss, J., Huber, M.C.E., Eds.; Springer: Dordrecht, The Netherlands, 2001; pp. 1325–1376. ISBN 978-94-010-0320-9.
40. Taylor, L.A.; Shervais, J.W.; Hunter, R.H.; Shih, C.-Y.; Bansal, B.M.; Wooden, J.; Nyquist, L.E.; Laul, L.C. Pre-4.2 AE Mare-Basalt Volcanism in the Lunar Highlands. *Earth Planet. Sci. Lett.* **1983**, *66*, 33–47. [CrossRef]
41. Che, X.; Nemchin, A.; Liu, D.; Long, T.; Wang, C.; Norman, M.D.; Joy, K.H.; Tartese, R.; Head, J.; Jolliff, B.; et al. Age and Composition of Young Basalts on the Moon, Measured from Samples Returned by Chang'e-5. *Science* **2021**, *374*, 887–890. [CrossRef] [PubMed]
42. Li, Q.-L.; Zhou, Q.; Liu, Y.; Xiao, Z.; Lin, Y.; Li, J.-H.; Ma, H.-X.; Tang, G.-Q.; Guo, S.; Tang, X.; et al. Two-Billion-Year-Old Volcanism on the Moon from Chang'e-5 Basalts. *Nature* **2021**, *600*, 54–58. [CrossRef]
43. Qian, Y.; She, Z.; He, Q.; Xiao, L.; Wang, Z.; Head, J.W.; Sun, L.; Wang, Y.; Wu, B.; Wu, X.; et al. Mineralogy and Chronology of the Young Mare Volcanism in the Procellarum-KREEP-Terrane. *Nat. Astron.* **2023**, *7*, 287–297. [CrossRef]
44. Chen, T.; Guestrin, C. XGBoost: A Scalable Tree Boosting System. In Proceedings of the 22nd ACM SIGKDD International Conference on Knowledge Discovery and Data Mining, San Francisco, CA, USA, 13–17 August 2016; Association for Computing Machinery: New York, NY, USA, 2016; pp. 785–794.

45. Khan, R.M.; Salehi, B.; Niroumand-Jadidi, M.; Mahdianpari, M. Mapping Water Clarity in Small Oligotrophic Lakes Using Sentinel-2 Imagery and Machine Learning Methods: A Case Study of Canandaigua Lake in Finger Lakes, New York. *IEEE J. Sel. Top. Appl. Earth Obs. Remote Sens.* **2024**, *17*, 4674–4688. [CrossRef]
46. Zhao, X.; Xia, N.; Xu, Y.; Huang, X.; Li, M. Mapping Population Distribution Based on XGBoost Using Multisource Data. *IEEE J. Sel. Top. Appl. Earth Obs. Remote Sens.* **2021**, *14*, 11567–11580. [CrossRef]
47. Zhang, Q.; Chen, J.; Xu, H.; Jia, Y.; Chen, X.; Jia, Z.; Liu, H. Three-Dimensional Mineral Prospectivity Mapping by XGBoost Modeling: A Case Study of the Lannigou Gold Deposit, China. *Nat. Resour. Res.* **2022**, *31*, 1135–1156. [CrossRef]
48. Ashourloo, D.; Aghighi, H.; Matkan, A.A.; Mobasheri, M.R.; Rad, A.M. An Investigation Into Machine Learning Regression Techniques for the Leaf Rust Disease Detection Using Hyperspectral Measurement. *IEEE J. Sel. Top. Appl. Earth Obs. Remote Sens.* **2016**, *9*, 4344–4351. [CrossRef]
49. Vohland, M.; Harbich, M.; Ludwig, M.; Emmerling, C.; Thiele-Bruhn, S. Quantification of Soil Variables in a Heterogeneous Soil Region With VIS–NIR–SWIR Data Using Different Statistical Sampling and Modeling Strategies. *IEEE J. Sel. Top. Appl. Earth Obs. Remote Sens.* **2016**, *9*, 4011–4021. [CrossRef]
50. Zhang, Y.; Liang, S.; Sun, G. Forest Biomass Mapping of Northeastern China Using GLAS and MODIS Data. *IEEE J. Sel. Top. Appl. Earth Obs. Remote Sens.* **2014**, *7*, 140–152. [CrossRef]
51. Lyon, R.J.P. Analysis of Rocks by Spectral Infrared Emission (8 to 25 Microns). *Econ. Geol.* **1965**, *60*, 715–736. [CrossRef]
52. Paige, D.A.; Foote, M.C.; Greenhagen, B.T.; Schofield, J.T.; Calcutt, S.; Vasavada, A.R.; Preston, D.J.; Taylor, F.W.; Allen, C.C.; Snook, K.J.; et al. The Lunar Reconnaissance Orbiter Diviner Lunar Radiometer Experiment. *Space Sci. Rev.* **2010**, *150*, 125–160. [CrossRef]
53. Williams, J.-P.; Paige, D.A.; Greenhagen, B.T.; Sefton-Nash, E. The Global Surface Temperatures of the Moon as Measured by the Diviner Lunar Radiometer Experiment. *Icarus* **2017**, *283*, 300–325. [CrossRef]
54. Liu, B.; Rostamian, A.; Kheirollahi, M.; Mirseyed, S.F.; Mohammadian, E.; Golsanami, N.; Liu, K.; Ostadhassan, M. NMR Log Response Prediction from Conventional Petrophysical Logs with XGBoost-PSO Framework. *Geoenergy Sci. Eng.* **2023**, *224*, 211561. [CrossRef]
55. Chen, M.; Liu, Q.-Y.; Chen, S.; Liu, Y.; Zhang, C.; Liu, R. XGBoost-Based Algorithm Interpretation and Application on Post-Fault Transient Stability Status Prediction of Power System. *IEEE Access* **2019**, *7*, 13149–13158. [CrossRef]
56. Osman, A.A.A.; Ahmed, A.N.; Chow, M.F.; Huang, Y.F.; El-Shafie, A. Extreme Gradient Boosting (Xgboost) Model to Predict the Groundwater Levels in Selangor Malaysia. *Ain Shams Eng. J.* **2021**, *12*, 1545–1556. [CrossRef]
57. Kennedy, J.; Eberhart, R. Particle Swarm Optimization. In Proceedings of the ICNN'95—International Conference on Neural Networks, Perth, WA, Australia, 27 November–1 December 1995; Volume 4, pp. 1942–1948.
58. Zhu, H.; Wang, Y.; Wang, K.; Chen, Y. Particle Swarm Optimization (PSO) for the Constrained Portfolio Optimization Problem. *Expert Syst. Appl.* **2011**, *38*, 10161–10169. [CrossRef]
59. Wang, X.; Zhang, J.; Ren, H. Lunar Surface Chemistry Observed by the KAGUYA Multiband Imager. *Planet. Space Sci.* **2021**, *209*, 105360. [CrossRef]
60. Dhanarajan, G.; Mandal, M.; Sen, R. A Combined Artificial Neural Network Modeling–Particle Swarm Optimization Strategy for Improved Production of Marine Bacterial Lipopeptide from Food Waste. *Biochem. Eng. J.* **2014**, *84*, 59–65. [CrossRef]
61. de Jong, S. SIMPLS: An Alternative Approach to Partial Least Squares Regression. *Chemom. Intell. Lab. Syst.* **1993**, *18*, 251–263. [CrossRef]
62. Li, L. Partial Least Squares Modeling to Quantify Lunar Soil Composition with Hyperspectral Reflectance Measurements. *J. Geophys. Res.* **2006**, *111*, E04002. [CrossRef]
63. Morota, T.; Haruyama, J.; Ohtake, M.; Matsunaga, T.; Honda, C.; Yokota, Y.; Kimura, J.; Ogawa, Y.; Hirata, N.; Demura, H.; et al. Timing and Characteristics of the Latest Mare Eruption on the Moon. *Earth Planet. Sci. Lett.* **2011**, *302*, 255–266. [CrossRef]
64. Green, D.H. Experimental Testing of "Equilibrium" Partial Melting of Peridotite under Water-Saturated, High-Pressure Conditions. *Can. Mineral.* **1976**, *14*, 255–268.

Disclaimer/Publisher's Note: The statements, opinions and data contained in all publications are solely those of the individual author(s) and contributor(s) and not of MDPI and/or the editor(s). MDPI and/or the editor(s) disclaim responsibility for any injury to people or property resulting from any ideas, methods, instructions or products referred to in the content.

remote sensing

MDPI

Article

Study on the Degradation Pattern of Impact Crater Populations in Yutu-2′s Rovering Area

Xinyu Ma [1], Meixi Chen [1], Teng Hu [1,2,*], Zhizhong Kang [1,2] and Meng Xiao [1]

[1] School of Land Science and Technology, China University of Geosciences, Beijing 100083, China; 1012214108@email.cugb.edu.cn (X.M.); 1012214109@email.cugb.edu.cn (M.C.); zzkang@cugb.edu.cn (Z.K.); 2012210008@email.cugb.edu.cn (M.X.)

[2] Subcenter of International Cooperation and Research on Lunar and Planetary Exploration, Center of Space Exploration, Ministry of Education of the People's Republic of China, Beijing 100083, China

* Correspondence: huteng@cugb.edu.cn

Abstract: A detailed analysis of the panoramic camera data from the 27th to 33rd lunar days was conducted on the high-resolution scenes captured by the Yutu-2 rover stations. This analysis aimed to determine the detailed morphological parameters of the 2015 impact craters within the inspection area. The levels of degradation observed in the impact craters were determined alongside the surface features. Subsequently, the degradation patterns of the impact craters located within the Yutu-2's roving area and the distribution patterns of the morphological parameters were analysed and investigated. The results of the analysis indicate that 94% of the impact craters exhibited severe degradation, 80% had depth-to-diameter ratios (DDRs) ranging from 0.07 to 0.17, and the remaining craters were moderately degraded. The DDRs of the impact craters exhibited a declining trend with an increase in the dimensions of the impact craters. Additionally, the degree of degradation of impact crater populations demonstrated a decreasing trend. In general, the impact craters along the rover's route exhibited severe degradation, with the population of degradation degrees gradually decreasing with increasing diameter.

Keywords: Yutu-2; rover images; impact craters; crater degradation patterns; the Moon

1. Introduction

Yutu-2 travelled to the Von Karman impact crater in the South Pole-Aitken Basin at the lunar south pole and has been used for lunar surface roving [1–3]. The paucity of sub-metre-scale impact crater data and related studies is a consequence of the resolution of orbiter images, which is limited to 0.5 m/pixel. The panoramic camera on the Yutu-2 rover, with the detection advantage of in situ close-range observation, provides valuable technical data for extracting the morphological parameters of sub-metre-scale impact craters, analysing the three-dimensional scene, and examining the pattern of the group's morphological characteristics [4]. The images record impact craters, with diameters ranging from sub-metre to metre, providing a data basis for studying the formation, degradation, and flux of sub-metre-scale impact craters. They are also significant for revealing the population patterns of these impact events on the lunar surface.

The degradation state of impact craters directly characterizes the age of their formation. Consequently, the morphology of impact craters changes over time, and it is indicative of the evolution and age of the lunar surface stratigraphy [5,6]. Morphology/age relationship analysis is the main research method used by most scholars to study the degradation pattern of impact craters based on morphological features. For example, Craddock (1972) and Haruyama et al. (2004) studied the degradation process of impact craters and described the relative age of geological units via the degradation parameter [7,8]; Wood (1977) and Ivanov et al. (2002) classified the degradation grade through the morphology of impact craters [9,10], and Craddock (1972) established a degradation model

and estimated the degradation and erosion rate of impact craters using the Clementine data [7]. Research on the saturation equilibrium state of the impact crater density is ongoing. Hartman (1997) and James (2009) studied the equilibrium state of the impact crater distribution using computer modelling methods [11,12]. Li Kun (2013) employed the data on impact craters in the typical Moon Sea area to investigate the morphology of the impact craters. He began by examining the degradation of the impact craters and then proceeded to identify the impact crater depth as a parameter for determining the degradation. The relationship between the production and chronological functions of the impact craters was employed to derive the time-series curves of ascending readings of impact crater size and establish the degradation model [13]. Previous studies have demonstrated that for impact craters of a similar size, the older the formation age is, the more apparent the degradation phenomenon is, and the smaller the scale of the impact crater is, the greater the probability of its disappearance is due to the effects of degradation.

Statistical studies on the morphology of degradation grades and other related features are of significant importance in order to gain an understanding of the correlation between the morphological evolution of impact craters and the age of the corresponding lunar surface in that region. The current methods for grading the degradation of impact craters are predominantly based on visual interpretation. In 1963, Arthur proposed four degradation types for the moon. The classification system proposed by Arthur comprises four classes, designated C1, C2, C3, and C4. C1 refers to fresh impact craters; C2 to initially degraded impact craters; C3 to impact craters with a severely eroded morphology; and C4 to completely flattened impact craters [14]. The studies by Mcgill and Wise (1972) and Basilevsky et al. (1976) proposed five degradation types for the moon. These were classified into three main classes—A, B, and C—and two transitional classes—AB and BC. The classes A, B, and C are used to indicate the following: Class A indicates a fresh impact crater, Class B indicates an initially degraded impact crater (with a smooth rim), and Class C indicates a completely flattened impact crater [15,16]. In order to study the morphological grading of impact craters, Yao Meijuan et al. (2016) employed the optimal grading method which involved the optimal division of diameters, resulting in 10 grades [17]. Overall, the statistics analysis of features related to the degradation level of impact craters is primarily based on orbiter image data with a limited image resolution. Furthermore, the dimensions of the extracted and analysed impact craters are relatively considerable, which makes it challenging to obtain the availability of in situ validation data on the lunar surface.

Given the characteristics of Yutu-2's data, we employed the rover's image data to construct a high-resolution three-dimensional scene of the roving area and generated a digital elevation model (DEM) and digital orthophoto model (DOM). Subsequently, the impact craters were manually extracted and identified all the impact craters in the images using the automatic extraction method for the impact craters' morphological parameters. This resulted in the accurate determination of the depth, diameter, and other morphological parameters for the identified impact craters. The degradation levels were classified according to the texture characteristics of the impact craters, and the degradation patterns of the impact crater groups in the patrol area and the distribution patterns of the morphological parameters were studied and analysed.

Section 2 presents the experimental data and data processing methods employed in this study. Section 3 presents the results of the manual identification of the impact craters along the rover's route and analyses their degradation. Section 4 presents a discussion and analysis of the degradation and degradation patterns of the population of small impact craters in the roving area, with a comparison to the existing data on the impact craters along the rover's route and the data on Chang'e-4's landing area.

2. Data and Methodology

2.1. Data

We used the DEM and DOM images produced by Yutu-2's panoramic camera [18] as the image data and assigned geo-referenced coordinates (GCS_Moon_2000). The resolu-

tions of DEM and DOM images are variable, with a resolution of 0.0011 m at close range and 0.004 m at longer range. The panoramic camera is equipped with two imaging modes: colour imaging and panchromatic imaging. These modes can be switched between the two modes during the shooting process. The image resolutions of the colour mode and the panchromatic imaging mode are 2352 × 1728 pixels and 1176 × 864 pixels, respectively. The camera's field-of-view angle is 19.6° × 14.5° [19]. The panoramic camera is designed to capture 360° images around the station by utilising the mast's up-down and left-right rotation. A total of 56 images can be captured in each turn, including 28 pairs of images in different directions at two altitude angles. Figure 1 displays a section of imagery captured by a panoramic camera. This enables the three-dimensional stereo imaging of the topography and landscape of the landing and roving areas [20]. Consequently, the panoramic camera on Yutu-2 can achieve clear imaging from the foot of the rover to the farthest point in the field of view, with a spatial resolution can reach the millimetre scale during close observation. As of 20 September 2023, the Chang'e-4 mission has completed its 62nd lunar day. The study utilised data from the panoramic camera images captured between the 27th and 33rd days of the lunar days.

2.2. Methodology

The panoramic camera images captured by Yutu-2 were processed to obtain the DEM and DOM images. Impact craters were then manually extracted from the images using algorithms to correct the centre of the extracted impact craters and extract the required morphological parameters. Subsequently, the degradation grades were classified in conjunction with the spatial morphology of the impact craters. Finally, the degradation grades and the corresponding morphological parameters of the craters were employed to conduct a study of the degradation patterns of the impact craters and the distribution patterns of the morphological parameters on the backside of the moon. The research method is illustrated in Figure 2.

2.2.1. Image Processing

The panoramic camera images were subjected to three processing stages. Firstly, the images were classified according to the time of shooting and divided into 10 stations, each including 122 image data. The images from each station were imported into the MetashapePro 1.7.4 software (https://www.agisoft.com/zh-cn/downloads/installer/, accessed on 21 March 2023) for processing. This involved camera calibration, scale scaling, and other procedures, resulting in the creation of a dense point cloud. The focal length and pixel size of panchromatic camera were 50.29 mm and 0.0148 mm, respectively, while those of the colour camera were 50.274 mm and 0.0074 mm. Both colour and panchromatic images were employed in the reconstruction of three-dimensional scenes and the generation of digital elevation models and digital orthophoto models. The scale scaling was calibrated based on the standard of Yutu-2's track, which was determined to be 15 cm. Finally, a grid image using the dense point cloud was generated to produce the DEM and DOM images, and the 3D model and corresponding texture were obtained simultaneously.

2.2.2. Impact Crater Identification

Impact craters have depressed circular features, so they are identified based by the contrast between light and dark features under lighting conditions. In this study, the impact craters in the generated DOM and DEM images were identified and marked using the CraterTools software (https://www.geo.fu-berlin.de/en/geol/fachrichtungen/planet/software/index.html, accessed on 2 June 2023).

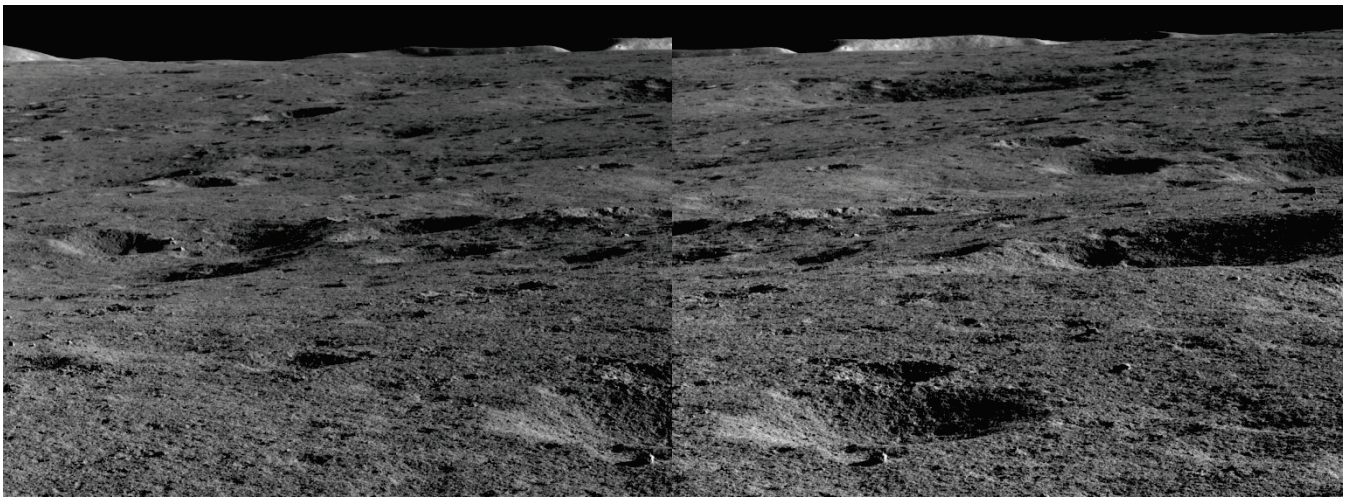


Figure 1. Parts of an original panoramic camera image.

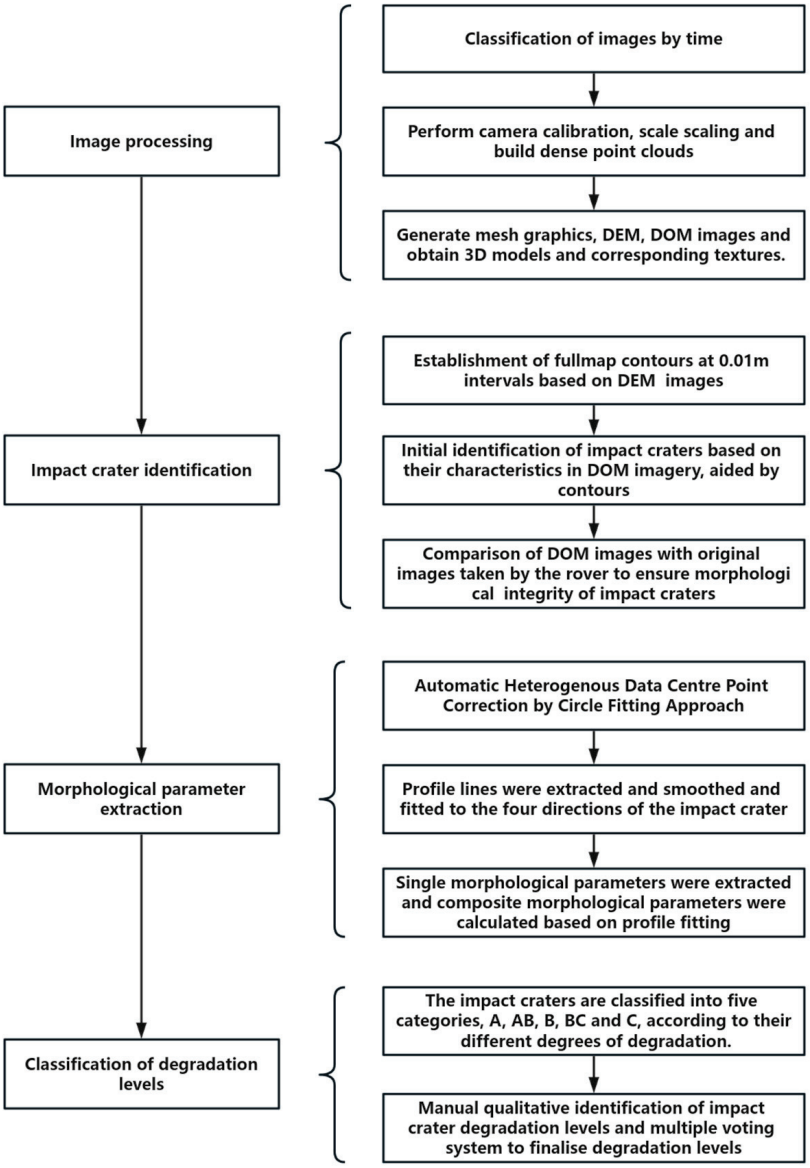
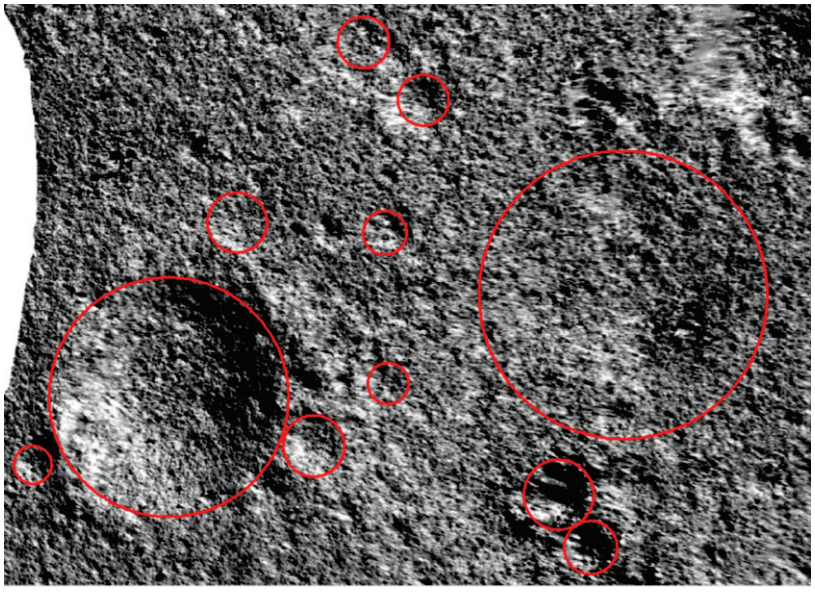
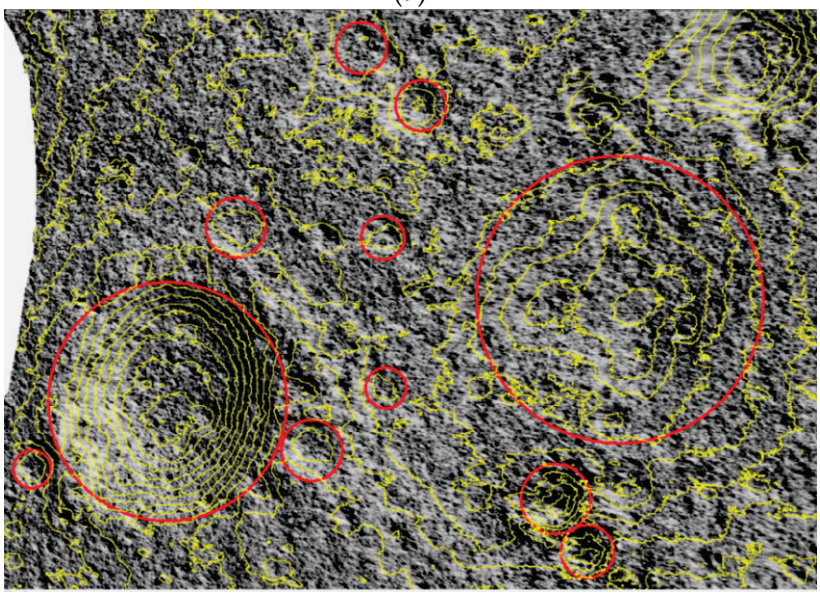


Figure 2. Step diagram of data processing.

We adopted a multi-source determination method in the identification process, as shown in Figure 3. Figure 3a shows the identification of impact craters in the DOM images based on the depressed circular and light–dark contrast features. Due to the limited field of view of the panoramic camera, some impact craters were not photographed all the way to the bottom. These incomplete craters were discarded in the identification process. The metre-scale impact craters were generally small-sized with shallow depths, resulting in a lack of obvious light–dark contrast, which cannot be quickly identified from the DOM images alone. To solve this problem, we created full map contours based on the DEM images to assist in the impact crater identification with the DOM images (with 0.01 m contour intervals). Figure 3b shows the impact craters identified based on the contours. The integrity of the fit in the centre of the impact crater cannot be clearly seen due to the impact of the resolution of the DOM image. Therefore, when identifying the impact craters, the DOM image was compared with the original rover image to ensure that the impact crater's morphology was complete. Figure 3c shows the original rover image of the rover corresponding to Figure 3a.



(**a**)



(**b**)

Figure 3. *Cont.*



(**c**)

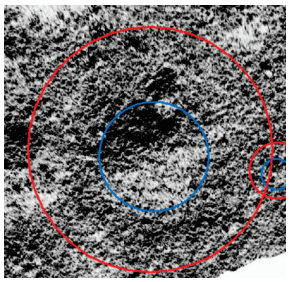
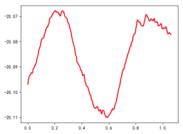
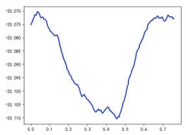
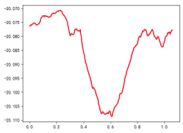
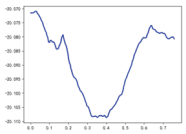
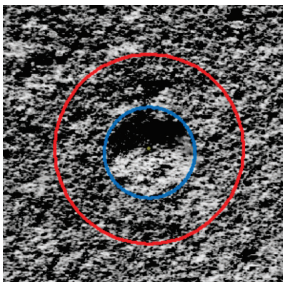
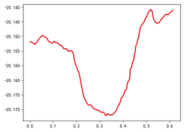
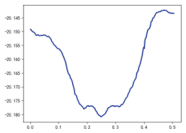
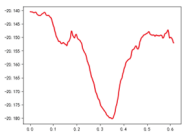
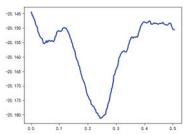
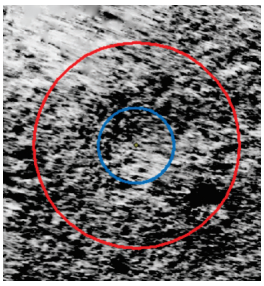
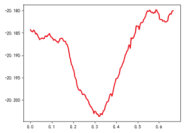
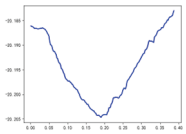
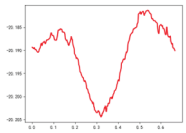
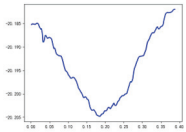
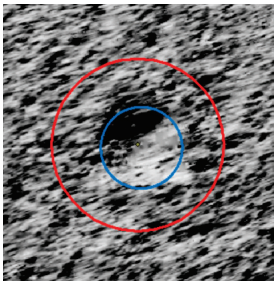
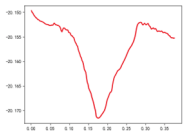
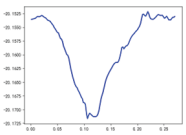
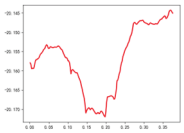
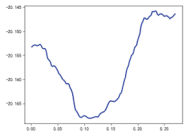
Figure 3. Impact crater identification method. (**a**) Impact crater marking with DOM as base map. (**b**) Contour-assisted recognition with DOM as base map. (**c**) Visual comparison of the original images of the rover. The red circle in the figure shows the approximate location of the impact crater, and the yellow line shows the contour lines.

2.2.3. Morphological Parameter Extraction

Since contours or elevation differences are not easily identifiable, it is possible to use an algorithm accurately calculate the peak locations to find the exact edges of impact craters and fit them to the actual centre. Therefore, after roughly extracting these impact craters, we used an algorithm to centre correct the extracted impact craters to find the correct location and extent of the impact craters, and based on this, we extracted the morphological parameters.

We used an automatic extraction algorithm to extract polymorphic parameters of the impact craters. The algorithm first corrected the offset problem of the centre point offset problem via circle fitting, so that the offset centre point was closer to the actual centre position of the impact crater. The aim of the algorithm was to automatically correct the centre point of the impact crater data from heterogeneous sources, to resolve the coordinate bias between these data, and to improve the data quality. A comparison of the results before and after the centre correction is shown in Table 1. The least squares algorithm was used to fit high order polynomials to the profile lines in the four directions of the impact craters. The higher order polynomial functions of the profile lines with a better fit were obtained to generate the fitted profile lines and polynomial models to describe the morphology of the impact crater profiles based on the mathematical and theoretical dimensions. Finally, eight morphological descriptors were designed, including individual and composite morphological parameters (including depth, internal and external slope, pit lip width, pit lip height, etc.) and composite morphological parameters (including roundness, the depth-to-diameter ratio, and the body shape ratio). In this paper, we mainly studied morphological parameters such as diameter, depth, and depth-to-diameter ratio, which can reflect the impact craters' shape, size, and evolution of impact craters.

Table 1. Before and after correction of impact crater centres. In the figure, red represents the position and profile line of the impact crater after the central correction, while blue represents the position and profile line before the central correction. In the table, X and Y represent the horizontal and vertical profile lines relative to the impact crater. The extraction process involves four directions, but only two are shown in this table. The horizontal and vertical axes of the profile map are all in meters.

Comparison of Centre Point Correction before and after	Profile Line Aspects	After Centre Point Correction	Before Centre Point Correction
	X		
	Y		
	X		
	Y		
	X		
	Y		
	X		
	Y		

2.2.4. Classification of Degradation Levels

According to McGill and Wise (1972) and Basilevsky et al. (1976) [15,16], impact craters are classified into five classes, namely A, AB, B, BC, and C, according to their different degrees of degradation. Category A indicates the freshest impact craters, while category C indicates the most degraded impact craters. However, while previous studies have focused on craters larger than a few tens of metre in diameter, this study focuses on sub-metre craters. The data used in this study have a higher resolution and show more detailed impact crater morphology than the satellite observations used by previous authors. The impact craters in this study are therefore categorized according to the descriptions of each type in previous studies. Figure 4 shows examples of impact craters with different types

of degradation: the Class A fresh impact craters have obvious bright or clear edges, large impact crater depths, and sharp contrasts between light and dark; the Class AB impact craters are slightly degraded, with more obvious contrasts between light and dark; the Class B impact craters have clear and intact edges, with traces of degradation, and obvious shadows; the Class BC impact craters have incomplete edges, with obvious degradation, and shallow depths with minor differences between light and dark; and the Class C impact craters have very faint and incomplete edges, severe degradation, shallow impact crater depths, and basically no shadows, and circular contours are visible when the image is stretched.

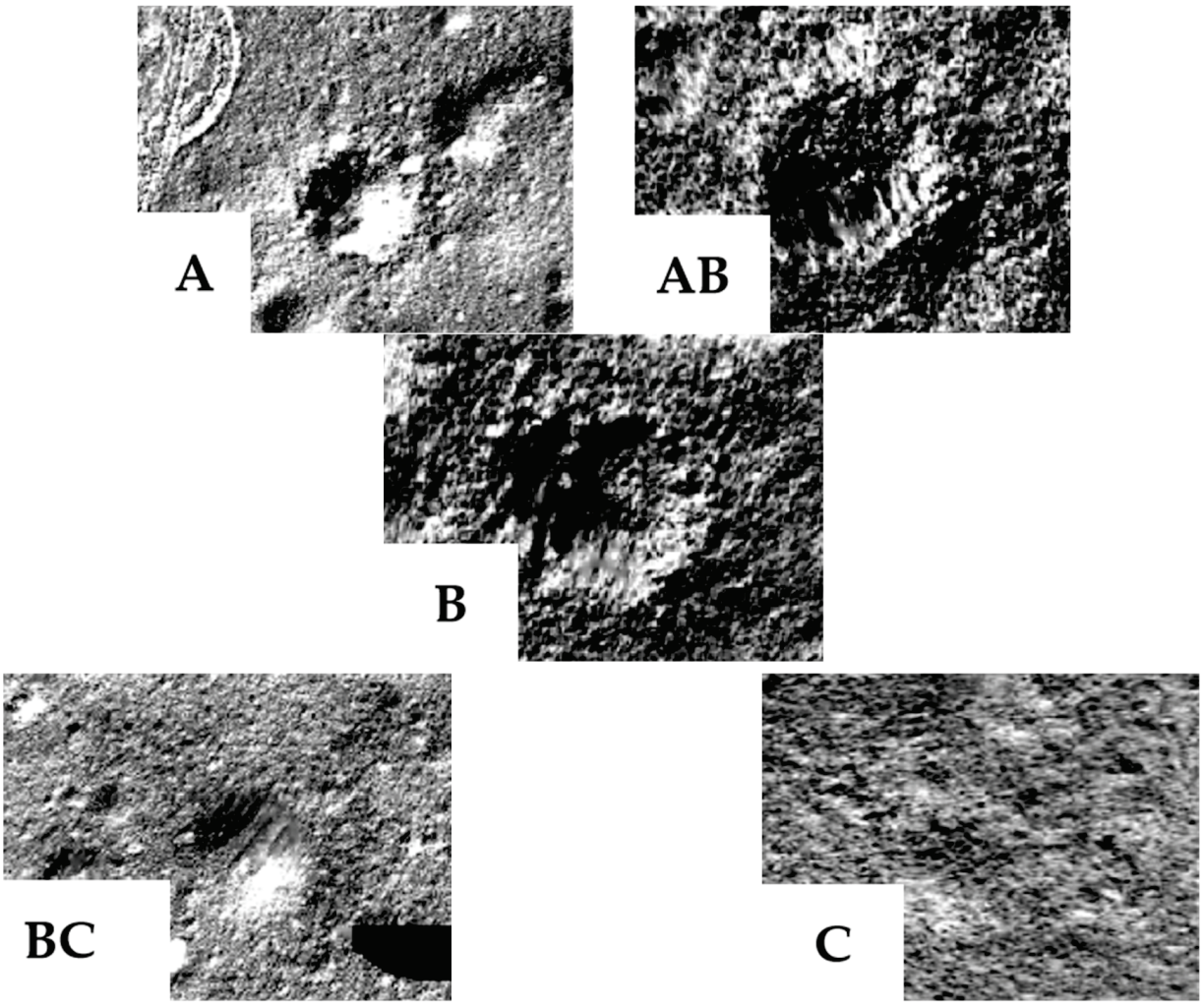


Figure 4. Examples of different types of impact crater degradation. The diagram shows the degradation levels of the impact crater. The levels are marked in the lower left corner.

We used manual qualitative identification of the impact crater degradation classes. Manual qualitative classification usually introduces human subjective factors, so errors in judgement are inevitable. For example, the Class BC impact craters in Figure 4 are similar to Class C impact craters and can be classified. Therefore, a multi-voting procedure was applied to all impact craters, where all impact craters were first assigned degradation classes by three researchers each. The resulting degradation classes of the impact craters were then summarized. If the degradation class of an impact crater was disputed, the three researchers discussed its degradation class based on the DOM image, original images, and other supporting data. In the end, the degradation classes of all impact craters were agreed upon by all, and the classification of impact crater degradation classes was completed.

3. Results

We carried out artificial identification and morphological parameter extraction for the impact craters photographed during the Yutu-2 rover's journey using the research methods described above. We then performed statistics and analysis on the degree of degradation.

3.1. Results of Impact Crater Extraction

We carried out scene reconstructions and generated DEM and DOM images for 10 stations based on Yutu-2's panoramic camera images, as shown in Figure 5. The DEM and DOM images were generated from the foot of the rover to approximately 10 m from the rover. Both the DEM and DOM images resolutions are variable values, with a resolution of 0.0011 m at close range and 0.004 m at longer range. The results demonstrate the high image resolution and high integrity of the impact crater images, which provided a good basis for the study of the impact craters in Yutu-2's orbit.

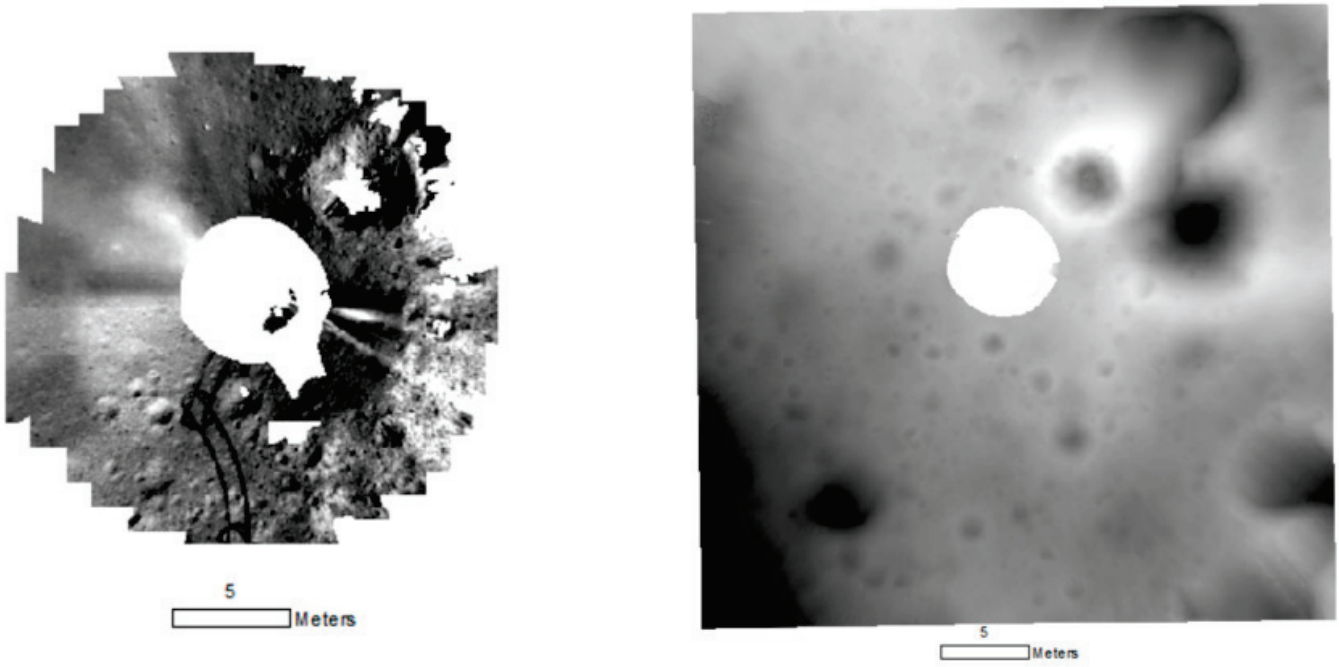


Figure 5. Generated images: (**a**) D0M image; (**b**) DEM image.

In this study, the DOM image of each station served as the basic study area. The specific study area was an annular area with an average outer and inner diameter of 11 m and 3 m, respectively, centred on the rover position. The largest and smallest outer diameters were 16 m and 9 m, respectively, as shown in Figure 6. The distribution of the impact craters in the DOM image is shown in Figure 7, where the impact craters are distributed in a radial pattern around the rover. The further away from the rover, the lower the density of impact craters that could be identified. A small number of complete impact craters were distributed outside the DOM image. The majority of impact craters were small, with the highest concentration near the centre of the rover. The distribution pattern of all the impact craters extracted from the ten stations was found to be consistent with that shown in Figure 7.

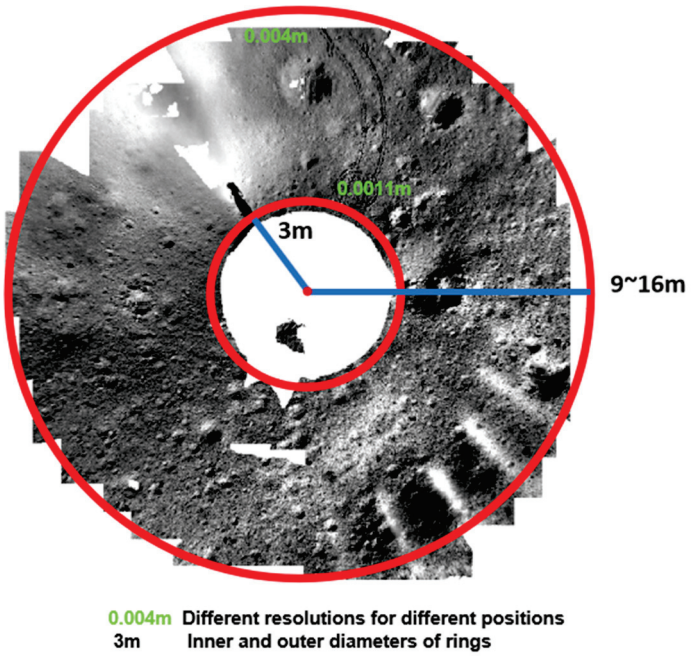


Figure 6. Schematic of DOM image range.The red ring in the figure represents the effective range of the image, and the meanings represented by the other colours are marked in the figure.

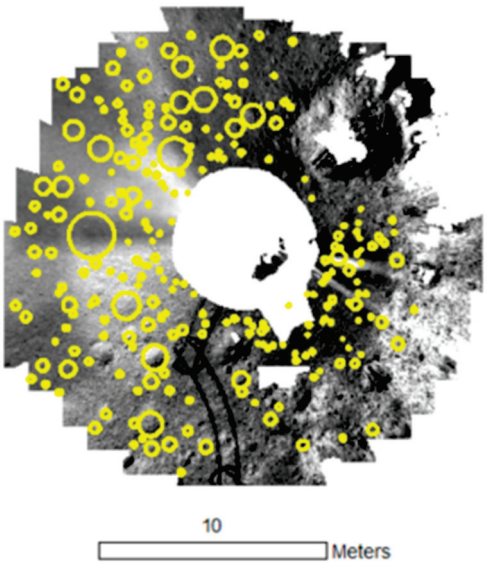


Figure 7. Distribution of impact craters in DOM images. The yellow circles represent the approximate locations of all extractable impact craters at the station in the diagram.

A total of 2110 impact craters were identified based on the DEM and DOM images. Some impact craters were not captured at the bottom due to the angle limitations of the panoramic camera. A comparison was made between the identified impact craters and the original images captured by the panoramic camera. Those the impact craters that were not photographed at the bottom were excluded. A total of 2015 complete impact craters were extracted. This result ensured the completeness of the impact crater data and furnished a robust foundation basis for the subsequent degradation parameter extraction, class classification, and statistical analysis.

The diameters of all impact craters at the ten stations were enumerated. The smallest impact crater diameter was 0.098 m, the largest was 4.077 m, and the mean value was 0.503 m. There were 19 impact craters with diameters greater than 2 m, 151 with diameters

greater than 1 m, and 79 with diameters less than 0.2 m. Figure 8 presents the size–frequency statistics of the impact craters with diameters of less than 2 m. The impact craters with diameters between 0.2 and 0.3 m exhibited the highest frequency, reaching 504, followed by those between 0.3 and 0.4 m, with a frequency of 466. The majority of the impact craters (over 80%) were concentrated in the diameter range of 0.2–0.8 m, with the 0.2–0.5 m range accounting for 64.4%. The data set primarily comprised sub-metre impact craters were extracted. The impact craters were numerous and concentrated in size, with a gradual increase infrequency as their diameters decreased with diameters below 2 m.

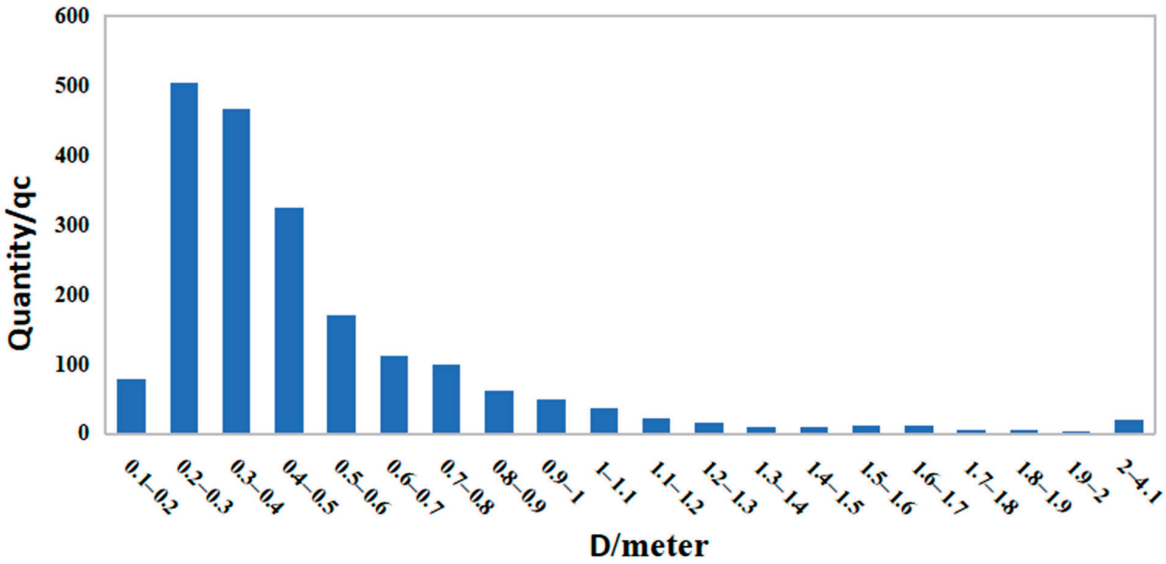


Figure 8. Size–frequency distribution of the impact craters up to 2 m in diameter.

3.2. Results of Morphological Parameter Extraction for Impact Craters

The depth and depth-to-diameter ratio parameters of the impact craters were extracted from the available impact crater information and subjected to statistical analysed.

Figure 9 presents the linear depth–diameter relationship, with a correlation coefficient exceeding 0.7 and high credibility. The depth-to-diameter ratios of the impact craters with a diameter of more than 2 m did not exceed 0.16, while those of impact craters with a diameter of less than 2 m were concentrated in the range of 0.05 to 0.20. The small size of the impact craters resulted in their generally small diameters and depth-to-diameter ratios.

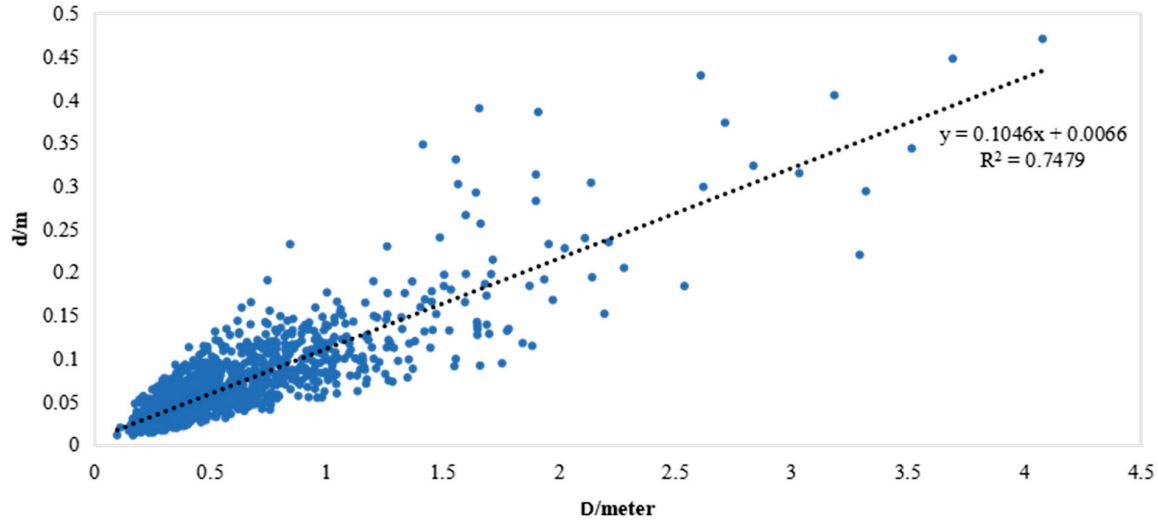


Figure 9. Depth–diameter relationship.

Figure 10 presents the frequency statistics of the depth-to-diameter ratio. The depth-to-diameter ratios of the impact craters exhibited a normal distribution, with values ranging from 0.053 and 0.29, a mean of 0.122, and a variance of approximately 0.039. The depth-to-diameter ratios were found to be concentrated in the range from 0.07 to 0.17, with more than 80% of the data falling within this range. Furthermore, 50% of the impact craters exhibited depth-to-diameter ratios in the range from 0.09 to 0.13.

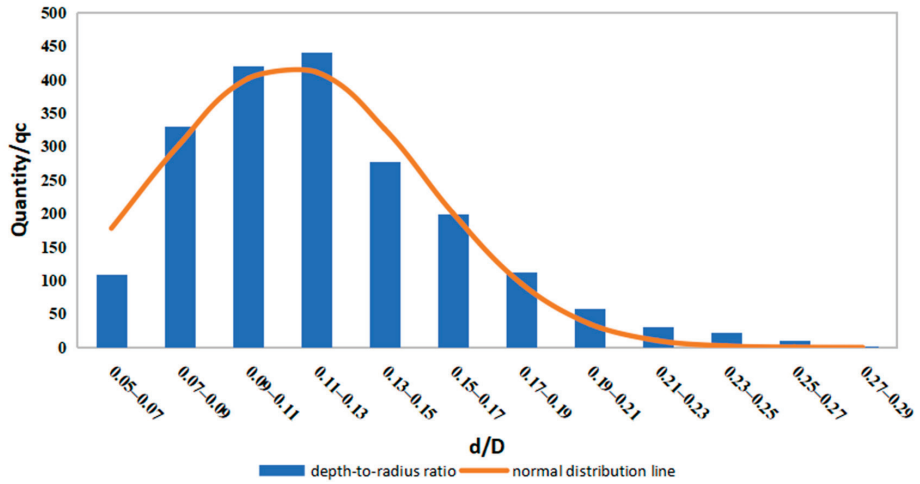


Figure 10. Frequency plot of depth-to-diameter ratios.

The relationship between the diameter and depth of an impact crater is depicted in Figure 11. The impact crater depth–diameter ratio values were distributed across a range of diameter segments from 0.1 to 2 m. The minimum depth–diameter ratio value was close to 0.06. The impact craters with diameters of less than 1 m exhibited a maximum depth–diameter ratio value of greater than 0.25. The maximum difference in the depth–diameter ratios was observed in the diameter range of 0.4 to 0.5 m. The mean value of the depth-to-diameter ratio was 0.22. The median and mean values of the depth–to-diameter ratio demonstrated a general downward trend with increasing diameter, although this decline was not particularly pronounced. The depth-to-diameter ratio values exhibited a notable increase increased at diameters of 1.4–1.5 m and 1.9–2.0 m. This may have been an inadvertent consequence of the limited data on impact craters with diameters of exceeding than 1 m. Overall, there was some variation in the depth-to-diameter ratio with diameter. The depth-to-diameter ratios of the impact craters with diameters below 2 m exhibited a decreasing trend with increasing size, although the degree of decrease was insignificant.



Figure 11. Diameter–depth ratio relationship.

3.3. Results of Impact Crater Degradation Classification

The degradation levels of the 2015 impact craters were obtained following the voting classification of the impact craters. The percentages are shown in Figure 12. There were no Class A and AB impact craters. Meanwhile, there were 1229, 686, and 100 Class C, BC, and B impact craters, accounting for 60%, 34%, and 6%, respectively. This indicates that the extracted impact craters at the 10 stations were mostly Class BC and C, exhibiting morphology that is not readily identifiable and a high degree of degradation.

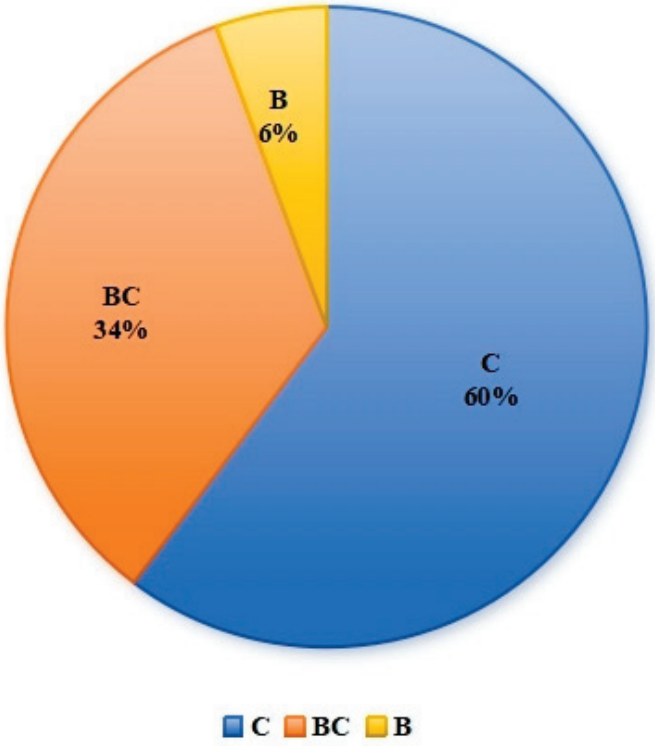


Figure 12. Degradation level classifications as percentages.

The relationship between the diameter of impact craters and their degradation is illustrated in Figure 13. The majority of Class C impact craters exhibited a high percentage (greater than 50%) in the majority of the diameter bands. The median diameters of the Class B, BC and C impact craters were 0.29 m, 0.35 m, and 0.42 m, respectively. The degradation level of the Class B impact craters in the size intervals of 0.1–0.5 m, 0.5–1 m, 1–1.5 m, and 1.5–2 m, varied in ratio from 5.83% to 3.67%, 2.11%, and 0%; that of Class BC impact craters varied from 37.32% to 26.88%, 32.63%, and 21.62%; and that of Class C impact craters changed from 56.85% to 69.45%, 65.26%, and 78.38%. The statistical analysis indicates show that the degradation of the small impact crater group was significant, with the majority impact craters formed by the impact of small objects on the lunar surface. The limited energy of these impacts prevented the occurrence of a violent melting process in the material, which, in turn, limited the size of the formed craters. In addition, the material strength of the walls of these craters was lower than that of large craters, making them susceptible to degradation. However, the presence of impact craters with diameters less than 1 m diameter with Class B degradation indicated that the small impact craters had both severely and moderately degraded parts. This, in turn, indicated that the small impact craters had a low degree of solidity and were easily degraded and that fresh impact craters could easily be generated under the influence of external forces and other factors, while the original impact craters were continuously degraded.

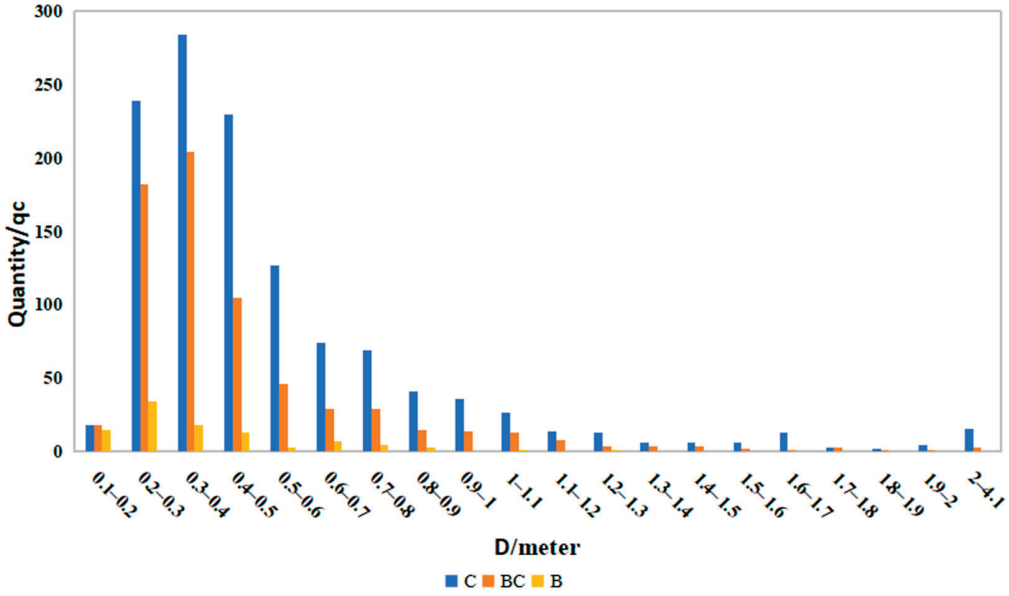


Figure 13. Diameter–degradation level relationship.

The relationship between impact crater depth and degradation class is shown in Figure 14. The average depth-to-diameter ratios of Class C, BC, and B impact craters were 0.112, 0.132, and 0.165, respectively, with 80% of the Class C impact craters having depth-to-diameter ratios in the range of 0.053–0.153; 80% of the Class BC impact craters having ratios in the range of 0.073–0.173; and 80% of the Class B impact craters having ratios in the range of 0.093–0.213. Overall, the ratios of the Class C impact craters increased and decreased with the increasing in the depth-to-diameter ratio, changing from 83.44% to 75.21%, 68.26%, 57.58%, 50.54%, 45.30%, 37.37%, 32.00%, 30.00%, 28.57%, 0.00%, 0.00%, and 0.00%, respectively. The ratio of Class B impact craters gradually increased from 0.63% to 0.85%, 3.42%, 4.55%, 7.73%, 17.17%, 22.00%, 26.67%, 28.57%, 55.56%, and 50.00%, showing that the number of impact craters with severe degradation increased as the depth-to-diameter ratio decreased.

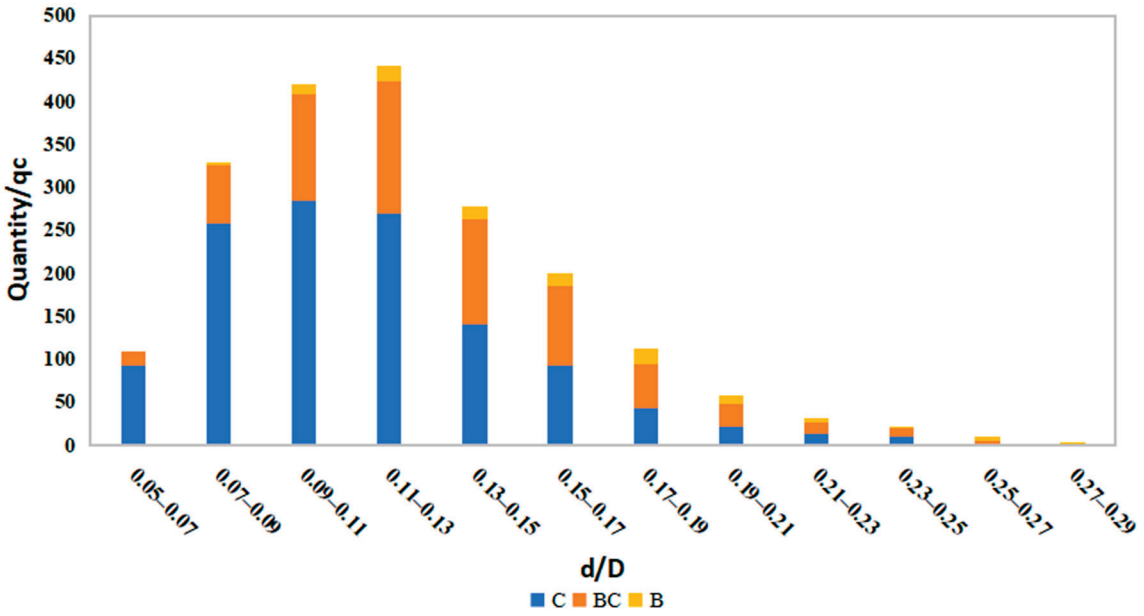


Figure 14. Relationship between depth-to-diameter ratio and degradation classification.

4. Discussion and Analysis

4.1. Comparison with Available Results

Yang et al. (2021) [21] studied sub-metre impact craters. In the statistical results of diameter–frequency, only 12 of the 371 impact craters had a diameter larger than 1 m, and more than 50% had a diameter of 0.1–0.3 m. In this paper, the statistical results of the 2015 impact craters show that 80% of the impact craters in the study area had a diameter concentrated in the range of 0.2–0.5 m, with a total of 1294. A total of 151 impact craters had diameters larger than 1 m, accounting for 7.4%. Compared to existing results, this study extracted a larger number of impact craters was extracted in this study, and the results are more general. However, the size of the impact craters was concentrated in the range of 0.1–2 m, and impact craters with sizes below 0.1 m and larger than 2 m were missing.

The frequency statistics of the depth-to-diameter ratios of 63 impact craters presented by Yang et al. (2021) [21] (Figure 15) revealed depth-to-diameter ratios ranging from 0.03 to 0.18, with a mean value of 0.12 and a variance of 0.03. A total of 78% of the impact craters exhibited depth-to-diameter ratios between 0.10 and 0.16. The statistical analysis of the data revealed that the depth-to-diameter ratios of the impact craters in the study area exhibited a wide distribution, ranging from 0.053 to 0.29. The mean value was 0.122, with a standard deviation of 0.039. The depth-to-diameter ratios were found to be concentrated in the range from 0.07 to 0.17, with more than 80% of the ratios falling within this range. Furthermore, and 50% of the impact craters exhibited depth-to-diameter ratios between 0.10 and 0.16. Both studies demonstrate a linear relationship between depth and diameter. The findings of this study align with those of previous research, indicating that the methodology and process employed in this study are highly reliable. However, the impact crater diameters were found to be larger and the depth-to-diameter ratios smaller than in previous studies. This was due to the larger number of impact craters counted in this study than in previous studies, which provided more accurate statistical analyses for studying the sub-metre impact craters.

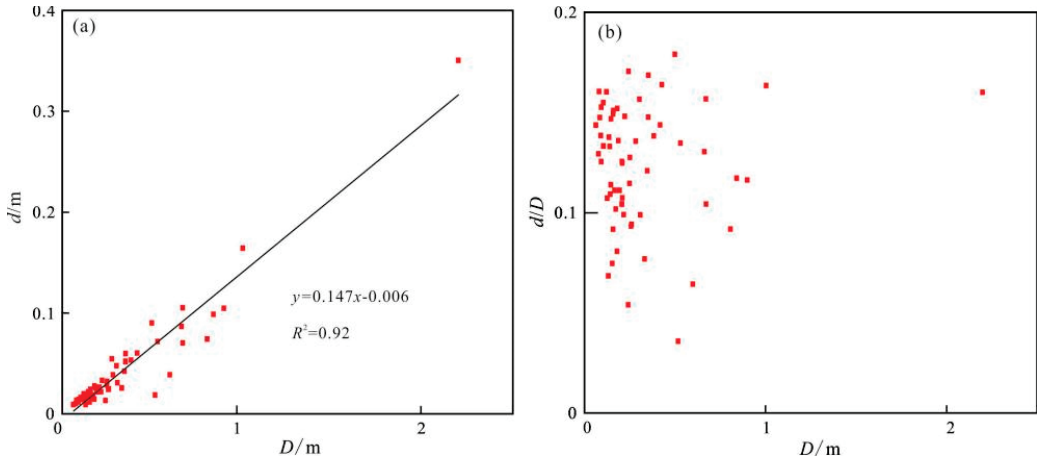


Figure 15. Results of the existing study. (**a**) shows a plot of diameter versus depth, and (**b**) shows a plot of diameter versus depth-to-diameter ratio.

4.2. Statistical Patterns of Regional Population of Micro-Impact Craters

The image data obtained from the landing zone of Chang'e-4 [22] and the image data collected along the rover's route were subjected to a comparative analysis in order to identify the statistical patterns present in the population of the small impact crater craters observed in the lunar back region. Firstly, both studies demonstrated an inverse relationship between the impact crater size and frequency. This inverse relationship can be described as follows: the smaller the impact crater was, the higher the frequency was, and the larger the impact crater size was, the lower the frequency was. Regarding the distributions, the landing camera's come-centre landing zone exhibited a higher image

ground resolution, with 975 impact craters with diameters ranging from 0.15 to 0.5 m in the 30 m range around the landing site. However, due to the limitations of the image resolution, the peripheral zones prevented the further extraction and identification of miniature impact craters. The resolution of the panoramic camera's close observation was sufficient to reach the millimetre level, which enabled the extraction of a greater number of smaller-sized impact craters. Nevertheless, it proved challenging to identify and extract impact craters with diameters exceeding 2 m due to the limitations of the panoramic camera's shooting imaging angle and height. In conclusion, a greater number of impact craters with diameters below 1 m were identified in the landing zone and along the rover's route, indicating a high density of impact craters.

With regard to the level of degradation, 6316 impact craters were extracted from the landing zone, with only 19 identified as fresh impact craters with a minimum diameter greater than 2 m. In contrast, 2015 impact craters were extracted along the rover's route, with no fresh impact craters observed. A mere 2.99% of the impact craters in the landing zone exhibited slight degradation, while 99.7% were severely degraded to varying degrees. The remaining 96.71% were moderately degraded or severely degraded. The proportion of severely degraded craters gradually increased as the size of the craters decreased, while the proportion of fresh craters gradually increased as the size of the craters increased. In parallel, all impact craters along the rover's route exhibited varying degrees of degradation, with 6% classified as moderately degraded. The results of the two studies indicate that the degradation of small impact craters in the region was significant. Nevertheless, 87 moderately degraded impact craters with diameters ranging from 0.1 to 1 m were identified along the rover's route, reflecting the ease with which such craters can be formed and degraded.

4.3. Analysis of Impact Crater Impact Saturation

As the number of impact craters continues to increase, the density of impact craters will eventually reach an upper limit [12,23], particularly for smaller-diameter craters. A cluster of smaller impact craters below a certain diameter is considered saturated when the rate of their creation is equal to the rate of their degradation [24]. The method of saturating the density of impact craters with empirical assessment, as proposed by Gault (1970) [25] and Hartmann (1984) [26], is a widely used approach. In this study, the CraterStats2 tool was used to plot the Hartmann saturation line of impact craters in the 10-station studied area, as illustrated in Figure 16. Figure 14 illustrates a clear inflexion point at 0.2 m, which is evident in the impact crater. A power law fit to the impact craters in the region was performed using Clausi et al. (1970)'s technique [25] to obtain cumulative SFD slopes and equilibrium onset diameters, as shown in Table 2. The cumulative SFD slope of the impact crater population at equilibrium from decimetres to hundreds of meters was -2, while the production slope was -3. This indicates that the impact craters in the study region were not saturated. The area traversed by the Yutu-2 rover's route may be of greater antiquity, exhibiting thicker weathering layers [27]. Therefore, several secondary impact craters may be distributed, which are more likely to be widely distributed in the sub-metre diameter range. Furthermore, smaller impact craters are challenging to saturate with impact craters due to their high probability of new cratering and greater likelihood of burial by ejecta from neighbouring impact craters.

Table 2. Saturation of impact craters in the statistical region.

Counting Areas	Cumulative SFD Slopes of Crater Population in Equilibrium	D_{eq} (m)
Area along the rover's route	−3.6898	0.8177

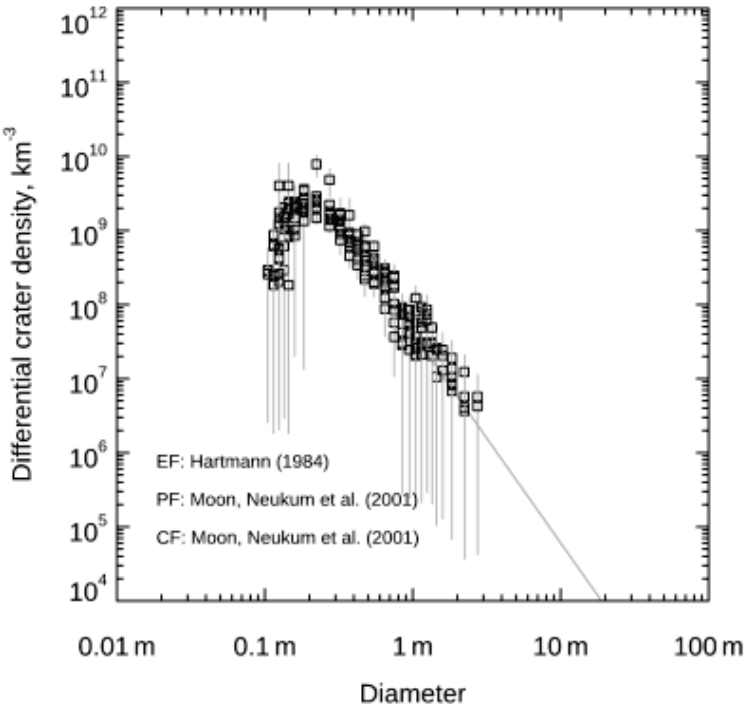


Figure 16. Craterstats2 programme-calculated equilibrium lines [26,28].

5. Conclusions

In this paper, we synthesized and analysed 2015 impact craters with diameters ranging from 0.08 to 4.07 m in panoramic camera images from the 27th to 33rd lunar days, alongside their morphological parameters and degradation levels. Our findings led to the following conclusions:

(1) The majority of the impact craters had diameters between 0.1 and 2 m, with the number of impact craters observed to decrease with increasing size. The distribution of the impact crater depth-to-diameter ratios exhibited a range from 0.053 to 0.29, with over 80% of the minor impact craters exhibiting depth-to-diameter ratios within the range from 0.07 to 0.17.

(2) A negative correlation was observed between the depth-to-diameter ratios and the diameters of minor impact craters. This correlation exhibited a decreasing trend in the depth-to-diameter ratio and a decreasing trend in the population degradation with increasing size.

(3) The area and impact craters along the rover's route exhibited severe degradation overall, with the groups' degradation degree progressively decreasing with increasing diameter.

(4) The achievement of saturation was challenging due to the high probability of the emergence of new craters emerging from sub-metre-scale (mainly below 2.0 m in diameter) impact craters and the high probability of burial by spatter.

The images captured by the Yutu-2 rover's panoramic camera can be used to compare and analyse the distribution and degradation of minor impact craters at the front and back of the moon. This will enable the exploration of the degradation and morphological parameter distribution laws of the impact crater population on the lunar surface.

Author Contributions: Conceptualisation, T.H. and Z.K.; data curation, X.M. and M.C.; formal analysis, X.M. and M.C.; methodology, T.H.; software, M.X.; visualisation, X.M.; writing—original draft, X.M. and M.C.; writing—review and editing, X.M., M.C. and T.H. All authors have read and agreed to the published version of the manuscript.

Funding: This work was supported by the National Natural Science Foundation of China (grant no. 41602215), the National Key Research and Development Program of China (2019YFE0123300),

and a pre-research project on Civil Aerospace Technologies (D020204) funded by the China National Space Administration (CNSA). 2023 University Students' Innovation and Entrepreneurship Training Project of China University of Geosciences, Beijing (S202311415157).

Data Availability Statement: The original contributions of this study are included in this article. Further inquiries can be directed to the corresponding authors.

Acknowledgments: We express our thanks to the "Ground Research and Application System (GRAS) of China's Lunar and Planetary Exploration Program, provided by China National Space Administration (http://moon.bao.ac.cn)" for providing the data set used in this study.

Conflicts of Interest: The authors declare no conflicts of interest.

References

1. Ou Yang, Z.Y.; Li, C.L.; Zou, Y.Y.; Liu, J.Z. Progress of scientific application and research of China's circumlunar exploration program. *Bull. Chin. Acad. Sci.* **2009**, *24*, 530–536.
2. Lin, H.; Chen, J.; Li, C.; Ding, C.; Xiao, X.; Huang, J.; Ji, J.; Gou, S.; Zhang, J.; Wei, Y.; et al. Research progress of remote sensing for the Chang'E lunar exploration mission. *Bull. Mineral. Petrol. Geochem.* **2023**, *42*, 478–493.
3. Michael, G.G.; Neukum, G. Planetary surface dating from crater size-frequency distribution measurements: Partial resurfacing events and statistical age uncertainty. *Earth Planet. Sci. Lett.* **2010**, *294*, 223–229. [CrossRef]
4. Yue, Z.Y.; Shi, K.; Di, K.C.; Lin, Y.T.; Gou, S. Progresses and prospects of impact crater studies. *Sci. China-Earth Sci.* **2023**, *66*, 2441–2451. [CrossRef]
5. Prieur, N.C.; Rolf, T.; Wünnemann, K.; Werner, S.C. Formation of Simple Impact Craters in Layered Targets: Implications for Lunar Crater Morphology and Regolith Thickness. *J. Geophys. Res.-Planets* **2018**, *123*, 1555–1578. [CrossRef]
6. Sun, S.J.; Yue, Z.Y.; Di, K.C. Investigation of the depth and diameter relationship of subkilometer-diameter lunar craters. *Icarus* **2018**, *309*, 61–68. [CrossRef]
7. Craddock, R.A.; Howard, A.D. Simulated degradation of lunar impact craters and a new method for age dating farside mare deposits. *J. Geophys. Res.-Planets* **2000**, *105*, 20387–20401. [CrossRef]
8. Haruyama, J.; Ohtake, M.; Matsunaga, T. Detectability of Degradation of Lunar Impact Craters by SELENE Terrain Camera. *ResearchGate* **2004**, *3*, 1496.
9. Wood, C.; Head, J.; Cintala, M. Crater Degradation on Mercury and the Moon: Clues to Surface Evolution. 1977. Available online: https://adsabs.harvard.edu/full/1977LPSC....8.3503W (accessed on 25 April 2024).
10. Ivanov, M.; Basilevsky, A. Morphology and Size–Frequency Distribution of Kilometer-Scale Impact Craters on Callisto and Ganymede Derived from Galileo Data. *Sol. Syst. Res.* **2002**, *36*, 447–457. [CrossRef]
11. Hartmann, W.K.; Gaskell, R.W. Planetary cratering 2: Studies of saturation equilibrium. *Meteorit. Planet. Sci.* **1997**, *32*, 109–121. [CrossRef]
12. Richardson, J.E. Cratering saturation and equilibrium: A new model looks at an old problem. *Icarus* **2009**, *204*, 697–715. [CrossRef]
13. Li, K. Study on Small-Scale Lunar Craters' Morphology and Degradation. Ph.D. Thesis, Wuhan University, Wuhan, China, 2013.
14. Arthur, D.; Agnieray, A.; Horvath, R.; Wood, C.; Chapman, C. The System of Lunar Craters, Quadrant I. *Commun. Lunar Planet Lab.* **1964**, *2*, 71–78.
15. Mcgill, G.E.; Wise, D.U. Regional variations in degradation and density of Martian craters. *J. Geophys. Res.* **1972**, *77*, 2433–2441. [CrossRef]
16. Basilevskii, A.T. On the evolution rate of small lunar craters. *Lunar Planet. Sci. Conf. Proc.* **1976**, *1*, 1005–1020.
17. Yao, M.J.; Chen, J.P.; Wang, X.; Xu, B. The grading and evolution analysis of lunar crater based on optimum partition and grading method. *Acta Petrol. Sin.* **2016**, *32*, 119–126.
18. Ground Research and Application System of China's Lunar and Planetary Exploration Program. Chang'E 4 Panoramic Cameras Dataset. China National Space Administration. 2020. Available online: http://moon.bao.ac.cn (accessed on 20 February 2023).
19. Dai, S.; Wu, J.; Sun, H.; Zhang, B.; Yang, J.; Fang, G.; Wang, J.; Wang, H.; An, J. Chang'E-3 Lunar Rover's Scientific Payloads. *Chin. J. Space Sci.* **2014**, *34*, 332–340. [CrossRef]
20. Jia, Y.; Zou, Y.; Xue, C.; Ping, J.; Yan, J.; Ning, Y. Scientific Objectives and Payloads of Chang'E-4 Mission. *Chin. J. Space Sci.* **2018**, *38*, 118–130. [CrossRef]
21. Yang, M.; Yue, Z.; Di, K.; Wan, W.; Liu, J.; Shi, K. Statistical Analysis of Secondary Craters in the Chang'E-4 Landing Area Based on Panoramic Camera Data. *Bull. Mineral. Petrol. Geochem.* **2021**, *40*, 720–729.
22. Hu, T.; Yang, Z.; Kang, Z.Z.; Lin, H.Y.; Zhong, J.; Zhang, D.Y.; Cao, Y.M.; Geng, H.M. Population of Degrading Small Impact Craters in the Chang'E-4 Landing Area Using Descent and Ground Images. *Remote Sens.* **2022**, *14*, 3608. [CrossRef]
23. Melosh, H.J. Impact Cratering: A Geologic Process. *Geol. Mag.* **1989**, *126*, 729–730. [CrossRef]
24. Xiao, Z.Y.; Werner, S.C. Size-frequency distribution of crater populations in equilibrium on the Moon. *J. Geophys. Res.-Planets* **2015**, *120*, 2277–2292. [CrossRef]
25. Gault, D.E. Saturation and Equilibrium Conditions for Impact Cratering on the Lunar Surface: Criteria and Implications. *Radio Sci.* **1970**, *5*, 273–291. [CrossRef]
26. Hartmann, W.K. Does crater "saturation equilibrium" occur in the solar system? *Icarus* **1984**, *60*, 56–74. [CrossRef]

27. Qiao, L.; Ling, Z.H.; Fu, X.H.; Li, B. Geological characterization of the Chang'e-4 landing area on the lunar farside. *Icarus* **2019**, *333*, 37–51. [CrossRef]
28. Neukum, G.; Ivanov, B.; Hartmann, W.K. Cratering records in the Inner solar system in relation to the lunar reference Space. *Sci. Rev.* **2001**, *96*, 55–86.

Disclaimer/Publisher's Note: The statements, opinions and data contained in all publications are solely those of the individual author(s) and contributor(s) and not of MDPI and/or the editor(s). MDPI and/or the editor(s) disclaim responsibility for any injury to people or property resulting from any ideas, methods, instructions or products referred to in the content.

remote sensing

MDPI

Article

Quantitative Inversion of Martian Hydrous Minerals Based on LSTM-1DCNN Model

Xinbao Liu [1,2,3], Ming Jin [1,2,*], Xiangnan Liu [3], Zhiming Yang [1,2], Zengqian Hou [1,2] and Xiaozhong Ding [1,2]

[1] Institute of Geology, Chinese Academy of Geological Sciences, Beijing 100037, China; liuxinbao@email.cugb.edu.cn (X.L.); zhiming.yang@cags.ac.cn (Z.Y.); houzengqian@126.com (Z.H.); xiaozhongding@sina.com (X.D.)
[2] National Geological Mapping Research Center of China Geological Survey, Beijing 100037, China
[3] School of Information Engineering, China University of Geosciences Beijing, Beijing 100083, China; liuxn@cugb.edu.cn
* Correspondence: jinmingjsh@163.com; Tel.: +86-134-0119-0327

Abstract: Hydrous minerals are significant indicators of the ancient aqueous environment on Mars, and orbital hyperspectral data are one of the most effective tools for obtaining information about the distribution of hydrous minerals on the Martian surface. However, prolonged weathering, erosion, and other external forces result in complex mixing effects, often weakening the spectral absorption features of individual minerals. This study proposes a quantitative inversion method for Martian hydrous minerals by integrating a radiative transfer model with a deep learning network. Based on the physics of the Hapke radiative transfer model, the single-scattering albedo spectra of mineral end members were obtained. Additionally, the Linear Spectral Mixture Model was employed to generate a large number of fully constrained mineral mixture samples, providing theoretical support for experimental data. An LSTM-1DCNN model was trained to establish a data-driven quantitative inversion framework. CRISM data were applied to the Eberswalde Crater region to retrieve the abundances of 21 hydrous minerals, including tremolite, opal, and serpentine. The average abundance of hydrous minerals was calculated to be 0.018, with a total area proportion of approximately 8%. Additionally, by analyzing the distribution areas of hydrous silicates, hydrous sulfates, and hydrous hydroxides, the water activity history of the region was inferred. The results align with findings from related studies and mineral spectral index results. By incorporating deep learning into traditional mixing models, this study identifies the distribution of various low-abundance hydrous minerals, enhancing the accuracy of Martian hydrous mineral inversion. It is expected to provide valuable references for the selection of landing sites for Tianwen-3 and support the smooth implementation of China's Mars exploration mission.

Keywords: spectral unmixing; quantitative inversion; Martian hydrous minerals; deep learning

1. Introduction

The precise detection of mineral compositions on the Martian surface is crucial for revealing potential signs of life on Mars and constraining its evolutionary history. As one of the nearest terrestrial planets to Earth within the scope of human detection, previous studies have speculated that Mars may have hosted a habitable environment during the Noachian period based on the analysis of layered silicates [1,2]. The widespread hydrous minerals on the Martian surface reveal the history of the early aqueous environment. Although

a large number of qualitative studies have provided limited clues regarding early water activities on Mars [3–5], quantitative research of mineral assemblages and their relative abundances on the Martian surface can offer deeper constraints on the degree of aqueous alteration, formation conditions, and geological evolutionary history [6,7]. Therefore, the use of spectral data to estimate mineral abundances is of significant scientific value in advancing our understanding of the history of water.

Orbital hyperspectral data are the most effective means of rapidly obtaining information on mineral abundance information over large areas of Mars. Current methods for quantitative inversion of Mars using hyperspectral data include absorption-depth conversion [8,9] and spectral unmixing [10]. The absorption-depth conversion method estimates the relative content of the target mineral by approximating the intensity of the spectral absorption peaks. The absorption peak is influenced by factors, such as spectral mixing effects, leading to considerable uncertainty in this method. Therefore, it is primarily used for the qualitative analysis of Martian minerals.

In contrast, spectral unmixing is more commonly employed for quantitative inversion studies of Martian minerals. This method decomposes a mixed spectrum into multiple end-member spectra and obtains the proportional content of each end member. The dense mixing characteristics of Martian minerals result in the strong nonlinear characteristics of their mixing in visible-shortwave infrared reflectance [11] and the mixing of single-scattering albedo spectra, which is approximately a linear addition [12]. Therefore, spectral unmixing models generally require a combination of radiative transfer models for mineral inversion on Mars [13–15]. In Martian mineral abundance inversion, two methods of spectral unmixing have been developed based on different emphases: Multiple End-member Spectral Mixture Analysis (MESMA) [16] and sparse unmixing [17]. The MESMA method allows each pixel to use different end-member combinations during the unmixing process, thereby emphasizing the flexibility of end-member combinations. Combe et al. [18] applied a multiple-end-member linear spectral unmixing model to the Mars OMEGA dataset to identify the abundances of pyroxenes, olivines, gypsum, and other minerals in regions, such as Sytis Major, Aram Chaos, and the Arctic. Le Mouélic et al. [19] applied this method to analyze global Mars OMEGA data to retrieve the distribution and abundance of minerals, such as olivine, clinopyroxene, and orthopyroxene, on the Martian surface. However, because of the exponential increase in the number of models with an increase in the number of end members, this method is computationally intensive and unsuitable for situations with a large number of end members or complex ground object mixing. Therefore, it is challenging to achieve precise unmixing in regions with concentrated distributions of hydrous minerals, such as ancient Martian valleys and lakes with multi-mineral mixing.

Another method is the sparse unmixing algorithm, which focuses on optimizing the unmixing process through sparse constraints and emphasizes finding a combination of fewer end members to explain the mixed spectrum, which is suitable for specific sparsity assumptions. Sparse unmixing conditions can be created by applying sparse regularization methods, effectively reducing the computational cost of the least-squares algorithm in the unmixing process. Zhang et al. [20] used the Sparse Unmixing via Variable Splitting Augmented Lagrangian and TV (SUnSAL-TV) algorithm [21] to quantitatively invert the Mars Science Laboratory (MSL) landing zone, obtaining the abundances of seven minerals, including saponite, and the results were consistent with in situ analyses conducted by the MSL rover "Curiosity". Lin et al. [22] used the proposed Modified Sparse Unmixing (MSU) algorithm with Compact Reconnaissance Imaging Spectrometer for Mars (CRISM) data to quantitatively invert the abundance of three major hydrous minerals, including Fe/Mg phyllosilicates, prehnite, and kieserite, in the Gale Crater. Their results were consistent with the in situ detection results of "Curiosity". Lin [23] also proposed a new methodology

driven by a sparse unmixing model, performing the quantitative inversion of six CRISM images from three regions—Nili Fossae, Northeast of Syrtis Major, and Kashira Crater—and detected putative serpentine in the Nili Fossae region for the first time. In summary, existing sparse unmixing algorithms are limited by their computational complexity and thus restrict the number of end members. Moreover, Martian hydrous minerals have characteristics such as low content, scattered distribution, and uncertain background minerals [24], which can easily lead to the omission of end members and affect the inversion results. Therefore, sparse unmixing algorithms have limitations in the fine quantitative inversion of hydrous Martian minerals.

The quantitative inversion method based on deep learning is a type of data-driven method. It has been widely used in the field of ground object spectral unmixing with high accuracy [25–28]. At the same time, compared with the hybrid spectral decomposition methods widely used for Mars, the deep learning method reduces the cyclic iteration process and improves inversion efficiency. However, as it is challenging to obtain a large number of measured spectral label samples for the inversion of Martian minerals, the application of deep learning models to Martian mineral inversion is restricted. To address this issue, we used the Linear Spectral Mixing Model (LSMM) to rapidly generate large, labeled datasets using simulated abundance data and Earth sample spectral data.

This study proposes a quantitative inversion model based on the LSTM-1DCNN architecture, which integrates the advantages of MESMA and sparse unmixing, allowing for the flexible selection of end-member types and quantities while progressively applying sparsity through multiple thresholds. In addition, by intentionally expanding the variety of hydrous minerals included in the database, the model is particularly well-suited for the quantitative inversion of hydrous minerals on Mars.

2. Data

The data used in this study included end-member spectral and orbital hyperspectral data. The former was used to construct a Martian mineral end-member spectral library, generate labeled datasets, and train the LSTM-1DCNN model; the latter was used for the orbital data application of the quantitative inversion model.

2.1. End-Member Spectral Data

The rationality of the mineral end-member spectral library content had a significant influence on the training speed and prediction accuracy of the Martian mineral quantitative inversion model. This study relied on the USGS Spectral Library data (https://crustal.usgs.gov/speclab/QueryAll07a.php, accessed on 15 February 2024) and the Reflectance Experiment Laboratory (RELAB) data (https://speclib.rsl.wustl.edu/, accessed on 20 March 2024) to screen for proven Martian minerals and minerals of interest to construct a Martian mineral end-member spectral library. The USGS Spectral Library uses its Spectral Library Version 7 dataset, a spectral database compiled by the United States Geological Survey Spectral Analysis Laboratory and the Center for Geological, Geophysical, and Geochemical Sciences, to measure the reflectance spectra of minerals using laboratory, field, and aerial spectrometers. Diverse mineral species are suitable for use in spectral libraries. The RELAB spectral database, produced by Brown University and hosted by the PDS Geosciences Node, provides multiple types of spectral information for the same mineral, supporting research on spectral variation phenomena and addressing the practical issues of spectral diversity for the same object.

The MRO CRISM Type Spectra Library (https://crismtypespectra.rsl.wustl.edu/, accessed on 25 March 2024) was referenced to construct the end-member spectral library. This spectral library contains 31 typical minerals within 6 major categories: iron oxides

and primary silicates, ices, sulfates, phyllosilicates, carbonates, and other hydrated silicates and halides. These spectra were compiled into the Minerals Identified through the CRISM Analysis library, and similar laboratory spectra were obtained.

Thus, this study incorporated multiple spectral data of the same mineral into the Martian mineral spectral library to fully account for the effects of spectral variability. Additionally, synthetic positive and negative slope end members, as well as a zero-slope end member, were included in the spectral library to reflect the effects of dust or low-reflectance materials on the Martian surface and explain the spectral slope differences between the CRISM and laboratory spectra [29]. The end-member spectral library contained 199 spectral curves from 47 mineral types. The specific mineral end-member spectral library is listed in Table 1. Linear interpolation in MATLAB R2021b was used to resample all spectra so that the spectral library was aligned with the CRISM data in terms of spectral resolution.

Table 1. Mineral end-member spectral library.

Number	Name	Chemical Formula	Mineral Types	Spectrum Number
1	Alunite	$KAl_3(SO_4)_2(OH)_6$	Hydrated Sulfate	6
2	Bassanite	$CaSO_4 \cdot 0.5H_2O$	Hydrated Sulfate	1
3	Copiapite	$(Fe^{2+})_6(Fe^{3+})_2(SO_4)_4(OH)_2 \cdot 20H_2O$	Hydrous Sulfate	8
4	Gypsum	$CaSO_4 \cdot 2H_2O$	Hydrous Sulfate	2
5	Halotrichite	$FeAl_2(SO_4)_4 \cdot 22H_2O$	Hydrous Sulfate	2
6	Jarosite	$KFe_3(OH)_6(SO4)_2$	Hydrated Sulfate	5
7	Kieserite	$MgSO_4 \cdot H_2O$	Hydrated Sulfate	2
8	Letovicite	$(NH_4)HSO_4$	Ammonium Sulfate	2
9	Mascagnite	$(NH_4)_2SO_4$	Ammonium Sulfate	2
10	PolyHydratedMagnesiumSulfate	$MgSO_4 \cdot 7H_2O$	Hydrated Sulfate	1
11	Analcime	$NaAlSi_2O_6 \cdot H_2O$	Hydrated Silicate	1
12	Beidellite	$(Al,Fe^{3+})_2(Si,Al)_4O_{10}(OH)_2 \cdot nH_2O$	Hydrous Silicate	8
13	Chlorite	$(Mg,Fe^{2+})_5Al(Si_3Al)O_{10}(OH)_8$	Hydrous Silicate	5
14	Clinopyroxene	$(Ca,Na)(Mg,Fe,Al)(Si,Al)_2O_6$	Silicate	11
15	Epidote	$Ca_2Al_3(SiO_4)_3(OH)$	Hydrated Silicate	3
16	Halloysite	$Al_2Si_2O_5(OH)_4 \cdot nH_2O$	Hydrated Silicate	5
17	Illite	$K < 1\ (Al, R^{2+})_2\ [(Si,Al)\ Si_3O_{10}]\ [OH]_2\ \cdot nH_2O$	Hydrated Silicate	5
18	Kaolinite	$Al_2Si_2O_5(OH)_4$	Hydrated Silicate	6
19	Margarite	$KAl_3(AlSi_3O_{10})(OH)_2$	Silicate	1
20	Maskelynite	$NaAlSi_3O_8$	Silicate	2
21	Montmorillonite	$(Na,Ca)_{0.5}(Al,Mg)_2Si_4O_{10}(OH)_2 \cdot nH_2O$	Hydrated Silicate	6
22	Muscovite	$KAl_2(AlSi_3O_{10})(OH)_2$	Hydrated Silicate	5
23	Nontronite	$(Fe^{3+},Al)_2(Si,Al)_4O_{10}(OH)_2 \cdot nH_2O$	Hydrated Silicate	3
24	Olivine	$(Mg,Fe)_2SiO_4$	Silicate	10
25	Fayalite	$Mg < Fe\ (Mg,Fe)SiO_4$	Silicate	1
26	Forsterite	$Mg > Fe\ (Mg,Fe)SiO_4$	Silicate	1
27	Opal	$SiO_2 \cdot nH_2O$	Hydrated Silicate	5
28	Orthopyroxene	$(Mg,Fe)_2Si_2O_6$	Silicate	9
29	Plagioclase	$(Na,Ca)(Si,Al)_4O_8$	Silicate	9
30	Prehnite	$Ca_2Al(AlSi_3O_{10})(OH)_2$	Hydrous Silicate	1
31	Saponite	$(Na,Ca)_{0.5}(Mg,Fe)_3(Si_4O_{10})(OH)_2 \cdot nH_2O$	Hydrated Silicate	6
32	Serpentine	$Mg_3Si_2O_5(OH)_4$	Hydrous Silicates	4
33	Talc	$Mg_3Si_4O_{10}(OH)_2$	Hydrated Silicate	3
34	Tremolite	$Ca_2(Mg,Fe)_5Si_8O_{22}(OH)_2$	Hydrated Silicate	2
35	Vermiculite	$(Mg,Fe,Al)_3(Al,Si)_4O_{10}(OH)_2 \cdot 4H_2O$	Hydrated Silicate	4
36	Calcite	$CaCO_3$	Evaporite	9
37	Chloride	$(NH_4)Cl$	Evaporite	1
38	Magnesite	$MgCO_3$	Evaporite	13
39	MagnesiumSulphate	$MgSO_4$	Evaporite	1
40	Perchlorate	$R^{2+}(ClO_4)_2$	Evaporite	5
41	Siderite	$FeCO_3$	Evaporite	4
42	Diaspore	$AlO(OH)$	Aluminum Hydroxide	8
43	Goethite	$FeO(OH)$	Iron Hydroxide	5
44	Akaganeite	$FeO(OH,Cl)$	Iron Oxide	1
45	Hematite	Fe_2O_3	Iron Oxide	1
46	H_2OIce	H_2O	Oxide	1
47	dust		Unknown	3

R^{2+} represents a divalent metal cation.

2.2. Orbital Hyperspectral Data

In this study, the orbital hyperspectral image data (FRT000060dd) of the Eberswalde crater region on Mars were used to evaluate and apply the model. The Eberswalde crater underwent significant modifications in later stages, with its center located at 24°8′S, 33°39′W on Mars with a diameter of approximately 63 km. This crater region was once a potential landing site for the Mars Perseverance rover and holds great value for studying the early history of the Martian aqueous environment. As shown in Figure 1, the alluvial fan landform area is located within the crater. The hydromorphic landforms provide a strong indication of the hydrous mineral distribution, facilitating research on Martian hydrous minerals. The data were acquired using the Compact Reconnaissance Imaging Spectrometer for Mars (CRISM) on the Mars Reconnaissance Orbiter (MRO) and provided by NASA's Planetary Data System (PDS) website (https://pds-geosciences.wustl.edu/, accessed on 21 February 2024). The CRISM spectrometer consists of two sensors: a visible and near-infrared sensor (VNIR, 0.36–1.06 μm) and an infrared sensor (IR, 1.00–3.94 μm), with a total of 544 channels in hyperspectral mode. It can observe the Martian surface in two spatial resolution modes: 18 m/pixel (FRT) and 36 m/pixel (HRL/HRS). After removing bad data channels and channels severely affected by emission spectra, this study retained 232 channels in the 18 m/pixel spatial resolution mode, specifically bands 3–235 in the FRT mode. Data preprocessing of CRISM included photometric, atmospheric, and geometric corrections. All steps were performed using the ENVI plug-in CRISM Analysis Toolkit (CAT) 7.4. The plug-in was downloaded from the PDS (https://pds-geosciences.wustl.edu/missions/mro/crism.htm, accessed on 14 March 2024).

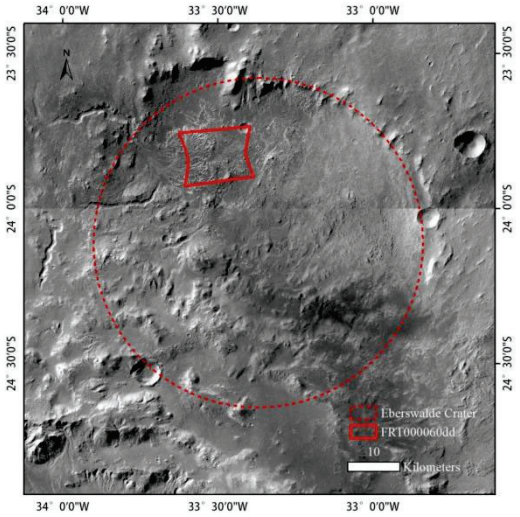


Figure 1. Overview map of the Eberswalde crater on Mars and the study area FRT000060dd. The Eberswalde crater underwent significant post-impact modifications, leaving only the northeastern crater rim intact. The FRT000060dd image is located northwest of the Eberswalde crater. The western part of the crater features a prominent valley where a river connects to the alluvial fan within the image coverage, forming a relatively complete aqueous landform. The base map data are CTX images.

3. Methods

The quantitative inversion model of Martian hydrous minerals constructed in this study involved three models: the radiative transfer model, the spectral mixing model, and the neural network model. Information flow was achieved between the models by assigning data features. The technical route used in this study is shown in Figure 2. This study's technical route mainly consisted of three parts. First, data preprocessing was performed, and the Hapke radiative transfer model was applied to enhance the spectral

features. Second, a spectral mixing model was used to construct a label dataset. Finally, a quantitative inversion model of Martian hydrous minerals was constructed based on the LSTM-1DCNN model, and CRISM images were used for the inversion of Martian hydrous minerals. The LSTM-1DCNN model is the core of the inversion model, which is composed of two sequential sub-networks: Long Short-Term Memory (LSTM) and a 1D Convolutional Neural Network (1DCNN). This design transforms the complex spectral unmixing problem into two simpler tasks: feature recognition and multivariate regression. By doing so, it reduces the overall complexity of the network structure while significantly enhancing the model's inversion speed. Each sub-network is only required to perform its respective task—qualitative identification or abundance inversion—based on the provided information. Consequently, the network depth does not need to be excessively deep, which further simplifies the structure. More importantly, this model allows the 1DCNN network to operate on the basis of qualitative identification, thereby reducing the impact of result non-uniqueness on inversion accuracy and effectively improving the inversion results.

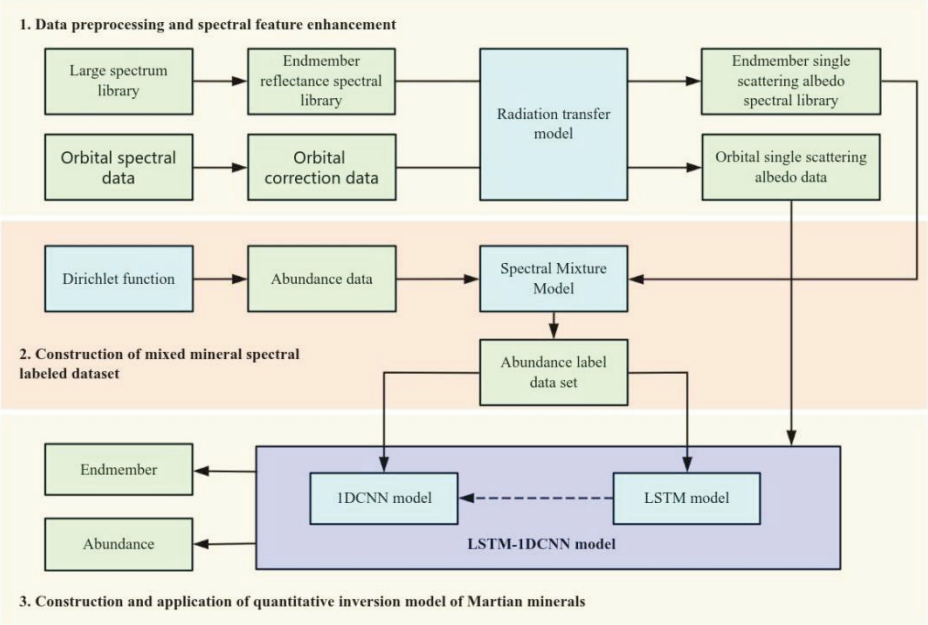


Figure 2. Technology roadmap.

3.1. Radiative Transfer Model

The quantitative inversion model in this study is essentially a data-driven model, so the accuracy of the simulated data is critical to the model's inversion performance. The mixing of various minerals on the Martian surface is a dense mixture that manifests as a highly nonlinear mixing pattern in the reflectance spectra. The direct application of linear spectral mixing methods results in a low accuracy. Therefore, this study introduced the Hapke radiative transfer model to convert reflectance into a single-scattering albedo, which represents the ratio of the part of the incident light scattered by the particle to the sum of the absorbed part and the scattered part of the particle [30]. This approach effectively reduced the spectral differences between the samples in the simulated dataset and the real samples, thereby improving inversion accuracy.

Bruce Hapke, the father of American planetary science, laid the foundation for a radiative transfer model of planetary surfaces. He established the Hapke radiative transfer model that connected macroscopic and microscopic properties to describe the scattering of sunlight on granular media, particularly on planetary regolith surfaces, and for the first time, derived the relationship between the reflectivity of mixed minerals and the optical and physical parameters of the medium when the particle size in a semi-infinite medium

was larger than the wavelength [30]. The function describing the relationship between reflectivity and single-scattering albedo is shown in Equation (1):

$$r = \frac{\omega\mu_0}{4(\mu_0+\mu)} \cdot [(1+B(g))P(g) + H(\mu_0,\omega)H(\mu,\omega) - 1] \quad (1)$$

where $\mu_0 = \cos(i)$, $\mu = \cos(e)$, i and e are the radiation incident angle and emission angle, respectively, g represents the phase angle, and ω is the single-scattering albedo, which is also the target of the radiative transfer model conversion. r represents the reflectance, which, in CRISM data, corresponds to the reflectance corrected for atmospheric and photometric effects. $B(g)$ is the backscatter function related to the phase angle g, describing the opposition effect. When the phase angle g is greater than 15°, the opposition effect can be ignored and the value of $B(g)$ begins to approach zero [11,22,31]. In this study, the phase angle of CRISM data FRT000060dd is greater than 42°, which is significantly beyond the 15° threshold identified in previous studies, so we set $B(g) = 0$. $P(g)$ is the phase function of the medium, which describes the probability of incident light being reflected in a certain direction. Assuming isotropic single scattering of particles, the phase function was set as $P(g) = 1$ [12]. $H(\mu,\omega)$ represents the multiple-scattering function. An approximation of $H(\mu,\omega)$ was proposed by Hapke, with an error within 4% compared to the true value [30], as shown in Equation (2):

$$H(\mu,\omega) = \frac{1+2\mu}{1+2\mu\sqrt{1-\omega}} \quad (2)$$

By substituting the above assumptions and Equation (2) into Equation (1), a simplified version of the Hapke radiative transfer model is derived, as shown in Equations (3) and (4). This simplified approach has been applied in Martian mineral inversion studies and its feasibility has been validated [22]. Considering that the phase angles and other parameters of the mineral end-member spectral library data and the FRT000060dd data from the study area meet the conditions for simplification, this study also adopts the simplified version of this model.

$$\sqrt{1-\omega} = \frac{\left[(\mu_0+\mu)^2\varphi^2 + (1+4\mu_0\mu\varphi)(1-\varphi)\right]^{1/2} - (\mu_0+\mu)\varphi}{1+4\mu_0\mu\varphi} \quad (3)$$

$$\varphi = 4\frac{\mu_0+\mu}{\mu_0}\frac{1}{(1+2\mu_0)(1+2\mu)}r \quad (4)$$

Based on Equations (3) and (4), the nonlinear solver function fsolve in MATLAB R2021b is used to calculate the single-scattering albedo data by inputting the reflectance data, the incidence, and the emission angle data.

3.2. Spectral Mixture Model

The single-scattering albedo spectrum of minerals exhibits an approximately linear additive relationship during the process of mineral mixing [30]. Therefore, a Linear Mixing Model (LMM) [9] was introduced to simulate spectral mixing, as shown in Equation (5). The study by Lin has already proven the feasibility of this simulated sample approach, with their results showing that the abundance error between simulated samples and real samples does not exceed 3% [23]. Although the accuracy of models trained on these data can only match the precision of the simulated data, it still meets the accuracy requirements for model predictions.

$$\omega_{\text{mix}} = \sum_{j=1}^{J} a_j\omega_j + k \quad (5)$$

where ω_{mix} represents the single-scattering albedo of the mixed minerals, ω_j is the single-scattering albedo of end-member j generated in Section 3.1, a_j is the end-member volume abundance produced by the Dirichlet distribution and satisfies the full constraints of $a_j > 0$

and $\sum a_j = 1$, and k is the generated random noise vector. Assuming that Martian surface minerals are uniformly mixed, the volume abundance is approximately equal to the relative geometric cross-section.

The role of the spectral mixing model is to simulate the single-scattering albedo of mixed minerals using the weighted average of the single-scattering albedo of the end members, thereby generating a large amount of label sample data. Based on the mineral complexity assumptions of the Martian surface, the number of effective end members within a pixel ranges from 5 to 8 [23]. The value of J was set to five mixing modes: 4, 5, 6, 7, and 8, representing the number of end members involved in the mixing. For each J value, 20,000 spectral label samples were randomly generated, resulting in a total of 100,000 spectral sample datasets. The dataset was randomly divided into training and test sets in a 4:1 ratio to train the model described in Section 3.3.

3.3. LSTM-1DCNN Model

3.3.1. LSTM Network

The task of mixed spectral end-member identification is similar to the multi-label classification problem in deep learning. Specific label features were extracted from the data, and binary existence labels were assigned to each label based on the confidence thresholds. This study specifically designed a qualitative network structure for the characteristics of Martian CRISM data. In this study, the LSTM network consists of a bidirectional long short-term memory (Bi-LSTM) layer, a dropout layer, a fully connected layer, and a sigmoid output layer. The input data for training the network consist of simulated mixed mineral spectral samples generated in Section 3.2, and the output is the existing confidence levels of 199 end members corresponding to the spectral library. The overall network structure is shown in Figure 3.

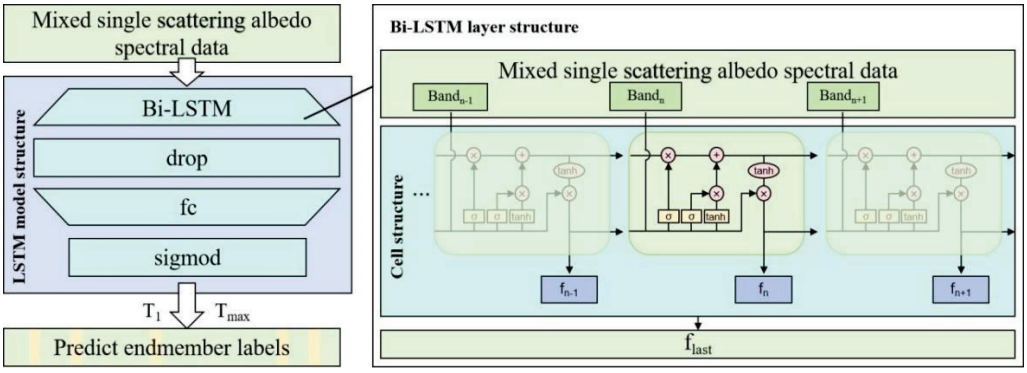


Figure 3. LSTM model structure diagram and Bi-LSTM layer structure diagram, where the LSTM layer neuron structure is referenced from Li et al. [32].

The Bi-LSTM layer is the feature extraction layer of the LSTM network. This layer has notable advantages in extracting one-dimensional data features through a unique gating mechanism, particularly when the data exhibit interdependence, which aligns well with the characteristics of hyperspectral data. The layered structure is illustrated in Figure 3. The cell uses the Forget Gate to select and discard cell state information. The sigm and tanh functions in the Input Gate determine which new information is stored in the cell state, allowing information to flow throughout the chain. Finally, the feature vector (f_n) is processed by sigm in the Output Gate, while tanh further updates the cell state. Each cell outputs features based on the previous cell state and input information [32], so that the final feature output (f_{last}) retains the information from the entire spectrum. The drop layer enhances the overall nonlinear prediction capability and generalization of the LSTM network. The fully connected layer aligns the number of features with the number of

end members, and the sigmoid layer converts the output into end-member confidence levels, facilitating the subsequent sparsification of end members based on a threshold. In this study, the LSTM network's outputs were binarized by setting a threshold T_1 for end-member confidence and the 199 output labels were divided into 0 and 1, where 0 represents an absence of an end member and 1 represents its presence. The T_1 threshold value was between 0 and 1 and primarily functioned to screen for potentially present end members. The specific value of T_1 should be determined based on the conditions of the study area and the CRISM data quality. The T_1 value is discussed in detail in Section 4.1 of this paper. Additionally, to ensure the number of identified end-member spectra did not exceed the input limit of the 1DCNN model, the total number of end members predicted as "1" was constrained by the T_{max} threshold, an integer greater than "0". This threshold ensures rational data transfer between the two subnetworks.

3.3.2. 1DCNN

This study addressed the problem of the process from end members to abundances by constructing a 1DCNN. To reduce model complexity and effectively extract features, the input section of the model was designed to consist of two concatenated parts, as shown in Figure 4. The first part of the input was the end-member spectral data output from the LSTM network in described Section 3.3.1, which was concatenated sequentially from left to right. If there were empty end-member spectral positions, they were filled with zeros, ensuring that the predicted end members were unified to the same size. The second part consisted of the corresponding mixed spectral data. In summary, the input format of the model was 232 × 11. The output of the model consists of abundance values for 10 corresponding spectra, satisfying the constraints of being greater than zero and summing to one. A network structure diagram of the 1DCNN, along with the input and output data flow, is shown in Figure 4.

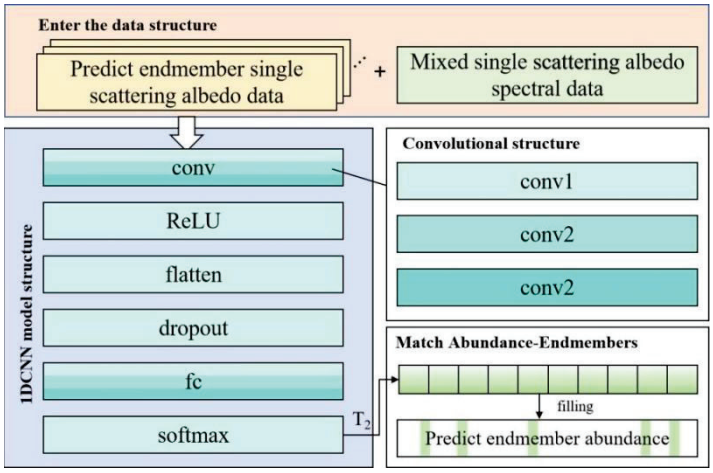


Figure 4. 1DCNN structure and data chart.

The 1DCNN was composed of three convolutional layers, the ReLU activation function layer, the flatten layer, three fully connected layers, and a softmax output layer. The three convolutional layers were used to progressively extract the features between the mixed spectra and the individual end-member spectra. The ReLU layer enhanced the nonlinear problem-solving capability of the model, and the weight relationship between the mixed mineral and end-member spectra was obtained by flatten layer and fully connected layers. The output of the 1DCNN achieved T_{max} fully constrained values through softmax. The prediction results were denoised by setting an abundance threshold of T_2 and retaining only end members with abundance values greater than T_2. This process effectively reduced

the impact of image noise on the experimental results and ensured the accuracy of the inversion outcomes. T_2 is a real number between 0 and 1 that serves to remove noise from the model's results. If T_2 is set too high, a large amount of valuable information may be lost; if set too low, the noise influence will be significant. Therefore, determining the value of T_2 requires expert judgment based on experimental results.

4. Results

4.1. LSTM Network Qualitative Training Result

The accurate identification of mineral end members is the basis for achieving refined abundance inversion. This study used an LSTM network implemented on the Kaggle platform (https://www.kaggle.com/, accessed on 20 September 2024) within the PyTorch 2.4.0 framework, leveraging a Tesla P100-PCIE-16GB GPU, a 4-core CPU, and 29GB of RAM. The LSTM network was trained using the binary cross-entropy loss function (BCELoss) and the Adam optimizer with a learning rate of 0.0005. The training dataset consisted of 80,000 samples, with 500 training epochs and a batch size of 64. The dataset used for training was generated using the Mineral End-member Spectral Library based on the Hapke radiative transfer model and the linear mixing model, resulting in a labeled dataset of 100,000 samples simulated in MATLAB 2021b. Each labeled sample consists of two parts: simulated spectra and end-member labels. The dataset was split into a training set and a test set in a 4:1 ratio. The input data comprise simulated mixed spectral data (80,000 $\times$ 232), where 80,000 represents the number of samples and 232 is the number of spectral bands. The data were simulated in MATLAB using the linear spectral mixing model. The output corresponds to the end-member label data (199 $\times$ 1), where 199 is the total number of end-member spectra. The output values are binary (0 or 1), indicating the presence or absence of the corresponding end-member. The output produced a variable number of labels based on the constraints of T_1 and $T_{\max}$. $T_{\max}$ was set to 10 according to the input structure of the 1DCNN. A comprehensive analysis of the LSTM network's output was conducted with respect to the T_1 value. The results for the LSTM network's accuracy, precision, recall, and F1 score on the test set as T_1 varies are shown in Figure 5: when $T_1 = 0.25$, the accuracy reaches its peak. Considering the class imbalance in the data, the F1 score is the primary metric of interest, peaking near $T_1 = 0.2$. Below this threshold, the recall continues to increase, indicating that some end members are still being missed. However, the precision drops sharply when $T_1 < 0.15$, indicating a significant increase in misclassification. Considering that an excessively high T_1 value in the qualitative network could lead to missed end-member extractions and a value too low could result in severe striping effects in the predicted results, this study determined that T_1 should be restricted to a range of 0.1–0.2 based on the combined performance of the four metrics mentioned above.

The LSTM network's output labels have a many-to-one relationship with mineral types. Identifications corresponding to different spectra of the same mineral should be considered successful. Therefore, we further merged the label results based on mineral types. This further reduces the possibility of non-uniqueness in the results and minimizes the errors caused by non-uniqueness. When $T_1 = 0.1$ and $T_{\max} = 10$, the results of the 20,000-sample test set are shown in Figure 6. The average recognition accuracy of the 47 mineral types in the LSTM network is 97.76%, with more than half of the minerals' identification accuracy above 95%. Among them, the identification accuracy of plagioclase, calcite, and magnesite is relatively low, which were all below 93%. Therefore, the qualitative results of these minerals should be manually verified for their authenticity during application.

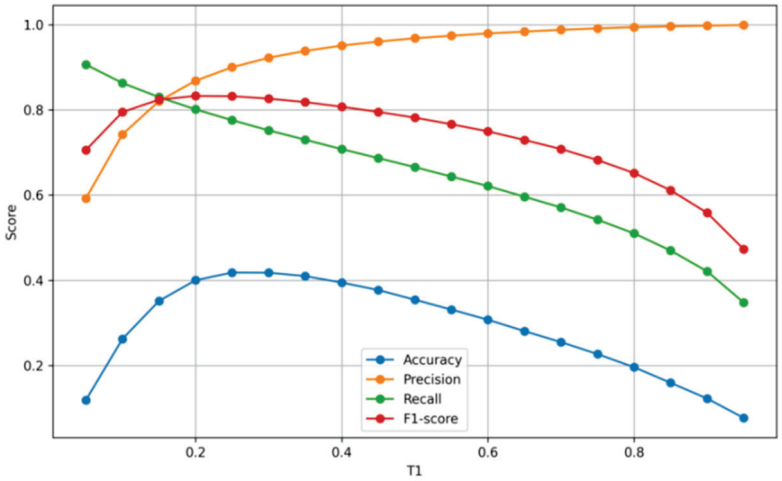


Figure 5. Model accuracy, precision, recall, and F1 score trends as T_1 changes.

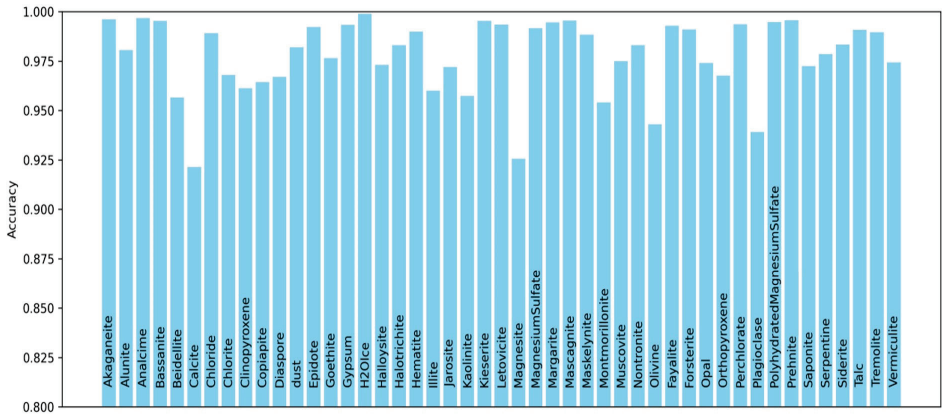


Figure 6. Qualitative network mineral identification accuracy chart.

4.2. 1DCNN Quantitative Training Results

The 1DCNN used was also implemented on the Kaggle platform using the PyTorch 2.4.0 framework with a Tesla P100-PCIE-16GB GPU, a 4-core CPU, and 29GB of RAM. The mean squared error (MSELoss) function and an Adam optimizer with a learning rate of 0.0005 were used to train the 1DCNN. The training dataset contained 80,000 samples, with a batch size of 64. The dataset used for training is similar to that used for the LSTM network, with the key difference being that the labeled samples consist of three parts: simulated mixed spectra, end-member spectral combinations, and abundance labels. The input data are a combination of mixed spectral data and end-member spectral data, with dimensions of 80,000 $\times$ 232 $\times$ 11, where 80,000 represents the number of samples, 232 is the number of spectral bands, and 11 corresponds to the mixed spectra and 10 individual end-member spectra. The output data consist of abundance labels for the 10 end members. The stability of the model's quantitative output is crucial for the inversion results. Training started with 100 batches and incrementally increased by 50 batches per round, continuing for six rounds. The correlation between predicted abundances on the test set and the true abundance labels for different training batches is shown in Figure 7, where a, b, c, d, e, and f represent the results for 1DCNN training batches of 100, 150, 200, 250, 300, and 350, respectively. The experimental results show that the average mean squared error (MSE) value on the test set was 0.0039 with smaller fluctuation, indicating the stability of the network's training results. The predicted results on the test set exhibited a significant positive correlation with the labels: the slope is k = 1 $\pm$ 0.04 and the intercept is b = 1 $\pm$ 0.012. Additionally, the scatter plot showed that as the label abundance value increased, the model's predictions

became more accurate, whereas lower abundance values resulted in greater prediction errors. This suggests that the randomness of the inversion results increased when the mineral abundance value was low, leading to noticeable noise in the image. Therefore, the T_2 threshold should be applied to remove the lower abundance results to reduce errors.

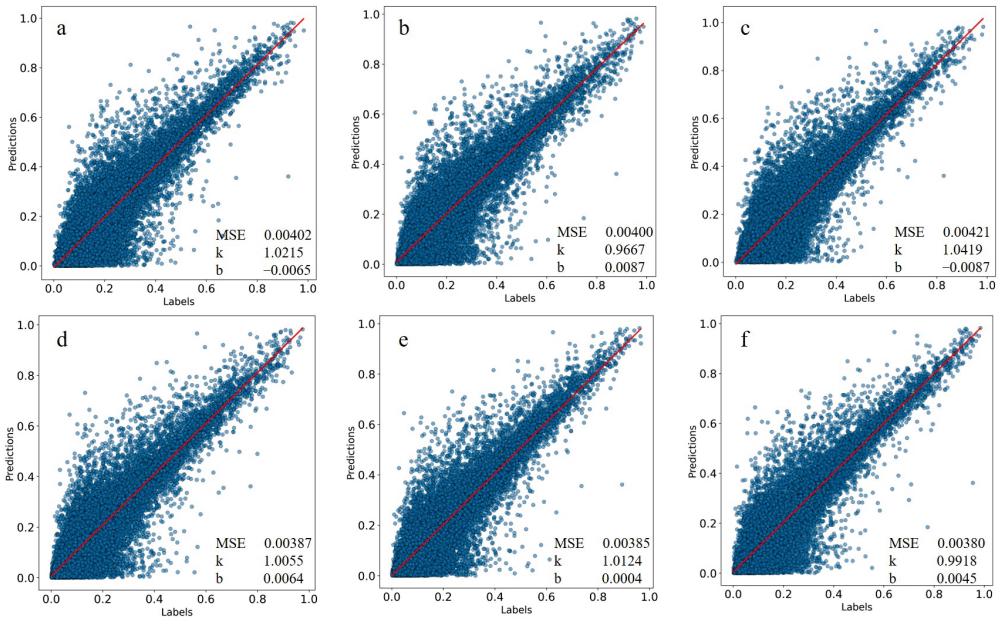


Figure 7. Scatter plot of the test set for multi-batch training of the quantitative network. Panels (**a**–**f**) represent the results for 1DCNN training batches of 100, 150, 200, 250, 300, and 350, respectively.

4.3. Application of LSTM-1DCNN Network Model in Track Data

The LSTM-1DCNN model was applied to the CRISM data for regional-scale mineral quantitative inversion to obtain an abundance of 35 minerals, with the statistical results shown in Figure 8, indicating that the inversion yielded abundance data for 35 minerals in the region. Excluding unknown mineral components, such as dust, the abundances of olivine, plagioclase, clinopyroxene, and maskelynite were generally high, with median abundance values of approximately 0.22, 0.24, 0.38, and 0.60, respectively. Other minerals generally had low abundances and were mostly concentrated below 0.2. The results indicated that the study area may contain a variety of low-abundance hydrous minerals and clay minerals. In addition, this study detected a small number of low-abundance H_2O ice signals. The abundance box plots reveal that the abundance of hydrous minerals of interest in this region is generally low, with an average abundance of 0.018. Before noise removal using the T_2 threshold, the median abundance of minerals like Kieserite was even as low as 0.01. A larger T_2 threshold has a significant impact on these important minerals. After comprehensive analysis, the T_2 threshold was set to 0.01 to retain information on hydrous minerals while removing noise. As shown in the figure, minerals such as letovicite and mascagnite exhibited high-abundance outliers, which were manually removed. This phenomenon may result from image noise, which significantly affects the spectra of the minerals.

Since a single pixel may contain multiple minerals, this study defined the total number of pixels occupied by all minerals as the total mineral distribution area. The ratio of the pixel count for each mineral to the total mineral distribution area was defined as the mineral area proportion. The inversion results, after removing mineral types significantly affected by noise such as mascagnite, letovicite, and copiaoite, were statistically analyzed, as shown in Figure 9. The figure illustrates the area proportion greater than 0.01% of 26 minerals within the study area. The statistical chart shows that the most widely distributed minerals in this

region are relatively ancient minerals, such as plagioclase, olivine, forsterite, clinopyroxene, and maskelynite, which is similar to the mineral distribution trend on the surface of Mars, which is generally dominated by ancient bedrock. Additionally, the statistical results also include 15 hydrous minerals with relatively low area proportions, such as epidote, tremolite, and opal, with a combined proportion of approximately 8%. Although the overall spatial distribution is relatively small, the hydrous mineral types are diverse and have various origins, providing diverse constraints for analyzing the evolutionary history of this region.

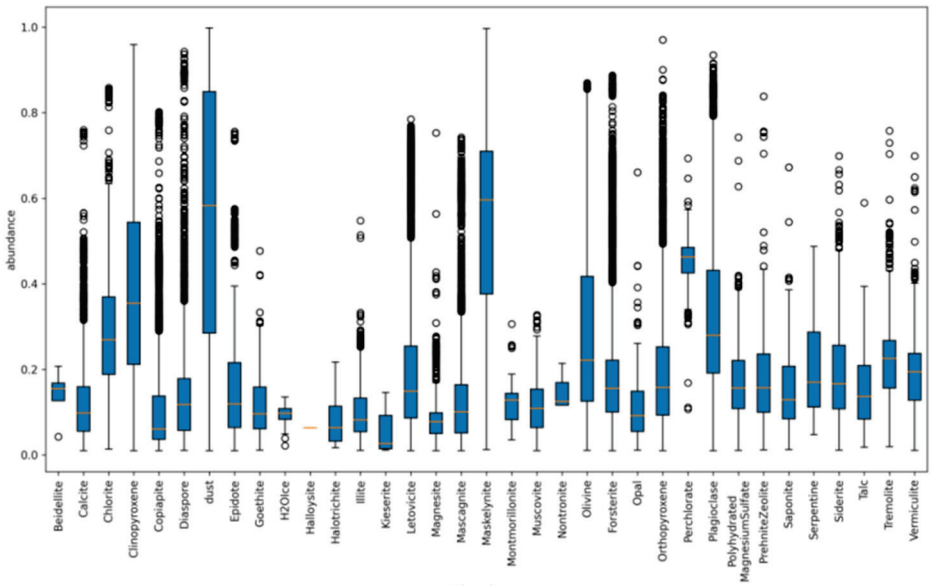


Figure 8. Box plot of predicted mineral abundance within the FRT000060dd map area.

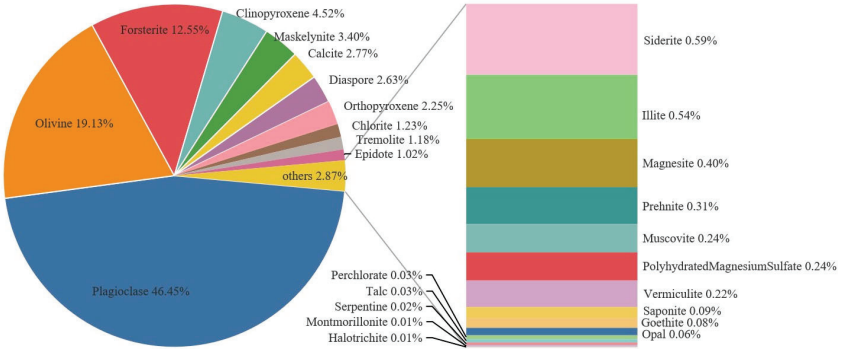


Figure 9. Statistical chart of the pixels occupied by major minerals.

Taking the inversion results of the highlights region in the northwest delta shown in Figure 10 as an example, the LSTM-1DCNN model developed in this study achieved accurate end-member and abundance predictions at the pixel scale. The pixel indicated by the red arrow in Figure 10a is located in the bright strip region of the delta. Its reflection characteristics in the image are significantly different from those of the background minerals. The inversion results of this study's model for this pixel identified 10 end members qualitatively, including 4 minerals: mascagnite, forsterite, orthopyroxene, and plagioclase, along with some low-reflectivity dust and unknown low-reflectivity materials. The identified end-member spectra overlap with the CRISM spectra at certain absorption peak positions. Additionally, a mixed spectrum was simulated using the end-member spectra and their corresponding abundances. It shows good consistency with the CRISM spectrum in both the absorption peak positions and overall absorption trends. The spectral angle

measurement between the two spectral curves was calculated as 0.004, and the inversion results of the LSTM-1DCNN model demonstrate a certain level of reliability.

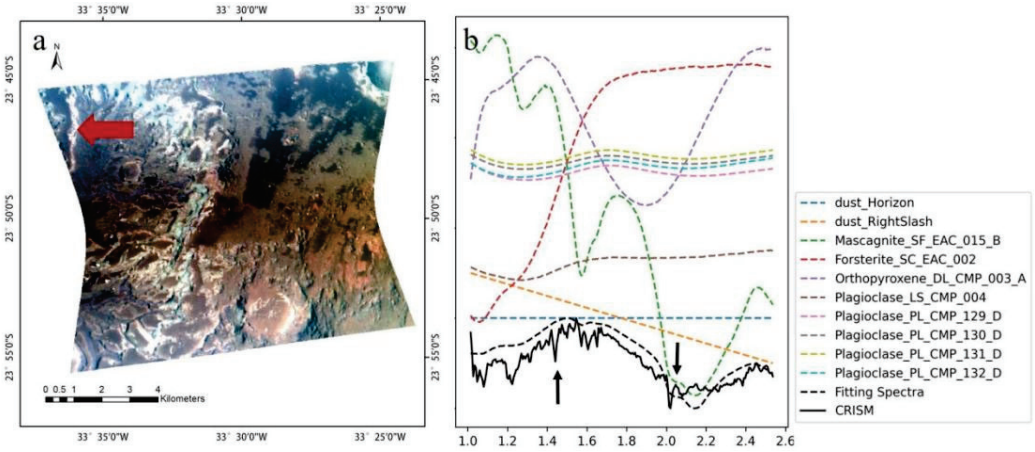


Figure 10. Comparison of model inversion results and CRISM data. (**a**) A false-color RGB image (red = 2.5295 μm, green = 1.5066 μm, blue = 1.0800 μm). The red arrow indicates the pixel location. In (**b**), the solid black line represents the orbital spectral curve of the pixel, whereas the dashed black line shows the simulated spectral curve based on the inversion results. The other dashed, colored lines correspond to the end-member spectra. The variations observed in the 1.4–1.55 μm range, marked by the arrow, result from instrumental errors [33], whereas the sharp peaks in the 1.9–2.1 μm range, also marked by an arrow, are due to atmospheric correction related to CO_2 [10].

The inversion results included 21 hydrous minerals, as shown in Figure 11. For clarity of analysis, the hydrous minerals were classified into three categories based on mineral type: hydrous sulfates, hydrous silicates, and hydrous hydroxides. The hydrous sulfate minerals, including halotrichite and kieserite, are primarily distributed in the high-brightness regions within the red rectangular areas (Figure 11a). Hydrous hydroxides, including diaspore and goethite, are mainly distributed in the low-elevation dark regions downstream of the delta (Figure 11b). Hydrous silicates are more diverse and include halloysite, illite, opal, and serpentine, which are primarily distributed in the bright regions of the figure, such as high-brightness outcrops at the edges of the delta and the rims of impact craters (Figure 11c).

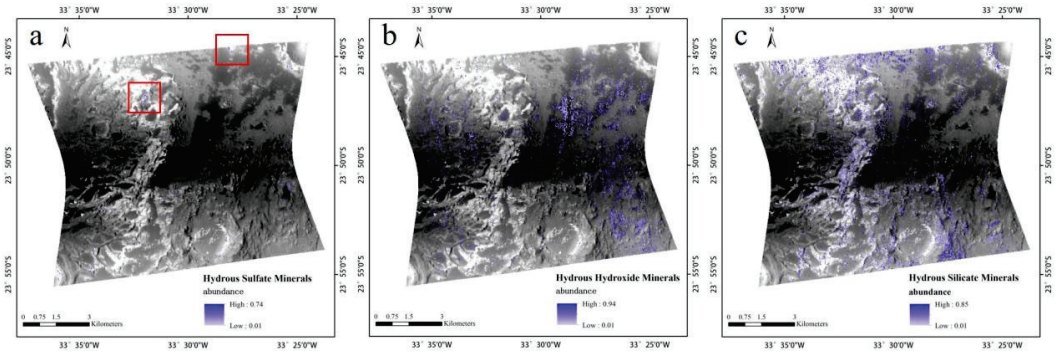


Figure 11. The distribution map of hydrous mineral types: (**a**) hydrous sulfate minerals, which have been highlighted with a red box, (**b**) hydrous hydroxide minerals, and (**c**) hydrous silicate minerals. The bottom figure is the gray-scale data for the 1.1652 μm.

5. Discussion

5.1. Mineral Type Identification

The qualitative study in this research uses an LSTM network combined with a T_1 threshold sparsity method to filter potential candidate end members from mixed spec-

tra. The experiments show that this identification method has advantages over existing Mars mineral identification methods in terms of identifying more end members and a faster recognition speed. Currently, Mars mineral identification studies mainly analyze spectral characteristics and use manually defined combinations of spectral characteristic parameters to determine mineral types [34,35]. However, spectral parameters typically only identify broad categories of minerals, and determining specific mineral subcategories often requires manual comparison, which is not only time-consuming but also highly subjective. In contrast, the LSTM qualitative network automatically extracts features through neural network layers and completes identification, improving speed while capturing more potential features. Additionally, Lin et al. [36] improved upon the Factor Analysis and Target Transformation [37] by proposing the Dynamic Aperture Factor Analysis and Target Transformation (DAFATT), which enables mineral type identification with spatial location information. However, only one end-member mineral can be identified at a time. The LSTM network achieved rapid identification of multiple minerals by leveraging end-member spectral libraries, significantly improving the efficiency of end-member recognition.

Previous studies have attempted to apply deep learning to Martian mineral spectral identification [38], demonstrating the feasibility of deep learning methods in Mars mineral identification. In this study, the LSTM network is considered part of the inversion process and needs to operate in coordination with the 1DCNN network. The output layer is configured for dynamic output, with fewer outputs than $T_{\max}$ and confidence greater than T_1, making the entire qualitative network more flexible. At the same time, some errors appeared in the qualitative identification results, with minerals exhibiting pronounced striping noise. Expert knowledge is required to assess these cases, posing a challenge to the accuracy of the LSTM network's identification.

5.2. Mineral Abundance Inversion

Extensive studies have been conducted on the mineral composition of the Martian surface. Kodikara et al. [39] proposed a method using deep neural networks to estimate the abundances of stilbite, montmorillonite, and epsomite from the reflectance spectra of ternary mineral mixtures. However, according to Hazen et al. [40], the confirmed number of Martian mineral species has reached 161, and many more Martian minerals remain undiscovered. In regions with hydrous mineral distribution, the mineral mixtures are more complex [24], and traditional binary and ternary mineral inversion methods are inadequate for the refined needs of Martian exploration. The quantitative inversion in this study is based on qualitative identification. The most widely used method for mineral abundance inversion on Mars is the least squares-based mathematical approach. This method iteratively identifies the mineral combinations and corresponding abundances that best match the measured spectra, thereby achieving abundance inversion. However, when there are five or more end members mixed within the model, least-squares regression often suffers from severe overfitting [41]. This overfitting leads to significant errors in the abundance inversion results. Moreover, least-squares regression involves extensive matrix computations, and the efficiency decreases exponentially with an increasing number of end members. Therefore, the number of end members in least-squares inversion is typically limited to 2–5. The goal of the quantitative model is similar to that of least-squares regression. This study addresses the problem by constructing a 1DCNN model, which simultaneously inputs the mixed spectra and the qualitative spectral results into the neural network. By utilizing multiple layers of neurons for nonlinear regression, the model identifies the weight relationships between the mixed spectra and the spectra of individual end members, thereby outputting the abundance values. This approach transforms the least-squares matrix-solving process into a deep learning-based nonlinear regression problem,

eliminating the iterative steps of least squares and significantly improving computational efficiency. The experimental results showed that using a ten-end-member mixture as an example, the 1DCNN model took 330.50 s to compute mineral abundances on the Kaggle platform with FRT000060dd data.

Additionally, the T_2 threshold was applied to the abundance inversion results to filter out end members with low contributions and poor stability during unmixing, thus enabling post-denoising of the model. Without setting a threshold, a wide distribution of low-abundance minerals may occur, making it difficult to ensure their authenticity. Considering the image quality of the FRT000060dd data in this study, the T_2 threshold was set to 0.01. If the image quality is lower, the T_2 value should be increased accordingly and further adjusted based on specific conditions.

5.3. Mineral Analysis of Typical Areas

The spectral index is an effective method for the rapid qualitative assessment of mineral distribution on the Martian surface. Generally, higher spectral index values indicate a higher abundance of the mineral. To ensure the accuracy of the experimental results, multiple inversion outcomes were integrated to derive more precise regional abundance data for specific minerals. The abundance of olivine and pyroxene obtained using the model in this study was compared with those obtained using the Olivine Index and the Pyronexe Index [42], as shown in Figure 12. The spatial distribution of minerals and their corresponding mineral indices in Figure 12 demonstrates a high degree of overlap, indicating that the mineral inversion results of this model are spatially reliable. Furthermore, panels (c) and (f) show a positive correlation between the model predictions abundance and the spectral index. This suggests that the abundance inversion results of this study are reliable in terms of abundance numerical trends. However, when the inversion abundance is low and the error is large, it is necessary to remove the low abundance mineral end element by the T_2 threshold, so as to improve the overall inversion accuracy and stability of the model. In Figure 12a, the two areas marked with red boxes have been identified by the model in this study as halloysite distribution zones. However, given that the absorption positions of halloysite and olivine overlap near 1 μm, and there is strong absorption around 1.36–1.45 μm, which is close to the band positions used in the Olivine Index, misidentification may have occurred. Therefore, the halloysite identified in this study has also been tentatively included to participate in the analysis of olivine abundance. The specific mineral type requires further investigation and discussion. Previously, Wu et al. [43] used collaborative sparse unmixing to quantitatively retrieve minerals in this region, obtaining six minerals, including pyroxene, which were validated using mineral spectra. The distributions of pyroxene, siderite, and plagioclase obtained in this study are consistent with their results, which validates the reliability of the inversion results in this research. Furthermore, this study identified 28 reliable mineral types in the same image, representing a significant improvement in the number of retrieved mineral end members. This demonstrates that the model is more suitable for mineral abundance inversion in scenarios with complex mineral mixing.

The typical delta landforms in this region indicate the presence of early liquid water activity [44]. In this study, the model's ability to accurately identify various mineral types was fully utilized, revealing a wide variety of hydrous minerals across the region. The inversion results show that the region exhibits overall characteristics of low hydrous mineral abundance, small area coverage, and high diversity of mineral types; moreover, their origins are mostly associated with water, consistent with the ancient environment implied by the deltaic water-related geomorphology. Furthermore, the presence of different types of hydrous minerals indicates diverse aqueous environments. High abundances of

pyroxene and other silicate rock-forming minerals, along with various hydrous silicate minerals, were found on the steep slopes of the bright regions along the delta edges, as shown in Figures 12 and 13. Based on the overall environmental context of the region, it is hypothesized that prolonged liquid water activity enabled silicates in the bedrock to either directly absorb water or chemically react with it to form hydrous minerals. Alternatively, hydrous minerals transported downstream by rivers may have been deposited in the alluvial fan, where steeper slopes facilitated the exposure of these ancient minerals. In contrast, dark regions with hydrous hydroxide minerals correspond to the low-elevation hillock in Figure 13, with little to no olivine or pyroxene present. This study suggests that the region once hosted a long-standing paleolake. Large quantities of cations in the lake water likely precipitated as hydroxides in an oxidizing environment, accumulating and covering the original silicate substrate—a process also observed in research on ancient marine environments on Earth [45]. The small crater in the northeast of the delta presented in Figure 1 shows no evidence of fluvial erosion, indicating that it formed after water activity ceased. However, its crater edges contain high abundances of hydrous minerals. These deep-seated minerals were likely excavated by the impact. Therefore, we hypothesize that more hydrous minerals may be buried under a layer of dust.

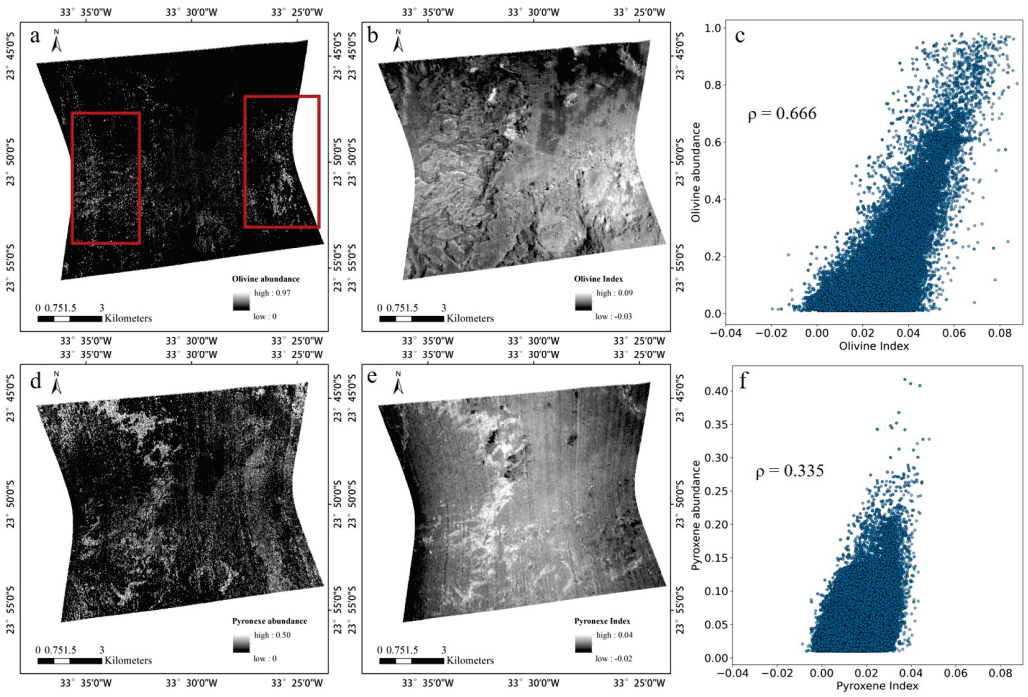


Figure 12. A comparison between mineral abundance inversion results and mineral spectral indices. Panels (**a**,**b**) represent the Olivine abundance and Olivine Index. The red rectangular region in Panel (**a**) represents a potential olivine distribution area. Panel (**c**) illustrates the scatter plot corresponding to the data presented in Panels (**a**,**b**); the Pearson Correlation Coefficient (ρ) between the two variables in Panel (**c**) is 0.666, indicating a moderately strong positive correlation. Panels (**d**,**e**) represent the Pyroxene abundance and Pyroxene Index. Panel (**f**) illustrates the scatter plot corresponding to the data presented in Panels (**d**,**e**); the ρ between the two variables in Panel (**f**) is 0.335, indicating a certain positive correlation.

The map area also displays a large number of low-abundance ammonium sulfate signals as shown in Figure 8. Previous, Manning et al. [46] hypothesized that ammonium sulfate minerals on Mars form when significant amounts of atmospheric nitrogen are fixed into soil nitrates and subsequently transported and enriched by groundwater in sulfur-rich environments. In this study, mascagnite and letovicite were included as end members in the mineral end-member spectral library because preliminary observations indicated that the

CRISM spectral absorption peaks in the study area overlapped with those of ammonium sulfate minerals. Sefton-Nash et al. [47] detected absorption signals of ammonium sulfate minerals, such as mascagnite and letovicite, in the Iani Chaos region. As Iani Chaos is near the Eberswalde Crater, similar environmental conditions were more likely to produce comparable mineral compositions, providing a reference for the mineral composition in the study area. However, the inversion results revealed that the spatial distribution trends closely aligned with the orbiter's movement direction, forming a distinct strip pattern inconsistent with the natural distribution of minerals. As a result, these minerals were manually removed by T_2 Threshold. This phenomenon may have resulted from image noise, which significantly affected the mineral spectra. Based on expert knowledge, these minerals were classified as unreliable, requiring further in-depth investigation in future studies.

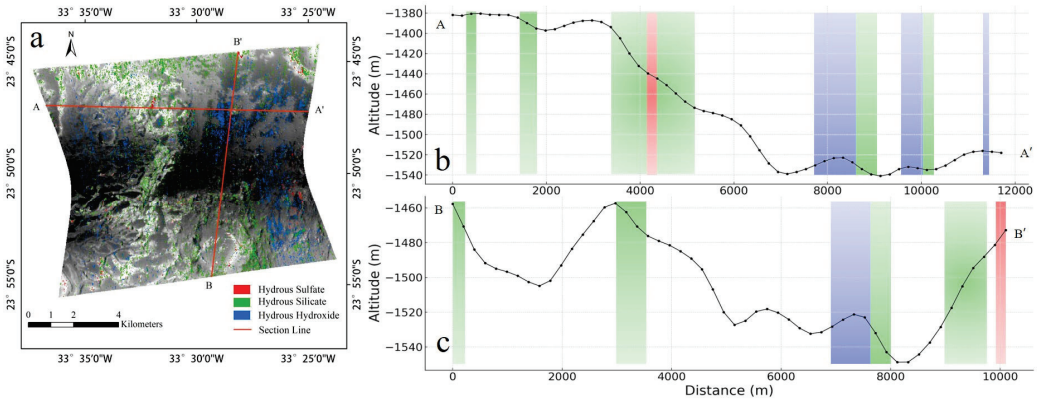


Figure 13. Horizontal and vertical elevation distribution maps of the three types of hydrous minerals. (**a**) The horizontal distribution of three types of hydrous minerals: hydrous sulfate minerals, hydrous hydroxide minerals, and hydrous silicate minerals. (**b**,**c**) The AA′ and BB′ cross-sectional profiles corresponding to (**a**), respectively, showing the elevation distribution of different minerals along and near the section lines.

6. Conclusions

This study presents a quantitative inversion model of Martian hydrous minerals based on the LSTM-1DCNN model for inversion Martian mineral abundances using CRISM hyperspectral data. The model comprises two subnetworks: the LSTM network, which is used for qualitative identification of end members in Martian mixed minerals, simplifies the overall model scale and enhances the accuracy of hydrous mineral inversion, while the 1DCNN performs quantitative determination of Martian mineral end members, effectively improving unmixing efficiency. The Hapke radiative transfer model is used to convert Martian mineral end-member spectra into single-scattering albedo spectra, and the Linear Spectral Mixing Method is employed to construct a labeled dataset for model training. The testing results show that this model achieves an average accuracy of 97.76% in qualitative recognition and an average MSE of 0.0039 in quantitative inversion. Using the LSTM-1DCNN model, the CRISM data enabled the inversion of the abundances of 31 high-confidence minerals in the Eberswalde crater area, including 21 hydrous minerals, with olivine and pyroxene abundance results showing high spatial correlation with mineral spectral indices. The model has high inversion accuracy and high potential to be applied to the entire Martian surface.

Author Contributions: Conceptualization, M.J. and X.L. (Xinbao Liu); methodology, M.J. and X.L. (Xinbao Liu); software, X.L. (Xinbao Liu); validation, X.L. (Xinbao Liu), M.J. and X.D.; formal analysis, X.L. (Xinbao Liu); investigation, X.L. (Xinbao Liu); resources, X.L. (Xinbao Liu); data curation, X.L. (Xinbao Liu); writing—original draft preparation, X.L. (Xinbao Liu); writing—review and editing,

X.L. (Xinbao Liu), M.J., X.L. (Xiangnan Liu), Z.Y., Z.H. and X.D.; visualization, X.L. (Xinbao Liu), M.J. and X.L. (Xiangnan Liu); supervision, M.J; project administration, M.J.; funding acquisition, M.J., Z.Y., Z.H. and X.D. All authors have read and agreed to the published version of the manuscript.

Funding: This research was funded by the National Natural Science Foundation of China (Grant No. 42302266), the Fundamental Research Funds of the Chinese Academy of Geological Sciences (Grant No. J2412), and the National Key Research and Development Program of China (2024YFF0807700).

Data Availability Statement: The original contributions presented in the study are included in the article, further inquiries can be directed to the corresponding author.

Conflicts of Interest: The authors declare no conflicts of interest.

References

1. Bishop, J.L.; Loizeau, D.; McKeown, N.K.; Saper, L.; Dyar, M.D.; Des Marais, D.J.; Parente, M.; Murchie, S.L. What the ancient phyllosilicates at Mawrth Vallis can tell us about possible habitability on early Mars. *Planet. Space Sci.* **2013**, *86*, 130–149. [CrossRef]
2. Bibring, J.-P.; Langevin, Y.; Mustard, J.F.; Poulet, F.O.; Arvidson, R.; Gendrin, A.; Gondet, B.; Mangold, N.; Pinet, P.; Forget, F.; et al. Global Mineralogical and Aqueous Mars History Derived from OMEGA/Mars Express Data. *Science* **2006**, *312*, 400–404. [CrossRef] [PubMed]
3. McKeown, N.K.; Bishop, J.L.; Noe Dobrea, E.Z.; Ehlmann, B.L.; Parente, M.; Mustard, J.F.; Murchie, S.L.; Swayze, G.A.; Bibring, J.P.; Silver, E.A. Characterization of phyllosilicates observed in the central Mawrth Vallis region, Mars, their potential formational processes, and implications for past climate. *J. Geophys. Res. Planets* **2009**, *114*, E00D10. [CrossRef]
4. Noe Dobrea, E.Z.; Bishop, J.L.; McKeown, N.K.; Fu, R.; Rossi, C.M.; Michalski, J.R.; Heinlein, C.; Hanus, V.; Poulet, F.; Mustard, R.J.F.; et al. Mineralogy and stratigraphy of phyllosilicate-bearing and dark mantling units in the greater Mawrth Vallis/west Arabia Terra area: Constraints on geological origin. *J. Geophys. Res. Planets* **2010**, *115*, E00D19. [CrossRef]
5. Ruesch, O.; Poulet, F.; Vincendon, M.; Bibring, J.P.; Carter, J.; Erkeling, G.; Gondet, B.; Hiesinger, H.; Ody, A.; Reiss, D. Compositional investigation of the proposed chloride-bearing materials on Mars using near-infrared orbital data from OMEGA/MEx. *J. Geophys. Res. Planets* **2012**, *117*, E00J13. [CrossRef]
6. Ehlmann, B.L.; Berger, G.; Mangold, N.; Michalski, J.R.; Catling, D.C.; Ruff, S.W.; Chassefière, E.; Niles, P.B.; Chevrier, V.; Poulet, F. Geochemical Consequences of Widespread Clay Mineral Formation in Mars' Ancient Crust. *Space Sci. Rev.* **2012**, *174*, 329–364. [CrossRef]
7. Poulet, F.; Carter, J.; Bishop, J.L.; Loizeau, D.; Murchie, S.M. Mineral abundances at the final four curiosity study sites and implications for their formation. *Icarus* **2014**, *231*, 65–76. [CrossRef]
8. Sunshine, J.M.; Pieters, C.M. Estimating Modal Abundances from the Spectra of Natural and Laboratory Pyroxene Mixtures Using the Modified Gaussian Model. *J. Geophys. Res. Planets* **1993**, *98*, 9075–9087. [CrossRef]
9. Poulet, F.; Mangold, N.; Loizeau, D.; Bibring, J.P.; Langevin, Y.; Michalski, J.; Gondet, B. Abundance of minerals in the phyllosilicate-rich units on Mars. *Astron. Astrophys.* **2008**, *487*, L41–L44. [CrossRef]
10. Keshava, N.; Mustard, J.F. Spectral unmixing. *IEEE Signal Process. Mag.* **2002**, *19*, 44–57. [CrossRef]
11. Mustard, J.F.; Pieters, C.M. Photometric phase functions of common geologic minerals and applications to quantitative analysis of mineral mixture reflectance spectra. *J. Geophys. Res. Solid Earth* **1989**, *94*, 13619–13634. [CrossRef]
12. Hapke, B. *Theory of Reflectance and Emittance Spectroscopy*; Cambridge University Press: Cambridge, UK, 2012.
13. Liu, Y.; Stachurski, F.; Liu, Z.; Zou, Y. Quantitative assessment of water content and mineral abundances at Gale crater on Mars with orbital observations. *Astron. Astrophys.* **2020**, *637*, A79. [CrossRef]
14. Liu, Y.; Glotch, T.D.; Scudder, N.A.; Kraner, M.L.; Condus, T.; Arvidson, R.E.; Guinness, E.A.; Wolff, M.J.; Smith, M.D. End-member identification and spectral mixture analysis of CRISM hyperspectral data: A case study on southwest Melas Chasma, Mars. *J. Geophys. Res. Planets* **2016**, *121*, 2004–2036. [CrossRef]
15. Liu, Y.; Goudge, T.A.; Catalano, J.G.; Wang, A. Spectral and stratigraphic mapping of hydrated minerals associated with interior layered deposits near the southern wall of Melas Chasma, Mars. *Icarus* **2018**, *302*, 62–79. [CrossRef]
16. Roberts, D.A.; Gardner, M.; Church, R.; Ustin, S.; Scheer, G.; Green, R.O. Mapping Chaparral in the Santa Monica Mountains Using Multiple Endmember Spectral Mixture Models. *Remote Sens. Environ.* **1998**, *65*, 267–279. [CrossRef]
17. Iordache, M.-D.; Bioucas-Dias, J.M.; Plaza, A. Sparse Unmixing of Hyperspectral Data. *IEEE Trans. Geosci. Remote Sens.* **2011**, *49*, 2014–2039. [CrossRef]
18. Combe, J.P.; Le Mouélic, S.; Sotin, C.; Gendrin, A.; Mustard, J.F.; Le Deit, L.; Launeau, P.; Bibring, J.P.; Gondet, B.; Langevin, Y.; et al. Analysis of OMEGA/Mars Express data hyperspectral data using a Multiple-Endmember Linear Spectral Unmixing Model (MELSUM): Methodology and first results. *Planet. Space Sci.* **2008**, *56*, 951–975. [CrossRef]

19. Mouélic, S.L.; Sarago, V.; Combe, J.-P.; Massé, M.; Bourgeois, O.; Mangold, N.; Bibring, J.-P.; Gondet, B.; Langevin, Y.; Sotin, C. Global Mapping of Minerals on Mars with OMEGA Hyperspectral Data: Results of a Linear Unmixing Approach. In Proceedings of the 40th Lunar and Planetary Science Conference, Woodlands, TX, USA, 23–27 March 2009.
20. Zhang, X.; Shuai, T.; Lin, H. Abundance retrieval of hydrous minerals around the mars science laboratory landing site. *Planet. Space Sci.* **2016**, *121*, 76–82.
21. Iordache, M.-D.; Bioucas-Dias, J.M.; Plaza, A. Total Variation Spatial Regularization for Sparse Hyperspectral Unmixing. *IEEE Trans. Geosci. Remote Sens.* **2012**, *50*, 4484–4502. [CrossRef]
22. Lin, H.; Zhang, X. Retrieving the hydrous minerals on Mars by sparse unmixing and the Hapke model using MRO/CRISM data. *Icarus* **2017**, *288*, 160–171. [CrossRef]
23. Lin, H.; Mustard, J.F.; Zhang, X. A methodology for quantitative analysis of hydrated minerals on Mars with large endmember library using CRISM near-infrared data. *Planet. Space Sci.* **2019**, *165*, 124–136. [CrossRef]
24. Carter, J.; Poulet, F.; Bibring, J.-P.; Mangold, N.; Murchie, S. Hydrous minerals on Mars as seen by the CRISM and OMEGA imaging spectrometers: Updated global view. *J. Geophys. Res. Planets* **2013**, *118*, 831–858. [CrossRef]
25. Chen, J.; Yang, C.; Zhang, L.; Yang, L.; Bian, L.; Luo, Z.; Wang, J. TCCU-Net: Transformer and CNN Collaborative Unmixing Network for Hyperspectral image. *IEEE J. Sel. Top. Appl. Earth Obs. Remote Sens.* **2024**, *17*, 8073–8089. [CrossRef]
26. Wang, B.; Yao, H.; Song, D.; Zhang, J.; Gao, H. SSF-Net: A Spatial–Spectral Features Integrated Autoencoder Network for Hyperspectral Unmixing. *IEEE J. Sel. Top. Appl. Earth Obs. Remote Sens.* **2023**, *17*, 1781–1794. [CrossRef]
27. Shao, Y.; Liu, Q.; Xiao, L. IVIU-Net: Implicit Variable Iterative Unrolling Network for Hyperspectral Sparse Unmixing. *IEEE J. Sel. Top. Appl. Earth Obs. Remote Sens.* **2023**, *16*, 1756–1770. [CrossRef]
28. Sun, L.; Chen, Y.; Li, B. SISLU-Net: Spatial Information-Assisted Spectral Information Learning Unmixing Network for Hyperspectral Images. *Remote Sens.* **2023**, *15*, 817. [CrossRef]
29. Poulet, F.; Mangold, N.; Platevoet, B.; Bardintzeff, J.M.; Sautter, V.; Mustard, J.F.; Bibring, J.P.; Pinet, P.; Langevin, Y.; Gondet, B.; et al. Quantitative compositional analysis of martian mafic regions using the MEx/OMEGA reflectance data. *Icarus* **2009**, *201*, 84–101. [CrossRef]
30. Hapke, B. Bidirectional reflectance spectroscopy: 1. Theory. *J. Geophys. Res. Solid Earth* **1981**, *86*, 3039–3054. [CrossRef]
31. Fraeman, A.A.; Arvidson, R.E.; Murchie, S.L.; Rivkin, A.; Bibring, J.P.; Choo, T.H.; Gondet, B.; Humm, D.; Kuzmin, R.O.; Manaud, N.; et al. Analysis of disk-resolved OMEGA and CRISM spectral observations of Phobos and Deimos. *J. Geophys. Res. Planets* **2012**, *117*, E00J15. [CrossRef]
32. Li, F.; Ren, G.; Lee, J. Multi-step wind speed prediction based on turbulence intensity and hybrid deep neural networks. *Energy Convers. Manag.* **2019**, *186*, 306–322. [CrossRef]
33. Langevin, Y.; Bibring, J.P.; Montmessin, F.; Forget, F.; Vincendon, M.; Douté, S.; Poulet, F.; Gondet, B. Observations of the south seasonal cap of Mars during recession in 2004–2006 by the OMEGA visible/near-infrared imaging spectrometer on board Mars Express. *J. Geophys. Res. Planets* **2007**, *112*, E08S12. [CrossRef]
34. Mustard, J.F.; Murchie, S.L.; Pelkey, S.M. Hydrated silicate minerals on Mars observed by the Mars Reconnaissance Orbiter CRISM instrument. *Nature* **2008**, *454*, 305–309. [CrossRef] [PubMed]
35. Ehlmann, B.L.; Mustard, J.F.; Swayze, G.A.; Clark, R.N.; Bishop, J.L.; Poulet, F.; Marais, D.J.D.; Roach, L.H.; Milliken, R.E.; Wray, J.J.; et al. Identification of hydrated silicate minerals on Mars using MRO-CRISM: Geologic context near Nili Fossae and implications for aqueous alteration. *J. Geophys. Res. Planets* **2009**, *114*, E00D08. [CrossRef]
36. Lin, H.; Tarnas, J.D.; Mustard, J.F.; Zhang, X.; Wei, Y.; Wan, W.; Klein, F.; Kellner, J.R. Dynamic aperture factor analysis/target transformation (DAFA/TT) for Mg-serpentine and Mg-carbonate mapping on Mars with CRISM near-infrared data. *Icarus* **2021**, *355*, 114168. [CrossRef]
37. Thomas, N.H.; Bandfield, J.L. Identification and refinement of martian surface mineralogy using factor analysis and target transformation of near-infrared spectroscopic data. *Icarus* **2017**, *291*, 124–135. [CrossRef]
38. Saranathan, A.M.; Parente, M. Adversarial feature learning for improved mineral mapping of CRISM data. *Icarus* **2021**, *355*, 114107. [CrossRef]
39. Kodikara, G.R.L.; McHenry, L.J.; van der Meer, F.D. Application of deep learning and spectral deconvolution for estimating mineral abundances of zeolite, Mg-sulfate and montmorillonite mixtures and its implications for Mars. *Planet. Space Sci.* **2022**, *223*, 105579. [CrossRef]
40. Hazen, R.M.; Downs, R.T.; Morrison, S.M.; Tutolo, B.M.; Blake, D.F.; Bristow, T.F.; Chipera, S.J.; McSween, H.Y.; Ming, D.; Morris, R.V.; et al. On the Diversity and Formation Modes of Martian Minerals. *J. Geophys. Res. Planets* **2023**, *128*, e2023JE007865. [CrossRef]
41. Jin, M.; Ding, X.; Han, H.; Pang, J.; Wang, Y. An improved method combining Fisher transformation and multiple endmember spectral mixture analysis for lunar mineral abundance quantification using spectral data. *Icarus* **2022**, *380*, 115008. [CrossRef]

42. Viviano, C.E.; Seelos, F.P.; Murchie, S.L.; Kahn, E.G.; Seelos, K.D.; Taylor, H.W.; Taylor, K.; Ehlmann, B.L.; Wiseman, S.M.; Mustard, J.F.; et al. Revised CRISM spectral parameters and summary products based on the currently detected mineral diversity on Mars. *J. Geophys. Res. Planets* **2014**, *119*, 1403–1431. [CrossRef]
43. Wu, X.; Zhang, X.; Lin, H. Retrieval of Mineral Abundances of the Delta Region in Eberswalde, Mars. *Int. Arch. Photogramm. Remote Sens. Spat. Inf. Sci.* **2017**, *42*, 171–176. [CrossRef]
44. Malin, M.C.; Edgett, K.S. Evidence for Persistent Flow and Aqueous Sedimentation on Early Mars. *Science* **2003**, *302*, 1931–1934. [CrossRef]
45. Heard, A.W.; Dauphas, N.; Guilbaud, R.; Rouxel, O.J.; Butler, I.B.; Nie, N.X.; Bekker, A. Triple iron isotope constraints on the role of ocean iron sinks in early atmospheric oxygenation. *Science* **2020**, *370*, 446–449. [CrossRef] [PubMed]
46. Manning, C.V.; McKay, C.P.; Zahnle, K.J. Nitrates on Mars: Evidence from the 15/14N isotopic ratio. In Proceedings of the AGU Fall Meeting, San Francisco, CA, USA, 10–14 December 2007; p. P13D-1556.
47. Sefton-Nash, E.; Catling, D.C.; Wood, S.E.; Grindrod, P.M.; Teanby, N.A. Topographic, spectral and thermal inertia analysis of interior layered deposits in Iani Chaos, Mars. *Icarus* **2012**, *221*, 20–42. [CrossRef]

Disclaimer/Publisher's Note: The statements, opinions and data contained in all publications are solely those of the individual author(s) and contributor(s) and not of MDPI and/or the editor(s). MDPI and/or the editor(s) disclaim responsibility for any injury to people or property resulting from any ideas, methods, instructions or products referred to in the content.

remote sensing

MDPI

Article

Comprehensive Evaluation of the Lunar South Pole Landing Sites Using Self-Organizing Maps for Scientific and Engineering Purposes

Hengxi Liu [1], Yongzhi Wang [1,2,*], Shibo Wen [1], Sheng Zhang [3], Kai Zhu [4,5] and Jianzhong Liu [4,5]

[1] College of Geoexploration Science and Technology, Jilin University, Changchun 130026, China; hxliu22@mails.jlu.edu.cn (H.L.); wensb23@mails.jlu.edu.cn (S.W.)
[2] Institute of Integrated Information for Mineral Resources Prediction, Jilin University, Changchun 130026, China
[3] College of Resources and Environment Engineering, Guizhou University, Guiyang 550025, China; shengzhang0110@yeah.net
[4] Institute of Geochemistry, Chinese Academy of Sciences, Guiyang 550081, China; zhukai@mail.gyig.ac.cn (K.Z.); liujianzhong@mail.gyig.ac.cn (J.L.)
[5] CAS Center for Excellence in Comparative Planetology, Chinese Academy of Sciences, Hefei 230026, China
* Correspondence: wangyongzhi@jlu.edu.cn; Tel.: +86-135-7892-4673

Abstract: The permanently shadowed regions of the lunar South Pole have become a key target for international lunar exploration due to their unique scientific value and engineering challenges. In order to effectively screen suitable landing zones near the lunar South Pole, this research proposes a comprehensive evaluation method based on a self-organizing map (SOM). Using multi-source remote sensing data, the method classifies and analyzes candidate landing zones by combining scientific purposes (such as hydrogen abundance, iron oxide abundance, gravity anomalies, water ice distance analysis, and geological features) and engineering constraints (such as Sun visibility, Earth visibility, slope, and roughness). Through automatic clustering, the SOM model finds the important regions. Subsequently, it integrates with a supervised learning model, a random forest, to determine the feature importance weights in more detail. The results from the research indicate the following: the areas suitable for landing account for 9.05%, 5.95%, and 5.08% in the engineering, scientific, and synthesized perspectives, respectively. In the weighting analysis of the comprehensive data, the weights of Earth visibility, hydrogen abundance, kilometer-scale roughness, and slope data all account for more than 10%, and these are thought to be the four most important factors in the automated site selection process. Furthermore, the kilometer-scale roughness data are more important in the comprehensive weighting, which is in line with the finding that the kilometer-scale roughness data represent both surface roughness from an engineering perspective and bedrock geology from a scientific one. In this study, a local examination of typical impact craters is performed, and it is confirmed that all 10 possible landing sites suggested by earlier authors are within the appropriate landing range. The findings demonstrate that the SOM-model-based analysis approach can successfully assess lunar South Pole landing areas while taking multiple constraints into account, uncovering spatial distribution features of the region, and offering a rationale for choosing desired landing locations.

Keywords: selection of lunar South Pole landing zones; self-organizing map; comprehensive evaluation

1. Introduction

Because of its exceptional potential to answer important scientific issues, the lunar South Pole has become a top target for further exploration [1–3]. Over geological timeframes, volatiles like water ice can be trapped in permanently shadowed regions (PSRs), which are created by the Moon's slight axial tilt of 1.5°. In addition to providing in situ resources for sustainable human exploration and the establishment of lunar bases, these volatiles are crucial for understanding the formation and evolution of the Moon [4,5].

Compared to the North Pole, the lunar South Pole has a greater number of large PSRs and adjacent elevated terrains that receive near-constant sunlight [6–9]. It also overlaps with the South Pole-Aitken (SPA) Basin, one of the oldest and deepest impact basins in the solar system, making it an important region for sampling early lunar crust and understanding the inner solar system's impact history [10–13].

In response to this scientific and strategic value, multiple nations have launched or are planning polar exploration missions, including NASA's Artemis program and VIPER rover [14,15], the ESA's HERACLES mission [16], the ISRO's Chandrayaan missions [17], ROSCOSMOS's Luna-25 [18], and China's Chang'E program [19]. These missions share a common challenge: selecting safe and scientifically valuable landing sites within complex polar terrains.

Landing site selection at the lunar South Pole must balance multiple and often conflicting objectives: scientific return, engineering feasibility, resource accessibility, and long-term sustainability [20]. Traditional selection methods, such as multi-criteria decision analysis and expert-guided models [3,17,21], have played a critical role in enabling early identification of candidate regions, integrating expert knowledge with available remote sensing data, and providing structured decision frameworks to inform mission planning and risk assessment. These approaches were especially useful when data were limited or expert judgment was required. However, they frequently rely on subjective weighting, are susceptible to prior assumptions, and struggle with high-dimensional, multi-source remote sensing datasets. Furthermore, manually integrating multiple data layers and engaging in expert consultation processes can be time-consuming and labor-intensive [22]. These constraints limit the scalability and efficiency of standard approaches when applied to vast and complex polar terrains.

Recent advances in machine learning have allowed for data-driven techniques to evaluate lunar landing sites. Supervised learning methods, such as weighted ranking models [23], extreme gradient boosting models [24], and CNN-based scoring systems [25], have demonstrated promise by leveraging labeled data to attain high prediction accuracy and interpretable decision-making in well-characterized regions. However, their effectiveness is limited by the scarcity of labeled landing site data, particularly in unexplored regions. Clustering-based approaches [26,27] provide an alternative, although they frequently fail to adequately integrate various scientific and engineering restrictions.

To address these limitations, this study presents an unsupervised learning framework based on the self-organizing map (SOM) algorithm [28], which is ideal for extracting latent patterns from high-dimensional geospatial data. SOM has been widely used in remote sensing for unsupervised classification, land cover analysis, and pattern recognition, especially in cases requiring high-dimensional and multi-source data, when labeled samples are limited or unavailable [29]. In contrast to conventional techniques, SOM eliminates human bias and subjective assumptions by automatically clustering regions based on the underlying structure of the input data without the need for labeled data. It is useful for recognizing different kinds of data, displaying their distribution, and assessing their landing suitability because of its capacity to capture nonlinear dependencies and project multidimensional input into a two-dimensional network.

A sliding-window preprocessing technique is presented in order to further minimize spatial bias and the possibility of missing appropriate micro-regions. This guarantees that local spatial details are not overlooked and permits ongoing assessment throughout the lunar South Polar region [26]. By minimizing trial and error and enhancing model stability, Bayesian optimization is used to identify important hyperparameters such as grid size and iteration in order to maximize the performance of the SOM model.

Moreover, the feature importance analysis based on a random forest is performed on the clustering results to improve interpretability and evaluate the influence of various characteristics. This hybrid SOM and random forest framework offers a thorough assessment model by combining the interpretability of supervised learning with the scalability and data-driven structure discovery of unsupervised learning.

Above all, the objective of this research is to develop an intelligent, interpretable, and automated evaluation model for selecting landing zones in the lunar South Pole. The proposed framework integrates a variety of scientific factors, such as hydrogen abundance, kernel density analysis of geological maps, distance analysis of exposed water ice, iron oxide abundance, and gravity anomalies, along with engineering factors like solar illumination, communication, slope, and surface roughness. Using this extensive data set, the framework can handle nonlinear relationships, avoid the need for subjective weights, and ensure full spatial coverage. This makes it an effective tool for future polar exploration missions, as it provides a data-driven approach to optimal landing site selection.

2. Study Area and General Framework

2.1. Study Area

The lunar South Pole, as an important area for lunar scientific exploration, holds unique scientific value and exploration potential. Located at the edge of the South Pole-Aitken (SPA) Basin, the terrain is rough, and extreme lighting conditions prevail due to the Moon's small axial inclination [9,13,30]. Despite this, certain locations within the region, such as the areas near the Shackleton Crater and De Gerlach Crater, as well as the ridge connecting them, have areas that receive nearly continuous sunlight for over 80% of the time, providing ideal locations for future scientific missions [31,32]. Additionally, the solar panel lighting conditions can be significantly improved with minimal height gain (2–10 m), providing a stable power supply and making these regions key targets for future lunar exploration missions [8,33,34].

The lunar South Pole's average annual surface temperature is as low as 38 K, with the PSRs having temperatures low enough to effectively trap condensed volatiles such as water ice [35,36]. Remote sensing data show that water ice may exist on the surface or subsurface of some PSRs, with a strong correlation between surface ice and surface reflectance anomalies from the Lyman Alpha Mapping Project (LAMP) and LOLA 1064 nm data, supporting the theory of water ice in these regions [37]. Moreover, the Moon Mineralogy Mapper (M3) data reveal diagnostic near-infrared absorption features of water ice [38]. Hydrogen concentration data from the Lunar Energetic Neutron Detector (LEND) and LPNS estimate the water-equivalent hydrogen (WEH) value in the South Pole area to be 0.3–0.5 wt.%, indicating potential deposits of water ice and other volatile substances [39,40].

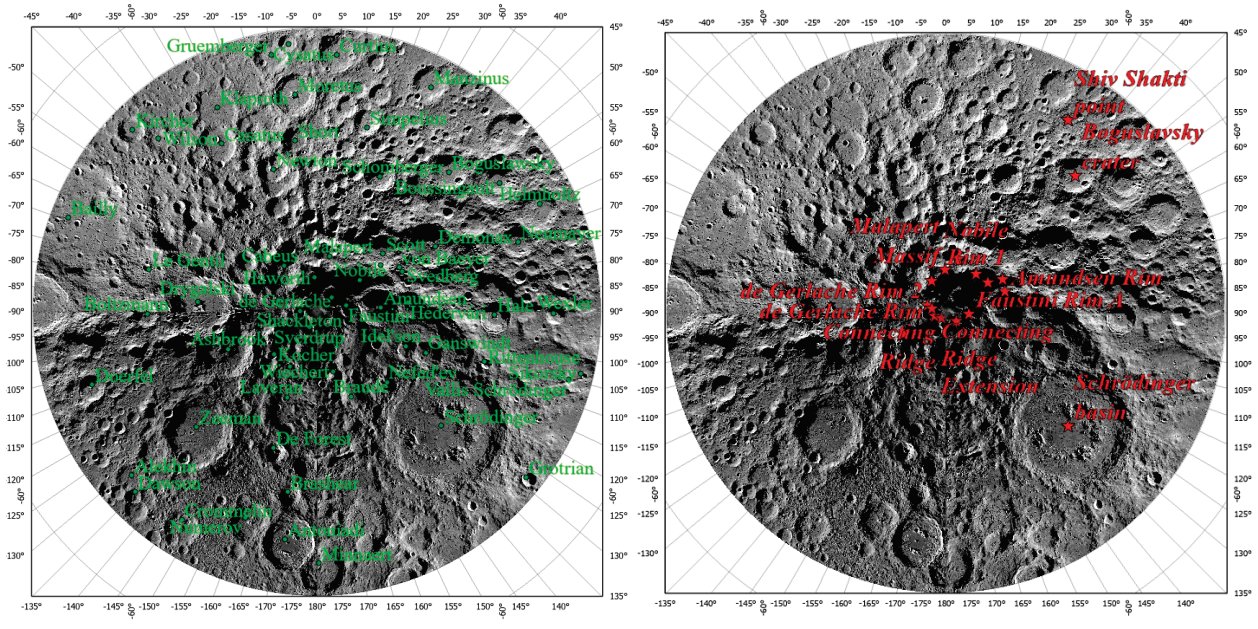
These characteristics of the lunar South Pole not only offer favorable environmental conditions for future long-term exploration on the Moon but also provide valuable insights into the volatile substance evolution of the solar system [41]. Recent observations, such as the impact plume from the LCROSS mission, revealed the presence of water ice and other volatile compounds, such as light hydrocarbons, sulfur compounds, and carbon dioxide, further confirming the South Pole's importance as a region for resource collection and energy utilization [42]. Additionally, the coexistence of high-illumination peaks and

PSRs at the South Pole offers unique opportunities for solar energy utilization and resource exploration [41,43]. These areas could contain frozen volatiles for consumables, radiation shielding, and propellants necessary for human habitation. Therefore, the lunar South Pole is not only a crucial area for scientific exploration but also a key location for future lunar exploration and utilization.

In an effort to resolve the debate over the presence of water ice and other cold-trapped volatiles at the lunar poles [2,36,38,44,45], different regions and organizations have announced new rounds of lunar South Pole exploration plans, as shown in Figure 1 and Table 1. This overview provides important context for the fundamental geographic distribution of landing site selections, and some of the sites listed are mentioned in the regional analysis presented in Section 4.3.

Table 1. Lunar South Pole exploration plans.

Region Name	Longitude°	Latitude°	Affiliated Organizations	Program	Country/Region	Date of Announcement
Amundsen Rim	69.35	−84.22	NASA	Artemis	USA	20 August 2022
Nobile Rim 2	58.83	−83.93	NASA	Artemis	USA	20 August 2022
Haworth	−22.8	−86.75	NASA	Artemis	USA	20 August 2022
Faustini Rim A	90.03	−87.87	NASA	Artemis	USA	20 August 2022
de Gerlache Rim 2	−64.42	−88.2	NASA	Artemis	USA	20 August 2022
Connecting Ridge Extension	−101.4	−89	NASA	Artemis	USA	20 August 2022
Connecting Ridge	−136.07	−89.05	NASA	Artemis	USA	20 August 2022
Nobile Rim 1	37.38	−85.42	NASA	Artemis	USA	20 August 2022
Peak Near Shackleton	123.37	−88.82	NASA	Artemis	USA	20 August 2022
de Gerlache Rim	−67.97	−88.07	NASA	Artemis	USA	20 August 2022
Leibnitz Beta Plateau	31.58	−85.4	NASA	Artemis	USA	20 August 2022
Malapert Massif	−0.42	−85.98	NASA	Artemis	USA	20 August 2022
de Gerlache-Kocher Massif	−116	−85.83	NASA	Artemis	USA	20 August 2022
Nobile Crater	53.49	−85.2	NASA	VIPER	USA	21 September 2021
Malapert A	12.88	−84.88	NASA	Nova-C	USA	25 May 2023
Schrödinger Basin	132.4	−74.98	ESA, JAXA, CSA	HERACLES	Europe, Japan, Canada	2015y
Boguslavsky Crater	43.2	−72.9	ROSCOSMOS	Luna-25	Russia	Late 1990s
Shiv Shakti Point	32.319	−69.373	ISRO	Chandrayaan-3	India	1 January 2020



(**a**) (**b**)

Figure 1. (**a**) WAC image map of the lunar South Pole superimposed with lunar place names and (**b**) landing sites associated with the lunar South Pole, with corresponding mission details provided in Table 1.

2.2. Framework

The general framework of SOM-based South Polar landing zone selection is given in Figure 2. This research uses a feature-level fusion strategy based on SOM to integrate multi-source scientific and engineering data, such as slope, Sun visibility, Earth visibility, and roughness, as well as water ice exposure, South Pole geologic maps, iron oxide abundance, gravity anomalies, and hydrogen abundance. The technique entails first resampling all input data to a consistent spatial resolution, then creating 10-dimensional feature vectors (corresponding to 10 input data sources) for each geographical unit, and finally applying min–max normalization to reduce scale variations.

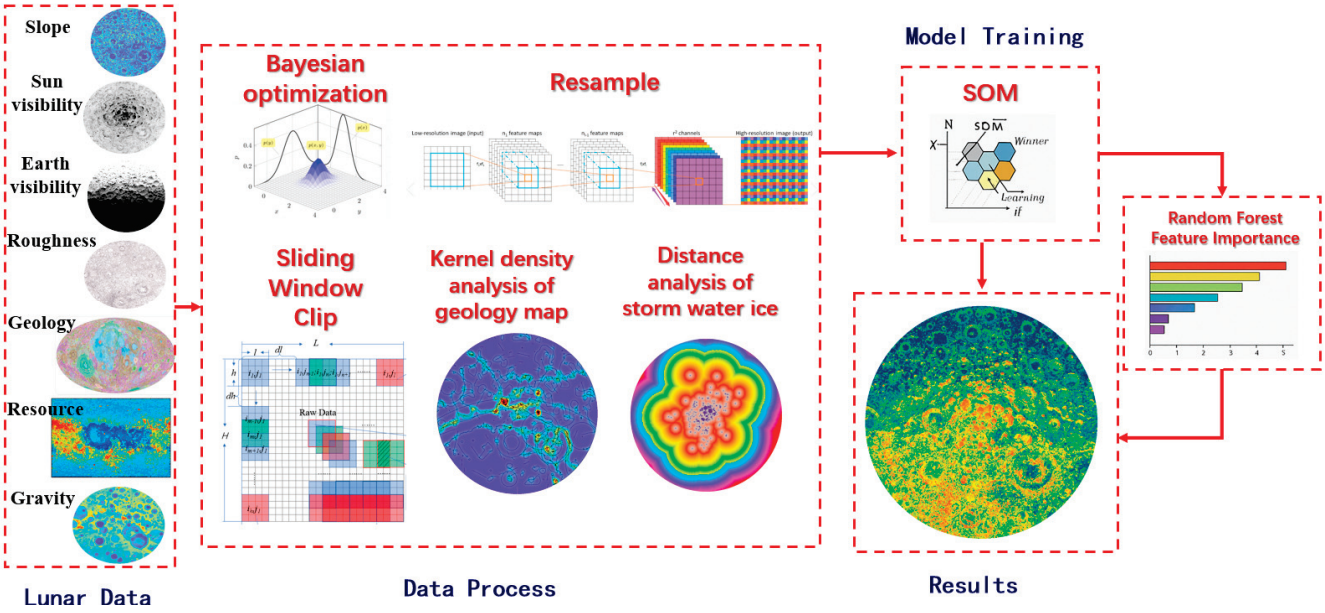


Figure 2. Schematic of SOM-based South Polar landing zone selection.

To address hyperparameter optimization in the SOM model, a Bayesian optimization technique automatically identifies the best network topology and training epoch and predicted improvement acquisition functions for efficient parameter space exploration. The input layer's neuron count is directly proportional to the data source dimensions (10 neurons for 10 data sources in the full model, or 5 neurons for 5 data sources in the engineering model), and all preprocessed feature data are supplied into the network at the same time.

The SOM automatically discovers nonlinear correlations between features using its competitive learning mechanism, resulting in synergistic grouping of multi-source data. To improve interpretability, post-training random forest analysis computes significance scores, which quantify each feature's contribution to clustering outcomes.

The final output neuron weight vectors indicate the best feature combination patterns, allowing for unsupervised clustering-based landing site selection. This strategy takes full advantage of SOM's topology-preserving properties to successfully retain high-dimensional feature associations in low-dimensional mapping space. By combining Bayesian optimization for automated parameter selection and random forest for feature importance analysis, the method achieves high-performance and interpretable data-driven feature-level fusion, offering dependable technological support for lunar South Polar landing site selection.

3. Materials and Methods

3.1. Data

For decades, research institutions and organizations have collected a large amount of remote sensing data that provide critical information on the presence or absence of cold-captured volatiles on the Moon. These data are categorized into engineering and scientific categories, and they include slope, Sun visibility, Earth visibility, and roughness, as well as water ice exposure, South Pole geologic maps, iron oxide abundance, gravity anomalies, and hydrogen abundance, as shown in Figure 3 and Table 2.

Table 2. Summary table of lunar South Pole remote sensing data.

	Data	Data Name	Resolution	Range
Engineering category	Slope	Lunar_LRO_LOLA_Global_SLOPE_118m_Mar2014	256 ppd	90N~90S
	Roughness m scale	LRO_LOLA_ClrRoughness_Global_16ppd_E8cu01	16 ppd	90N~90S
	Roughness km scale	LRO_LOLA_ClrRoughness_Global_16ppd_E8cu16	16 ppd	90N~90S
	Sun visibility	AVGVISIB_65S_240M_201608	240 m	65S~90S
	Earth visibility	AVGVISIB_65S_240M_201608_EARTH_SP	240 m	65S~90S
Science category	Iron oxide abundance	LRO_LOLA_Kaguya_SP_FeO_Abundance_SP_1km	1000 m	50S~90S
	Hydrogen abundance	Hydrogen_Abundances_PolarS	-	65S~90S
	Water ice	SP_IceLoc_280m	-	
	Gravitational anomaly	gggrx_1200a_anom_l1200.tif	5 km	90N~90S
	PSR	LOLA_81S_SP_PSR_STEREOGRAPHIC_10KM2_20170227.shp	-	80S~90S
	Geological map	LQ30.gdb	-	65S~90S

Engineering category:

Slope: The LOLA team mapped products describing the slope of the lunar surface at a resolution of 255 ppd (120 m over the equator) based on shape data from SLDEM2015 [46,47], and they are available from the Planetary Data System LOLA Data node (http://imbrium.mit.edu/EXTRAS/SLDEM2015/ (accessed on 18 June 2018)).

Sun visibility (illumination) and Earth visibility: LOLA-based solar and Earth visibility is obtained by time-averaging the results of computational modeling performed hourly for about 18.6 years, with a resolution of 240 m/pixel [9]. Mean visibility is a fraction of time equal to 0 when the Sun/Earth is not visible and 1 when any part of the Sun/Earth is visible. Illumination values represent the proportion of time that the Sun is visible from a given location.

Roughness: Kreslavsky et al. provided maps of the roughness of the lunar terrain on scales of meters and kilometers, derived from distance profiles obtained by the LOLA instrument (the Lunar Orbiting Laser Altimeter) onboard the Lunar Reconnaissance Orbiter LRO spacecraft, revealing features of the terrain that could not be analyzed with LOLA-based raster topographic maps at a resolution of 16 ppd [48].

Scientific category:

FeO: Lemelin et al. obtained an absolute reflectance data cube based on the Kaguya Spectral Profiler dataset depicting the first map of iron oxide (FeO) minerals in the polar regions with a spatial resolution of 1 km/pixel [49].

Hydrogen Abundance Map: Peplowski et al. corrected for variations in rare-earth elements by conducting an analysis similar to that of scholars who quantitatively understood rare-earth and thermal neutron variations [50]. A key aspect of this correction uses a quantitative baseline of rare earth element variations in the composition of lunar samples and applies these corrections to orbital data, yielding a complete global map of bulk hydrogen abundances across the lunar surface.

Gravity: GRAIL free-air gravity or gravitational perturbations were obtained at 16 pixels/degree with a reference radius of 1738 km using the GRGM1200A gravity model with an expansion of L = 660. They show the "free-air" variations as measured by the spacecraft and, therefore, include contributions from the surface relief and from any subsurface interfaces [51].

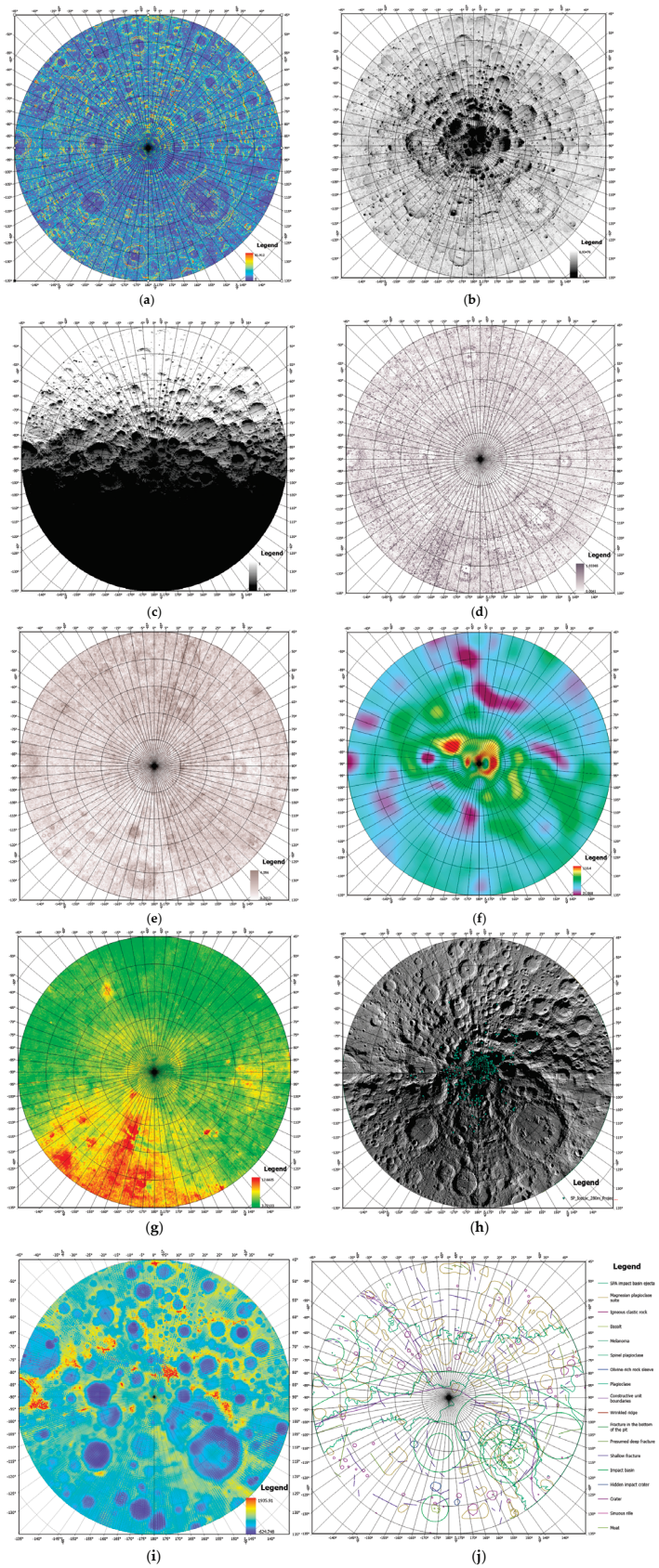


Figure 3. Summary of lunar South Pole data: (**a**–**j**) slope, Sun visibility, Earth visibility, roughness at the hm and km scales, hydrogen abundance, iron oxide content, exposed water ice, gravity anomalies, and a geological map. (**a**) Slope, (**b**) Sun visibility, (**c**) Earth visibility, (**d**) hectometer-scale roughness, (**e**) kilometer-scale roughness, (**f**) hydrogen abundance, (**g**) FeO, (**h**) exposed water ice, (**i**) gravity anomalies, and (**j**) geological map.

PSR: This study calculated horizon elevations in the polar regions (up to ∼75° latitude) from LOLA data and modeled the lighting conditions in the two polar regions (extending to ~80° latitude) to obtain the locations of the permanently shaded areas and the polar regions that are most well illuminated [9].

Geological map: Jinzhu Ji et al. [52] provided a 1:2,500,000 scale global geological map of the Moon, mainly using data from the China Lunar Exploration Project (CLEP) and international exploration missions, with distortions reduced by the division of 30 regions with different map projections, and mapped using the ESRI ArcMap platform. The lunar geological map is divided into three periods, Eolunarian, Paleolunarian, and Neolunarian, according to the geological time scale, and defines 90 geological units covering impact craters, basin formation, endogenous orogeny, and so on. The map illustrates lunar impact basins, craters, rock types, and geological structures, providing key data on the Moon's geological evolution and support for lunar base construction.

Water ice exposure: The process of detecting surface-exposed water ice in the lunar polar regions involves using near-infrared (NIR) reflectance spectral data obtained from the Moon Mineralogy Mapper (M^3). After thermal calibration and projection processing, shadowed regions are identified by combining LOLA topographic data. By analyzing the absorption features of water ice in the spectra and comparing them with laboratory water ice spectra, the presence and distribution of water ice are ultimately confirmed [38].

In the selection of lunar South Pole landing sites, the above data can be used for a comprehensive assessment of the suitability of candidate regions. Slope, illumination, Earth visibility, and roughness are engineering factors that directly impact landing safety and mission feasibility; for example, smaller slopes aid in stable landings, areas with continuous illumination provide reliable energy, good communication conditions ensure data transmission, and lower surface roughness reduces mechanical damage risks. However, water ice exposure, South Pole geological maps, iron oxide abundance, gravity anomalies, and hydrogen abundance are scientific factors that determine the research value and resource utilization potential of landing sites. For example, water ice resources can be used for fuel production and life support; geological features reveal the moon's evolutionary history; ilmenite ($FeTiO_3$), concentrated in high-FeO terrains (lunar maria), offers a readily reducible source of oxygen and titanium for in situ construction and manufacturing and can be a potential source of helium-3 [53,54]; gravity anomalies reflect subsurface structures; and hydrogen abundance suggests possible volatile distributions. Through the SOM method, these factors can be comprehensively analyzed to identify the optimal landing regions that satisfy both engineering and scientific requirements.

3.2. Method

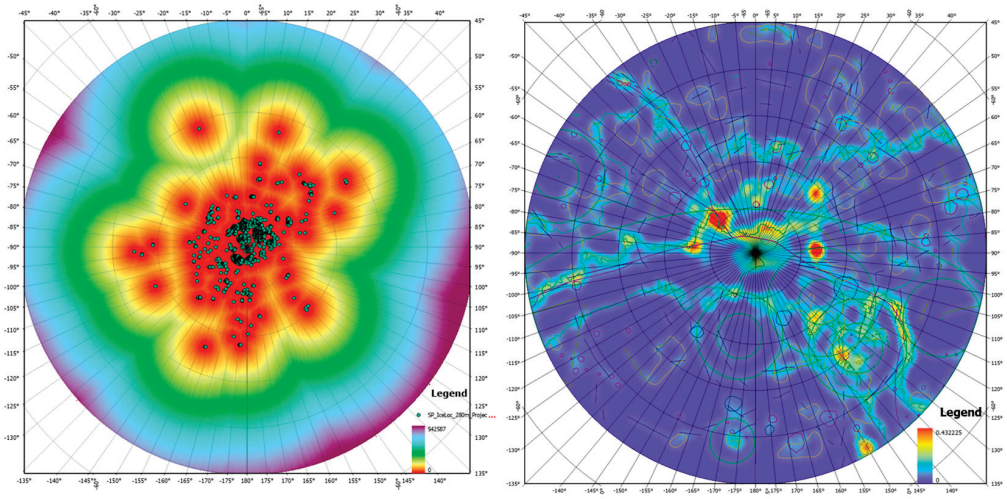
A self-organizing map (SOM) is an unsupervised learning algorithm. The proposed artificial neural network is capable of mapping high-dimensional data into a low-dimensional representation space. It is a popular tool for high-dimensional analysis, dimensionality reduction, classification, and visualization. Its applications can be found in many research fields (robotics, healthcare, social sciences, and document mining). The nodes of the SOM can be trained without supervision and are able to preserve the topology of the input data, which facilitates the understanding of the intrinsic relationships of the data. In this study, a SOM is trained as a landing suitability model for learning site selection based on engineering elements, scientific elements, and integrated elements.

3.2.1. Preprocessing of Datasets

Before the training process, in order to obtain the dataset for model training, first, the resolution is unified for all of the data using the resampling method; then, the sliding

window method is used for the data to slide in a window with a spatial step of 0.03125° and a sliding interval of 0.015°. The data points within a single window are averaged, and with the area of 65°S–90°S for any data range, 1599 × 23,039 data points are obtained.

For the vector layers (water ice exposure and geological maps) that could not be input as a quantitative form for model training, different quantitative treatments were performed; for the water ice exposure in the South Pole region, the distance analysis method was utilized, where each window of the South Pole division was regarded as the Euclidean distance between the point and the nearest exposed water ice point. This technique was implemented using the toolbox of ArcGIS Pro 3.0.2. The results are shown in Figure 4a.



(**a**) (**b**)

Figure 4. (**a**) Analysis of water ice distances; (**b**) Kernel density analysis of the geologic map.

For the geological map, the quantitative results of the scientific element set were obtained using kernel density analysis, which was used to calculate the density of an element in its surrounding neighborhood. For the predicted density of (*x*,*y*) predicted points,

$$\text{Density} = \frac{1}{(radius)^2} \sum_{i=1}^{n} \left[\frac{3}{\pi} \cdot pop_i \left(1 - \left(\frac{dist_i}{radius} \right)^2 \right)^2 \right] \quad For(dist < radius) \tag{1}$$

where $i = 1, \ldots, n$ are the input points. Only the points in the sum are included if they lie within a radius distance of the (*x*,*y*) location. pop_i is the value of the population field for point *i*, which is an optional parameter. *disti* is the distance between point *i* and the location (*x*,*y*). The calculated density is then multiplied by the number of points, or by the sum of the population fields, if any. This correction makes the spatial integral equal to the number of points (or the sum of the population field) rather than always equal to 1. This implementation uses a quadratic kernel. Separate equations need to be computed for each location where density is to be estimated. Since a raster is being created, the calculation will be applied to the center of each pixel in the output raster.

The formula used to determine the default search radius (also known as the bandwidth) is as follows:

$$SearchRadius = 0.9 \cdot \min\left(SD, \sqrt{\frac{1}{In(2)}} \cdot D_m \right) \cdot n^{-0.2} \tag{2}$$

D_m is the (weighted) median distance from the (weighted) center of the mean. *n* is the number of points for which the *population* field is not used, and *n* is the sum of the values

of the *population* field if one is supplied. *SD* is the standard distance, which is computed as follows:

$$SD = \sqrt{\frac{\sum_{i=1}^{n}(x_i - \overline{X})^2}{n} + \frac{\sum_{i=1}^{n}(y_i - \overline{Y})^2}{n} + \frac{\sum_{i=1}^{n}(z_i - \overline{Z})^2}{n}} \quad (3)$$

where x_i, y_i, and z_i are the coordinates of element i denoting the mean center of the element, and N is equal to the total number of elements. The kernel density analysis of the geological map is shown in Figure 4b.

3.2.2. Working Mechanism of the SOM

The working process of the SOM can be divided into the following stages.

The SOM has a two-layer network structure. The input layer has n nodes corresponding to the n feature dimensions of the input samples. The output layer, also called the competition layer, has a node distribution that usually has a lower dimension (commonly two dimensions).

As can be seen from the learning process later, each node in the competitive layer is also represented by a feature vector of dimension. Therefore, each node can be regarded as a "clustering center", and the learning process of the SOM is to map each input datum to a node in the competitive layer and to make closer the input data that are closer in the input space to the geometric position of the nodes in the competitive layer.

The number of nodes in the competitive layer determines the size of the SOM, which should have a sufficient number of nodes to ensure the accuracy and generalization ability of the model. An empirical formula for the minimum number of nodes that a 2D competitive network layer should have is given in the following equation:

$$\mathrm{Nodes}_{\min} = \sqrt{5\sqrt{\mathrm{n}}} \quad (4)$$

where $Nodes_{min}$ refers to the minimum number of nodes required for the network layer and n represents the number of input features.

Weight update: The weight vector of the node is updated using the following formula:

$$w_j(t+1) = w_j(t) + a(t)h_{j,w_c}(t)(x(t) - w_j(t)) \quad (5)$$

where $w_j(t)$ is the weight vector of node j, $a(t)$ is the learning rate, $h_{j,wc}(t)$ is the neighborhood function, and $x(t)$ is the input vector. As the number of training times increases, the learning rate and neighborhood radius gradually decrease, and the SOM network gradually converges, eventually forming a topological mapping to the input data.

3.2.3. Model Evaluation Parameters

The quantization error is a measure of the average of the distances between the input data points and their best-match units (BMUs). It reflects the accuracy of the SOM model's representation of the input data. The smaller the quantization error, the more accurate the SOM model's representation of the input data.

$$QE = \frac{1}{N}\sum_{i=1}^{N} \parallel x_i - wBMU_i \parallel \quad (6)$$

The topological error measures whether the BMUs and sub-BMUs (i.e., second closest neurons) of the input data points are neighbors. A smaller topological error indicates that the SOM network performs better in maintaining the topology of the data.

$$TE = \frac{1}{N}\sum_{i=1}^{N} e_i \tag{7}$$

The contour coefficient is a metric used to assess the quality of clustering. It combines the distance of each data point from data points within the same cluster and its distance from the nearest other clustered data points. The contour coefficient can take values between -1 and 1. The larger the value, the more suitable the data point is for the cluster that it is in and the better the clustering effect. For any sample i in the dataset, the procedure for calculating the contour coefficient $s(i)$ is as follows:

For the cluster distance ($a(i)$), for the sample i in the cluster C, calculate the average distance between i and all other points in C, which is written as $a(i)$:

$$a(i) = \frac{1}{|C|-1}\sum_{j\in C, j\neq i} d(i,j) \tag{8}$$

where $d(i,j)$ denotes the distance between sample i and sample j.

Calculation of the inter-cluster distance ($b(i)$): For the cluster C where sample i is located, we calculate the average distance between i and all points in other clusters C', denoted as $b(i)$. Among all other clusters, we choose the smallest average distance $b(i)$.

$$b(i) = \min_{C\prime\neq C}\frac{1}{|C\prime|}\sum_{j\in C\prime} d(i,j) \tag{9}$$

Calculation of the contour coefficient ($s(i)$): Based on the intra-cluster distance and inter-cluster distance, we calculate the contour coefficient of sample i.

$$s(i) = \frac{b(i)-a(i)}{\max(a(i),b(i))} \tag{10}$$

The overall profile coefficient of the dataset is the average of all sample profile coefficients:

$$s = \frac{1}{n}\sum_{i=1}^{n} s(i) \tag{11}$$

Contour coefficients close to 1 indicate good clustering, those close to 0 indicate that the data points lie on the boundary of two clusters, and negative values indicate that samples may be misclassified into the wrong cluster.

3.2.4. Bayes Optimization Approach in SOM Parameter Selection

In order to improve the performance of the SOM model, this study uses Bayesian optimization to optimize the key parameters of the SOM, including the learning rate, neighborhood radius, and the number of training iterations. Bayesian optimization approximates the objective function by constructing an agent model and using the model to select the next set of parameters, thus finding the optimal parameter combination within a limited number of evaluations.

Bayesian optimization is a global optimization method based on probabilistic models and is a strategy used for global optimization that is particularly suitable for optimizing computationally expensive black-box functions. Bayesian optimization finds the optimal solution in the least number of function evaluations by constructing an agent model (usually a Gaussian process or a tree-structured model), approximating the objective function, and

using the agent model to select the next sampling point. The main steps include the following:

Surrogate model: Bayesian optimization uses a surrogate model to approximate the objective function $f(x)$. The commonly used surrogate model is a Gaussian process.

A Gaussian process is a nonparametric Bayesian model used to define the prior distribution of the distribution function $f(x)$. Suppose that the true value of the objective function $f(x)$ is y; then,

$$y \sim GP(m(x), k(x, x\prime)) \tag{12}$$

where $m(x)$ is the mean function and $k(x, x')$ is the covariance function. In the simple case, the mean function is usually set to zero, $m(x) = 0$. The covariance function usually uses a kernel function, the radial basis function:

$$k(x, x\prime) = \sigma_f^2 \exp(-\frac{\| x - x\prime \|^2}{2l^2}) \tag{13}$$

where σf^2 is the signal variance and l is the length scale. The next set of parameters is selected for evaluation by maximizing the expected improvement (EI) or other sampling strategies. A commonly used collection function is the expected improvement, which is defined as follows:

$$\partial EI(x) = E\big[\max\big(f(x) - f(x^+), 0\big)\big] \tag{14}$$

where x^+ is the current optimal point. For specific calculations, assuming that the current optimum is $f(x^+)$, and the mean and variance at the new point x are $\mu(x)$ and $\sigma(x)$, respectively, the expected improvement can be expressed as follows:

$$\partial EI(x) = \big(\mu(x) - f(x^+) - \xi\big)\varphi(Z) + \sigma(x)\phi(Z) \tag{15}$$

$$Z = \frac{\mu(x) - f(x^+) - \xi}{\sigma(x)} \tag{16}$$

where $\Phi(Z)$ is the cumulative distribution function of the standard normal distribution, $\phi(Z)$ is the probability density function of the standard normal distribution, and ξ is a tuning parameter for balancing exploration and exploitation.

We set the objective function as follows: quantization error + topology error—profile coefficient.

Parameter update: We update the agent model using the results of the new evaluation and repeat the process until the stopping condition is satisfied.

Based on the training records of Bayesian hyperparameter optimization from Table 3 and Figure 5b, the optimal grid size is found to be 10, and the optimal number of iterations is 69.

Table 3. Table of Bayesian hyperparametric optimization processes.

Iteration	Evaluation Result	Objective	Best (Observed)	Best (Estimation)	Grid Size	Epoch
1	Best	3.05	3.05	3.05	6	40
2	Best	2.82	2.82	2.82	9	49
3	Best	2.73	2.73	2.73	10	46
4	Accept	2.8	2.73	2.73	9	204
5	Accept	3.05	2.73	2.73	6	592
6	Accept	2.80	2.73	2.73	9	587
7	Accept	2.90	2.73	2.73	8	464

Table 3. *Cont.*

Iteration	Evaluation Result	Objective	Best (Observed)	Best (Estimation)	Grid Size	Epoch
8	Accept	2.73	2.73	2.73	10	264
9	Accept	2.76	2.73	2.73	10	547
10	Accept	2.87	2.73	2.73	8	1008
11	Accept	2.74	2.73	2.73	10	11
12	Best	2.73	2.73	2.73	10	141
13	Best	2.72	2.72	2.72	10	90
14	Accept	2.76	2.72	2.72	10	1010
15	Accept	2.74	2.72	2.72	10	753
16	Accept	3.17	2.72	2.72	5	1009
17	Accept	2.74	2.72	2.72	10	85
18	Accept	2.74	2.72	2.72	10	379
19	Accept	2.74	2.72	2.72	10	88
20	Accept	2.80	2.72	2.72	9	99
21	Accept	2.80	2.72	2.72	9	118
22	Accept	2.74	2.72	2.72	10	114
23	Best	2.71	2.71	2.71	10	69
24	Accept	2.72	2.71	2.71	10	29
25	Accept	2.72	2.71	2.71	10	100
26	Accept	2.87	2.71	2.71	8	10
27	Accept	2.88	2.71	2.71	8	150
28	Accept	2.79	2.71	2.71	9	1009
29	Accept	2.79	2.71	2.71	9	74
30	Accept	3.17	2.71	2.71	5	84

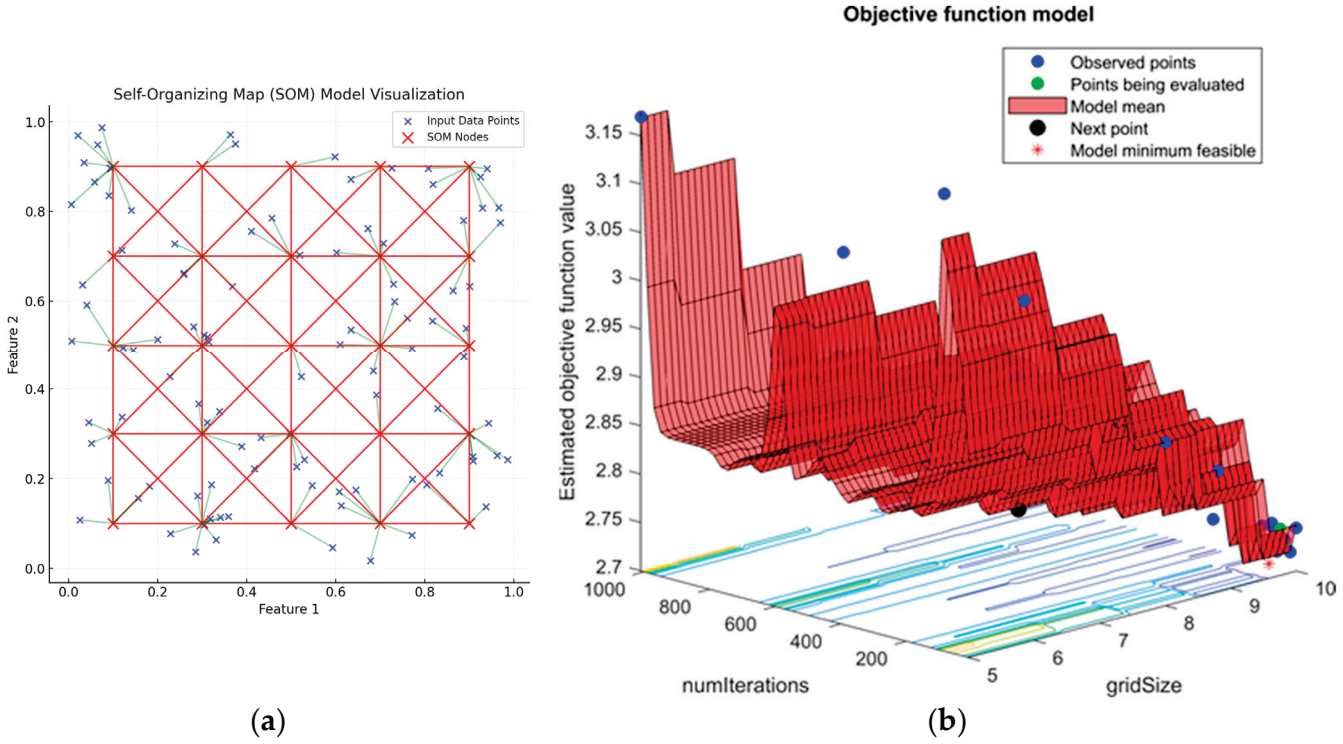


Figure 5. (**a**) Schematic diagram of the SOM model. (**b**) Bayesian hyperparametric optimization graph.

3.2.5. Reordering of Clustering Centers

Since the classification results of the clustering model are unordered, for this specific problem of landing zone selection, it is possible to obtain classification results that meet the

needs by reordering the clustering centers. For example, by arranging the clustering centers of each class of the slope data in a descending order, the first class of the classification results will have the lowest value for the slope, which is in line with the needs of landing engineering purposes.

3.2.6. Calculation of Feature Importance

Among the landing area selection considerations, the weight contribution of individual data to suitable landings is also of interest, and there is a lack of data-driven references for obtaining the weights of individual site selection element data in the landing site selection problem. However, the SOM method itself does not directly output how much each feature contributes to the classification results, as it is an unsupervised learning algorithm. The SOM helps to discover patterns or clustering structures in the data by mapping the data to a two-dimensional or low-dimensional space. The feature contribution can be indirectly obtained from the SOM model through a number of analytical methods. Thus, the importance of random forest features using machine learning can be indirectly obtained from the data weights by using the SOM clustering labels as classification targets and the features of the original input data as feature inputs to the model. A random forest is an integrated learning algorithm that classifies data by constructing multiple decision trees and, at the same time, is able to provide feature importance assessments. In this case, the random forest model can estimate the impact of each feature on the classification labels to obtain the importance weights of each siting data element on the classification results.

Feature importance assessment in random forests is based on the information gain (or reduction in impurity) calculated during node splitting, which reflects the importance of a feature in helping the decision tree to correctly classify it. When the decision tree is constructed, one feature at a time is selected to split the nodes, and this selection is based on the reduction in impurity (impurity). Impurity can be measured using Gini impurity or entropy. Suppose that there is a node t and the feature X_j. X_j is used to split the node into child nodes t_L and t_R, and then the reduction in impurity brought about by the feature can be expressed as follows:

$$\Delta i(t, X_j) = i(t) - (\frac{Nt_L}{N_t} i(t_L) + \frac{Nt_R}{N_t} i(t_R)) \tag{17}$$

where $i(t)$ is the impurity of node t (e.g., Gini impurity or entropy).

Nt_L and Nt_R are the numbers of samples of the left and right child nodes.

Nt is the total number of samples of node t.

The importance of each feature can be measured using the cumulative reduction in impurity it induces in all trees:

$$\text{Feature Importance}(X_j) = \sum_T \sum_{t \in T} \Delta i(t, X_j) \tag{18}$$

That is, in all decision trees, the impurity reduction from each node split is part of the feature's contribution to the final classification decision. Finally, the feature importance is normalized to between 0 and 1. The higher the feature importance, the higher the contribution of the feature to the classification result.

4. Results

The landing suitability evaluation results obtained using big data on the lunar polar region underwent a series of steps, including data resampling, vector data conversion, sliding window traversal, and SOM modeling. Next, the weight contribution of each type of data to the landing suitability was obtained using the characteristic importance method

with a random forest; after that, the SOM evaluation results of the combined data were re-screened according to the principle of threshold selection, the results were categorized into two categories of suitable and unsuitable landing, and the results were compared with the South Pole landing sites selected by Zhang et al. [55]. These elements demonstrate the results of SOM landing zone preferences in the following three subsections: (1) lunar South Polar zone results for rating the suitability of landing zones with the SOM method, (2) landing assessment results from a data-driven perspective providing the weighted contribution of each site selection element and categorizing the combined data from the SOM evaluation results into two categories of suitable versus unsuitable landings by using the threshold filtering principle, and (3) superimposing the South Pole landing sites selected by Zhang et al. as well as preselected South Pole landing areas by various organizations to compare with the local areas of the integrated SOM results.

4.1. SOM-Based Evaluation of Lunar South Landing Zones

The SOM-based South Pole landing evaluation model integrates rich scientific data and engineering data and utilizes the sliding-window method for data slicing; the window sizes of $1^\circ \times 1^\circ$, $0.5^\circ \times 0.5^\circ$, and $0.03125^\circ \times 0.03125^\circ$ are selected, and the step sizes in both directions are set to be 0.5°, 0.25°, and 0.015625°, respectively. The data are processed by the SOM model, and the clustering centers are reordered. The SOM evaluation results for the lunar polar region landing based on engineering data, scientific data, and comprehensive data are shown in Figure 6. In addition, 49×719, 99×1439, and $1599 \times 23{,}039$ landing suitability rating windows were obtained in the processing range of 65°S~90°S at the South Pole, respectively. The South Pole is superimposed with the center point of the Artemis 3 landing preselection area declared by NASA on 20 August 2022 (https://www.nasa.gov/news-release/nasa-provides-update-on-artemis-iii-moon-landing-regions/ (accessed on 28 October 2024)), as well as the preselected landing area centroids associated with South Pole landings by organizations collated in Table 1.

Figure 6a–c provide an analysis of the conditions for landing in the South Polar region of the Moon based on engineering data and the SOM methodology. Among the rating metrics in the 100 categories of the legend, the results of category 1 indicate that it is the category with the lowest clustered central mean among the five categories of engineering data, thus representing the most suitable areas for landing, which have excellent performance in terms of light, communication, slope, and roughness, and are suitable for a future landing mission. The 100th category represents the category with the highest cluster-centered mean, which may be due to steep terrain, poor light conditions, or other unfavorable factors. The number of windows in the first through fifth categories that are most suitable for landing is 33,334,467, which is 9.05% of the total windows. The results demonstrate that factors such as illumination, communication, slope, and roughness combine to determine a window's suitability for landing. Comparing Figure 3c, which shows the Earth visibility data in the polar region of the lunar South Pole, with the boundary from 90°W to 90°E, the data plot demonstrates a clear and gradual change in Earth visibility from high to low values from the upper to lower half of the boundary. In Figure 6a–c, containing the SOM results, most of the blue areas, which are suitable for landing, are distributed above the boundary, and the red areas, which are unsuitable for landing, are distributed below this boundary; this distribution feature is more obvious in the window sizes of 1° and 0.5°, which is consistent with the data distribution features for the Earth's visibility. Comparing with Figure 3b, which shows the solar visibility data to indicate the lunar illumination, the boundary is from 90°W to 90°E. The impact craters above the boundary between 90°W and 90°E have lower illumination in the upper part of the crater wall, and the crater wall above the boundary is shown as a red range that is unsuitable for landing in the SOM result map; then, the

area near the South Pole has lower illumination, and there are several permanently shaded areas, which are shown as unsuitable for landing in the SOM evaluation results with a small window size (0.03125°), which is in line with the illumination data. The area near the South Pole is shown as suitable for landing, but there is a contradiction in comparison with the illumination data, which is caused by the lower slope data and roughness data in the pole region that make it suitable for landing; therefore, the contribution of each data weight in the SOM results is also an issue to be considered. Comparing the data representing the lunar slope and roughness maps in Figure 3a,d–f, the bottoms of the impact craters within the study area are lower in terms of their slope and roughness values. Low values of slope and roughness at the bottom of an impact crater within the study area are also shown to be suitable for landing in the plot of the engineering results, while high values of slope and roughness at the wall portions of craters are shown to be unsuitable for landing relative to the bottom areas of craters in the plot of engineering results, which demonstrates a good correlation of the SOM results with the slope data and roughness data. Therefore, the polar region engineering landing evaluation results of the SOM absorb the distribution characteristics of each type of engineering data and are a comprehensive representation of the suitability of multidimensional engineering data for landing in the polar region, proving that the SOM method can integrate multidimensional data into a two-dimensional space, provide intuitive visualization results, and help decision makers to identify optimal regions quickly. In addition, the delineation of landing suitability is more refined as the window size decreases. Comparing the SOM engineering results in Figure 6a–c, the outline of the impact crater morphology in the polar region is clearer in Figure 6a–c. Comparing this with the Schrödinger Basin region declared by the HERACLES program, it is not suitable for landing when using the large window size, while it is suitable for landing when using the small window size due to the larger data values included in the model with the large window size and the higher values in the crater. This is due to the fact that the model contains more data values with the large window size, and the higher values in the edge portion of the impact crater affect the window mean. Therefore, the SOM results for the small window size (0.03125°) are better than those for the large window size when assessing the suitability of a polar region for landing.

Figure 6d–f provide an analysis of the conditions for landing in the South Polar region of the Moon based on scientific data and the SOM methodology, incorporating factors such as hydrogen content abundance, nuclear density analysis of geological maps, distance analysis of water ice, iron oxide abundance, and gravity anomalies. Of the 100 categories of rating metrics in the legend, the results in category 1 indicate that it is the category with the highest mean of the five scientific data clustering centers, representing the most suitable landing area that contains the highest scientific value. The number of windows in categories 1–5 of the most suitable landing areas containing the highest scientific value is 2,191,821, or 5.95%. The results demonstrate that, from a scientific point of view, the range suitable for landing is distributed in the region around the South Pole, which is consistent with the abundance of hydrogen content, the clustering of high values in geological maps and density analyses, and the distribution characteristics of water ice. The outlines of impact craters in the South Pole region in the SOM result maps are similar to those of the gravity anomaly data map, and the lower-left part of the boundary from 90°W to 90°E has a higher iron oxide content than the surrounding area. This is a similar feature to that seen in the SOM result map. The SOM result map also shows that the distribution of suitable areas for landing increases with decreasing latitude, which is consistent with the characteristics of the analysis of the distance to water ice. This feature is consistent with the analysis of water ice distances. Therefore, the scientific landing evaluation results of the SOM for the polar region have absorbed the distribution characteristics of each type of scientific data

and are a comprehensive representation of the suitability of multidimensional scientific data for landing in the polar region.

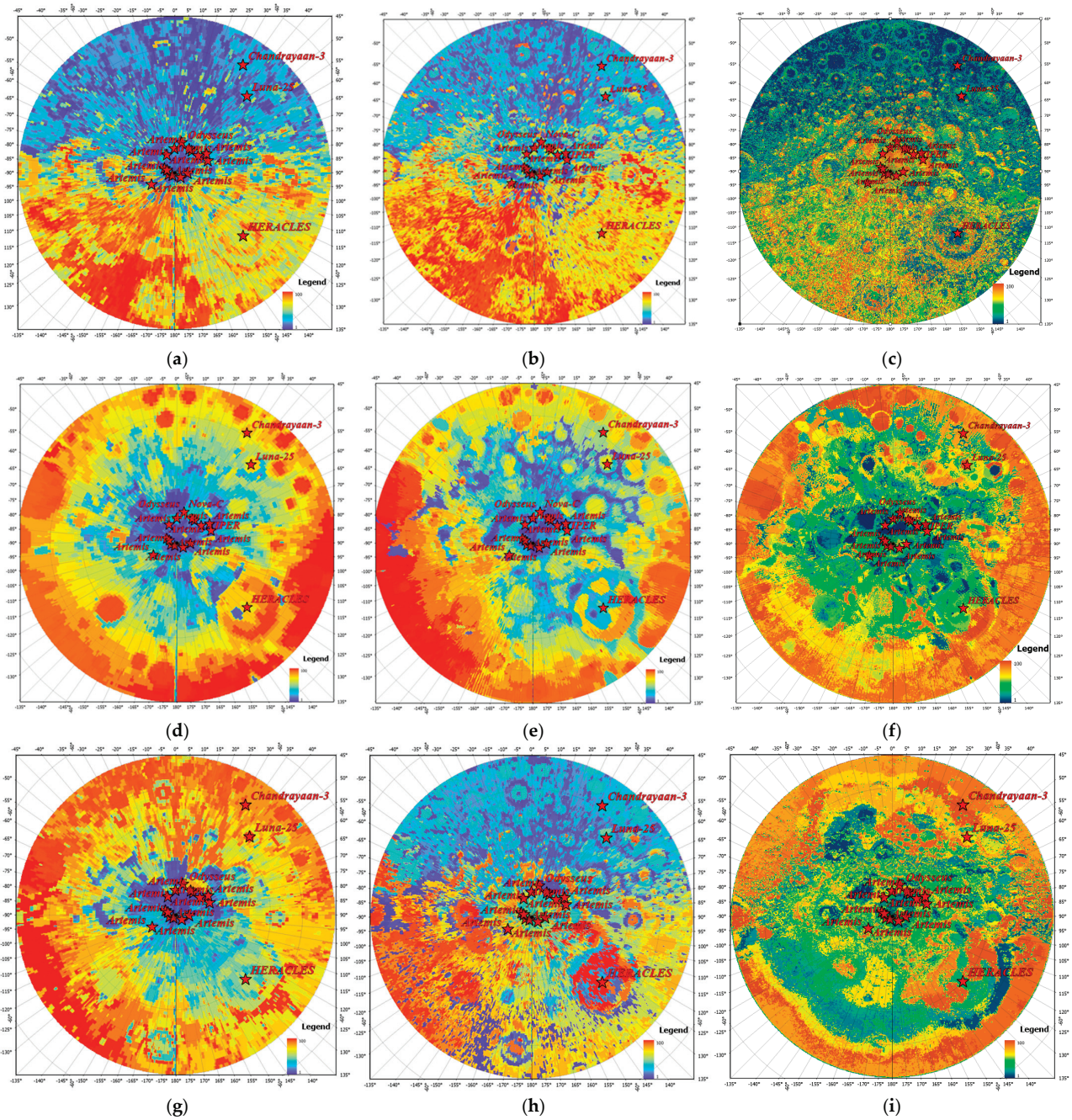


Figure 6. SOM evaluation of lunar South Pole landing zones, where the legend represents the results of the categorization, blue represents the most suitable landing zones, and red represents the least suitable landing zones. The first through third rows represent engineering, scientific, and comprehensive evaluations, respectively. The first through third columns represent the evaluation results for the 1°, 0.5°, and 0.03° windows, respectively. (**a**) Engineering evaluation of the 1° window, (**b**) 0.5° window, (**c**) 0.03° window, (**d**) Scientific evaluation of the 1° window, (**e**) 0.5° window, (**f**) 0.03° window, (**g**) Comprehensive evaluation of the 1° window, (**h**) 0.5° window, and (**i**) 0.03° window.

Figure 6g–i provides a comprehensive analysis of conditions for landing in the South Polar region of the Moon based on engineering and scientific data using the SOM methodology, incorporating factors such as light, communication, slope, roughness, hydrogen content abundance, core density analysis of geological maps, distance analysis of water

ice, iron oxide abundance, and gravity anomalies. Of the 100 categories of rating metrics in the legend, the results in category 1 represent the category with the most compatible landing conditions for the mean of the 10 engineering and scientific data clustering centers, representing the blue areas that are most suitable for landing. The number of windows for the most suitable landing areas in categories 1–5 is 1,872,531, or 5.08%. The green and yellow-green areas shown in the clustering results represent places with better-integrated conditions that are suitable as landing sites. The 18 existing landing site plans in Table 1 are clustered in these excellent areas except for the Shiv Shakti point landing site of Moon Ship III, which verifies the reliability of the SOM evaluation model. The Moon Ship III landing site near 69°S latitude has good engineering landing conditions, but it is far away from the permanently shaded area near the pole and has high values in the geological map kernel density analysis, and the low evaluation of its scientific value results in its unsuitability for landing. However, comparing the results of the SOM synthesis evaluation in Figure 6g with the data in Figure 6h, it can be seen that different conclusions are produced in the evaluation results with a window size of 1° versus 0.5°. Figure 6g demonstrates unsuitability for landing in the area above the boundary from 90°W to 90°E, and the general trend is similar to the characteristics of the SOM evaluation results for scientific data. Figure 6h demonstrates the suitability of landing in the area above the boundary from 90°W to 90°E, and the general trend is similar to the characteristics of the SOM evaluation results for engineering data. This contradiction may be caused by the following two reasons: 1. the weight contribution of each type of data in the SOM evaluation model is not consistent during the training process, which may cause a higher weight contribution of the scientific data to be shown in the SOM evaluation results, and therefore, it is necessary to analyze the data by obtaining the contribution of each type to the weights on the basis of that analysis. 2. From the perspective of meeting the landing conditions based on scientific and engineering data, there is a data conflict, and the overall trend is similar to that of the scientific data. There is a data conflict between the scientific data and the engineering data from the perspective of landing conditions. In permanently shaded areas, the higher hydrogen content abundance and water ice data are more suitable for landing because they reflect the scientific value of the area as a landing zone, but from the engineering point of view, there is very low light and communication, which is unsuitable for landing, so it is necessary to reclassify the clustering results of the SOM evaluation in order to alleviate this contradiction.

4.2. Weight Contributions of Multidimensional Features and Reclassification of the Synthesized Results

4.2.1. Weight Contributions of Multidimensional Features

Among the landing zone selection considerations, the weight contribution of individual data to suitable landings is also a matter of interest. For the SOM unsupervised learning algorithm, the feature contribution can be indirectly obtained from the SOM model through random forest special importance extraction. The SOM clustering labels are used as the classification targets, and the features of the original input data are used as the feature inputs to the random forest model. The weight contribution of each type of data within the target for engineering, scientific, and integrated landing objectives for suitable landing classification is shown in Figure 7.

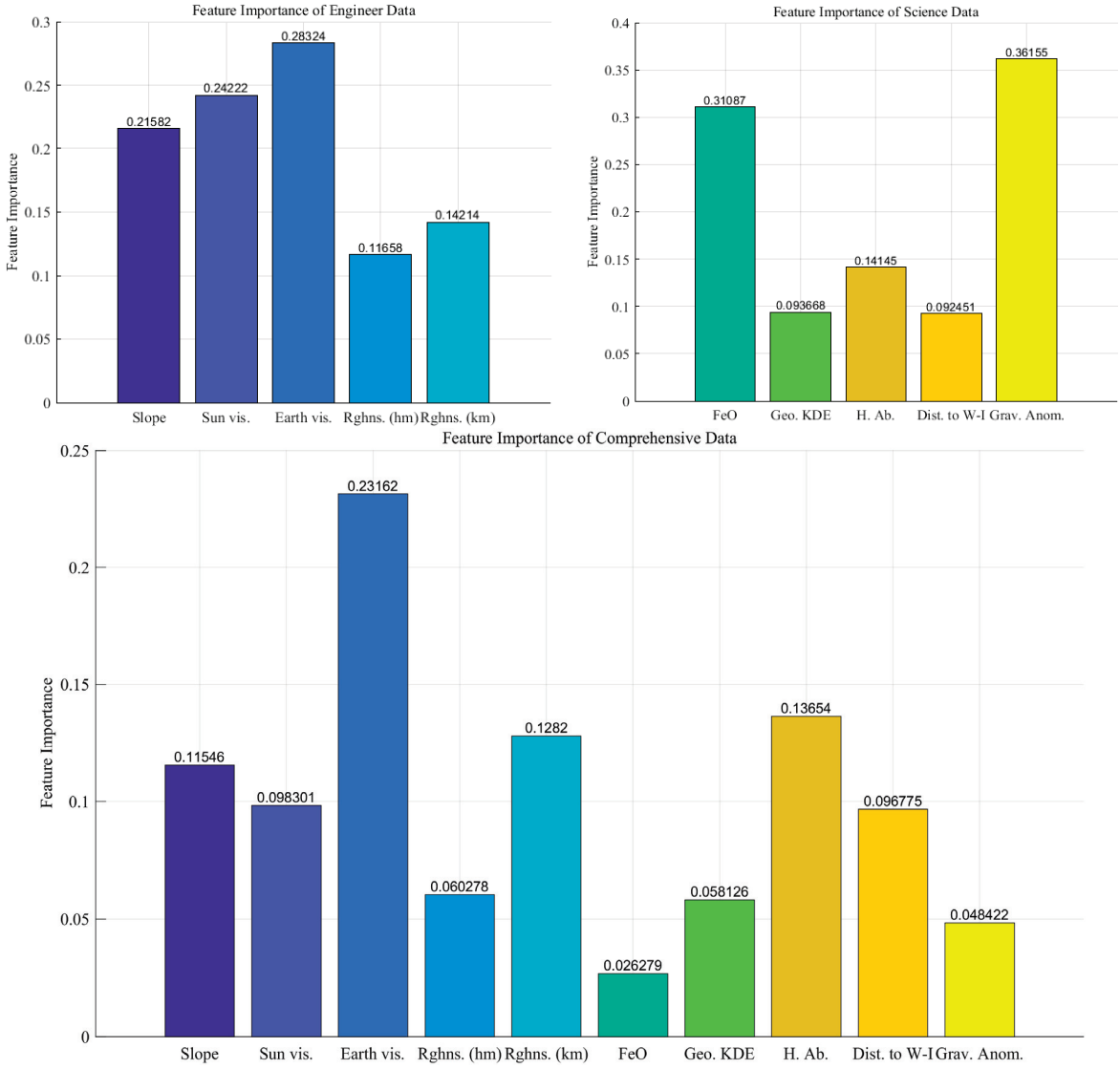


Figure 7. Feature importance for the engineering, scientific, and comprehensive datasets.

In terms of the random forest feature importance results shown in Figure 7, the weighting of the influence of the characteristics of each type of engineering data (slope, light, communication, roughness, etc.) on site selection is analyzed as follows. Earth visibility (0.28324): The highest feature importance value in the figure is the most important engineering factor for a successful landing from a data-driven point of view, which is in line with the results of the South Pole SOM for the project in Figure 6c and is consistent with the conclusion that the characterization of the communication data is reflected. Stability of communications is associated with ensuring that the lander is able to communicate effectively with the Earth. Sun visibility (0.24222): Lighting conditions are the second most important feature, with sufficient sunlight helping to maintain the rover's energy supply and ensure that the equipment operates properly in the harsh environment of the lunar South Pole. Slope (0.21582): The slope comes in a close second, indicating that the flatness of the terrain directly affects the safety of the lander's landing. Lower slopes are beneficial in reducing the risk of the lander being in contact with the ground, thus reducing the likelihood of hard landings and capsizes. Roughness (km, 0.14214) and roughness (hm, 0.11658): Roughness is less important but still has some influence. Roughness reflects the smoothness of the surface and affects the stability of the lander's landing. Earth visibility,

Sun visibility, and slope are the main considerations in the current automated site selection, reflecting the priority of communication, energy supply, and the flatness of the surface of the landing zone in the engineering mission.

From the graph of the feature importance of scientific data, it can be seen that the contributions of scientific features for lunar South Pole landing site selection are as follows: Gravity anomalies (0.36155): Gravity anomalies have the highest feature importance in the scientific data, and the South Pole region is consistent with the conclusion that gravity anomalies characterize the data embodied in the results of the SOM evaluation in Figure 6c. This also suggests that gravity anomalies are the primary factor in automated site selection as scientific landing targets, as they are correlated with the internal structure of the Moon, geological activity, and topographic features, and can reveal hidden subsurface resources or inhomogeneous mass distributions, thus providing scientifically significant discoveries. FeO (0.31087): Iron oxide content follows closely, showing the importance of iron oxide abundance in scientific site selection. Areas of high iron oxide content hint at the presence of abundant metallic mineral resources on the Moon, which is important for future mineral extraction and resource utilization. Hydrogen abundance (0.14145): Hydrogen abundance is also a key scientific feature. The presence of hydrogen indicates the distribution of water ice, which in turn affects the detection of water resources on the Moon. Geo. KDE (0.093668) and Distance to W–I (0.092451): Geological kernel density estimation and the distance to the distribution of water ice are of low importance; geological maps reveal details of the Moon's geological structure, and the distribution of the distance to water ice affects the ease of detecting direct evidence of water ice. Gravity anomalies, FeO, and hydrogen abundance are the main considerations in the current automated site selection for scientific landings, reflecting the prioritization of geological properties and resource potential in missions.

From the results of the feature importance analysis of the synthesized data, after combining the features of the engineering data and the scientific data, the feature importance was as follows: Earth visibility (0.23162): Communication remains the most important feature, showing that Earth visibility continues to be prioritized in ensuring communication between the lander and Earth. This is consistent with the needs of the engineering mission, where the reliability of communications is most important to mission success during the automated siting of the combined factors. Hydrogen abundance (0.13654): Hydrogen abundance became the second most important feature, indicating that the availability of water is critical for future missions in resource utilization and scientific exploration of the lunar South Pole. Roughness (km, 0.1282): Roughness increased in weight and is the third most important of the combined factors, which is related to the fact that roughness data at the kilometer scale not only affects landing safety but also reflects the bedrock geology as a feature for science. Slope (0.11546): The slope also has a higher weight and is an important factor in ensuring landing safety, especially for the lunar South Pole region, which has a more complex terrain. Sun visibility (0.098301) and distance to water ice (0.096775): Light and the distribution of the distance to water ice also carry considerable weight, indicating that ease of energy supply and access to resources were considered in site selection. FeO (0.060278): Iron oxide content decreased in importance but still reflects value in future mining and resource utilization. Geo. KDE (0.058126) and gravity anomalies (0.048422): The geological kernel density estimates and gravity anomalies have lower weights, but they provide information on geology and gravitational fields to provide complementary support for scientific exploration. In the synthesized data, communication (Earth visibility), hydrogen abundance, kilometer-scale roughness, and slope all have a weighting of more than 10% and are considered to be the four most important factors in the automated site selection process integrating scientific objectives and engineering needs. Of these, the kilometer-scale roughness data were slightly elevated in the combined weighting,

consistent with the conclusion that these data reflect not only surface roughness from an engineering perspective but also bedrock geology from a scientific perspective [48].

4.2.2. Reclassification of the Consolidated Results

As mentioned in the previous section, there is a data conflict between the scientific data and the engineering data from the point of view of meeting the landing conditions; in permanently shaded areas, a higher hydrogen abundance and more water ice data are more reflective of the scientific value as a landing area and suitability for landing, but there is a very low illumination from the engineering point of view, which is unsuitable for landing, and the clustering results of the SOM evaluations need to be reclassified in order to alleviate this conflict. Specifically, for the clustering of composite conditions, the mean screening of cluster centers produces a disorder in the ordering of the classification results due to the conflict between the light data in engineering and the hydrogen content abundance and water ice distance data in science. Therefore, the principle of threshold screening was used to reclassify the results of the comprehensive SOM evaluation. To ensure a safe landing, fixed thresholds were determined for factors related to engineering safety: a slope less than 12°, solar visibility greater than 35%, and Earth visibility greater than 15%; this restriction meets the safety redundancy requirements in current Mars rover design [25,56]. Considering that exploration for water and other volatiles is the primary scientific objective, an elemental hydrogen abundance greater than 100 ppm was selected as the specific scientific limit [3,19].

The original clustering results of seven classes of all classifications satisfying this threshold condition were obtained, containing classes 1, 3, 21, 43, 47, 72, and 74, as the classification results for suitable landing, and they were superimposed on the preselected landing plan in Table 1, as well as 10 landing sites in four regions of the South Pole selected by Zhang et al. according to the engineering conditions. The WAC imagery maps were used as the base maps, with the blue areas as the suitable landing ranges after the screening of the integrated condition thresholds to obtain Figure 8.

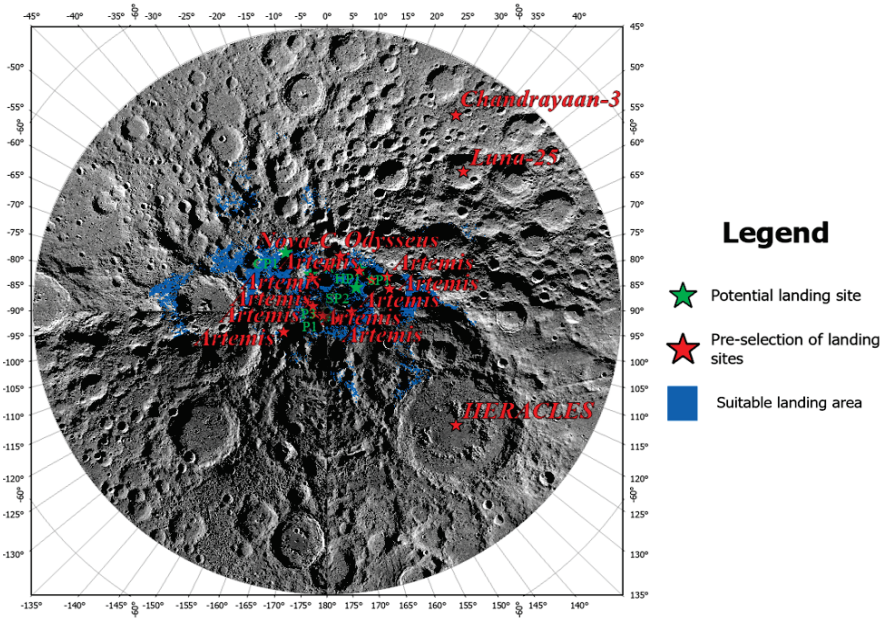


Figure 8. Comprehensive SOM evaluation results based on threshold screening.

Figure 8 demonstrates the final classification of suitable ranges of landing zones based on the integrated data and the SOM methodology after the use of the threshold screening principle, after the zones were classified as suitable (blue) or unsuitable and

then superimposed on the WAC image map, in combination with the display of landing sites and potential landing sites; thus, the distribution and selection of landing zones were visualized. This reflects the following characteristics: 1. The blue areas representing the most suitable landing zones in the integrated SOM evaluation results for the South Pole are mostly distributed near the poles; their distribution is similar to the characteristics of the range of hydrogen abundance of >100 ppm and similar to the characteristics of the SOM evaluation results for the scientific data. The number of blue windows suitable for landing is 2,457,515, accounting for 6.67% of the total. 2. Most of the blue areas suitable for landing are located on the rims of peaks, terraces, and ridges of craters, making them close to the permanently shaded impact craters, which is conducive to the discovery of the evidence of the presence of water ice and avoids the engineering limitation of the lack of light for the operation of detectors; in permanently shadowed areas, the tension between the scientific value of high hydrogen abundance and the technical requirements of weak illumination is partially eased. The edges of these impact crater peaks and ridges being identified as suitable landing areas is also consistent with the recommendation by Flahaut et al. [3] that small altitude increases using solar panels can significantly improve sunlight harvesting and provide a near-continuous power supply. 3 Since most South Pole exploration programs recommend suitable landing areas rather than landing sites, Zhang et al. [55] screened potential landing sites based on the principles of light conditions and local terrain flatness for comparison, and the results showed that all 10 potential landing sites in the four regions fell within the suitable landing range of the synthesized SOM results for the South Pole. The high overlap between the SOM results and the potential landing sites indicates that there is a high level of consistency between the existing scientific knowledge and the results of the SOM method, which also improves the reliability of the site selection model. This comprehensive analysis combines imagery, clustering results, and points from external authorities to show the most suitable areas for landing more clearly and provide a reference for practical operations. A local-area SOM evaluation at the South Pole in relation to an exploration program is specifically analyzed in the next section.

4.3. Regional Site Evaluation

After the above analysis of the SOM model results for the lunar South Pole, the localized areas associated with a South Pole exploration program can be given a recommended scope and in-depth analysis from a data-driven perspective. The following is an analysis of Zhang et al. and nine other regional scopes.

4.3.1. Malapert Massif

The Malapert Massif is a mountain range located south of the Malapert Crater (84.9S, 7.3E) at the lunar South Pole; it has a long sunshine period due to its high relief and is located on the edge of the inner ring of the SPA Basin [57]. It is considered one of the preferred locations for the Artemis III lunar exploration mission, as it contains a potential landing site.

The results in Figure 9 reflect the engineering, scientific, and comprehensive data and SOM landing suitability evaluations for the Malapert Massif, and they are analyzed as follows. 1. The SOM engineering evaluations show that the central part of the area is strip-shaped and suitable for landing, as it is located in the flat area of the mountain peaks, thus avoiding the higher slopes in the northern part and the roughness and low visibility of the illuminated Earth in the southern part. 2. The results of the scientific evaluation of the SOM of the region are similar to the characteristics of gravity anomalies in the region, which is consistent with the conclusion that the characteristics of gravity anomalies are the most important in the scientific SOM model. The relative proximity of the landing area to

exposed water ice, as determined from the water ice distance data, increases the potential for scientific exploration of the area. 3. The combined results of the SOM evaluations show similar characteristics to the engineering data for the suitable landing range, with the central area being striped and suitable for landing, as it is located in a broadly flat area on the peak of the Malapert Massif, and with the HP1 potential landing site falling within the suitable landing range.

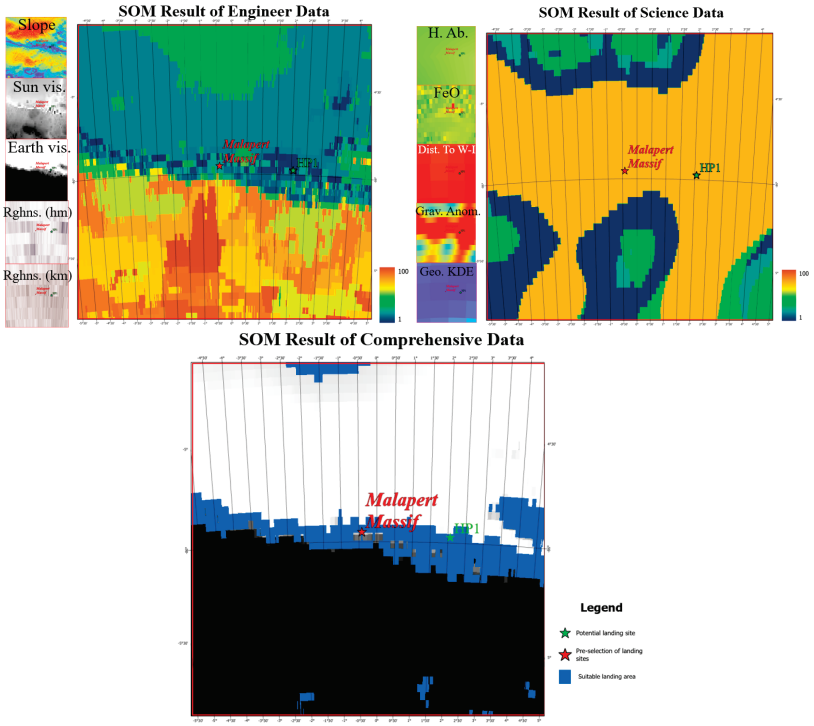


Figure 9. Results of the SOM landing suitability evaluation of the Malapert Massif from three perspectives: engineering, scientific, and comprehensive perspectives.

Overall, the Malapert Massif region has excellent energy and communication conditions, with long periods of light helping to address the critical issue of energy supply, and due to the site's high altitude, it can have almost direct visibility of the Earth, making it suitable for long-term exploration missions. In terms of scientific exploration, the region's proximity to key scientific hotspots at the Moon's South Pole could provide important support for future lunar resource development and scientific research.

4.3.2. Shackleton

The Shackleton impact crater, located at 89.7°S, 129.2°E, is 21 km in diameter, was formed during the Eratosthenian, and was excavated from an unconformity that exposed blocks containing probably the purest plagioclase on one side of the caldera and a layered outcrop on the other side of the caldera with a permanently shaded area of approximately 235 km^2 in extent [13]. Layered outcrops on the other side of the crater contain a permanently shaded area of approximately 235 km^2, which may be located in the inner ring of the SPA and, thus, demonstrate the deeper geology of the Shackleton crater and the South Pole of the Moon, and part of the crater rim (0.01 km^2) is a permanently shaded area, and such a large permanently shaded area must have had a significant impact on the volatility of the moon [58]. It is a promising site for SPA investigations and water ice discovery near the South Pole. The nearby connecting ridge crater, which connects the Shackleton and Henson craters (known as the "connecting ridge" of the Artemis III potential landing zone) and the peak near Shackleton, is in permanent proximity to the center of the polar regions.

This location is characterized by very specific geographic and environmental conditions. The extreme light conditions, temperatures, and topography of this location have made it a potential landing site in several lunar exploration and human lunar exploration programs, and it is considered one of the preferred sites for the Artemis III lunar exploration mission, with the region containing four potential landing sites.

The results in Figure 10 reflect the data and SOM landing suitability evaluation results for the Shackleton region from three perspectives: engineering, scientific, and synthesized. 1. The SOM engineering evaluation results show that there is a suitable landing range at the edge of the Shackleton crater location, and the connecting ridge location selected in the Artemis III mission falls into the suitable landing range. 2. The scientific SOM evaluation results in this region show that the scientific value of the Shackleton impact crater is higher than that of the surrounding area. 3. The combined results of the SOM evaluations show similar characteristics to the engineering data for suitable landing ranges, suggesting that the Shackleton edge and connect ridge are suitable for landing and that the four potential landing sites in the region, P1, P2, P3, and P4, fall within the suitable landing ranges.

The results in Figure 11 reflect the data and SOM landing suitability evaluation results for the region of the peak near the Shackleton region from three perspectives: engineering, scientific, and synthesized. 1. The engineering SOM evaluation results show that the region of peak near Shackleton falls into a suitable landing range because of the gentle slope of the peak region, good illumination, and communication. 2. The scientific SOM evaluation results for this region show that the area near the peak has a higher scientific value than the surrounding area. 3. The synthesized SOM evaluation results show similar characteristics to those of the suitable landing range according to the engineering data, and it is concluded that there is a suitable landing range in and around the peak area. Overall, the Shackleton area is close to the permanently shaded area, is a priority impact crater for the detection of evidence of the presence of volatiles in the polar region, and has suitable conditions for engineering landings at the edge of the impact crater and on the connecting ridge. Despite the technical challenges of terrain and communications, its abundant water ice resources and unique polar environment offer great strategic value for long-term lunar exploration missions.

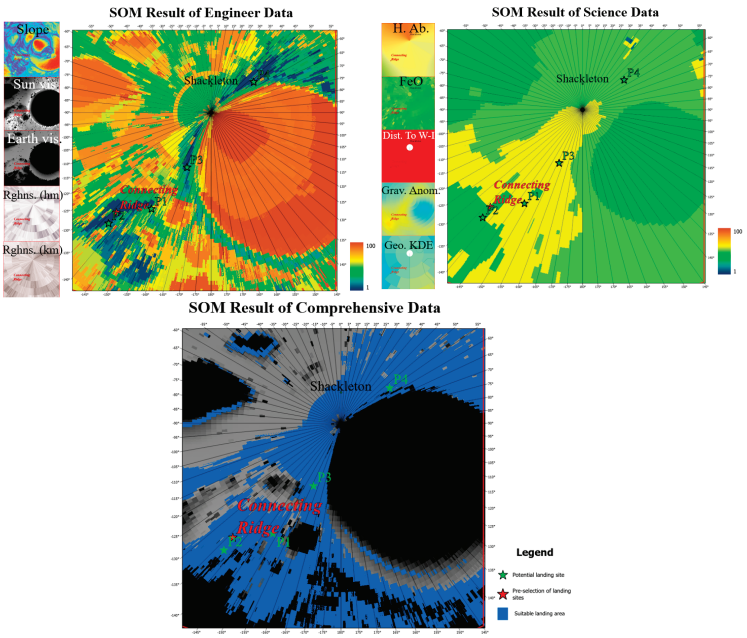


Figure 10. Results of the SOM landing suitability evaluation of the Shackleton region from three perspectives: engineering, scientific, and comprehensive.

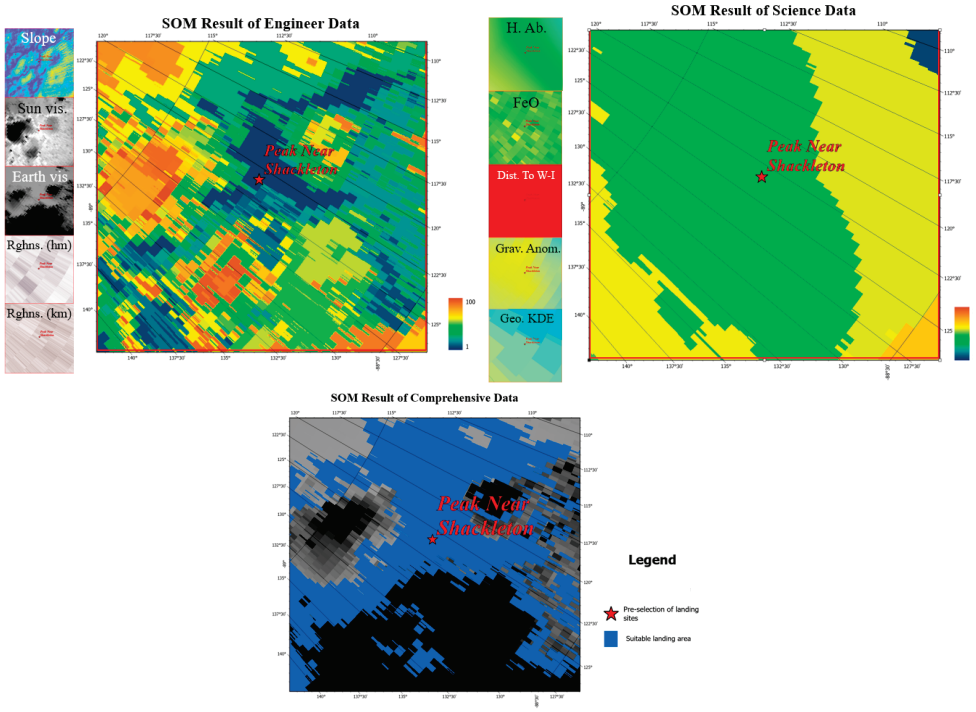


Figure 11. Results of the SOM landing suitability evaluation for the peak near Shackleton from three perspectives: engineering, scientific, and comprehensive.

4.3.3. Haworth

Haworth Crater is a sub-pentagonal impact crater with a diameter of 35 km located in the South Polar region of the Moon. Approximately 4.76 km^2 of the crater floor is permanently shadowed [58]. The Lunar Prospector neutron instrument detected hydrogen abundances of 142–144 ppm on the crater floor [37]. Thermal infrared (TIR) imaging indicates that the temperature at the bottom of the crater is very low, only 15–54 K (average temperature of 32–38 K), which allows for the long-term preservation of many volatiles, including water ice [11]. It is considered one of the preferred landing sites for the Artemis III mission, and it contains two potential landing sites.

The results in Figure 12 reflect the engineering, scientific, and integrated data and the SOM landing suitability evaluation of the Haworth region, and they are analyzed as follows. 1. The engineering SOM evaluation shows that the suitable landing area is distributed around the edge of the impact crater, avoiding the right part of the area with a high roughness and slope. 2. The characteristics of the scientific SOM evaluation are similar to the distribution of gravity data. 3. The comprehensive SOM evaluation results are similar to the characteristics of the engineering evaluation results, and the lower part of the comprehensive evaluation results has a wider range of suitable landing areas than the engineering results, which is caused by the higher values of the kernel density analysis (KDA) of the geological map in the lower part of the region, which absorbs the characteristics of the scientific data. In addition, the two potential landing sites in the region, CP2 and HP2, fall into the suitable landing range. Overall, the Haworth impact crater has been listed as one of the alternative landing sites by many international lunar exploration missions, and the rich resource potential of the region makes it a hotspot for international cooperation and research on lunar exploration and the utilization of lunar resources.

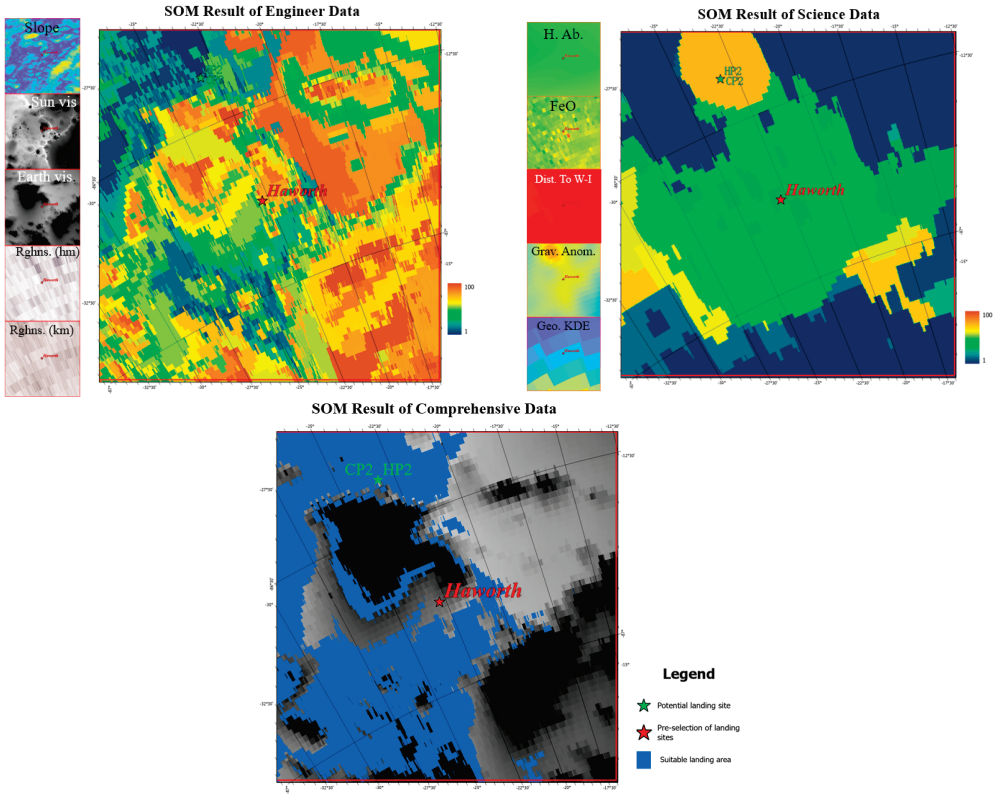


Figure 12. Results of the SOM landing suitability evaluation in the Haworth from three perspectives: engineering, scientific, and comprehensive.

4.3.4. Cabeus

Cabeus Crater, located at 84.9°S 35.5°W, is an abraded formation with an average depth of 4 km at the base of the crater, a width of 60 km, and a slope of the crater wall of 10–15°. The crater is located at 84.9°S 35.5°W, and it has an average depth of 4 km at the base of the crater and a width of 60 km [59]. The temperature in the shadowed region is below 100 K (-173 °C), which would allow water ice to remain on or near the crater surface for billions of years without sublimating [60]. NASA's LCROSS mission in 2009 successfully detected evidence of the presence of large amounts of water ice in the Cabeus crater. Water vapor and volatiles released by the impact further confirmed water ice reserves in the region, which contains one potential landing site.

The preselected landing area is located on the ridge north of the Cabeus impact crater. The results in Figure 13 reflect the data from three perspectives—engineering, scientific, and synthesized—and the results of the SOM landing suitability evaluation of the Cabeus region. 1. The engineering SOM evaluation results show a suitable landing area that is consistent with the low-slope ridge strike characteristics. 2. The characteristics of the scientific SOM evaluation results are similar to the characteristics of the gravity data distribution in the SOM, and the scientific value of the impact crater is higher than that of the ridge. 3. The comprehensive SOM evaluation results are similar to the engineering evaluation results; the potential landing site in the northern part of the Cabeus crater is close to it with a high scientific value, and the potential landing site CP1 falls into the range of suitable landings.

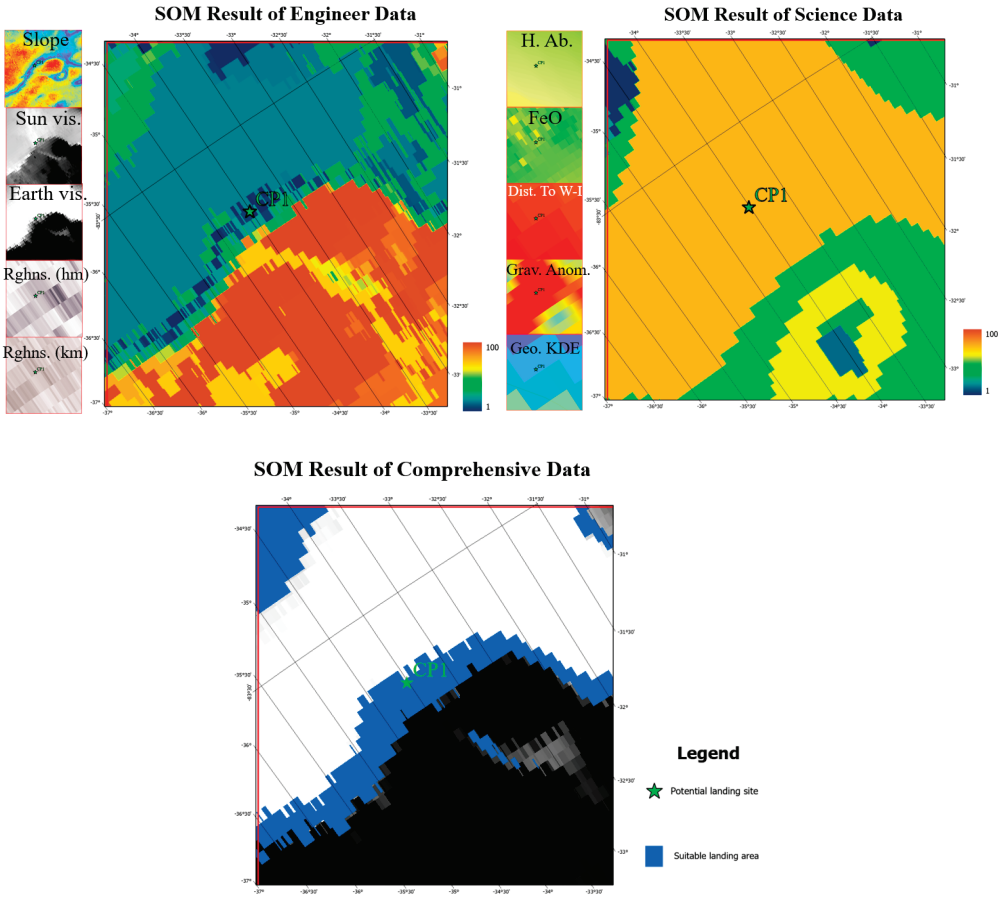


Figure 13. Results of the SOM landing suitability evaluation for the Cabeus region from three perspectives: engineering, scientific, and comprehensive.

4.3.5. Shoemaker

Shoemaker Crater is located at 88.1°S, 44.9°E, with a diameter of about 51 km. Much of the crater floor is permanently shadowed, making it one of the largest permanently shadowed areas in the South Polar region of the Moon. A large number of impact spatter accumulations are distributed on the crater floor [61]. The hydrogen abundance at the bottom of the crater reaches 158–159 ppm. The temperature is very low, only 15–54 K (average temperature is 32–35 K), and this low temperature allows the long-term preservation of volatiles, including water ice, CO, CN, NH, etc.; therefore, it is one of the most probable areas on the Moon for the presence of a large number of volatiles of multiple types [11]. It contains the Nobile preselected landing area and potential landing site SP2.

The results in Figure 14 reflect the results of the potential landing site in the SP area according to the engineering and scientific data and the SOM landing suitability evaluation, and the following is the specific analysis. 1. The engineering SOM evaluation results show that SP2 is located at the edge of the impact crater, and the good slope, light, and communication conditions make this area suitable for landing, but the roughness is poor. 2. The scientific SOM evaluation results for this area show that the scientific value of the center area is higher than that of the edge area. 3. The comprehensive SOM evaluation results show that after combining the scientific features and engineering features, the edge area of the impact crater is considered suitable for landing, as it is conducive to safe landing and nearby detection. The potential landing site SP2 falls within the suitable landing range.

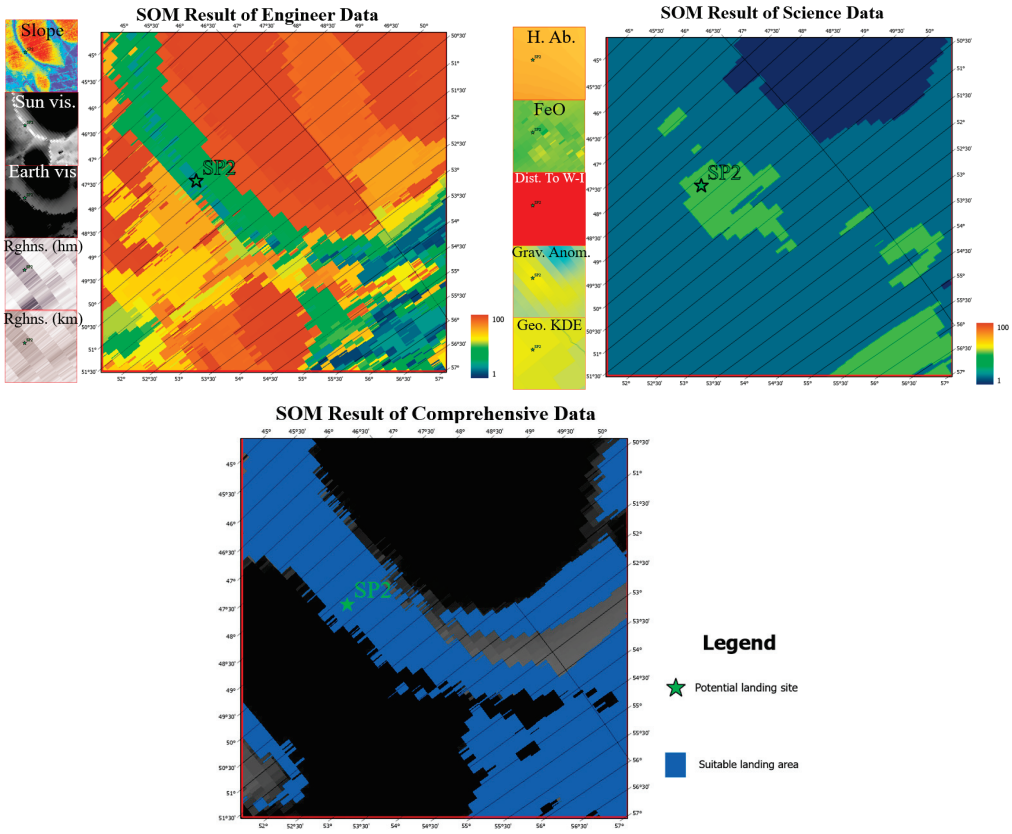


Figure 14. Results of the SOM landing suitability evaluation for the Shoemaker region from three perspectives: engineering, scientific, and comprehensive.

The Rim 1 region of the Nobile impact crater is close to the South Pole of the Moon and is adjacent to the Shoemaker crater, and Figure 15 reflects the results of the engineering and scientific data and the SOM landing suitability evaluation of the Nobile Rim 1 region, which are analyzed as follows. 1. The engineering SOM results show that the ridges and highlands receive solar irradiation for a longer period of time, that the communication and topographic conditions are more favorable, and that the ridge region is suitable for landing. 2. The scientific SOM evaluation results in this region show that the center area of the impact crater has a higher scientific value than the ridge area. 3. The combined SOM results absorb the characteristics of the scientific and engineering results, and the ridge area is suitable for landing; there is also a suitable range of landing sites with suitable slopes in the low-lying area of the impact crater, and the potential landing site SP1 falls into the suitable landing range.

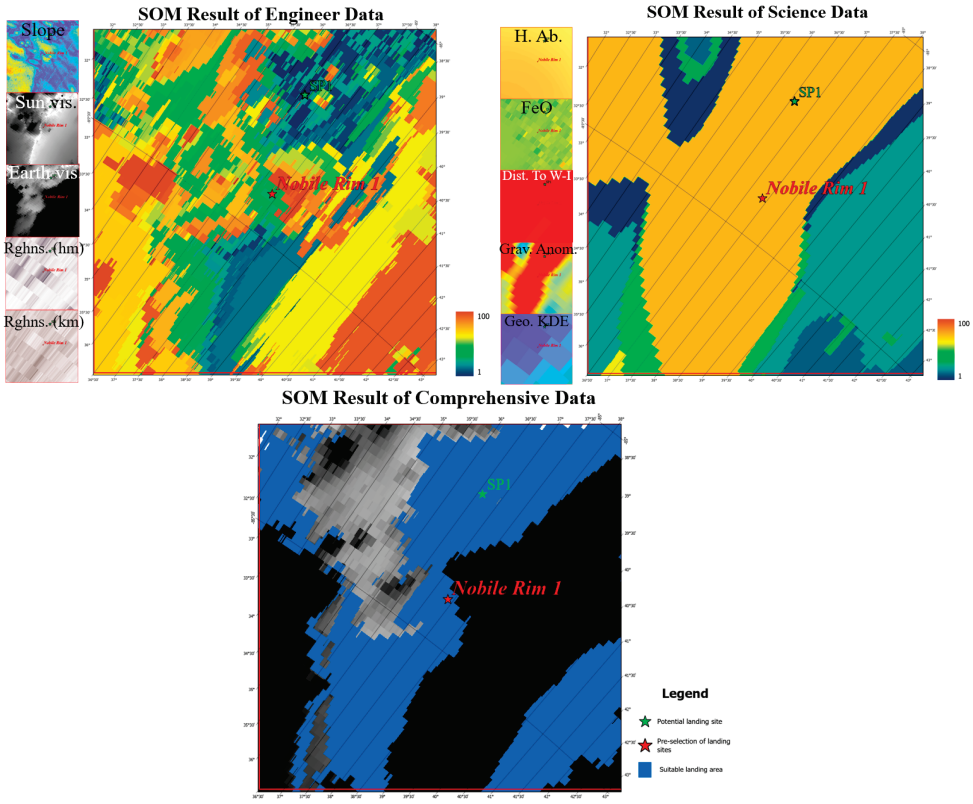


Figure 15. Results of the SOM landing suitability evaluation for Nobile Rim 1 near the Shoemaker crater from three perspectives: engineering, scientific, and comprehensive.

4.3.6. Chandrayaan-3 and Luna-25 Landing Zone Assessment

The Chandrayaan-3 landing site is located in the South Polar region of the Moon, and Shiv Shakti Point is located between the lunar craters Manzinus C and Simpelius N at 69.373°S 32.319°E. A rover was repositioned by jumping and repositioning itself by 30–40 cm from the landing site. The Pragyan rover separated from the lander on 24 August 2023 and was surveyed in situ throughout the lunar day. Sulfur (S), aluminum (Al), calcium (Ca), manganese (Mn), ferrous (iron or ferrous), titanium (Ti), chromium (Cr), silicon (Si), and oxygen (O) were all successfully discovered by the rover. It also searched for hydrogen in the southernmost polar region of the Moon [17].

The results in Figure 16 reflect the results of the engineering and scientific data and the SOM landing suitability evaluation of the Shiv Shakti Point area, which are analyzed as follows: 1. The terrain in the area is relatively flat, with small slopes, which is conducive to a safe landing, and the lighting conditions meet the energy needs of landers, while the communication conditions are good for data transmission between Earth and the rover. The lighting conditions are good, as they meet the energy demands of the lander, and the communication conditions are also good, which is good for data transmission between the Earth and the rover. The engineering SOM results show that most of the area is suitable for landing, and there is already a landing site, Shiv Shakti Point, that falls into the range of suitability for landing. 2. This landing site is adjacent to the South Pole region of the Moon, which has potential for water ice exploration, and this is suitable for resource assessment and proximity. The results of the scientific SOM evaluation show that there is a range of outstanding scientific value in the vicinity of Shiv Shakti Point.

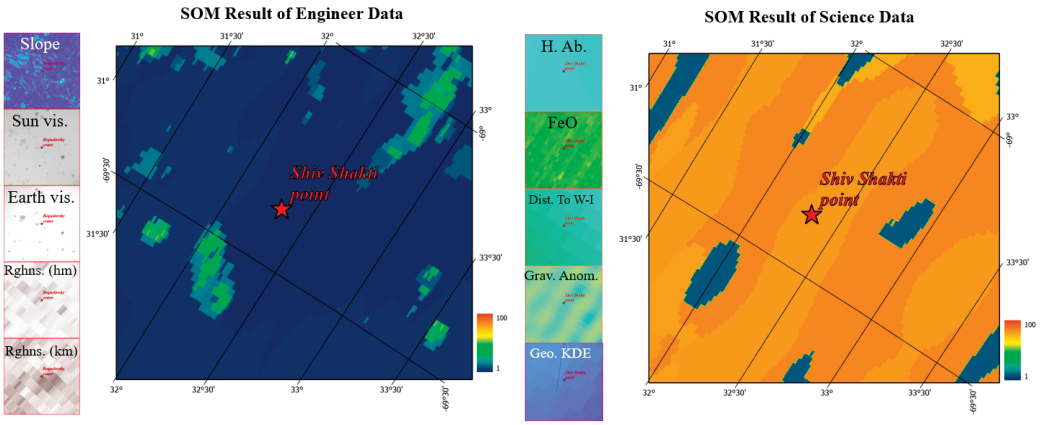


Figure 16. Results of the SOM landing suitability evaluation for Shiv Shakti Point from the engineering and scientific perspectives.

The landing site of the Luna 25 is located at Guslavsky Crater in the South Polar region of the Moon at the coordinates 69.5°S, 43.5°E [62]. The maximum estimated mass fraction of water in the surface layer is 0.5%, suggesting the possible presence of water ice in the subsurface [63].

The results in Figure 17 reflect the results of the engineering and scientific data and the SOM landing suitability evaluation for the Boguslawsky region, and they are analyzed as follows. 1. The region has low relief, good lighting conditions, and good communications, and the engineering SOM results show that the Boguslawsky region contains a large area that is suitable for landing, and the preselected landing sites fall within the suitable landing range. 2. The results of the SOM scientific evaluation in this area show that there is a range of outstanding scientific interest to the east of Boguslawsky crater.

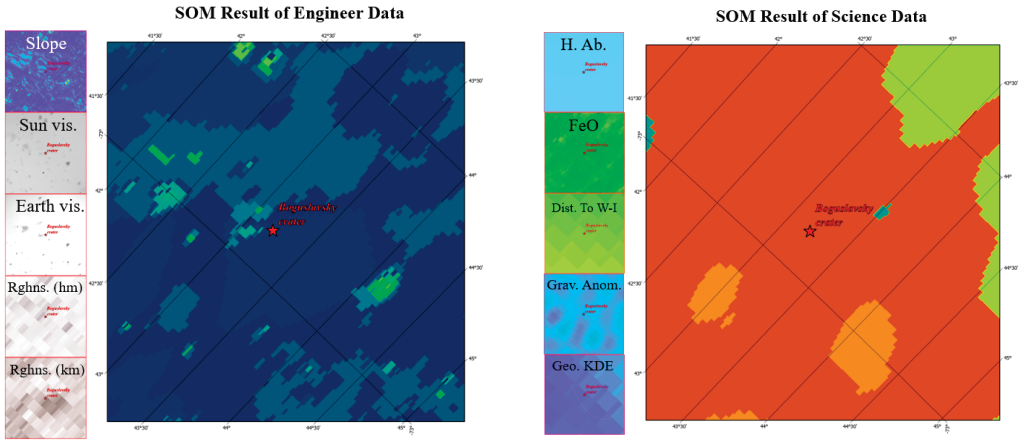


Figure 17. Results of the SOM landing suitability evaluation for the Boguslawsky region from the engineering and scientific perspectives.

4.3.7. Summary of Regional Site Selection

Malapert Massif, with its high elevation, prolonged sunlight exposure, and excellent Earth visibility, has been identified as a preferred site for the Artemis III mission, making it suitable for long-term exploration missions. Its proximity to key scientific hotspots near the lunar South Pole further enhances its scientific exploration potential. Shackleton Crater, along with the nearby regions of the connecting ridge and peak near Shackleton, is a focal area for volatile detection due to its extensive permanently shadowed regions and extreme temperature conditions. Despite challenges related to terrain and communication, the area's abundant water ice resources and unique environment offer significant strategic value

for long-term lunar exploration. Haworth Crater, characterized by its low temperatures and high hydrogen abundance, has become a hotspot for international lunar missions. Suitable landing zones are primarily distributed along the crater's edges, avoiding areas with high roughness and steep slopes. Cabeus Crater, known for its low-temperature environment and water ice deposits, which were confirmed by the LCROSS mission, is a critical area for scientific exploration. The proposed landing site on the northern ridge is close to the scientifically valuable crater floor. Shoemaker Crater and the adjacent Nobile Rim1 region, with their vast permanently shadowed areas and rich volatile potential, are ideal locations for detecting water ice and other volatiles. Suitable landing zones are mainly concentrated along the crater edges and ridges. The Shiv Shakti Point landing site of Chandrayaan-3, with its flat terrain, favorable illumination, and communication conditions, is well suited for safe landing and resource exploration, while its proximity to the lunar South Pole offers potential for water ice detection. The Boguslawsky Crater, selected for the Luna 25 mission, benefits from good illumination and communication conditions, as well as potential water ice resources, making it a prime area for scientific exploration. The proposed landing site is located on the eastern side, which exhibits high scientific value. Additionally, the 10 potential landing sites proposed by Zhang et al. all fall within suitable landing zones. Overall, the selection of these regions integrates both engineering considerations (such as slope, illumination, and communication) and scientific value (such as water ice resources and volatile detection), providing critical reference points for future lunar exploration missions.

5. Discussion

The application of the self-organizing mapping (SOM) method to the optimal selection of lunar South Pole landing zones is an efficient and innovative idea. The method downscales and visualizes multidimensional feature data (e.g., slope, illumination and communication conditions, surface roughness, hydrogen abundance, water ice resources, etc.) to help identify potentially preferable landing areas.

First, the SOM method has the risk of information loss when dealing with multidimensional data, especially in regions such as the lunar South Pole, with its complex terrain and uneven distribution of resources. Although the SOM method is able to demonstrate the clustering patterns of data through dimensionality reduction and visualization, due to the high dimensionality and complexity of the data, certain key features may be weakened or lost during the dimensionality reduction process, resulting in less accurate clustering results. Improvements can include introducing more advanced dimensionality reduction techniques to minimize the information loss and combining this with multi-source data fusion techniques to enhance the ability to capture key features.

Second, the SOM approach has limitations in feature importance analysis. Since the SOM method itself cannot directly provide the contribution of each feature to the clustering results, the feature importance needs to be indirectly assessed by introducing supervised learning models (e.g., with a random forest). However, this approach still cannot fully address the problem of complex relationships among features, especially when the weights of different features are inconsistent. Future improvements can explore combining deep learning models to more accurately reflect the relative importance between features through automatic feature extraction and weight assignment, thus enhancing the interpretability and reliability of clustering results.

Moreover, as an unsupervised method, SOM has the advantage of revealing inherent patterns and structures within the data without relying on pre-labeled ground truth. However, this does present limitations, as there is no direct validation of the identified "optimal" sites, and there is a potential risk of identifying landing sites that might be less

optimal due to unmodeled hazards. For example, the SOM might group similar regions together based on the input features, but without ground truth data, we cannot fully verify whether these sites are truly optimal or if they contain hidden hazards (e.g., small craters, rocks, or uneven surface features) that were not captured in the input data. To mitigate this risk, future studies could involve cross-validation with known landing sites or integration of additional information from other sources, such as past mission data, high-resolution imagery, or field observations, to validate the suitability of the identified sites.

Finally, data quality and preprocessing have a significant impact on the clustering effect of the SOM method. Due to the inhomogeneity of data collection in the South Polar region of the Moon, feature data in some regions may be under-sampled, resulting in uneven spatial distribution of clustering results. In addition, the SOM method is sensitive to outliers, and normalization and denoising in data preprocessing are crucial. Improvements can include the development of more robust data preprocessing algorithms to minimize the interference of outliers and noise on the clustering results, and data enhancement techniques can be developed to compensate for the under-sampling problem so as to improve the applicability and stability of the SOM method in lunar South Pole landing zone selection.

Overall, the SOM method demonstrates great potential in lunar South Pole landing zone selection, but it still needs to be combined with more advanced data processing and analysis techniques to overcome its limitations and better support future lunar exploration missions.

6. Conclusions

The self-organizing mapping (SOM) method provides an effective means of clustering and visualizing multidimensional feature data during the selection of lunar South Pole landing zones. By downscaling data such as slope, light, communication conditions, roughness, hydrogen abundance, and water ice resources, the SOM method is able to identify potentially preferable areas that meet specific engineering and scientific needs. Combined with a supervised learning model such as a random forest, the clustering results of the SOM method are further analyzed to calculate the importance weights of each feature. This combined approach effectively compensates for the limitations of the SOM method in feature contribution analysis and allows for enhanced explanatory power and rationalization of landing zone selection, leading to the following conclusions.

1. The results of the engineering, scientific, and comprehensive SOM evaluation of the South Pole combined with 10 kinds of data were obtained, and the ranges of regions at the South Pole suitable for landing from engineering, scientific, and comprehensive perspectives accounted for 9.05%, 5.95%, and 5.08%, respectively.

2. The feature importance of each data point was weighted based on SOM automated site selection. In the engineering results, the weights from high to low were as follows: communication (0.28), light (0.24), slope (0.22), kilometer-scale roughness (0.14), and hectometer-scale roughness (0.12). In the scientific results, the weights from high to low were as follows: gravity anomaly (0.36), iron oxide (0.31), hydrogen abundance (0.14), geological map kernel density analysis (0.09), and water ice distance analysis (0.09). In the synthesized results, the weights were, in descending order, communication (0.23), hydrogen abundance (0.14), kilometer-scale roughness (0.13), slope (0.12), water ice distance analysis (0.10), light (0.10), hectometer-scale roughness (0.06), geological map kernel density analysis (0.06), gravity anomaly (0.05), and iron oxide (0.03). In the middle, the kilometer-scale roughness data were slightly elevated in the combined weights, which was consistent with the conclusion that these data reflect not only the surface roughness from

the engineering point of view but also the bedrock geology from the scientific point of view [48].

3. Binary classification results of the South Pole landing suitability were obtained after threshold screening, and the results showed that 10 of the 10 preselected landing sites selected from Zhang et al. [55] fell within the suitable landing range, proving the effectiveness of the SOM model. Then, nine preselected landing zones were analyzed.

Although the SOM method has its challenges in scenarios with uneven data or complex correlations, its application in landing zone preselection shows good adaptability and provides reliable support for multi-feature integrated analysis for future lunar exploration missions. Through rational data preprocessing and adaptive screening methods, the SOM method can play an important role in the planning and resource assessment of lunar South Pole missions, providing a key reference for landing zone selection decisions.

Author Contributions: Conceptualization, Y.W. and H.L.; methodology, Y.W. and H.L.; software, H.L.; validation, S.W.; formal analysis, H.L. and S.W.; resources, S.Z.; data curation, J.L., K.Z. and S.Z.; writing—original draft preparation, H.L.; writing—review and editing, Y.W. and S.W.; visualization, H.L. and S.Z.; supervision, J.L. and K.Z.; project administration, Y.W.; funding acquisition, Y.W. All authors have read and agreed to the published version of the manuscript.

Funding: This research was funded by the National Key Research and Development Program of China (grant number: 2022YFF0503100).

Data Availability Statement: In this study, the WAC image data used in Figure 1 can be downloaded at: https://astrogeology.usgs.gov/search/map/moon_lro_lroc_wac_global_morphology_mosaic_100m (accessed on June 2013). The lunar South Pole remote sensing data used in Figure 2 can be found at the following locations: slope (Planetary Data System LOLA Data node (http://imbrium.mit.edu/EXTRAS/SLDEM2015/ (accessed on 24 January 2022))), Sun visibility and Earth visibility [9], roughness [48], FeO [49], hydrogen abundance [50], water ice exposure [38], geological map [52], and gravity [51].

Acknowledgments: The authors express their thanks to the people who helped with this study and the providers of the data used in this article, and they acknowledge the valuable suggestions from the peer reviewers.

Conflicts of Interest: The authors declare no conflicts of interest regarding the publication of this paper.

References

1. Watson, K.; Murray, B.; Brown, H. On the possible presence of ice on the Moon. *J. Geophys. Res.* **1961**, *66*, 1598–1600. [CrossRef]
2. Hayne, P.O.; Hendrix, A.; Sefton-Nash, E.; Siegler, M.A.; Lucey, P.G.; Retherford, K.D.; Williams, J.-P.; Greenhagen, B.T.; Paige, D.A. Evidence for exposed water ice in the Moon's south polar regions from Lunar Reconnaissance Orbiter ultraviolet albedo and temperature measurements. *Icarus* **2015**, *255*, 58–69. [CrossRef]
3. Flahaut, J.; Carpenter, J.; Williams, J.P.; Anand, M.; Crawford, I.A.; van Westrenen, W.; Füri, E.; Xiao, L.; Zhao, S. Regions of interest (ROI) for future exploration missions to the lunar South Pole. *Planet. Space Sci.* **2020**, *180*, 104750. [CrossRef]
4. Lin, Y.; Tronche, E.J.; Steenstra, E.S.; van Westrenen, W. Evidence for an early wet Moon from experimental crystallization of the lunar magma ocean. *Nat. Geosci.* **2017**, *10*, 14–18. [CrossRef]
5. Lin, Y.; van Westrenen, W. Isotopic evidence for volatile replenishment of the Moon during the Late Accretion. *Natl. Sci. Rev.* **2019**, *6*, 1247–1254. [CrossRef]
6. Vasavada, A.R.; Paige, D.A.; Wood, S.E. Near-Surface Temperatures on Mercury and the Moon and the Stability of Polar Ice Deposits. *Icarus* **1999**, *141*, 179–193. [CrossRef]
7. Mazarico, E.; Barker, M.K.; Jagge, A.M.; Britton, A.W.; Lawrence, S.J.; Bleacher, J.E.; Petro, N.E. Sunlit pathways between south pole sites of interest for lunar exploration. *Acta Astronaut.* **2023**, *204*, 49–57. [CrossRef]
8. Gläser, P.; Oberst, J.; Neumann, G.A.; Mazarico, E.; Speyerer, E.J.; Robinson, M.S. Illumination conditions at the lunar poles: Implications for future exploration. *Planet. Space Sci.* **2018**, *162*, 170–178. [CrossRef]
9. Mazarico, E.; Neumann, G.A.; Smith, D.E.; Zuber, M.T.; Torrence, M.H. Illumination conditions of the lunar polar regions using LOLA topography. *Icarus* **2011**, *211*, 1066–1081. [CrossRef]

10. Flahaut, J.; Blanchette-Guertin, J.F.; Jilly, C.; Sharma, P.; Souchon, A.; van Westrenen, W.; Kring, D.A. Identification and characterization of science-rich landing sites for lunar lander missions using integrated remote sensing observations. *Adv. Space Res.* **2012**, *50*, 1647–1665. [CrossRef]
11. Lemelin, M.; Blair, D.M.; Roberts, C.E.; Runyon, K.D.; Nowka, D.; Kring, D.A. High-priority lunar landing sites for in situ and sample return studies of polar volatiles. *Planet. Space Sci.* **2014**, *101*, 149–161. [CrossRef]
12. Gawronska, A.J.; Barrett, N.; Boazman, S.J.; Gilmour, C.M.; Halim, S.H.; Harish; McCanaan, K.; Satyakumar, A.V.; Shah, J.; Meyer, H.M.; et al. Geologic context and potential EVA targets at the lunar south pole. *Adv. Space Res.* **2020**, *66*, 1247–1264. [CrossRef]
13. Spudis, P.D.; Bussey, B.; Plescia, J.; Josset, J.-L.; Beauvivre, S. Geology of Shackleton Crater and the south pole of the Moon. *Geophys. Res. Lett.* **2008**, *35*, L14201. [CrossRef]
14. NASA. NASA's Plan for Sustained Lunar Exploration and Development. Available online: https://www.nasa.gov/sites/default/files/atoms/files/a_sustained_lunar_presence_nspc_report4220final.pdf (accessed on 6 April 2023).
15. Fong, T.; Bluethmann, B.; Bridgwater, L. Overview of the Volatiles Investigating Polar Exploration Rover. In Proceedings of the Lunar Surface Innovation Consortium Meeting, Bowie, MD, USA, 31 August 2021.
16. Hiesinger, H.; Landgraf, M.; Carey, W.; Karouji, Y.; Haltigin, T.; Osinski, G.; Mall, U.; Hashizume, K.; Heracles Science Working Group. HERACLES: An ESA-JAXA-CSA Joint Study on Returning to the Moon. In Proceedings of the 50th Lunar and Planetary Science Conference, Woodlands, TX, USA, 18–22 March 2019.
17. Kanu, N.J.; Gupta, E.; Verma, G.C. An insight into India's Moon mission—Chandrayan-3: The first nation to land on the southernmost polar region of the Moon. *Planet. Space Sci.* **2024**, *242*, 105864. [CrossRef]
18. Kazmerchuk, P.V.; Shirshakov, A.E. The Luna-25 Spacecraft: Return to the Moon. *Sol. Syst. Res.* **2021**, *55*, 496–508. [CrossRef]
19. Hu, T.; Yang, Z.; Li, M.; van der Bogert, C.H.; Kang, Z.; Xu, X.; Hiesinger, H. Possible sites for a Chinese International Lunar Research Station in the Lunar South Polar Region. *Planet. Space Sci.* **2023**, *227*, 105623. [CrossRef]
20. Grant, J.A.; Golombek, M.P.; Wilson, S.A.; Farley, K.A.; Williford, K.H.; Chen, A. The science process for selecting the landing site for the 2020 Mars rover. *Planet. Space Sci.* **2018**, *164*, 106–126. [CrossRef]
21. Turchinskaya, O.I.; Slyuta, E.N. Landing site choice for Luna-27 mission in the Moon South Polar Region. *Acta Astronaut.* **2024**, *222*, 346–358. [CrossRef]
22. Golombek, M.P.; Grant, J.A.; Parker, T.J.; Kass, D.M.; Crisp, J.A.; Squyres, S.W.; Haldemann, A.F.C.; Adler, M.; Lee, W.J.; Bridges, N.T.; et al. Selection of the Mars Exploration Rover landing sites. *J. Geophys. Res. Planets* **2003**, *108*, 8072. [CrossRef]
23. Zeng, X.; Mu, L. Lunar Spatial Environmental Indicators Dynamically Modeling Based Exploration Area Selection. *Geomat. Inf. Sci. Wuhan Univ.* **2017**, *42*, 91–96. [CrossRef]
24. Wen, S.; Wang, Y.; Gong, Q.; Liu, J.; Kang, X.; Liu, H.; Chen, R.; Zhu, K.; Zhang, S. A New Robust Lunar Landing Selection Method Using the Bayesian Optimization of Extreme Gradient Boosting Model (BO-XGBoost). *Remote Sens.* **2024**, *16*, 3632. [CrossRef]
25. Feng, Y.; Li, H.; Tong, X.; Li, P.; Wang, R.; Chen, S.; Xi, M.; Sun, J.; Wang, Y.; He, H.; et al. Optimized Landing Site Selection at the Lunar South Pole: A Convolutional Neural Network Approach. *IEEE J. Sel. Top. Appl. Earth Obs. Remote Sens.* **2024**, *17*, 10998–11015. [CrossRef]
26. Liu, H.; Wang, Y.; Wen, S.; Liu, J.; Wang, J.; Cao, Y.; Meng, Z.; Zhang, Y. A New Blind Selection Approach for Lunar Landing Zones Based on Engineering Constraints Using Sliding Window. *Remote Sens.* **2023**, *15*, 3184. [CrossRef]
27. Cao, Y.; Wang, Y.; Liu, J.; Zeng, X.; Wang, J. Selection of Whole-Moon Landing Zones Based on Weights of Evidence and Fractals. *Remote Sens.* **2022**, *14*, 4623. [CrossRef]
28. Kohonen, T. The self-organizing map. *Proc. IEEE* **1990**, *78*, 1464–1480. [CrossRef]
29. Wickramasinghe, C.S.; Amarasinghe, K.; Manic, M. Deep Self-Organizing Maps for Unsupervised Image Classification. *IEEE Trans. Ind. Inform.* **2019**, *15*, 5837–5845. [CrossRef]
30. Bussey, D.B.J.; McGovern, J.A.; Spudis, P.D.; Neish, C.D.; Noda, H.; Ishihara, Y.; Sørensen, S.A. Illumination conditions of the south pole of the Moon derived using Kaguya topography. *Icarus* **2010**, *208*, 558–564. [CrossRef]
31. De Rosa, D.; Bussey, B.; Cahill, J.T.; Lutz, T.; Crawford, I.A.; Hackwill, T.; van Gasselt, S.; Neukum, G.; Witte, L.; McGovern, A.; et al. Characterisation of potential landing sites for the European Space Agency's Lunar Lander project. *Planet. Space Sci.* **2012**, *74*, 224–246. [CrossRef]
32. Gläser, P.; Scholten, F.; De Rosa, D.; Marco Figuera, R.; Oberst, J.; Mazarico, E.; Neumann, G.A.; Robinson, M.S. Illumination conditions at the lunar south pole using high resolution Digital Terrain Models from LOLA. *Icarus* **2014**, *243*, 78–90. [CrossRef]
33. McGovern, J.A.; Bussey, D.B.; Greenhagen, B.T.; Paige, D.A.; Cahill, J.T.S.; Spudis, P.D. Mapping and characterization of non-polar permanent shadows on the lunar surface. *Icarus* **2013**, *223*, 566–581. [CrossRef]
34. Speyerer, E.J.; Robinson, M.S. Persistently illuminated regions at the lunar poles: Ideal sites for future exploration. *Icarus* **2013**, *222*, 122–136. [CrossRef]
35. Zhang, J.A.; Paige, D.A. Cold-trapped organic compounds at the poles of the Moon and Mercury: Implications for origins. *Geophys. Res. Lett.* **2009**, *36*, L16203. [CrossRef]

36. Paige, D.A.; Siegler, M.A.; Zhang, J.A.; Hayne, P.O.; Foote, E.J.; Bennett, K.A.; Vasavada, A.R.; Greenhagen, B.T.; Schofield, J.T.; McCleese, D.J.; et al. Diviner Lunar Radiometer Observations of Cold Traps in the Moon's South Polar Region. *Science* **2010**, *330*, 479–482. [CrossRef]
37. Fisher, E.A.; Lucey, P.G.; Lemelin, M.; Greenhagen, B.T.; Siegler, M.A.; Mazarico, E.; Aharonson, O.; Williams, J.-P.; Hayne, P.O.; Neumann, G.A.; et al. Evidence for surface water ice in the lunar polar regions using reflectance measurements from the Lunar Orbiter Laser Altimeter and temperature measurements from the Diviner Lunar Radiometer Experiment. *Icarus* **2017**, *292*, 74–85. [CrossRef]
38. Li, S.; Lucey, P.G.; Milliken, R.E.; Hayne, P.O.; Fisher, E.; Williams, J.-P.; Hurley, D.M.; Elphic, R.C. Direct evidence of surface exposed water ice in the lunar polar regions. *Proc. Natl. Acad. Sci. USA* **2018**, *115*, 8907–8912. [CrossRef]
39. Lawrence, D.J. A tale of two poles: Toward understanding the presence, distribution, and origin of volatiles at the polar regions of the Moon and Mercury. *J. Geophys. Res. Planets* **2017**, *122*, 21–52. [CrossRef]
40. Sanin, A.B.; Mitrofanov, I.G.; Litvak, M.L.; Bakhtin, B.N.; Bodnarik, J.G.; Boynton, W.V.; Chin, G.; Evans, L.G.; Harshman, K.; Fedosov, F.; et al. Hydrogen distribution in the lunar polar regions. *Icarus* **2017**, *283*, 20–30. [CrossRef]
41. Jawin, E.R.; Valencia, S.N.; Watkins, R.N.; Crowell, J.M.; Neal, C.R.; Schmidt, G. Lunar Science for Landed Missions Workshop Findings Report. *Earth Space Sci.* **2019**, *6*, 2–40. [CrossRef]
42. Colaprete, A.; Schultz, P.; Heldmann, J.; Wooden, D.; Shirley, M.; Ennico, K.; Hermalyn, B.; Marshall, W.; Ricco, A.; Elphic, R.C.; et al. Detection of Water in the LCROSS Ejecta Plume. *Science* **2010**, *330*, 463–468. [CrossRef]
43. Crawford, I.A. Lunar resources: A review. *Prog. Phys. Geogr. Earth Environ.* **2015**, *39*, 137–167. [CrossRef]
44. Anand, M. Lunar Water: A Brief Review. *Earth Moon Planets* **2010**, *107*, 65–73. [CrossRef]
45. Arnold, J.R. Ice in the lunar polar regions. *J. Geophys. Res. Solid Earth* **1979**, *84*, 5659–5668. [CrossRef]
46. Smith, D.E.; Zuber, M.T.; Neumann, G.A.; Mazarico, E.; Lemoine, F.G.; Head Iii, J.W.; Lucey, P.G.; Aharonson, O.; Robinson, M.S.; Sun, X.; et al. Summary of the results from the lunar orbiter laser altimeter after seven years in lunar orbit. *Icarus* **2017**, *283*, 70–91. [CrossRef]
47. Barker, M.K.; Mazarico, E.; Neumann, G.A.; Zuber, M.T.; Haruyama, J.; Smith, D.E. A new lunar digital elevation model from the Lunar Orbiter Laser Altimeter and SELENE Terrain Camera. *Icarus* **2016**, *273*, 346–355. [CrossRef]
48. Kreslavsky, M.A.; Head, J.W.; Neumann, G.A.; Rosenburg, M.A.; Aharonson, O.; Smith, D.E.; Zuber, M.T. Lunar topographic roughness maps from Lunar Orbiter Laser Altimeter (LOLA) data: Scale dependence and correlation with geologic features and units. *Icarus* **2013**, *226*, 52–66. [CrossRef]
49. Lemelin, M.; Lucey, P.G.; Camon, A. Compositional Maps of the Lunar Polar Regions Derived from the Kaguya Spectral Profiler and the Lunar Orbiter Laser Altimeter Data. *Planet. Sci. J.* **2022**, *3*, 63. [CrossRef]
50. Lawrence, D.J.; Peplowski, P.N.; Wilson, J.T.; Elphic, R.C. Global Hydrogen Abundances on the Lunar Surface. *J. Geophys. Res. Planets* **2022**, *127*, e2022JE007197. [CrossRef]
51. Lemoine, F.G.; Goossens, S.; Sabaka, T.J.; Nicholas, J.B.; Mazarico, E.; Rowlands, D.D.; Loomis, B.D.; Chinn, D.S.; Neumann, G.A.; Smith, D.E.; et al. GRGM900C: A degree 900 lunar gravity model from GRAIL primary and extended mission data. *Geophys. Res. Lett.* **2014**, *41*, 3382–3389. [CrossRef]
52. Ji, J.; Guo, D.; Liu, J.; Chen, S.; Ling, Z.; Ding, X.; Han, K.; Chen, J.; Cheng, W.; Zhu, K.; et al. The 1:2,500,000-scale geologic map of the global Moon. *Sci. Bull.* **2022**, *67*, 1544–1548. [CrossRef]
53. Ciazela, J.; Bakala, J.; Kowalinski, M.; Pieterek, B.; Steslicki, M.; Ciazela, M.; Paslawski, G.; Zalewska, N.; Sterczewski, L.; Szaforz, Z.; et al. Lunar ore geology and feasibility of ore mineral detection using a far-IR spectrometer. *Front. Earth Sci.* **2023**, *11*, 1190825. [CrossRef]
54. Zwierzyński, A.J.; Ciążela, J.; Boroń, P.; Binkowska, W. Lunar Cold Microtraps as Future Source of Raw Materials—Business and Technological Perspective. *Appl. Sci.* **2023**, *13*, 3030. [CrossRef]
55. Zhang, H.; Du, Y.; Li, F.; Zhang, H.; Ma, J.; Sheng, L.; Wu, K. Proposals for Sites Selection of Soft Landing on Lunar South Polar Region. *J. Deep Space Explor.* **2020**, *7*, 232–240. [CrossRef]
56. Heldmann, J.L.; Colaprete, A.; Elphic, R.C.; Bussey, B.; McGovern, A.; Beyer, R.; Lees, D.; Deans, M. Site selection and traverse planning to support a lunar polar rover mission: A case study at Haworth Crater. *Acta Astronaut.* **2016**, *127*, 308–320. [CrossRef]
57. James, P.B.; Smith, D.E.; Byrne, P.K.; Kendall, J.D.; Melosh, H.J.; Zuber, M.T. Deep Structure of the Lunar South Pole-Aitken Basin. *Geophys. Res. Lett.* **2019**, *46*, 5100–5106. [CrossRef]
58. Xiao, L.; Qiao, L.; Xiao, Z.; Huang, Q.; He, Q.; Zhao, J.; Xue, Z.; Huang, J. Major scientific objectives and candidate landing sites suggested for future lunar explorations. *Sci. Sin. Phys. Mech. Astron.* **2016**, *46*, 29602. [CrossRef]
59. Kozlova, E.A.; Lazarev, E.N. Crater Cabeus as Possible Cold Trap for Volatiles Near South Pole of the Moon. In Proceedings of the 41st Annual Lunar and Planetary Science Conference, The Woodlands, TX, USA, 1–5 March 2010; p. 1779.
60. Feldman, W.C.; Maurice, S.; Lawrence, D.J.; Little, R.C.; Lawson, S.L.; Gasnault, O.; Wiens, R.C.; Barraclough, B.L.; Elphic, R.C.; Prettyman, T.H.; et al. Evidence for water ice near the lunar poles. *J. Geophys. Res. Planets* **2001**, *106*, 23231–23251. [CrossRef]

61. Campbell, B.A.; Campbell, D.B. Regolith properties in the south polar region of the Moon from 70-cm radar polarimetry. *Icarus* **2006**, *180*, 1–7. [CrossRef]
62. Djachkova, M.V.; Mitrofanov, I.G.; Sanin, A.B.; Litvak, M.L.; Tret'yakov, V.I. Characterization of the Luna-25 Landing Sites. *Sol. Syst. Res.* **2021**, *55*, 509–528. [CrossRef]
63. Mitrofanov, I.G.; Zelenyi, L.M.; Tret'yakov, V.I.; Kalashnikov, D.V. Luna-25: The First Polar Mission to the Moon. *Sol. Syst. Res.* **2021**, *55*, 485–495. [CrossRef]

Disclaimer/Publisher's Note: The statements, opinions and data contained in all publications are solely those of the individual author(s) and contributor(s) and not of MDPI and/or the editor(s). MDPI and/or the editor(s) disclaim responsibility for any injury to people or property resulting from any ideas, methods, instructions or products referred to in the content.

remote sensing

MDPI

Article

Characteristics and Climatic Indications of Ice-Related Landforms at Low Latitudes (0°–±30°) on Mars

Yan Zhou [1], Yu-Yan Sara Zhao [1,2,*], Xiaoting Xu [1] and Yiran Wang [3]

[1] Research Center for Planetary Science, College of Earth and Planetary Sciences, Chengdu University of Technology, Chengdu 610059, China; zhouyan092@stu.cdut.edu.cn (Y.Z.); xuxt@cdut.edu.cn (X.X.)
[2] CAS Center for Excellence in Comparative Planetology, Hefei 230026, China
[3] Department of Earth and Space Sciences, Southern University of Science and Technology, Shenzhen 518055, China; wangyr@sustech.edu.cn
* Correspondence: zhaoyuyan@cdut.edu.cn

Abstract: The deposition and evolution of ice-rich materials on Martian surfaces offer valuable insights into climatic evolution and the potential driving forces behind global climate change. Substantial evidence indicates that the mid-latitudes of Mars played a crucial role in the formation and development of glacial and periglacial landforms during the Amazonian period. However, few studies have comprehensively examined ice-related landforms in the low-latitude region of Mars. Whether extensive glacial activity has occurred in the equatorial region of Mars and whether there are any potential geological records of such activities remain unclear. In this study, we analyzed remote sensing data from the Martian equatorial region (0°–±30°) and identified existing glacial/periglacial features, as well as remnant landforms of past glaciation. Our findings reveal that glaciation at low latitudes is more widespread than previously thought, with ice-related remnants extending as far equatorward as 13°N in the northern hemisphere and 19°S in the southern hemisphere, highlighting a broader latitudinal range for ice-related landforms. These landforms span multiple episodes of Martian geological history, supporting the hypothesis on the occurrence of repeated glaciation and various high-obliquity events. Evidence of dynamic interactions between ice deposition and sublimation in low-latitude regions demonstrates substantial ice loss over time, leaving ice-related remnants that provide valuable insights into Mars' climatic evolution. Based on volumetric estimates of the concentric crater fill (CCF), the low-latitude regions of Mars may contain up to 1.05×10^3 km^3 of ice. This corresponds to a global equivalent ice layer thickness ranging from 21.7 mm (assuming a pore ice with 30% ice content) to 65.1 mm (assuming glacial ice with 90% ice content), suggesting a potentially greater low-latitude ice reservoir than previously recognized.

Keywords: Mars; equatorial; buried ice; glacial; periglacial; climate evolution

1. Introduction

Numerous studies have emphasized the critical role of the mid-latitudes (±30°–60°) of Mars in the formation and evolution of glacial and periglacial landforms during the Amazonian period (~3.1 Ga–present) [1–5]. These regions host a variety of glacial landforms (Figure 1), including lineated valley fills (LVFs), lobate debris aprons (LDAs), concentric crater fills (CCFs), and glacier-like forms (GLFs) [6–9]. Recent studies suggest that many of these landforms were formed from debris-covered glaciers, with ice contents of up to 90% [10,11]. Radar interpretation results indicate that substantial quantities of ice are preserved in the subsurface [2,12].

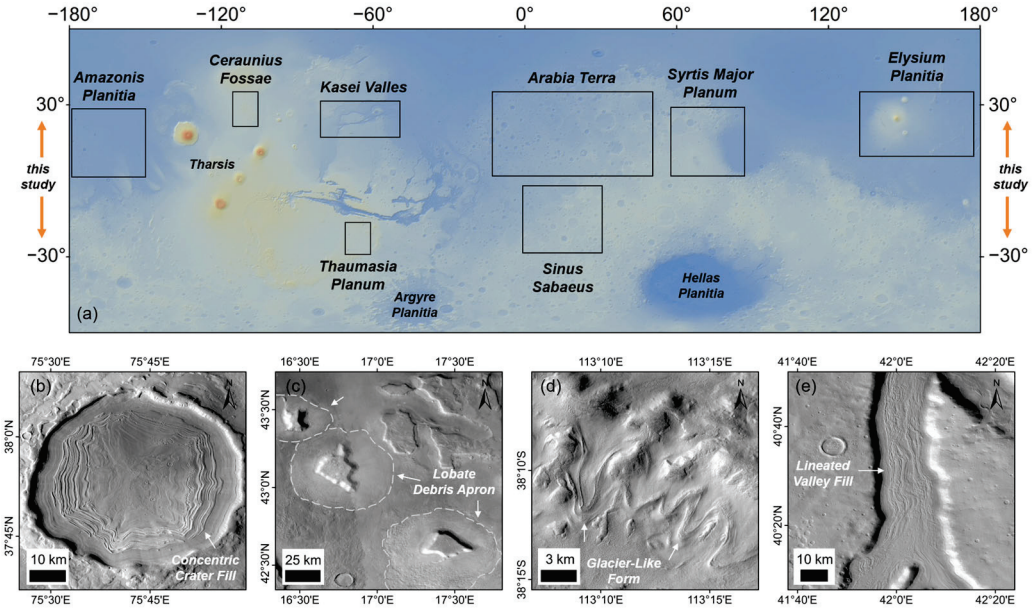


Figure 1. (**a**) Context map of Mars Orbiter Laser Altimeter (MOLA/HRSC) DEM data superimposed on Blendshade. Red represents high elevation, and blue represents low elevation. The map represents the study area of this research (0°–±30°). To more accurately depict the locations of ice-related landforms, the place names of the regions are labeled on the map. (**b**) Example of concentric crater fill (37.88°N, 75.71°E). (**c**) Example of lobate debris apron (42.57°N, 17.26°E). (**d**) Example of a glacier-like form (−38.10°N, 113.12°E). (**e**) Example of a lineated valley fill (40.42°N, 42.02°E).

Ring-mold craters (RMCs) and "brain-terrain" textures are frequently observed on the surfaces of these glacial landforms. RMCs are interpreted as the result of impacts on ice-rich substrates [7,13,14], causing plastic deformation of buried ice that uplifted the crater rim into the characteristic ringed morphology. While they currently lack direct terrestrial analogs, partially collapsed pingos in permafrost regions may bear a superficial resemblance to RMCs, although their origins differ significantly. "Brain-terrain" textures appear as irregular surface patterns on features such as LDAs, LVFs, and CCFs. Although these textures resemble polygonal patterned ground in terrestrial permafrost settings, such as Alaska and Siberia, they likely form due to different mechanisms. On Earth, patterned ground typically results from seasonal freeze–thaw processes, while Martian "brain-terrain" textures are interpreted to develop via the sublimation of ice-rich materials, thermal contraction cracking, and glacio-tectonic deformation [15]. Therefore, despite morphological similarities, "brain-terrain" textures on Mars represent a cold desert, sublimation-dominated analog rather than a freeze–thaw feature. In addition, small-scale polygonal patterns are widely distributed in the mid- to high-latitude regions of Mars and are considered to be closely related to thermal contraction and differential sublimation processes [16]. In contrast, large-scale polygons may indicate the potential presence of freeze–thaw cycles [16].

Global circulation models (GCMs) suggest that Mars' fluctuating orbital obliquity drives the periodic sublimation of polar ice, with ice being transported to equatorial regions during periods of high obliquity [17,18]. At an average obliquity of 35°, ice is primarily stabilized at mid-latitudes, whereas at higher obliquities, such as 45°, ice can extend into equatorial regions [19]. The current interglacial period has led to unstable ice-rich materials near the equator [20,21]. Mars may have experienced multiple ice ages, with glaciers at mid-latitudes forming during periods of high obliquity, particularly in the middle to late Amazonian period [22,23]. Recent studies suggest that glacier-like forms (GLFs) represent remnants of the most recent obliquity shift, providing insights into regional glaciation and

revealing stratigraphic relationships [24,25]. The "brain-terrain" textures observed in mid- to high-latitude mantle polygons reflects the sequential interaction between earlier glacial-like deposition events and subsequent modification by ice-rich mantling and thermal contraction cracking, during more recent cold-climate periods [15]. These findings support the idea of repeated glaciation during high-obliquity events.

Despite extensive research on Martian ice-related features at mid-latitudes, there is a notable gap in terms of studies focusing on low-latitude regions (0°–±30°). While some evidence suggests that the equatorial regions may have experienced glacial/periglacial activity during periods of high obliquity [26–28], comprehensive studies documenting the ice-associated features in these areas are lacking. Previous studies have largely concentrated on mid- and high-latitude regions, where glacial features are more prominent [4,29–32]. For example, large tropical glaciers in regions such as Tharsis Montes and Olympus Mons [33], as well as candidate ice-rich materials in Sinus Sabaeus [34], may have formed during early high-obliquity periods, but the overall extent of ice-related landforms at low latitudes remains unclear. Consequently, it remains unclear whether the absence of documented ice-related features at low latitudes indicates a lack of glacial activity or if these features have been overlooked due to insufficient coverage. Recent evidence revealed elevated hydrogen levels in central Valles Marineris, suggesting that this equatorial region may be a promising site for investigating subsurface water ice [35].

The primary goal of this study is to extend previous investigations by mapping glacier-related landforms in the low-latitude region of Mars (0°–±30°) and analyzing these features in greater detail via high-resolution remote sensing images. We focus on the spatial distribution and key parameters of ice-related landforms, including crater diameter, fill elevation, slope, aspect, and volume, and compare them to similar features found at mid- and high latitudes. By integrating datasets from different latitudes and sources, we seek to identify global patterns in the distributions of ice-related features. Additionally, chronological crater counts were conducted in representative areas to estimate the formation ages of these ice-related deposits, offering new insights into the geological and climatic evolution of Mars during the late Hesperian to Amazonian period.

2. Materials and Methods

2.1. Image Datasets and Surface Property Data

Image mosaics from the Mars Reconnaissance Orbiter (MRO) context camera (CTX; ~5–6 m/pixel) [36] and high-resolution image data from the high-resolution imaging science experiment (HiRISE; ~25 cm/pixel) [37] were used for visual interpretation and detailed geomorphological mapping. Topographic parameters, including elevation, slope, and aspect, were extracted and analyzed using the Mars MGS MOLA-MEX HRSC blended DEM (global, 200 m resolution) [38], which integrates data from the Mars Orbiter Laser Altimeter (MOLA) [39], aboard the NASA Mars Global Surveyor (MGS), and the High-Resolution Stereo Camera (HRSC; 2 m/pixel) [31] on the ESA Mars Express (MEX) spacecraft. The image databases were sourced from the Planetary Data System (PDS) Cartography and Imaging Science Discipline (CISD) Node and the Mars Orbital Data Explorer (ODE). All the CTX images covering the Martian low latitudes (0°–±30°) were systematically examined through detailed visual interpretation. This thorough, frame-by-frame assessment ensured complete coverage and consistency across the entire study area.

2.2. Mapping of a Global Database of Published Characteristics of Typical Glaciers and the Distribution of Buried Water Ice Resources

The identification and mapping of typical glacial surface features on Mars follow the frameworks summarized in previous studies [15,24,40]. Potential ice-related land-

forms, similar to those shown in the work of Diot et al. [41], were identified primarily as depressions and cracks within craters [42].

To distinguish glacial and periglacial landforms from morphologically similar features formed by other geological processes, we apply multiple diagnostic criteria, including morphology, context, and associated surface textures. For example, several crater floor depressions in the study area exhibit concentric talus scarp rings, linear depressions composed of pits, and crack networks. These features are interpreted as remnants of glacial ice-rich fill that underwent sublimation. Their circular symmetry, continuous talus scarp distribution, and a lack of evidence of flood discharge/fluvial erosion or slope collapse suggest that these depressions are not simply the result of gravitational mass wasting, but rather indicate progressive ice loss from crater interiors. Furthermore, their frequent occurrence in association with other glacial morphologies, such as lineated valley fills and lobate debris aprons, reinforces this interpretation. Outside of craters, the identified possible sublimation depressions (PSDNs) exhibit linear depressions and/or steep scarps, as well as depressions with concentric patterns and circular ridges, and lack fracture control or roof collapse structures typical of lava tubes or karstic subsidence features. Their geomorphic appearance, combined with their spatial clustering near known ice-related landforms (e.g., ring-mold craters), supports an interpretation that they are of an ice-related origin, most likely as surface expressions of ground ice sublimation and associated surface collapse or compaction. This integrated geomorphic analysis allows us to differentiate ice-related features from other surface processes and supports the interpretation of widespread glacial/periglacial activity at low latitudes (0°–±30°) on Mars.

To quantify crater fill in the lower latitudes of Mars, we extracted key parameters from the Mars Global ≥1 km Impact Crater Database [43] for craters intersecting our mapped regions. These parameters, including latitude, longitude, and diameter, were extracted to facilitate the calculation of the crater depth and fill volume.

Using the distribution of buried water ice resources mapped by the Mars Subsurface Water Ice Mapping (SWIM) team, we incorporated data from the geomorphology database and composite ice-consistency maps for depths of 1–5 m and >5 m [44]. These datasets are analyzed together in our discussion. We attempted to examine several glacial/periglacial features using publicly available SHARAD data; however, no clear subsurface reflections were detected. As a result, no new SHARAD radar data were processed in this study. The radar-related observations presented are based on previously published datasets and are used here for contextual interpretation.

2.3. Volume Calculation of Concentric Crater Fill (CCF)

To estimate the volume of concentric crater fill (CCF) with the most pronounced surface features at low latitudes, we employed the volume calculation method outlined by Levy et al. [22]. First, the depth of the unfilled impact crater (d) was calculated via the crater diameter (D), and this depth–diameter relationship was established by Garvin et al. [45]. Next, the depth of the fill within the crater (d_f) was determined by subtracting the fill thickness (d_m) from the depth of the unfilled crater (d). The fill thickness (d_m) was calculated as the difference between the maximum rim elevation of the crater and the average elevation of the fill within the crater. Finally, the final filled volume of the CCF was calculated by applying the cavity shape function from Garvin et al. [45] and integrating it over the crater diameter range from 0 to d_f.

2.4. Crater Size–Frequency Distribution (CSFD)

CSFD analysis [46,47] was used to estimate the absolute modeled ages of the deposits within craters in different typical regions. Small craters within these regions were identified

through the use of CTX and HiRISE images. Georeferencing and measurements were performed via ArcGIS 10.8.1 software (https://www.esri.com; accessed on 1 September 2022), crater mapping was conducted via CraterTools (v2.1) [48], and the data analysis was conducted via Craterstats 2.0 software [49]. Crater identification was automated via an automatic crater detection (ACD) tool [50], supplemented by basic visual interpretation and manual corrections. To improve the reliability of the age estimates, we excluded from the statistics both craters superposed on crater wall deposits and those with diameters smaller than 30 m (d < 30 m). After excluding these factors, we applied the production function by Hartmann and Daubar [51] and the chronology function by Hartmann [47] to assess the absolute modeled ages of the deposits.

3. Results

This study surveyed entire low-latitude regions of Mars (0° to ±30°) and identified a total of 4307 ice-related landforms. These features were classified into five major morphological types, listed here in descending order by abundance: crater fills (CFs), lobate debris aprons (LDAs), possible sublimation depressions (PSDNs; non-crater forms), glacier-like forms (GLFs), and lineated valley fills (LVFs) [22].

3.1. Characteristics and Global Distribution of Ice-Related Landforms at Low Latitudes

3.1.1. Crater Fill (CF)

Crater fill (CF) features are the most abundant ice-related landforms in the lower latitudes of Mars, accounting for approximately 85% of the 4307 mapped features across the surveyed low-latitude regions of Mars. We classify CFs into four types on the basis of their morphology: concentric crater fill (CCF) (Figure 2), crater irregular fill (Figure 3), crater directional fill (Figure 4), and crater depression (Figure 5).

CCFs at low latitudes resemble those at mid-latitudes, with the crater floors displaying concentric rings or linear structures (Figure 2). The surface features commonly include "brain-terrain" textures [15] and/or RMC morphologies [13] (Figure 2b,d). Crater irregular fills exhibit ice-related textures (Figure 3), often characterized by linear, ice flow-like patterns and pits, which are likely formed by the sublimation of near-surface ice (Figure 3b). In addition, depressions and scarps near the crater floor edges resemble talus deposits, indicative of glacial retreat [6]. Unique features on the crater floors include circular mesas, degraded craters, and RMCs, although linear or "brain-terrain" textures are less common (Figure 3d). Circular mesas are generally considered erosional remnants, potentially shaped by wind or water-related processes, and, in some cases, may also be linked to sublimation-induced collapse in ice-rich terrains. On Earth, these landforms are part of a morphological continuum, akin to terrestrial plateaus, mesas, and buttes, distinguished by their size. RMCs are present on the surface of the deposited material, with cracks observed on the central mesa (Figure 3e), and a network of polygonal cracks is visible on smooth deposited surfaces (Figure 3c,e). Crater directional fills display the occurrence of deposits on the walls of polar-facing craters (Figure 4). For example, Figure 4a shows the directional filling within the interior of a double-layer ejecta rampart crater in Sabaea Terra. Crack networks are distributed across the depositional surface on the crater floor (Figure 4b). Crater depressions are widespread at low latitudes and exhibit a ring of talus, steep scarps parallel to the crater rim, linear depressions composed of pits, and linear cracks (Figures 5, A1 and A2). These materials are thicker near the crater center and thinner toward the rim (Figure A3). Newly observed ice-rich materials are located near 47°E, 15°N (Figure A1e).

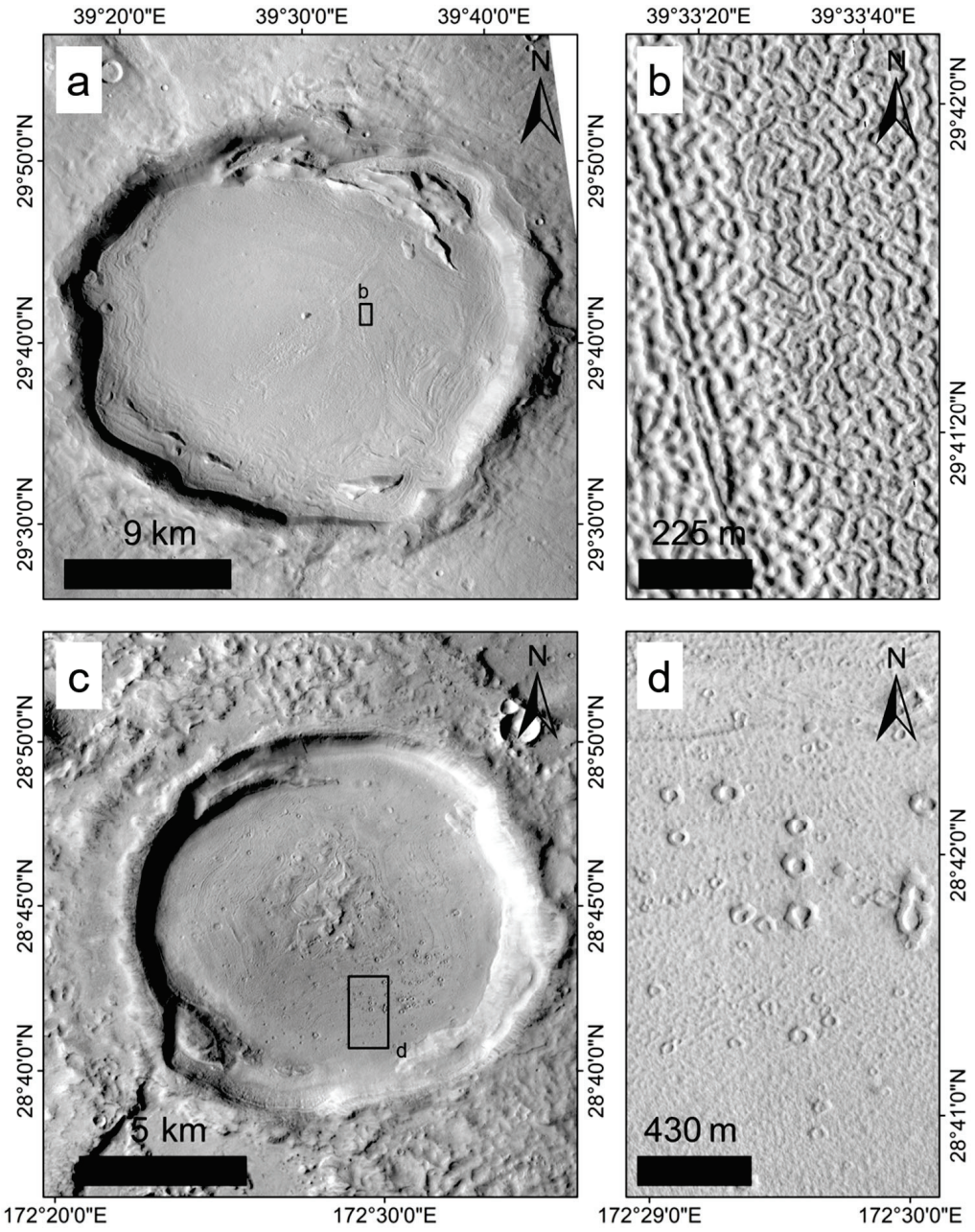


Figure 2. Examples of CCFs at low latitudes on Mars, with the images on the right corresponding to the HiRISE magnified image within the box on the left. (**a**) CCF in Arabia Terra (B16_016062_2119_XI_31N320W; centered at 39.50°E, 29.68°N). (**b**) "Brain-terrain" texture on the CCF surface (ESP_054843_2100_RED). (**c**) Concentric filling pattern on the CCF surface (U23_080080_2106_XN_30N187W; centered at 172.47°E, 28.74°N). (**d**) CCF surfaces characterized by ring-mold craters (RMCs) (ESP_053981_2090_RED).

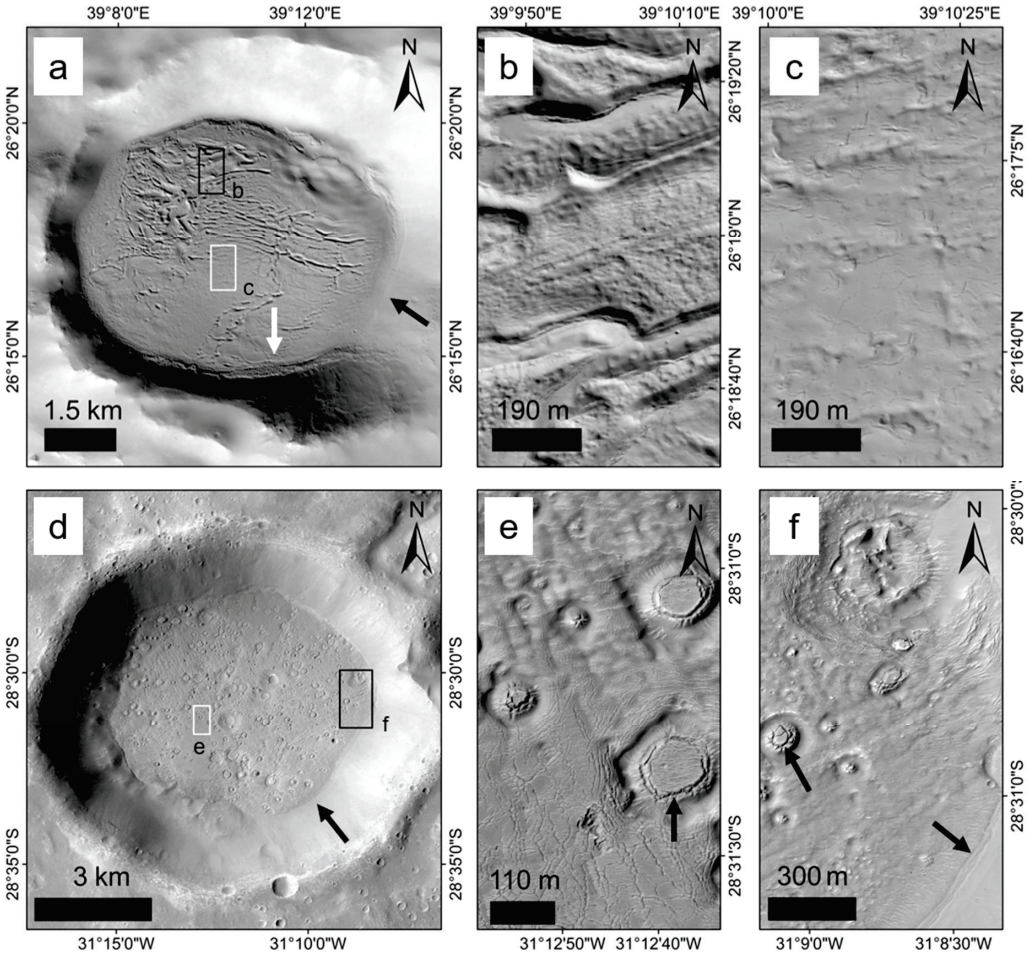


Figure 3. Examples of crater irregular fill at low latitudes on Mars, with the two images on the right (**b**,**c**,**e**,**f**) corresponding to the HiRISE magnified image within the box on the left (**a**,**d**). (**a**) The fill material on the floor of this crater flows like icy surface features, and the surface of the overall floor exhibits linear, but nonconcentric, textures similar to CCFs (glacial flow features). Its surface also contains pits that may have been formed by sublimation of near-surface ice, as well as elongated depressions. Additionally, ice-rich material is present on the pole-facing slope of the crater (indicated by the white arrow in (**a**); J11_049028_2065_XN_26N320W; centered at 39.17°E, 26.28°N). On the floor edge of the crater, a ring of steep talus scarps, parallel to the crater rim, can be observed (black arrow). They are evidence of glacial sublimation and retreat. (**b**) Characterization of ice flow features on the floor of the crater (ESP_049028_2065_RED). (**c**) Depositional surface cluttered with polygon-like cracks (ESP_049028_2065_RED). (**d**) Morphological pattern of the crater irregular fill in Noachis Terra (G06_020535_1510_XI_29S031W; centered at −31.19°E, 28.51°N). The scarps are located on the floor edge of the crater (shown by the black arrow). Crater floors contain circular mesas, fresh bowl craters, ring-mold craters (RMCs), and degraded craters with "oyster shells", a term referring to distinctive layered, curved surface textures that resemble the overlapping structure of oyster shells [7]. Uniquely, the surfaces of deposited materials rarely have a prominently linear or "brain-terrain" texture. (**e**) RMCs on the surface of the deposited material, with cracks appearing on the central mesa. Additionally, polygonal cracks are formed around the RMCs (ESP_020535_1510_RED). **(f**) A heavily degraded crater is visible in the upper part of the panel and is situated on the surface of a crater irregular fill deposit. The black arrows highlight cracks in the central highlands of the RMC and steep talus scarps along the crater walls (ESP_020535_1510_RED). Note that although irregular fills lack the organized tongue-shaped morphology of typical glacier-like forms, their ice flow textures, debris cover, and sublimation-related modifications are broadly consistent with the behavior of rock glaciers on Earth, where ice–debris mixtures undergo slow, ice-supported deformation, similar to those in periglacial settings.

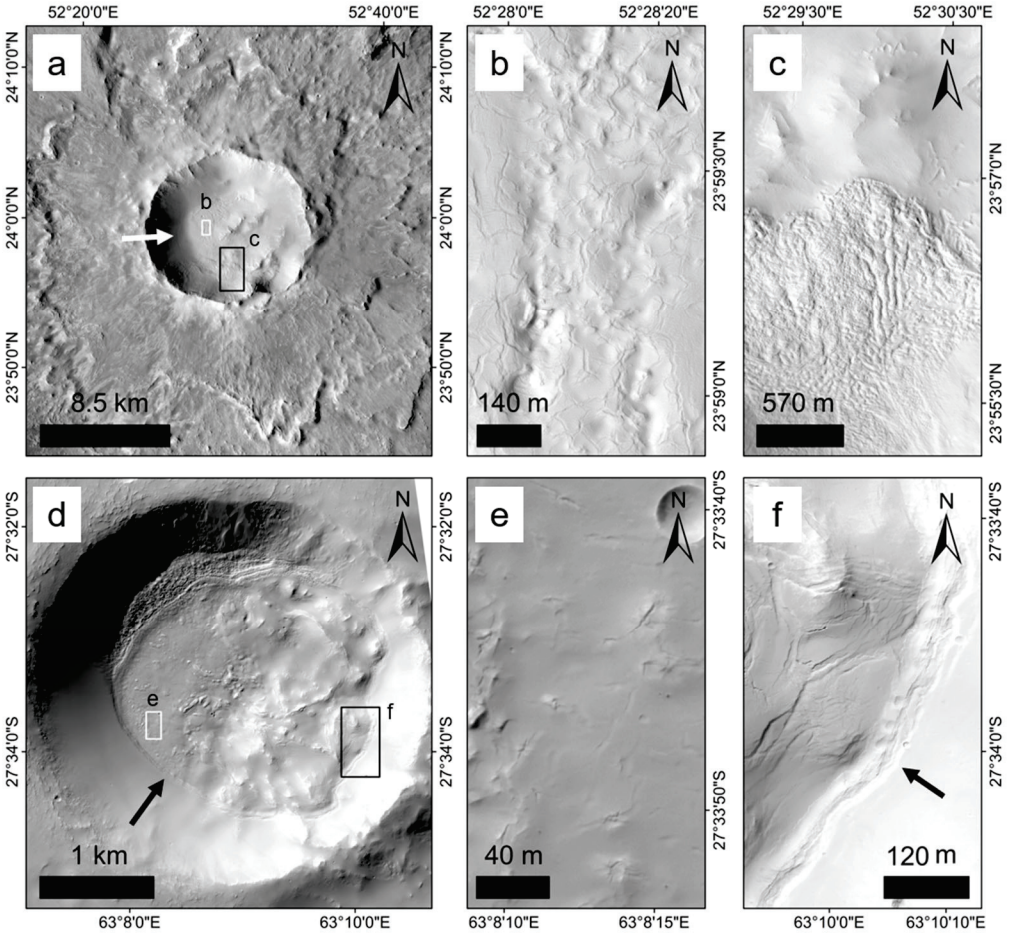


Figure 4. Examples of crater directional fill at low latitudes on Mars, with the two images on the right (**b**,**c**,**e**,**f**) corresponding to the HiRISE magnified image within the box on the left (**a**,**d**). (**a**) Directional filling of the interior of the double-layer ejecta rampart crater in Sabaea Terra (J04_046285_2044_XN_24N307W; centered at 52.49°E, 23.98°N). The scarps are located on the floor edge of the crater (shown by the white arrow). (**b**) Crack network on the deposited surface on the floor of the crater (ESP_046285_2045_RED). (**c**) Deposits on the walls of predominantly poleward-facing craters (ESP_046285_2045_RED). (**d**) Crater directional fill northwest of Hellas Planitia (ESP_034338_1520_RED; centered at 51.07°E, −27.55°N). (**e**) A shallow network of cracks on the deposited surface on the floor of the crater (ESP_034338_1520_RED). (**f**) The black arrows indicate the scarps located on the floor edge of the crater (ESP_034338_1520_RED). The crack networks in (**b**) are morphologically similar to terrestrial patterned ground commonly found in terrestrial permafrost regions, likely formed by thermal contraction in cold-climate regions.

CF features are mostly concentrated in Arabia Terra and northern Syrtis Major Planum in the northern hemisphere, as well as around northern Hellas in the southern hemisphere (Figure 6). In the northern hemisphere (15°–30° latitude), the number of CFs increases significantly with the latitude, and the types become more diverse. The CFs are also distributed west of Elysium, northwest of Amazonis Planitia, near Tartarus Colles, and around the northern edge of Hellas, with additional scattered occurrences in the southern highlands near the 30° latitude across longitudes −90° to 90°. Owing to the dichotomy of Martian north–south topography, the mean elevation of the CFs in the northern hemisphere (−1165 m) is significantly lower than that in the southern hemisphere (552 m). In the northern hemisphere, most CFs occur at negative elevations, referring specifically to the height of the deposit surface measured below the Martian datum (0 m), except in areas such as Ceraunius Fossae, parts of Syrtis Major Planum, and Elysium, where the elevations are positive. In the southern hemisphere, CFs near Uzboi Vallis and north of Hellas are

generally below 0 m, whereas the CFs in other areas at similar latitudes tend to occur above 0 m, particularly north of Thaumasia, where elevations exceed 1700 m.

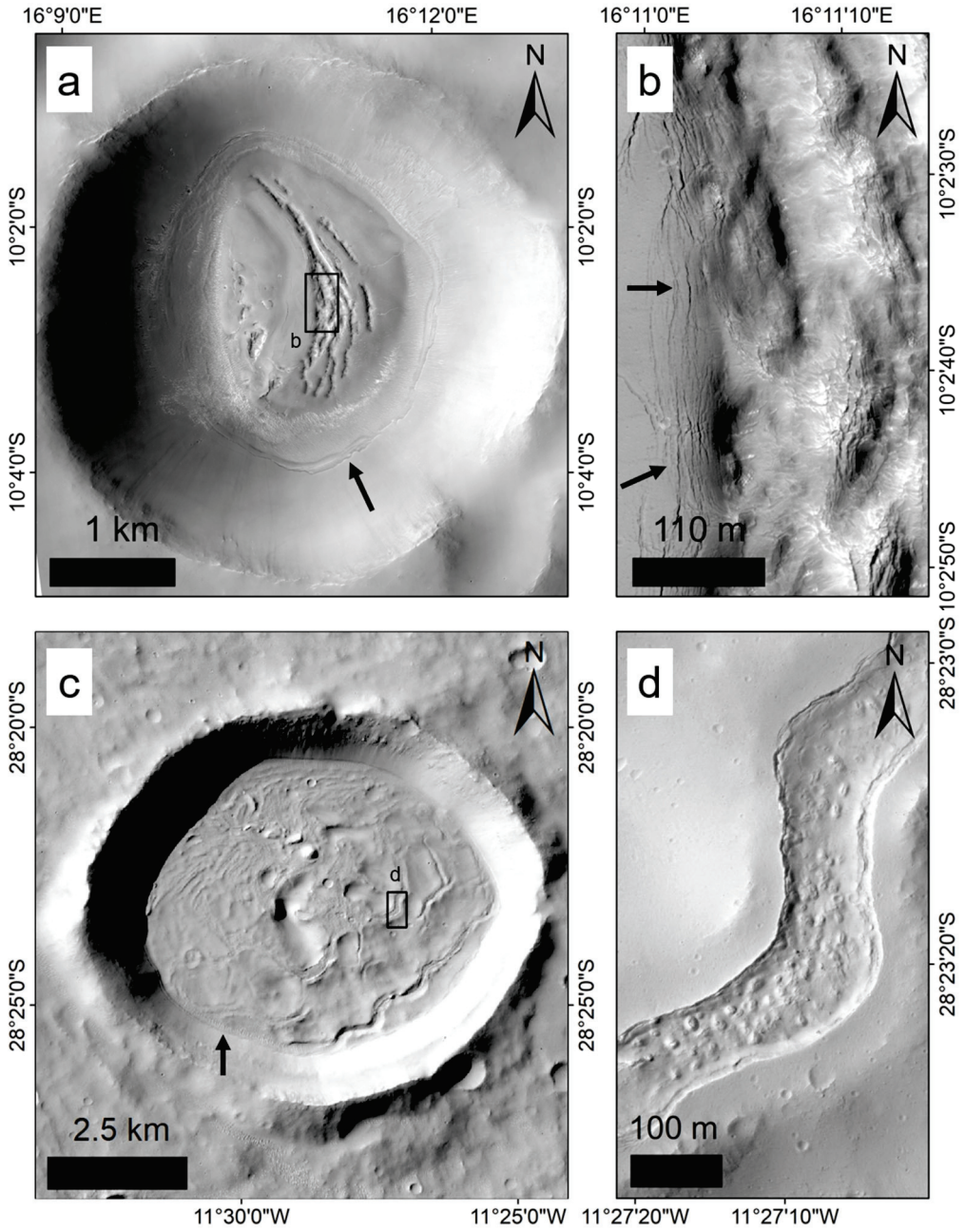


Figure 5. Examples of crater depression at low latitudes on Mars, with the images on the right corresponding to the HiRISE magnified image within the box on the left. (**a**) Crater depression in Sabaea Terra, classified as a subtype of crater fill (ESP_020019_1700_RED; centered at 13.65°E, −10.04°N). (**b**) The pits on the deposited surface have formed linear depressions. Closely spaced linear cracks are observed around the linear depressions (shown by the black arrow). (**c**) Crater depression at Noachis Terra (ESP_081643_1515_RED; centered at −11.47°E, −28.38°N). (**d**) Depression on the floor of the crater. The deposited surface around the depression was much smoother (ESP_081643_1515_RED).

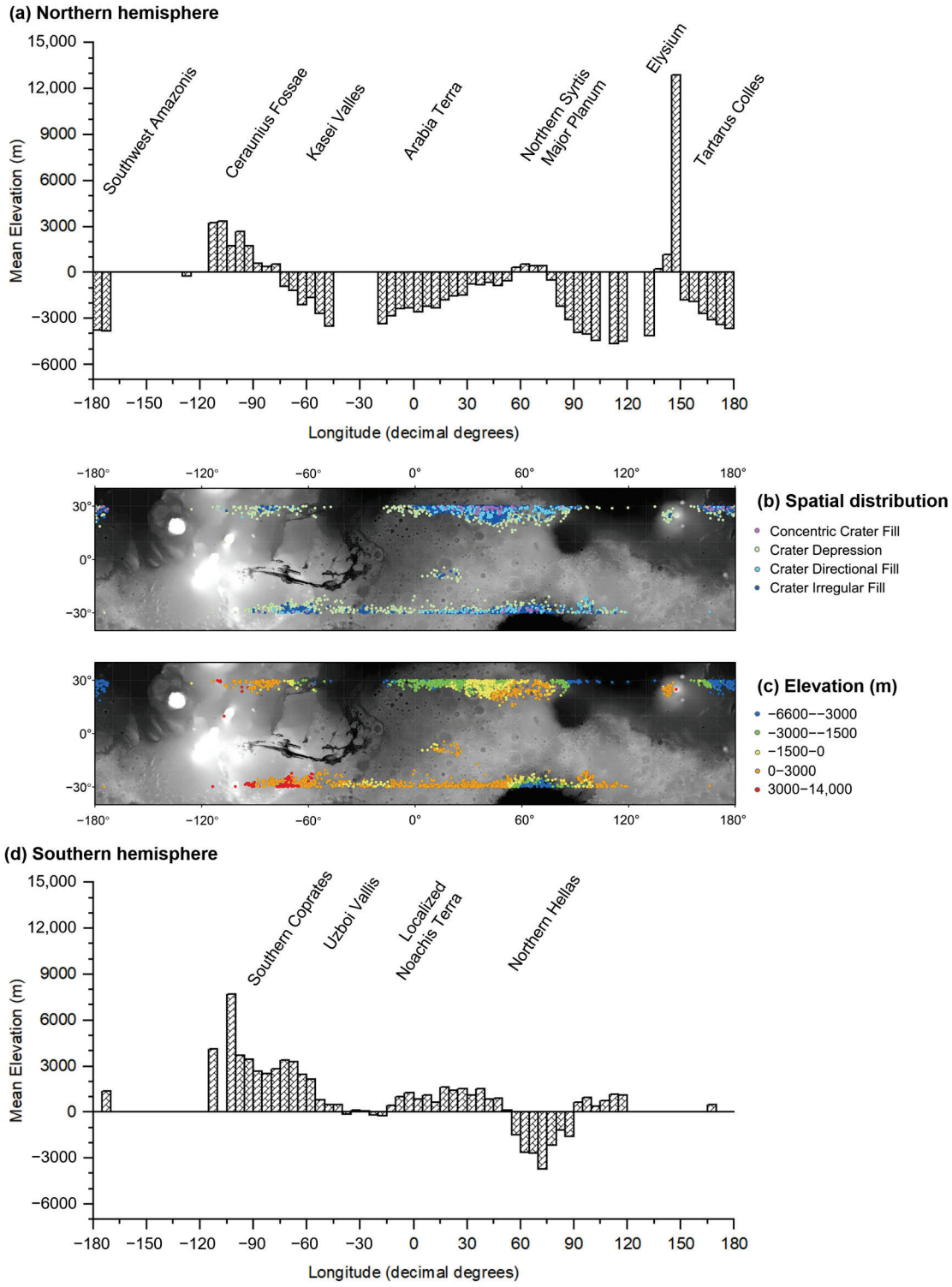


Figure 6. Spatial and elevation distribution analysis map of crater fill (CF). (**a**) Bar plot of the mean elevation of the CF landforms, based on a 5° longitude scale, in the northern hemisphere. Spatial distributions (**b**) and elevations (**c**) of various types of CFs in the low-latitude region of Mars. A total of 3653 CFs were mapped globally. (**b**) A spatial distribution map of 89 CCFs (purple dots; 2.44%), 368 crater directional fills (light blue dots; 10.07%), 1949 crater irregular fills (navy blue dots; 53.35%), and 1247 crater depressions (grass green dots; 34.14%). (**c**) Elevation distributions: dark red shading represents higher elevations, whereas dark blue shading indicates lower elevations. (**d**) Bar plot of the mean elevation of the CF landforms, based on a 5° longitude scale, in the southern hemisphere.

The majority of CCFs are concentrated in central Arabia Terra and Tartarus Colles, near the 30°N latitude in the northern hemisphere, and are also locally observed in northern Hellas in the southern hemisphere. Crater irregular fill and crater directional fill are distributed across similar latitudes, with additional occurrences between Uranius Fossae and Labeatis Fossae in the northern hemisphere. In the southern hemisphere, these types of crater fill are found south of Coprates, including eastern Solis Planum, Thaumasia Planum, and parts of Noachis Terra. In contrast, crater depressions are more abundant and geographically widespread than other crater fill types. They typically occur closer to the Martian equator, near 13°N and 19°S. In the northern hemisphere, prominent occurrences are found around Uranius Mons, localized areas of Ceraunius Fossae, the North Kasei Channel, and the Elysium Mons. In the southern hemisphere, crater depressions are most densely clustered between longitudes −95° and 110°, notably within the Sinus Sabaeus region [34]. A distinct spatial transition in crater fill morphology is observed from equatorial to mid-latitude regions, progressing from crater depressions to directional fills, then to irregular fills, and culminating in concentric crater fills at higher latitudes. This pattern may reflect latitudinal variations in climate-related ice deposition and degradation processes.

3.1.2. Lobate Debris Aprons (LDAs)

LDAs, the second largest category, account for approximately 6.6% of the total identified features and are almost exclusively distributed in the northern hemisphere (Figure 7). The morphology of LDAs at low latitudes differs somewhat from that at mid-latitudes, as their formation is constrained by specific geographical environments, possibly indicating distinct formation mechanisms. LDAs are located primarily in northwestern Amazonis Planitia, Kasei Valles, Arabia Terra, and northeastern Elysium Planitia.

In the northeastern Elysium Planitia and northwestern Amazonis Planitia, particularly around Tartarus Colles and Phlegra Dorsa, the surface morphology of LDAs becomes increasingly similar to that of mid-latitude LDAs as they approach the 30°N latitude. These LDAs exhibit an apron-like form, uniformly scattered around mesas or knolls (Figure 7a,b,d). Closer to the equator, the volume and number of LDAs decrease significantly, as shown in Figure 7c. On the western side of Orcus Patera, the apron-like morphology nearly disappears, leaving only the outermost ridge, as indicated by the black arrow in Figure 7e,f.

In Kasei Valles, LDAs exhibit topographic depressions, also known as moats, which encircle mesas or run parallel to hillocks (Figure 7g,h). Hauber et al. [52] interpreted these features as remnants of former LDAs, possibly eroded flood materials, lava flows, or debris flows analogous to volcanic mudflows, which solidified at the front edge of the LDAs. Owing to climate change, these features retreated and formed depressions over time (Figure 7g,h). In Arabia Terra, we identified outwardly parallel ridges on the inner walls of certain craters, extending from the crater rim to the base of the cliffs, and categorized them as LDAs (indicated by black arrows in Figure 7i,j), which is consistent with the classification used in the GIS datasets [11,22].

In the southern hemisphere, LDA-like features are sparse and sporadic, including moat-like structures around hills and ridges at their outermost edges (Figure A4). Possible sublimation lag deposits (Figure A4a,b) occur in the Mangala Valles [53]. In the Peta Crater and nearby craters (Figure A4c), former ice flow or sliding is suggested to have formed ridges [54,55]. This limited distribution may be due to the generally higher elevations of the southern highlands, which reduce the potential for ice accumulation and preservation compared with similar latitudes in the north.

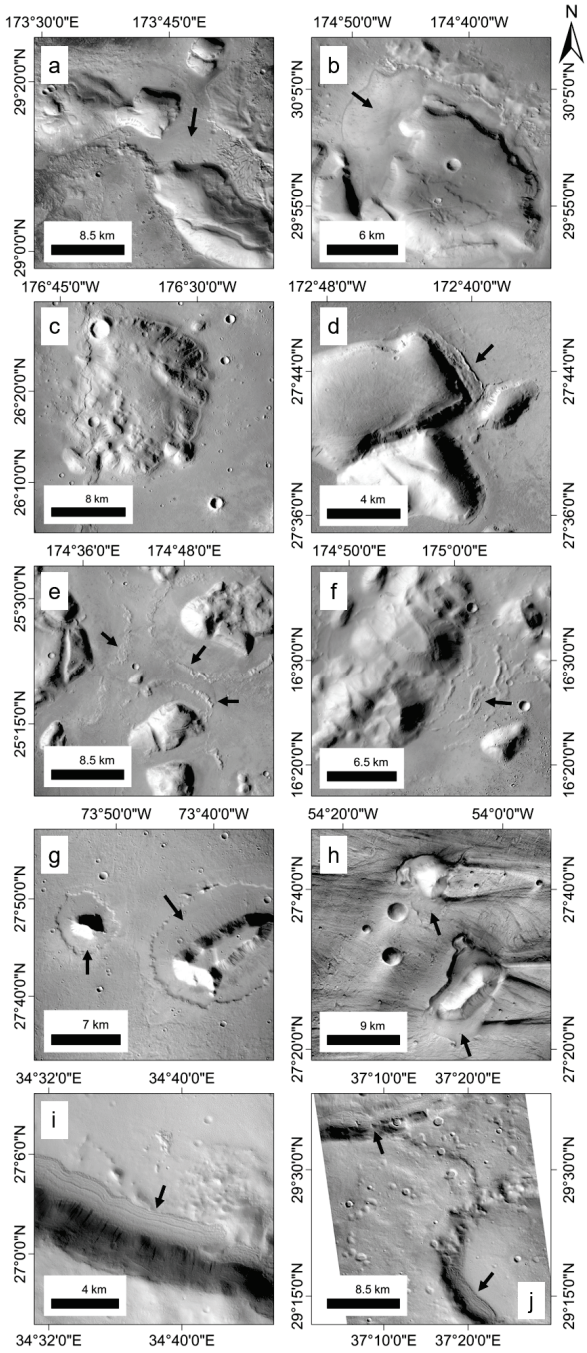


Figure 7. Examples of LDAs (lobated debris aprons) at low latitudes on Mars. (**a**) LDA in northwestern Amazonis Planitia (N09_066021_2094_XN_29N186W; centered at 173.79°E, 29.17°N). (**b**) Apron-like form uniformly scattered around mesas or knolls in Tartarus Colles (J16_050961_2111_XN_31N175W; centered at −174.77°E, 29.90°N). (**c**) LDA in northwestern Amazonis Planitia (K04_054785_2049_XN_24N176W; centered at −176.61°E, 26.34°N). (**d**) The black arrow indicates the position of the LDA (G21_026355_2084_XN_28N172W; centered at −172,71°E, 27.69°N). (**e**) The LDA sublimated, leaving the outermost ridge on the western side of Orcus Patera (B19_016901_2053_XN_25N185W; centered at 174.77°E, 25.29°N). (**f**) The most distal ridge of the LDA remnant in the Tartarus Colles region (P22_009925_1977_XN_17N185W; centered at 174.94°E, 16.50°N). (**g**) The former extent of lobate debris aprons in northern Kasei Valles (P22_009609_1977_XN_17N185W; centered at −73.80°E, 27.79°N). (**h**) Remnants of former LDAs (D17_033735_2076_XN_27N054W; centered at −54.10°E, 27.54°N). (**i**) Parallel ridges extending outward from the inner wall of the crater in Arabia Terra (D17_033735_2076_XN_27N054W; centered at 34.67°E, 27.11°N). (**j**) Parallel ridges extending outward from the inner wall of the crater (J08_048026_2096_XN_29N322W; centered at 37.27°E, 29.34°N).

3.1.3. Possible Sublimation Depressions (Non-Crater) (PSDNs)

In addition to crater-associated depressions, we identified depressions outside craters that may have formed due to the sublimation of near-surface ice. The surface of the area is characterized by linear depressions, which are termed "possible sublimation depressions (non-crater)" (PSDNs), based on their morphological features and spatial distribution.

The PSDNs include two subtypes: (1) linear depressions and/or steep scarps, which are typically located within valleys (Figure 8b,d,e,h), and (2) depressions, which exhibit concentric patterns and circular ridges (Figure 8f,g). The latter, as noted by Levy et al. [56], may have resulted from interactions between volcanic activity and subsurface ice. Additionally, staggered and continuous depressions are observed in Lycus Sulci, which are located near hills (Figure 8a). In Ceraunius Fossae, viscous flow material is present within graben floors, with surfaces covered by ice-rich material and ring-mold craters (Figure 8b,c). Valley-associated depressions represent the most common type of PSDNs (Figure 8b,d,e,h). These features are predominantly concentrated in the northern hemisphere, particularly near Lycus Sulci, Ceraunius Fossae, Kasei Valles, and Elysium Mons. In contrast, distinctive concentric depressions with circular ridges are rare, sparsely distributed, and found only in a few isolated locations (Figure 8f,g). No additional morphological subtypes indicative of ice-related processes were identified within the PSDN category, based on the available imagery and mapping resolution.

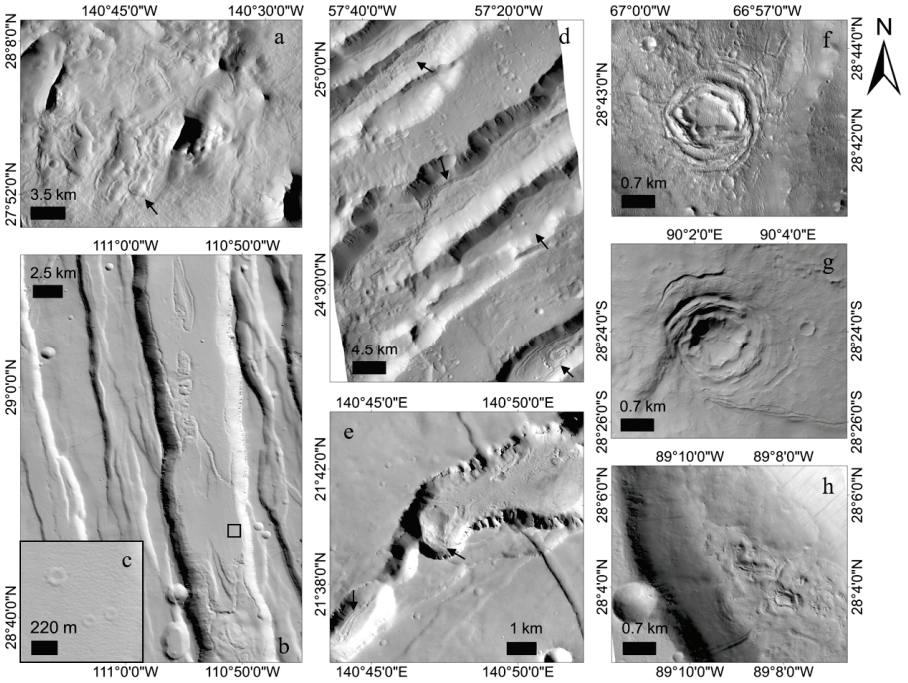


Figure 8. Typical examples of possible sublimation depressions (non-crater) (PSDNs) at low latitudes. The black arrows indicate the locations of the depressions. (**a**) Staggered and continuous depressions in the vicinity of the hills in Lycus Sulci (F03_037127_2103_XI_30N141W; centered at −140.68°E, 28.01°N). (**b**) Very thin ice-rich deposits are present within graben floors in Ceraunius Fossae (K12_057882_2090_XI_29N111W; centered at −110.89°E, 28.93°N). (**c**) Magnification of the area framed by the black box in the principal panel, showing RMCs on the surface of the VFF. (**d**) Linear depression and steep scarps at the edge of the valley floor in Nilokeras Fossa (G01_018439_2053_XN_25N057W; centered at −57.42°E, 24.64°N). (**e**) Linear depressions on the valley graben floor (U16_077035_2041_XN_24N219W; centered at 140.77°E, 21.65°N). (**f**) Ringed ridges in Kasei Valles (ESP_074115_2090_RED; centered at −66.97°E, 28.71°N). (**g**) Depression with concentric features (ESP_052297_1515_RED; centered at 80.74°E, −28.40°N). (**h**) Linear depressions on the valley floor near Kasei Valles (ESP_050351_2085_RED; centered at −79.74°E, 28.06°N).

3.1.4. Glacier-like Form (GLF)

The surface morphology of GLFs at low latitudes is similar to that at mid-latitudes, with textures that flow along topographic gradients (Figure 9). For instance, the boundaries of GLFs are well-defined and terminate in distinct moraine-like ridges (Figure 9a,c,e,i; indicated by the black arrow). In contrast, Figure 9g,h shows less clearly defined boundaries, although the surface textures still exhibit flow patterns, aligned with the topographic gradient.

In the northern hemisphere, GLFs are predominantly distributed at an average latitude of 28.12°. They generally have small volumes and are confined within alcoves strongly influenced by the topography, primarily occurring on north-facing slopes. In the southern hemisphere, GLFs are distributed at an average latitude of 25.12°, tend to have large volumes, and are found mainly on southeast-facing slopes, along the inner or outer walls of craters (Figure 9e,f,I,j). While GLFs are slightly more abundant than LVFs, they remain relatively rare overall.

GLFs are more common in the northern hemisphere than in the southern hemisphere and are sprinkled near Olympus Mons (Figure 9a), where the broad glacial deposits have not yet been fully mapped, although individual GLFs have been identified. They are also observed in central Arabia Terra (Figure 9b) and near the north–south dichotomy of Syrtis Major, possibly indicating multiple glacial events northwest of Nili Fossae (Figure 9c,d). In the southern hemisphere, GLFs are predominantly found around northern Hellas (Figure 9e–j). Examples include moraine-like ridges in the Isil Crater [57,58] (Figure 9e), steep scarps and trim lines formed by glacial sublimation retreat and contraction in the Nako Crater [59] (Figure 9g), and craters on the northwest edge of the Terby Crater [60] (Figure 9h).

3.1.5. Lineated Valley Fills (LVFs)

At low latitudes, the morphology of LVFs resembles that observed in mid-latitude regions, with flow characteristics aligned parallel to the valley walls (Figure 10). However, the linear features on the surface of the LVFs in low-latitude regions are less distinct than those in mid-latitude areas. The occurrence of LVFs at low latitudes is extremely limited, with an average distribution near 28.3° north and south latitudes. LVFs are slightly more prevalent in the northern hemisphere than in the southern hemisphere. In the southern hemisphere, LVFs more clearly exhibit tightly spaced or folded linear features on their surfaces (Figure 10e,g,h). In the northern hemisphere, LVFs are primarily concentrated in Arabia Terra and some valleys to the east, such as the lower reaches of Auqakuh Vallis [61] (Figure 10f). In the southern hemisphere, LVFs are distributed mainly in Thaumasia Planum (Figure 10e,g,h) and the northern part of the Hellas Basin (Figure 10i,j).

3.1.6. Elevation Distribution of Ice-Related Landforms at Low Latitudes

The global mapping results are shown in Figure 11. A total of 4307 features were identified: 3653 crater fills (CFs; 84.82%), 284 LDAs (6.59%), 139 PSDNs (3.23%), 137 other types (3.18%), 79 GLFs (1.83%), and 15 LVFs (0.35%).

We analyzed the elevation distributions of these landforms via MOLA and HRSC blended DEM data, calculated the mean elevation for each 5° longitude interval (Figure A5a) and generated elevation maps for the low-latitude regions (Figure A5b). From 150°E to 225°E (−135°E), the ice-related landforms are mostly confined to the northern hemisphere near −2000 m, with elevations ranging from −4246.81 m to 1529.24 m (average −3061.71 m). From −135°E to −55°E, the average elevation of the ice-related landforms is 1726.58 m, ranging from −3213.14 m to 14,911.33 m. From −55°E to 95°E, the elevation ranges from −6530.90 m to 3082.36 m, with a mean of −824.96 m. From 95°E to 150°W, the elevation ranges from −4631.43 m to 13,624.03 m, with an average of 876.37 m.

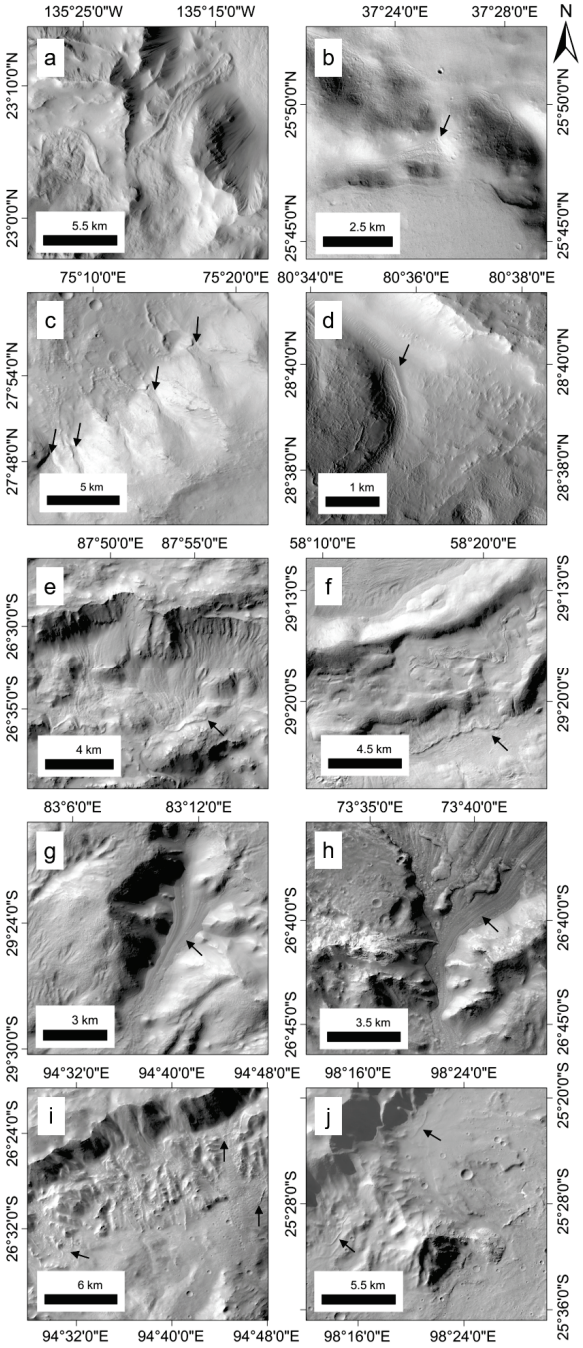


Figure 9. Examples of GLFs (glacier-like forms) at low latitudes on Mars. The black arrows indicate the terminals of the GLF. (**a**) GLF in Olympus Mons (B17_016464_2034_XI_23N135W; −135.35°E, 23.06°N). (**b**) N08_065472_2047_XN_24N322W; 37.41°E, 25.80°N. (**c**) Evidence of possible multiple glacial events northwest of Nili Fossae (D21_035550_2073_XI_27N284W; centered at 75.27°E, 27.83°N). (**d**) GLF in the Nilosyrtis region (ESP_055132_2090_RED; centered at 70.31°E, 28.65°N). (**e**) GLF within the Isil Crater (D17_033730_1526_XI_27S272W; centered at 87.85°E, −26.61°N). (**f**) GLFs on the outer wall of a crater in the southern hemisphere (G16_024448_1519_XN_28S301W; centered at 58.24°E, −29.27°N). (**g**) GLF within the Nako Crater (D18_034139_1509_XN_29S277W; centered at 83.17°E, −29.42°N). (**h**) GLF in a crater on the northwest edge of the Terby Crater (D14_032557_1531_XI_26S286W; centered at 73.63°E, −26.69°N). (**i**) Example of GLFs (D15_033255_1551_XI_24S265W; centered at 94.53°E, −26.52°N). (**j**) The black arrows point to the moraine-like ridges of the GLF (P18_008109_1536_XI_26S261W; centered at 98.31°E, −25.47°N).

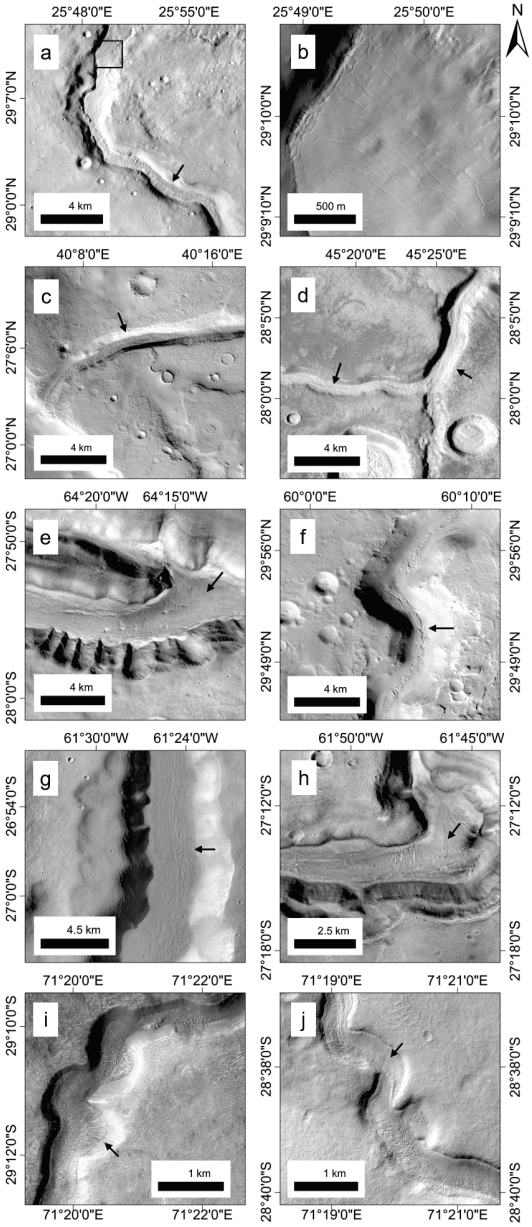


Figure 10. Examples of LVFs at low latitudes on Mars. (**e**,**g**–**j**) LVFs in the southern hemisphere with larger deposition volumes and more pronounced linear features on their surfaces than those in the northern hemisphere (**a**–**d**,**f**). (**a**) Example of LVF in the northern hemisphere (P18_007940_2082_XI_28N334W; centered at 25.87°E, 29.03°N). (**b**) Magnified HiRISE view of the area within the black box in (**a**). A possible sublimation-induced linear depression is present at the terminal end of the LVF (ESP_052114_2095_RED; centered at 25.83°E, 29.16°N). (**c**) Example of LVF in the northern hemisphere (N10_066171_2068_XN_26N319W; centered at 40.17°E, 27.10°N). (**d**) LVF in Arabia Terra (B16_016075_2091_XN_29N314W; centered at 45.33°E, 28.00°N). (**e**) Linear features characterize the LVF in Thaumasia Planum (J07_047674_1519_XN_28S064W; centered at −64.27°E, −27.90°N). (**f**) Channel at the bottom of Auqakuh Vallis showing remnants interpreted as lobate debris flow (LVF) deposits (P08_003970_2091_XI_29N299W; centered at 60.18°E, 29.90°N). While a fluvial origin (e.g., terrace formation) cannot be ruled out, the morphology and regional context favor a glacial interpretation. (**g**) Linear features characterize the LVF in Thaumasia Planum (B02_010620_1529_XI_27S061W; centered at −61.41°E, −26.96°N). (**h**) Linear features characterize the LVF in the southern hemisphere (G11_022659_1527_XN_27S061W; centered at −61.82°E, −27.23°N). (**i**) ESP_030461_1505_RED; centered at 60.10°E, −29.17°N. (**j**) ESP_016378_1510_RED; centered at 60.12°E, −28.65°N.

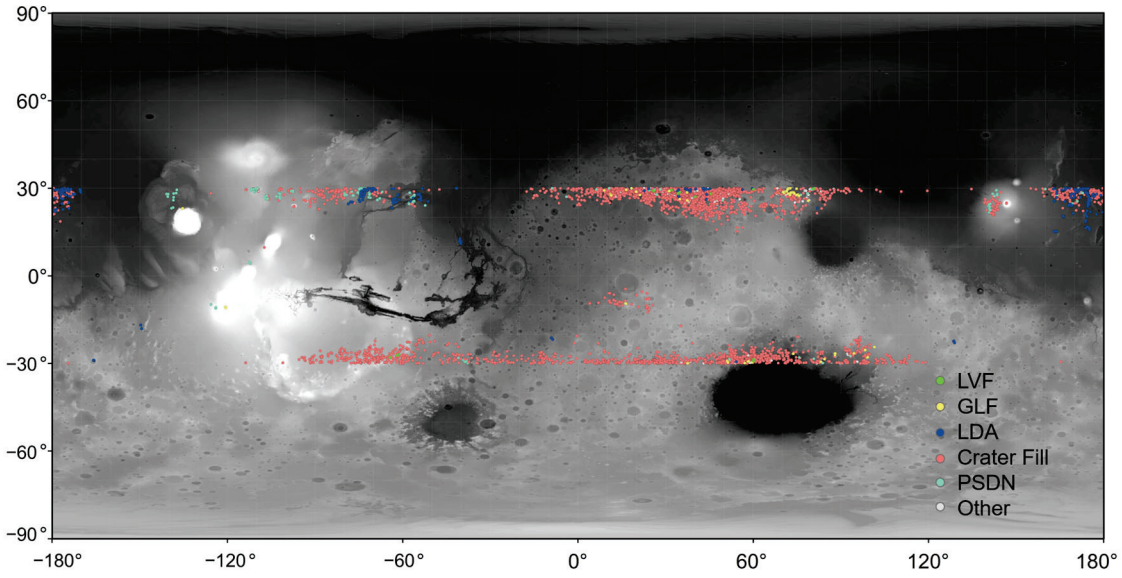


Figure 11. Spatial distribution of ice-related landforms in the low-latitude regions of Mars identified in this study. The legend indicates the color corresponding to each landform type. The base map is a $10^\circ \times 10^\circ$ grid, based on the MOLA dataset.

Most ice-related landforms occur in regions with negative elevations, such as the eastern Elysium Planitia, western Amazonis Planitia, parts of Kasei Valles, Arabia Terra, and northern Hellas Basin. Ice-related landforms in other areas occur primarily at positive elevations.

3.2. Crater Fills (CFs) in Low-Latitude Regions

3.2.1. Statistical Analysis of the CFs

The slope and aspect measurements are based on a blend of DEM data. The number of CFs is notably greater in the northern hemisphere than in the southern hemisphere (Figures A6a, A7 and A8), with CFs mainly distributed in regions characterized by gentle slopes, based on MOLA–HRSC blended DEM data at a 200 m/pixel resolution (Figure A6b). Furthermore, the majority of fill materials are concentrated in craters less than 20 km in diameter (Figure A6c). The orientation of the CFs is determined by the directionality of the three fill types, other than CCFs. At low latitudes, the orientation of CCFs is less distinct, possibly because of the smaller number of CCFs. Crater irregular fill and crater directional fill are symmetrically distributed across the different hemispheres: the northern hemisphere predominantly features north- and northeast-facing slopes, whereas the southern hemisphere has south- and southeast-facing slopes. On the other hand, crater depressions tend to exhibit fill movement toward the east and southeast, with a surface morphology characterized by depression-dominated crater floors.

The morphological characteristics and slope variations also differ among the fill types. CCFs are typically found in craters 2–15 km in diameter, with slopes not exceeding 4°. Crater irregular fill is observed in craters 2–10 km in diameter, with fill slopes up to 6°. Crater directional fill occurs in craters of all sizes (1–30 km diameter), with slopes ranging from 1° to 13°. Crater depressions are found in relatively flat regions within craters less than 20 km in diameter and with slopes of 12° or less (Figures A7 and A8).

3.2.2. Total Volume of Identified CCFs at Low Latitudes

The volume of the CCF was estimated based on the described calculation method. The total volume of CCF deposits in low-latitude regions was calculated to be approximately 1048.98 km^3. To estimate the ice content in these deposits, we considered two hypotheses

regarding their origin [22]: glacial ice with 90% ice content [11] and pore ice with 30% ice content [62]. Based on these assumptions, the total ice inventory of low-latitude CCFs was estimated to be 944.08 km^3 for glacial ice and 314.69 km^3 for pore ice, corresponding to globally equivalent ice thicknesses of 65.1 mm and 21.7 mm, respectively. No error estimations are provided for the estimated volume and ice content in this study, due to inherent limitations in the resolution of the DEM data and uncertainties associated with interpolating the full dataset [22]. As a result, the volume estimate of 30% pore space is a reasonable minimum value for these landforms, following previous studies [22]. This estimate includes only concentric fills within craters, excluding irregular and directional fills. Consequently, the actual ice content in the low-latitude region of Mars is likely even greater than these calculated values.

3.2.3. Age Estimates for the CFs

We analyzed the CSFDs of different crater fill types to estimate their model ages (Table A1). The surveyed area covers approximately 140 km^2, within which 291 small craters were identified on the crater fill surface for chronological analysis. The model ages of the CCFs (220 $\pm$ 20 Ma, 140 $\pm$ 50 Ma) (Figure 12a,b) are broadly consistent with the depositional ages (100 Ma−700 Ma) reported for mid-latitude viscous flow glacial features in previous studies [63,64]. However, the CSFDs of irregularly filled craters reveal variations in the model ages depending on their surface morphologies. Deposits with only RMCs on the surface, lacking any flow patterns (Figure 12c,d), exhibit older model ages in the late Hesperian (~3.4 Ga) and early Amazonian (~2.8 Ga) periods. For an impact crater within the Arabia Terra region (52.49°E, 23.98°N), we analyzed the model ages for the crater directional fill (Figure A9). Although accurately measuring the age of the deposits on the polar-facing interior wall was difficult, only the region on the crater floor was selected for counting, and its modal age (4.2 $\pm$ 0.8 Ma) suggests a relatively young depositional period.

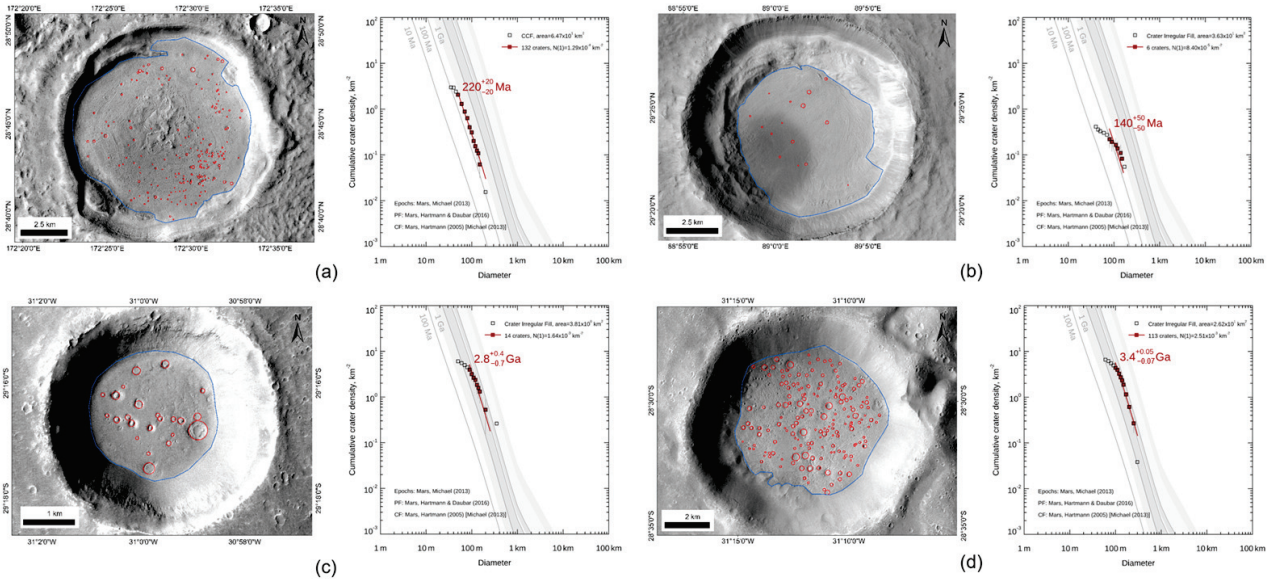


Figure 12. Age estimation of ice-rich material in impact craters. The blue outline indicates regions where impact craters were counted, whereas the red outline marks the measured craters. (**a**) Centered at 172.47°E, 28.74°N; (**b**) centered at 89.03°E, 29.39°N; (**c**) centered at −30.99°E, −29.27°N; and (**d**) centered at −31.19°E, −28.51°N. The age estimations in the figures are based on the following references: epoch boundaries from Michael (2013) [65]; production function from Hartmann and Daubar (2016) [51]; and chronology functions from Hartmann (2005) [47] and Michael (2013) [65].

However, owing to the limited number and small size of the craters superposed on the deposit surface, the modeled ages should be regarded as approximate estimates. Furthermore, dating results may also be subject to uncertainty due to many other factors. For example, candidate craters that are too small in diameter may lead to biased dating. In addition, the accuracy of diameter identification for some RMCs with heavily degraded boundaries may also affect the results.

4. Discussion

At the global low-latitude scale, ice-related features are primarily found up to 13°N in the northern hemisphere and 19°S in the southern hemisphere. The previously observed restriction of ice indicating features restricted to latitudes above 32°N in the northern hemisphere is no longer consistent, aligning with predicted ice accumulation in the low-latitude Thaumasia region (110°W–60°W) of the southern hemisphere [66]. Levrard et al. [67] predicted that surface water ice accumulation at 40° obliquity would primarily occur near the Tharsis Volcanic Province and the Schiaparelli Basin. In the Tharsis region, water ice is likely deposited on the windward sides of volcanoes under monsoon-like atmospheric circulation [33,68]. In addition, remnant deposition in Sinus Sabaeus most likely occurred due to past obliquity-driven climate change [34].

At low latitudes, ice-related landforms exhibit less pronounced surface textures and are fewer in number and distribution than those at mid-latitudes. This is primarily because current Martian climatic conditions are unfavorable for stable accumulation and long-term preservation of ice-rich materials in low-latitude regions. In addition, intense surface degradation processes, such as aeolian activity or erosion, are more active at lower latitudes and may obscure or erode ice-related features. In many cases, any near-surface ice that may exist is likely buried beneath the regolith layer, thereby limiting its geomorphic expression on the surface. Like the GLFs and LVFs, these features are sporadically distributed in Arabia Terra and Syrtis Major near the dichotomy boundary in the northern hemisphere and in Thaumasia Planum and northern Hellas in the southern hemisphere. LDAs, predominantly located in Tartarus Colles and Kasei Valles, with some occurrences in Arabia Terra, are interpreted as glacial remnants at low latitudes [52]. In contrast, the CFs and PSDNs extend closer to the equator and exhibit broader distributions. Ice-related landforms in the northern hemisphere generally occur at significantly lower elevations than those in the southern hemisphere and are likely influenced by the Mars global dichotomy and atmospheric circulation patterns, which suggests a link between the local topography and favorable conditions for glacial ice accumulation and preservation [69]. A detailed analysis of the CFs revealed that northeast-facing (northern hemisphere) and southeast-facing (southern hemisphere) orientations dominated at low latitudes. This orientation may reflect local climatic and insolation conditions, allowing ice to persist in colder crater regions [5,31,70].

Figure 13 integrates previously published datasets with our results, illustrating the distribution of ice-related landforms on Mars from mid-latitudes to the equator. The two columns on the right of the legend represent prior datasets [8,22,71], which focus primarily on glacial features between 30° and 60° north and south latitudes. Our study extends this mapping into low-latitude regions, addressing a significant data gap. The comparative analysis reveals that our low-latitude results align well with the previous mid-latitude data near 30°N and 30°S, indicating spatial continuity in the landform distribution. Importantly, we introduce newly defined subcategories of ice-related landforms in low-latitude regions. Within the crater fill (CF) category, three subtypes, excluding concentric crater fill (CCF), are newly proposed in this study, based on distinct morphological patterns not previously classified as glacial or periglacial features. In addition, the total number of ice-related

landforms mapped at low latitudes in our dataset exceeds that reported in earlier works. These additions provide a more comprehensive and refined characterization of Martian glaciation at low latitudes, enhancing our understanding of the spatial and morphological diversity of ice-related processes beyond the traditionally studied mid-latitude zones. Our results also show uniform coverage across both hemispheres as the dataset extends toward the equator, particularly in regions such as Arabia Terra in the northern hemisphere and northern Hellas in the southern hemisphere, where crater fill features are dominant.

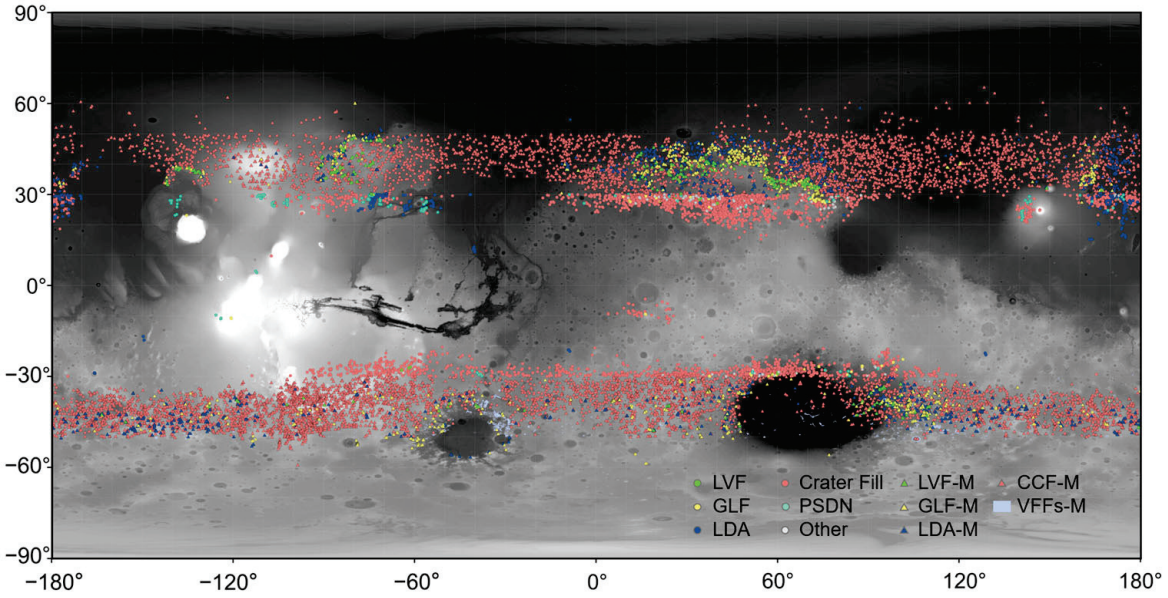


Figure 13. Integration with previously published datasets reveals ice-related landforms extending from the mid-latitudes to the equator on Mars. Figure legends for LVF, GLF, LDA, crater fill, PSDN, and other represent data from this study for low-latitude regions (±30°), whereas LVF-M, GLF-M, LDA-M, CCF-M, and VFFs-M represent previously published data for mid-latitude regions. Data sources for mid-latitudes: GLF-M [8]; LVF-M, LDA-M, CCF-M [22]; VFFs-M [71].

We compared our dataset with the ice consistency maps generated by the SWIM team, which represent the inferred burial depths of subsurface ice, categorized as 1–5 m and >5 m [44]. To facilitate the comparison, we mapped the geomorphological features (a), alongside SWIM-derived data indicating estimated depths to subsurface ice in the range of 1–5 m (b) and >5 m (c) (Figure 14). Good agreement between our dataset and the SWIM results was observed in several key regions. In the northern hemisphere, the key regions include Tartarus Colles (160°–185°E), Uranius Fossae to Tempe Mensa (270°–292°E), and Arabia Terra to Nili Fossae (10°–80°E). In the southern hemisphere, the key regions include the northern Argyre margins (298°–350°E) and northern Hellas margins (39°–100°E). In addition, our findings in the Sinus Sabaeus (3°–15°E) region align well with observations by Shean [34]. Several other blue regions near the equator, some of which are associated with the Medusa Fossae Formation, contain pedestal craters, a landform type not covered by the data in this study. In Figure 14b, the dust layer in certain areas may influence the ground radar signals [40]. We examined several landforms with distinct glacial/periglacial features, using publicly available SHARAD radar data; however, no subsurface reflections were detected. This may be attributed to factors such as steep crater walls or the small, discontinuous nature of the ice-related deposits, which can generate surface clutter that overwhelms the radar signal. Additionally, the absence of reflections may result from the loss of near-surface volatiles or the presence of ice-rich material that is too thin to be detected by SHARAD.

This study suggests that extensive glacial activity occurred in the low-latitude regions of Mars during past periods of high Martian obliquity, potentially preserving substantial subsurface ice within large crater deposits. The crater retention ages of concentric crater fills (CCFs) and other ice-related landforms range from as early as the late Hesperian (~3.4 Ga) to as recent as ~3 Ma, indicating multiple episodes of ice accumulation and reworking. Sinha and Vijayan [5] summarized and compared the geomorphic and topographic characteristics of four typical late Amazonian glacial/periglacial flow features (LVF/LDA, CCF, and VFF), along with their age estimates and obliquity considerations. The flow feature is interpreted to have formed during a period between ~10 and 100 Ma, under obliquity conditions (~30°–45°), similar to those associated with the formation of LDA and LVF landforms [5]. These settings are analogous to the crater directional fill observed in this study, particularly those preserved on pole-facing slopes, suggesting shared climatic control. The wide age range of low-latitude ice-related features may reflect episodic glacial activity linked to successive high-obliquity intervals during the Amazonian period, which is consistent with orbital simulations and stratigraphic correlations across Martian mid- and low-latitudes. However, further constraints, such as regional thermal models and crater degradation analyses, are needed to better resolve the timing, duration, and climatic thresholds of each glaciation episode.

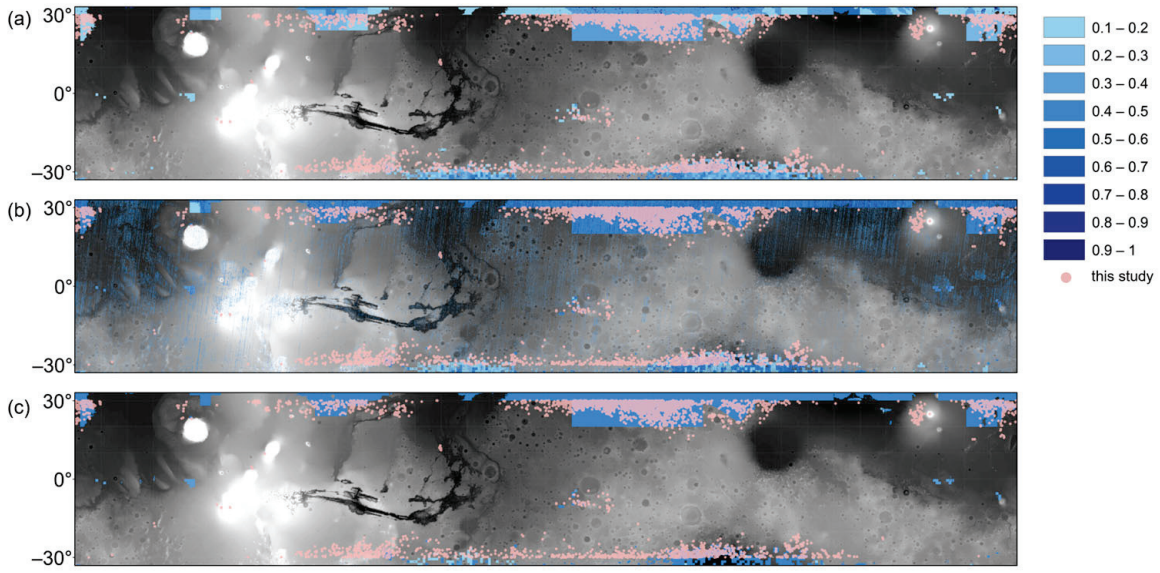


Figure 14. Integrated ice consistency maps, published by the SWIM team, with our data, including geomorphology (**a**) and subsurface ice depth categories of 1–5 m (**b**) and >5 m (**c**), representing the inferred burial depth of ground ice. The darker the blue color is, the strong the glacial/periglacial signal. Data sources: pink dots (data from this study); blue dots (ground ice distribution from the SWIM team) [44].

Hauber et al. [52] suggested that LDAs at 25°−30°N formed at approximately 1 Ga, with the current landscapes representing glacial remnants. This aligns with models that predict Martian climatic evolution under relatively high obliquity [20]. Similarly, crater irregular fill features only RMCs on their sediment surfaces, without significant flow patterns, and likely formed during high-obliquity periods, hundreds of millions of years ago. The formation of CCF viscous flow features at low latitudes appears to have aligned temporally with mid-latitude glaciation events, which are estimated to have occurred between 100 Ma and 700 Ma [63,64]. The observed geomorphological features reflect a complex interplay between ice deposition and ice loss through both sublimation and glacial recession. For example, impact crater floor cracks and talus accumulations along crater

edges [6] suggest extensive sublimation of near-surface ice. Moreover, the presence of ice-rich debris on crater sidewalls may indicate former glacial activity and downslope transport, indicating transitions between periods of ice accumulation and recession, likely driven by variations in Martian obliquity.

The modal age of polar-facing crater wall deposits (4.2 ± 0.8 Ma) corresponds to relatively recent glaciation during the late Amazonian period, comparable to the CSFDs of small VFFs in Nereidum Montes (2.7 ± 0.8 Ma) [71]. These sediments likely represent the outcomes of recent glacial activity and depositional processes. Our findings are consistent with those of previous analyses, supporting the hypothesis that multiple debris-covered glacial events occurred during the late Amazonian period on Mars. These observations emphasize the dynamic and episodic nature of Martian glaciation, which was driven by climatic changes over geologic timescales. The preservation of young, debris-covered deposits on pole-facing slopes suggests that Martian glaciers may share key similarities with terrestrial rock glaciers. It is likely that past glaciers on Mars contained more extensive clean ice, which progressively transitioned to debris-covered forms through sublimation and surface armoring. While the internal ice content of these flow-like landforms cannot yet be fully explained, their morphology and spatial context strongly indicate past ice activity during their formation and emplacement.

A 3D calculation was performed in regard to the residual glacial landforms (i.e., CCFs in this study) on Mars, with an estimated total volume of 1048.98 km^3. Assuming an ice content of 90%, this corresponds to a global ice layer thickness of 65.1 mm; with an ice content of 30%, it corresponds to a global ice layer thickness of 21.7 mm. These estimates are provided as end-member scenarios, assuming ice contents of 90% and 30%, respectively. While the higher end of this range would support an interpretation involving glacial processes, the lower end may indicate debris-dominated rock glaciers or other forms of periglacial activity. However, due to the current lack of direct subsurface ice measurements at these locations, we cannot draw definitive conclusions regarding the dominant process type. The volume of glaciers at low latitudes is much smaller than that of glaciers in mid- to high-latitude areas. Note that we did not estimate the ice volumes of subcategories other than CCFs for several reasons. First, the distributions of GLFs and LVFs are sparse, and their boundaries are often indistinct, making precise definitions challenging. Second, some LDAs are remnants of glacier ice or features resulting from glacial retreat, exhibiting complex characteristics that complicate measurements. Additionally, the sublimation of ice can create depressions and cracks inside or outside craters, further complicating accurate mapping of terrain changes. As only the volume of CCFs was measured, other subcategories were excluded, suggesting that the actual ice content at low latitudes is likely underestimated.

5. Conclusions

In this study, we conducted a detailed visual survey of the entire Martian low-latitude (0°–±30°) region and identified a total of 4307 ice-related landforms in these regions. The identified features include 3653 crater fills (CFs; 84.82%), 284 lobate debris aprons (LDAs; 6.59%), 139 possible sublimation depressions (non-crater) (PSDNs; 3.23%), 79 glacier-like forms (GLFs; 1.83%), and 15 lineated valley fills (LVFs; 0.35%). The remaining 137 features (3.18%) were categorized as “others”, referring to potential ice deposits that may have occurred on plains. The crater fill features were further classified into four subtypes, namely concentric crater fill (CCF), crater irregular fill, crater directional fill, and crater depression. By mapping and analyzing these features, we have expanded the understanding of Martian glacial/periglacial processes, particularly in regions closer to the equator, that were previously underexplored. The key findings are summarized as follows:

1. Ice-related landforms in the lower latitudes of Mars are more extensive than previously thought. The latitudinal extent of ice-related remnants has extended equatorially to 13°N in the northern hemisphere and 19°S in the southern hemisphere, highlighting a broader range for ice-related landforms;
2. The identified ice-related landforms were formed during multiple episodes of Martian geologic history, indicating that Mars has experienced repeated glacial/periglacial processes. These findings support the hypothesis that surface ice extends closer to the equator during periods of high obliquity;
3. Evidence of a dynamic interplay between ice accumulation and ice loss (sublimation) has been observed at low latitudes. These regions had significantly higher ice contents in the past and have since undergone extensive sublimation and removal. Many ice-related remnants have been preserved;
4. Crater fills (CFs) are the most abundant type of ice-related landform at low latitudes, comprising approximately 85% of all the observed features. Among these, irregular fill is the most prevalent subtype. CFs in the northern hemisphere are at lower average elevations (−1165 m) than those in the southern hemisphere (552 m), but their numbers are significantly greater. The elevation contrast between the northern and southern CFs reflects both Martian hemispheric topography and possible differences in climate-driven ice stability. Directional fills are primarily found on the polar-facing walls of craters;
5. The total volume of CCFs at low latitudes on Mars was approximately 1.05×10^3 km^3. Assuming an ice content of 90%, this corresponds to a global equivalent ice layer thickness of 65.1 mm; based on a more conservative assumption of 30% ice content, the equivalent thickness is 21.7 mm. The ice content at low latitudes is likely higher than that suggested by previous studies, necessitating a revised estimate.

Author Contributions: Conceptualization, Y.-Y.S.Z.; investigation, Y.Z.; writing—original draft preparation, Y.Z. and Y.-Y.S.Z.; writing—review and editing, Y.Z., Y.-Y.S.Z., X.X. and Y.W.; visualization, Y.Z.; supervision, Y.-Y.S.Z., X.X. and Y.W.; funding acquisition, Y.-Y.S.Z. All authors have read and agreed to the published version of the manuscript.

Funding: This research was funded by the National Natural Science Foundation of China (Nos. 42441803; 42373042).

Data Availability Statement: All the data generated and analyzed during this study are included in this published article and Appendix A.

Acknowledgments: The authors thank Joseph Levy for his constructive comments and suggestions throughout the project. The authors sincerely thank the four anonymous reviewers for their thorough reviews and constructive comments, which greatly improved the quality and clarity of the manuscript.

Conflicts of Interest: The authors declare that there are no conflicts of interest.

Appendix A

The supporting information includes nine figures (Figures A1–A9) and one table (Table A1).

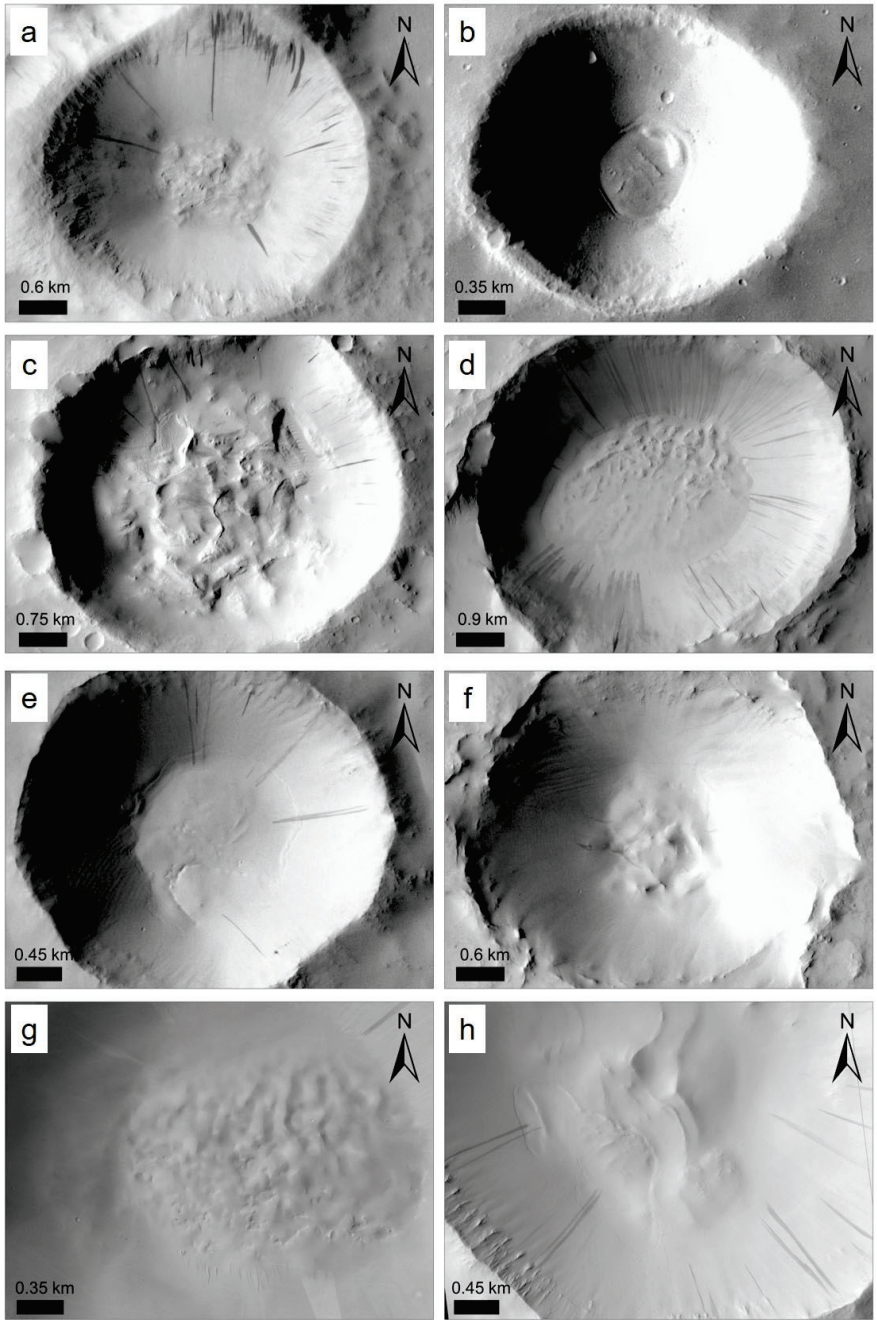


Figure A1. Representative examples of crater depressions in the northern hemisphere. The morphology of the features illustrated in (**a**,**c**,**f**,**h**) is similar to those described by Diot et al. (2015) [41] in Figures 10 and 11, with circular rimless depressions. (**a**) J22_053229_2052_XN_25N175W; centered at −175.48°E, 25.25°N. (**b**) G22_026919_2066_XN_26N089W; centered at −90.02°E, 26.39°N. (**c**) D21_035490_2026_XI_22N088W; centered at −88.59°E, 22.85°N. (**d**) B01_009957_2030_XI_23N326W; centered at 33.65°E, 23.52°N. (**e**) Candidate ice-rich materials close to 47°E, 15°N. J01_045138_1954_XN_15N312W; centered at 47.42°E, 15.83°N. (**f**) N02_063256_1958_XI_15N303W; centered at 56.26°E, 16.54°N. (**g**) ESP_035261_2005_RED; centered at 43.64°E, 20.10°N. (**h**) ESP_044914_2000_RED; centered at 41.84°E, 19.73°N.

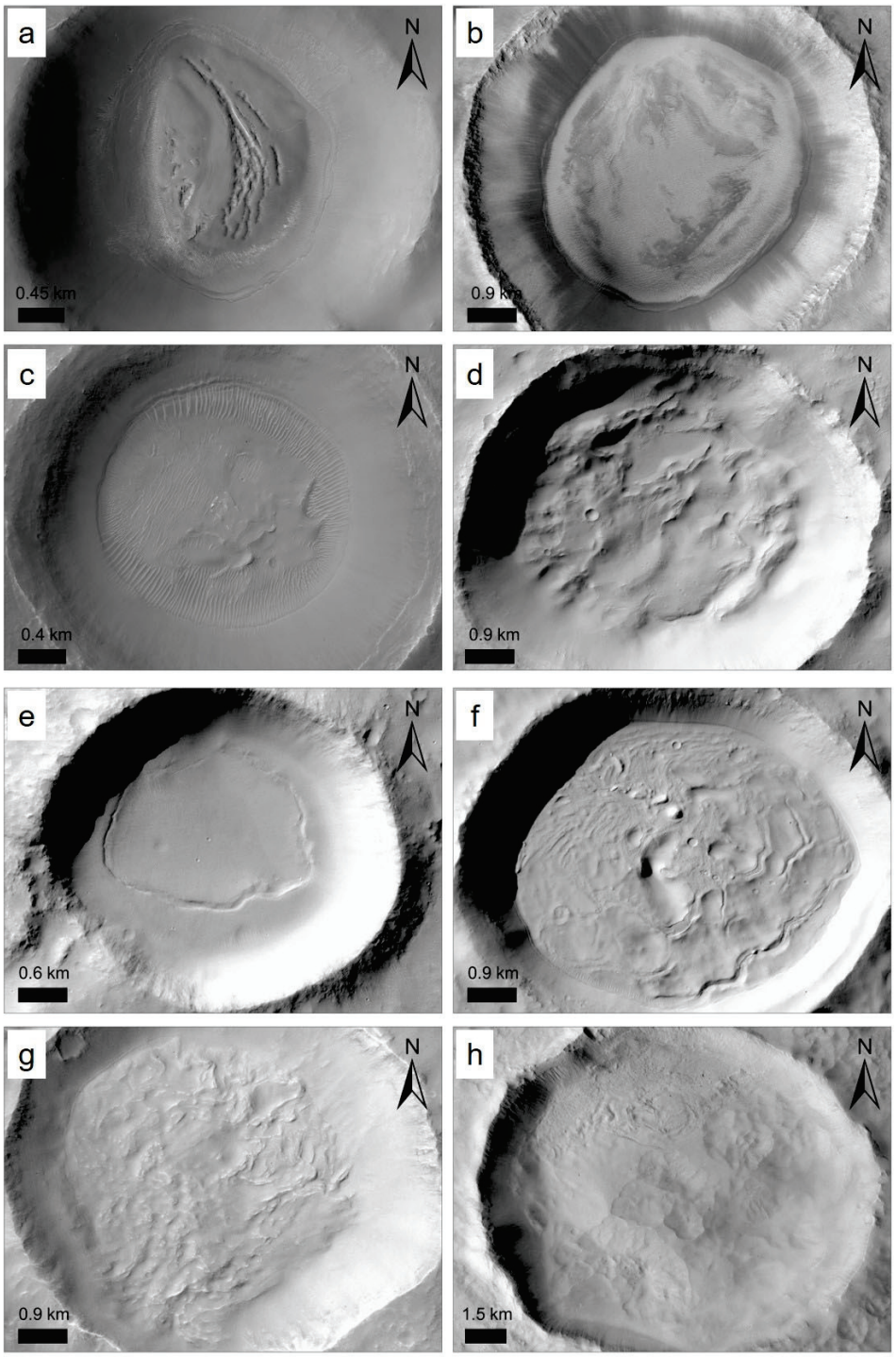


Figure A2. Representative examples of crater depressions in the southern hemisphere. Circular linear textures on the crater floor edges parallel to the crater rims, as well as interspersed linear depressions present in the middle of the crater floor, are widespread at low latitudes. (**a**) ESP_020019_1700_RED; centered at 13.65°E, −10.04°N. (**b**) The surface morphology of this material ranges from smooth to dissected, exhibiting a number of pits, cracks, and ridges. These features are similar to those of the candidate ice-rich material within craters mentioned by Shean (2010) [34]. G10_022142_1744_XN_05S349W; centered at 10.93°E, −5.97°N. (**c**) ESP_024690_1520_RED; centered at −69.09°E, −27.83°N. (**d**) G23_027089_1558_XN_24S043W; centered at −44.13°E, −23.02°N. (**e**) U19_078531_1530_XN_27S013W; centered at −12.96°E, −26.31°N. (**f**) F03_036872_1534_XN_26S011W; centered at −11.47°E, −28.38°N. (**g**) U14_076562_1524_XN_27S263W; centered at 96.30°E, −26.02°N. (**h**) F08_039057_1488_XI_31S252W; centered at 107.69°E, −29.94°N.

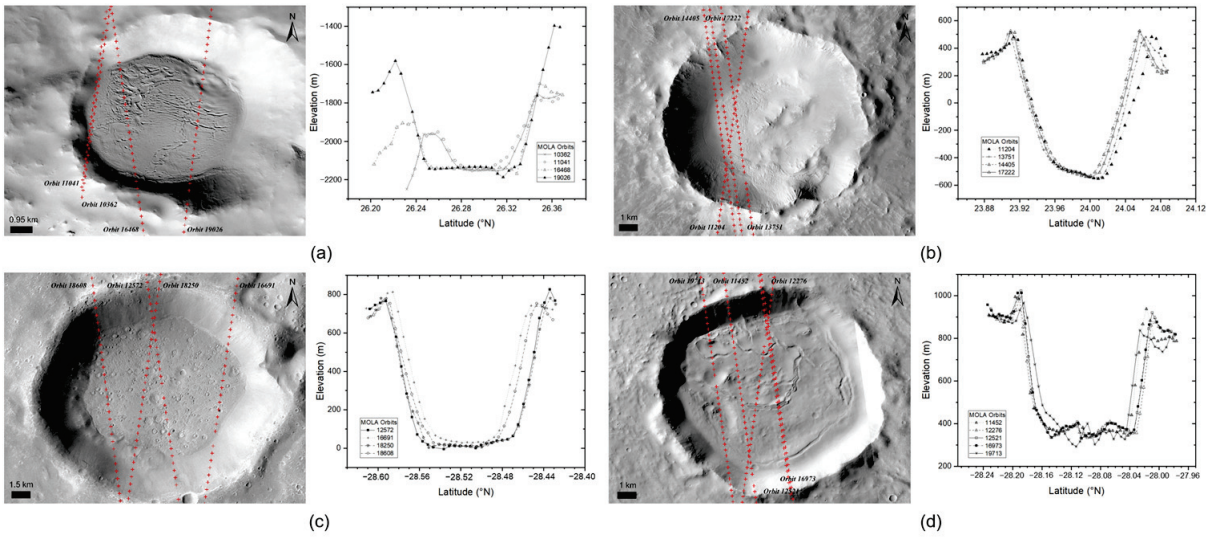


Figure A3. Elevation profiles of four representative types of crater fill based on MOLA shot data. The red dots on the left side of each panel represent different orbital tracks, and the corresponding elevation trend profiles are shown on the right. (**a**) Crater irregular fill (centered at 39.17°E, 26.28°N). (**b**) Crater directional fill (centered at 52.49°E, 23.98°N). (**c**) Crater irregular fill (centered at −31.19°E, −28.51°N). (**d**) Crater depression (centered at −11.33°E, −28.10°N).

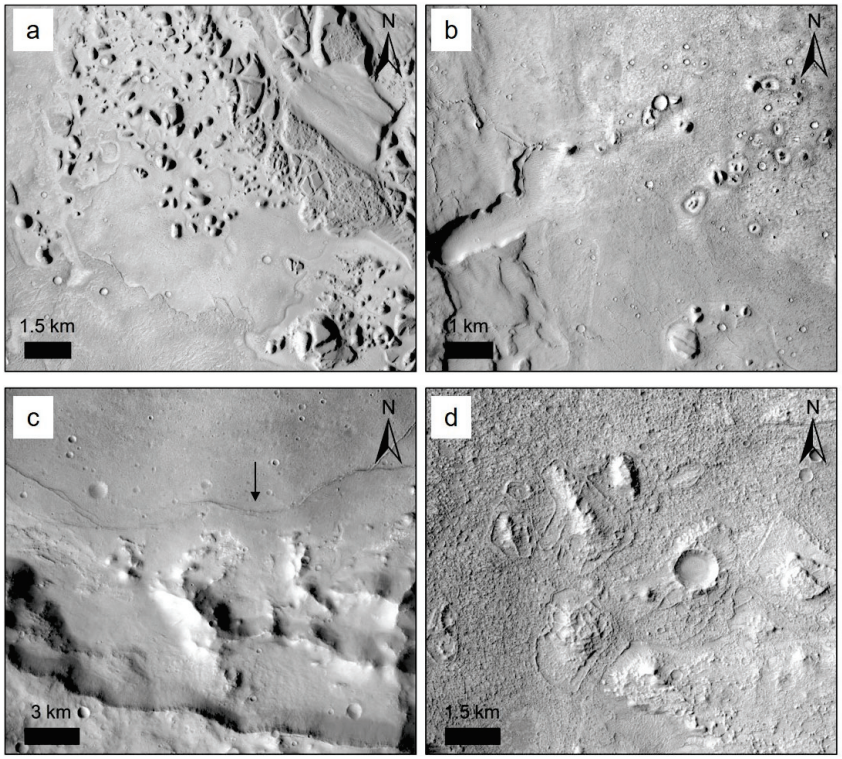


Figure A4. Examples of LDA-like characteristics in the southern hemisphere. All images shown are derived from CTX data. (**a**) LDA-like features in Mangala Valles (P05_002857_1629_XN_17S149W; centered at −149.72°E, −16.72°N). (**b**) Distinct ridges on the periphery of the pits in Mangala Valles (P05_002857_1629_XN_17S149W; centered at −149.43°E, −17.94°N). (**c**) Ring ridges in the Peta Crater, as indicated by the black arrows (U09_074601_1587_XI_21S009W; centered at −9.17°E, −21.69°N). (**d**) Ring of ridges around small hills (P13_006117_1584_XN_21S231W; centered at 128.90°E, −22.96°N).

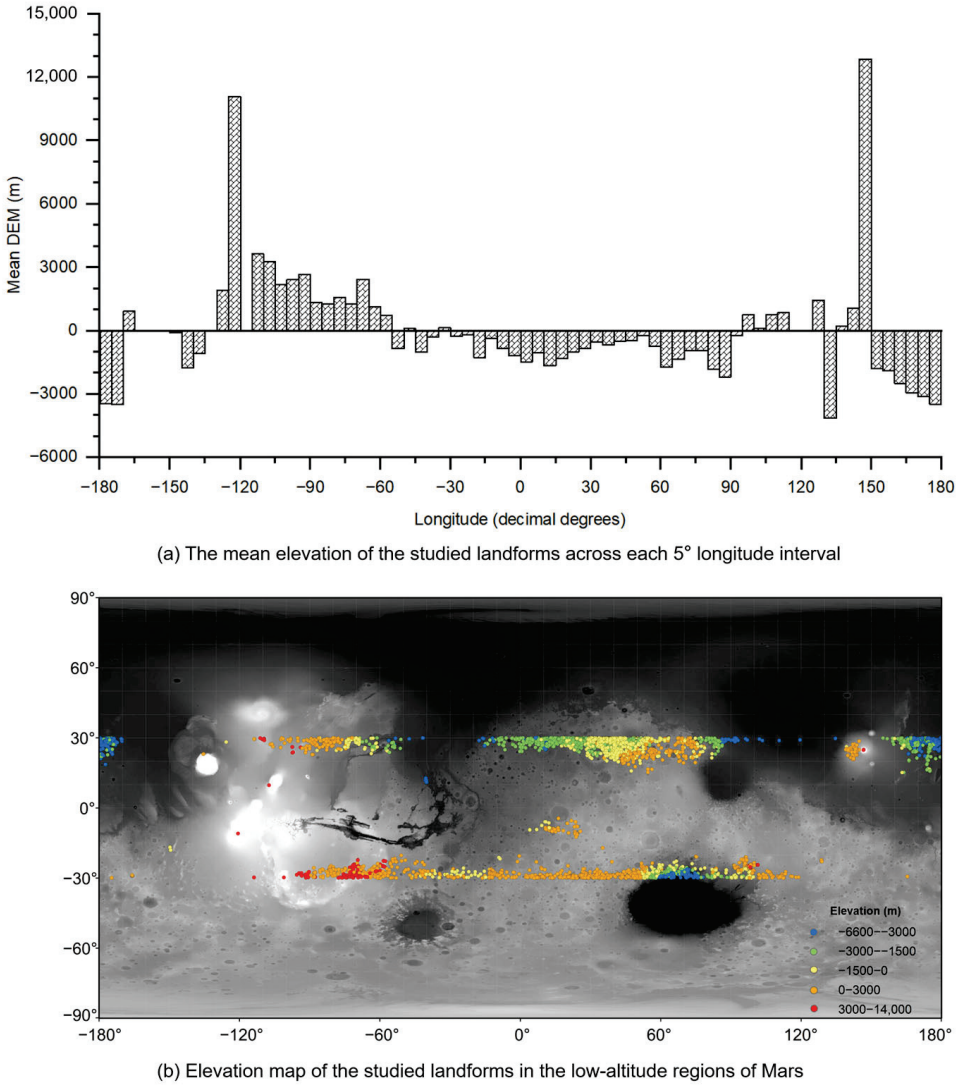


Figure A5. (**a**) Bar plot illustrating the mean elevation of the studied landforms across each 5° longitude interval. (**b**) Elevation map displaying all the studied landforms in the low-latitude regions of Mars. Different altitudes are represented by distinct colors, with red indicating higher elevations and blue representing lower elevations.

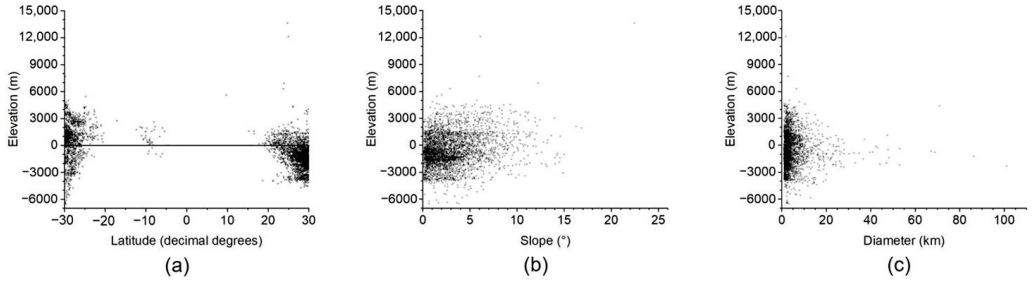


Figure A6. Distributions in terms of elevation with latitude (**a**), slope (**b**), and crater diameter (**c**) for the CFs in the lower-latitude regions of Mars.

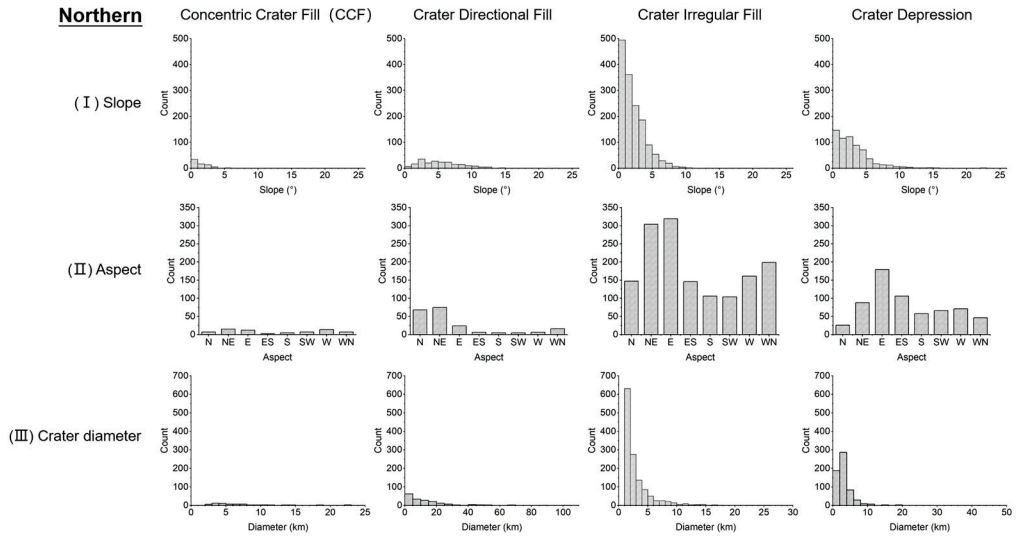


Figure A7. Quantification of four crater fill subtypes (concentric crater fill, crater directional fill, crater irregular fill, and crater depression) in the low-latitude regions of Mars, categorized by slope (**I**), aspect (**II**), and crater diameter (**III**), for the northern hemisphere. In the aspect plot (**II**), the horizontal axis indicates the direction of the deposits (e.g., ES represents southeast facing).

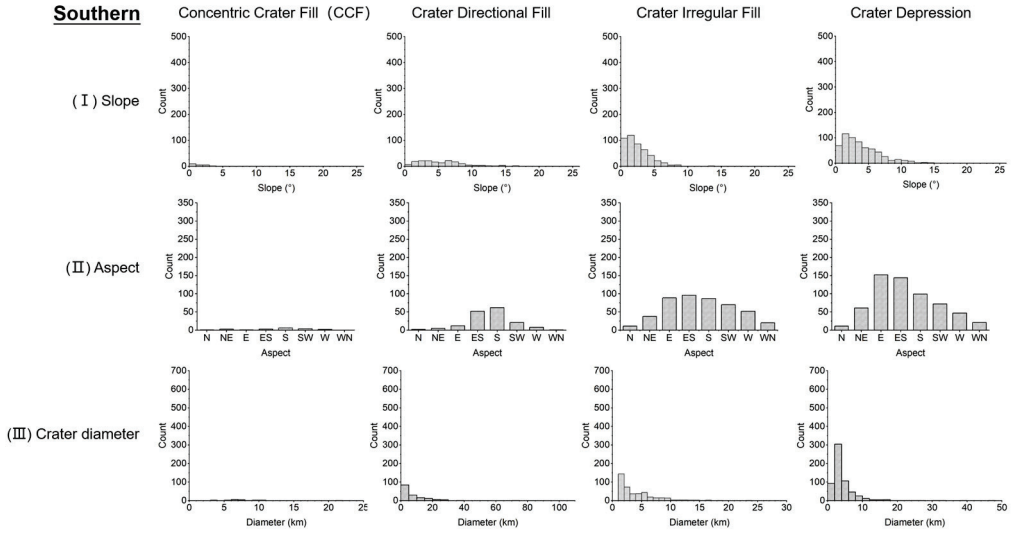
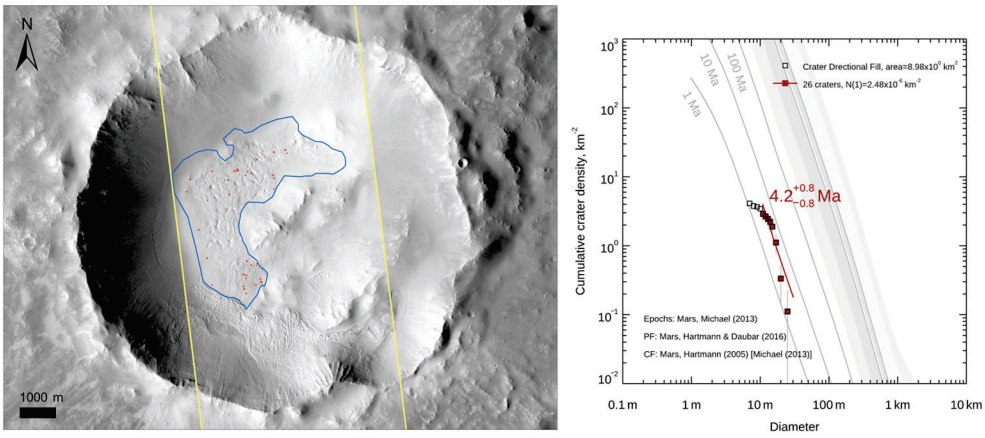


Figure A8. Quantification of four crater fill subtypes (concentric crater fill, crater directional fill, crater irregular fill, and crater depression) in the low-latitude regions of Mars, categorized by slope (**I**), aspect (**II**), and crater diameter (**III**), for the southern hemisphere. In the aspect plot (**II**), the horizontal axis indicates the direction of the deposits (e.g., ES represents southeast facing).

Table A1. Summary of crater size–frequency measurements for crater fill landforms.

Types	Specific Images	Area Size	Number of Craters	Estimated Age with Errors
Centric crater fill	Figure 12a	6.47×10^1 km^2	132	220 ± 20 Ma
Crater irregular fill 1	Figure 12b	3.63×10^1 km^2	6	140 ± 50 Ma
Crater irregular fill 2	Figure 12c	3.81×10^0 km^2	14	2.8 + 0.4 Ga/2.8 − 0.7 Ga
Crater irregular fill 3	Figure 12d	2.62×10^1 km^2	113	3.4 + 0.05 Ga/3.4 − 0.07 Ga
Crater directional fill	Figure A9	8.98×10^0 km^2	26	4.2 ± 0.8 Ma



(a) (b)

Figure A9. Age estimates of ice-rich material within the crater directional fill (52.49°E, 23.98°N). (**a**) Blue contours indicate areas where craters were analyzed, with red outlines marking measured craters. The yellow box highlights the HiRISE detailed image. (**b**) Crater size-frequency distribution (SFD) for the crater floor depression region. The age estimations in the figures are based on the following references: epoch boundaries from Michael (2013) [65]; production function from Hartmann and Daubar (2016) [51]; and chronology functions from Hartmann (2005) [47] and Michael (2013) [65].

References

1. Carr, M.H. Mars Global Surveyor observations of Martian fretted terrain. *J. Geophys. Res. Planets* **2001**, *106*, 23571–23593. [CrossRef]
2. Holt, J.W.; Safaeinili, A.; Plaut, J.J.; Head, J.W.; Phillips, R.J.; Seu, R.; Kempf, S.D.; Choudhary, P.; Young, D.A.; Putzig, N.E. Radar sounding evidence for buried glaciers in the southern mid-latitudes of Mars. *Science* **2008**, *322*, 1235–1238. [CrossRef]
3. Sinha, R.K.; Ray, D. Extensive glaciation in the Erebus Montes region of Mars. *Icarus* **2021**, *367*, 114557. [CrossRef]
4. Séjourné, A.; Costard, F.; Swirad, Z.M.; Łosiak, A.; Bouley, S.; Smith, I.; Balme, M.R.; Orgel, C.; Ramsdale, J.D.; Hauber, E. Grid mapping the Northern Plains of Mars: Using morphotype and distribution of ice-related landforms to understand multiple ice-rich deposits in Utopia Planitia. *J. Geophys. Res. Planets* **2019**, *124*, 483–503. [CrossRef]
5. Sinha, R.K.; Vijayan, S. Geomorphic investigation of craters in Alba Mons, Mars: Implications for Late Amazonian glacial activity in the region. *Planet. Space Sci.* **2017**, *144*, 32–48. [CrossRef]
6. Levy, J.S.; Head, J.W.; Marchant, D.R. Lineated valley fill and lobate debris apron stratigraphy in Nilosyrtis Mensae, Mars: Evidence for phases of glacial modification of the dichotomy boundary. *J. Geophys. Res. Planets* **2007**, *112*, E08004. [CrossRef]
7. Mangold, N. Geomorphic analysis of lobate debris aprons on Mars at Mars Orbiter Camera scale: Evidence for ice sublimation initiated by fractures. *J. Geophys. Res. Planets* **2003**, *108*, 8021. [CrossRef]
8. Souness, C.; Hubbard, B.; Milliken, R.E.; Quincey, D. An inventory and population-scale analysis of martian glacier-like forms. *Icarus* **2012**, *217*, 243–255. [CrossRef]
9. Van Gasselt, S.; Hauber, E.; Neukum, G. Lineated valley fill at the Martian dichotomy boundary: Nature and history of degradation. *J. Geophys. Res. Planets* **2010**, *115*, E08003. [CrossRef]
10. Baker, D.M.; Head, J.W.; Marchant, D.R. Flow patterns of lobate debris aprons and lineated valley fill north of Ismeniae Fossae, Mars: Evidence for extensive mid-latitude glaciation in the Late Amazonian. *Icarus* **2010**, *207*, 186–209. [CrossRef]
11. Head, J.W.; Marchant, D.R.; Dickson, J.L.; Kress, A.M.; Baker, D.M. Northern mid-latitude glaciation in the Late Amazonian period of Mars: Criteria for the recognition of debris-covered glacier and valley glacier landsystem deposits. *Earth Planet. Sci. Lett.* **2010**, *294*, 306–320. [CrossRef]
12. Plaut, J.J.; Picardi, G.; Safaeinili, A.; Ivanov, A.B.; Milkovich, S.M.; Cicchetti, A.; Kofman, W.; Mouginot, J.; Farrell, W.M.; Phillips, R.J. Subsurface radar sounding of the south polar layered deposits of Mars. *Science* **2007**, *316*, 92–95. [CrossRef] [PubMed]
13. Kress, A.M.; Head, J.W. Ring-mold craters in lineated valley fill and lobate debris aprons on Mars: Evidence for subsurface glacial ice. *Geophys. Res. Lett.* **2008**, *35*, L23206. [CrossRef]
14. Pedersen, G.B.M.; Head, J.W. Evidence of widespread degraded Amazonian-aged ice-rich deposits in the transition between Elysium Rise and Utopia Planitia, Mars: Guidelines for the recognition of degraded ice-rich materials. *Planet. Space Sci.* **2010**, *58*, 1953–1970. [CrossRef]
15. Levy, J.S.; Head, J.W.; Marchant, D.R. Concentric crater fill in Utopia Planitia: History and interaction between glacial "brain terrain" and periglacial mantle processes. *Icarus* **2009**, *202*, 462–476. [CrossRef]

16. Levy, J.; Head, J.; Marchant, D. Thermal contraction crack polygons on Mars: Classification, distribution, and climate implications from HiRISE observations. *J. Geophys. Res. Planets* **2009**, *114*, E01007. [CrossRef]
17. Forget, F.; Haberle, R.M.; Montmessin, F.; Levrard, B.; Head, J.W. Formation of glaciers on Mars by atmospheric precipitation at high obliquity. *Science* **2006**, *311*, 368–371. [CrossRef]
18. Jakosky, B.M.; Carr, M.H. Possible precipitation of ice at low latitudes of Mars during periods of high obliquity. *Nature* **1985**, *315*, 559–561. [CrossRef]
19. Bina, A. The Periglacial Landscape of Mars: Insight into the 'Decameter-scale Rimmed Depressions' in Utopia Planitia. Master's Thesis, The University of Western Ontario, London, ON, Canada, 2018.
20. Laskar, J.; Correia, A.C.; Gastineau, M.; Joutel, F.; Levrard, B.; Robutel, P. Long term evolution and chaotic diffusion of the insolation quantities of Mars. *Icarus* **2004**, *170*, 343–364. [CrossRef]
21. Madeleine, J.-B.; Forget, F.; Head, J.W.; Levrard, B.; Montmessin, F.; Millour, E. Amazonian northern mid-latitude glaciation on Mars: A proposed climate scenario. *Icarus* **2009**, *203*, 390–405. [CrossRef]
22. Levy, J.S.; Fassett, C.I.; Head, J.W.; Schwartz, C.; Watters, J.L. Sequestered glacial ice contribution to the global Martian water budget: Geometric constraints on the volume of remnant, midlatitude debris-covered glaciers. *J. Geophys. Res. Planets* **2014**, *119*, 2188–2196. [CrossRef]
23. Morgan, G.A.; Head III, J.W.; Marchant, D.R. Lineated valley fill (LVF) and lobate debris aprons (LDA) in the Deuteronilus Mensae northern dichotomy boundary region, Mars: Constraints on the extent, age and episodicity of Amazonian glacial events. *Icarus* **2009**, *202*, 22–38. [CrossRef]
24. Brough, S.; Hubbard, B.; Hubbard, A. Area and volume of mid-latitude glacier-like forms on Mars. *Earth Planet. Sci. Lett.* **2019**, *507*, 10–20. [CrossRef]
25. Hepburn, A.J.; Holt, T.; Hubbard, B.; Ng, F. Creating HiRISE digital elevation models for Mars using the open-source Ames Stereo Pipeline. *Geosci. Instrum. Methods Data Syst.* **2019**, *8*, 293–313. [CrossRef]
26. Kadish, S.J.; Head, J.W.; Fastook, J.L.; Marchant, D.R. Middle to Late Amazonian tropical mountain glaciers on Mars: The ages of the Tharsis Montes fan-shaped deposits. *Planet. Space Sci.* **2014**, *91*, 52–59. [CrossRef]
27. Shean, D.E.; Head, J.W.; Marchant, D.R. Origin and evolution of a cold-based tropical mountain glacier on Mars: The Pavonis Mons fan-shaped deposit. *J. Geophys. Res. Planets* **2005**, *110*, E05001. [CrossRef]
28. Williams, J.M.; Scuderi, L.A.; Newsom, H.E. Numerical Analysis of Putative Rock Glaciers on Mount Sharp, Gale Crater, Mars. *Remote Sens.* **2022**, *14*, 1887. [CrossRef]
29. Butcher, F.E.G. Water Ice at Mid-Latitudes on Mars. In *Oxford Research Encyclopedia of Planetary Science*; Oxford University Press: Oxford, UK, 2022.
30. Chuang, F.C.; Crown, D.A. Surface characteristics and degradational history of debris aprons in the Tempe Terra/Mareotis fossae region of Mars. *Icarus* **2005**, *179*, 24–42. [CrossRef]
31. Dickson, J.L.; Head, J.W.; Fassett, C.I. Patterns of accumulation and flow of ice in the mid-latitudes of Mars during the Amazonian. *Icarus* **2012**, *219*, 723–732. [CrossRef]
32. Souness, C.; Hubbard, B. Mid-latitude glaciation on Mars. *Prog. Phys. Geogr.* **2012**, *36*, 238–261. [CrossRef]
33. Neukum, G.; Jaumann, R.; Hoffmann, H.; Hauber, E.; Head, J.; Basilevsky, A.; Ivanov, B.; Werner, S.; Van Gasselt, S.; Murray, J. Recent and episodic volcanic and glacial activity on Mars revealed by the High Resolution Stereo Camera. *Nature* **2004**, *432*, 971–979. [CrossRef] [PubMed]
34. Shean, D.E. Candidate ice-rich material within equatorial craters on Mars. *Geophys. Res. Lett.* **2010**, *37*, L24202. [CrossRef]
35. Mitrofanov, I.; Malakhov, A.; Djachkova, M.; Golovin, D.; Litvak, M.; Mokrousov, M.; Sanin, A.; Svedhem, H.; Zelenyi, L. The evidence for unusually high hydrogen abundances in the central part of Valles Marineris on Mars. *Icarus* **2022**, *374*, 114805. [CrossRef]
36. Malin, M.C.; Bell, J.F.; Cantor, B.A.; Caplinger, M.A.; Calvin, W.M.; Clancy, R.T.; Edgett, K.S.; Edwards, L.; Haberle, R.M.; James, P.B.; et al. Context Camera Investigation on board the Mars Reconnaissance Orbiter. *J. Geophys. Res. Planets* **2007**, *112*, E05S04. [CrossRef]
37. McEwen, A.S.; Ojha, L.; Dundas, C.M.; Mattson, S.S.; Byrne, S.; Wray, J.J.; Cull, S.C.; Murchie, S.L.; Thomas, N.; Gulick, V.C. Seasonal flows on warm Martian slopes. *Science* **2011**, *333*, 740–743. [CrossRef]
38. Fergason, R.L.; Hare, T.M.; Laura, J. HRSC and MOLA Blended Digital Elevation Model at 200m v2. Astrogeology PDS Annex, US Geological Survey. 2018. Available online: https://astrogeology.usgs.gov/search?target=&system=&p=1&accscope=&searchBar= (accessed on 19 July 2023).
39. Smith, D.E.; Zuber, M.T.; Frey, H.V.; Garvin, J.B.; Head, J.W.; Muhleman, D.O.; Pettengill, G.H.; Phillips, R.J.; Solomon, S.C.; Zwally, H.J.; et al. Mars Orbiter Laser Altimeter: Experiment summary after the first year of global mapping of Mars. *J. Geophys. Res. Planets* **2001**, *106*, 23689–23722. [CrossRef]
40. Head, J.W.; Nahm, A.L.; Marchant, D.R.; Neukum, G. Modification of the dichotomy boundary on Mars by Amazonian mid-latitude regional glaciation. *Geophys. Res. Lett.* **2006**, *33*, L08S03. [CrossRef]

41. Diot, X.; El-Maarry, M.R.; Guallini, L.; Schlunegger, F.; Norton, K.P.; Thomas, N.; Sutton, S.; Grindrod, P.M. An ice-rich flow origin for the banded terrain in the Hellas basin, Mars. *J. Geophys. Res. Planets* **2015**, *120*, 2258–2276. [CrossRef]
42. Adeli, S.; Hauber, E.; Kleinhans, M.; Le Deit, L.; Platz, T.; Fawdon, P.; Jaumann, R. Amazonian-aged fluvial system and associated ice-related features in Terra Cimmeria, Mars. *Icarus* **2016**, *277*, 286–299. [CrossRef]
43. Robbins, S.J.; Hynek, B.M. A new global database of Mars impact craters $\geq$1 km: 1. Database creation, properties, and parameters. *J. Geophys. Res. Planets* **2012**, *117*, E05004. [CrossRef]
44. Putzig, N.E.; Morgan, G.A.; Sizemore, H.G.; Hollibaugh Baker, D.M.; Petersen, E.I.; Pathare, A.V.; Dundas, C.M.; Bramson, A.M.; Courville, S.W.; Perry, M.R.; et al. Ice Resource Mapping on Mars. In *Handbook of Space Resources*; Springer: Cham, Switzerland, 2023; pp. 583–616.
45. Garvin, J.; Sakimoto, S.; Frawley, J. Craters on Mars: Global geometric properties from gridded MOLA topography. In Proceedings of the Sixth International Conference on Mars, Pasadena, CA, USA, 20–25 July 2003.
46. Hartmann, W.; Daubar, I. Martian cratering 11. Utilizing decameter scale crater populations to study Martian history. *Meteorit. Planet. Sci.* **2017**, *52*, 493–510. [CrossRef]
47. Hartmann, W.K. Martian cratering 8: Isochron refinement and the chronology of Mars. *Icarus* **2005**, *174*, 294–320. [CrossRef]
48. Kneissl, T.; van Gasselt, S.; Neukum, G. Map-projection-independent crater size-frequency determination in GIS environments—New software tool for ArcGIS. *Planet. Space Sci.* **2011**, *59*, 1243–1254. [CrossRef]
49. Michael, G.; Neukum, G. Planetary surface dating from crater size–frequency distribution measurements: Partial resurfacing events and statistical age uncertainty. *Earth Planet. Sci. Lett.* **2010**, *294*, 223–229. [CrossRef]
50. Wang, Y.R.; Zhuo, M.; Zhang, X.R. *Automatic Crater Detection Tool for Moon, Mars, and Mercury [DS/OL]*; Science Data Bank: Beijing, China, 2024.
51. Hartmann, W.; Daubar, I. Utilizing Small Impact Craters to Clarify the History of Martian Surfaces. In Proceedings of the 79th Annual Meeting of the Meteoritical Society, Berkeley, CA, USA, 27–31 July 2016; p. 6435.
52. Hauber, E.; van Gasselt, S.; Chapman, M.G.; Neukum, G. Geomorphic evidence for former lobate debris aprons at low latitudes on Mars: Indicators of the Martian paleoclimate. *J. Geophys. Res. Planets* **2008**, *113*, E02007. [CrossRef]
53. Levy, J.S.; Head, J.W. Evidence for remnants of ancient ice-rich deposits: Mangala Valles outflow channel, Mars. *Terra Nova* **2005**, *17*, 503–509. [CrossRef]
54. Guallini, L. Esker-Like Ring-Shaped Ridges in Peta, Novara and Two Other Unnamed Craters on Mars: Evidences of Ancient Glaciers? *Space Sci. Rev.* **2017**, *110*, 85–130.
55. Parker, T. Sinuous Ridges in Peta Crater, Mars. In Proceedings of the 42nd Annual Lunar and Planetary Science Conference, The Woodlands, TX, USA, 7–11 March 2011; p. 2776.
56. Levy, J.S.; Goudge, T.A.; Head, J.W.; Fassett, C.I. Candidate volcanic and impact-induced ice depressions on Mars. *Icarus* **2017**, *285*, 185–194. [CrossRef]
57. Baliyan, S.; Hayne, P.; Vijayan, S. Isil Crater on Mars: Insights into Volcanic and Glacio-Fluivial Processes. *LPI Contrib.* **2024**, *3007*, 3384.
58. Zhang, M.; Zhao, J.; Xiao, L.; Xu, Y.; Bugiolacchi, R.; Wang, J. Fan-shaped deposits in the northern Hellas region, Mars: Implications for the evolution of water reservoir and climate. *Icarus* **2023**, *395*, 115470. [CrossRef]
59. Galofre, A.G.; Howard, A.D.; Morgan, A.M.; Wilson, S.A.; Moore, J.M. Glacial sculpting of a martian cratered landscape on the northeastern flank of the Hellas basin. *Icarus* **2024**, *420*, 116211. [CrossRef]
60. Wilson, S.A.; Howard, A.D.; Moore, J.M.; Grant, J.A. Geomorphic and stratigraphic analysis of Crater Terby and layered deposits north of Hellas basin, Mars. *J. Geophys. Res. Planets* **2007**, *112*, E08009. [CrossRef]
61. Moore, J.M. Nature of the mantling deposit in the heavily cratered terrain of northeastern Arabia, Mars. *J. Geophys. Res. Solid Earth* **1990**, *95*, 14279–14289. [CrossRef]
62. Squyres, S.W.; Carr, M.H. Geomorphic evidence for the distribution of ground ice on Mars. *Science* **1986**, *231*, 249–252. [CrossRef]
63. Fassett, C.I.; Levy, J.S.; Dickson, J.L.; Head, J.W. An extended period of episodic northern mid-latitude glaciation on Mars during the Middle to Late Amazonian: Implications for long-term obliquity history. *Geology* **2014**, *42*, 763–766. [CrossRef]
64. Fastook, J.L.; Head, J.W. Amazonian mid-to high-latitude glaciation on Mars: Supply-limited ice sources, ice accumulation patterns, and concentric crater fill glacial flow and ice sequestration. *Planet. Space Sci.* **2014**, *91*, 60–76. [CrossRef]
65. Michael, G. Planetary surface dating from crater size–frequency distribution measurements: Multiple resurfacing episodes and differential isochron fitting. *Icarus* **2013**, *226*, 885–890. [CrossRef]
66. Vincendon, M.; Forget, F.; Mustard, J. Water ice at low to midlatitudes on Mars. *J. Geophys. Res. Planets* **2010**, *115*, E10001. [CrossRef]
67. Levrard, B.; Forget, F.; Montmessin, F.; Laskar, J. Recent ice-rich deposits formed at high latitudes on Mars by sublimation of unstable equatorial ice during low obliquity. *Nature* **2004**, *431*, 1072–1075. [CrossRef]
68. Montmessin, F.; Bertaux, J.-L.; Quémerais, E.; Korablev, O.; Rannou, P.; Forget, F.; Perrier, S.; Fussen, D.; Lebonnois, S.; Rébérac, A. Subvisible CO_2 ice clouds detected in the mesosphere of Mars. *Icarus* **2006**, *183*, 403–410. [CrossRef]

69. Mischna, M.A.; Richardson, M.I.; Wilson, R.J.; McCleese, D.J. On the orbital forcing of Martian water and CO_2 cycles: A general circulation model study with simplified volatile schemes. *J. Geophys. Res. Planets* **2003**, *108*, 5062. [CrossRef]
70. Head, J.W.; Mustard, J.F.; Kreslavsky, M.A.; Milliken, R.E.; Marchant, D.R. Recent ice ages on Mars. *Nature* **2003**, *426*, 797–802. [CrossRef] [PubMed]
71. Berman, D.C.; Chuang, F.C.; Smith, I.B.; Crown, D.A. Ice-rich landforms of the southern mid-latitudes of Mars: A case study in Nereidum Montes. *Icarus* **2021**, *355*, 114170. [CrossRef]

Disclaimer/Publisher's Note: The statements, opinions and data contained in all publications are solely those of the individual author(s) and contributor(s) and not of MDPI and/or the editor(s). MDPI and/or the editor(s) disclaim responsibility for any injury to people or property resulting from any ideas, methods, instructions or products referred to in the content.

remote sensing

MDPI

Article

A Generative Adversarial Network for Pixel-Scale Lunar DEM Generation from Single High-Resolution Image and Low-Resolution DEM Based on Terrain Self-Similarity Constraint

Tianhao Chen [1,2], Yexin Wang [2,*], Jing Nan [2,3], Chenxu Zhao [2,3], Biao Wang [2,3], Bin Xie [2,3], Wai-Chung Liu [2], Kaichang Di [2], Bin Liu [2] and Shaohua Chen [1]

[1] School of Instrumentation Science and Opto-Electronics Engineering, Beijing Information Science & Technology University, Beijing 100192, China; 2023020180@bistu.edu.cn (T.C.); 20172056@bistu.edu.cn (S.C.)
[2] State Key Laboratory of Remote Sensing and Digital Earth, Aerospace Information Research Institute, Chinese Academy of Sciences, Beijing 100101, China; nanjing23@mails.ucas.ac.cn (J.N.); zhaochenxu22@mails.ucas.ac.cn (C.Z.); wangbiao221@mails.ucas.ac.cn (B.W.); xiebin21@mails.ucas.ac.cn (B.X.); liaowc@aircas.ac.cn (W.-C.L.); dikc@aircas.ac.cn (K.D.); liubin@radi.ac.cn (B.L.)
[3] University of Chinese Academy of Sciences, Beijing 100101, China
* Correspondence: wangyx@aircas.ac.cn; Tel.: +86-10-64807987

Abstract

Lunar digital elevation models (DEMs) are a fundamental data source for lunar research and exploration. However, high-resolution DEM products for the Moon are only available in some local areas, which makes it difficult to meet the needs of scientific research and missions. To this end, we have previously developed a deep learning-based method (LDEMGAN1.0) for single-image lunar DEM reconstruction. To address issues such as loss of detail in LDEMGAN1.0, this study leverages the inherent structural self-similarity of different DEM data from the same lunar terrain and proposes an improved version, named LDEMGAN2.0. During the training process, the model computes the self-similarity graph (SSG) between the outputs of the LDEMGAN2.0 generator and the ground truth, and incorporates the self-similarity loss (SSL) constraint into the network generator loss to guide DEM reconstruction. This improves the network's capacity to capture both local and global terrain structures. Using the LROC NAC DTM product (2 m/pixel) as the ground truth, experiments were conducted in the Apollo 11 landing area. The proposed LDEMGAN2.0 achieved mean absolute error (MAE) of 1.49 m, root mean square error (RMSE) of 2.01 m, and structural similarity index measure (SSIM) of 0.86, which is 46.0%, 33.4%, and 11.6% higher than that of LDEMGAN1.0. Both qualitative and quantitative evaluations demonstrate that LDEMGAN2.0 enhances detail recovery and reduces reconstruction artifacts.

Keywords: lunar exploration; digital elevation model; generative adversarial network; self-similarity loss

1. Introduction

In lunar exploration missions, applications, such as lunar surface feature identification, landing site selection, rover navigation, and positioning, rely on high-precision and high-resolution lunar digital elevation models (DEMs) [1–3]. Lunar DEMs are regular grids

with corresponding elevation values to represent surface topography. They contribute to both scientific research and the safety of lunar landing missions. Before landing on the surface, DEMs are utilized to support the study of stratigraphy, volcanic activity, and impact history, as well as analyses of slope, illumination condition, communication, flight trajectory, etc., to determine the landing site and ensure safety landing [4–6]. After landing, DEMs, including those constructed by orbiter images and those constructed by images captured on the lander/rover, play important roles in post-land operations such as rover navigation and positioning, path planning, in situ analysis support, etc. [7].

In early studies, lunar DEM-generation approaches have been broadly classified into two types: stereo photogrammetry and laser altimetry-based interpolation [8]. Stereo photogrammetry requires stereo images to cover the target area. However, there are currently few high-resolution orbiters designed for direct stereo imaging. It is impossible to obtain sufficient multi-view image data to ensure adequate overlap and achieve global multi-coverage detection [9]. The altimeter is limited by launch plans and orbit coverage density [10]. Due to the differences in the orbit altitude and a large laser spot size, the distribution of the lunar surface elevation points is not uniform, and the spacing between sampling points is large [11]. For example, LOLA's sampling strategy produces five parallel profiles along LRO's sub-spacecraft ground track. Profiles are 10–12 m apart, with observations within each profile separated by 56 m [12]. Consequently, the accuracy of the DEM reconstructed through elevation interpolation varies across different regions, making it challenging to achieve high-resolution and high-precision DEMs.

Given the scarcity of high-resolution stereo or multi-coverage images of the lunar surface, recent studies have focused on extracting lunar elevation information from a single image to construct lunar DEMs [13]. Single-image DEM reconstruction methods are primarily based on surface reflectance modeling, such as shape from shading (SFS) and shape and albedo from shading (SAFS) [14,15]. These methods leverage variations in surface brightness to estimate parameters such as relative heights or surface normal vectors at each point, thereby deriving the elevation information and generating terrain data. However, single-image SFS often requires extra constraints to produce reliable results [16], such as using regularization models [17] or incorporating low-resolution DEMs [18], which improve both accuracy and robustness in shape recovery and absolute elevation values.

The advancement of deep learning has transformed the unconstrained single-image 3D reconstruction problem into a nonlinear mapping problem [19]. Neural networks can learn the "hidden" mapping relationships between two types of data and perform end-to-end transformations with sufficient training samples [20]. Deep neural networks extract features from input monocular images and utilize the depth information inherent in these features to generate high-resolution DEMs [21]. These methods mainly include convolutional neural networks (CNNs) and generative adversarial networks (GANs) [22]. CNN-based methods are trained with a large number of images and corresponding depth information to implicitly establish a mapping between images and normalized depth information, enabling terrain reconstruction from a single image [23]. However, these methods rely on high-quality large-scale data and struggle to accurately recover terrain scale information under monocular conditions. To address this challenge, researchers introduced low-resolution DEMs as global constraints, which improved scale-recovery accuracy [24]. Although low-resolution DEMs are used as constraints to improve the overall accuracy and consistency of terrain reconstruction, they still struggle to capture fine-scale terrain features and remain heavily reliant on the quality of low-resolution DEM data. Subsequently, researchers combined low-resolution DEMs and image data as inputs to a CNN, allowing for the network to learn multi-scale terrain features and generate more accurate high-resolution DEMs [25]. With the development of deep neural networks, GANs offer self-supervised adversarial

learning frameworks for both image generation and transformation. Later approaches incorporate multi-scale reconstruction strategies alongside single-scale optimization inference mechanisms, effectively addressing the trade-off between reconstruction resolution and global consistency [26,27]. Additionally, combining single images with low-resolution DEMs has been integrated into GAN frameworks [28,29], which improves the accuracy and robustness of single-image DEM reconstruction. However, when significant resolution discrepancies exist between input and output DEMs, existing methods frequently exhibit artifacts such as detail loss and spurious structures in texture-rich areas. This limitation may arise from the generator's inadequate representational capacity, while discriminators may struggle to effectively identify and constrain subtle differences induced by resolution gaps or inherent model limitations within these texture-rich areas. Thus, mitigating artifact generation (e.g., detail loss and spurious structures) in texture-rich areas constitutes a pivotal challenge for achieving high-fidelity, high-resolution DEM reconstruction.

Self-similarity of terrain originates from the similarity of statistical laws and structural patterns at different DEM data in the same terrain. Introducing self-similarity loss into GANs helps the generator to maintains consistency with the real terrain, effectively improving the authenticity and detail accuracy of the generated images and enhancing the generalization ability of the model. Therefore, based on the principle that the same terrain exhibits self-similarity across different DEM data, this paper improves upon the previously developed single-image lunar DEM reconstruction network (LDEMGAN1.0) [29], which suffers from issues such as detail loss and spurious structures (the features that appear in the DEM reconstructed by LDEMGAN1.0, but are absent in the corresponding real images) in complex terrain structures, and proposes an enhanced version named LDEMGAN2.0. By constructing a self-similarity graph (SSG) and calculating self-similarity loss (SSL) to guide the training process of the DEM reconstruction network, this approach quantifies the correlations between the generated DEM and ground truth, thereby reducing information loss and achieving high-resolution DEM reconstruction. In this study, a lunar reconnaissance orbiter camera (LROC) narrow-angle camera (NAC) digital terrain model (DTM) is used as the ground truth to reconstruct pixel-scale DEMs from LROC NAC imagery of the Apollo 11 landing area. Please note that, for lunar topography, DEM and DTM are interchangeable, as no vegetation or buildings exist. A comprehensive evaluation was conducted by comparing the DEMs generated by LDEMGAN2.0, LDEMGAN1.0, and Ames Stereo Pipeline (ASP) SFS [30] against the ground truth to assess the reconstruction accuracy and generalization performance of the proposed model.

2. Materials and Methods

2.1. Previous Work: LDEMGAN1.0

We previously developed a single-image lunar DEM reconstruction network (LDEMGAN1.0) based on the GAN model [29]. This network uses a single high-resolution digital orthophoto map (DOM) image combined with a low-resolution DEM as input. The low-resolution DEM serves as auxiliary control information, allowing for the network to capture low-frequency terrain features. For this study, the LRO LOLA digital elevation model co-registered with Selene data 2015 (SLDEM2015, ~60 m/pixel) was selected as the low-resolution DEM and up-sampled to the same spatial resolution as the input DOM prior to network input. The reconstruction process is composed of two phases: network training and DEM reconstruction. In the network training phase, high-resolution DOMs are combined in SLDEM2015 with the same spatial resolution to create dual-channel image data. This data is used as input to LDEMGAN1.0, with the corresponding NAC DTM serving as the ground truth for supervised training to obtain the reconstruction network. In the DEM reconstruction phase, high-resolution DOMs and the up-sampled SLDEM2015 data covering the same re-

gion are fed into LDEMGAN1.0 to produce DEMs with the same spatial resolution as input images. Since the input data needs to be normalized before entering the generative network for better convergence, the output value of the network fall within [0, 1] as well. Therefore, the output is scaled to convert the generated DEM from relative elevation to absolute value. Although LDEMGAN1.0 has shown promising performance in DEM-reconstruction tasks, it shows certain limitations in representing complex terrain structures and preserving high-frequency details (e.g., impact crater rims, ridges, and textured geological features) in some reconstruction results. These limitations may cause minor structural distortions and partial detail loss in some cases, which can cause local inconsistencies in the geometry and texture of the reconstructed terrain, as shown in Figure 1.

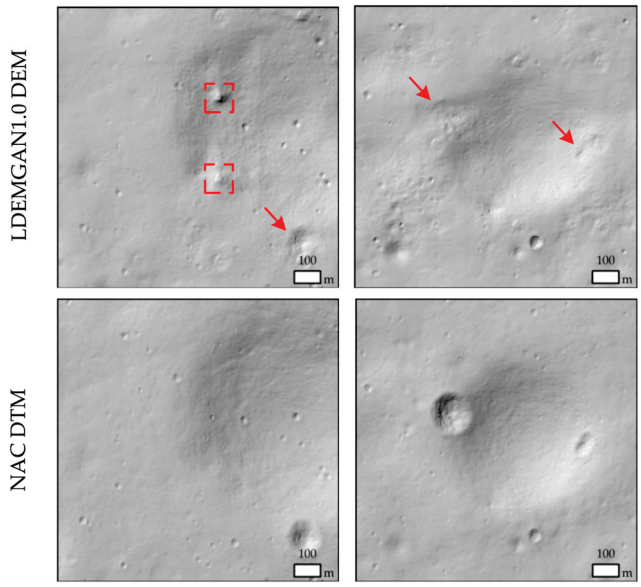


Figure 1. LDEMGAN1.0 exhibits minor spurious structures and a degree of detail loss in some cases. The dashed box highlights LDEMGAN1.0 local spurious structures, while red arrows point to its areas with detail loss.

We posit that this may be attributed to the inadequate consideration of the local elevation differences between the reconstructed DEM and the ground truth within the same terrain. Accordingly, in LDEMGAN2.0, we introduced a terrain self-similarity constraint to regularize the network training process.

2.2. Improvement in This Work: LDEMGAN2.0

In order to address the issues identified in the LDEMGAN1.0 network, we propose an improved version, termed LDEMGAN2.0, which leverages the inherent structural self-similarity in different DEM data of the same lunar terrain. Compared to LDEMGAN1.0, LDEMGAN2.0 constructs SSGs between the reconstructed DEM and the ground truth to calculate SSL during training, which in turn guides parameter updates, optimizes the network architecture, and supervises the generation of image structures and details. The training process is illustrated in Figure 2.

During the network training process, the NAC DOM and SLDEM2015, preprocessed and resampled to 2 m/pixel, are used as inputs to LDEMGAN2.0 for DEM reconstruction. The reconstructed DEM is then compared with the ground truth NAC DTM, and SSGs are calculated for the LDEMGAN2.0 generator output and NAC DTM, focusing on the regions with edge and texture information on the ground truth. The resulting SSL is calculated and integrated into the generator's loss function to guide the optimization of the entire training process.

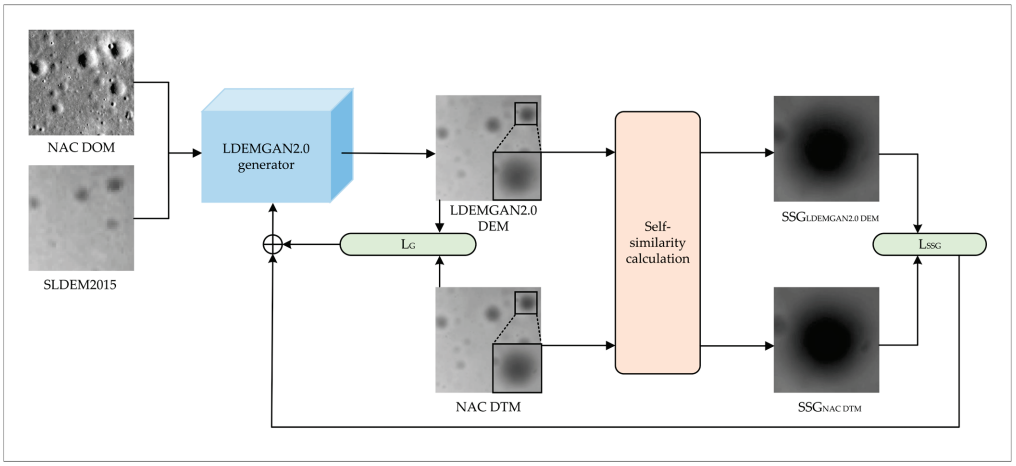


Figure 2. LDEMGAN2.0 training process.

2.3. DEM Self-Similarity Loss

Based on the principle that the terrain morphology and surface texture in different lunar DEM data exhibit similar statistical distribution patterns and scale invariance at the same lunar terrain, we utilize the principle of self-similarity to calculate SSGs between the reconstruction results of the LDEMGAN2.0 generator and the ground truth during the network training process. SSL is then integrated into the loss function to guide the recovery of the details and structure in the reconstructed DEM.

2.3.1. Self-Similarity Principle

Self-similarity is the statistical property of images, meaning that, for images from the same area, their structural patterns and texture features exhibit similar statistical laws and scale invariance across different data or resolutions [31]. It is widely applied in fields such as image registration, feature matching, and super-resolution reconstruction in computer vision and remote sensing [32]. Figure 3 illustrates the self-similarity of the same lunar region's different DEM data.

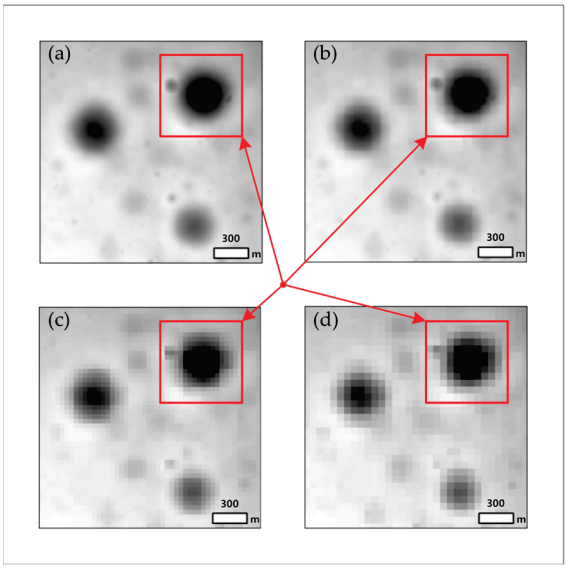


Figure 3. Schematic diagram of the self-similarity of the lunar surface appearing in DEMs with different data and resolutions. (**a**) NAC DTM (2 m/pixel), (**b**) NAC DTM (60 m/pixel), (**c**) SLDEM2015 (2 m/pixel), (**d**) SLDEM2015 (60 m/pixel). The impact craters (highlighted with red squares) exhibit inherent structural self-similarity across different data and resolutions.

2.3.2. Binary Mask Image

Using the above principle, we calculated the self-similarity between the output DEM of generator and the ground truth DEM to construct the SSGs. However, calculating global SSGs incurs a high training cost. In fact, it is unnecessary to compute the self-similarity for each pixel, as we aimed for LDEMGAN2.0 not only to maintain low training costs, but also to focus on the edge and texture areas to reduce reconstruction artifacts, especially on high-frequent features. Therefore, we reused a binary mask of edge and texture pixels for the ground truth DEM [33], indicating where the SSGs should be calculated during the training process.

The Laplace operator is denoted as L, the ground truth is denoted as DTM_{NAC}, and the calculated value from the convolution operation is denoted as E, as shown in Formula (1):

$$E = L \otimes DTM_{NAC} \tag{1}$$

The regions where E values exceed the empirical threshold t are considered to have significant edge and texture information are marked as 1. Conversely, the regions where E values are below the threshold t are considered smooth regions and are marked as 0. This forms a binary mask, denoted as *Mask*, as shown in Equation (2):

$$Mask = \begin{cases} 0, \ E \ \leq \ t \\ 1, \ E \ > \ t \end{cases} \tag{2}$$

here, t represents the threshold, which is empirically set to 165 to preserve most of the true edge pixels while filtering out smooth terrain features.

2.3.3. Self-Similarity Graph

Centered on the pixels marked as 1, the search areas for both the LDEMGAN2.0 DEM and the NAC DTM are defined, each having a size of 5×5 pixels. A local sliding window is then applied within the search areas. The local sliding windows for LDEMGAN2.0 DEM and NAC DTM are denoted as $P_{LDEMGAN2.0}$ and P_{NAC}, respectively, each with a size of 3×3 pixels. As shown in Equation (3), the squared differences between each pixels and its neighboring pixels in $P_{LDEMGAN2.0}$ and P_{NAC} is calculated, respectively, denoted as $d^2_{LDEMGAN2.0}(\mu_{i,j})$ and $d^2_{NAC}(\eta_{i,j})$.

$$\begin{aligned} d^2_{LDEMGAN2.0}(\mu_{i,j}) &= \frac{1}{c} \sum_{i=0}^{f} \sum_{j=0}^{f} (\mu_{i,j} - \mu_{i+1,j+1})^2 \\ d^2_{NAC}(\eta_{i,j}) &= \frac{1}{c} \sum_{i=0}^{f} \sum_{j=0}^{f} (\eta_{i,j} - \eta_{i+1,j+1})^2 \end{aligned} \tag{3}$$

here, c represents the number of channels in the image, f represents the size of the block, and $\mu_{i+1,j+1}$, $\eta_{i+1,j+1}$ represents the neighboring pixels of the origin pixel $\mu_{i,j}$, $\eta_{i,j}$ in the local sliding window.

Therefore, the self-similarity value of $P_{LDEMGAN2.0}$ and P_{NAC} is denoted as $S(d^2_{LDEMGAN2.0}(\mu_{i,j}))$ and $S(d^2_{NAC}(\eta_{i,j}))$, as shown in Equation (4):

$$\begin{aligned} S(d^2_{LDEMGAN2.0}(\mu_{i,j})) &= e^{-\frac{d^2_{LDEMGAN2.0}(\mu_{i,j})}{h}} \\ S(d^2_{NAC}(\eta_{i,j})) &= e^{-\frac{d^2_{NAC}(\eta_{i,j})}{h}} \end{aligned} \tag{4}$$

here, h is the proportional factor, $h > 0$. $0 \ \leq S(d^2(\mu_{i,j})) \ \leq 1$, the closer it is to 1, the higher similarity between $\mu_{i,j}$, $\eta_{i,j}$ and $\mu_{i+1,j+1}$, $\eta_{i+1,j+1}$.

In order to enhance the contrast of small values and reduce storage requirements and memory usage, a logarithmic transformation is applied to map the values $S(d^2_{LDEMGAN2.0}(\mu_{i,j}))$ and $S(d^2_{NAC}(\eta_{i,j}))$ to the range of 0–255, denoted as $SSG(S(d^2(\mu_{i,j})))$, as shown in Equation (5).

$$SSG(S(d^2(\mu_{i,j}))) = \frac{\log(1+S(d^2(\mu_{i,j})))}{\log(1+S_{max}(d^2(\mu_{i,j})))} \times 255 \tag{5}$$

where $S_{max}(d^2(\mu_{i,j}))$ represents the maximum value in self-similarity.

The SSGs of $P_{LDEMGAN2.0}$ and P_{NAC} are generated using Equation (5), denoted as $SSG_{predict}$ and SSG_{NAC}, respectively. These graphs illustrate the distribution of inherent structural similarities in the DEMs, as shown in Figure 4.

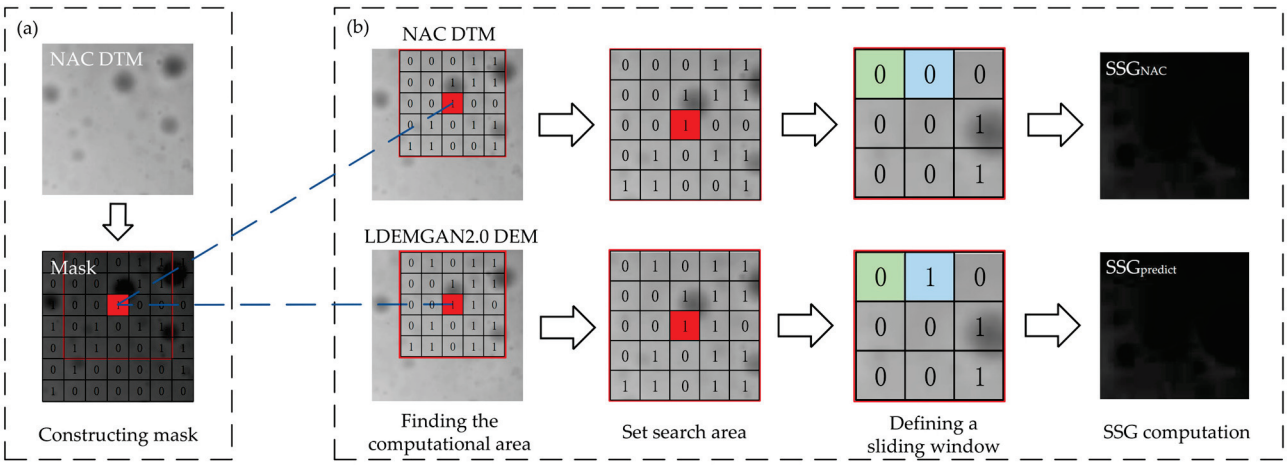


Figure 4. Illustration of the SSGs calculation process. (**a**) A mask is constructed based on the ground truth to indicate regions where the SSG should be calculated during the training process. (**b**) For pixels marked as 1, a 5 × 5 pixel calculation area is defined, and a 3 × 3 pixel sliding window is used to calculate the SSG within the area.

2.3.4. Loss Function

Based on the principle of self-similarity, this paper leverages the inherent structural self-similarity of different DEM data from the same lunar terrain. By calculating SSL between the LDEMGAN2.0 DEM and the ground truth as a constraint, the network training process is optimized, enhancing the network's ability to constrain both local and global terrain structures and improving the accuracy of terrain reconstruction.

$SSG_{predict}$ and SSG_{NAC} represent the SSGs of the LDEMGAN2.0 DEM and the ground truth, respectively. The differences between them is used to supervise the network training. In this paper, the self-similarity loss is constructed using the Kullback–Leibler (KL) divergence and regularization loss [33], denoted in Equation (6):

$$L_{SSG} = D_{KL}(SSG_{NAC} \parallel SSG_{predict}) + \varepsilon \left| SSG_{predict} - SSG_{NAC} \right| \tag{6}$$

here, ε represents the balance parameter factor and $D_{KL}(\cdot)$ represents the KL divergence, which is used to quantify the distribution difference between SSG_{NAC} and $SSG_{predict}$, as shown in Equation (7):

$$D_{KL}(SSG_{NAC} \parallel SSG_{predict}) = H(SSG_{NAC}, SSG_{predict}) - H(SSG_{NAC}) \tag{7}$$

Among them, $H(SSG_{NAC}, SSG_{predict})$ represents the cross-entropy between SSG_{NAC} and $SSG_{predict}$, which quantifies the reconstruction error between SSG_{NAC} and $SSG_{predict}$, and

$H(SSG_{NAC})$ represents the entropy of SSG_{NAC}, reflecting the inherent information content in SSG_{NAC}.

L_{SSG} is added to the loss function of the LDEMGAN1.0 generator's loss function L_G [29], with the total loss denoted as L_{Gtotal}, as shown in Equation (8). The model is then retrained.

$$L_{Gtotal} = L_G + \delta L_{SSG} \tag{8}$$

where $L_G = \alpha L_{Huber} + \beta L_{grad} + \gamma L_{GAN} + L_D$ and $\alpha, \beta, \gamma, \delta$ represent the balanced parameter factors.

2.4. Network Training

The dataset for the network training consists of training samples created from 10 selected regions, as shown with the yellow points in Figure 5. To ensure optimal reconstruction quality, we selected images within our suggested range of 25–70° from past experience, specifically within the range of 45–70°, and avoided those containing shadows with a grayscale value approaching 0 or overexposed regions with a grayscale value approaching 1 (normalized value). The training data consists of LROC NAC DOMs (0.5–2 m/pixel) covering these regions, along with their corresponding LROC NAC DTMs (2 m/pixel) and SLDEM2015 (~60 m/pixel). These data can be downloaded from https://ode.rsl.wustl.edu/moon/ (accessed on 1 May 2025). The information of the LROC NAC DOM image used is shown in Table 1.

In this paper, the training data are resampled to a resolution of 2 m/pixel for subsequent comparative analysis under the same experimental conditions. The resampled LROC NAC DOM and its corresponding SLDEM2015 for the same area are served as the first and second bands, respectively, to synthesize dual-channel image data. The LROC NAC DTM served as the ground truth. To enhance the generalization ability of the network, data augmentation techniques are applied, including training samples with different lunar geomorphologies (e.g., impact craters, volcanos, ridges, and so on) and training samples after rotation or flipping. As a result, a total of 51,222 sets of 256 × 256 pixels dual-band input data and corresponding high-resolution DEMs are generated and divided into a training set and a validation set in an 8:2 ratio for the model training and performance evaluation.

For the reconstruction network training, the experimental hyperparameters are set as follows: block size of 256 × 256 pixels, batch size of 64, and 300 training epochs. The initial learning rate is set to 2×10^{-4}, which begins to decay after 100 epochs, and is linearly reduced to 10^{-6}. The coefficients in Equation (4) is set to $h = 0.004$, which effectively captures the fine structures in the image while also avoiding the excessive amplification of noise. The coefficients in Equation (8) are set to $\alpha = 0.5$, $\beta = 0.5$, $\gamma = 0.8$, and $\delta = 0.5$. The GPU used in the experimental hardware environment is the NVIDIA GeForce RTX 4090, with a machine RAM of 64 GB. The experiments are implemented in Python 3.10 and PyTorch 2.3.1 + cu121 deep learning framework, with CUDA 12.1 used for acceleration. The total training time was 36 h. To ensure the comparability of the experimental results, all experiments in this paper are conducted in the same environment and with identical parameter settings.

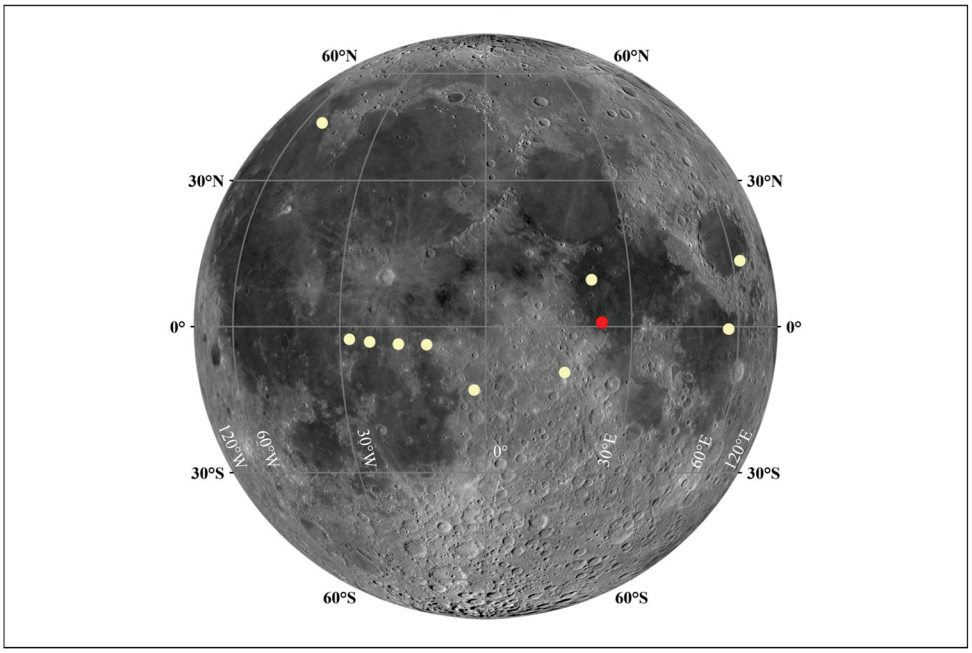


Figure 5. Distribution of data for training and experiment (Projection: Orthographic; False Easting: 0.0°; False Northing: 0.0°; Longitude of center: 0.0°; Latitude of center: 0.0°). The yellow points represent the training regions, while the red point represent the experimental area.

Table 1. Information of the training data.

ID	Area	LROC NAC Image ID
1	Apollo 12	M120005333LE, M120005333RE
2	Apollo 13	M160139273LE, M160139273RE
3	Apollo 14	M150633128LE, M150633128RE
4	Apollo 16	M159847331LE, M159847331RE
5	Apollo 17	M144708115LE, M144708115RE
6	LUNA 16	M159582808LE, M159582808RE
7	LUNA 24	M144219225LE, M144219225RE
8	RANGER 6	M144483945LE, M144483945RE
9	RANGER 9	M12930938LE, M12930938RE
10	RIMASHARP 3	M173252954LE, M173252954RE

3. Results

3.1. Experimental Area

To evaluate the reconstruction performance of LDEMGAN2.0, the Apollo 11 landing area, located around 0.77°N, 23.44°E, is selected as the experimental area, which differs from training data area. The location is indicated by the red dot in Figure 5. The area is mostly flat with minor terrain undulations, and is primarily composed of lunar mare

basalts, predominantly consisting of low-lying basalt plains. Small impact craters are scattered locally, with their diameters ranging from several to hundreds of meters [34].

3.2. Evaluation Indicators

To evaluate the reconstruction performance of the improved algorithm model, this paper uses the mean absolute error (MAE) and root mean square error (RMSE) as statistical evaluation metrics to quantitatively assess the elevation accuracy deviation, overall error distribution, and local error variations.

MAE is defined in statistics as the average of the absolute differences between the predicted values and the ground truth. It is used to measure the network's average prediction error, as shown in Equation (9):

$$MAE(y_i, \hat{y}_i) = \frac{1}{n}\sum_{i=1}^{n}|y_i - \hat{y}_i| \tag{9}$$

where n represents the number of samples, y_i represents the ground truth, and $\hat{y}_i$ represents the network's predicted value. Please note that, as there is no absolute elevation value, the LROC NAC DTM is considered the ground truth.

RMSE is a commonly used metric in statistics and regression analysis to measure the average deviation between the network's predicted values and the ground truth, as shown in Equation (10):

$$RMSE(y_i, \hat{y}_i) = \sqrt{\frac{1}{n}\sum_{i=1}^{n}(y_i - \hat{y}_i)^2} \tag{10}$$

Additionally, to ensure that the DEM evaluation not only focuses on numerical accuracy deviations, but also reflects the overall stability and spatial consistency of the terrain structure, the structural similarity index measure (SSIM) was used to assess the similarity between the DEM reconstructed by the improved network reconstructed DEM and the NAC DTM in terms of spatial feature distribution, terrain gradient changes, and texture details [35], as shown in Equation (11):

$$SSIM(y_i, \hat{y}_i) = \frac{(2\mu_{\hat{y}_i}\mu_{y_i} + C_1)(2\sigma_{\hat{y}_i y_i} + C_2)}{\left(\mu_{\hat{y}_i}^2 + \mu_{\hat{y}_i}^2 + C_1\right)\left(\sigma_{\hat{y}_i}^2 + \sigma_{\hat{y}_i}^2 + C2\right)} \tag{11}$$

where $\mu_{\hat{y}_i}$ and μ_{y_i} represents the mean of $\hat{y}_i$ and y_i respectively, $\sigma_{\hat{y}_i}^2, \sigma_{y_i}^2$ represents the variance in $\hat{y}_i$ and y_i respectively, $\sigma_{\hat{y}_i y_i}$ represents the covariance of $\hat{y}_i$ and y_i, and C_1, C_2 are constants.

The elevation differences between each reconstructed DEM (LDEMGAN2.0, LDEMGAN1.0, ASP SFS [30]) and the ground truth DEM are calculated individually to generate absolute difference maps for error analysis. Additionally, a hillshade map is created to simulate the terrain illumination variations under the same solar altitude angle of the input images. Finally, elevation profiles are used to analyze and compare the morphological characteristics.

3.3. Reconstruction and Analysis

3.3.1. Analysis and Evaluation of Overall Reconstruction Results

In this study, the images used for testing the network performance were M150368601LE and M150368601RE, which include both left and right experimental data record (RE) images, with a solar elevation angle of 46.26° and an image resolution of 0.53 m/pixel. Since there is a significant resolution difference between the NAC DOM and SLDEM2015, an iterative reconstruction procedure was adopted. First, the input data consists of the LROC NAC

DOM was down-sampled to 10 m/pixel, and the SLDEM2015 was up-sampled to the same resolution of 10 m/pixel. They were fed into the network to generate a reconstructed DEM at 10 m/pixel resolution. Subsequently, the generated 10 m/pixel DEM was up-sampled to 2 m/pixel and combined with the LROC NAC DOM, which was also down-sampled to 2 m/pixel, to generate a final DEM at 2 m/pixel resolution. Finally, the mean and standard deviation of the SLDEM2015 were calculated, based on which the reconstructed elevation was stretched to obtain the absolute height. Geographic information was subsequently added to the restored height, and scale restoration was completed. The LROC NAC DTM (2 m/pixel) was used as the ground truth to reconstruct the DEM of the Apollo 11 landing area. Please note that by configuring the appropriate hierarchical structures, LDEMGAN2.0 can generate DEMs at the same grid resolution as the input data. The down-sampling to 2 m/pixel was primarily used to facilitate comparative analysis with the ground truth.

Meanwhile, the key parameters of the ASP SFS DEM reconstruction method were set as follows: the shadow threshold was set to 0.003, and the smoothness weight was set to 0.04 to achieve a balance between detail recovery and terrain continuity. The reflectance model chosen was the Lunar-Lambertian model (reflectance type 1) [36], which is suitable for the lunar surface. The maximum number of iterations was set to 20 to ensure full convergence. To improve the image fusion effect, the blending distance was set to 10 pixels, and the minimum blending area width was set to 100 pixels [30].

The elevation accuracy of the reconstruction results was evaluated using the metrics described above. The reconstruction results of LDEMGAN2.0 in the Apollo 11 experimental area are shown in Figure 6.

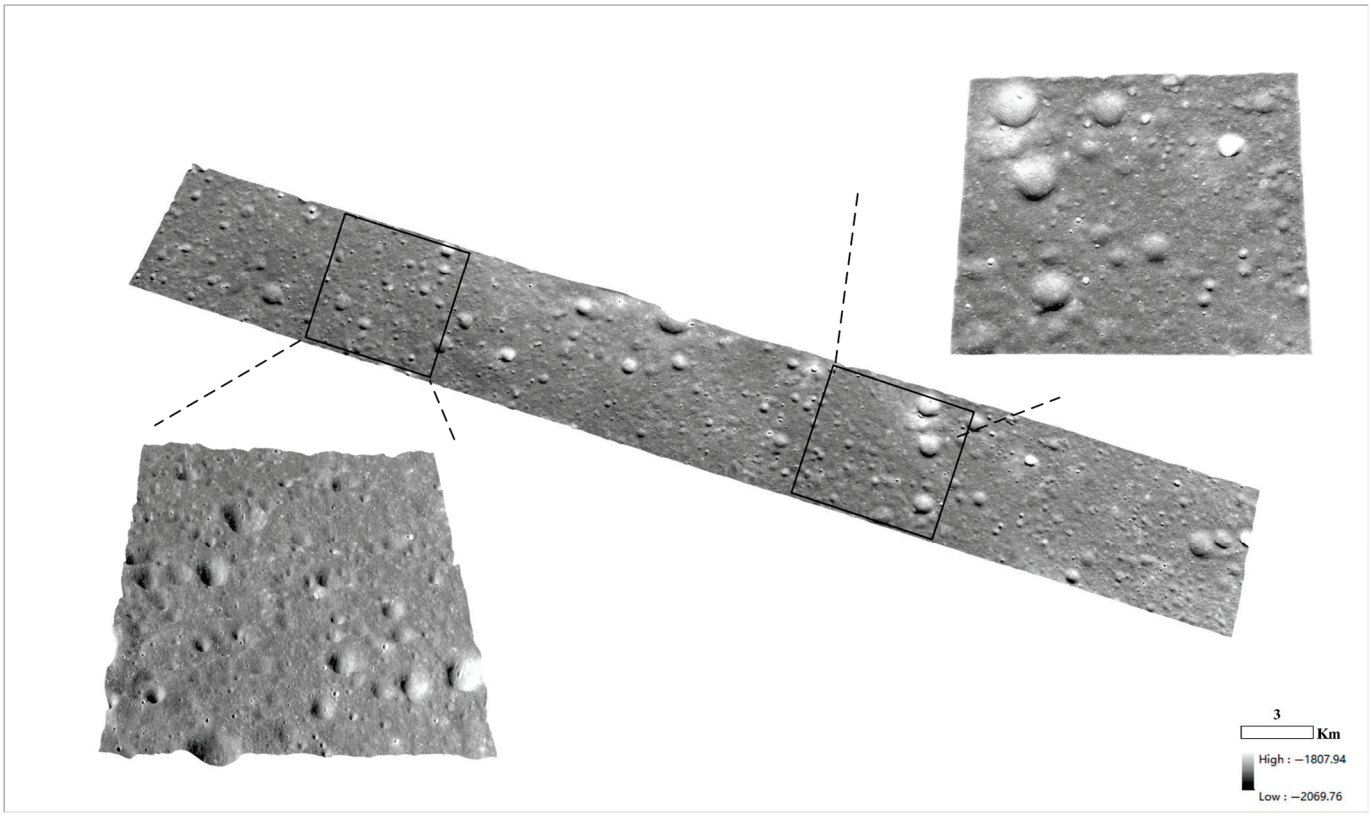


Figure 6. Reconstruction results of the Apollo 11 experimental area rendered with NAC DOM are shown in 3D-perspective view, with two zoomed-in views. (Height exaggeration factor: 10). The scalebar corresponds to the entire Apollo 11 experimental area.

The absolute difference maps for the LDEMGAN2.0-reconstructed DEM, LDEMGAN1.0-reconstructed DEM, and ASP SFS DEM, with respect to the NAC DTM, were calculated, as shown in Figure 7.

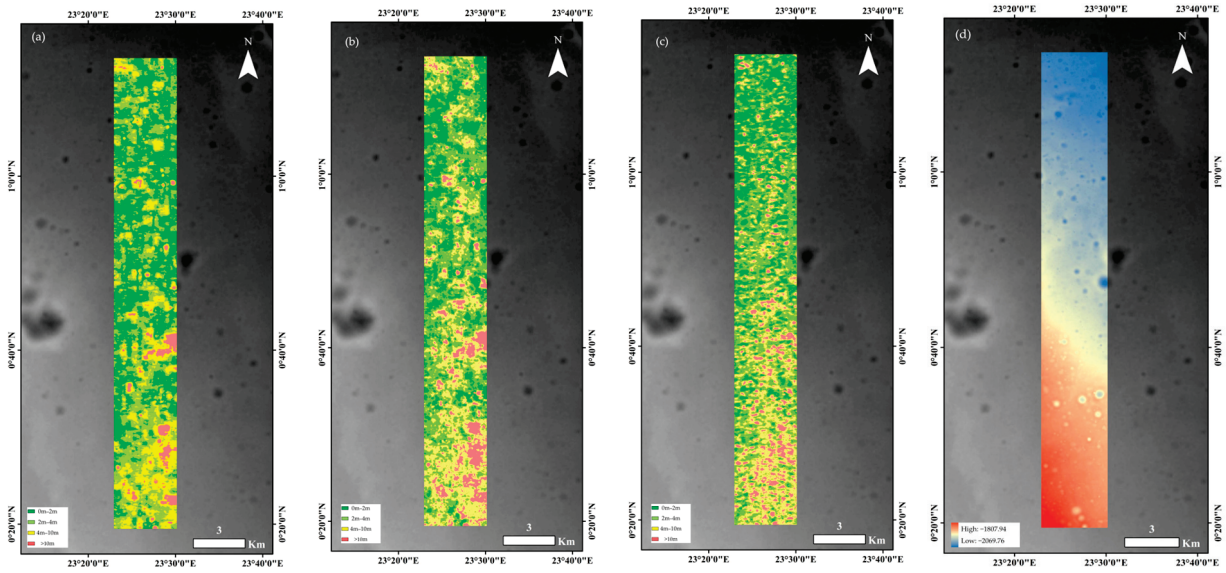


Figure 7. Comparison of absolute difference maps overlaid on the sldem2015: (**a**) absolute difference map between the DEM reconstructed by LDEMGAN2.0 and the NAC DTM; (**b**) absolute difference map between the DEM reconstructed by LDEMGAN1.0 and the NAC DTM; (**c**) absolute difference map between the DEM reconstructed by ASP SFS and the NAC DTM; (**d**) NAC DTM (2 m/pixel).

As shown in Figure 7, the LDEMGAN2.0 network has enhanced its ability to recover terrain details. Approximately 55% of the pixels have an elevation difference of less than 2 m, and about 95% of the pixels have an elevation difference of less than 10 m. The overall accuracy of the DEM has improved. The statistical results of detailed elevation residuals with the ground truth for the reconstruction results of the Apollo 11 experimental area using LDEMGAN 2.0, LDEMGAN 1.0, and ASP SFS are shown in Figure 8. From the figure, it is obvious that our proposed LDEMGAN 2.0 has the lowest errors.

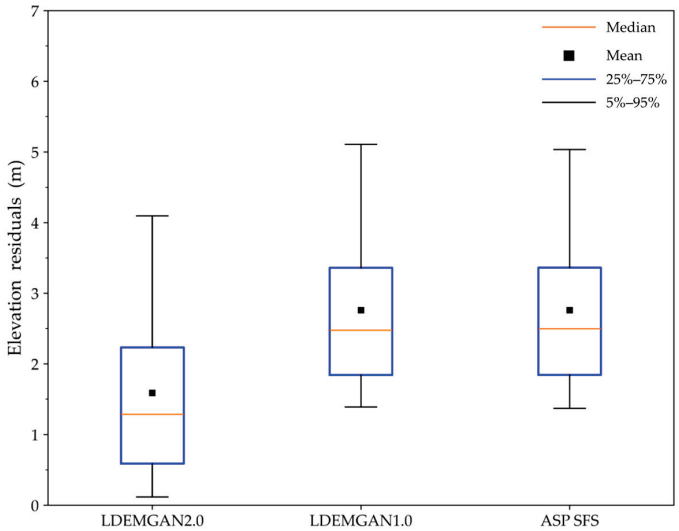


Figure 8. Box-plot of elevation residuals. Statistical results of detailed elevation residuals with the ground truth for the reconstruction results of the Apollo 11 experimental area using LDEMGAN 2.0, LDEMGAN 1.0, and ASP SFS.

Statistics of the overall reconstruction error in the experimental area of the three methods are demonstrated in Table 2. As shown in Table 2, using the LROC NAC DTM (2 m/pixel) as the ground truth, the MAE for the entire experimental area is 1.491 m, the RMSE is 2.015 m, and the SSIM is 0.86, which is 46.0%, 33.4%, 11.6% higher than that of LDEMGAN1.0, and 29.3%, 45.8%, 17.8% higher than that of ASP SFS, respectively.

Table 2. Statistics of the overall reconstruction error in the experimental area.

Method	Reconstruction Error <2 m (%)	Reconstruction Error <4 m (%)	Reconstruction Error <10 m (%)	MAE (m)	RMSE (m)	SSIM	Rebuild Speed (h)
LDEMGAN2.0	56.16	87.25	95.10	1.49	2.01	0.86	~0.05
LDEMGAN1.0	48.32	73.06	91.54	2.76	3.02	0.77	~0.05
ASP SFS	42.17	66.24	88.02	2.11	3.71	0.73	~12.5

In terms of reconstruction speed, LDEMGAN2.0 incorporates self-similarity loss during training without affecting the generator's structure, allowing for its reconstruction speed to remain consistent with that of LDEMGAN1.0. It takes 3 min to reconstruct the 4 km × 27 km DEM of the Apollo 11 experimental area. In contrast, ASP SFS requires multiple iterations over each pixel, of which the computational workload grows exponentially as the resolution increases. Nonetheless, LDEMGAN2.0 is a pre-trained model which does not need optimization case by case, while ASP SFS is akin to neural radiance field (NeRF) and Gaussian Splatting, which require substantial training for each mapping task. Under the same experimental conditions, to ensure that the SFS reconstruction results are comparable to other methods in terms of spatial resolution and detail representation, enabling subsequent quantitative analysis and comparison, we used the key parameters mentioned in Section 3.3.1 in ASP SFS. As a result, the 2 m/pixel DEM of the experimental area was reconstructed, taking approximately 12.5 h in total.

3.3.2. Detailed Analysis of the Reconstruction Results

To further analyze the reconstruction results, this study selected four 1 km × 1 km sub-regions (labeled I–IV in Figure 9) for further examination. For comparison with the ground truth, the image resolution was down-sampled to 2 m/pixel and overlaid on the SLDEM2015, as shown in Figure 9.

Figure 10 shows hillshade maps of the LDEMGAN2.0 DEM, LDEMGAN1.0 DEM, ASP SFS DEM, and NAC DTM for the zoomed-in sub-region I–IV shown in Figure 9. As shown in Figure 10, the elevation information in the LDEMGAN2.0 DEM is finer than that in LDEMGAN1.0, with significant improvements in detail recovery and terrain consistency. The elevation changes in sub-region I are relatively minor, and the DEMs reconstructed by all three methods exhibited higher consistency with the ground truth. For the small impact craters with diameters of approximately 160 m and 55 m located in the lower-right corner of the image in sub-region II and III, as indicated by the red arrows, the DEM reconstructed by ASP SFS exhibits irregular shapes (e.g., deformed impact crater rims). For such small-scale illumination-sensitive terrain, it is prone to edge perturbations caused by noise and to distortions of crater-floor morphology induced by photometric artifacts, thereby resulting in irregular shapes. In contrast, LDEMGAN2.0 calculates SSL by leveraging the self-similarity of terrain in the same area at different DEM data, thereby constraining the training process of the DEM reconstruction network. This effectively suppresses detail loss while preserving local detail features. In sub-region II and IV, the dashed box highlights that LDEMGAN1.0 DEM displays more terrain details, such as spurious structures with diameters of approximately 50 m. However, upon comparison with the original NAC

DOM, it was determined that these fine terrain features are not actual surface features. By integrating structural self-similarity loss during training, LDEMGAN2.0 effectively suppressed these unrealistic reconstructions, improving the model's ability to represent the actual terrain structure and maintain consistency. Compared to LDEMGAN1.0, LDEMGAN2.0 effectively reduces structural distortions and detail loss in some cases, enhances the terrain consistency (i.e., LDEMGAN2.0 DEM shows closer agreement with the NAC DTM in overall terrain morphology, including topographic trends and structural details), better preserves geomorphic features. It even overcomes the stripe artifacts in sub-area IV in the NAC DTM.

Based on the reconstruction results of LDEMGAN2.0, the reconstruction error statistics for the four selected sub-regions (labeled I–IV in Figure 9) are presented in Table 3. In terms of elevation change, sub-region I shows the smallest elevation change at 42.76 m. Sub-regions II and III exhibit relatively large terrain fluctuations, with values of 76.00 m and 69.10 m. Sub-region IV shows the elevation change at 62.01 m. Regarding accuracy, sub-region I achieves RMSE of 2.78 m and SSIM of 0.79. Sub-region II, which exhibits the largest elevation change, achieves RMSE of 2.23 m and SSIM of 0.85, suggesting that the model demonstrates strong robustness and generalization capability in these areas. Sub-region III performs well across various evaluation metrics, with a MAE of 1.25 m, RMSE of 2.06 m, and SSIM of 0.84, indicating that the reconstruction results in this region are highly consistent with the ground truth in terms of both overall structure and local details. In addition, sub-region IV shows RMSE of 2.74 m, a maximum error of 7.75 m, and SSIM of 0.77.

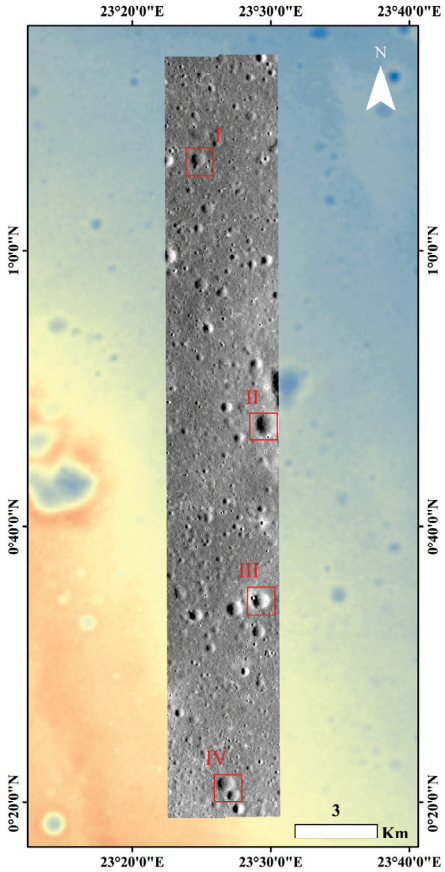


Figure 9. LROC NAC DOM of the experimental area overlaid on SLDEM2015. Four sub-regions are marked in red rectangles and labeled for further analysis.

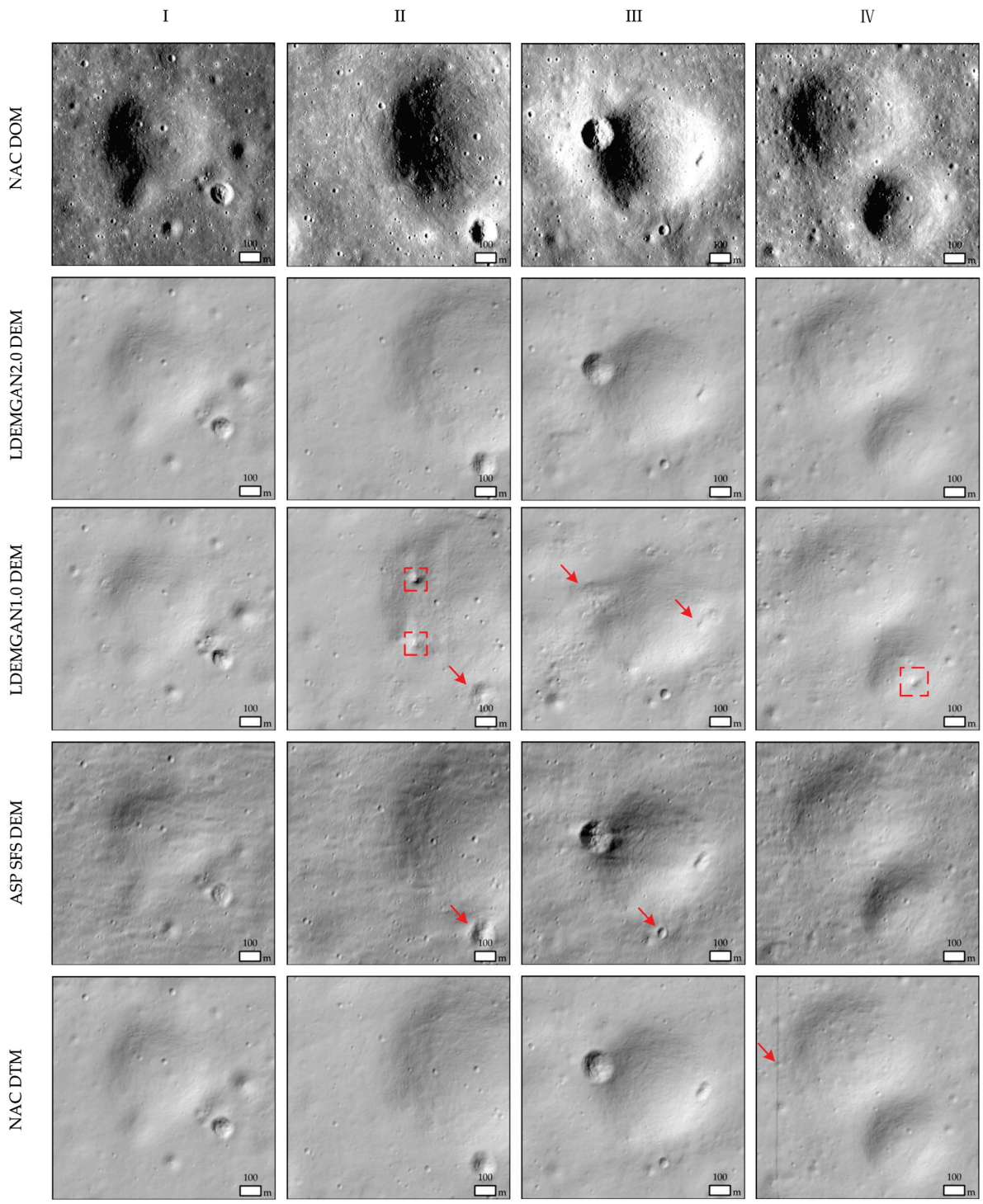
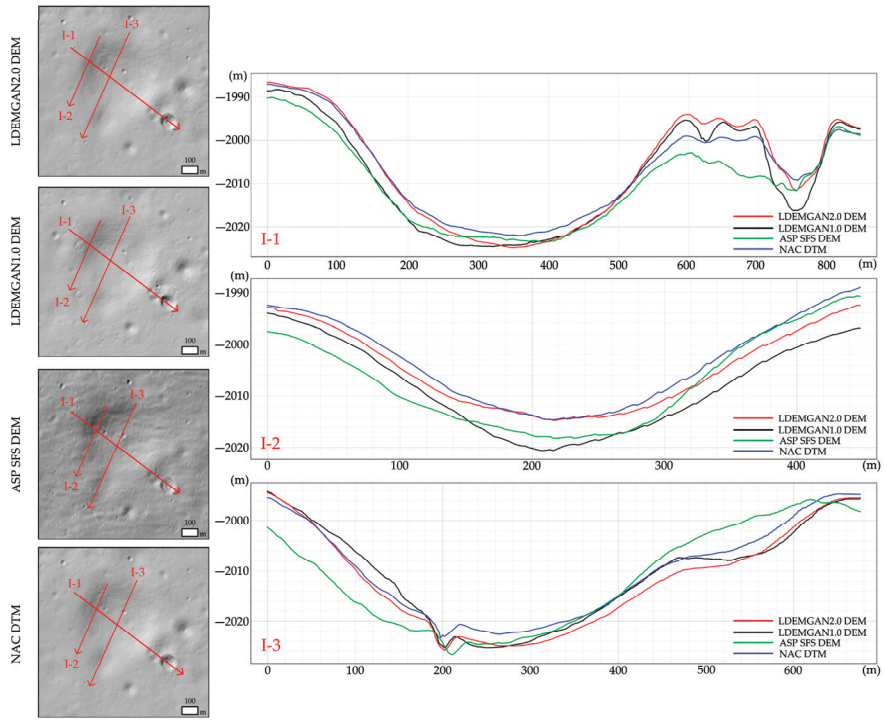


Figure 10. Local terrain reconstruction results of sub-region I–IV. The dashed box highlights local false textures and structural artifacts, while red arrows point to areas with obvious reconstruction errors or seams.

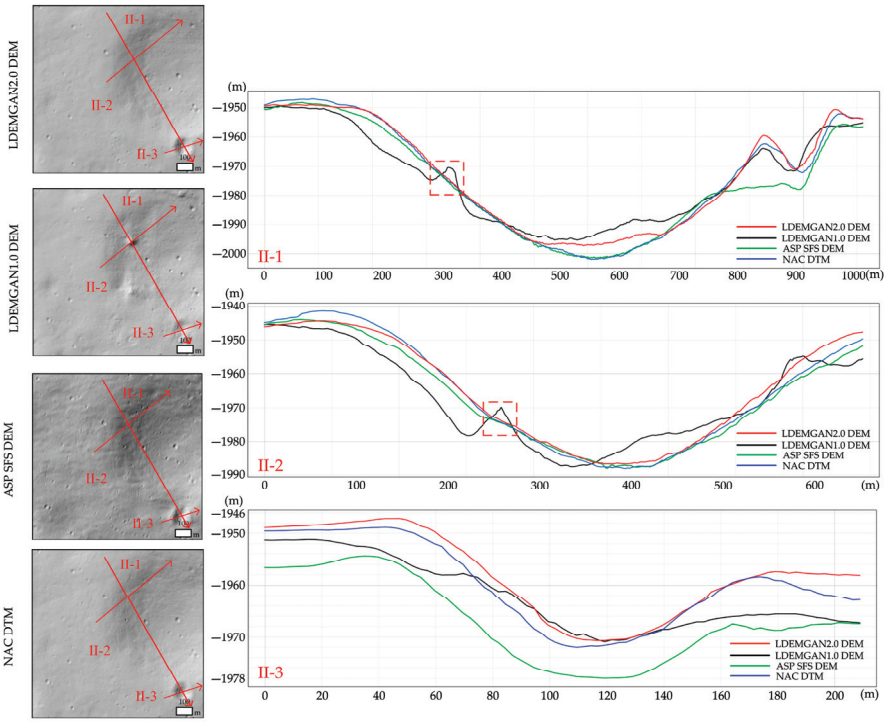
Table 3. Statistics of reconstruction errors for sub-regions shown on Figure 9 based on LDEMGAN2.0.

Sub-Region	Elevation Change (m)	MAE (m)	RMSE (m)	SSIM	Maximum Error (m)
I	42.76	1.92	2.78	0.79	7.01
II	76.00	1.84	2.23	0.85	4.72
III	69.10	1.25	2.06	0.84	5.24
IV	62.01	1.77	2.74	0.77	7.75

In addition, we conducted a detailed profile analysis of the four selected 1 km × 1 km sub-regions (labeled I–IV in Figure 9). For each area, we measured three DEM profiles to show the terrain differences and provide a detailed comparison among the LDEMGAN2.0 DEM, LDEMGAN1.0 DEM, ASP SFS DEM, and NAC DTM, as shown in Figure 11.

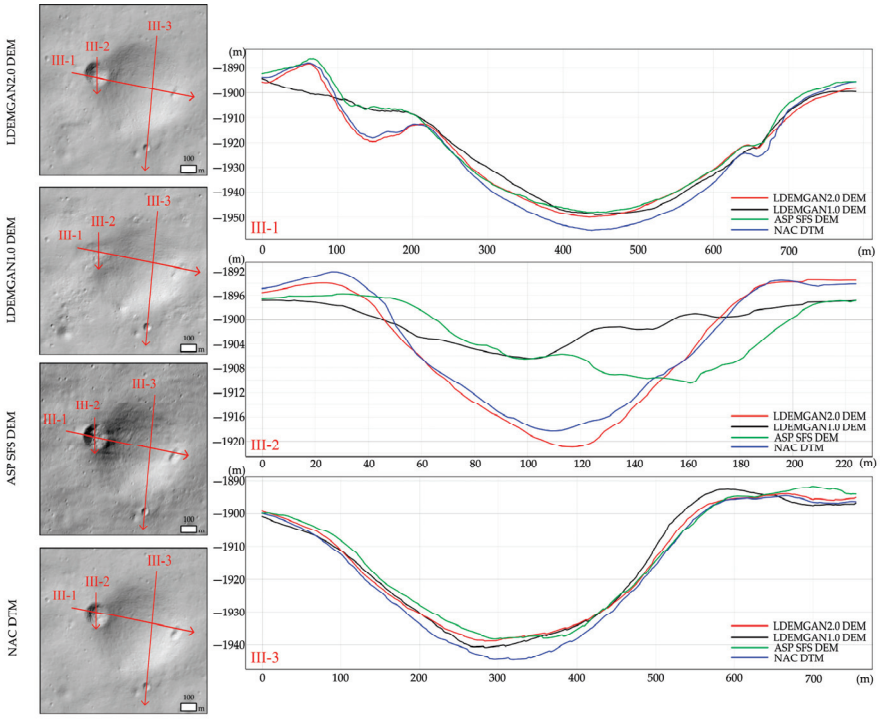


(**a**)

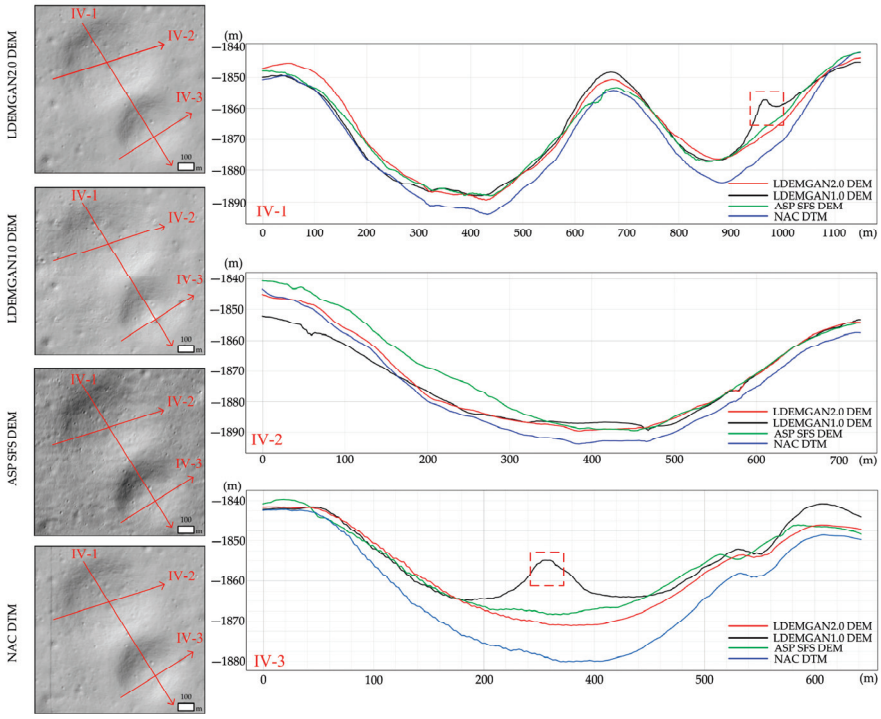


(**b**)

Figure 11. *Cont.*



(**c**)



(**d**)

Figure 11. (**a**) Profiles of the 2 m/pixel LDEMGAN2.0 DEM, LDEMGAN DEM, ASP SFS DEM, and NAC DTM in sub-region I (location shown in Figure 9). (**b**) Profiles of the 2 m/pixel LDEMGAN2.0 DEM, LDEMGAN DEM, ASP SFS DEM, and NAC DTM in sub-region II (location shown in Figure 9). (**c**) Profiles of the 2 m/pixel LDEMGAN2.0 DEM, LDEMGAN DEM, ASP SFS DEM, and NAC DTM in sub-region III (location shown in Figure 9). (**d**) Profiles of the 2 m/pixel LDEMGAN2.0 DEM, LDEMGAN DEM, ASP SFS DEM, and NAC DTM in sub-region IV (location shown in Figure 9).

Figure 11 shows that the DEM reconstructed using LDEMGAN2.0 preserves the terrain undulation characteristics compared to the ground truth. The maximum elevation error between the LDEMGAN2.0 DEM and the ground truth (NAC DTM) are 7.01 m, 4.72 m, 5.24 m, and 7.75 m in sub-regions I, II, III, and IV, respectively. These results indicate that LDEMGAN2.0 maintains a high degree of consistency with the ground truth in terms of overall trends, and shows better detail preservation ability. The elevation profiles in sub-region I of Figure 11a and region IV of Figure 11d further verify the conclusion of Figure 10, which indicates that LDEMGAN2.0 effectively reduces detail loss and spurious structures, enhancing the terrain authenticity of the DEM. This is attributed to the lack of LDEMGAN1.0 consideration for the self-similarity between the reconstructed DEM and the ground truth at the same terrain, resulting in weak constraints on local features in areas with strong texture information. In contrast, most of the fine terrain features reconstructed by LDEMGAN2.0 align with the ground truth, which demonstrates that LDEMGAN2.0 improves stability and consistency in terrain detail recovery compared to LDEMGAN1.0.

In summary, based on the analysis of the reconstruction results of the four sub-regions, the LDEMGAN2.0 network has improved its ability to restore terrain details after incorporating self-similarity loss, particularly in areas with significant changes in crater shape, slope, and elevation gradient. The reconstruction results align more closely with the NAC DTM in both overall trends and local fluctuations, demonstrating an improvement in feature structure and terrain consistency. This makes LDEMGAN2.0 more suitable for high-precision DEM reconstruction tasks.

4. Discussion

This study conducts experiments and analyzes the method of reconstructing high-resolution DEMs based on the self-similarity of different DEM data for the same lunar terrain. According to the findings and challenges encountered in this research, the following points should be further explored and improved in future work:

(1) In our previous work [29], as reported in our experiments, when the solar altitude angle is within approximately 25–70°, the reconstruction accuracy remains stable and the errors are within an acceptable range. When the solar altitude angle is not within this range, factors such as the underexposure or overexposure of the image may lead to additional reconstruction errors. Based on this experience, we suggest employing imagery acquired within the recommended range and excluding imagery acquired under extreme illumination conditions or undergoing image preprocessing before use so as to ensure stable network convergence and maintain reconstruction accuracy.

(2) In the current high-resolution DEM-reconstruction task, a single data source is often limited by factors such as acquisition conditions, observation angles, and spatial resolution, making it difficult to fully capture the complexity of terrain structures. Thus, optimizing multi-source data-fusion strategies is a crucial direction for improving system accuracy and robustness. Moreover, attention should be paid to the spatial registration and error-propagation mechanisms between data sources to ensure geometric consistency and elevation accuracy during fusion process. This will provide a solid foundation for high-quality DEM reconstruction.

(3) The approach proposed in this study can be applied to other places of the Moon (e.g., south pole) [37,38] and also to the surfaces of other planets through transfer learning with a relatively small amount of additional data. For the Moon's south pole, as the illumination conditions are much worse compared to those in the data used in this study, preprocessing methods such as image enhancement should be considered. Moreover, images captured from different times and sources (e.g., ShadowCam onboard the Korea Pathfinder Lunar Orbiter) should be employed. For other planetary applications—take

Mars, for example—as there are some geomorphologies that do not exist on the Moon (e.g., aeolian features), data containing them should be added.

5. Conclusions

This paper proposes a DEM construction network LDEMGAN2.0, the improved version of version LDEMGAN1.0, by utilizing the self-similarity of different DEM data in the same lunar terrain. During the training process, the model incorporates the SSL constraint into the network generator loss to guide DEM reconstruction so as to solve issues such as detail loss and spurious structures in complex terrain structures in the previous network. To evaluate the performance of LDEMGAN2.0, we conducted experiments in the Apollo 11 landing area. The reconstructed DEM was compared with LDEMGAN1.0, ASP SFS DEM, and NAC DTM using both qualitative analysis and quantitative metrics, including MAE, RMSE, and SSIM.

The experimental results show that, compared to LDEMGAN1.0, ASP SFS, and NAC DTM, the DEM reconstructed by LDEMGAN2.0 achieves the best metrics: MAE for the entire experimental area is 1.49 m, RMSE is 2.01 m, and SSIM is 0.86, which is 46.0%, 33.4%, 11.6% higher than that of LDEMGAN1.0, and 29.3%, 45.8%, 17.8% higher than that of ASP SFS, respectively. These results validate the feasibility and effectiveness of the improved reconstruction network. Moreover, it is shown that adding SSL to the DEM reconstruction network during training significantly enhances the network's ability to recover local details. The mechanism enables the network to learn the similarity between SSGs in the local scale, thereby further strengthening the constraints on detail and structural consistency in DEM reconstruction and helping to reduce the generation of detail loss and the appearance of spurious structures during the reconstruction process.

This method is valuable for scientific and engineering applications such as terrain feature analysis, landing site selection, navigation and localization, path planning, and decision support.

Author Contributions: Conceptualization, Y.W. and T.C.; methodology, T.C. and Y.W.; software, T.C. and Y.W.; validation, Y.W., W.-C.L., B.L. and K.D.; formal analysis, Y.W. and K.D.; investigation, K.D., Y.W. and S.C.; resources, C.Z., B.W. and B.X.; data curation, T.C. and Y.W.; writing—original draft preparation, T.C.; writing—review and editing, Y.W., J.N., W.-C.L. and K.D.; visualization, T.C. and Y.W.; supervision, K.D., Y.W. and S.C.; project administration, T.C. and Y.W.; funding acquisition, K.D. and Y.W. All authors have read and agreed to the published version of the manuscript.

Funding: This research was funded by the National Key Research and Development Program of China (Grant No. 2022YFF0503100), International Partnership Program of Chinese Academy of Sciences (for Grand Challenges, No. 313GJHZ2024034GC), and Science and Disruptive Technology Program, AIRCAS (Grant No. 2024-AIRCAS-SDTP-13).

Data Availability Statement: The data used to support the findings of this study are available from the corresponding author upon reasonable request.

Acknowledgments: The authors thank all those who worked on the NASA Planetary Data System archive to make the LROC imagery and SLDEM2015 available.

Conflicts of Interest: The authors declare no conflicts of interest.

Abbreviations

The following abbreviations are used in this manuscript:

ASP	Ames Stereo Pipeline
CNN	Convolutional neural network
DEM	Digital elevation model

DTM	Digital terrain model
DOM	Digital orthophoto map
GAN	Generative adversarial network
KL	Kullback–Leibler
LE	Left-experimental data record
LOLA	Lunar Orbiter Laser Altimeter
LROC	Lunar Reconnaissance Orbiter camera
MAE	Mean absolute error
NAC	Narrow angle camera
NeRF	Neural radiance field
RE	Right-experimental data record
RMSE	Root mean squared error
SFS	Shape from shading
SAFS	Shape and albedo from shading
SSL	Self-similarity loss
SSG	Self-similarity graph
SLDEM2015	LRO LOLA Digital Elevation Model Co-registered with Selene Data 2015
SSIM	Structural similarity index measure

References

1. Liu, J.J.; Zeng, X.G.; Li, C.L.; Ren, X.; Yan, W.; Tan, X.; Zhang, X.X.; Chen, W.L.; Zuo, W.; Liu, Y.X.; et al. Landing Site Selection and Overview of China's Lunar Landing Missions. *Space Sci. Rev.* **2021**, *217*, 6–30. [CrossRef]
2. Di, K.C.; Liu, B.; Liu, Z.Q.; Zou, Y.L. Review and prospect of lunar mapping using remote sensing data. *J. Remote Sens.* **2016**, *20*, 1230–1242.
3. Formisano, M.; De Sanctis, M.C.; Boazman, S.; Frigeri, A.; Heather, D.; Magni, G.; Teodori, M.; De Angelis, S.; Ferrari, M. Thermal modeling of the lunar South Pole: Application to the PROSPECT landing site. *Planet. Space Sci.* **2024**, *251*, 105969. [CrossRef]
4. Fassett, C.I.; Head, J.W.; Kadish, S.J.; Mazarico, E.; Neumann, G.A.; Smith, D.E.; Zuber, M.T. Lunar impact basins: Stratigraphy, sequence and ages from superposed impact crater populations measured from Lunar Orbiter Laser Altimeter (LOLA) data. *J. Geophys. Res. Planets* **2012**, *117*, E00H06. [CrossRef]
5. Wu, B.; Li, F.; Ye, L.; Qiao, S.; Huang, J.; Wu, X.Y.; Zhang, H. Topographic mapping and analysis at the landing site of Chang'E-3 on the moon. *Earth Planet. Sci. Lett.* **2014**, *405*, 257–273. [CrossRef]
6. Wu, B.; Li, F.; Hu, H.; Zhao, Y.; Wang, Y.R.; Xiao, P.P.; Li, Y.; Liu, W.C.; Chen, L.; Ge, X.M.; et al. Topographic and geomorphological mapping and analysis of the Chang'E-4 landing site on the far side of the Moon. *Photogramm. Eng. Remote Sens.* **2020**, *86*, 247–258. [CrossRef]
7. Di, K.C.; Liu, Z.Q.; Wan, W.H.; Peng, M.; Liu, B.; Wang, Y.X.; Gou, S.; Yue, Z.Y. Geospatial technologies for Chang'e-3 and Chang'e-4 lunar rover missions. *Geo-Spat. Inf. Sci.* **2020**, *23*, 87–97. [CrossRef]
8. Wu, B.; Guo, J.; Zhang, Y.; King, B.A.; Li, Z.; Chen, Y. Integration of Chang'E-1 Imagery and Laser Altimeter Data for Precision Lunar Topographic Modeling. *IEEE Trans. Geosci. Remote Sens.* **2011**, *49*, 4889–4903.
9. Liu, C.B.; Bo, Z.; Zhang, P.; Zhou, M.Y.; Liu, W.Y.; Huang, R.; Niu, R.; Ye, Z.; Yang, H.Z.; Liu, S.J.; et al. Current status and future prospects of lunar topographic remote sensing and mapping. *J. Geo-Inf. Sci.* **2025**, *27*, 801–819.
10. Shan, J.; Tian, X.; Li, S.; Li, R.F. Advances of spaceborne laser altimetry technology. *Acta Geod. Cartogr. Sin.* **2022**, *51*, 964–982.
11. Wu, B.; Hu, H.; Guo, J. Integration of Chang'E-2 imagery and LRO laser altimeter data with a combined block adjustment for precision lunar topographic modeling. *Earth Planet. Sci. Lett.* **2014**, *391*, 1–15. [CrossRef]
12. Smith, D.E.; Zuber, M.T.; Neumann, G.A.; Lemoine, F.G.; Mazarico, E.; Torrence, M.H.; McGarry, J.F.; Rowlands, D.D.; Head, J.W., III; Duxbury, T.H.; et al. Initial observations from the lunar orbiter laser altimeter (LOLA). *Geophys. Res. Lett.* **2010**, *37*, L18204. [CrossRef]
13. Wu, B.; Liu, W.C.; Grumpe, A.; Wöhler, C. Shape and Albedo from Shading (SAFS) for pixel-level DEM generation from monocular images constrained by low-resolution DEM. *Int. Arch. Photogramm. Remote Sens. Spat. Inf. Sci.* **2016**, *41*, 521–527. [CrossRef]
14. Liu, W.C.; Wu, B.; Wöhler, C. Effects of illumination differences on photometric stereo shape-and-albedo-from-shading for precision lunar surface reconstruction. *ISPRS J. Photogramm. Remote Sens.* **2018**, *136*, 58–72.
15. Horn, B.K.P. Shape from Shading: A Method for Obtaining the Shape of a Smooth Opaque Object from One View. Ph.D. Thesis, Massachusetts Institute of Technology, Cambridge, MA, USA, 1970.

16. Ju, Y.K.; Zhou, J.C.; Zhou, S.T.; Xie, H.; Zhang, C.; Xiao, J.; Yang, C.X.; Sun, J. Three-dimentional reconstruction of underwater side-scan sonar images based on shape-from-shading and monocular depth fusion. *Intell. Mar. Technol. Syst.* **2024**, *2*, 4. [CrossRef]
17. Santo, H.; Samejima, M.; Matsushita, Y. Numerical shape-from-shading revisited. *IPSJ Trans. Comput. Vis. Appl.* **2018**, *10*, 8. [CrossRef]
18. Grumpe, A.; Belkhir, F.; Wöhler, C. Construction of lunar DEMs based on reflectance modelling. *Adv. Space Res.* **2014**, *53*, 1735–1767. [CrossRef]
19. Buyukdemircioglu, M.; Kocaman, S.; Kada, M. Deep Learning for 3D Building Reconstruction: A Review. In Proceedings of the 24th ISPRS Congress on Imaging Today, Foreseeing Tomorrow, Nice, France, 6–11 June 2022.
20. Masoumian, A.; Rashwan, H.A.; Cristiano, J.; Asif, M.S.; Puig, D. Monocular Depth Estimation Using Deep Learning: A Review. *Sensors* **2022**, *22*, 5353. [CrossRef] [PubMed]
21. Cao, J.R.; Huang, R.; Ye, Z.; Xu, Y.S.; Tong, X.H. Generative 3D Reconstruction of Martian Surfaces using Monocular Images. *Int. Arch. Photogramm. Remote Sens. Spat. Inf. Sci.* **2024**, *48*, 51–56. [CrossRef]
22. Ge, L. Research on 3D Reconstruction Methods Based on Deep Learning. *Trans. Comput. Sci. Intell. Syst. Res.* **2024**, *5*, 678–684. [CrossRef]
23. Eigen, D.; Puhrsch, C.; Fergus, R. Depth Map Prediction from a Single Image using a Multi-Scale Deep Network. In Proceedings of the 27th International Conference on Neural Information Processing Systems (NIPS 2014), Montreal, QC, Canada, 8–13 December 2014.
24. Chen, Z.; Wu, B.; Liu, W.C. Mars3DNet: CNN-Based High-Resolution 3D Reconstruction of the Martian Surface from Single Images. *Remote Sens.* **2021**, *13*, 839. [CrossRef]
25. Chen, H.; Hu, X.Y.; Gläser, P.; Xiao, H.F.; Ye, Z.; Zhang, H.Y. CNN-Based Large Area Pixel-Resolution Topography Retrieval From Single-View LROC NAC Images Constrained With SLDEM. *IEEE J. Sel. Top. Appl. Earth Obs. Remote Sens.* **2022**, *15*, 9398–9416. [CrossRef]
26. Tao, Y.; Xiong, S.T.; Conway, S.J.; Muller, J.P.; Guimpier, A.; Fawdon, P.; Thomas, N.; Cremonese, G. Rapid Single Image-Based DTM Estimation from ExoMars TGO CaSSIS Images Using Generative Adversarial U-Nets. *Remote Sens.* **2021**, *13*, 2877. [CrossRef]
27. Tao, Y.; Muller, J.; Xiong, S.; Conway, S. MADNet 2.0: Pixel-Scale Topography Retrieval from Single-View Orbital Imagery of Mars Using Deep Learning. *Remote Sens.* **2021**, *13*, 4220. [CrossRef]
28. Grassa, R.L.; Gallo, I.; Re, C.; Cremonese, G.; Landro, N.; Pernechele, C.; Simioni, E.; Gatti, M. An Adversarial Generative Network Designed for High-Resolution Monocular Depth Estimation from 2D HiRISE Images of Mars. *Remote Sens.* **2022**, *14*, 4619. [CrossRef]
29. Liu, Y.; Wang, Y.X.; Di, K.C.; Peng, M.; Wan, W.H.; Liu, Z.Q. A Generative Adversarial Network for Pixel-Scale Lunar DEM Generation from High-Resolution Monocular Imagery and Low-Resolution DEM. *Remote Sens.* **2022**, *14*, 5420. [CrossRef]
30. Alexandrov, O.; Beyer, R.A. Multiview Shape-From-Shading for Planetary Images. *Earth Space Sci.* **2018**, *5*, 652–666. [CrossRef]
31. Bodensteiner, C.; Huebner, W.; Juengling, K.; Mueller, J.; Arens, M. Local multi-modal image matching based on self-similarity. In Proceedings of the IEEE International Conference on Image Processing, Hong Kong, China, 26–29 September 2010.
32. Chang, K.; Ding, P.; Li, B.X. Single image super-resolution using collaborative representation and non-local self-similarity. *Signal Process.* **2018**, *149*, 49–61. [CrossRef]
33. Chen, D.; Zhang, Z.Q.; Liang, J.; Zhang, L. SSL: A Self-similarity Loss for Improving Generative Image Super-resolution. In Proceedings of the 32nd ACM International Conference on Multimedia (MM '24), New York, NY, USA, 28 October–1 November 2024.
34. Iqbal, W.; Hiesinger, H.; van der Bogert, C. Geological mapping and chronology of lunar landing sites: Apollo 11. *Icarus* **2019**, *333*, 528–547. [CrossRef]
35. Wang, Z.; Bovik, A.C.; Sheikh, H.R.; Simoncelli, E.P. Image quality assessment: From error visibility to structural similarity. *IEEE Trans. Image Process.* **2004**, *13*, 600–612. [CrossRef] [PubMed]
36. McEwen, A.S. Photometric functions for photoclinometry and other applications. *Icarus* **1991**, *92*, 298–311. [CrossRef]
37. Kereszturi, A. Polar Ice on the Moon. In *Encyclopedia of Lunar Science*; Cudnik, B., Ed.; Springer: Cham, Switzerland, 2023; pp. 971–980.
38. Long, X.X.; Wang, C.; Sanlang, S.J.; Feng, Y.J.; Xu, X.; Xie, H.; Tong, X.H. Retrieving water ice abundance in representative regions of the Moon's South Pole using topography corrected SELENE MI images. *Geosci. Lett.* **2025**, *12*, 33. [CrossRef]

Disclaimer/Publisher's Note: The statements, opinions and data contained in all publications are solely those of the individual author(s) and contributor(s) and not of MDPI and/or the editor(s). MDPI and/or the editor(s) disclaim responsibility for any injury to people or property resulting from any ideas, methods, instructions or products referred to in the content.

MDPI AG
Grosspeteranlage 5
4052 Basel
Switzerland
Tel.: +41 61 683 77 34

Remote Sensing Editorial Office
E-mail: remotesensing@mdpi.com
www.mdpi.com/journal/remotesensing



Disclaimer/Publisher's Note: The title and front matter of this reprint are at the discretion of the Guest Editors. The publisher is not responsible for their content or any associated concerns. The statements, opinions and data contained in all individual articles are solely those of the individual Editors and contributors and not of MDPI. MDPI disclaims responsibility for any injury to people or property resulting from any ideas, methods, instructions or products referred to in the content.





Academic Open
Access Publishing

mdpi.com

ISBN 978-3-7258-7854-3